Transactions of the ASME®

Journal of Fluids Engineering

Published Quarterly by The American Society of Mechanical Engineers

VOLUME 123 • NUMBER 3 • SEPTEMBER 2001

(Contents continued on inside back cover)

Transactions of the ASME, Journal of Fluids Engineering (ISSN 0098-2202) is published quarterly (Mar., June, Sept., Dec.) by The American Society of Mechanical Engineers, Three Park Avenue, New York, NY 10016. Periodicals postage paid at New York, NY and additional mailing offices.
POSTMASTER: Send address changes to Transactions of the ASME, Journal of Fluids Engineering, c/o THE AMERICAN SOCIETY OF MECHANICAL ENGINEERS, 22 Law Drive, Box 2300, Fairfield, NJ 07007-2300.
CHANGES OF ADDRESS must be received at Society headquarters seven weeks before they are to be effective. Please send old label and new address.
STATEMENT from By-Laws. The Society shall not be responsible for statements or opinions advanced in papers or ... printed in its publications (B7.1, Par. 3).

INDEXED by Applied Mechanics Reviews and Engineering Information, Inc. Canadian Goods & Services Tax Registration #126148048.

This journal is printed on acid-free paper, which exceeds the ANSI Z39.48-1992 specification for permanence of paper and library materials. ♾™
♻ 85% recycled content, including 10% post-consumer fibers.

(Contents continued)

TECHNICAL BRIEFS

ERRATA

ANNOUNCEMENTS

(Contents continued on facing page)

Journal of Fluids Engineering Volume 123, Number 3 SEPTEMBER 2001

Journal of Fluids Engineering

Editorial

This volume contains eight papers on turbomachinery covering CFD applications, detailed flow measurements on unsteady flow, new design methods and control devices, and conventional empirical approaches. Shi and Tsukamoto succeeded in predicting pressure fluctuations caused by the interaction between a centrifugal impeller and diffuser vanes, using a Navier-Stokes code with standard $k-\varepsilon$ turbulence model. Using a commercial code, Gu et al. succeeded in predicting the performance of a single-stage centrifugal compressor and studied the volute/diffuser flow in detail at design and off design conditions. By combining a scheme called the Single-Sweep Method with an algebraic eddy viscosity model, Kochevsky made a parametric study of the energy loss in annular diffusers with a rotating hub and inlet flow swirl, with the purpose of minimizing the loss in annular diffusers. These papers suggest that CFD is now becoming capable of predicting not only steady flows under design flow conditions, but also unsteady flows and off-design flows. Sinha, Pinarbasi and Katz, using PIV and pressure fluctuation measurements, made detailed observations of unsteady flow process during the onset and developed stages of rotating stall within a vaned diffuser of a centrifugal pump. This work is useful for refining CFDs so that they can predict local flow process, as well as for obtaining a physical understanding of the stalling process. The combination of those efforts in CFD and detailed flow measurements will lead CFDs to more useful design tools that require less experience and fewer empirical factors, and also to methods for clarifying the flow physics in turbomachinery.

New production technologies can expand the applications of turbomachinery. Liu, Nishi and Yoshida have shown that a high efficiency mini turbopump is possible by employing a larger outlet blade angle and a larger number of blades with a smaller outlet/inlet area ratio, combined with high precision manufacturing technology. Two papers propose new control methods. Saha et al. propose the application of radial grooves on the casing walls between impeller exit and vaned diffuser throat, to control vaned diffuser rotating stall in radial centrifugal impellers. In many cases the suppression was realized at the cost of head decrease, but it was shown that shallow grooves can decrease the rotating stall onset flow rate with acceptable head decrease. A pitch-flap coupling mechanism to control the output power of a horizontal axis wind turbine was studied by Shimizu and Kamada to determine the optimum pitch angle to flap angle ratio and also the flow physics of control.

Despite the developments of CFD as mentioned before, we still need to depend largely on empirical relations in various aspects of turbomachinery design. Lazzarotto et al. studied the influence of Reynolds number on the performance of cross flow fans with various casing geometry. Engin and Gur studied the effects of solid particles on the performance of open type centrifugal pump impellers with various tip clearance. Such empirical studies will remain a requirement for the practical design of various types of turbomachinery.

Yoshinobu Tsujimoto
Associate Editor

Numerical Study of Pressure Fluctuations Caused by Impeller-Diffuser Interaction in a Diffuser Pump Stage

F. Shi
Research Lecturer,
Satellite Venture Business Lab.

H. Tsukamoto
Professor,
Department of Biological Functions and Engineering,
Graduate School of Life Science and Systems Engineering
Kyushu Institute of Technology
Kitakyushu-shi, 804-8550, Japan

Two-dimensional and three-dimensional, unsteady state Reynolds-averaged Navier-Stokes (RANS) equations with standard k-ε turbulence models were solved within an entire stage of a diffuser pump to investigate pressure fluctuations due to the interaction between impeller and diffuser vanes. A complete solution of transient flows due to the interaction between components in the whole pump without approximating the blade count ratio of impeller to diffuser was obtained by employing an Arbitrary Sliding Mesh. The unsteady numerical results were compared with experimental data and values calculated by the singularity method. As a result of the present study, the Navier-Stokes code with the k-ε model is found to be capable of predicting pressure fluctuations in the diffuser. Furthermore, extensive numerical studies identified sources contributing to the pressure fluctuations in the diffuser, and helped to understand the mechanism of impeller-diffuser interactions in the diffuser pump. [DOI: 10.1115/1.1385835]

Introduction

In a diffuser pump, the centrifugal impeller interferes with its successive diffuser vanes and produces pressure fluctuations downstream of the impeller. In the case of a small radial gap between the impeller and diffuser vanes, the magnitude of these pressure fluctuations may become as large as the total pressure rise across the pump (Arndt et al., [1,2]; and Tsukamoto et al. [3]). These fluctuations not only generate noise and vibration that cause unacceptable levels of stress and reduce component life due to fatigue, but also introduce unfavorable characteristics of pump performance even at or near the design point. Therefore, there is a need to understand the sources of unsteadiness (i.e., potential and wake interactions) to control the pressure fluctuations and to improve the overall pump performance and reliability.

Dring et al. [4] indicated two distinct mechanisms of rotor-stator interaction: (i) wake interactions and (ii) potential interactions. Potential interactions are presently fully understood as potential flow effects induced by inviscid interaction due to the relative motion between rotor blades and stator vanes. Wake interaction is far more complicated than potential interaction. It originates from the impingement and convection of wakes shed from the impeller passages and moving through the successive diffuser passages. Rotor-stator interactions have been studied extensively in axial-type gas turbomachines (Gallus et al., [5]; Fleeter et al., [6]; Rai, [7]; Giles et al., [8]; Lewis et al., [9]; Rao et al., [10]; Sharma et al., [11]; Ho et al., [12]; Valkov et al., [13]; Arnone et al., [14]; Chung et al., [15]). However, only a few studies have focused on impeller-diffuser interaction in hydraulic machines, especially in centrifugal pumps. Some experimental contributions to wake interactions in pumps may be attributed to the extensive PIV measurements by Dong et al. [16], and Akin et al. [17], and hot wire measurement by Ubaldi et al. [18]. However, it is difficult to understand the flow phenomena due to impeller-diffuser interaction from only experimental studies because of the complicated flow structures in centrifugal pumps. A 2-D unsteady flow calculation was presented by Fortes-Patella et al. [19], who studied the interaction between the impeller and volute in a volute pump. They used ''over-lapping'' mesh and ''phase-lagged'' periodic boundary conditions. Bert et al. [20] carried out an unsteady flow calculation in a centrifugal pump using a finite element method. Schulz et al. [21] did calculations of steady/unsteady 3D viscous flow in hydrodynamic torque converters. Qin and Tsukamoto [22] calculated an unsteady flow caused by impeller-diffuser interaction in a diffuser pump with singularity method. Ruprecht et al. [23] performed a numerical modeling of unsteady flow in a francis turbine. All these works contributed to the understanding of impeller-diffuser interaction in pumps, however, we have not reached the stage in which the unsteady flow due to the impeller-diffuser interaction can be predicted with sufficient accuracy.

Following the recent theoretical works by Qin and Tsukamoto [22], the present study uses RANS code to calculate the pressure fluctuations downstream of the diffuser pump impeller. Full Navier-Stokes equations with k-ε turbulence model were solved within a diffuser pump stage and the results were compared with experimental data to validate the CFD calculations. The results were also compared with values predicted by the singularity method to differentiate the potential interaction contribution from unsteady pressures. These comparisons lead to identify the contributions to pressure fluctuation resulting from various sources (potential and wake-diffuser interactions), and will enhance our understanding of the mechanism of impeller-diffuser interaction in diffuser pumps.

Description of the Model and Computational Method

Pump Model and Experimental Data. The test pump was a single-stage diffuser pump with five impeller blades, eight diffuser vanes, and volute casing as shown in Fig. 1(a). A detailed description of the pump is given by Tsukamoto et al. [3]. Measured unsteady pressure in the vaned diffuser passage was compared with values calculated by the singularity method (Qin and Tsukamoto, [22]). Specifications of the essential components are summarized in Table 1.

A comprehensive survey of instantaneous pressure within the diffuser passages was made by Tsukamoto et al. [3]. The unsteady pressures were measured by semi-conductor-type pressure transducers, which were installed directly on the pressure taps to pre-

Contributed by the Fluids Engineering Division for publication in the JOURNAL OF FLUIDS ENGINEERING. Manuscript received by the Bioengineering Division October 21, 1998; revised manuscript received April 12, 2001. Associate Editor: B. Schiavello.

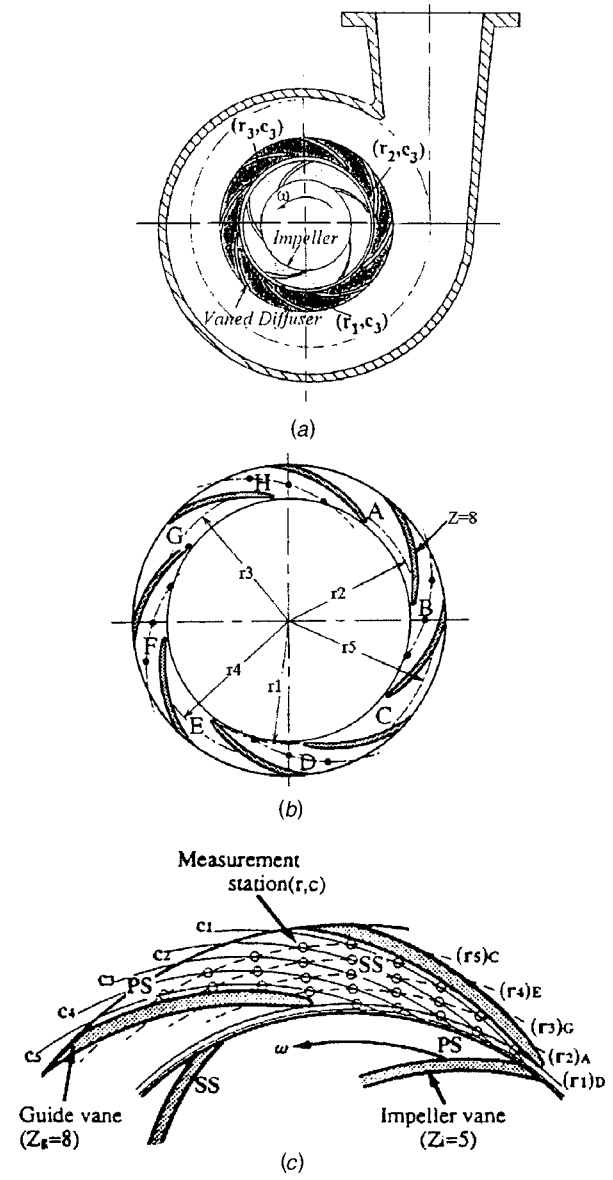

Fig. 1 Schematics of test diffuser pump. (a) Test diffuser pump; (b) pressure measurement stations for test vaned diffuser; (c) shifted static pressure tap position in blade-to-blade passage

vent the decrease of natural frequency in the pressure measurement systems. Figures 1(b) and 1(c) illustrate the unsteady pressure measurement stations on the shroud casing side of the diffuser in the test pump. Because of the limited space in the measuring sections the pressure taps for tangential traverse were located only at one radial location in each passage of the diffuser. The subscript of the radial traverse position represents the passage ID (e.g. $(r_5)_c$ means that the static pressure tap is on the r_5 line in the passage C). The blade-to-blade distributions of unsteady pressure were identified by a phase shift of the measured data. The coordinates of the static pressure taps were formed by the cross of five radial grid lines and five stream-wise grid lines in a blade-to-blade passage as shown in Fig. 1(c).

Mathematical Method, CFD Code. In this study, unsteady incompressible Reynolds-averaged Navier-Stokes equations were employed to execute the time-accurate calculations associated with true transient impeller-diffuser interaction in a diffuser pump. The present CFD code is a commercial software package STAR-CD [24]. One application of this code to turbomachinery flows can be found from Schachenmann et al. [25]. The pressure-based, fully conservative, finite volume method is used in the code. The turbulent viscosity was calculated using the standard k-ε model. An implicit first-order scheme was used for the time-dependent term. To avoid excessive numerical dissipation, a third-order accurate interpolation scheme (QUICK) was used for the discretization of the convection terms and central difference scheme was used for diffusion terms. The discrete governing equations were solved with the PISO (Pressure Implicit Split Operation) algorithm.

Computational Domain and Grid Topology. The number of blade passages is usually limited in computational domains to reduce the computer memory and running time for unsteady rotor-stator interaction analysis. Obviously, this sort of treatment incurs difficulties not only in modifying the blade configurations for the match of the count ratio of rotor to stator, but also in specifying the boundary condition for single component calculations. Since there is no common factor available between the present impeller blades and diffuser vanes, numerical calculations were made for the whole stage of pump from impeller inlet to volute casing outlet. At the first step of study, the pump model was simplified down to 2-D flow to reduce the computational cost and memory requirements and to make the calculation possible on an EWS (Engineering Work Station). Then 3-D pump model was performed using the same CFD code to determine the differences between 2D and 3D calculations.

As shown in Fig. 2, the Hexahedron mesh was generated by ICEM-CFD and the multi-block computational domain was comprised of three sub-domains: impeller, diffuser and volute casing. The grids were arranged carefully within the small gap (4 mm) between impeller and diffuser. The total number of cells was 41,800 for the 2-D pump model and 338,460 for the 3-D pump model with higher density of cells in the diffuser region where more detailed flow structure was desired. The finer grids of 61,480 cells were used to check the grid-independence of numerical results in the 2-D flow model. Grid-independent results for 3-D calculations were not pursued due to limitations of our computer resources. A special technique called Arbitrary Sliding Mesh was used in the present transient solution to accommodate the relative motion between the impeller and stationary parts of diffuser vanes

Table 1 Specifications of test pump

Impeller	Diffuser	Volute casing
Number of blades $Z_i=5$	Number of vanes $Z_d=8$	Volute width $b_v=76.9$ mm
Inlet diameter $D_1=132$ mm	Inlet diameter $D_3=258$ mm	Base circle diameter=478.8 mm
Outlet diameter $D_2=250$ mm	Outlet diameter $D_4=325$ mm	
Outlet width $b_2=41.6$ mm	Inlet and outlet width $b_3=b_4=45.8$ mm	
Blade inlet angle $\beta_1=20.4$ deg	Blade inlet angle $\beta_3=16.97$ deg	
Blade outlet angle $\beta_2=22.5$ deg	Blade outlet angle $\beta_4=15.44$ deg	
Design point:	Flow rate $Q_0=6.21$ m^3/min. ($\varphi_0=Q_0/\pi D_2 b_2 U_2=0.117$)	
	Total head rise $H=29.2$ m ($\psi_0=gH/U_2^2=0.393$)	
	Rotational speed $N=2066$ rpm	

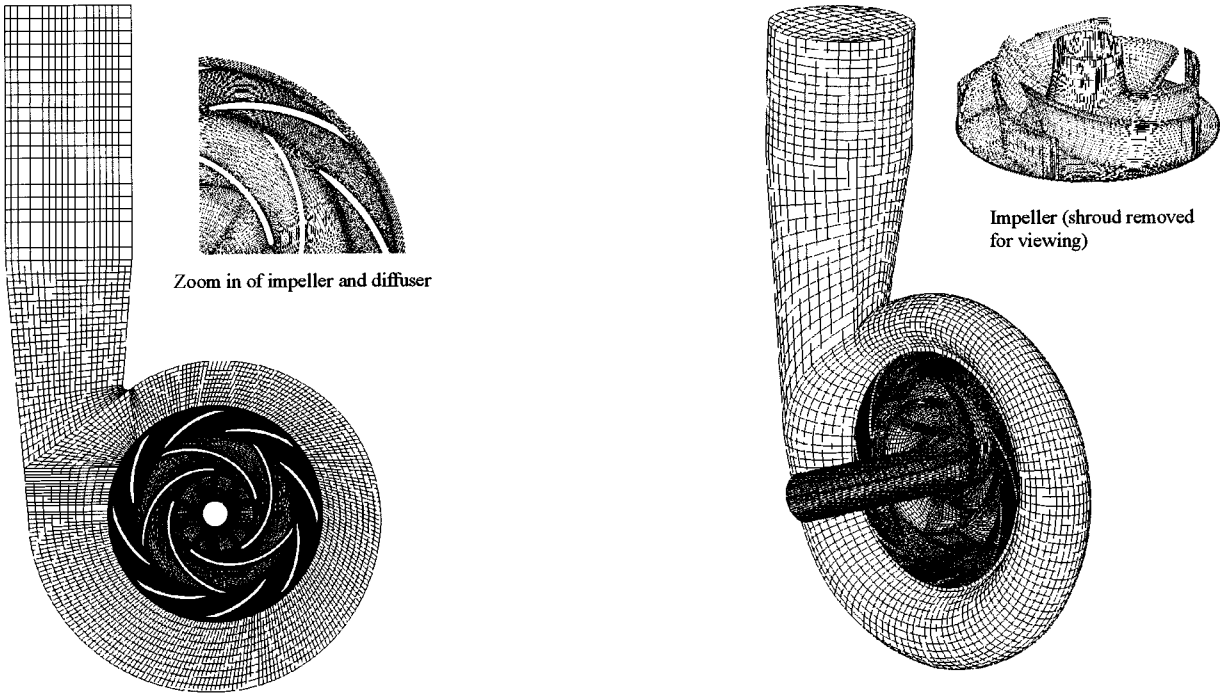

Fig. 2 Computational grid. (a) 2-D computational grid (41,800 cells); (b) 3-D computational grid (338,460 csells)

and volute casing. This allowed portions of mesh in the rotary part of the impeller to slide in small incremental moments relative to those of the stationary part during transient simulations.

Boundary Conditions. Since the computational domain incorporated the entire stage of the diffuser pump, the boundary conditions were easily specified at the inlet and outlet of the pump. Corresponding to the specified flow rate, a steady uniform radial velocity for 2-D calculations or axial inflow velocity distribution for 3-D calculations was given at the inlet boundary and the inlet boundary was located as far from the impeller blades leading edge, as possible. The outlet boundary was imposed at the end port of the volute casing, and simple extrapolation boundary conditions were employed. Further changes in locations of inlet and outlet boundaries did not show differences in predicted static pressure fluctuations. Nonslip wall boundary conditions were specified for the impeller blades surface, diffuser vanes surface and volute casing wall. The so-called ''wall functions'' were employed within the sub-layer adjacent to all the surfaces. Also, the boundary values of turbulence energy and turbulence dissipation rate were carefully set to make the solution stable and accurate. Zero gradients of k and ε are specified at the outlet, while the following relationships are selected for k and ε at inlet,

$$k_1 = 0.005(U_1^2 + V_1^2 + W_1^2) \quad \text{and} \quad \varepsilon_1 = k_1^{1.5}/0.01D_2$$

where U_1, V_1, and W_1 are inlet mean velocity components, and D_2 the outlet diameter of the pump impeller. Variations in these parameters showed little effect on the pressure fluctuation in the diffuser. The sliding interface between the impeller and diffuser was treated as an additional fluid zonal boundary in transient calculations with sliding meshes, and was updated implicitly after the interior of computational domain has been updated.

Convergence Judgment and Numerical Error Control. All the computations were performed on a computer VT-Alpha 500AXP (500 MHz Alpha processor, 512 MB RAM). The time step, which is related to rotational speed and angular displacement of the impeller between two successive computations, was set to 1.0×10^{-4} (290 time steps per revolution). The combination of mesh density and time step was chosen such that the maximum cell Courant number (defined as $C=|V|\Delta t/\Delta x$, where V is the estimated local velocity, and Δx, the corresponding local mesh dimension) was less than 50. This was found to be necessary for time accuracy and numerical stability. Normally, correctors between 5 and 8 are necessary within each time step for the PISO algorithm to reduce the residual below an acceptable value. 5-6 revolutions of the impeller are necessary to get the convergence to a periodic unsteady solution. Figure 3 shows the time histories of velocity and static pressure near the leading edge suction side of diffuser vanes during the first five revolutions of impeller. The final numerical results for the comparisons with experimental data in this paper were extracted from the sixth revolution of the impeller. To determine the sensitivity of numerical results to the magnitude of the time step, the results at 290 and 580 time steps per revolution were compared. As shown in Fig. 4, the magnitude of the time step has no significant effect on the pressure fluctuation. The sensitivity of the model to grid size was checked by performing the calculations for the 2-D model on two grid systems, one with 41,800 cells and the other with 61,480 cells, as shown in Fig. 5. The numerical results showed that accurate computations are expected from 290 time steps per revolution and 61,480 grids in the present unsteady calculation. Furthermore, various spatial difference schemes, such as, the first-order UD (Upwind Differencing), the second-order LUD (Linear Upwind Differencing) and the third-order QUICK (Quadratic Upstream Interpolation of Convective Kinematics) as well as a multidimensional second-order MARS (Monotone Advection and Reconstruction Scheme) were tested at the mesh density of 61,480 cells. The differences in the results were negligible. The numerical tests based on two grid systems and different convective flux formulations indicated that the well-known numerical diffusion (a form of numerical truncation error) and numerical dispersion (a kind of numerical instability) diminished to maximum extent. Moreover, the influences of boundary locations and boundary specifications were reduced to their respective minimums. Therefore, for the

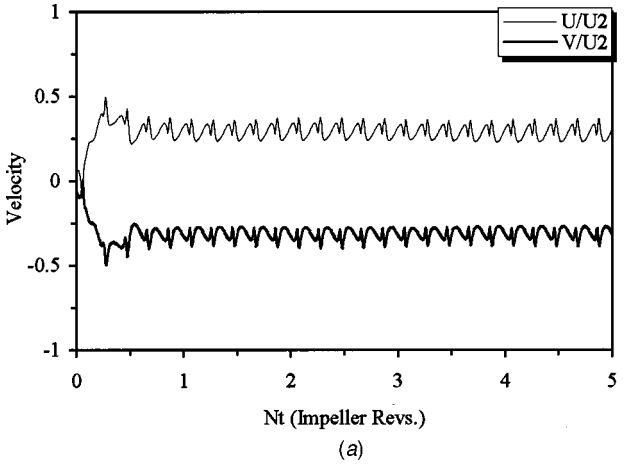

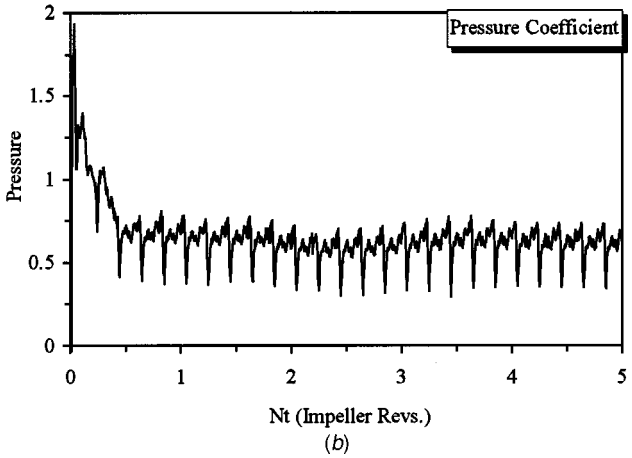

Fig. 3 Convergence history of time accurate computation during five rotations. (a) velocity fluctuation; (b) pressure fluctuation

present 2-D calculations, the numerical deviations from the experimental data can be attributed to physical modeling errors: (1) 2-D and 3-D difference; (2) difference between CFD pump modeling and real pump modeling; (3) pump geometry deviation; and (4) turbulence models. While for the present 3-D simulations, the discretization error due to inadequate grid resolution is a major concern.

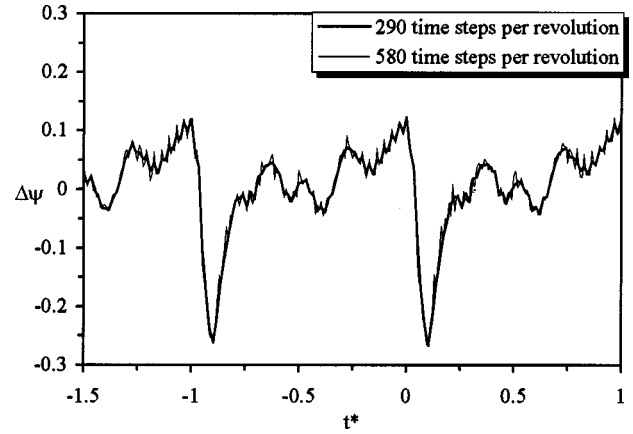

Fig. 4 Effect of time step on pressure fluctuation at station (r_1, c_1) for rated condition

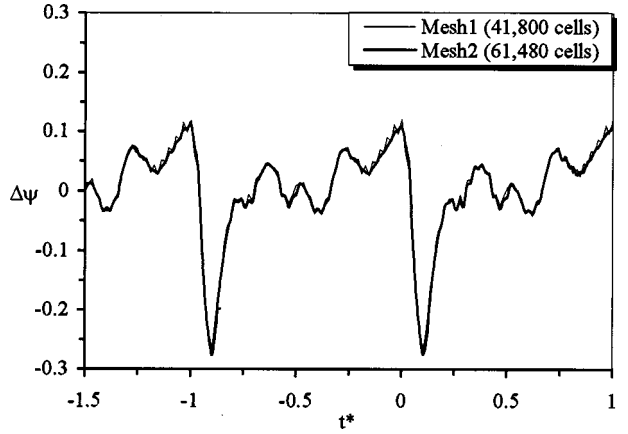

Fig. 5 Effect of grid density on pressure fluctuation at station (r_1, c_1) for rated condition

Calculations by Singularity Method. Qin and Tsukamoto [22] calculated pressure fluctuations downstream of the present test diffuser using singularity method. In their 2D, inviscid, and incompressible flow analysis, they chose three kinds of vortices for the fundamental analysis on impeller-diffuser interaction: steady bound vortices on the impeller, unsteady bound vortices on the diffuser vanes and free vortices shed from the diffuser vane trailing edge. The present CFD results were compared with the unsteady static pressures calculated by singularity method.

Results and Discussion

Unsteady Pressure in Diffuser Vane Passage. Figure 6 indicates the time histories of the unsteady part of the instantaneous pressure coefficient on a representative pressure tap $(r_1, c_1)_D$ positioned close to the diffuser vane leading edge on the suction side (see Fig. 1(b)). The relative position between impeller I-1 and diffuser vane D-1 at $t^* = 0.0$ is shown in Fig. 1(c). The wave form of unsteady pressure predicted by CFD shows better agreement with the experimental one than a wave form calculated by the singularity method which is comprised of only low frequency components. The poor waveform predicted by the singularity method was due to exclusion of the blade thickness and viscous wake-diffuser interaction from the calculation. As shown in Fig. 7, the incorporation of the wake vortices from the impeller passages into the singularity method with some assumptions can improve, to some degree, the unsteady static pressure in terms of the fluctuation wave form (Qin [26]). The valley of instantaneous

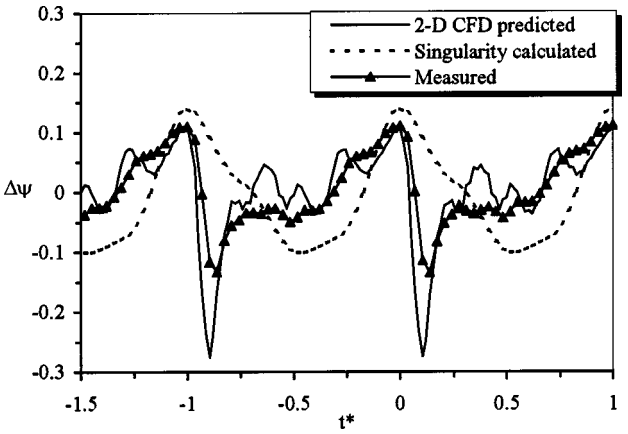

Fig. 6 Time histories of unsteady pressure $\Delta\psi$ at (r_1, c_1); Experimental Uncertainty in $\Delta\psi = 7.1$ percent

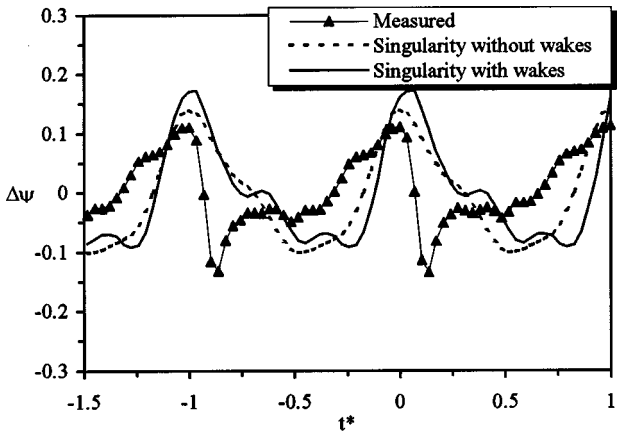

Fig. 7 Unsteady pressure $\Delta\psi$ at (r_1, c_1) predicted by Singularity method accounting for the viscous effects

pressure modeled by CFD is lower than observed in the experimental data or predicted by the singularity method but follows the general pattern.

Figure 8 shows the blade-to-blade distributions of the peak-to-peak values of unsteady pressure coefficient in the test diffuser shown in Fig. 1(c). As compared to the results from the singularity method and the experimental data, the present CFD approach is capable of predicting global trends in the pressure variations, which are found to be larger on the suction side of diffuser vane than on the pressure side at a given radius, and that unsteady pressure decreases with increasing radius. The absolute magnitude of the unsteady pressure coefficient from CFD simulation with the two-equation model is larger than the experimental value. At the current stage, nevertheless, the general features of the pressure variations can be captured with the Navier-Stokes Solver. The results obtained are in agreement with the available experimental data in spite of the deviation in the magnitude of pressure fluctuations. Figure 9 shows both the measured and the CFD predicted unsteady pressures in frequency domain at the location of $(r_1, c_1)_D$ in the diffuser (Fig. 1(b)). The frequencies are extracted from the time domain with an external FFT program. The present simulations demonstrate that the pressure in the diffuser passage fluctuates with the impeller blade passing frequency $Z_i N$ and its high harmonics, which cannot be accounted for in the singularity method without viscous wake interactions. In conclusion, the present whole stage calculations can predict frequency components of unsteady static pressures well, and provide fair approximations of pressure amplitudes.

Contour of Instantaneous Static Pressure (2-D CFD Results). Figure 10(a) and (b) shows the contour of instantaneous static pressure in the stage of the test pump at two instants corresponding to P1 and P3 in Fig. 11 that indicates four pressure peaks occurring at the pressure tap $(r_1, c_3)_D$ within one pitch angular displacement of the impeller. At $t^* = 0$, when impeller blade I-1 approaches closest to the leading edge of the diffuser vanes D-1, static pressure at $(r_1, c_3)_D$ reaches the highest peak P1. This pressure peak is due to potential interactions between impeller blades and diffuser vanes as indicated by the potential flow analysis (Qin and Tsukamoto, [22]). When the trailing edge of the impeller blade I-1 is passing by the pressure tap $(r_1, c_3)_D$, the pressure at $(r_1, c_3)_D$ is responding to another peak P3. This is attributed by the wake interference from impeller blade I-1 as described later.

Contour of Turbulent Kinetic Energy (2-D CFD Results). Figure 12(a) and (b) shows the CFD calculated contour of turbulent kinetic energy in the stage of the studied pump at two instants. The impeller wake with high level turbulent kinetic energy moves out of the impeller discharge (e.g., I-1 in Fig. 12(a)), and is chopped by diffuser vane when it approaches the leading edge of the diffuser vanes. Then the wakes decay gradually in the diffuser passage becoming insignificant after passing through the diffuser passage, as can be seen in Fig. 12. The pressure peak P2 in Fig. 11 happens at the moment when the viscous wake shed from blade I-1 passes by the location $(r_1, c_3)_D$, as shown in Fig.

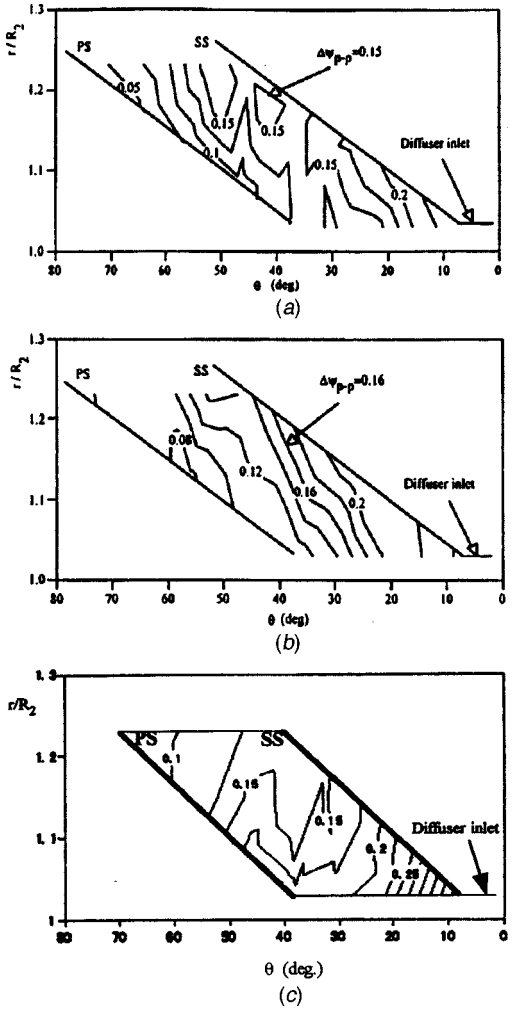

Fig. 8 Contour map of magnitude of $\Delta\psi_{p\text{-}p}$ of pressure fluctuation in vaned diffuser passage at rated condition; experimental uncertainty in $\Delta\psi_{p\text{-}p}$=7.1 percent. (a) Measured; (b) calculated by singularity method; (c) CFD predicted

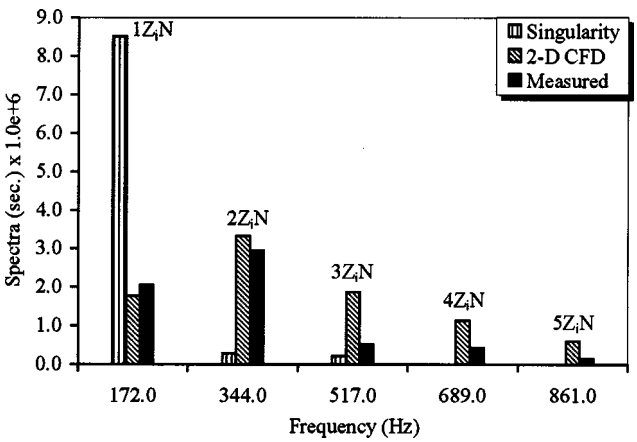

Fig. 9 Pressure fluctuation at (r_1, c_1) in frequency domain

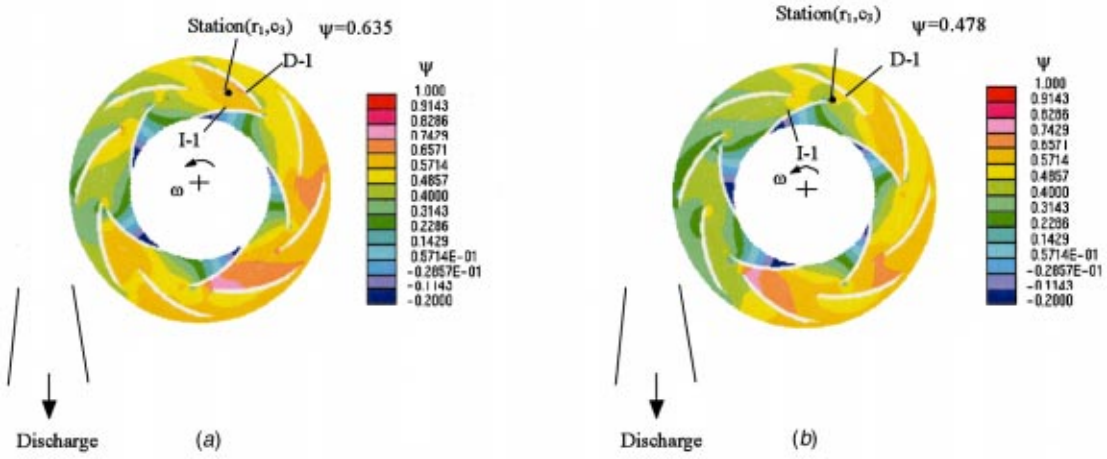

Fig. 10 2-D CFD predicted static pressure at two instants. (a) $t^*=0.0$; (b) $t^*=0.41378$

12(b). In other words, the viscous wake shed from impeller passage can be interpreted as a kind of ''phantom blade'' causing additional impeller-diffuser interactions.

Vorticity Contours (2-D CFD Results). Figures 13(a) and (b) show the present CFD predicted contour of vorticity ζ in the stage of the test pump at two different instants. The wakes shed from the impeller blade trailing edge traverse with the main flow from the impeller and are chopped into segments by diffuser vanes. Then the wake segments are sheared and stretched within the diffuser passage, and continue migrating while decaying gradually. From Fig. 13(a) and (b), it might be deduced that the pressure peaks, P3 and P4, shown in Fig. 11 are possibly produced by the passing of wakes shed from the trailing edge of impeller blade I-1. In addition to the outstanding pressure peaks occurring at the monitored location $(r_1,c_3)_D$, a series of small increases in pressure are introduced by wake stretching and decaying. Consequently, this wake interaction generates fluctuations in the velocity and static pressure in the diffuser passage. Whereas the detailed viscous wake-diffuser interactions can be detected with the present CFD model, the present singularity method cannot explain the interaction and migration of the wakes downstream of impeller passages, thus the frequency components calculated by the singularity analysis cannot cover wide frequency ranges, even though the present singularity method can identify the potential interaction in pumps.

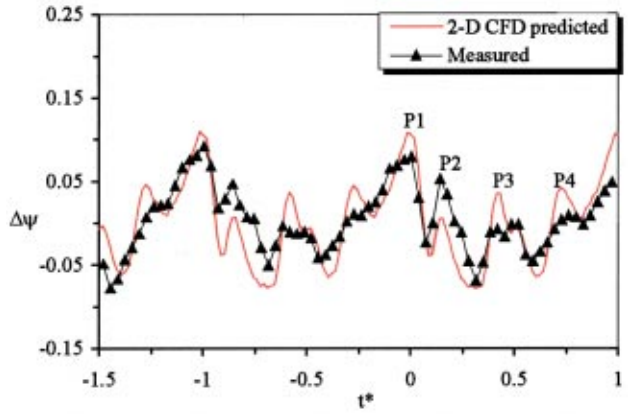

Fig. 11 Unsteady pressure $\Delta\psi$ at position (r_1,c_3) for rated condition

Comparison Between 2-D and 3-D Calculations. Figure 14 presents a comparison between 2-D and 3-D calculations on the static pressure fluctuation at stations $(r_1,c_1)_D$, $(r_1,c_3)_D$, $(r_2,c_3)_A$ and $(r_3,c_3)_G$. The wave form is improved by the 3-D computation, especially between the two pressure peaks. It seems that the sampling time of 0.0002 second for the measurements may be too long to be able to capture the detail fluctuations of pressure as predicted by CFD calculations. Generally, the agree-

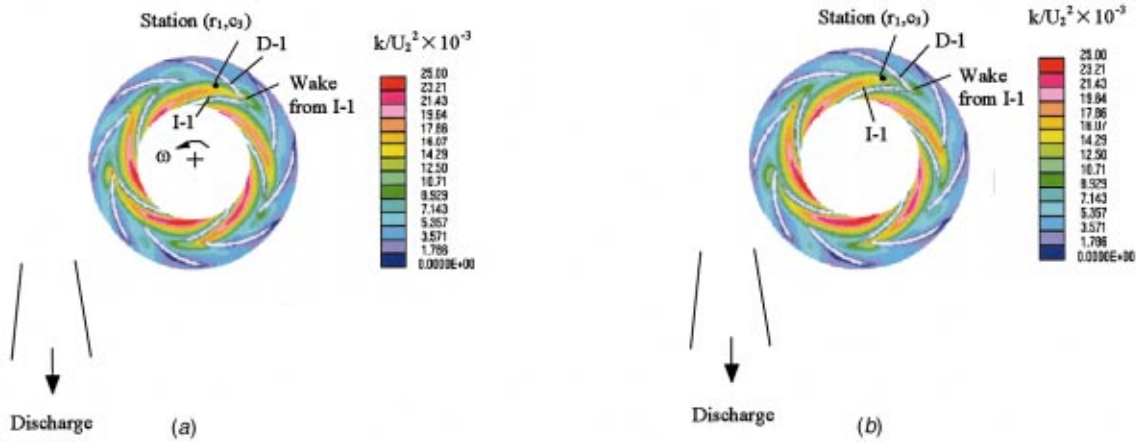

Fig. 12 2-D CFD predicted turbulent kinetic energy at two instants. (a) $t^*=0.0$; (b) $t^*=0.13788$

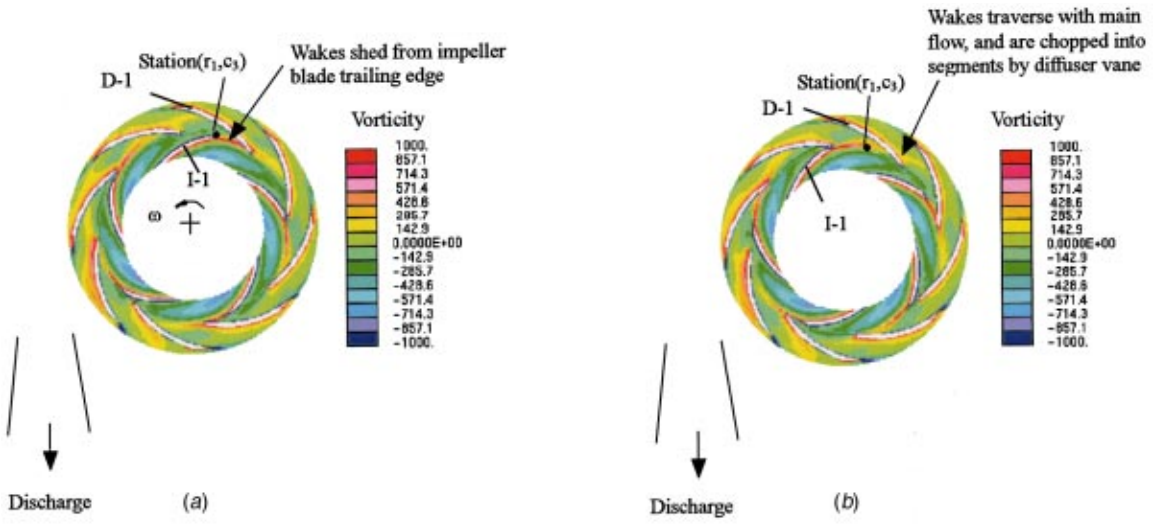

Fig. 13 2-D CFD predicted contour of vorticity at two instants. (a) $t^*=0.41378$; (b) $t^*=0.72418$

ment between CFD and experimentation becomes worse at higher radii, especially at position $(r_2,c_3)_A$ in the diffuser passage A, which is oriented to the tongue of the volute. This is because the complicated interaction processes at the rear part of the diffuser or near the tongue area cannot be captured accurately by the present calculation. Using the present CFD studies on the test pump, the unsteady effects can be categorized as potential interactions that propagate downstream and upstream, and wake effects that convect downstream. At the rear part of the diffuser, both of these effects become very complicated, and hence the real physics of the interaction processes becomes more difficult to model with the current RANS CFD solver.

Figure 15 presents the contours of relative velocity magnitude at the discharge of the test pump impeller from the unsteady 3-D calculation at two instants, and indicates a small, time-dependent region with the well-known ''jet-wake'' structure near the shroud suction corner at the outlet of the centrifugal impeller. This flow structure cannot be predicted by the 2-D calculation due to its failure to capture the secondary flow motion in the impeller. The slight discrepancy between 2-D and 3-D calculations shown in Fig. 14 may come from such flow structure differences. Surprisingly, 3-D calculations did not present as satisfactory results as expected. This can be explained in that the present impeller-diffuser interactions are dominated by potential interaction and

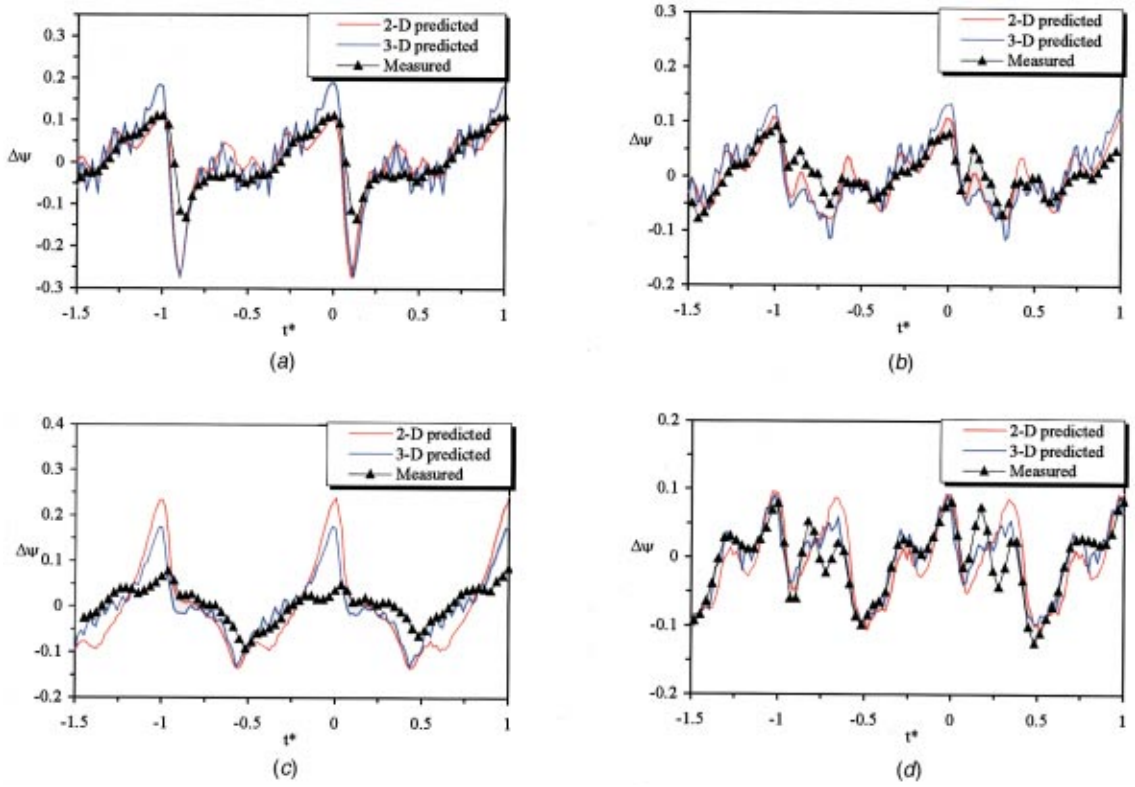

Fig. 14 Comparisons between 2-D and 3-D calculations. (a) (r_1,c_1); (b) (r_1,c_3); (c) (r_2,c_3); (d) (r_3,c_3)

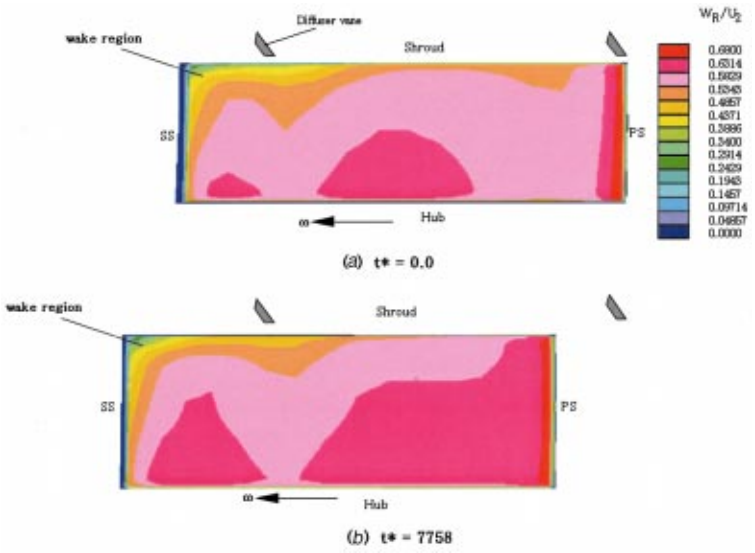

Fig. 15 Contours of relative velocity at the impeller discharge based on unsteady 3-D calculation. (a) $t^*=0.0$; (b) $t^*=0.7758$

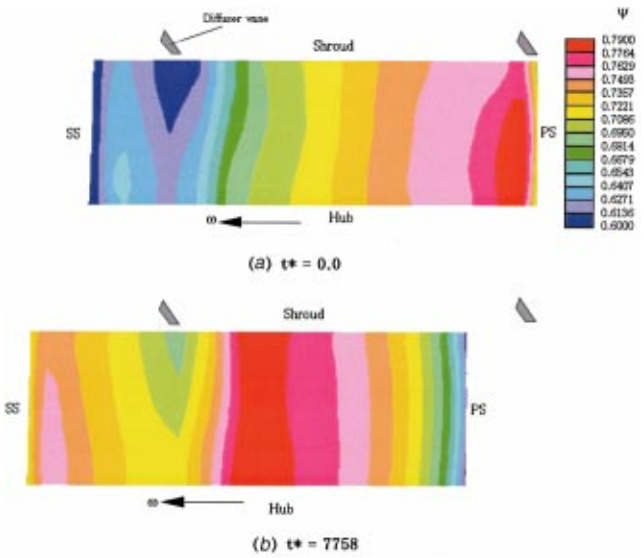

Fig. 16 Static pressure contour at the impeller discharge based on unsteady 3-D calculation. (a) $t^*=0.0$; (b) $t^*=0.7758$

hence the wake effects are relatively small. The time-dependent static pressure distribution from hub to shroud based on the unsteady 3-D calculation at two instants as shown in Fig. 16, does not indicate marked distortion and follows a trend toward 2-D patterns.

Conclusions

A 2-D and 3-D unsteady incompressible Reynolds-averaged Navier-Stokes equations with two equation turbulence models was computed for the whole stage of a diffuser pump without approximating the count ratios of rotor to stator. The calculated results provided insights toward a better understanding of complicated unsteady rotor-stator interaction phenomena in a diffuser pump. As a result of the comparison of the CFD predictions with singularity calculations and experimental data, the following conclusions are derived:

1 Sources contributing to the pressure fluctuations in the diffuser passage of the present diffuser pump stage have been captured with a 2-D RANS solver: potential interactions cause the highest peak of pressure in the diffuser; viscous wakes shed from the impeller interfere with the successive diffuser vanes and result in the presence of additional high pressure peaks.

2 The frequency components of the pressure fluctuations in the diffuser passage are comprised mainly of the impeller blade passing frequency Z_iN and its higher harmonics of $2Z_iN$ and $3Z_iN$. This indicates that the impeller-diffuser interaction is caused chiefly by potential interaction and wake impingement with the diffuser vanes.

3 The ''jet-wake'' flow structure at impeller discharge affects the wake-diffuser interaction, but it is relatively small compared with stronger viscous wake interactions in the present pump.

Further work is being focused on the numerical solutions on real pump models including the leakage flow, which is believed to be important factors for impeller-diffuser simulations in pumps.

Acknowledgments

The work in this paper is a portion of the special program of SBVL (Satellite Venture Business Laboratory) at Kyushu Institute of Technology. This study was supported by the Japanese Ministry of Education, Science and Culture under a grant-in-aid for Scientific Research, No. 09450081; This support is gratefully acknowledged. The authors' thanks extended also to Messrs. M. Uno, Y. Narimatsu for their useful suggestions and help in this work.

Nomenclature

c = symbol of pressure traverse line
D = diameter
k = turbulence energy
f = frequency
N = rotational speed
PS = pressure side
P_s = total pressure at pump suction port
p = instantaneous static pressure $=\overline{p}+\tilde{p}$
$\overline{p}$ = time average p
$\tilde{p}$ = unsteady component of p
p^* = relative pressure $=p-P_s$
R,r = radius

SS = suction side
T = period of one revolution of impeller
T_i = time required to traverse one pitch of impeller blade
t = time
t^* = non-dimensional time $= t/T_i$
U,V,W = x-, y- and z- velocities in Cartesian coordinates
U_2 = peripheral speed of impeller
Z = number of blades
$\Delta\psi$ = non-dimensional unsteady pressure $= \tilde{p}^*/\rho U_2^2/2$
$\Delta\psi_{p\text{-}p}$ = peak-to-peak magnitude of $\Delta\psi$
ε = dissipation rate of turbulence energy
ρ = density
ψ = instantaneous pressure coefficient $= (p - \mathrm{P}_s)/(\rho U_2^2/2)$
ζ = vorticity $= \partial v/\partial x - \partial u/\partial y$

Subscripts

A,D,G = individual diffuser passage shown in Fig. 1(b)
d = diffuser
i = impeller
1, 2 = impeller inlet and outlet
3, 4 = diffuser vane inlet and outlet

References

[1] Arndt, N., Acosta, A J., Brennen, C. E., and Caughey, T. K., 1989, ''Rotor/Stator Interaction in a Diffuser Pump,'' ASME J. Turbomach., **111**, pp. 213–221.

[2] Arndt, N., Acosta, A J., Brennen, C. E., and Caughey, T. K., 1990, ''Experimental Investigation of Rotor/Stator Interaction in a Centrifugal Pump with Several Vaned Diffusers,'' ASME J. Turbomach., **111**, pp. 213–221.

[3] Tsukamoto, H., Uno, M., Hamafuku, H., and Okamura. T., 1995, ''Pressure Fluctuation Downstream of a Diffuser Pump Impeller,'' The 2nd Joint ASME/JSME Fluids Engineering Conference, Forum of Unsteady Flow, FED-Vol. 216, pp. 133–138.

[4] Dring, R. P., Joslyn, H. D., Hardwin, L. W., and Wagner, J. H., 1982 ''Turbine Rotor-Stator Interaction,'' ASME J. Eng. Power, **104**, pp. 729–742.

[5] Gallus, H. E., 1979, ''Unsteady Flows in Turbines,'' VKI Lecture Series LS-1979-3, Vol. 2, Von Karman Institute.

[6] Fleeter, S., Jay, R. L., and Bennett, W. A., 1981, ''Wake Induced Time-Variant Fluids Aerodynamics Including Rotor-Stator Axial Spacing Effects,'' ASME J. Fluids Eng., **103**, pp. 59–66.

[7] Rai, M. M., 1987, ''Unsteady Three-Dimensional Navier-Stokes Simulations of Turbine Rotor Stator Interactions,'' AIAA Paper No. 87–2058.

[8] Giles, M. B., 1988, ''Calculation of Unsteady Wake/Rotor Interaction,'' J. Propul. Power, **4**, No. 4, pp. 356–362.

[9] Lewis, J. P., Delaney, R. A., and Hall, E. J., 1989, ''Numerical Prediction of Turbine Vane-Blade Aerodynamic Interaction,'' ASME J. Turbomach., **111**, pp. 387–393.

[10] Rao. K. V., and Delaney, R. A., 1992, ''Investigation of Unsteady Flow Through a Transonic Turbine Stage, Part. I, Analysis,'' AIAA Paper No. 90-2408.

[11] Sharma, O. P., Pickett, G. F., and Ni, R. H., 1992, ''Assessment of Unsteady Flows in Turbines,'' ASME J. Turbomach., **114**, pp. 79–90.

[12] Ho, Y.-H., and Lakshiminarayana, B., 1995, ''Computation of Unsteady Viscous Flow Through Turbomachinery Blade Row Due to Upstream Rotor Wakes,'' ASME J. Turbomach., **117**, pp. 541–552.

[13] Valkov, T., and Tan, C. S., 1995, ''Control of the Unsteady Flow in a Stator Blade Row Interacting with Upstream Moving Wakes,'' ASME J. Turbomach., **117**, pp. 97–105.

[14] Arnone, A., and Pacciani, R., 1996, ''Rotor-Stator Interaction Analysis Using the Navier-Stokes Equations and a Multigrid Method,'' ASME J. Turbomach., **118**, pp. 679–689.

[15] Chung, M.-H., and Wo, A. M., 1997, ''Navier-Stokes and Potential Calculations of Axial Spacing Effect on Vortical and potential Disturbances and Gust Response in an Axial Compressor,'' ASME J. Turbomach., **119**, pp. 472–481.

[16] Dong, R., Chu, S., and Katz, J., 1992, ''Quantitative-Visualization of the Flow Within the volute of a Centrifugal Pump. Part B: Results,'' ASME J. Fluids Eng., **114**, No. 3, pp. 396–403.

[17] Akin, O., and Rockwell, D., 1994, ''Flow Structure in a Radial Flow Pumping System Using High-Image-Density Particle Image Velocimetry,'' ASME J. Fluids Eng., **116**, pp. 538–544.

[18] Ubaldi, M., Zunino, P., Barigozzi, G., and Gattanei, A., 1996, ''An Experimental Investigation of Stator Induced Unsteadiness on Centrifugal Impeller Outflow,'' ASME J. Turbomach., **118**, pp. 41–54.

[19] Fortes-Patella, R., Longatte, F., Kueny, J-L., and Croba, D., 1995, ''Numerical Analysis of Unsteady Flow in a Centrifugal Pump,'' ASME Fluid Machinery, FED-Vol. 222, pp. 41–46.

[20] Bert, P. F., Combes, J. F., and Kueny, J. L., 1996, ''Unsteady Flow Calculation in a Centrifugal Pump Using a Finite Element Method,'' XVIII IAHR Symposium on Hydraulic Machinery and Cavitation, Valencia, Spain.

[21] Schulz, H., Greim, R., and Volgmann, W., 1996, ''Calculation of Three-Dimensional Viscous Flow in Hydrodynamic Torque Converters,'' ASME J. Turbomach., **118**, pp. 578–589.

[22] Qin, W., and Tsukamoto, H., 1997, ''Theoretical Study of Pressure Fluctuations Downstream of a Diffuser Pump Impeller-Part 1: Fundamental Analysis on Rotor-Stator Interaction,'' ASME J. Fluids Eng., **119**, pp. 647–652.

[23] Ruprecht, A., Heitele, M., Helmrich, T., Faigle, P., and Moser, W., 1998, ''Numerical Modeling of Unsteady Flow in a Francis Turbine,'' XIX IAHR Symposium on Hydraulic Machinery and Cavitation, Singapore.

[24] STAR-CD Documentation, Version 3.0, Computational Dynamics Ltd., London, 1996.

[25] Schachenmann, A., Muggli, F., and Guelich, J. F., 1993, ''Comparison of Three Navier-Stokes Codes with LDA-Measurements on an Industrial Radial Pump Impeller,'' ASME FED-Vol. 154, Pumping Machinery, pp. 247–252.

[26] Qin, W., 1995 ''Study of Pressure Fluctuations Downstream a Diffuser Pump Impeller Due to Rotor-Stator Interaction,'' Ph.D. thesis (in Japanese), Kyushu Institute of Technology, Japan.

Fahua Gu

Abraham Engeda

Turbomachinery Lab,
Michigan State University,
East Lansing, MI 48824

Mike Cave

Jean-Luc Di Liberti

Solar Turbines Inc.,
9280 Sky Park CT.,
San Diego, CA 92123

A Numerical Investigation on the Volute/Diffuser Interaction Due to the Axial Distortion at the Impeller Exit

A numerical simulation is performed on a single-stage centrifugal compressor using the commercially available CFD software, CFX-TASCflow. The steady flow is obtained by circumferentially averaging the exit fluxes of the impeller. Three runs are made at the design condition and off-design conditions. The predicted performance is in agreement with experimental data. The flow details inside the stationary components are investigated, resulting in a flow model describing the volute/diffuser interaction at design and off-design conditions. The recirculation and twin vortex structure are found to explain the volute loss increase at lower and higher mass flows, respectively.
[DOI: 10.1115/1.1385515]

Introduction

A single-stage centrifugal compressor consists of impeller, diffuser (vaned or vaneless), and volute. Impeller and diffuser flows have been studied extensively, and volute flow study has appeared as an interesting research field for further improving the compressor performance. Van den Braembussche and Hande [1] measured a straight model of a centrifugal compressor volute. Based on their measurement, they described the volute flow as:

- The fluid entering close to the tongue at small radii fills the center of the volute
- New fluid entering further downstream at a larger radius starts rotating around the upstream fluid
- Vortex tubes of increasing radius are wrapped around each other and each vortex tube remains at constant radius

Ayder et al. [2,3] gave a detailed measurement and numerical simulation of the flow structure of the volute at design and off-design conditions. Hagelstein et al. [4] presented a detailed flow measurement of a rectangular volute at an off-design condition of higher mass flow rate.

The interaction between volute and impeller was studied experimentally by Hagelstein et al. [5]. At off-design conditions, the volute produces a peripheral pressure distortion, leading to a periodic throttling of the impeller flow and oscillating of the radial force on the impeller shaft. Flathers et al. [6] satisfactorily predicted the variation of radial force magnitudes and directions with the mass flow rates using CFX-TASCflow. Sorokes et al. [7] experimentally investigated the circumferential static pressure nonuniformity on a multi-stage compressor. The numerical study of Hillewaert [8] showed that the pressure oscillation at the vaneless diffuser inlet could be up to 10% of the mean value for the near choke flow.

This paper numerically investigates the flow structure inside the compressor under distorted impeller exit pressure due to the volute. Except for the use of some models (Hillewaert and Van Den Braembussche [8]), the numerical investigation of the pressure circumferential distortion at the impeller exit is very expensive because all the impeller passages have to be simulated together, and the unsteady flow has to be resolved at tiny time steps. However, since the upstream effect of the volute has previously been studied and found to be $\frac{1}{2}$ that at the diffuser exit, as shown by Hagelstein et al. [4] and Sorokes et al. [7], it is therefore deemed reasonable to simply circumferentially average the impeller exit fluxes as a starting flow for the diffuser/volute analysis. Because of the circumferential averaging, this paper limits the discussion to the flow axial distortion at the averaging station. A flow model is proposed to describe the flow inside the volute of the compressor.

Contributed by the Fluids Engineering Division for publication in the JOURNAL OF FLUIDS ENGINEERING. Manuscript received by the Fluids Engineering Division February 2, 1000; revised manuscript received April 17, 2001. Associate Editor: Yi Tsujimoto.

CFD Models

The commercially available CFD software, CFX- TASCflow, is employed for this study. The validation of this code for the configuration of centrifugal compressors can be found, for example, in the work of Flathers [6,9]. The code solves the Reynolds averaged Navier-Stokes equations in primitive variable form. The effects of turbulence were modeled using the standard $\kappa-\varepsilon$ turbulent model. To make the simulation timely economical, a wall function is used to resolve the wall flows. The simulation is believed converged when nondimensionalized maximum residuals are reduced to 1.E-4. The dependence of the solution on turbulence models has not been conducted in this study, but a comprehensive assessment has been made by Lakshminarayana [10] on the computation of turbomachinery flows using κ-ε turbulence model. The CFD results of Flathers and Bache [6] satisfactorily agreed with the experiment using this turbulence model for a similar compressor as will be discussed in this paper.

The code allows for connecting simple blocks into a multiblock assembly. A convenient feature of TASCflow is that the grids are not required to match at the connect interface. This makes it easy to connect volute grids at the critical surface, where one side is of the smallest area and the other side of the largest one. A self-coded volute grid generator was used to generate the volute and vaneless diffuser grid. The grid of the volute is of butterfly section to reduce the grid skewness (Fig. 1). For the sake of clarity, the impeller inlet bell mouth is not shown in this figure. The convention of the compressor is defined in Fig. 2. The commercial impeller grid generator, TASCgen, is employed to generate the impeller grid. In this study, the simulations were run on both fine meshes and coarse meshes to remove the dependence of the solution on the grid density. One fine grid size is $121\times27\times25=81{,}675$ for one passage of the impeller and 231,710 for the volute. One coarse grid size is $87\times16\times13=18{,}096$ points for one passage of the impeller and 145,535 for the volute. For all the

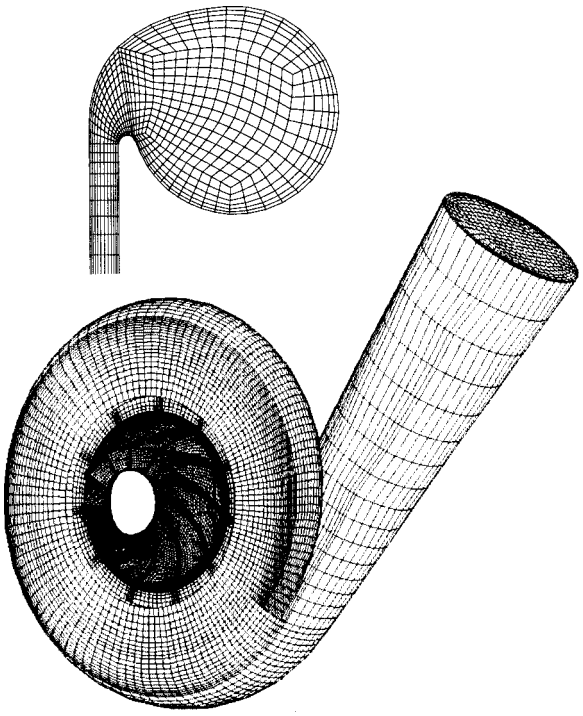

Fig. 1 Compressor grid

runs, same wall function was used, and the y^+ of the first grid point on the wall is in the range of logarithmic sub-layer of the boundary layer. The comparison shows that the differences of the computed compressor efficiencies and pressure ratios are negligible, less than 0.5%. The flow structure in the volute remains conceptually the same.

In this assembly, as shown in Fig. 1, there are two distinct components: impeller that is rotating, and volute and vaneless diffuser that are stationary. A mixing grid interface between these two components is defined as ''stage interface'' using TASCflow grid attachment facility. It tangentially averages the exit fluxes of impeller for the inflow of the diffuser; thus, it is not necessary to simulate all the passages of the impeller. In this study only one passage is modeled. The validation of this model can be found in Galpin et al., [11]. Periodic boundary condition is assigned to the blade grid tangential surfaces. The flows in all the components are solved simultaneously.

The inflow boundary condition was assigned at station 0-0 upstream of the impeller as total temperature, total pressure, and flow angles. Mass flow rate was imposed on the exit of the cone 8-8 as the outflow boundary condition. The CFD study ran at the design and two off-design conditions: 75% and 125% of the design mass flow. Because CFX-TASCflow does not require a uniform exit, the cone was not artificially extended, and no separation was found in the cone for all the mass flow rates.

There are mainly three disadvantages of this CFD model. The first one is that the circumferential distortion is smoothed out at the stage interface; it can affect the volute flow structure. This paper therefore focuses on the dependence of the volute flow structure on the axial distortion at vaneless diffuser inlet. The second one is the use of wall function. Even though this practice is economical for daily design process, the fine turbulent boundary layer structures will not be analyzed. The last disadvantage is that all the conclusions from the CFD analysis would be more convincible if more experimental data were available.

Results

The compressor was designed for pipeline applications. The tip machine Mach number is 0.65 at design point. The diffuser ratio D_5/D_2 is 1.9 and b/r_2 is 0.125. The volute area, including the 90

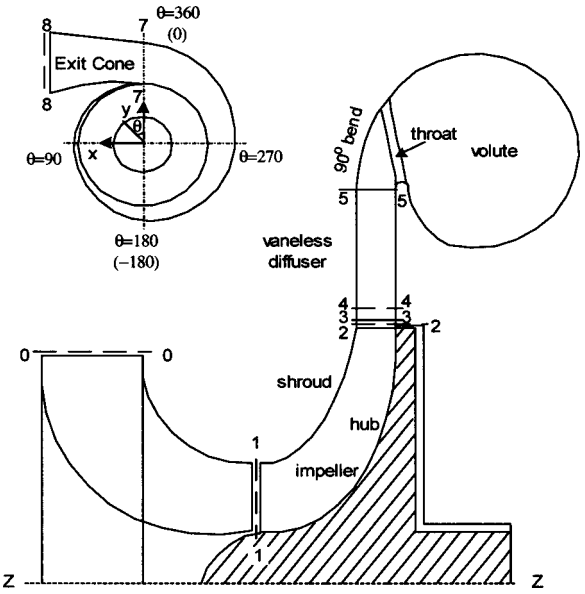

Fig. 2 Compressor convention

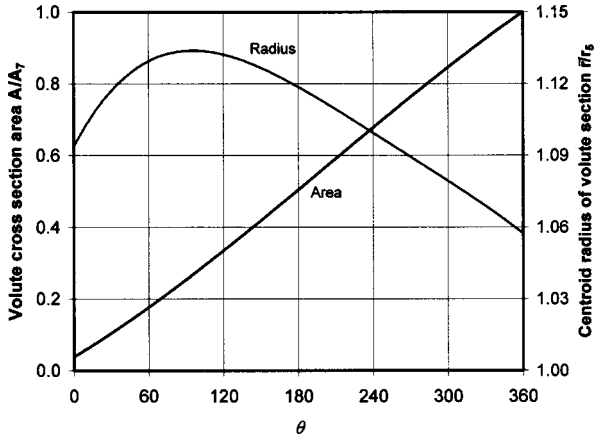

Fig. 3 Volute sectional area and radius

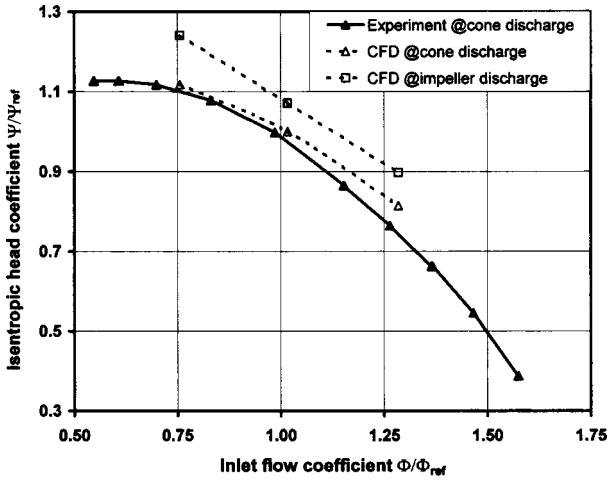

Fig. 4 Compressor performance

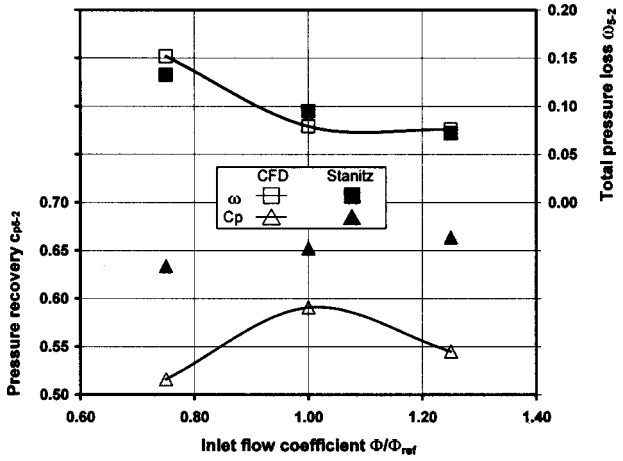

Fig. 5 Vaneless diffuser performance

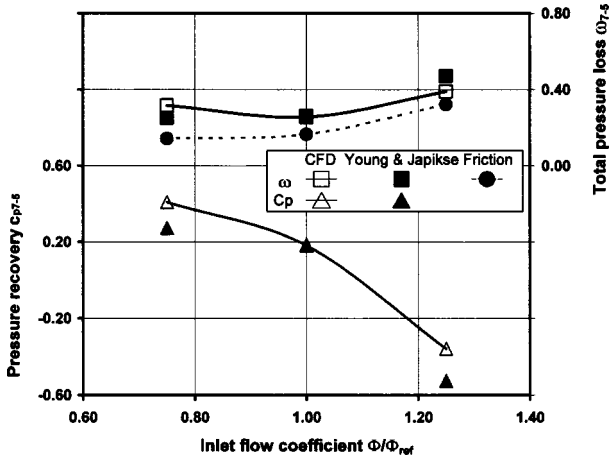

Fig. 6 Volute performance

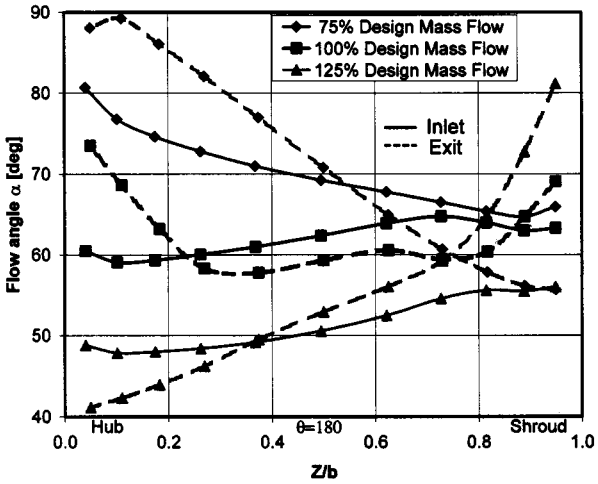

(a)

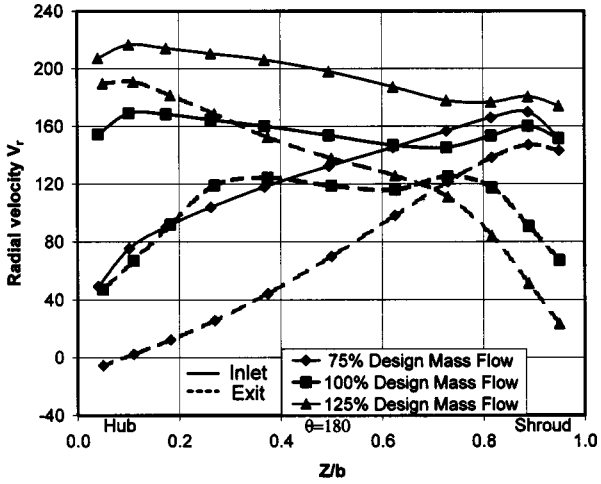

(c)

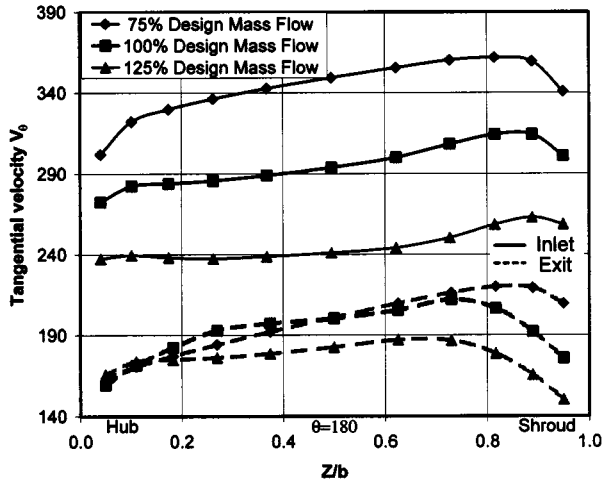

(b)

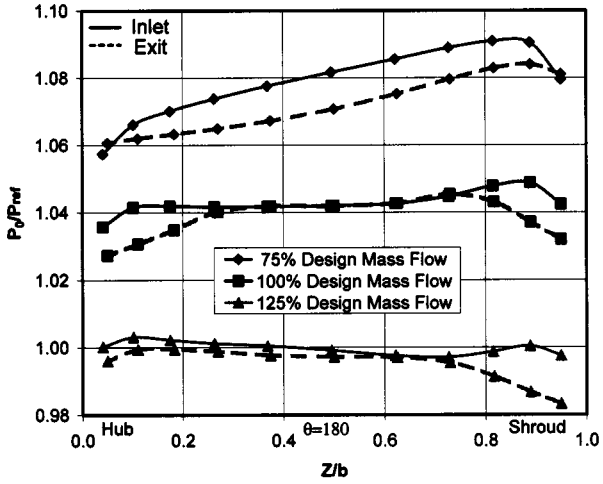

(d)

Fig. 7 Diffuser flows flow angle variation in axial direction radial velocity variation in axial direction tangential velocity variation in axial direction total pressure variation in axial direction

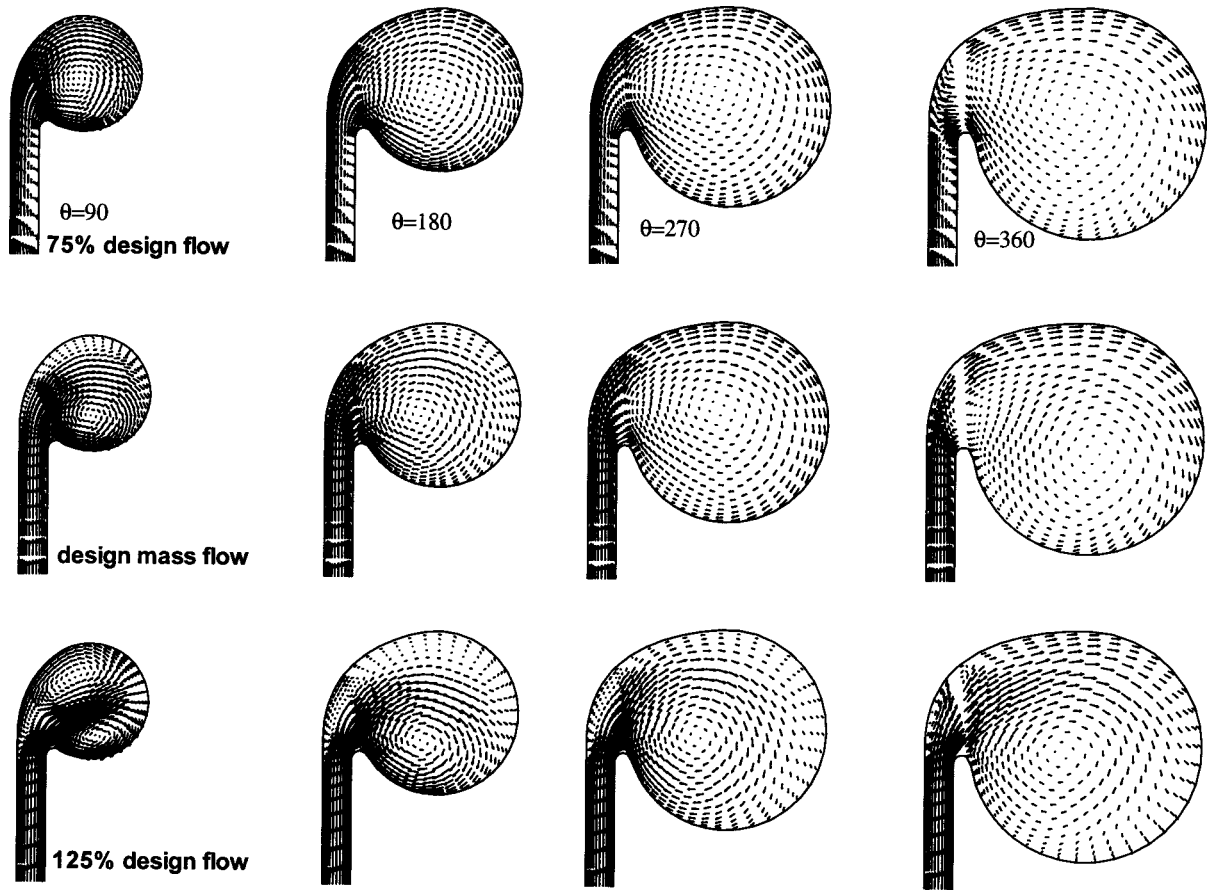

Fig. 8 Surface vectors of swirling flows

deg bend, increases linearly with area ratio of $AR=A_7/A_5=0.668$ while the centroid radius initially increases then decreases consistently as shown in Fig. 3. The performance test was conducted at Solar Turbines air test facility. The performances were measured from flange to flange following the ASME PTC10 guidelines. No flow details were measured between flanges. The working fluid was air at ambient conditions.

Compressor Performance. The experiment was run at several rotation speeds, while the CFD study was conducted only at 10,530 rpm. The experimental curve presented in Fig. 4 was obtained from the data at 10,901 rpm. The difference between the rotation speeds comes from the fact that the CFD study was blinded from the experimental one. The CFD data was obtained by mass-weighted averaging over the grid surface of stations.

It can be seen that the three points from CFD are in good agreement with experiment data. The CFD points are above the experimental curve due to the fact that the CFD model did not incorporate the leakage flow in the labyrinth between the shroud outer wall and the case. The performance of the impeller is also presented in Fig. 4. It can be seen that the performance of the impeller can be rather different from that of the compressor, even in the tendency. The difference between the curves of the impeller discharge and cone discharge shows the effect of the stationary components on the compressor performance.

The performance of each stationary component is presented in Table 1 in terms of total-to-total efficiency. It can be seen that the impeller efficiency drops more at lower mass flow than at higher mass flow. The losses in the stationary components (vaneless diffuser and volute, $\eta_{8-1}-\eta_{2-1}$) make the compressor efficiency drop by from 7.25%–10.40%. The losses in the vaneless diffuser ($\eta_{5-1}-\eta_{2-1}$) decreases consistently as the mass flow increases. The efficiency drop in the volute ($\eta_{8-1}-\eta_{5-1}$) accounts for less than 2/5 for lower and design mass flow, but more than 3/5 for higher mass flow of the total losses in the stationary components.

The vaneless diffuser performance was compared in Fig. 5 with the well-known equations introduced by Stanitz [12]. The equations was integrated from station 2 to station 5. The friction losses on the wall were considered in the equations, but the blockage due to the boundary layers on the walls was excluded. The skin friction coefficient c_f is calculated by the equation suggested by Japikse [13],

$$c_f=k\left(\frac{1.8\times10^5}{\mathrm{Re}}\right)^{0.2} \tag{1}$$

Here, the Reynolds number is based on the inlet diameter and velocity,

$$\mathrm{Re}=\frac{\rho_2 V_2 D_2}{\mu} \tag{2}$$

The constant k was given a value of 0.01 also suggested by Japikse [13]. It can be seen that the total pressure losses are in good agreement with each other, indicating that friction is the

Table 1 Efficiencies of each component

flow rate/design flow	0.75	1.00	1.25
$\eta_{2-1}-\eta_{\mathrm{ref}}$	−1.23%	0.00%	−0.16%
$\eta_{5-1}-\eta_{\mathrm{ref}}$	−7.89%	−4.37%	−3.90%
$\eta_{5-1}-\eta_{2-1}$	−6.66%	−4.37%	−3.74%
$\eta_{8-1}-\eta_{2-1}$	−10.40%	−7.25%	−9.58%
$\eta_{8-1}-\eta_{5-1}$	−3.74%	−2.28%	−5.85%
$(\eta_{8-1}-\eta_{5-1})/(\eta_{8-1}-\eta_{2-1})$	35.98%	39.74%	61.02%

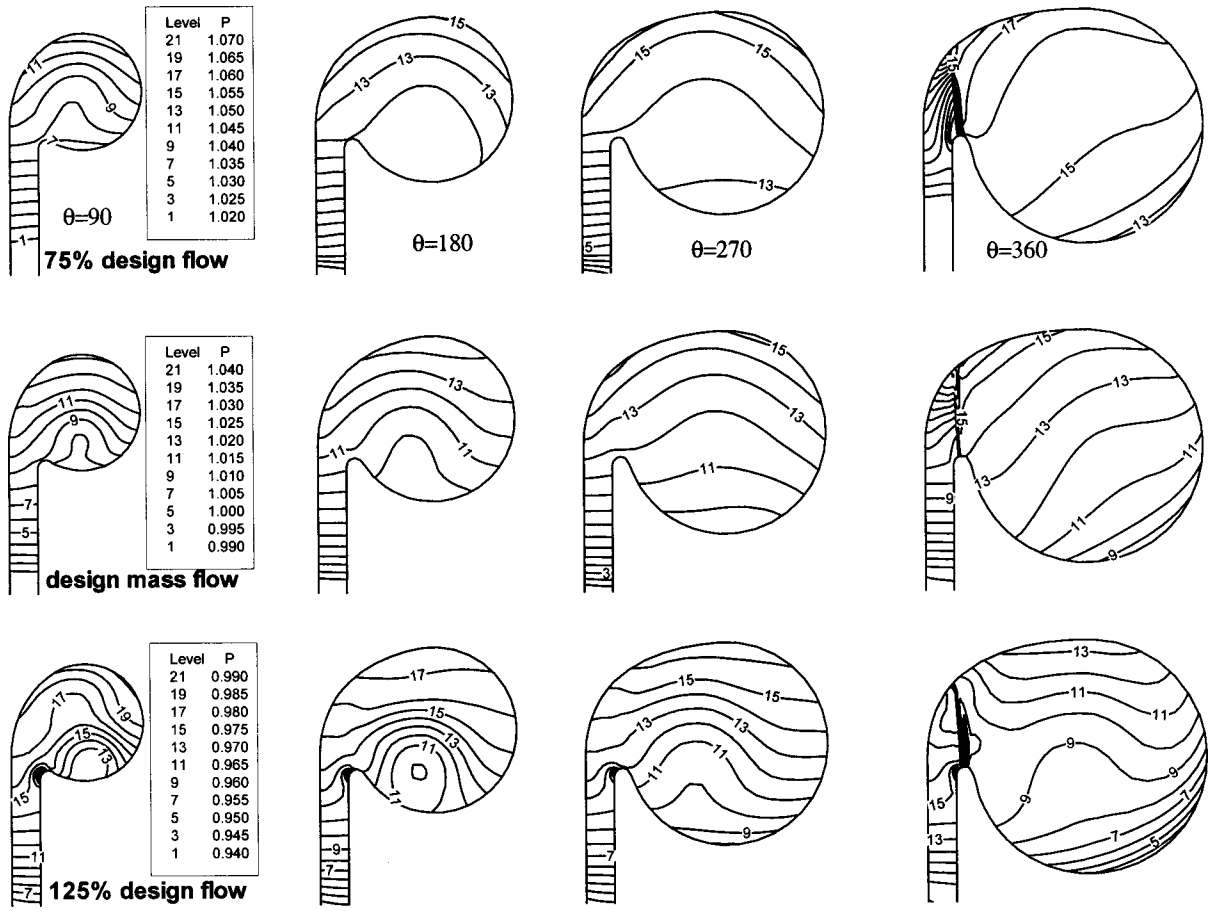

Fig. 9 Contours of static pressure

main source of vaneless diffuser loss when there is no flow separation. The higher loss for the lower mass flow results from the longer particle path. The Stanitz equations predicted higher pressure recovery due to the neglect of the aerodynamic blockage of the boundary layers on the walls

The volute performance is further investigated by comparing the pressure recovery and total pressure loss with the model of Young and Japikse [13], which is supported by experimental study. At the design point, both the total pressure loss and pressure recovery are in good agreement with each other. The Young and Japikse model gives lower total pressure loss and lower pressure recovery at the lower mass flow and higher acceleration and higher loss at higher mass flow. The fundamental assumption made in Young and Japikse model is that the meridional velocity coming into the volute is totally lost, and there is an additional loss, modeled as a sudden expansion mixing process, when the flow is decelerated in the volute passage. To tell whether the inlet meridional velocity is totally lost, it is necessary to distinguish the loss caused by the through flow and the loss caused by the swirling flow due to the inlet meridional velocity. The through flow causes friction losses in the volute passage that are approximated by White's formula cited by Schilichting [14] as shown in Fig. 6. The volute passage is modeled as a curved pipe with the section area equal to the critical area of the volute and length equal to the volute centroid passage. The pressure loss in the equivalent curved pipe is calculated as (see Appendix A)

$$\omega_{7-5} = \pi\Lambda \frac{R_5}{r_7} \frac{1}{(AR)^2} \frac{1}{\lambda^2+1} \tag{3}$$

The comparison suggests that for the design and higher mass flow rates, the friction loss due to the through flow accounts for more than half of the volute losses. It implies that the assumption in Young and Japikse's model is too pessimistic; at least half of the inflow meridional kinetic energy is preserved. For the lower mass flow, the friction loss only takes a small part of the total loss; it indicates that there should be some other loss mechanisms. The obvious one is the diffusion loss, which is not considered in the friction model. Unfortunately, there are few available publications dealing with diffusers with area ration less than 1.25 (Japikse and Baines [15]). For the small mass flow, the equivalent diffuser ratio λAR is 1.228. The flow structure in the volute will be investigated attempting to find out some loss mechanisms.

Flow at Diffuser Inlet and Exit. The comparison of the flows at the diffuser inlet and exit on section $\theta=180$ deg is presented in Fig. 7, which shows the flow variation in the axial direction. Senoo et al. [16] carried out a detailed measurement and calculation of the flow in the vaneless diffuser. The diffuser investigated by Senoo (Fig. 10 and Fig. 11 of the reference) has similar b/r_2 as used in the current study. The inlet swirling angles (Fig. 7a) of the current study also fall into the range as studied by Senoo. Senoo showed that the flow begins as a mixture of core and boundary layer flows; eventually, the boundary layers develop symmetrically on both walls and merge together.

At the design mass flow, the inlet radial velocity (Fig. 7b) is relatively uniform compared with the off-design conditions, and the exit radial velocity distribution indicates that the boundary layers symmetrically developed on both walls, which is in agreement with Senoo's observation. However, at off-design conditions, the distortion of the radial velocity is exaggerated from the inlet to the exit, indicating that there is an axial mass migration; mass migrates from the hub wall to the shroud wall at the lower mass flow, and from the shroud wall to the hub wall at the higher

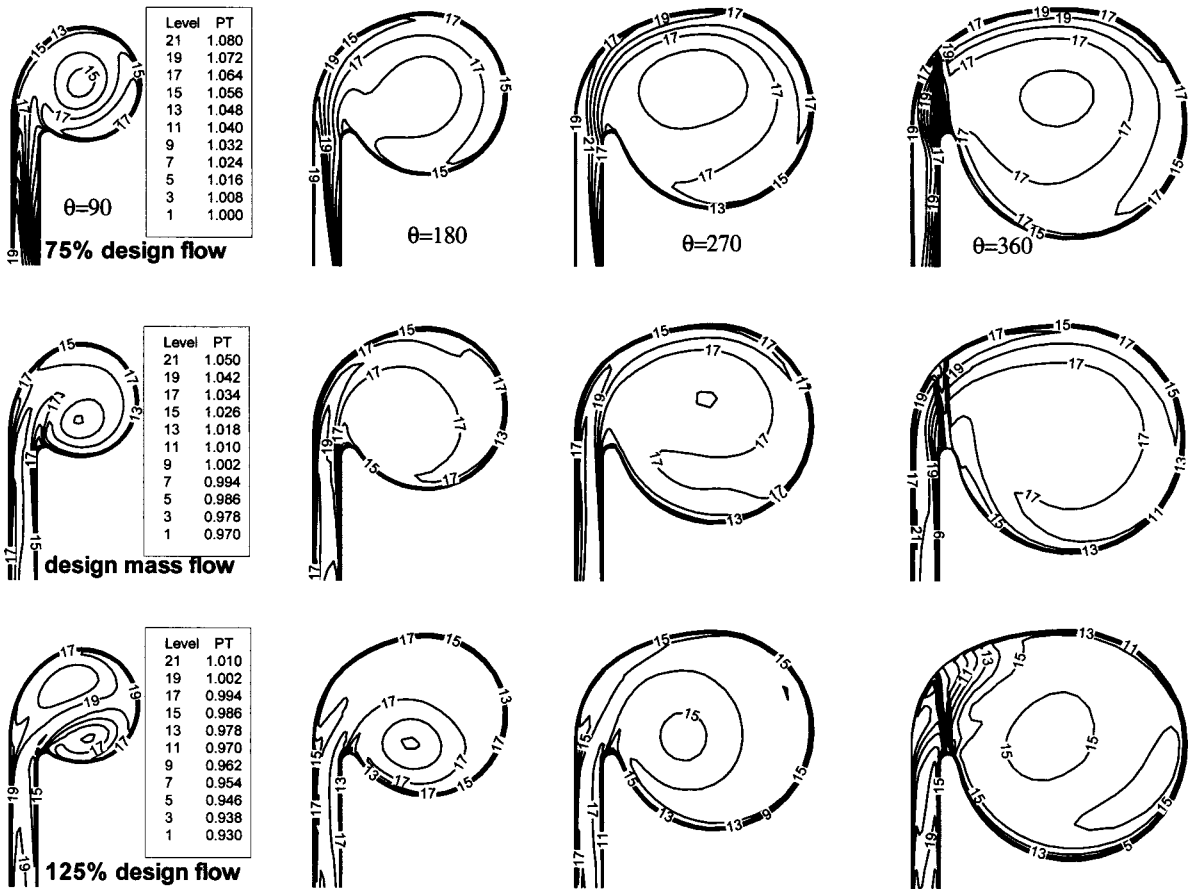

Fig. 10 Contours of total pressure

mass flow. At lower mass flow, the exit radial velocity distribution shows that the thicker boundary layer on the hub wall has merged with the thinner boundary layer on the shroud wall. At the higher mass flow, the radial velocity distribution also shows that the boundary layers have merged with a thicker boundary layer on the shroud wall. It therefore can be inferred that the asymmetrical distortion at the inlet accelerates the development and merge of the boundary layers.

For all the mass flow rates, the inlet tangential velocity (Fig. 7c) shows an identical distribution with higher velocity on the shroud side. At the exit the velocity distribution tendency remains, but the shroud side shows more velocity reduction for both design and higher mass flow rates. The total pressure distribution (Fig. 7d) confirms that higher total pressure losses occur on the shroud side at these two flow rates. This is due to the fact that the inflow is more tangential at these two mass flow rates, resulting in longer flow path inside the vaneless diffuser. This mechanism also applies to the flow at the lower mass rate where the inflow is more tangential over the vaneless diffuser width.

Flow in Volute. The different inflow patterns result in different flow structures in the volute, even though the variation of the inlet patterns is influenced by the volute itself. The flow field from the CFD analysis is presented in terms of surface vectors (Fig. 8), static pressure contours (Fig. 9), and total pressure contours (Fig. 10) on selected sections. The flows in the vaneless diffuser are also shown together.

Figure 8 shows that at all mass flows the flows from the diffuser are turned from radial direction to horizontal in the 90 degree bend. The swirling flow exists over all the sections. It indicates that the inlet meridional velocity component is not totally lost; it creates the swirling flow in the volute. At the design point from section $\theta=90$ deg to $\theta=360$ deg the flow shows a typical forced vortex flow pattern of clockwise rotation in the core. A narrow shell of free vortex flow also can be seen on the wall on section $\theta=90$ deg and $\theta=180$ deg. A mechanism will be proposed later to explain the pattern differences of the swirling flow. Of interest is that the center of the forced vortex does not move in one consistent radial direction as the flow travels from $\theta=90$ deg to $\theta=360$ deg, which results from the irregular variation of the centroid radius of the volute (Fig. 3). The flow pattern at the lower mass flow rate is similar to that at the design mass flow, but no free vortex region can be spotted on the wall. The higher mass flow pattern differs from the others in the twin opposite rotating vortices on the first two sections. The clockwise rotating vortex initially occupies a small region; then as it goes downstream, its size grows. The counter-clockwise rotating vortex initially takes almost half the area at section $\theta=90$ deg, then it gradually disappears, and a free vortex zone appears on the periphery of the forced vortex. The production and diffusion of the counter clockwise vortex are believed to be additional sources that causes the volute loss to increase at higher mass flow.

The common feature of the static pressure distribution (Fig. 9) at all the mass flow rates is that the contour curves align in axial direction and become more radial at section of $\theta=360$ deg. The curvature of the volute channel produces a radial pressure gradient, which makes the contour horizontal. The swirling flow creates a pressure gradient centered at the vortex core. As the flow approaches the exit, volute channel curvature becomes smaller; the pressure gradient by this curvature is therefore weakened. The pressure gradient from the sectional swirling exhibits more power in shaping the contours, resulting in the change of the contour orientation. As the mass flow increases, the change of the contour orientation is reduced. It means that the pressure gradient from the

volute passage curvature is still strong enough to shape the pressure contours due to the increased through flow velocity.

The total pressure contours (Fig. 10) shows that the low total pressure zone occurs in the sections of small azimuth angles (θ=90 deg), indicating that the total pressure loss mostly happens in the small area sections immediately downstream of the tongue. For the higher mass flow, two low total pressure zones can be found at section θ=90 deg, corresponding to the twin vortices. The high loss region remains at section θ=180 deg and θ=270 deg. It means the fluids coming from the twin vortex have lost their swirling energy and accumulated in the center of swirling flow vortex. The reason for the increase of loss at lower mass flow will be investigated.

Swirling flow models. The different swirling flow patterns (single versus twin vortices, free vortex versus forced vortex) are now being further investigated using streamlines. Figure 11 shows the streamlines starting from section θ=250 deg and θ=335 deg (section D) at the three mass flow rates. Because the streamlines from section θ=335 deg will go through the critical surface (tongue section), they will be investigated in detail. Thereafter, streamlines refer to these from section θ=335 deg, unless indicated otherwise.

At design mass flow, the streamline pattern (Fig. 11a) can be summarized as:

- Streamlines on the hub side (blue) go into the volute first and fill the center region of section A while rotating at high frequency. They compose the forced vortex.
- Streamlines on the shroud side (red) go into the volute later, and rotate at larger radii and at lower rotate frequencies. They compose the free vortex.
- After they travel 360 deg, the streamlines from the hub side go closer to the forced vortex center; these from the shroud side have been entrained into the forced vortex. The streamlines from θ=250 deg (yellow) rotate around these from θ=335 deg.
- By comparing the relative positions of streamlines from shroud side on section B and C, it can be seen that some of the streamlines rotate counter-clockwise (from section B to C, they are supposed to go farther away from the shroud wall in the axial direction if they rotate clockwise).
- The streamlines at lower flow (Fig. 11b) are described as:
- Since the inflow is axially distorted, the streamlines are twisted in the vaneless diffuser, resulting in the streamlines on the shroud side going into volute first. But all the streamlines (from both hub and shroud sides) rotate at an identical frequency, indicating that the flow is of solid body motion (forced vortex). The only difference between the streamlines is the phase lag.
- The fluids on the shroud side have higher total pressure, or radial velocity, which prevents their streamlines from counter-clockwise rotation (this will be explained).
- The streamlines from θ=250 deg separate into two groups. The shroud side group rotates around the streamlines already in the volute and exits from the volute. The hub side group is of lower total pressure (Fig. 7b) therefore cannot reach the volute under the radial pressure gradient before it arrives at the tongue section. It simply degenerates into recirculation mass, and moves in the center of the forced vortex.

The streamlines at higher mass flow (Fig. 11c) show a rather different pattern (for clarity, the streamlines from θ=250 deg are not plotted), and are described as:

- Streamlines on the hub side go directly into the cone diffuser, resulting in a reduction in mass flow inside the volute. Streamlines on the shroud side go into the volute, rotating in counter-clockwise direction.
- Streamlines from the mid passage follow different paths: the streamline close to the hub exits to the cone; the one close to the shroud side goes into volute; the one at mid goes into volute first, then turns back, goes over the tongue, and exits from the volute.

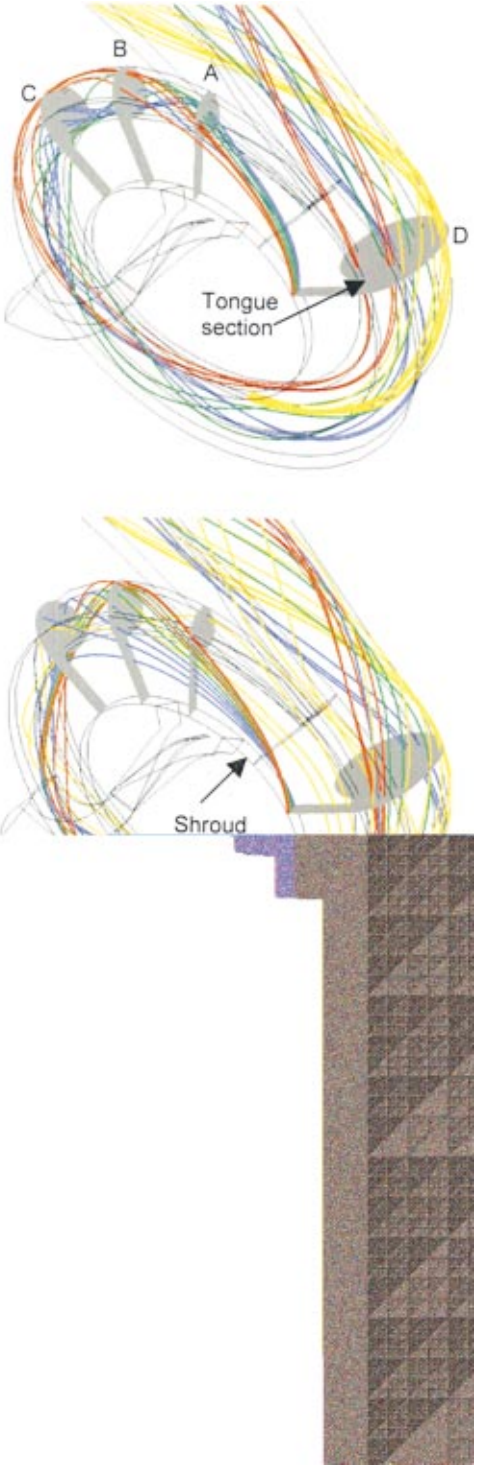

Fig. 11 Streamlines (images are presented in color) design mass flow 75% mass flow 125% mass flow

- After 360 deg, the streamlines going inside the volute are found at larger radius with respect to the forced vortex center. The fluids on these streamlines compose the free vortex flow.

The essence of the observed flow patterns at different mass flow rates is the same as Van den Braembussche's model: new coming fluids rotate around the old ones. However, the new models take into account the axial distortion of vaneless diffuser inflow. At design and higher mass flows, the hub side streamlines from section θ=335 deg start the opposite rotation downstream of the

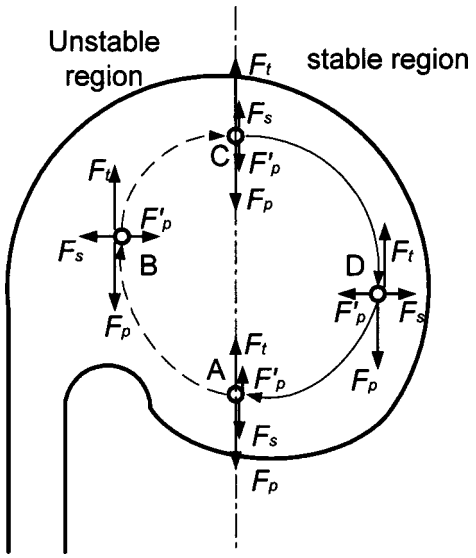

Fig. 12 Force analysis

tongue, then develop into free vortex flow, and at last are entrained into the forced vortex. Because of the opposite rotation, the counter-clockwise rotating streamline suffers more energy losses. This explains why the loss is increased at higher mass flow. Recirculations are found at the lower mass flow: the flow in the volute does not exit, instead, it turns into the volute again. This explains why the loss is increased at lower mass flow.

Figure 12 explains the generation of the opposite rotation vortex using force analysis on the section A downstream of the tongue. The fluid particle is balanced under the act of centrifugal forces and pressure gradient forces

$$\vec{F}_p+\vec{F}'_p+\vec{F}_t+\vec{F}_s=0 \tag{4}$$

Here, $\vec{F}_t,\vec{F}_s$ are the centrifugal forces due to the through flow and the swirling flow. $\vec{F}_p,\vec{F}'_p$are the force due to the pressure gradients caused by the through flow and swirling flow, respectively. Because of the pressure gradient from the through flow, which is guided by the volute channel, a particle moves from A to B to C will be decelerated, and from C to D to A will be accelerated. If the particle does not possess enough through flow velocity or if its path is of high radius of curvature than that of the volute passage, its centrifugal force is reduced; thus, it can be retarded or turned back when moving along the path A-B-C. Therefore, for the fluid particles, the left side of the volute is an unstable region, the upper left region being the most unstable one.

At lower mass flow, the particle from the shroud side possesses higher radial velocity (Fig. 7d); it is therefore strong enough to go through the adverse pressure gradient region. This is why no opposite rotation happens at this flow rate. On the contrary, at design and higher mass flows, the particle from the shroud side possesses lower radial velocity (Fig. 7d). Under the adverse pressure gradient, the heavily retarded particle will be pulled tangentially by the inner particle of forced vortex flow, resulting in the free vortex flow on the wall. The particles that are turned back by the adverse radial pressure gradient compose the opposite rotation flow. This is the generation of the twin vortex structure.

Conclusions

A numerical investigation of the flow structure inside the stationary components of a centrifugal compressor is performed in this paper. The following conclusions have been reached:

- The losses in the vaneless diffuser and volute make the compressor efficiency drop by 7.25% at design mass flow and by up to 10.40% at lower mass low. At lower and design mass flows the losses in the vaneless diffuser account for more than 3/5, while at higher mass flow, the volute losses take more than 3/5 of the total loss in the stationary components.
- The inlet distortion of the vaneless diffuser accelerates the development and merge of the boundary layers on the diffuser walls.
- In the volute, the flow basically follows Van den Braembussche's model. A new model is proposed to take into account the axial distortion at the vaneless diffuser inlet. At lower mass flow, the lower total pressure fluids from the hub side upstream of the tongue cannot exit the volute. Instead, they move into the force vortex center, resulting in recirculation. At higher mass flow, a twin vortex structure is found downstream of the tongue. The recirculation and the twin vortex structure are attributed to the increase of total pressure losses at off-design conditions.

Acknowledgments

The authors would like to thank Solar Turbines Incorporated for the permission to publish this paper.

Nomenclature

A = area
AR = area ratio, $\mathrm{AR}=A_7/A_5$
b = passage width
C_p = specific heat at constant pressure
c_f = skin friction coefficient
c_p = pressure recovery, $c_{p,i-j}=p_i-p_j/p_{0j}-p_j$
D = diameter
F = force
k = specific heat ratio, constant
p = pressure
Q = volume flow rate
R = radius from the machine axis
Re = Reynolds number
r = radius from the volute section center
$\overline{r}$ = centroid radius of the volute section, $\overline{r}=\int RdA/\int dA$
T = temperature
U = blade speed
u_τ = wall-friction velocity
V = velocity
Y^+ = nondimensional distance to the wall, $y^+=yu_\tau/\nu$
Z = axial direction
α = flow angle from radial
Φ = flow coefficient, $\Phi=Q_0/\frac{\pi}{4}\times D_{tip}^2\times U_{tip}$
Λ,Λ_0 = resistance coefficient
λ = swirling factor
η = efficiency, $\eta_{isen,t-t,i-j}=(p_{0i}/p_{0j})^{k-1/k}-1/T_{0i}/T_{0j}-1$
ν = kinematic viscosity
θ = angle of volute section
ω = total pressure loss coefficient, $\omega_{i-j}=p_{0j}-p_{0i}/p_{0j}-p_j$
Ψ = isentropic head coefficient, $\Psi=2C_pT_{00}((p_{08}/p_{00})^{(k-1))/k}-1)/U_{tip}^2$

Subscripts

i,j = index of station
isen = isentropic
p = pressure
r = radial
ref = reference condition
t-t = total-to-total
tip = tip of the impeller
0 = stagnation, inlet flange
1 = inlet of impeller
2 = exit of impeller
3 = inlet of diffuser
4 = grid interface between impeller and diffuser
5 = diffuser exit

7 = critical surface, $\theta=0$
8 = exit flange of the compressor

Appendix A: Derive of Friction Loss in Curved Pipe

Schlichting ([14] p. 627) cited White's work, giving the resistance coefficient for turbulent flow in a curved pipe

$$\frac{\Lambda}{\Lambda_0}=1+0.075\mathrm{Re}^{1/4}\left(\frac{r_7}{R_5}\right)^{1/2}$$

Λ_0 is calculated from Prandtl's universal law of friction for smooth pipes (p. 611)

$$\frac{1}{\sqrt{\Lambda_0}}=2.0\log(\mathrm{Re}\Lambda_0)-0.8$$

Here Re is the Reynolds number, defined as $\mathrm{Re}=\rho V_7 d_7/\mu$. The friction loss is calculated from $\Delta p=\Lambda L/d_7 1/2\rho V_7^2$. L is approximated as the periphery of the vaneless diffuser exit, $L=2\pi R_5$, for the volute of constant centroid radius, which is equal to the radius of the vaneless diffuser exit, R_5. The pressure loss coefficient is defined as $\omega_{7-5}=\Delta p/\frac{1}{2}\rho V_5^2$. The volute inlet velocity is related with the swirling factor $\lambda=\tan(\alpha_5)$ by $V_5=V_{5r}\sqrt{\lambda^2+1}$. From mass continuity, $V_{5r}A_5=V_7A_7$, the velocity ratio is related with the area ratio by $V_7/V_{5r}=A_5/A_7=1/\mathrm{AR}$.

Eventually, the pressure loss coefficient due to friction is calculated as

$$\omega_{7-5}=\pi\Lambda\frac{R_5}{r_7}\frac{1}{(\mathrm{AR})^2}\frac{1}{\lambda^2+1}$$

References

[1] Van den Braembussche, R. A., and Hande, B. M., 1990, ''Experimental and Theoretical Study of the Swirling Flow in Centrifugal Compressor Volutes,'' ASME J. Turbomach. **112**, pp. 38–43.

[2] Ayder, E., Van den Braembussche, R., and Brasz, J. J., 1993, ''Experimental and Theoretical Analysis of the Flow in a Centrifugal Compressor Volute,'' ASME J. Turbomach. **115**, pp. 582–589.

[3] Ayder, E., and Van den Braembussche, R., 1994, ''Numerical Analysis of the Three-dimensional Swirling Flow in Centrifugal Compressor Volutes,'' ASME J. Turbomach. **116**, pp. 462–468.

[4] Hagelstein, D., Hillewaert, K., Van den Braembussche, R. A., Engeda, A., Keiper, R., and Rautenberg M., 1999, ''Experimental and Numerical Investigation of the Flow in a Centrifugal Compressor Volute,'' ASME 99-GT-79.

[5] Hagelstein, D., Van den Braembussche, R. A., Keiper, R., and Rautenberg M., 1997, ''Experimental Investigation of the Circumferential Static Pressure Distortion in Centrifugal Gas Compressor Stages,'' ASME Paper No. 97- GT-50.

[6] Flathers, M. B., and Bache, G. E., 1999, ''Aerodynamically Induced Radial Forces in a Centrifugal Gas Compressor: Part 2 - Computational Investigation,'' ASME J. Eng. Gas Turbines Power **121**, pp. 725–734.

[7] Sorokes, J. M., Borokes, C., and Koch, J. M., 1998, ''Investigation of the Circumferential Static Pressure Non-Uniformity Caused by a Centrifugal Compressor discharge Volute,'' ASME Paper No. 98-GT-326.

[8] Hillewaert, K., and Van den Braembussche, R. A., 1999, ''Numerical Simulation of Impeller-Volute Interaction in Centrifugal Compressors,'' ASME J. Turbomach. **121**, pp. 603–608.

[9] Flathers, M. B., Bache, G. E., and Rautensberger, R., 1994, ''An Experimental and Computational Investigation of Flow in a Radial Inlet of An Industrial Pipeline Centrifugal Compressor,'' ASME Paper No. 94-GT-134.

[10] Lakshminarayana, B., 1991, ''An Assessment of Computational Fluid Dynamics Techniques in the Analysis and Design of Turbomachinery,'' ASME J. Fluids Eng. **113**, pp. 315–352.

[11] Galpin, P. F., Broberg, R. B., and Hutchinson, B. R., 1995, ''Three-Dimensional Navier Stokes Predictions of Steady State Rotor/Stator Interaction with Pitch Change,'' CFD 95 - CFD Society of Canada, Banff, Alberta, Canada.

[12] Stanitz, J., 1952, ''One Dimensional Compressible Flow in Vaneless Diffusers of Radial and Mixed Flow Compressors Including Effects of Friction, Heat Transfer and Area Change,'' NACA TN 2610.

[13] Japikse, D., 1996, ''Centrifugal Compressor Design and Performance,'' Concepts ETI Inc.

[14] Schlichting, H., 1979, *Boundary-Layer Theory*, McGraw-Hill, Seventh Edition, NY.

[15] Japikse, D. and Baines, N, 1998, ''Diffuser Design Technology,'' Concepts ETI Inc.

[16] Senoo, Y., Kinoshita, Y., 1977, ''Influence of Inlet Flow Conditions and Geometries of Centifugal Vaneless Diffusers on Critical Flow Angle for Reverse Flow,'' ASME J. Fluids Eng. **99**, pp. 98–103.

Numerical Investigation of Swirling Flow in Annular Diffusers With a Rotating Hub Installed at the Exit of Hydraulic Machines

A. N. Kochevsky
Junior Scientist,
Department of Fluid Mechanics,
Sumy State University, 40007,
Rimsky-Korsakov str., 2, Sumy, Ukraine

A single sweep method for the solution of Navier-Stokes equations is used for numerical investigation of flow in annular diffusers formed by a cylindrical casing and a converging conical hub, with the presence of inlet swirl and/or hub rotation. It is shown that counter-swirlwise hub rotation prevents reverse flow from appearing. The paper discusses the efficiency characteristics of diffusers installed at the exit of hydraulic machines. It is shown that the energy losses in a diffuser and in a channel behind the diffuser become minimal in the presence of small inlet swirl in the opposite direction to hub rotation.
[DOI: 10.1115/1.1385384]

Introduction

Annular diffusers, including those with a rotating hub, are widely used in engineering, in particular, as outlet devices of pumps and turbines. In this case, the swirl intensity at the diffuser inlet, as a rule, is close to minimal value at the nominal capacity and increases as the capacity increases or decreases. When the diffuser hub rotates together with the rotor and the capacity is above nominal, the main flow is swirled in the opposite direction to hub rotation. The diffuser is designed so that the flow within it has minimal energy loss and is therefore nonseparating within the operating range of a hydraulic machine. As the systematic experimental data on the coefficient of energy losses for a wide range of geometrical parameters and swirl intensities are absent, it makes sense to investigate this flow numerically. For this purpose we applied an appropriate calculation technique and conducted a comparison of results obtained from experimental data in which the physical effects inherent to these flows are clearly expressed. The satisfactory correspondence of results as well as the analysis of influence of separate terms in the momentum equations upon the velocity distribution makes it possible to predict the flow pattern under the simultaneous display of these effects.

To date, rather few papers are devoted to explorations of swirling flows in annular diffusers. Howard et al. [1] performed experimental research of flow in diffusers with a cylindrical hub and showed the dependence of the pressure recovery coefficient on internal angle, area ratio and swirl intensity. Small area ratios and a strong decrease of hub radius downstream are often inherent to diffusers used as outlet devices of hydraulic machines. The flows in such diffusers were investigated by Kanemoto et al. [2] and Ji-jun et al. [3]. Lohmann et al. [4] found out the effectiveness of diffusers with different area ratios and different angles of inner and outer wall. Agrawal et al. [5] and Singh et al. [6] explored the swirling flow in channels with diverging inner and outer walls, including a case of rotating the inner wall in the direction of swirl.

The universal scheme for calculating the strongly swirling flows is TEACH [7]. The finite difference methods for solving the Navier–Stokes equations with reference to swirling flows in diffusers are elaborated by Armfield. An assumption of the multi-sweep scheme [8] is the dependence of velocity in each point of flow only on upstream conditions. According to this scheme, the velocity components are calculated as a result of iterated sweeps from inlet to outlet section, while the elliptic equation is solved only to calculate pressure corrections. By discarding the highest order terms in the Navier–Stokes equations, the system of these equations becomes parabolic. That provides the possibility to calculate the flow by a single sweep in the flow direction [9]. One more widely used approach is to divide the region of flow into the inviscid core and the boundary layer [3], but the calculation technique in this case becomes too complex. When the flow is assumed to be inviscid in the whole region [10], it allows the determination of the separation point but doesn't allow for the influence of a rotating hub and doesn't allow the calculation of energy losses.

In this research, we give preference to a single sweep method due to its simplicity and its ability to take into account the hub rotation and related physical effects. More exact results may be obtained by applying the complete Reynolds equations [11]. However, in this paper, we ignore lesser factors affecting the flow, in order to clarify the main physical effects that determine the flow pattern. For the same reason we use the algebraic eddy viscosity model, though for swirling flows it yields less exact results than more complex models [12].

Mathematical Model

The results presented below are obtained using the single-sweep scheme similar to one described in [9]. The main difference is found in the equations in the curvilinear coordinate system, in order to calculate axisymmetrical flows in annular diffusers with arbitrary wall shape. After discarding the highest order terms the Reynolds equations and the continuity equation are as follows:

$$\frac{u}{H_1}\frac{\partial u}{\partial q_1}+\frac{v}{H_2}\frac{\partial u}{\partial q_2}-\frac{w^2}{H_1H_3}\frac{\partial H_3}{\partial q_1}+\frac{1}{H_2}\frac{\partial(\overline{u'v'})}{\partial q_2}+\frac{(\overline{u'v'})}{H_1^2H_2H_3}\frac{\partial(H_1^2H_3)}{\partial q_2}=-\frac{1}{H_1}\frac{\partial p}{\partial q_1}+\frac{1}{\mathrm{Re}}\left(\frac{1}{H_2^2}\frac{\partial^2 u}{\partial q_2^2}+\frac{1}{H_1H_2H_3}\frac{\partial u}{\partial q_2}\frac{\partial(H_1H_3/H_2)}{\partial q_2}\right); \tag{1}$$

$$\frac{\partial p_r}{\partial q_2}=\frac{w^2}{H_3}\frac{\partial H_3}{\partial q_2}; \tag{2}$$

Contributed by the Fluids Engineering Division for publication in the JOURNAL OF FLUIDS ENGINEERING. Manuscript received by the Fluids Engineering Division November 21, 2000; revised manuscript received May 10, 2001. Associate Editor: Y. Tsujimoto

$$\frac{u}{H_1}\frac{\partial w}{\partial q_1}+\frac{v}{H_2}\frac{\partial w}{\partial q_2}+\frac{uw}{H_1H_3}\frac{\partial H_3}{\partial q_1}+\frac{vw}{H_2H_3}\frac{\partial H_3}{\partial q_2}+\frac{1}{H_2}\frac{\partial(\overline{v'w'})}{\partial q_2}+\frac{(\overline{v'w'})}{H_1H_2H_3^2}\frac{\partial(H_1H_3^2)}{\partial q_2}=\frac{1}{\mathrm{Re}}\left(\frac{1}{H_2^2}\frac{\partial^2 w}{\partial q_2^2}+\frac{1}{H_1H_2H_3}\frac{\partial w}{\partial q_2}\frac{\partial(H_1H_3/H_2)}{\partial q_2}+\frac{w}{H_1H_2}\frac{\partial}{\partial q_2}\left(\frac{H_1}{H_2H_3}\frac{\partial H_3}{\partial q_2}\right)\right); \tag{3}$$

$$\frac{1}{H_1H_2H_3}\left(u\frac{\partial(H_2H_3)}{\partial q_1}+v\frac{\partial(H_3H_1)}{\partial q_2}\right)+\frac{1}{H_1}\frac{\partial u}{\partial q_1}+\frac{1}{H_2}\frac{\partial v}{\partial q_2}=0. \tag{4}$$

The system of equations is closed by the condition of constant flow rate:

$$\int_0^{Q_2} uH_2H_3\,dq_2=\mathrm{const}, \tag{5}$$

where Q_2 is the coordinate q_2 at the casing wall.

The turbulent terms are modeled using the Boussinesq approximation:

$$\overline{u'v'}=-\frac{1}{\mathrm{Re}}\frac{\nu_x}{\nu}\frac{1}{H_2}\frac{\partial u}{\partial q_2},$$

$$\overline{v'w'}=\frac{1}{\mathrm{Re}}\frac{\nu_\phi}{\nu}\left(-\frac{1}{H_2}\frac{\partial w}{\partial q_2}+\frac{\partial H_3}{\partial q_2}\frac{w}{H_2H_3}\right).$$

In the given research we use the algebraic eddy viscosity model suggested in [13] and generalized for the calculation of swirling flow in [14]. According to this model the algebraic eddy viscosity in the core region is calculated by the Clauser formula, and in the near casing wall region the following formulas are used:

$$\frac{1}{\mathrm{Re}}\frac{\nu_x}{\nu}=\frac{r}{R}l_x^2\left[\left(\frac{1}{H_2}\frac{\partial u}{\partial q_2}\right)^2+\frac{1}{\sigma}\left(-\frac{1}{H_2}\frac{\partial w}{\partial q_2}+\frac{\partial H_3}{\partial q_2}\frac{w}{H_2H_3}\right)^2\right]^{1/2}, \tag{6}$$

$$\frac{1}{\mathrm{Re}}\frac{\nu_\phi}{\nu}=\frac{r}{R}l_\phi^2\left[\left(\frac{1}{H_2}\frac{\partial u}{\partial q_2}\right)^2+\frac{1}{\sigma}\left(-\frac{1}{H_2}\frac{\partial w}{\partial q_2}+\frac{\partial H_3}{\partial q_2}\frac{w}{H_2H_3}\right)^2\right]^{1/2}, \tag{7}$$

where l_x, l_ϕ are the mixing lengths in the longitudinal and circumferential direction, $\sigma=\nu_x/\nu_\phi$. The formulas, for the near hub wall region are similar.

Calculation Technique

The domain is swept in the q_1 direction. At each step in this direction the w momentum Eq. (3) is calculated to obtain the circumferential velocity and Eq. (2) is calculated to obtain the radial pressure correction as it is done in [9]. However, the way of calculating the axial pressure gradient used in that paper is only acceptable for the calculation of nonseparating flows. Further steps of the algorithm are fulfilled according to [15], where a technique for calculating nonswirling separating flows is suggested.

In the regions of separation the term $u\partial u/(H_1\partial q_1)$ is expressed according to the Flügge–Lotz approximation:

$$\frac{u}{H_1}\frac{\partial u}{\partial q_1}=C\frac{|u|}{H_1}\frac{\partial u}{\partial q_1}, \tag{8}$$

where C is zero or a small positive constant.

Besides, the convective terms are discretized using the Newton linearization with the coupled solution of continuity {Eq. (4)} and u-momentum {Eq. (1)}. It is convenient to introduce the stream function ψ as follows:

$$uH_2H_3=-\frac{\partial\psi}{\partial q_2};\quad vH_3H_1=\frac{\partial\psi}{\partial q_1}.$$

Then the algebraic formulation of finite difference analogues of (1) and (4) is recorded in the following way:

$$\psi_{j-1}^{n+1}-\psi_j^{n+1}+b_j(u_{j-1}^{n+1}+u_j^{n+1})=0, \tag{9}$$

$$B_ju_{j-1}^{n+1}+D_ju_j^{n+1}+A_ju_{j+1}^{n+1}+E_j\psi_j^{n+1}=H_j\chi^{n+1}+C_j, \tag{10}$$

where $b_j, A_j, B_j, C_j, D_j, E_j, H_j$ are known coefficients; $n+1$ is the number of a current calculation layer; and j is the number of a node in transverse direction.

The system of Eqs. (9) and (10) has the block tridiagonal matrix with the blocks of 2×2 elements. Besides, the unknown parameter χ^{n+1} connected with the axial pressure gradient lies beyond the diagonal. The ad hoc algorithm for solving this matrix with minimal computational expenses is suggested in [15].

Results

Swirling Flow in Channels With a Nonrotating Hub. For a comparison of results we use the results of the experimental research of velocity field in diffusers with different internal angles and different swirl intensity [2]. The scheme of flow is presented in Fig. 1. The convergent angle of hubs were $2\alpha=16$, 24, and 36 deg, the Reynolds number was about 100,000. The inlet swirl was generated by guide vanes, and the swirl intensity was characterized by the angle of vanes setting β.

The inlet section is assumed at $x/H=0$, and the exit section at $x/H=14$. In order to secure the grid independent results here we use computational grids with 101 nodes in the radial direction. The steps increase in geometric progression while moving away from the casing and from the hub. The radial steps at the walls are about 0.001 of the inlet diameter. The axial step gradually increases from 0.01 of a diameter at the inlet to 0.05 of a diameter at the exit.

In the nonswirling flow the boundary layer thickness along the hub wall increases faster than that along the casing wall, and the flow separates just at the hub wall. Figure 2 shows the velocity distributions in the nonswirling flow and Figs. 3 and 4 those in the swirling flow. The radius of flow lines decreases downstream. The circumferential velocity increases downstream according to Eq. (3), and its distribution changes to a free vortex pattern. As the channel diverges, the pressure along the casing wall increases, but the pressure difference between the casing and hub walls also increases according to Eq. (2). As a result the pressure along the hub wall decreases downstream. Figure 5 shows calculated isolines of the nondimensional pressure $(p-p_1)/\rho U_0^2$, where U_0 is the maximal longitudinal velocity at the inlet section, and p_1 is the diffuser inlet pressure at the casing wall.

It may be noted that Eq. (1) has the following differences in comparison with the nonswirling flow:

- taking into account Eq. (2), the axial pressure gradient $\partial p/\partial q_1$ becomes nonconstant through a section;
- the term $(w^2\partial H_3)/(H_1H_3\partial q_1)$ appears, and its value increases

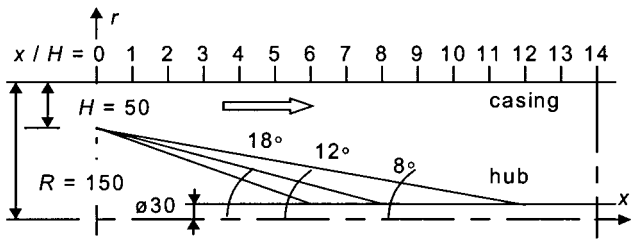

Fig. 1 Scheme of flow

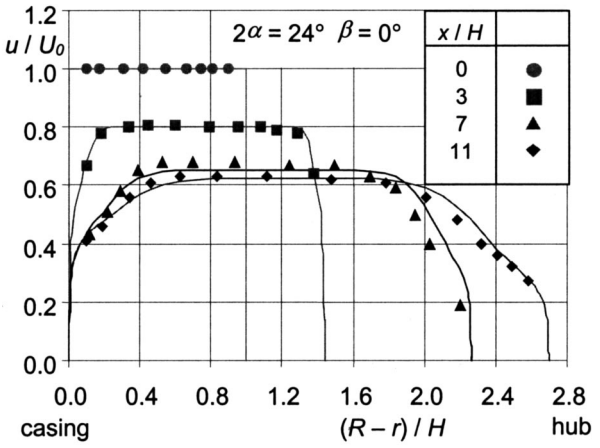

Fig. 2 Axial velocity distribution in the non-swirling flow

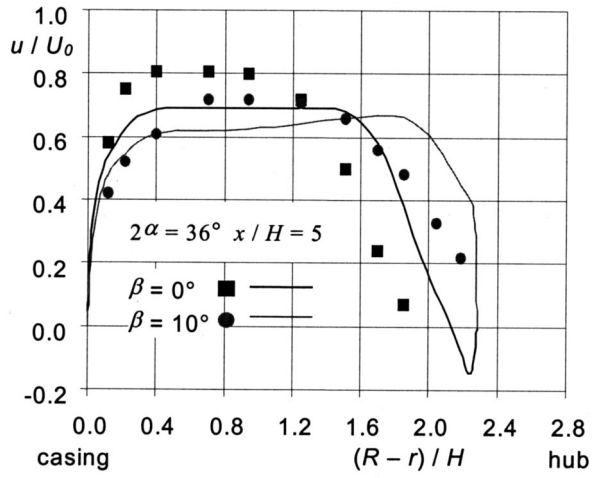

Fig. 3 Axial velocity distribution in the swirling flow

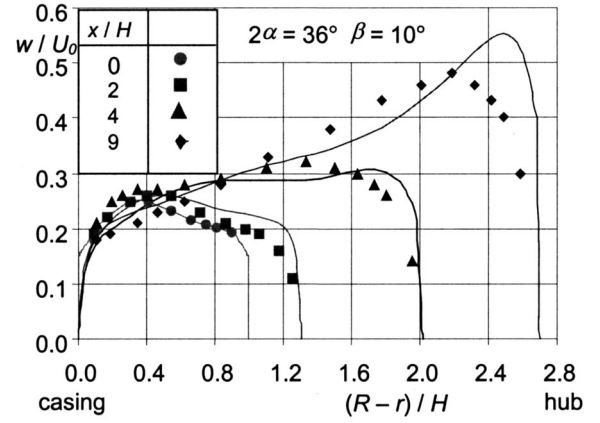

Fig. 4 Circumferential velocity distribution in the swirling flow

along with the increase of circumferential velocity and the increase of angle of flow lines inclination;

- according to Eq. (6), the algebraic eddy viscosity ν_x starts to depend on circumferential velocity.

The uneven distribution of the axial pressure gradient deforms the longitudinal velocity distribution according to Eq. (1), pressing it to the hub. As the swirl decays along the cylindrical section, the axial pressure gradient reaches its maximal value near the

$2\alpha = 36° \quad \beta = 10°$

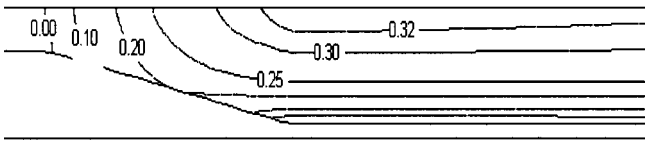

Fig. 5 Pressure isolines in the swirling flow

channel axis, pressing the longitudinal velocity distribution to the casing. When the swirl intensity is large enough, the reverse flow appears in the near axis region. Additionally, when the swirl intensity is still larger, the term $(w^2\partial H_3)/(H_1H_3\partial q_1)$ in Eq. (1) becomes large enough to cause the flow separation well before the start of the cylindrical section.

As one can see, this calculation technique allows the calculation of the flow pattern with sufficient accuracy until the appearance of reverse flow, though in a region of strong swirl the results are not very satisfactory. In should be mentioned that the near hub separation (Fig. 3) was successfully calculated by applying the Flügge-Lotz approximation, Eq. (8).

Nonswirling Flow in Channels With a Rotating Hub. Parr [16] carried out measurements in the flow along a rotating spinner inside a wind tunnel. The spinner radius decreased downstream. The most significant parameter affecting the flow pattern is the rotation parameter θ. This parameter varied from 0–4. The Reynolds number calculated by the inlet spinner radius was about 600,000 and had a weak influence upon the flow pattern.

The most important question in Parr's experiments was the position of the separation point. Figure 6 shows the scheme of flow as well as the experimental and computational results. Separation takes place at the whole range of rotational speed. According to calculations, and the experiments of Kanemoto et al. [2], there is no separation when a hub does not rotate and when the angle at the hub vertex is small enough. In Parr's experiments, with zero rotational speed the separation evidently took place due to a too blunt hub vertex. As can be seen in Fig. 6, the point of separation first moves downstream while θ increases to 1–1.5, and then reverses to move upstream again while θ continues to increase further.

Such complicated behavior of the separation point may be explained by analyzing the influence of different terms in Eq. (1) on the distribution of longitudinal velocity. As the flow moves downstream, the hub forces the nearest shears of fluid to rotate. The uneven distribution of the axial pressure gradient assists in pressing the flow toward the hub; however, the term $(w^2\partial H_3)/(H_1H_3\partial q_1)$ has a predominant influence upon the position of the separation point, and it advances the separation. The movement of the separation point downstream when $\theta=1$ is explained by an increase of the turbulent friction. The eddy viscosity increases together with the circumferential velocity according to Eq. (6). In order to confirm this, the flow was calculated without taking into account the terms in Eq. (6) that depend on the circumferential velocity:

$$\frac{1}{\mathrm{Re}}\frac{\nu_x}{\nu} = \frac{r}{R}l_x^2\left|\frac{1}{H_2}\frac{\partial u}{\partial q_2}\right|. \tag{11}$$

As Fig. 6 shows, there would be no movement of the separation point downstream in this case. As the rotation parameter increases further, the term $(w^2\partial H_3)/(H_1H_3\partial q_1)$ strongly increases, and that presses the flow from the hub and leads to flow separation. As one can see, the results obtained using the single - sweep scheme are in good agreement with the experimental data.

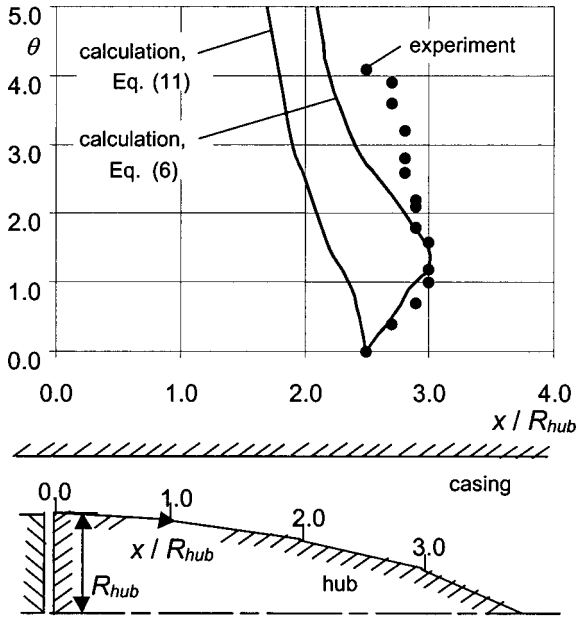

Fig. 6 Dependence of separation point position on the rotation parameter of the spinner

Swirling Flow in Channels With a Rotating Hub. The influence of hub rotation upon the swirling flow is investigated numerically. The flow in a channel of the same configuration as in Kanemoto's experiments [2] is calculated as an example (see Fig. 1). The angle at the hub vertex is 24 deg. The results of the calculations are demonstrated in the figures below.

Figure 7 shows the circumferential velocity distributions in a section near the hub vertex at different hub rotational speeds. When the hub does not rotate, the velocity field is typical for a free vortex pattern. A sharp velocity peak is observed near the hub wall. As one can see, this peak increases together with the rotational speed in the direction of the swirl. An increase in the swirl intensity accelerates the appearance of the reverse flow in the cylindrical section behind the hub.

As the hub rotates in the direction opposite of the swirl of the flow, the velocity peak near the hub is restrained. As the hub rotation ratio increases, the swirl intensity at the diffuser inlet can be increased proportionately without causing a separation of the flow. Figure 8 shows the range of swirl intensity at the diffuser inlet and the hub rotation parameters that allow flow without separation through the entire channel.

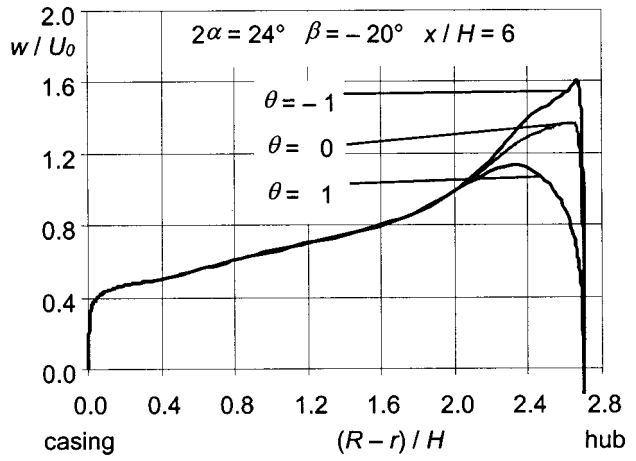

Fig. 7 Influence of the hub rotation upon the circumferential velocity distribution

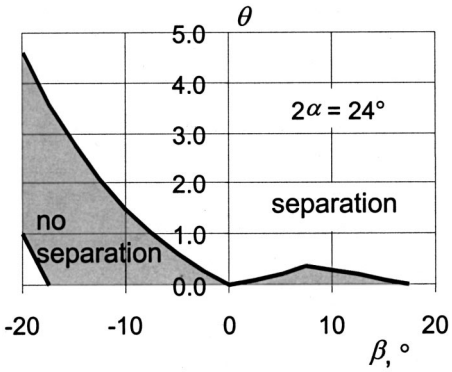

Fig. 8 Range of modes of non-separating flow

When a shaft rotates in the direction of the swirl, the reverse flow appears at small rotation parameters. When a shaft rotates in the direction opposite to the swirl, the range of modes of nonseparating flow appears to be much wider. When the rotational speed is large enough, the term $(w^2\partial H_3)/(H_1H_3\partial q_1)$ plays a predominant role, and the flow separates at the beginning of the hub cone, even if the shaft rotates in the direction opposite to the swirl.

Determining the Swirl Intensity at the Diffuser Inlet

In order for a hydraulic machine to have the highest efficiency, its wetted parts should be designed in such a way that the swirl intensity created by guidevanes and an impeller at the diffuser inlet in the operating range leads to the lowest energy losses in the diffuser. The coefficient of energy losses in the diffuser is calculated as follows:

$$\xi=\frac{\int_{S_1}(p+0.5\rho V^2)udS-\int_{S_2}(p+0.5\rho V^2)udS}{\int_{S_1}0.5\rho V^2udS}, \qquad (12)$$

where V is the absolute velocity, S_1 is the inlet section area, and S_2 is the outlet section area.

When a diffuser is installed at the exit of a hydraulic machine, the kinetic energy associated with the swirl at the exit section will be irretrievably lost due to friction in a pipe or a reservoir downstream. In order to estimate this kinetic energy we introduce the coefficient of residual swirl ξ_{SW}, that characterizes the hydraulic losses downstream of the diffuser due to swirl decay:

$$\xi_{SW}=\frac{\int_{S_2}0.5\rho w^2udS}{\int_{S_1}0.5\rho V^2udS}=\frac{\int_{S_2}w^2udS}{\int_{S_1}V^2udS}. \qquad (13)$$

Thus, as a criterion of diffuser effectiveness we can consider the total coefficient of energy losses ξ_{SUM}:

$$\xi_{SUM}=\xi+\xi_{SW}. \qquad (14)$$

This coefficient characterizes the energy losses inevitable in transforming the flow from the diffuser inlet to the state necessary for a customer.

Attention should also be paid to the energy transferred between the rotating hub and the fluid flow. When the flow swirls in the same direction as the hub rotates, and the hub rotation speed exceeds the speed of flow swirl, then the hub imparts to the flow the additional energy. The source of that energy is the external drive. In the opposite case the hub takes the energy from the flow. When

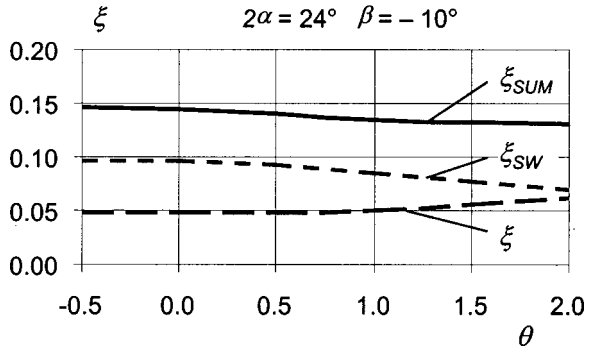

Fig. 9 Influence of hub rotation parameter upon the integral parameters of flow

the fluid flow and the hub rotate in opposite directions, the energy of the flow as well as the mechanical energy of the hub is dissipated. The energy absorbed or lost by the flow due to the hub rotation, strictly speaking, can be also taken into account in Eq. (14), but it goes beyond the present research.

The following results concern a channel of the same configuration as that in Kanemoto's experiments [2] (see Fig. 1), but at a different hub rotation parameter θ. As a rule the parameter θ is predetermined by the design of a hydraulic machine. However, here we consider the dependence of coefficients ξ and ξ_{SW} on the parameter θ under different swirl rates. When the flow at the inlet section does not swirl or swirls in the direction of hub rotation, both the coefficients ξ and ξ_{SW} increase together with the parameter θ, since the hub imparts to the flow additional swirl. When the hub rotates counter-swirlwise and the parameter θ increases, the swirl weakens, and therefore the coefficient ξ_{SW} decreases. The coefficient ξ increases due to an increase in the difference in velocity between the neighboring fluid shears that rotate in opposite directions. Figure 9 shows the typical dependence of the coefficients ξ and ξ_{SW} on the parameter θ.

In the nonswirling flow with a nonrotating hub, the maximal angle at the hub vertex allowing the flow without separation is $2\alpha = 24$ deg. One should note that the small irregular swirl and the increased level of turbulence exist behind the impeller of a hydraulic machine even at the optimal flow rate. The small irregular swirl [17] and the increased level of turbulence [18] restrain the separation, and allow the internal angle of the diffuser to increase a bit. In the swirling flow the separation does not occur even at $2\alpha = 36$ deg. The calculated results are shown only for that range of the angle 2α for which the experimental data are available [2]. The dependence $\xi(2\alpha)$ shown in Fig. 10 for the case $\theta = 1$ does not vary significantly in the range $-0.5 < \theta < 2$. The

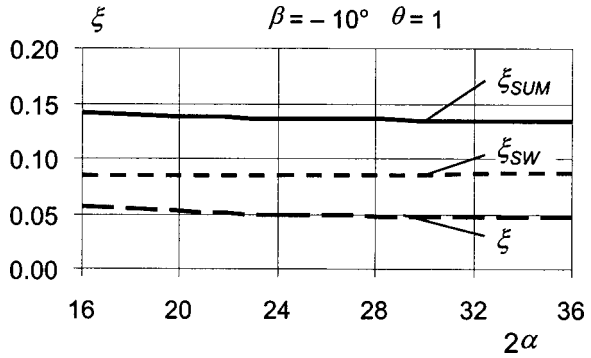

Fig. 10 Influence of angle at the hub vertex upon the integral parameters of flow

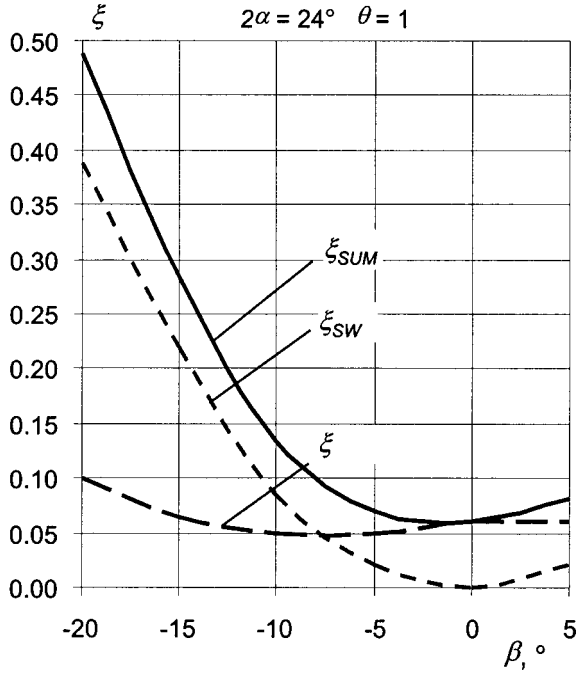

Fig. 11 Influence of swirl intensity upon the integral parameters of flow

coefficient ξ_{SW} at $\theta = 1$ increases slightly as the angle 2α increases, due to reducing the length of the hub that rotates and thus suppresses the swirl of the main flow.

Figure 11 shows the dependence of the coefficient of energy losses in the diffuser and the channel behind the diffuser on the swirl intensity when the rotation parameter $\theta = 1$. The calculation technique used here is useful to calculate only non-separating or weakly separating flows, so the results are presented mostly for a case when the hub rotates opposite to flow swirl. The coefficient ξ reaches a minimum at about $\beta = -8$ deg. According to Fig. 8 this swirl rate corresponds to the appearance of reverse flow in the channel. The coefficient ξ_{SW} has a minimum at $\beta = 0$ deg. Both coefficients ξ and ξ_{SW} increase together with the swirl intensity β in the direction opposite to hub rotation. The coefficient ξ_{SW} increases much more rapidly because only a small part of the swirl decays inside the diffuser, and the greater part of the swirl decays in a channel behind the diffuser. Thus the total coefficient of energy losses ξ_{SUM} reaches a minimum when the hub rotates counter-swirlwise and the swirl intensity β is close to zero. As the parameter θ increases, according to Fig. 8, the coefficient ξ reaches a minimum at larger swirl intensities β. Thus the optimal swirl intensity at the diffuser inlet will evidently increase somewhat.

Conclusions

1 A single-sweep technique of calculating the flow in a channel is realized in curvilinear orthogonal coordinates. It is shown that this technique allows the calculation of, with satisfactory accuracy, the nonseparating and weakly separating axisymmetrical swirling flows in annular channels with a rotating hub, where the radius of flow lines decreases downstream.

2 The hub rotation in the direction of flow swirl increases the intensity of flow swirl and advances the reverse flow. The hub rotation in the opposite direction, on the contrary, decreases the intensity of flow swirl and prevents the flow from reversing.

3 When the hub rotational speed is large enough, the flow separates soon after the beginning of hub converging.

4 The energy losses in the diffuser and in the channel behind the diffuser reach minimal value when the flow at the diffuser inlet is weakly swirling in the direction opposite to hub rotation.

Acknowledgments

The present research was conducted under leadership of Asst. Prof. A. A. Evtushenko and V. G. Nenya and under support of the collective of the department of fluid mechanics.

Nomenclature

u, v, w = longitudinal, transverse and circumferential velocity components
p = $p_l(q_1)+p_r(q_1,q_2,q_3)$-static pressure
ρ = fluid density
q_1, q_2, q_3 = longitudinal, transverse and circumferential coordinates
H_1, H_2, H_3 = Lamé coefficients
ν_x, ν_ϕ = eddy viscosity coefficients in longitudinal and circumferential direction
α = half-angle at the vertex of conical hub
β = angle of blade setting at the channel inlet, the measure of swirl intensity at the inlet section
x = axial coordinate
r = radial coordinate
R = radius of the casing wall
R_{hub} = hub radius
H = channel height at the inlet section
θ = rotation parameter (ratio of circumferential velocity at the hub surface to the average longitudinal velocity at the inlet section)
ξ = coefficient of energy losses in the diffuser
ξ_{SW} = coefficient of energy losses in a channel behind the diffuser
ξ_{SUM} = total coefficient of energy losses

References

[1] Howard, J. H. G. et al., 1967, ASME Paper, 67-WA/FE-21.
[2] Kanemoto, T., Toyokura, T., and Kurokawa, J., 1982, ''Flow in Annular Diffuser,'' 1st Report, Internal Flow and Performance, Bull. JSME, **25**, No. 204, June, pp. 912–918.
[3] Ji-jun, Y., Zhao-gang, Y., and Ming-de, W., 1992, ''On the Throughflow with Swirling Flow in Annular Diffuser,'' Appl. Math. Mech., **13**, No. 3, Shanghai, China, pp. 241–254.
[4] Lohmann, R. P., Markowski, S. J., and Brookman, E. T., 1979, ''Swirling Flow Through Annular Diffusers With Conical Walls,'' ASME J. Fluids Eng., **101**, No. 2, pp. 224–229.
[5] Agrawal, D. P., Singh, S. N., Sapre, R. N., and Malhotra, R. C., 1989, ''Effect of hub rotation on the mean flow of wide angle annular diffusers,'' HYDROTURBO 89, Vol. 1, pp. 231–240, Ostrava.
[6] Singh, S. N., Agrawal, D. P., Sapre, R. N., and Malhotra, R. C., 1994, ''Effect of inlet swirl on the performance of wide-angled annular diffusers,'' Indian Journal of Engineering and Materials Sciences, **1**, pp. 63–69.
[7] Gosman, A. D., and Pun, W. M., 1974, ''Calculation of Recirculation Flows,'' Report HTS/74/2, Department of Mechanical Engineering, Imperial College.
[8] Armfield, S. W., 1987, ''Numerical Simulation of Incompressible Turbulent Swirling Flow in Conical Diffusers,'' Ph.D. thesis, University of Sydney, Australia.
[9] Armfield, S. W., and Fletcher, C. A. J., 1986, ''Numerical simulation of swirling flow in diffusers,'' Int. J. Numer. Methods Fluids, **6**, pp. 541–556.
[10] Clausen, P. D., 1987, ''Measurements and predictions of swirling flow behind wind turbine blades and through an axisymmetric diffuser,'' Ph.D. thesis, University of Newcastle, Australia.
[11] Armfield, S. W., and Fletcher, C. A. J., 1986, ''A Comparison of Single and Multi-Sweep Techniques for Reduced Navier-Stokes Equations,'' Comp. Tech. and Appl. CTAC 85, pp. 431–442, Amsterdam, North Holland.
[12] Armfield, S. W., and Fletcher, C. A. J., 1986, ''Simulation of Internal Swirling Flow Using Mixing Length and $k-\varepsilon$ Turbulence Models,'' Proc. Int. Symp. Comp. Fluid Dyn. in Tokyo, pp. 740–751, Amsterdam, North Holland.
[13] Cebeci, T., and Smith, A. O. M., 1974, *Analysis of Turbulent Boundary Layers*, Academic Press, New York.
[14] Armfield, S. W., and Fletcher, C. A. J., 1985, ''Application of the Dorodnitsyn finite element method to swirling boundary layer flow,'' Int. J. Numer. Methods Fluids, **5**, pp. 443–462.
[15] Kwon, O. K., Pletcher, R. H., and Lewis, J. P., 1984, ''Prediction of Sudden Expansion Flows Using the Boundary-Layer Equations,'' ASME J. Basic Eng., **106**, pp. 285–291.
[16] Parr, O., 1963, ''Untersuchungen der dreidimensionalen Grenzschicht an rotierenden Drehkorpern bei axialer Anstromung,'' Ing. Arch., **32**, pp. 393–413.
[17] Shimizu, Y., Nagafusa, M., and Kuzuhara, S., 1982, ''Effects of Approaching Flow Types on the Performances of Straight Conical Diffusers,'' Bull. JSME, **25**, No. 208, pp. 1506–1512.
[18] Hoffman, J. A., 1981, ''Effects of Free-Stream Turbulence on Diffuser Performance,'' ASME J. Fluids Eng., **103**, No. 3, pp. 385–390.

The Flow Structure During Onset and Developed States of Rotating Stall Within a Vaned Diffuser of a Centrifugal Pump

Manish Sinha
Ali Pinarbasi
Joseph Katz

Department of Mechanical Engineering,
The Johns Hopkins University,
Baltimore, MD 21218

Particle Image Velocimetry (PIV) and pressure fluctuation measurements are used for investigating the onset and development of rotating stall within a centrifugal pump having a vaned diffuser. The experiments are performed in a facility that enables measurements between the diffuser vanes, within part of the impeller, in the gap between them and in the volute. The diffuser is also instrumented with pressure transducers that track the circumferential motion of rotating stall in the stator. The timing of low-pass-filtered pressure signals are also used for triggering the acquisition of PIV images. The data include detailed velocity distributions, instantaneous and phase-averaged, at different blade orientations and stall phases, as well as auto- and cross-spectra of pressure fluctuations measured simultaneously in neighboring vane passages. The cross-spectra show that the stall propagation rate is 0.93 Hz, 6.2 percent of the impeller speed, and that the stall travels from the passages located on the exit side of the volute toward the beginning side, crossing the tongue region in the same direction as the impeller, where it diminishes. Under stall conditions the flow in the diffuser passage alternates between outward jetting, when the low-pass-filtered pressure is high, to a reverse flow, when the filtered pressure is low. Being below design conditions, there is a consistent high-speed leakage flow in the gap between the impeller and the diffuser from the exit side to the beginning of the volute. Separation of this leakage flow from the diffuser vane causes the onset of the stall. The magnitude of the leakage and the velocity distribution in the gap depend on the orientation of the impeller blade. Conversely, the flow in a stalled diffuser passage and the occurrence of stall do not vary significantly with blade orientation. With decreasing flow-rate the magnitudes of leakage and reverse flow within a stalled diffuser passage increase, and the stall-cell size extends from one to two diffuser passages.
[DOI: 10.1115/1.1374213]

1 Introduction

At reduced flow rates, the performance, flow rate, and pressure of a compressor or a pump become increasingly unstable. When substantial flow fluctuations are propagating at a low frequency along the circumference, but are limited to parts of components (e.g., rotor, diffuser, or volute), the phenomenon is typically referred to as rotating stall. In spite of considerable efforts devoted to the study of rotating stall in compressors and pumps, the mechanics of this phenomenon are not yet well understood. Emmons et al. [1] provide a coherent explanation of rotating stall using cascade theory. While rotating stall may occur in any turbomachine, the phenomenon is most frequently observed and studied in compressors with a large number of blades. Its occurrence has also been reported in the impeller and in the diffuser/volute of centrifugal pumps (e.g., Lenneman and Howard [2]) with specific geometries. In a more recent research Yoshida et al. [3] investigate the rotating stall instability in a 7-bladed centrifugal impeller with a variety of diffusers. They observe that multiple stall cells occur, both in the impeller and in the vaned diffuser. The stall propagation speed in the diffuser is less than 10 percent of the impeller speed and is most evident when the clearance between impeller and diffuser vanes is large. In the present study, we examine the occurrence of stall in a centrifugal pump with a vaned diffuser that has a gap of 20 percent of the impeller radius and 15.4 percent of the diffuser chord length. This gap is larger than most of the available data for pumps.

Ogata et al. [4] report on measurements of pressure fluctuations and velocity fields, using hot wire measurements, in a vane diffuser of a centrifugal compressor. They conclude that the presence of a volute casing causes circumferentially nonuniform conditions at the outlet from the diffuser and that this nonuniformity is a large factor in the inception of rotating stall. Their velocity measurements indicate the existence of reverse flow in the vane passages with the lowest pressure field, but being point measurements, they cannot provide details on the flow structure and onset mechanisms. They also suggest that the propagation mechanism of a stall cell from one vane passage to another is more complex than the conventional explanation. Additional relevant reference material on stall and instabilities, including empirical correlations for the behavior of impellers and diffuser vanes can be found in Ribi [5], Tsujimoto [6], Miyake and Nagata [7] as well as Tsurusaki and Kinoshita [8]. Some recent computational work is described, for example, by Cao et al. [9] and Longatte and Kueny [10].

In spite of these efforts, there is still very little experimental data on the detailed flow structures within a stalled centrifugal turbomachine, the mechanism causing the onset of stall as well as on the effects of blade orientation and flow rate on the flow structure within a stalled pump. In this paper we use PIV to measure the velocity distributions within a vaned diffuser, part of the impeller, the gap between the diffuser and the impeller, and within the volute of a stalled pump. The experimental setup and test

Contributed by the Fluids Engineering Division for publication in the JOURNAL OF FLUIDS ENGINEERING. Manuscript received by the Fluids Engineering Division October 27, 2000; revised manuscript received March 15, 2001. Associate Editor: Y. Tsujimoto.

procedures are described in Section 2. The present measurements cover regions located on both sides of the tongue (cut water). Conditionally sampled data using the signal of a pressure transducer located within the diffuser is used for studying characteristic flow structures at different phases of the stall (Section 3). Pressure signals from several transducers located in adjacent blade passages are also used for measuring the propagation of the stall. The measured propagation frequency is only 6.2 percent of the impeller speed, but the propagation speed varies from one blade to the next, and stops at the beginning of the volute. The measurements are performed at different impeller orientations and different flow rates, starting from conditions for which the diffuser is not stalled down to conditions for which the stall cell covers more than one diffuser passage simultaneously. We show that high-speed leakage (circumferential flow) in the gap between the diffuser and the impeller, from the exit side to the volute to the beginning side, plays a major role in causing the onset of stall. It is also shown that the flow in the vane passage alternates between outward jetting when the passage is not stalled to strong reverse flow in a stalled passage (or two passages, depending on flow rate).

2 Experimental Setup and Procedures

2.1 Setup. A schematic description of the centrifugal pump used in the present study is presented in Fig. 1 and relevant details on the pump geometry are presented in Table 1. The pump is vibration isolated and separated from the rest of the facility using 50 m of coiled flexible hoses. A converging nozzle and flow straighteners (honeycombs and screens) at the entrance to the pump insure smooth inflow into the impeller. Further details on the test loop can be found in Sinha and Katz [11] and Sinha et al. [12].

The impeller has backswept blades with a logarithmic profile and the vaned diffuser has straight walls with a constant cross section. The configuration (radius) of the perimeter of the volute, r_v, in cm is given by:

$$r_v = 17.78 + 24.46 \times (\theta/360) \quad (\theta \text{ varies between } 0°\text{-}360°).$$

In the present configuration the tip of the tongue is located at $\theta = 29$ deg. Beyond $\theta = 360$ deg the outer perimeter is straight. The 24.46×1.27 cm^2 exit is gradually expanded to a 10.16 cm pipe by imposing a maximum expansion angle of less than 7 deg to avoid separation. Parts of the original stainless-steel blades and outer shroud of the impeller were removed and replaced with acrylic to allow visual access in the flow within the impeller. The entire diffuser and outer perimeter of the volute are also transparent. This setup allows illumination, flow visualization, and PIV measurements in both the horizontal (parallel to the shrouds) and vertical (parallel to the shaft) planes. The pump is also instrumented with flush mounted piezoelectric pressure transducers (PCB 105B02) that are mounted on the hub surface, along the centerline, in six adjacent vane passages. They are labeled A–F in Fig. 1.

Table 1 Geometric data and operating conditions

Impeller:	
Inlet diameter	8.51 cm
Discharge diameter	20.32 cm
Number of blades	5 backswept
Exit angle of blade	21.3°
Diffuser:	
Number of vanes	9
Inside diameter	24.45 cm
Discharge diameter	30.5 cm
Inlet angle of vane	10.6°
Outlet angle of vane	10.97°
Chord length	13.44 cm
Suction side radius	14.15 cm
Pressure side radius	24.79 cm
Axial width	1.27 cm
Operating conditions:	
Rotor speed	890 rpm
Design flow rate	5.67 l/s
Design Flow coefficient, $\varphi = Q/\pi DBU_t$ Q is the flow rate, D, B and U_t are the impeller diameter, width and tip speed, respectively.	0.118
Design specific speed	0.49
Flow-rate during the present experiments	2.52 l/s – 3.78 l/s
Flow coefficient during the present experiments	0.052-0.078

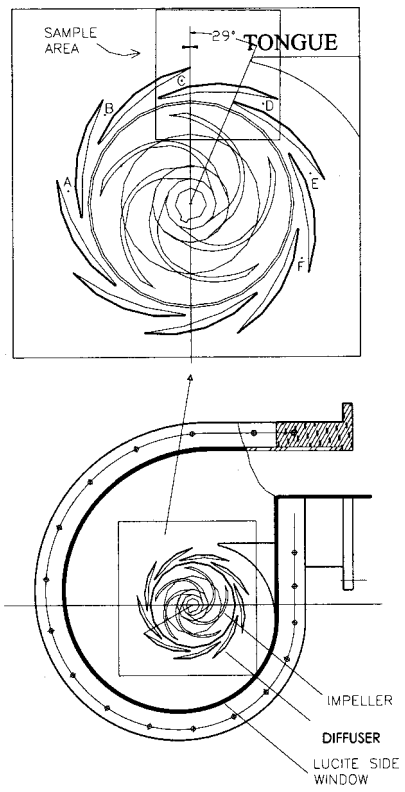

Fig. 1 The pump geometry and location of the present measurements

2.2 PIV system. All the data included in the present paper focus on the flow near the exit of the pump and the sample area is specified in Fig. 1. All the measurements are performed in the mid-section, i.e., in the 50 percent plane between the hub and the shroud. The optical setup of the PIV system is illustrated in Fig. 2. A 350 mJ/pulse, Nd-Yag laser and sheet forming optics are similar to the setup used in previous experiments [11,12] where one can find reference data on the flow at design conditions. The images are recorded by a 2048×2048 pixels, 4 frames/s digital camera that incorporates fast digital image shifting [11,12] to overcome directional ambiguity. The images are recorded at the desired impeller orientation using a shaft encoder. In addition, the electronic control unit provides trigger signals during maximum, minimum and zero-crossing phases of the low-pass-filtered signal of the transducer located at C (see Fig. 1). As will be shown in the next section, this signal is associated with the stall.

The acquired images are enhanced using an in-house histogram equalization algorithm and analyzed with in-house auto-correlation software [13–15]. The window size is 64×64 pixels

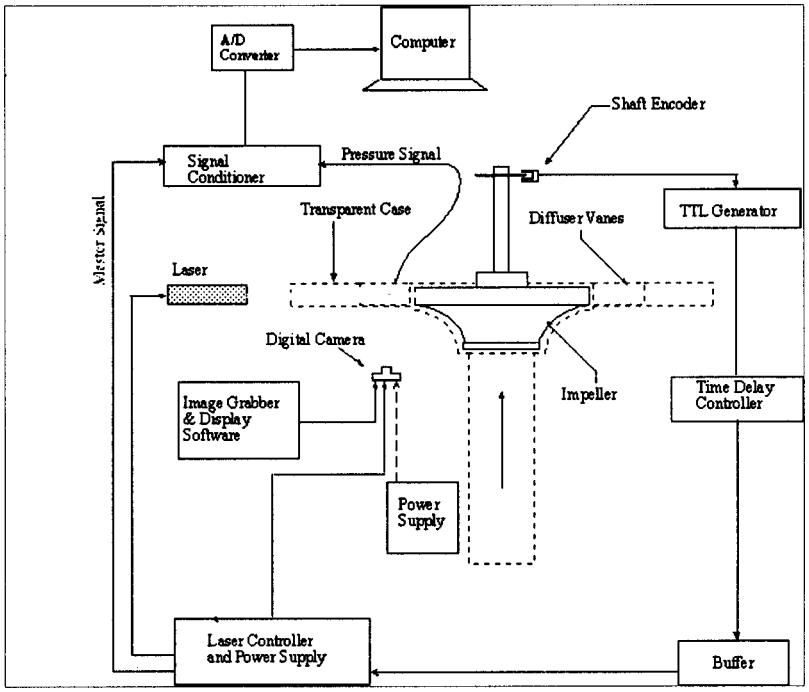

Fig. 2 The optical and control systems

and the vectors are calculated every 32 pixels, i.e., 50 percent overlap between neighboring windows. The water is seeded with 20 μm, neutrally buoyant fluorescent particles. The fluorescent particles enable us to install a high-pass filter in front of the camera that cuts the green laser light but allows unobstructed transmission of the yellow fluorescence. Consequently, reflections from solid boundaries, such as blades, vanes, and shrouds do not obscure the particles' traces, even very close to the blade surfaces. The uncertainty has been determined, calibrated, and discussed in detail in several of our previous papers (e.g., Dong et al. [16], Roth et al. [17], [13–15], Sridhar [18]). The standard deviation of the difference between the exact and measured velocities in both experimental and computer-generated images has been found to be about 0.2 pixels, provided there are sufficient number of particles per interrogation window. Consequently, the uncertainty in velocity measurements is in the 0.2–0.4 pixels range (depending on how stringent one chooses to be) and we have opted to use 0.3 pixels as a characteristic value. To achieve this uncertainty the particle concentration must be maintained at a level that ensures a distribution of at least 7—8 image pairs per interrogation window. This requirement is consistent with results of other studies of uncertainty in PIV measurements (Adrian [19]). Consequently, for a characteristic displacement of 20 pixels between exposures, the uncertainty is about 1.5 percent.

3 Results

3.1 Performance, Pressure Fluctuations and Propagation Rate. A performance curve of the present pump is presented in Fig. 3. At flow coefficients below 0.06 there is a change in the slope of the performance curve and as a result it is believed that the pump is close to the onset condition of rotating stall. Sample power spectra of the pressure signals in passage C under conditions of stall and no-stall are presented in Fig. 4(*a*). The pump shaft frequency is 14.83 Hz, but at this frequency there is only a change in slope. The peaks at twice and three times this frequency on design conditions are clear. There are five impeller blades, which means that the frequency at which blades pass by the same vane passage is 74.2 Hz. The largest peak in Fig. 4(*a*) (on design conditions) corresponds to this passing frequency. Its first super harmonic at 148.4 Hz is also evident. There are nine diffuser vanes, which means that the rate at which the same impeller blade passes by the diffuser vanes is 133.5 Hz. There is a clear spectral peak at this frequency too. There is another peak at ~122 Hz that we cannot explain and the reasons for its occurrence are beyond the scope of this paper. Under stalled conditions the peaks at 29.6, 74.2, 122, and 133.5 Hz are smaller, but they are higher at 44.5 Hz and at frequencies below 14.8 Hz. In particular, there is an increase of about 5 db below 1 Hz. Under a stalled condition, the power spectrum in fact yields an additional peak at 0.93 Hz in the signals of the transducers in passages A, B, C, D, and E, but not in the signal of transducer F. Samples of auto-spectra for passages, A, B, E, and F are presented in Fig. 4(*b*). The spectra for passages C and D are not shown since they are almost identical to those in passages A and B. Clearly, unlike passages A–E, there is no distinct spectral peak at frequencies below 15 Hz in passage F.

Figure 5(*a*) shows a sample of the magnitude of the cross-spectrum between the pressure signals A and B, and Fig. 5(*b*) provides the phase information A similar analysis was performed

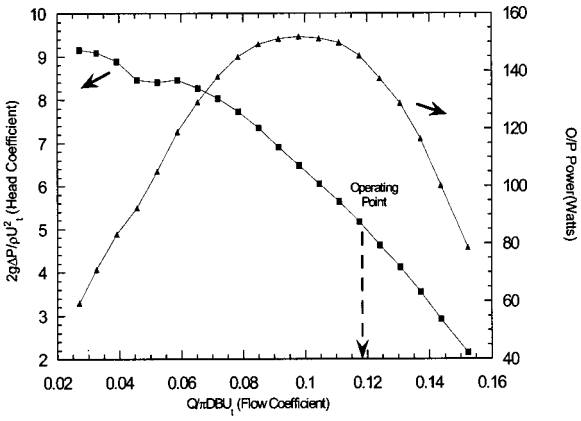

Fig. 3 The performance curve (squares) and output power (triangles) of the pump

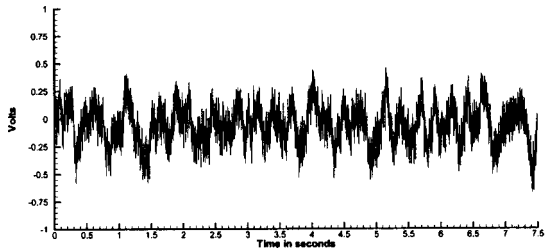

(a)

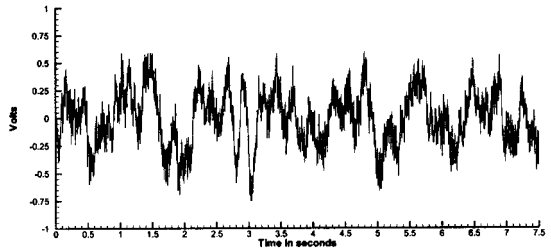

(b)

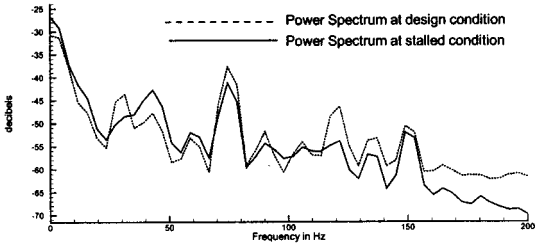

(c)

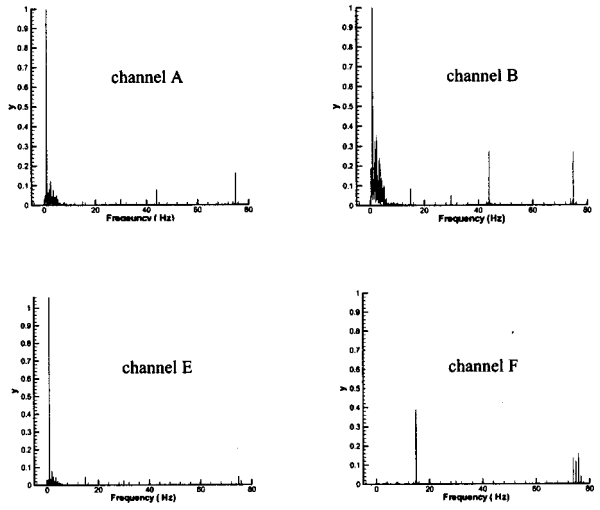

(d)

Fig. 4 A typical pressure signal of transducer C at: (*a*) design conditions (φ=0.118), (*b*) stalled conditions (φ=0.062), (*c*) power spectra of the signals in 4(*a*) and 4(*b*), (*d*) auto spectrum of Channels A, B, E, and F

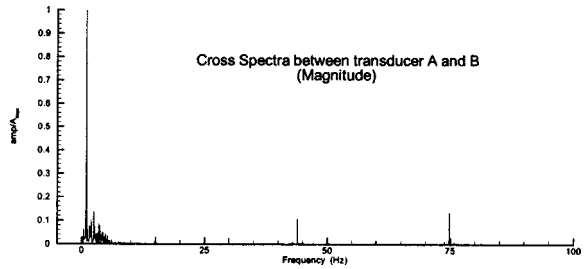

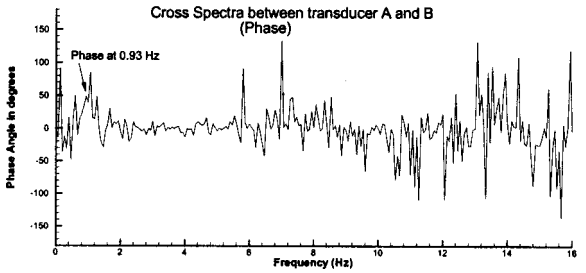

Fig. 5 (*a*) Sample cross spectrum magnitude of transducer signals in vane passages A and B; (*b*) phase difference between the signals of tranducers A and B

between each pair of transducer signals. The peaks are at frequencies that are common to the two signals and the phase is indicative of the time lag/lead between them. We obtain data at 0.93 Hz for passages ''A''-''E,'' since there is no peak in the spectra involving passage ''F.'' The phase angles by which the pressure signal of sensor ''A'' leads the signals in the other passages are tabulated in Table 2.

Clearly, the time delay varies as the phenomenon moves from one passage to another. The propagation speed initially increases as the tongue is approached. The time lag between sensor A and B is 0.145 s, whereas the lag between B and C is 0.06 s. Between C and D the lag increases only slightly to 0.08 s, but then it increases substantially to 0.44 s between D and E and disappears completely in F. The decaying propagation speed suggests the influence of the non-uniform flow conditions (circumferential pressure gradients) that exist, according to Ogata et al. [4], in the volute casing outside the diffuser, or in the gap between the impeller and the diffuser, as the present velocity measurements indicate. Since the propagation speed is not uniform we cannot use the Hanover diagram (Japikse et al. [20]) for estimating the number of stalled cells that exist at a given instant of time.

RMS values of pressure fluctuation in passages A–F, are recorded at different flow rates, starting from 5.67 1/s and lower (Fig. 6). The rms values start increasing at around 3.78 1/s in channels A, B, C, D, and E. The pressure fluctuations at D are initially lower than the levels in the other passages and it starts to rise at the same flow rate. However, it continues to rise well after the signals at A, B, C, and E reach maximum levels and peaks only at about 2.84 1/s. For the A–E passages, the rms levels decrease to a lower, but still elevated, levels below 2.75 1/s. Passage F does not follow the same trend. There, the fluctuations remain at almost the same level until 2.75 1/s where there is a sharp increase followed by an immediate decrease to an elevated

Table 2 Measured phase and time lead at 0.93 Hz obtained from cross-spectra of the pressure signals in passages A, B, C, D, and E. Transducer F has no peak at 0.93 Hz.

Transducers:	A&B	A&C	A&D	A&E	A&F
Angular separation	40.0 deg	80.0 deg	120.0 deg	160.0 deg	200.0 deg
Phase lead	48.49 deg	68.59 deg	94.06 deg	258.0 deg	not stalled
Time lead (s)	0.145	0.205	0.281	0.717	not stalled

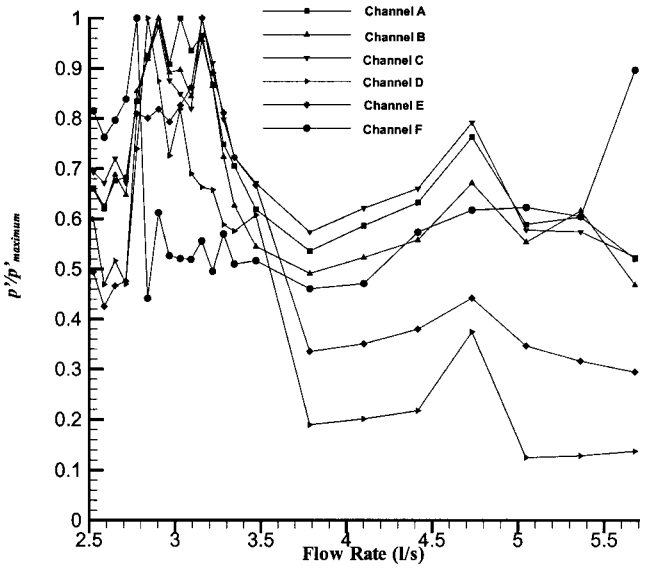

Fig. 6 RMS values of pressure fluctuations as a function of flow rate

level. Thus, at 3 1/s (φ=0.062) passages A, B, C, D, E are experiencing high pressure fluctuations whereas passage F is not. Consistent with the spectral analysis, and confirmed by the velocity distributions, discussed in the next section, the increased level of fluctuation is caused by massive flow oscillations, from being stalled (reverse flow) to having a jet flowing through (forward outflow) in the vane passage. Since the increase in pressure fluctuations begins at around 3.78 1/s, to study the onset of stall PIV images are recorded at and below 3.78 1/s, down to 2.52 1/s. We record data when the stall related, low-pass-filtered, pressure signal is maximum, minimum and during zero crossing (growth or decay). Reference data on the flow in other vane passages when the pump operates on design conditions can be found in Sinha et al. [11,12].

3.2 Flow Structures at Different Phases. Sample instantaneous vector maps at different phases of the stall, when the low-pass-filtered transducer signal at C is minimum, during zero crossing and maximum, all at φ=0.062, are presented in Figs. 7(*a*–*c*), respectively. The blade orientation is the same in all three cases. At minimum pressure, there is a reverse flow in van passage C. The magnitude of reverse velocity is only about 10 percent of the impeller tip speed. There is also clear evidence of flow separation at the trailing edge of the vane. During zero crossing (Fig. 7(*b*), i.e., as the pressure in C is rising, the flow in passage C is in the process of recovering from the reverse flow, whereas there is still backward flow in passage D above it. Interestingly, in Fig. 7(*b*) there is a negative radial velocity on the pressure side of the impeller blade, i.e., there is a backward flow into the impeller.

At a pressure-maximum phase, there is a strong outward flow (Fig. 7(*c*)) through passages C and D. The velocity at D is higher, presumably due to the lower mean pressure at the beginning of the volute when the pump operates below design conditions. The outflow from passage C separates from the convex side of the vane and is aimed directly toward the exit. In all cases there is a strong leakage flow in the gap between the impeller and the diffuser from the exit side to the beginning of the volute. The leakage velocity exceeds 50 percent of the impeller tip speed. The secondary flow downstream of the diffuser is complex but is significantly slower.

3.3 Effect of Blade Orientation. Figure 8(*a*–*c*) and Fig. 9(*a*–*c*) show sample phase averaged data (averages of 10 images, each) during minimum and maximum pressure phases, at 3 different impeller orientations, −4 (356), 26, and 56 deg, respectively. A complete set, every 10 deg, can be found in Sinha [21].

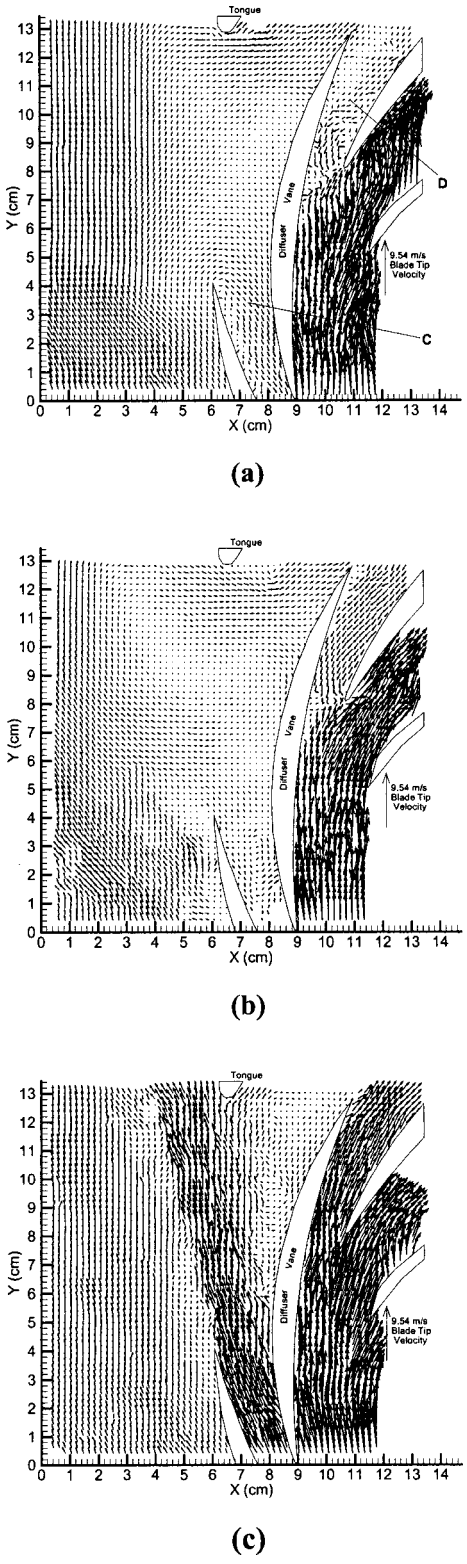

Fig. 7 Sample Instantaneous velocity maps at: (*a*) minimum, (*b*) zero-crossing (on the rise), and (*c*) maximum phases of the low-pass-filtered pressure signal at passage C (φ=0.062)

At minimum pressure-phase (Fig. 8), the phase-averaged data shows a reverse flow into passage C and a slow outward flow in passage D. As the flow turns around back into the passage C it

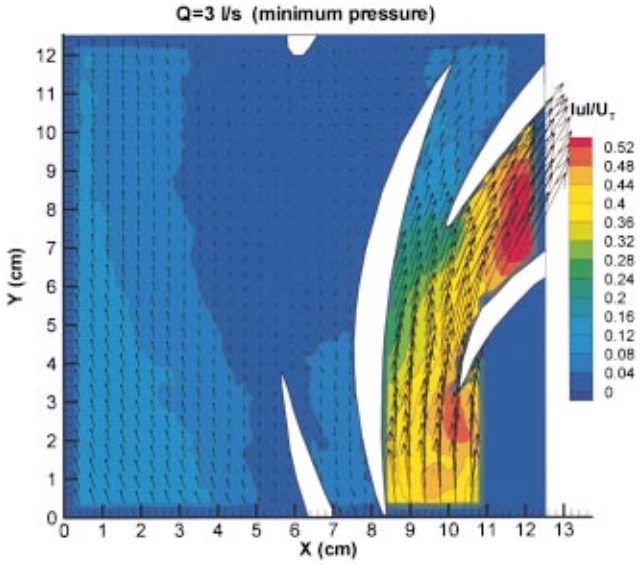

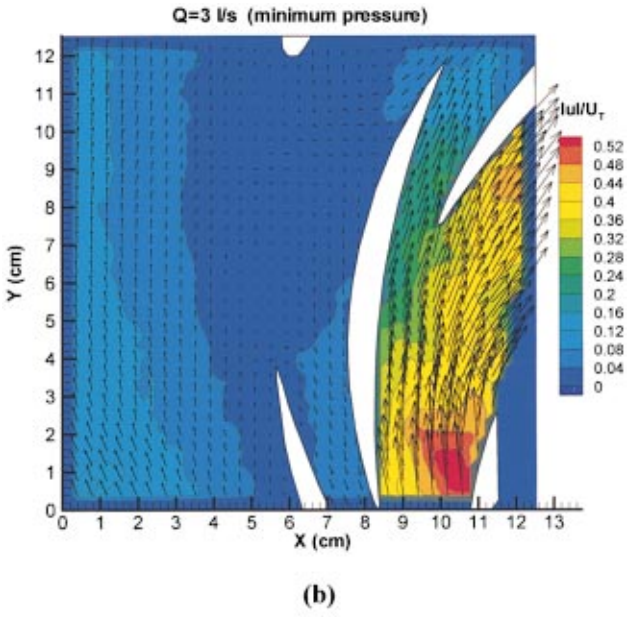

Fig. 8 Phase averaged velocity maps at a minimum pressure phase when the blade is at: (*a*) −4 deg, (*b*) 26 deg, and (*c*) 56 deg. The colors indicate velocity magnitude and a reference vector is provided in Fig. 7. Only alternate vectors are shown for clarity.

separates near the trailing edge of the lower diffuser vane, creating a pocket of no flow at the trailing edge, on the concave side of the lower vane. Several relatively weak vortex structures/large eddies can also be seen outside of the diffuser, in the vicinity of the tongue. Between instantaneous realizations these eddies vary both in strength and spatial locations.

As indicated before, the most dominant phenomenon is the high speed-leakage flow between the impeller and the diffuser, from the exit side of the pump (left side of the tongue) toward the beginning of the volute. The magnitude of the phase-averaged leakage velocity also exceeds 50 percent of the impeller tip speed. The magnitude and orientation of the leakage flow varies with blade orientation due to the ''jetting'' in the pressure side of the impeller blade and the ''wake'' region behind the blade. The impeller orientation, still at minimum pressure phase, also affects the out flux from passage D. It is at maximum in Fig. 8(*b*), when the vane passage faces the pressure side of the blade, and minimum in Fig. 8(*a*), when passage D is exposed to the suction side of the blade. Conversely, the phase-averaged flow outside of the diffuser is very slow, with very little secondary flow from the exit side to the beginning of the volute or from the beginning to the exit side. This trend indicates that the circumferential pressure gradients causing the leakage flow are confined to the narrow gap between the impeller and the diffuser. The pressure gradients outside of the diffuser are weak.

At a maximum pressure phase (Fig. 9), there is an outward jet from the vane passage with velocity magnitude of about 60 percent of the typical values on design condition (available in Sinha and Katz [11]). The jet is aimed directly toward the exit and there is no indication that it is affected by circumferential pressure gradients in the volute. The jet velocity is slightly higher when vane passage C is exposed to the pressure side of the blade (Fig. 9(*a*)), and the separation point on the convex side of the diffuser vane (separating passages C and D) shifts as the impeller blade passes by, but these fluctuations are small. There is essentially no (phase-averaged) flow to the right of the jet and the tongue. The out flux from passage D also increases when the inlet to this passage is exposed to the pressure side of impeller blade (Fig. 9(*b*)).

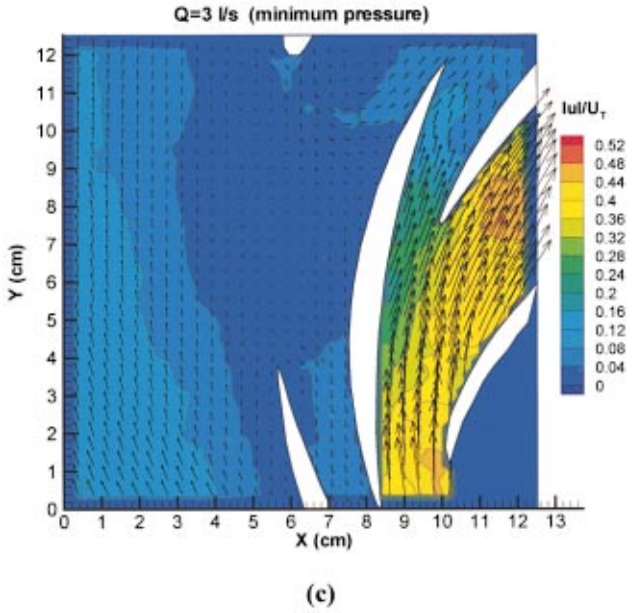

Fig. 8 (*Continued*)

In the gap between the impeller and diffuser the fast leakage flow persists in the maximum pressure phase of the stall. In fact, the characteristic leakage velocity is even higher than that of the minimum pressure phase. The velocity distribution depends, but not to a great extent, on the orientation of the impeller. The velocity is typically higher, exceeding 50 percent of the tip speed, on the pressure side of the impeller blade (ahead of the tip), and decreases as much as 40–45 percent in other regions. The decrease is particularly evident when the blade is located near the diffuser vane separating passages D and E (Fig. 9(*a*)). In summary, it is shown that the phase-averaged flow structure under stalled conditions shows some, but not substantial, dependence on the impeller orientation. Most of the effects are confined to the immediate vicinity of the blade (which is not surprising) and there is limited impact on the flow within the diffuser during maximum pressure phase. A probable cause for this limited effect is the high speed circumferential leakage flow that separates between the impeller and the diffuser.

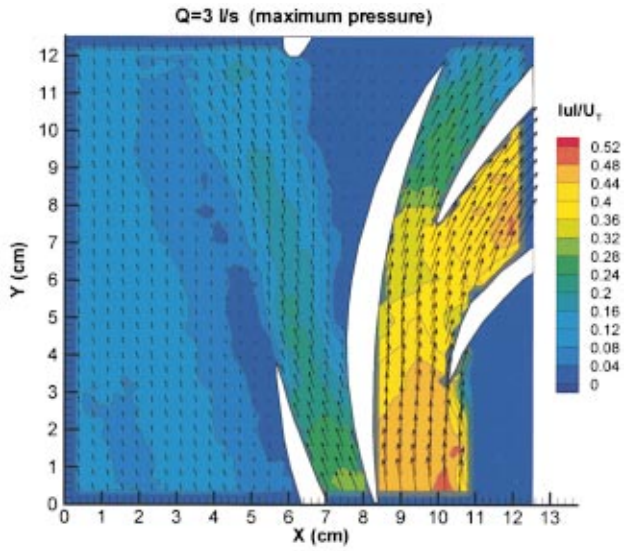

(a)

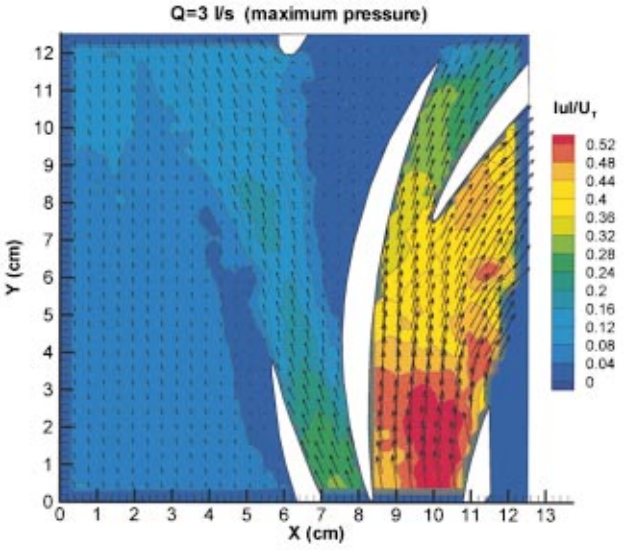

(b)

Fig. 9 Phase averaged velocitiy maps at a minimum pressure phase when the blade is at: (*a*) −4 deg, (*b*) 26 deg, and (*c*) 56 deg. The colors indicate velocity magnitude and a reference vector is provided in Fig. 7. Only alternate vectors are shown for clarity.

3.4 Effect of Flow Rate and Onset of Stall. Figures 10(*a*,*b*)–13(*a*,*b*) contain representative samples of instantaneous and phase averaged velocity maps (this time an average of 20 each) at 3.78 1/s (φ=0.078), 3.28 1/s (φ=0.068), 3.02 1/s (φ =0.062), and 2.52 1/s (φ=0.052), respectively, all at a minimum pressure phase and at the same blade orientation. These four characteristic examples are selected from an available series of 11 sets that covers the range φ=0.052–0.078 available in Sinha [21]. They are selected to demonstrate the transition, with decreasing flow rate, from a flow that is not stalled to conditions of massive stall that covers more than one blade passage simultaneously. In all cases the flow is below design conditions. As Figs. 3 and 6 indicate, at φ=0.078 (the upper bound), the flow is clearly not stalled. This condition is still far from the local minimum in performance curve and the pressure fluctuations are still relatively

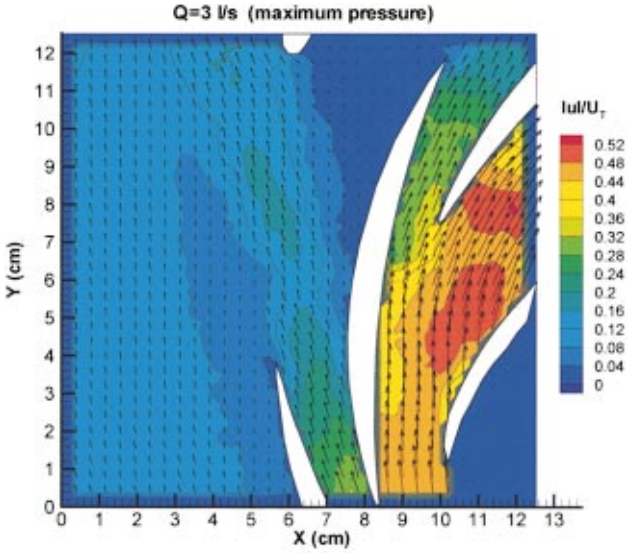

(c)

Fig. 9 (*Continued*)

low. With decreasing flow rate there is a range of conditions with high pressure fluctuations that are caused by the rotating stall. The highest fluctuations occur at φ~0.062. As the flow is decreased further the pressure fluctuations decrease again. The lower bound of our range of samples, φ=0.052, is already well below the range of flow rates with high pressure fluctuations. The latter is also close to the local minimum in the performance curve.

Typical narrow jetting near the concave side of the vane with a wide separated region in the convex side dominate the flow in and downstream of the diffuser at 3.78 1/s (φ=0.078), as shown in Fig. 10(a,b). At this flow rate the outward jet always exists. Part of the jet exiting from the previous diffuser passage (passage B), 40 deg upstream, is also evident, both in the instantaneous and phase averaged velocity distributions. This phenomenon is similar to that shown by Johnston and Dean [22] for off-design flow rates and similar (but lower velocity) to the phenomena occurring at higher flow rates in this pump [11] . Note also that there is a secondary flow from the beginning side of the volute (right of the tongue) toward the exit. This phenomenon indicates that the pressure gradients near the tongue are in the opposite direction compared to the gradients in the gap between the impeller and the diffuser, where the flow leaks to the beginning of the volute. The secondary flow around the tongue disappears at lower flow rates.

With decreasing flow rate the characteristic jet velocity decreases and the traces of the jet from passage B eventually disappear. Conversely, the leakage flow increases substantially, as is evident by comparing the samples in Fig. 10–13. In addition, the velocity in the outer sections of the volute (low x in the examples shown) becomes consistently higher than the flow in the vicinity of the tongue, a trend that is characteristic to operation off design conditions [16]. At about φ=0.068 the flow in passage C stops intermittently and even becomes negative, but the phase-averaged flow is still positive (Fig. 11(*b*)). In Fig. 11(*a*) the flow through passage D is positive, and quite fast, and there are traces of the jetting from passage B. Thus, only passage C is stalled, which is characteristic to the size of the stall cell at this flow rate.

The frequency of reverse flow increases with decreasing flow rate and eventually even the phase-averaged velocity in passage C becomes negative (Fig. 12(*b*)) during minimum pressure phase. At and below φ=0.065 (data not shown–the pattern is similar to Fig. 12(*a*,*b*)) the instantaneous stalled area starts covering two diffuser vane passages intermittently although the phase average distribution only covers one passage. The reverse flow magnitude also

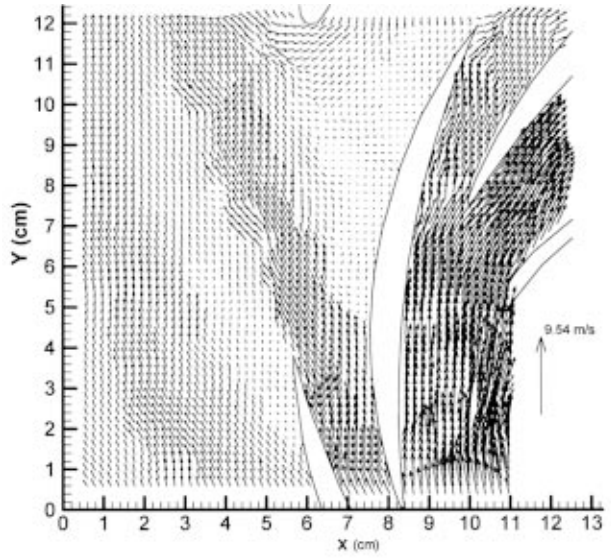

(a)

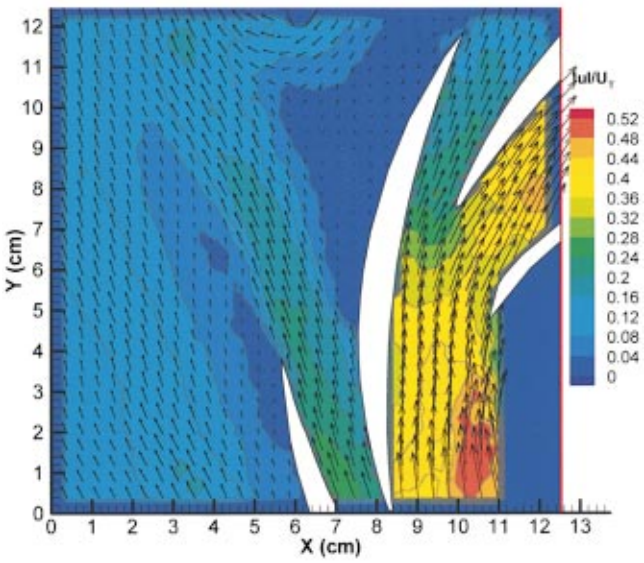

Fig. 10 Sample (*a*) instantaneous; and (*b*) phase averaged velocity maps (only alternate vectors are shown in *b*) at a minimum pressure phase. The flow rate is 3.78 1/s (φ=0.078) and the blade orientation is 6 deg.

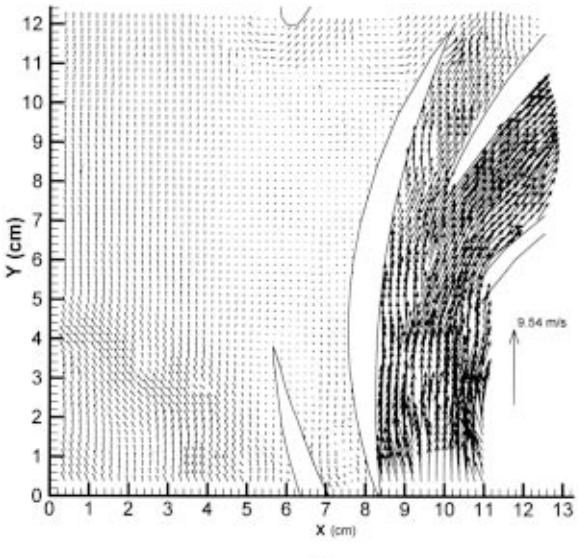

(a)

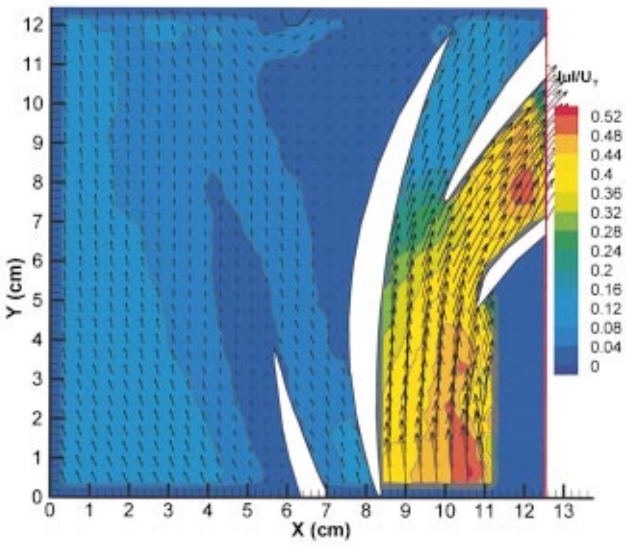

(b)

Fig. 11 Sample (*a*) instantaneous and (*b*) phase averaged velocity maps (only alternate vectors are shown in *b*) at a minimum pressure phase. The flow rate is 3.28 1/s (φ=0.068) and the blade orientation is 6 deg.

continues to increase. At φ=0.062 reverse flow regularly occurs in passage C during minimum pressure phase and at φ=0.052 (Fig. 13) the flow is consistently reversed in both passages C and D. Consequently, even the phase-averaged flow is negative.

Before concluding, it is of interest to identify exactly where the stall process starts. Our ability is limited since all the velocity measurements are performed in the same central plane and the flow is three-dimensional. A clear illustration that the flow is three-dimensional is the fact that the backward flow into passage D in Fig. 12(*a*) faces a flow in the opposite direction at the entrance to the passage. Obviously, to satisfy continuity there has to be a flow in the opposite direction in other planes. However, examination of the velocity distributions as the stall develops provides sufficient information to follow the process. As an illustration, let us examine the flow in passage D in Fig. 14 (φ=0.059) that shows a characteristic velocity distribution during early stages of transition from forward to reverse flow in the passage. In this example, the flow is separated on the concave surface but there is still an outward flow along the convex surface. The same trend, i.e., that the stall starts as the flow separates on the concave side of the passage, occurs also in passage C but typically at higher flow rate, due to the location of the trigger transducer. This phenomenon is most likely associated with the fast leakage flow that makes a turn near the narrowest point of the diffuser. Combined with the adverse pressure gradients in the passage (especially during a minimum pressure phase) the concave surface becomes prone to massive flow separation and stalling. As a vane passage stalls the leakage velocity increases which further increases the pressure gradients at the point where the leakage flow turns at the entrance to a passage. Thus, stalling of passage C increases the likelihood of subsequent stalling of passage D, i.e., a rotating stall. This process stops when the pressure gradients in a passage become favorable for outward flow. Due to the circumferential pres-

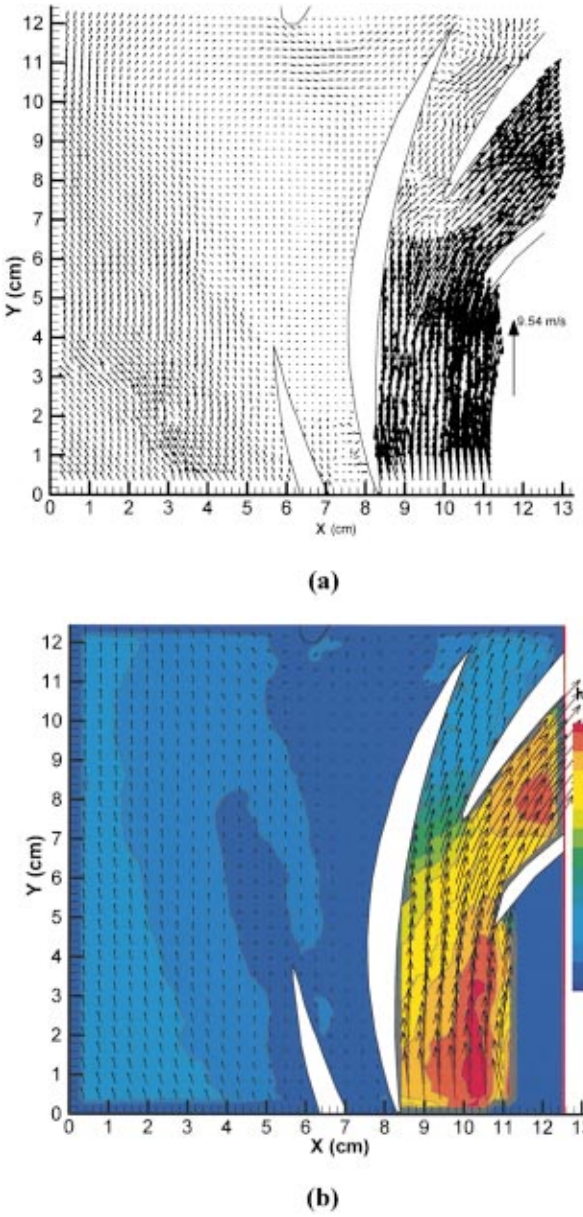

Fig. 12 Sample (*a*) instantaneous and (*b*) phase averaged velocity maps (only alternate vectors shown in *b*) at a minimum pressure phase. The flow rate is 3.08 1/s (φ=0.062) and the blade orientation is 6 deg.

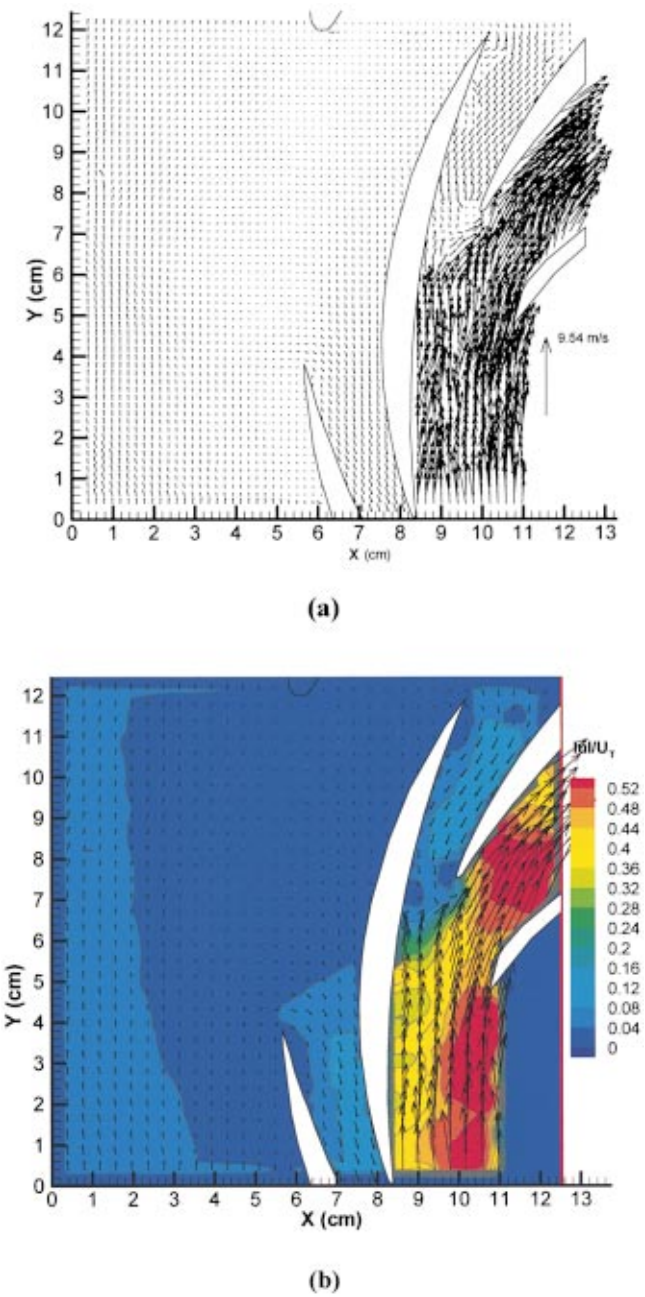

Fig. 13 Sample (*a*) instantaneous and (*b*) phase averaged velocity maps (only alternate vectors are shown in *b*) at a minimum pressure phase. The flow rate is 2.52 1/s (φ=0.052) and the blade orientation is 6 deg.

sure gradients below design conditions (Iversen et al. [23], [14,16], that in the present pump seem to be confined to the gap between the impeller and the diffuser, eventually the leakage flow finds a passage (most likely passage F above 2.8 1/s) where it can flow out. Consequently, in the present pump, passage F is not stalled at 3.02 1/s, as the spectral analysis demonstrates.

4 Summary and Conclusions

PIV and pressure fluctuation measurements are used for studying the flow structure within a centrifugal pump with a vaned diffuser under stall conditions. Cross spectra of the pressure signals at neighboring passages, as well as the RMS levels of pressure fluctuations confirms that a rotating stall occurs at a frequency of 0.93 Hz, 6.2 percent of the impeller speed. The stall is detected at the exit side of the pump and propagates with varying speeds to the beginning side, where it is quenched. The quenching of the stall occurs in a vane passage at the beginning of the volute where the pressure gradients for outflow are more favorable. Thus, unlike axial turbomachines, the circumferential pressure variations in the diffuser/volute confine the stall to a small part of the diffuser. This observation is consistent with the conclusions of Ogata et al. [4], that circumferential pressure nonuniformities affect the conditions for the onset of stall.

When the pump is stalled the flow in the diffuser passage alternates between an outward jetting, when the low-pass-filtered pressure signal in the vane passage is high, to a reverse flow, when the filtered pressure is low. Being below design conditions, there is a consistent high-speed leakage flow in the gap between the impeller and the diffuser from the exit side to the beginning of the volute. Separation of this leakage flow from the concave side of the diffuser vane causes the onset of the stall. The magnitude of

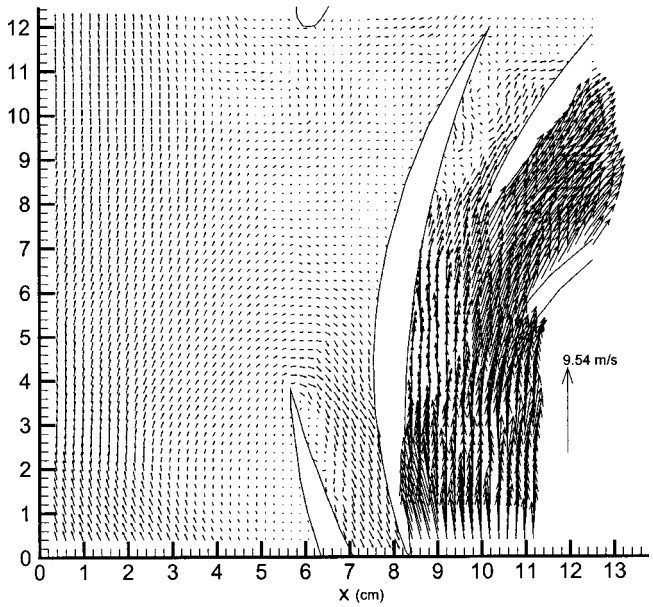

Fig. 14 Sample instantaneous velocity distribution at a minimum pressure phase as massive flow separation and the onset of stall occur in passage D. The flow rate is 2.89 1/s (φ=0.060) and the blade orientation is 6 deg.

the leakage and the velocity distribution in the gap depend on the orientation of the impeller blade. Conversely, the flow in a stalled diffuser passage does not vary significantly with impeller blade orientation. With decreasing flow-rate the magnitudes of leakage and reverse flow within a stalled diffuser passage increase and the stall-cell size extends from one to two diffuser passages. Unlike the gap between the impeller and the diffuser, there is very little leakage flow in the volute downstream of the diffuser, indicating that the circumferential pressure gradients in the volute are substantially smaller than those in the gap. This phenomenon is probably related to the uncharacteristic large gap between the impeller and the diffuser of the present pump (2.07 cm, 10.2 percent of the impeller diameter and 15.4 percent of the diffuser vane chord length). As indicated in Yoshida et al. [3], increasing the gap between the impeller and the diffuser also increases the likelihood and effect of the stall. Narrower gaps will not allow such a strong leakage flow in the gap, and will most likely thus ''push'' the circumferential pressure gradients and leakage into the volute.

Acknowledgment

This work has been funded in part by the Office of Naval Research through NSWC contract No: N000167-96-C-0086 (T. Calvert is program director at NSWC) and ONR grant No. N00014-98-1-0221 (P. Purtell, program officer) and in part by the Air Force Office of Scientific Research under grant No. F49620-97-1-0110 (T. Beutner, program director). We would also like to thank T. Calvert for providing the pump and S. King for construction of the electronics.

References

[1] Emmons, H. W., Kronauer, R. E., and Rockett, J. A., 1959, ''A survey of stall propagation–experiment and theory,'' ASME J. Basic Eng. **81**, pp. 409–416.
[2] Lennemann, E., and Howard, J. H. G., 1970, ''Unsteady flow phenomena in rotating centrifugal impeller passages,'' ASME J. Eng. Power **92**, 65–72.
[3] Yoshida, Y., Murakami, Y., Tsurusaki, T., and Tsujimoto, Y., 1991, ''Rotating Stalls in Centrifugal Impeller/Vaned Diffuser Systems,'' *Proc. First ASME/JSME Joint Fluids Engineering Conference*, **FED-107**, pp. 125–130.
[4] Ogata, M., and Ichiro A., 1995, ''An Experimental Study of Rotating Stall in a Radial Vaned Diffuser,'' *Unsteady Aerodynamics and Aeroelasticity of Turbomachines*, pp. 625–641.
[5] Ribi, B., 1996, ''Instability Phenomena in Centrifugal Compressors,'' *Flow in Radial Turbomachines*, Von Karman Institute Lectures series No. 1966-01, R. A. Van den Braembussche, ed.
[6] Tsujimoto, Y., 1996, ''Vaneless Diffuser Rotating Stall and Its Control,'' *Flow in Radial Turbomachines*, Von Karman Institute Lecture series No. 1996-01, R. A. Van den Braembussche, ed.
[7] Miyake, Y., and Nagata, T., 1999, ''Full Simulation of a Flow in a Single Stage Axial-Rotor in Rotating Stall,'' FEDSM-7197, ASME Fluids Eng. Conf., San Francisco.
[8] Tsurusaki, H., and Kinoshita T., 1999, ''Flow Control of Rotating Stall in a Radial Vaneless Diffuser,'' FEDSM99-7199, ASME Fluids Eng. Conf., San Francisco.
[9] Cao, S., Goulas, A., Wu, Y., Tsukamoto, H., Peng, G., Liu, W., Zhao, L., and Cao, B., 1999, ''Three-Dimensional Turbulent Flow in a Centrifugal Pump Impeller Under Design and Off-Design Operating Conditions,'' FEDSM-6872 Proceedings of the ASME Fluids Engineering Division, July 18–23, San Francisco.
[10] Longatte F., and Kueny J. L., 1999, ''Analysis of Rotor Stator Circuit Interactions in a Centrifugal Pump,'' FEDSM-6866, ASME Fluids Eng. Conf., San Francisco.
[11] Sinha, M. and Katz, J., 2000, ''Quantitative Visualization of the Flow in a Centrifugal Pump with Diffuser Vanes, Part A: On Flow Structure and Turbulence,'' ASME J. Fluids Eng. **122**, No. 1, pp. 97–107.
[12] Sinha, M., Katz, J., and Meneveau, C., 2000, ''Quantitative Visualization of the Flow in a Centrifugal Pump with Diffuser Vanes, Part B: Addressing Passage-Averaged and LES Modeling Issues in Turbomachinery Flows,'' ASME J. Fluids Eng. **122**, No. 1, pp. 108–116.
[13] Roth, G., Mascenik, D. T., and Katz, J., 1999, ''Measurements of the Flow Structure And Turbulence Within A Ship Bow Wave,'' Phys. Fluids **11**, No. 11, pp. 3512–3523.
[14] Roth G., and Katz J., 1999, ''Parallel Truncated Multiplication and Other Methods for Improving the Speed and Accuracy of PIV Calculations,'' FEDSM-6998, Proc. ASME Fluids Eng. Conf., San Francisco.
[15] Roth, G. and Katz, J., 2000, ''Five Techniques for Increasing the Speed and Accuracy of PIV Interrogation,'' Meas. Sci. Technol. **12**, p. 238–245.
[16] Dong, R., Chu, S., and Katz, J., 1992, ''Quantitative Visualization of the Flow Structure within the Volute of a Centrifugal Pump, Part B: Results,'' ASME J. Fluids Eng. **114**, No. 3, pp 396–403.
[17] Roth G., Hart, D., and Katz J., 1995, ''Feasibility of Using the L64720 Video Motion Estimation Processor (MEP) to Increase Efficiency of Velocity Map Generation for Particle Image Velocimetry,'' ASME/EALA Sixth Int. Conf. on Laser Anemometry, Hilton Head, South Carolina.
[18] Sridhar, G., and Katz, J., 1995, ''Lift and Drag Forces on Microscopic Bubbles Entrained by a Vortex,'' Phys. Fluids **7**, No. 2, pp. 389–399.
[19] Adrian, R. J., 1991, ''Particle-imaging Techniques for Experimental Fluid Mechanics,'' Annu. Rev. Fluid Mech. **23**, 261–304.
[20] Japikse, D., 1998, ''Rotating Stall Investigations Expand,'' SPIN, **7**, pp. 4–5.
[21] Sinha, M., 1999, ''Rotor-Stator Interactions, Turbulence Modeling and Rotating Stall in a Centrifugal Pump with Diffuser Vanes,'' Ph.D. dissertation, The Johns Hopkins University, Baltimore, MD.
[22] Johnston, J. P., and Dean, R. C., 1966, ''Losses in Vaneless Diffusers of Centrifugal Compressors and Pumps,'' ASME J. Eng. Power **88**, pp. 49–62.
[23] Iversen, H. W., Rolling, R. E., and Carlson, J. J., 1960, ''Volute Pressure Distribution, Radial Forces on the Impeller, and Volute Mixing Losses of a Radial Flow Centrifugal Pump,'' ASME J. Eng. Power **82**, pp. 136–144.

Impeller Geometry Suitable for Mini Turbo-Pump

Shuhong Liu
e-mail: oo9803jr@tobata.isc.kyutech.ac.jp

Michihiro Nishi
e-mail: nishi@mech.kyutech.ac.jp

Kouichi Yoshida
e-mail: yoshida@mech.kyutech.ac.jp

Department of Mechanical Engineering,
Kyushu Institute of Technology,
Sensui-cho 1-1, Tobata,
Kitakyushu, 804-8550, Japan

The objective of the present study is to investigate the suitable impeller geometry for a mini turbo-pump, which is defined as the size having impeller diameter between around 5 mm and 50 mm. This is treated because those pumps having the above size are regarded as low efficiency machines if efficiency is less than 40 percent or 50 percent. Considering that not only low Reynolds number and tip clearance but the design method are the major causes for low performance, we carried out the performance test experimentally using two semi-open centrifugal impellers: one is named as Impeller B of 36 mm diameter and the other is Impeller C of 34 mm diameter. And the former is designed by a conventional method and the latter is based on the proposed method. In the performance tests, rotational speed was varied between 3000 rpm and 10,000 rpm and the axial clearance at the blade tip of impeller exit was between 0.2 mm and 0.8 mm. It is clearly seen from the results that Impeller C gives the better hydraulic performance. It is also clarified that the effect of tip clearance on Impeller C performance is much smaller than that of the Impeller B. Further, we conducted numerical calculation of impeller performance, where the commercial CFD code named TASCflow was used with k-ω turbulence model. From the results, the turbulent flow analysis is reasonably usable to study the flow in the above mini impellers. [DOI: 10.1115/1.1385385]

Keywords: Mini, Turbo-pump, Impeller, Geometry, Performance, Tip Clearance, Numerical Analysis

Introduction

In recent years, due to the global environmental problems, it is essential to promote effective and efficient usage of energy and to develop mini technologies in many areas. For the turbo-pump, being the key machine for liquid transportation, its further development is always desirable. Impellers of around 50 mm diameter have still been adopted for a blood pump, a turbo-pump for a heat control system in a space laboratory, though they are expected to be as small as possible.

Though a great many research works have been done for the larger size pump, whose suction-pipe diameter is larger than 32 mm, rather a few studies have treated a mini turbo-pump of impeller diameter between 10 mm and 50 mm. It may be because many textbooks and handbooks usually show the classical results, which demonstrate the pump efficiency being decreased with decrease of the discharge [1]. The major causes are manufacturing accuracy, surface roughness, clearance effect, low specific speed, and low Reynolds number. However, some of these problems will be solved now by the remarkable development of various technologies. The production technology can reduce the effect of the first two or three at low cost. As an electric motor with inverter has become very popular in recent years, it will be possible to introduce a variable speed turbo-pump without an additional cost. Thus, a pump having not low but desirable specific speed will be selectable if higher rotational speed of a motor than the rated speed is utilized. Due to the higher rotational speed, we can set Reynolds number larger than 10^5, which is regarded as the limit to avoid the predominant deterioration of efficiency [2].

The major remaining problem must be the effect of axial tip clearance on the hydraulic performance, because a centrifugal semi-open impeller will be the standard type since higher head and smaller discharge will generally be expected for a mini turbo-pump. Engeda and Rautenburg did a systematic study on semi-open impellers and showed that the tip clearance had an obvious effect on pump performance [3]. Senoo and Ishida did fundamental studies on the pressure losses due to the tip clearance using centrifugal blowers, and demonstrated the prediction method for them [4–6]. It should be noted that all these studies were carried out for the larger size impeller. And it is still unclear how much the tip clearance affects the mini-impeller performance, although they are useful contributions.

Besides those causes mentioned above, a hydraulic design method for mini turbo-pumps should be the most important key. Though it is said that the method has already been established [1], it is not yet clear that the conventional design method is also applicable to the mini turbo-pumps. From consideration of the mini turbo-pump application, primary attention can be paid to higher load with smaller impeller-size and better hydraulic performance near the design point rather than higher cavitation performance and wider operating range. Thus, the following design concepts may be suitable for a mini turbo-pump having a centrifugal semi-open impeller: (1) larger blade angle at outlet (measured from tangential direction), (2) larger number of blades and (3) smaller outlet/inlet area-ratio. The objective of the present study is to investigate the impeller geometry suitable for the mini turbo-pump experimentally and numerically. We used two kinds of centrifugal semi-open impellers, one being designed by a conventional method and the other based on the concepts described above. As the first step, we focus on an impeller having specific speed (Type number) around 0.8 and specific diameter around 4.

Test Apparatus and Method

Test Impellers. Figure 1 shows the photos of test centrifugal impellers specified as Impeller B of 36 mm diameter and Impeller C of 34 mm diameter. The meridional shape is shown in Fig. 2, and major specifications are summarized in Table 1. It is noted that Impeller B having five two-dimensional blades is designed by the conventional method [1] and Impeller C is based on the proposed concepts. Typical geometrical features of the latter are outlet blade angle of 60 deg, blade number of 12, and outlet/inlet area ratio of 0.9.

Contributed by the Fluids Engineering Division for publication in the JOURNAL OF FLUIDS ENGINEERING. Manuscript received by the Fluids Engineering Division February 26, 2001; revised manuscript received April 28, 2001. Associate Editor: Y. Tsujimoto.

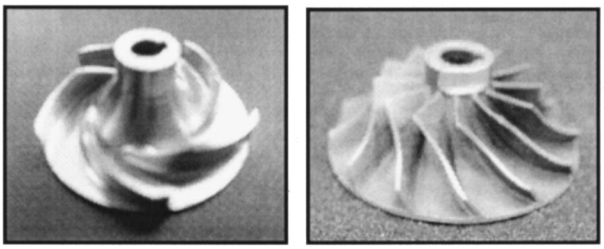

Impeller B (D_2=36mm) Impeller C (D_2=34mm)

Fig. 1 Test impellers

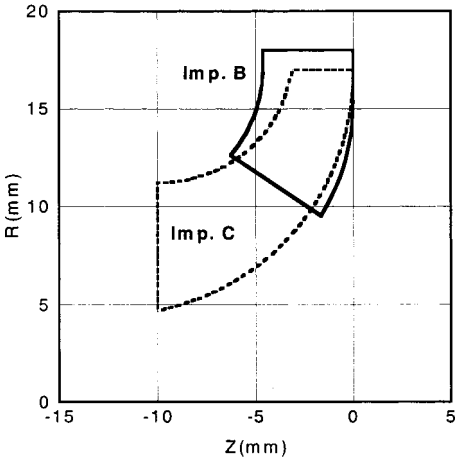

Fig. 2 Meridional shape of impeller

Table 1 Impeller specifications

	Symbols	Imp. B	Imp. C
Outlet diameter (mm)	D_2	36.0	34.0
Inlet diameter at hub (mm)	D_{1h}	18.0	9.0
Inlet diameter at tip (mm)	D_{1t}	25.0	22.0
Outlet width (mm)	b_2	4.4	2.9
Blade outlet angle	β_2	22.5°	60°
Blade number	Z	5	12
Outlet/inlet area ratio	A_2/A_1	1.36	0.9

Test Apparatus. The test impellers in turn are installed in the casing of a mini turbo-pump, a cross-sectional view of which is shown in Fig. 3. Considering the reaction factor of Impeller C, a vaneless diffuser portion is located between the impeller and the spiral casing. The pump inlet (suction pipe) diameter is 20 mm and the exit (delivery pipe) is 15 mm. Pressure taps are provided on the wall of the front cover to measure static pressures near the diffuser exit for Impeller C and near the diffuser inlet and exit for Impeller B. Axial clearance between the blade tip and the shroud casing is adjusted by inserting a lining sheet between the front cover and the casing to study the tip clearance effect. Thus, the diffuser width also varied with the thickness of the sheet. It is noted that the same diffuser and casing were used in this study, as our attention was primarily paid to the hydraulic performance of the impeller. Figure 4 schematically shows the test rig used for the measurement of pump performance. The test pump is driven by a three-phase induction motor with an inverter, which is adjustable from 1200 rpm–12,000 rpm. Input power was measured by a

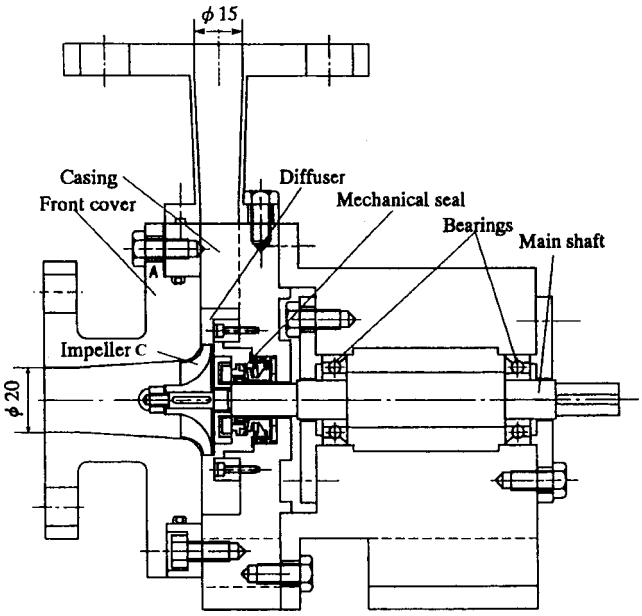

Fig. 3 Cross-sectional view

torque detector, the pump discharge was by a magnetic flowmeter and head rise between pump inlet and outlet was by U tube manometer.

Nondimensional Parameters. Following the standard test code [7], the pump performance is studied and the characteristics are represented by the nondimensional parameters shown below:

a. Discharge Coefficient: ϕ.

$$\phi=(Q_d/60000)/(U_2A_2) \tag{1}$$

where Q_d: discharge (*L*/min), U_2: peripheral speed at impeller outlet $=\pi D_2 n/60$ (m/s), A_2: cross-sectional area at impeller outlet $=\pi D_2 b_2$ (m^2) .

b. Head Coefficient: ψ.

$$\psi=H/(U_2^2/2g) \tag{2}$$

where H: pump total head (m), g: gravitational acceleration (m/s^2).

c. Power Coefficient: τ_p, τ_{in}, τ_w .

$$\tau_p=P_p/(\rho A_2 U_2^3/2) \tag{3}$$

$$\tau_w=P_w/(\rho A_2 U_2^3/2) \tag{4}$$

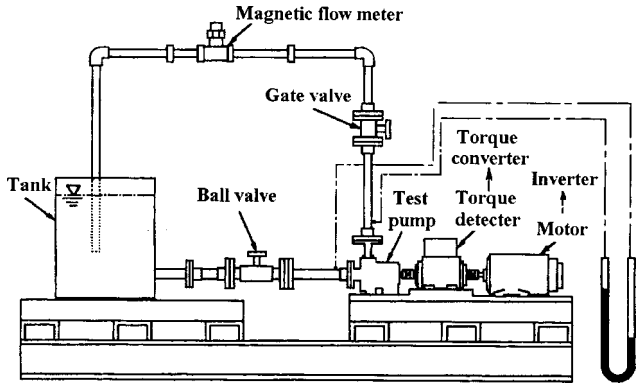

Fig. 4 Test rig

where ρ: water density (kg/m^3), P_p: shaft power (W), P_w: water power $=\rho g(Q_d/60{,}000)$ H (W).

Since the mechanical power losses due to the bearings and mechanical seal may be relatively large in the case of a mini pump, the following input power coefficient τ_{in} is introduced.

$$\tau_{in}=P_{in}/(\rho A_2 U_2^3/2) \tag{5}$$

where P_{in}: shaft power excluding bearings and mechanical seal losses (W). To obtain P_{in} experimentally, we carried out the shaft-torque measurement once the casing was emptied, assuming that the identical losses occurred in those cases with and without water as the working fluid.

d. Pump efficiency: η_p, η_{in}. Pump total efficiency is given by

$$\eta_p=\eta_v\eta_h\eta_m=\eta_v\eta_h\eta_{md}\eta_{me}=P_w/P_p \tag{6}$$

where η_v: volumetric efficiency, η_h: hydraulic efficiency, η_m: mechanical efficiency, η_{me}: external mechanical efficiency, η_{md}: internal mechanical efficiency related to the loss due to the disk and cylindrical friction on outer surfaces of impeller.

Considering the feature of the mini pump where mechanical loss is one of major losses, the **pump internal efficiency** η_{in} is used:

$$\eta_{in}=\eta_v\eta_h\eta_{md}=\tau_w/\tau_{in}=P_w/P_{in} \tag{7}$$

e. Loss Coefficient: ζ. The loss coefficient is defined by

$$\varsigma=H_L/(U_2^2/2g) \tag{8}$$

where H_L: head loss (m).

f. Dimensionless Tip Clearance: λ_2. The following dimensionless parameter is used as the measure to evaluate the effects of tip clearance.

$$\lambda_2=c_2/b_2 \tag{9}$$

where, c_2 is the axial clearance between blade tip and the casing wall at the impeller outlet location. As it is assumed that the thickness of the lining sheet corresponds to the increment of tip clearance, no measurement was made under the operating condition in the present study.

g. Reynolds Number: Re. Concerning Reynolds number, the following definition is adopted:

$$R_e=U_2(D_2/2)/\nu \tag{10}$$

where, ν is the kinematic viscosity (m^2/s).

Test Procedure. Table 2 shows the test conditions to study the effects of tip clearance and Reynolds number on the hydraulic performances of test pumps. The test range of Reynolds number and dimensionless tip clearance are summarized in Table 3 and Table 4, respectively. The performance test is made under constant rotational speed at each test condition.

Table 2 Test conditions

T: tested

n (rpm)	c_2 (mm)						
	0.2	0.3	0.4	0.5	0.6	0.7	0.8
3000	T						T
4000	T						T
5000	T						T
6000	T	T	T	T	T	T	T
8000	T						T
10000	T						T

Table 3 Reynolds number Re($\times 10^{-5}$)

n(rpm)	3000	4000	5000	6000	8000	10000
Imp. B	1.01	1.35	1.69	2.02	2.70	3.37
Imp. C	0.9	1.2	1.5	1.8	2.4	3.0

Table 4 Tip clearance ratio λ_2

c_2(mm)	0.2	0.3	0.4	0.5	0.6	0.7	0.8
Imp. B	0.045	0.068	0.091	0.114	0.136	0.159	0.182
Imp. C	0.069	0.103	0.138	0.172	0.207	0.241	0.276

Numerical Calculation

In order to make clear the applicability of CFD to the performance prediction of mini impellers, the numerical analysis of three-dimensional turbulent flow was made based on RANS equations and k-ω turbulence model. The commercial CFD code of TASCflow [8] was used for this purpose, and the flow in Impeller C was calculated to compare with the experimental results. As the effect of axial tip clearance on the performance of a semi-open impeller was a major concern, one impeller channel was treated assuming that the incoming flow was axisymmetric. Figure 5 shows the computational domain, which is generated by CFX-TurboGrid. It consists of two parts: blade and tip clearance. The total grid number is 96,200, in which for the blade is $65\times40\times29$, and for tip clearance is $65\times40\times8$. As for the boundary conditions, the absolute axial velocity was given by $U_a=Q_d/A_1$ at the inlet section, while the average static pressure was given as 0 at the outlet section of the domain. Shroud casing (front cover) is set as absolute stationary, and the surfaces of blade and hub are the relative stationary.

Convergence for the simulation varied, but a typical range is 150-200 iterations to research maximum normalized residuals less than the value of 1.0E-4. This is a finer convergence tolerance than is really required, since the solution is converged beyond the point where local or global flow changes are significant. Approximately 3-4 hours on a Dell computer workstation 420866M were required for each solution.

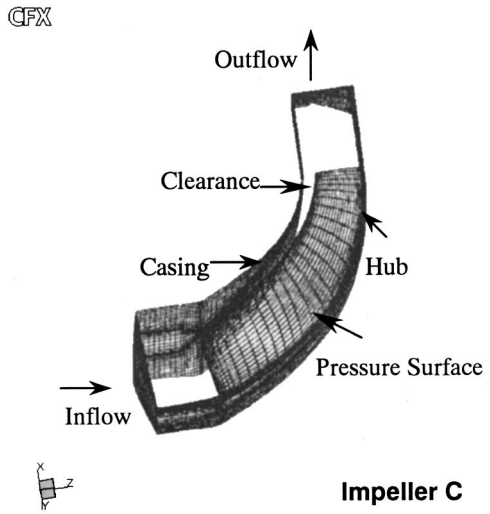

Fig. 5 Computational domain (displayed are the following grids: inflow and outflow planes, casing and hub surfaces, and pressure surface of blade)

Results and Discussions

Pump Performances. Performance curves for pumps having Impeller B and C tested under the rotational speed of 6000 rpm and axial tip clearance of 0.2 mm are shown in Fig. 6(*a*) and (*b*), where pump head H and input power P_{in} are plotted against the discharge Q_d. Theoretical head H_{th} is derived from measured input power and estimated disk-friction-loss [7]. A line of $H_{\text{th-inf}}$ shows the characteristic of theoretical head for the infinite number of impeller blades. Using wall pressures measured at four circumferential positions near the diffuser inlet and exit for Impeller B and those measured at four positions near the diffuser exit for Impeller C, we estimated total head rises at the impeller outlet and diffuser outlet, H_{imp} and H_{dif} respectively. Those results are also shown in the figure to see the performance of each component, impeller, vaneless diffuser and spiral casing. It is noted that H_{imp} in Fig. 6(*b*) corresponds to the calculated results, as we applied the numerical analysis to Impeller C at three operating points. Thus, the calculated input power $P_{\text{in-cal}}$ curve and theoretical head H_{th} are shown for comparison in Fig. 6(*b*).

Figure 7 shows the comparison of pump characteristics ψ, τ, and η versus ϕ, which were obtained from those results in Fig. 6.

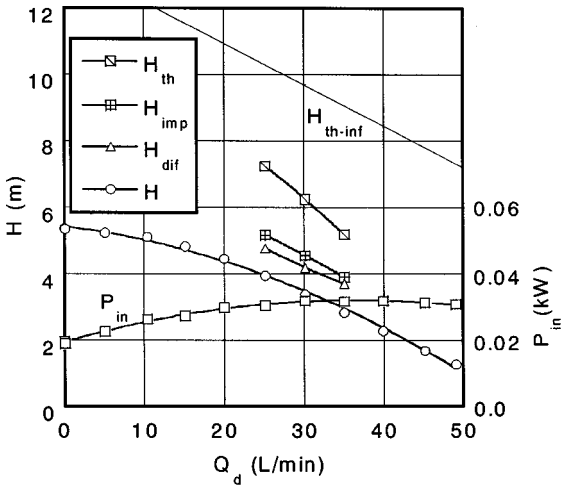

(a) IMPELLER B

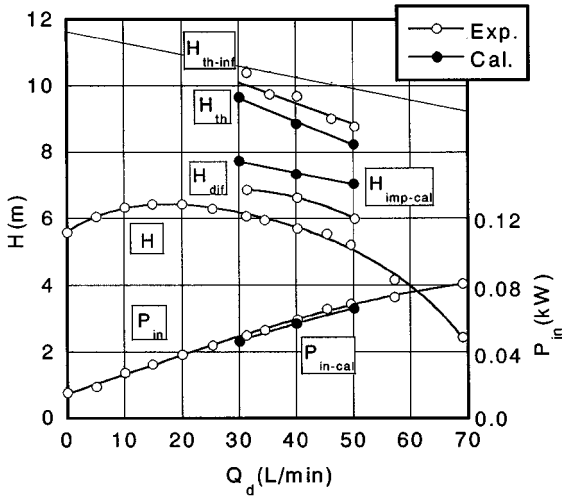

(b) IMPELLER C

Fig. 6 Performance of impeller (n=6000 rpm, c_2=0.2 mm) (Uncertainty of Q_d=±0.5 percent, of H=±0.3 percent, and of P_{in}=0.11 percent)

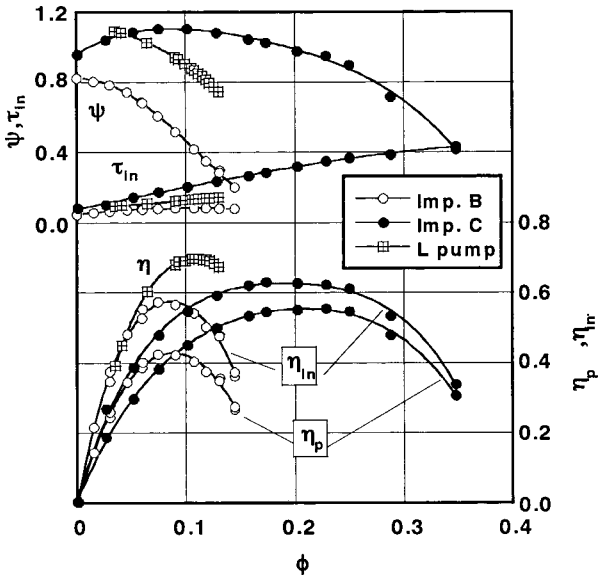

Fig. 7 Comparison of pump characteristics (Imp. B and C: n=6000 rpm, c_2=0.2 mm) (Uncertainty of ϕ=±0.52 percent, of ψ=±0. percent, and of τ_{in}=±0.15 percent, η=±1.5 percent)

Comparison of typical non-dimensional parameters at the best efficiency point is summarized in Table 5. Further, to see the effect of impeller size, the results demonstrated by Engeda-Rautenberg [3] using the following similar semi-open impeller are reproduced in the figure specified as L pump:

Specific speed (or Type number): n_s=0.83
Impeller diameter: D_2=219 mm
Outlet angle of blade: β_2=26 deg
Number of blade: Z=6
Tip clearance: λ_2=0.0523
From the above results, the following features are seen:

1 57 percent is the best pump internal efficiency for the pump having Impeller B, which is designed by the conventional method. According to the chart shown in textbooks, this value for a mini turbo-pump is regarded as not very low.

2 Impeller B provides the stable head-discharge curve observed in the whole operating range.

3 Better performances except the unstable characteristics in the lower flow range are provided by the pump having Impeller C, which is based on the proposed concepts.

Table 5 Comparison of Impeller B and C

(At the best efficiency point)

	Imp. B	Imp. C
ϕ	0.0902	0.202
ψ	0.515	0.978
ψ_{dif}	0.623	1.14
ψ_{imp}	0.678	1.26 (cal)
τ_{in}	0.0819	0.315
η_{in}	56.6%	62.6%
η_{imp}	73.5%	80.6%
ζ_{dif}	0.0553	0.125
ζ_{cas}	0.109	0.160

Note: η_{imp} and ζ_{dif} are estimated using the numerical result of ψ_{imp}.

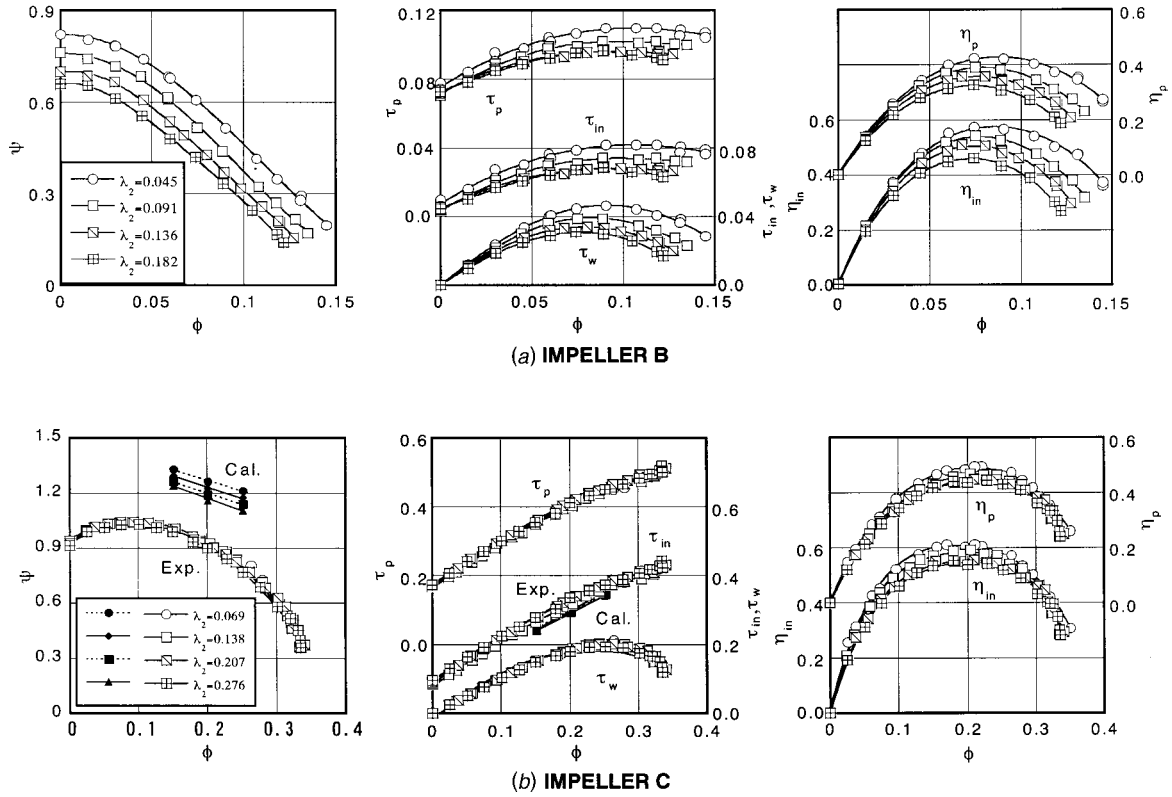

Fig. 8 Effect of tip clearance (n=6000 rpm) (Uncertainty of ϕ=±0.52 percent, of ψ=±0.3 percent, and of τ_{in}=±0.15 percent, η=±1.5 percent)

4 The best pump internal efficiency for Impeller C reaches 63 percent, and the efficiency more than 60 percent is secured in the operating range between 0.13 and 0.26 of ϕ.

5 The discharge and pump head are remarkably increased in the case of Impeller C, diameter of which is a little bit smaller than that of Impeller B.

6 The relatively large difference between pump internal efficiency and total efficiency in both pumps indicates that the mechanical power losses caused by bearings and seals cannot be disregarded for mini-size turbo-pump treated here.

7 The maximum efficiencies of Impeller B and C are smaller than that of L pump. The scale effect will be one of the causes.

8 Good agreement between measured and calculated input power (and theoretical head) of Impeller C case indicates that the turbulent flow analysis based on the RANS equations with k-ω turbulence model will be reasonably applicable to predict the hydraulic performance of turbo-pump even with mini-size.

Effect of Tip Clearance. As stated in the previous section, the tip clearance will be one of the major causes of deterioration of the performance of a turbo-pump having a semi-open impeller. Thus, the performance tests were repeated changing the axial tip clearance for Impeller B and C. Using dimensionless clearance λ_2 as a parameter, characteristic curves are shown in Fig. 8.

From Fig. 8(a) for Impeller B, it is seen that all coefficients, pump-head, power and efficiency are decreased with increasing λ_2. However, relatively smaller effects of λ_2 on the performances are observed in Fig. 8(b) for Impeller C. Especially, dependence on λ_2 is hardly seen among the results of the input power. Here, the numerical analysis was also made to study the effect of axial tip clearance on the performances of Impeller C at three operating points. Their results plotted in Fig. 8(b) show reasonable prediction. The difference of head between the experiment and the calculation largely corresponds to the losses that occurred in the vaneless diffuser and the spiral casing, for the head rise in the impeller is treated in the calculation. Concerning the input power, the numerical results also show the clearance effect being negligibly small.

$$\Delta H^* = (H_0 - H_\phi)/H_0 \tag{11}$$

Using the dimensionless head-drop ΔH^* given above, the clearance effect is examined as shown in Fig. 9, where, H_ϕ as a function of λ_2 denotes the pump head at a certain value of discharge ϕ near the best efficiency point. ϕ=0.09 and 0.2 were adopted for Impeller B and C in this study. H_0 is the pump head at ϕ for zero tip clearance. H_0 was obtained from the extrapola-

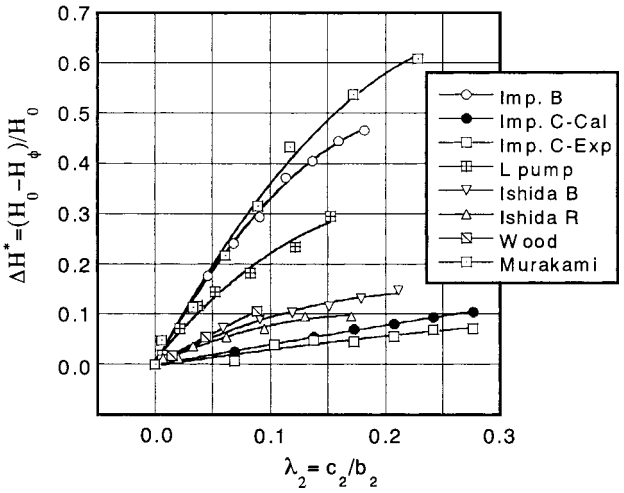

Fig. 9 ΔH^* VS. λ_2

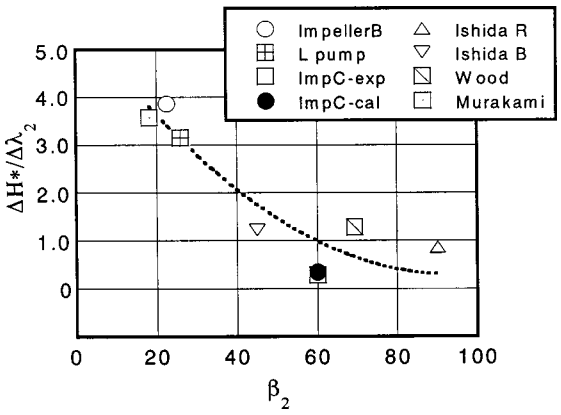

Fig. 10 $\Delta H^*/\Delta\lambda_2$ **VS.** β_2

tion of H_ϕ curve. Further, the numerical result for Impeller C and the test result for larger size pump [3,4,9,10] are included in the figure for comparison. The following features are seen in the figure:

1 Every result demonstrates that the larger the tip clearance is, the larger the head-drop is.

2 Good agreement between experiment and calculation for Impeller C is recognized.

3 Head-drop of Impeller C is much smaller than that of Impeller B and those of other larger size pumps.

4 Thus, the clearance effect does not primarily depend on the impeller size.

From Fig. 9, the correlation between head-drop gradient $\Delta H^*/\Delta\lambda_2$ and β_2 is made and plotted in Fig. 10. It is seen that the gradient is influenced by β_2, i.e., the larger the blade angle will be, the smaller the head-drop will be, which was pointed out by Senoo and Ishida [4–6].

Effect of Reynolds Number. In order to examine the effect of Reynolds number on pump performance, both impellers were tested under different rotational speeds from 3000 rpm–10,000 rpm, following the plan shown in Table 3.

From the macroscopic point of view, similitude is recognized in various characteristic curves excluding the η_p-ϕ curve. As a typical example, the relationship between efficiency and Reynolds number is shown in Fig. 11, where internal pump efficiency η_{in} and pump efficiency η_p are plotted against Re. The drop-off characteristic of pump efficiency η_p is observed with decrease of Reynolds number. This is understandable because the hydraulic power loss is a function of n^3, besides the external mechanical power loss is nearly proportional to n. Regarding the internal efficiency which is related to various hydraulic losses in the pump, the effect of Reynolds number looks considerably small, even though there is such a weak trend that the efficiency is decreased with decrease of Reynolds number. It is suspected that major losses in both pumps are caused by flow mixing which is not related to the effect of Reynolds number.

Further Consideration. It is made clear from the present experiment that the effect of tip clearance on the hydraulic performance of Impeller C is remarkably smaller than that of Impeller B. The experimental results in Fig. 8 show that the typical difference is observed in the characteristics of input power. Though it is decreased with increasing the tip clearance in the case of Impeller B, which is regarded as usual, it is nearly constant for Impeller C.

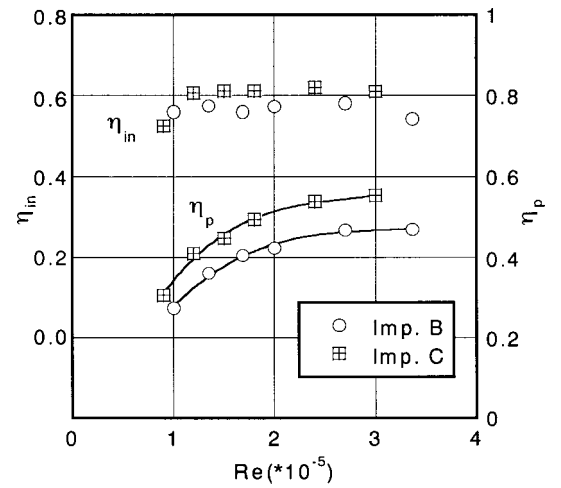

Fig. 11 η_{in}, η_p **VS. Re**

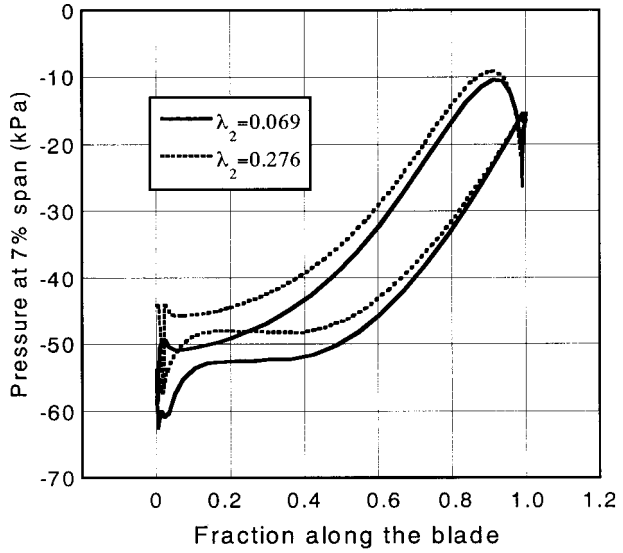

(*a*) **Near the hub**

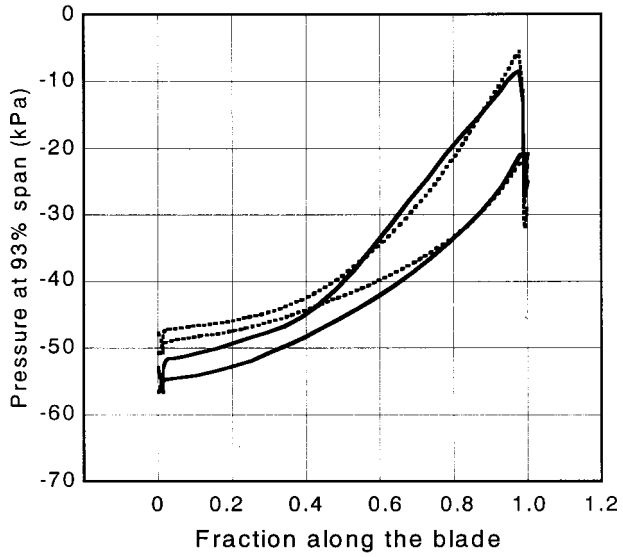

(*b*) **Near the blade tip**

Fig. 12 Pressure distribution along the blade of Impeller C

To find the reason, we calculated the pressure distributions around the blade of Impeller C from the numerical results. The distributions near the hub and the blade tip are shown in Fig. 12(*a*) and (*b*), respectively. It is seen that the difference of pressures on pressure surface and suction surface greatly changes near the upstream side of blade depending on the tip clearance, but it hardly changes near the downstream side. Since the latter largely decides the magnitude of impeller torque, it is explained that Impeller C based on the proposed concepts has the nature to provide almost the same input power under various tip clearance conditions.

Conclusions

The following conclusions can be drawn from the present experimental and numerical study on suitable impeller-geometry of mini turbo-pump, which provides good hydraulic performance:

1 The impeller geometry, which is designed based on the following design concepts, provides better hydraulic performance than that designed by the conventional method.

   (1) Larger outlet blade angle is selected (ex.: $\beta_2 = 60$ deg for Impeller C).
   (2) The number of blade greater than several blades is selected (ex.: $Z = 12$ for Impeller C).
   (3) Outlet/inlet area ratio A_2/A_1 less than 1.0 is selectable if the diffusion factor W_2/W_1 takes a reasonable value (ex.: $A_2/A_1 = 0.9$ for Impeller C).

2 If we use the turbo-pump having the proposed impeller of 34 mm diameter, the following performance is achievable under the rotational speed 10,000 rpm: pump head =15.8 m, discharge =66.8 L/min, and pump internal efficiency =63 percent.
3 The effect of tip clearance will be attenuated by the impeller geometry such as larger outlet blade angle. Its effect on the proposed impeller is remarkably smaller than that of the conventional impeller.
4 The law of similitude was observed for the pump characteristics in the range of Reynolds number larger than 1.0×10^5.
5 The numerical three-dimensional flow analysis based on RANS equations with k-ω turbulence model may be reasonably applicable to study the hydraulic performance of mini impellers.

Acknowledgments

The authors gratefully acknowledge the support from the Harada Memorial Scholarship foundation at the initiation of this study and that from the Ministry of Education, Science and Culture under the Grant-in-Aid for Scientific Research (c) (No.11650179) as a nice driving force. They are grateful to Dr. Y. Senoo, Professor Emeritus of Kyushu University, for his helpful comments during the preparation of this paper. The authors would also like to thank Prof. Tsukamoto, Prof. Kanemoto and the members of KIT Fluid Engineering Group for their assistance throughout the course of the present investigation, which has been conducted as one of projects in the KIT Satellite Venture Business Laboratory.

Nomenclature

A = area (m^2)
b = width (mm)
c = axial clearance (mm)
D = diameter (mm)
H = pump total head (m)
n = rotational speed (rpm)
P = power (W)
Q_d = discharge (L/min)
Re = Reynolds number
U = peripheral speed (m/s)
W = relative velocity (m/s)
Z = blade number
β = blade angle (deg)
ΔH^* = dimensionless head-drop, see Eq. (11)
ζ = loss coefficient, see Eq. (8)
η = efficiency, see Eq. (6)
λ = clearance ratio, see Eq. (9)
τ = power coefficient, see Eq. (3)
ϕ = flow coefficient, see Eq. (1)
ψ = head coefficient, see Eq. (2)

Subscripts

1 = inlet
2 = outlet
cal = calculation
cas = casing
dif = diffuser
h = hub, hydaulic
in = internal
imp = impeller
L = loss
p = power
t = tip
th = theoretical
th-inf = theoretical (perfectly guided)
w = water

References

[1] Stepanoff, A. J., 1957, *Centrifugal and Axial Flow Pumps*, 2ed., Wiley, NY.
[2] Tanaka, K., and Ohashi, H., 1984, ''Performance of Centrifugal Pumps at Low Reynolds Number,'' Trans. Jpn. Soc. Mech. Eng., Ser. B, **50**, No. 449, pp. 279–285 (in Japanese).
[3] Engeda, A., and Rautenberg, M., 1988, ''Partial Flow Performance Comparisons of Semi-open and Closed Centrifugal Impellers,'' ImechE, C334/88.
[4] Ishida, M., and Senoo, Y., 1981, ''On the Pressure Losses Due to the Tip Clearance of Centrifugal Blowers,'' ASME J. Eng. Gas Turbines Power, **103**, pp. 271–278.
[5] Senoo, Y., and Ishida, M.,1986, ''Pressure Loss Due to the Tip Clearance of Impeller Blades in Centrifugal and Axial Blowers,'' ASME J. Eng. Gas Turbines Power, **108**, pp. 32–35.
[6] Senoo, Y., and Ishida, M., 1987, ''Deterioration of Compressor Performance Due to Tip Clearance of Centrifugal Impellers,'' ASME J. Turbomach., **109**, pp. 55–61.
[7] JSME S008, 1989, Performance Conversion Method for Hydraulic Turbines and Pumps.
[8] CFX-TASCflow, Version 2.10, Primer Manual, AEA Technology Engineering Ltd.
[9] Wood, G. M., Welna, H., and Lamers, R. P., 1965, ''Tip-clearance Effect in Centrifugal Pumps,'' Trans. ASME, **85**, pp. 932–940.
[10] Murakami, M., and Minemura, Y., 1976, ''Effects of Side Clearance of Semi-open Impeller Pumps under Air Admitting Conditions,'' Trans. Jpn. Soc. Mechm. Eng. **42**, No. 354, pp. 489–496 (in Japanese).

Sankar L. Saha
Graduate Student,
Graduate School of Engineering
e-mail: saha@mach.me.ynu.ac.jp

Junichi Kurokawa
Professor
e-mail: kuro@mach.me.ynu.ac.jp

Jun Matsui
Associate Professor
e-mail: jmat@post.me.ynu.ac.jp

Hiroshi Imamura
Research Associate
e-mail: ima@post.me.ynu.ac.jp

Department of Mechanical Engineering,
Yokohama National University,
79-5 Tokiwadai, Hodogaya-ku,
Yokohama, 240-8501, Japan

Passive Control of Rotating Stall in a Parallel-Wall Vaned Diffuser by J-Grooves

In order to control and suppress instabilities caused by swirl flow, the authors have proposed a very simple passive method utilizing shallow grooves mounted on a casing wall or diffuser wall(s) parallel to the pressure gradient. The groove is termed a ''J-groove.'' The method is theoretically analyzed and experimentally proved capable of suppressing rotating stall in a vaneless diffuser. The performance curve instability is characterized by the positive slope of the head-capacity curve of a mixed flow pump for the entire flow range. In continuation, this work is aimed at realizing experimentally the effect of J-grooves on suppressing rotating stall in the vaned diffuser of a centrifugal turbomachine. Thirteen double curvature vanes with various radial positions, various setting angles, and J-grooves of different dimensions are tested in a parallel wall vaned diffuser with a semi-open radial impeller with and without J-grooves. The results show that J-grooves can also suppress rotating stall in the vaned diffuser for the entire flow range. [DOI: 10.1115/1.1374214]

1 Introduction

Rotating stall, the subsynchronous rotating velocity fluctuations of unsteady flow phenomenon, can be generated either by a destabilization of the impeller flow [1–3] or by a destabilization of the diffuser flow [4–6]. Centrifugal compressors are now increasingly being used in the automotive and utilities industries. The development of radial flow compressors has progressed to the point where a key factor for improved system performance is the vaned diffuser [7]. Both the efficiency and surge-to-choke operating range of a centrifugal compressor depend strongly on the performance of the vaned diffuser [8]. Rotating stall in the vaneless and vaned diffusers not only limits the stable operating range of pumps, fans, and compressors but also may cause severe damage to bearings [9].

To continue the development of high performance radial flow compressors, additional design information on diffuser performance, and a qualitative understanding of the flow mechanisms occurring in the vaned diffuser are being sought [7,8,10–17].

Research into the prediction and control of rotating stall and its detrimental effects has been pursued for many years. Among these, casing treatment and active control techniques are noteworthy. Casing treatments (axial, skewed and circumferential slots, tapered or straight holes, honeycombs, recess vane, air-separator etc.) have been popular since 1900, as reported by Osborn and Moore [18], Prince et al. [19], Amann et al. [20], Takata and Tsukuda [21], Greitzer et al. [22], Fujita and Takata [23], Smith and Cumptsy [24], Miyake et al. [25], and Azimian et al. [26]. The idea of extending the compressor operating range through the use of active control techniques was first published in the open literature by Epstein et al. [27], and since then successful experiments have been carried out by Day [28], Paduano et al. [29], D'Andrea et al. [30], and Gysling and Greitzer [31]. Both passive control (casing treatment) and active control methods have limitations such as an increase in stall or instability margin up to only a few percent, and insufficient to affect the entire flow range. Most of them require complicated mechanisms and utilize additional machinery that eventually decrease the overall efficiency and reliability. Recently, Day et al. [32] mentioned that the variety of the stalling patterns, and the ineffectiveness of stall warning procedures, suggest that the ultimate goal of a flightworthy active control system remains some way off. Therefore, there is as yet a strong need to find a simple method of suppressing rotating stall.

Kurokawa et al. [33] proposed a very simple passive method utilizing shallow grooves mounted on a casing wall or diffuser wall(s) parallel to the pressure gradient called J-grooves. Although J-grooves can be considered as the conventional casing treatment, yet their defined location, direction and mechanism are different from those of the conventional casing treatment. The mechanism of the J-groove is explained theoretically and the effectiveness is realized experimentally for suppressing rotating stall in the vaneless diffuser [33] and performance curve instability characterized by the positive slope of head-capacity curve of a mixed flow pump [34].

The present study is thus aimed at revealing experimentally the effects of J-grooves on suppressing rotating stall in a parallel-wall vaned diffuser with a purely radial impeller. There are few related publications; hence the papers on rotating stall in compressors are quoted, as they indicate that the present method can also be applicable to the compressor diffusers. First, the characteristics of rotating stall in the parallel-wall vaneless and vaned diffuser are studied experimentally. Second, the effect of J-grooves on suppressing rotating stall in the same vaned diffuser is determined experimentally. Finally, the results are compared. Hereafter groove means J-groove.

2 Experimental Apparatus and Procedures

The parallel-wall vaned diffuser test stand with a vertical axis used in this experiment is shown in Fig. 1. The outlet of the diffuser is exposed to the atmosphere. A swirl stop is mounted about 2 mm upstream of the impeller inlet. Fine wire net is set upstream of the impeller to aid uniform suction, to minimize the inlet velocity distortion, and also to prohibit the wake behind the supports of the impeller drive motor. The dimensions and the notations of the impeller and the diffuser are shown in Table 1.

The semi-open radial type impeller, n_s 170 used in this experiment had 8 vanes and outlet width b_2 equal to the diffuser channel width b. The tip clearance between the front shroud and the impeller was kept fixed at 0.8 mm. A variable speed motor and a supplemental blower (upstream) were used to control the speed of the impeller and to regulae the flow through it. The configuration of diffuser and vane is shown in Fig. 2(*a*) and configuration of

Contributed by the Fluids Engineering Division for publication in the JOURNAL OF FLUIDS ENGINEERING. Manuscript received by the Fluids Engineering Division April 27, 2000; revised manuscript received March 1, 2001. Associate Editor: Y. Tsuijimoto.

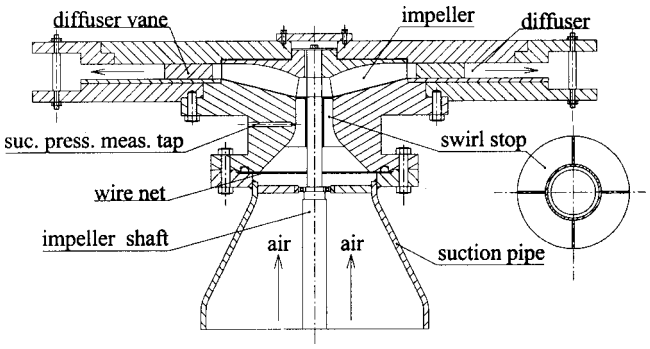

Fig. 1 Details of the test section

diffuser, vane and J-groove is shown in Fig. 2(*b*). Air flow rate was calculated from the pressure difference measured directly by a manometer across a nozzle orifice made according to Japan Industrial Standard No. B8616. Pressure fluctuation at the diffuser wall was measured with semiconductor pressure transducers of cut off frequency 10 kHz. The pressure transducers were set at $r/r_i=1.10$ for three different tangential positions, namely 0 deg, 55.4 deg, and 138.5 deg, as shown in Fig. 2(*c*). The number of rotating stall cells were calculated from their phase differences. Time averaged velocity distribution was measured by traversing a 3-hole Pitot probe at $r/r_i=1.10$ as shown in Fig. 2(*c*).

Thirteen double curvature diffuser vanes were used for all experiments. By changing their radial setting position, i.e., $r_v/r_i=1.05$, 1.10, and 1.15 where r_v is the vane setting radial position at the vane leading edge, and the vane setting angle, i.e., $\beta_v=8$ deg, 12 deg and 16 deg from the tangential direction, several sets of experiments were performed for the ungrooved and the J-grooved cases. The region of the diffuser wall(s) where grooves were to be formed was machined to the depth of the groove. Then the grooves were formed by pasting pieces of rubber plates onto the diffuser wall(s) with a very thin double layer coated gum tape of sufficient adhesive strength to keep the diffuser width constant. The diffuser vanes were also affixed to the diffuser channel walls with a very thin double layer coated gum tape. The grooves were radial and their depth and width were kept fixed radially for one set of experiments. Because the vaneless space/inlet region of the diffuser is considered to be a sensitive area and plays a dominant role in dictating diffuser performance, grooves were mounted from the diffuser inlet to the vane edge as shown in Fig. 2(*b*). It was predicted that the grooves would increase the flow angle and therefore would improve the choke flow between adjacent vanes to suppress rotating stall. The dimensions of the J-groove tested were $w=5\sim15$ mm, $d=1\sim3$ mm, $l=$approximately $12\sim28$ mm and $n=39\sim182$. In these test the impeller speed was kept fixed at 3000 rpm and the corresponding Reynolds number $R_e=U_2r_2/\nu$ was 3.3×10^5. The total head was calculated from the suction gauge pressure (measured at the impeller suction side) head and the velocity head between the suction of the impeller and the outlet of the parallel wall.

Table 1(Dimensions, notations of impeller and diffuser)

Vaneless and vaned diffuser:		Radial impeller (semi-open type, $n_s=170$):	
outer radius	$r_o=315$ mm	outlet radius	$r_2=125$ mm
		inlet radius	$r_1=25$ mm
inner radius	$r_i=126$ mm	outlet width	$b_2=20$ mm
		inlet width	$b_1=26$ mm
channel width	$b=20$ mm	outlet angle	$\beta_2=90$ deg
		inlet angle	$\beta_1=90$ deg

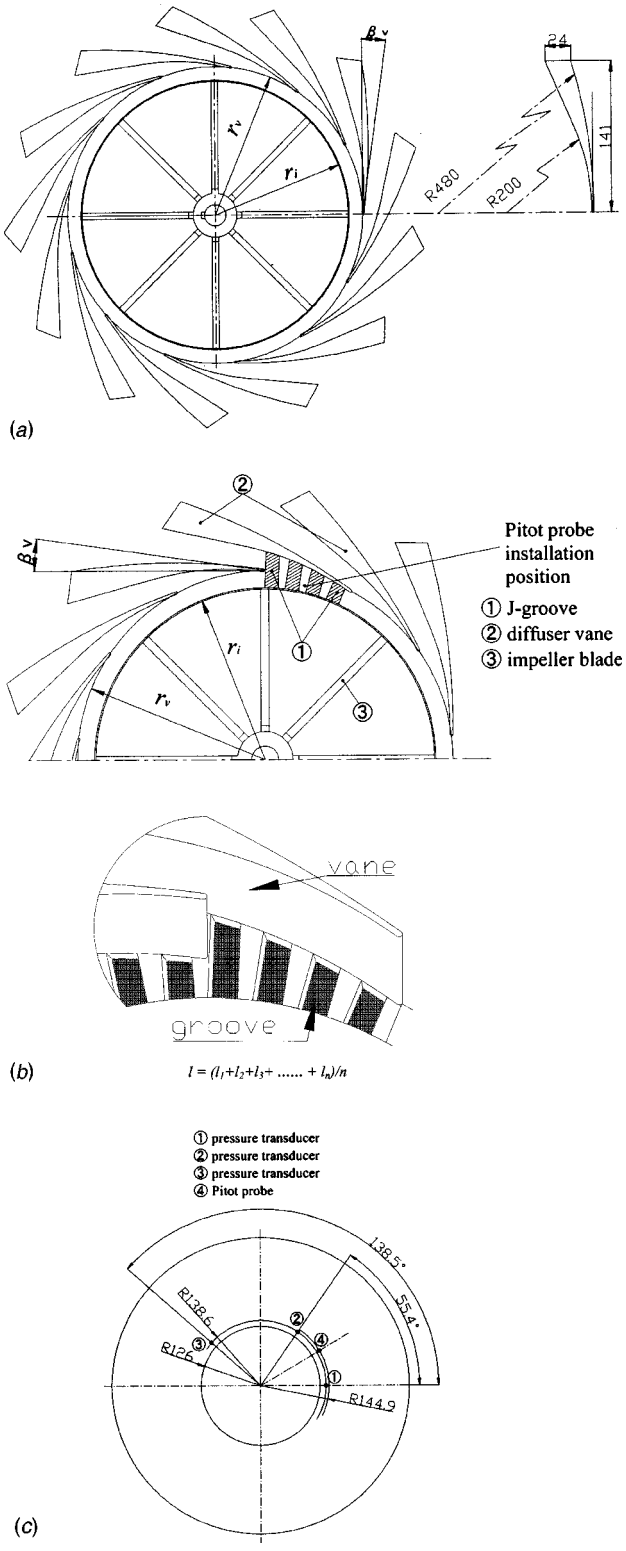

Fig. 2 (*a*) Configuration of diffuser and vane; (*b*) configuration of diffuser, vane and J-groove; (*c*) layout of the semiconductor pressure transducer and Pitot probe

3 Experimental Results and Discussions

3.1 Characteristics of Rotating Stall in the Vaneless Diffuser. As a reference, the characteristics of the vaneless diffuser were determined first by removing the vanes from the diffuser channel. The head-capacity curve is shown in Fig. 3(*a*). The wall

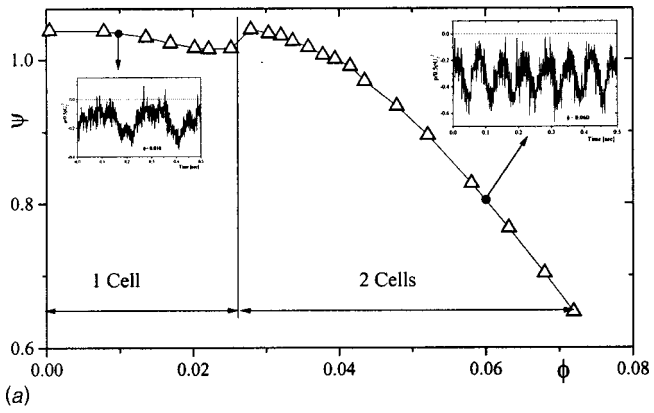

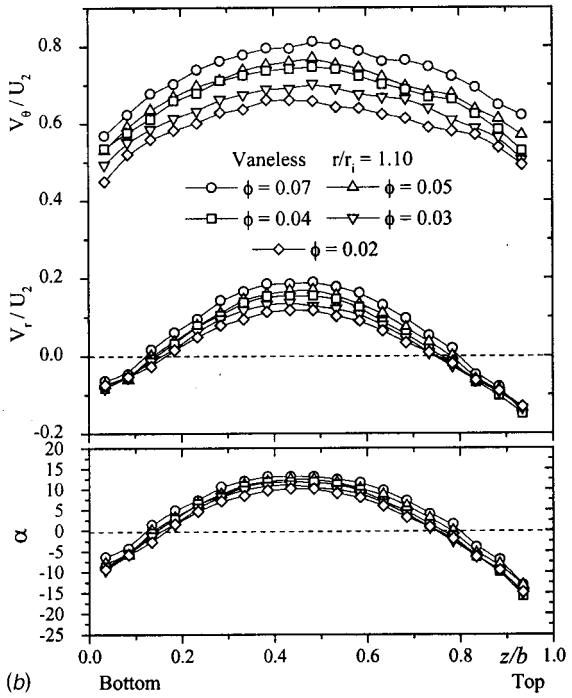

Fig. 3 (*a*) Characteristic curve of the vaneless diffuser ($r_o/r_i = 2.5$). Uncertainties of ψ & ϕ are ±1.5 percent and ±1.7 percent, respectively. (*b*) Velocity distribution at $r/r_i = 1.10$ in the vaneless diffuser. Uncertainties of V_θ/U_2; V_r/U_2; α & z/b are ±3.23 percent; ±3.23 percent; ±1.5 percent and ±2.24 percent, respectively.

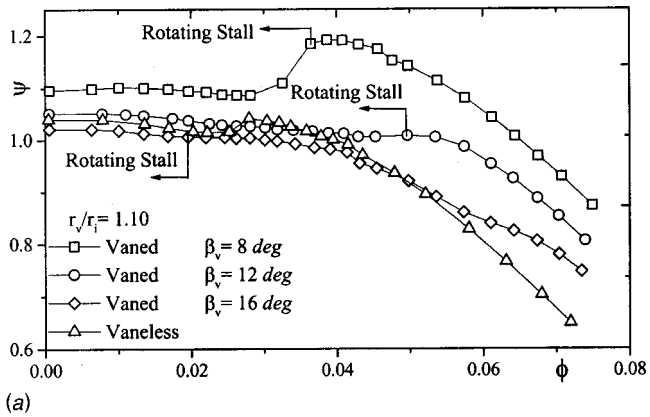

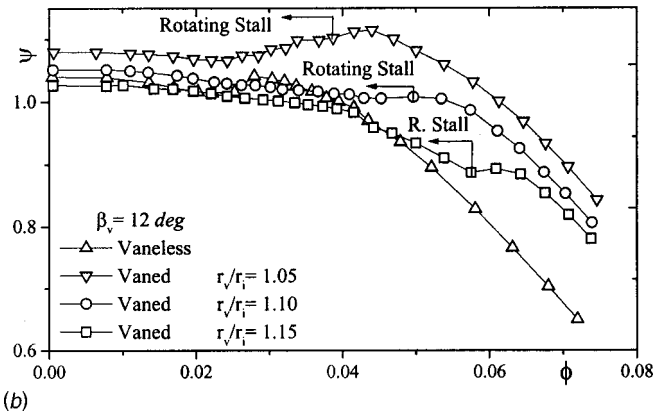

Fig. 4 Characteristics of vaneless, vaned diffuser and rotating stalled flow range. Uncertainties of ψ & ϕ are ±1.5 percent and ±1.17 percent, respectively. (*a*) for different vane setting angles; (*b*) for different vane setting locations.

static pressure fluctuation (shown in the same figure as window view) and their phase difference revealed that the rotating stall in the vaneless diffuser occurred in the entire flow range and even in the negative slope side, where stable operation is normally expected. The same phenomenon is also observed by Frigne and Van Den Braembussche [35]. A typical triangular oscillation with constant frequency $\Omega = 0.178$ was observed in the high flow region. But it changed to a sinusoid wave of moderate amplitude and low frequency, $\Omega = 0.127$ at low flow region. In the same figure at about $\phi = 0.026$, there can be seen a sudden positive slope in the head-capacity curve. From the frequency analysis of the wall static pressure fluctuation, it was understood that, limiting the flow at this point, there were two-cell oscillation in the high flow range and one-cell oscillation in the low flow range. Hence it can be predicted that the sudden positive slope of head-capacity curve is caused when two-cell oscillation is suddenly changed to one-cell with a decrease in ϕ. The reason for this is not yet clear. However, Kurokawa et al. [33], have also observed the same phenomenon in a vaneless diffuser with a pump impeller of $\beta_2 = 40$ deg. This implies that the appearance of positive slope is independent of β_2 but dependent on the number of stall cells. Another probable reason may be a growth of 3D reverse flow at the diffuser walls, and expansion up to the diffuser outlet forming a wide developed and stable reverse flow. In the case of a large vaneless diffuser where $r_o/r_i = 4.8$, the pattern of rotating stall changes gradually from two cells to one cell [33], but in the small diffuser case, it changes suddenly.

The time averaged tangential and radial velocity components measured at $r/r_i = 1.10$ for five flow coefficients for the vaneless case are shown in Fig. 3(*b*). The tangential velocity components are seen to decrease with the decrease in flow coefficient, which is characteristic of a radial vane impeller [36]. The reverse flow is seen for the entire measured region where rotating stall is also observed. This result is in agreement with Jansen [4] who has concluded that rotating stall in a vaneless diffuser is generated when a local flow reversal ($V_r < 0$) occurs. Considering the net flow region of the radial velocity distribution, the average net flow angle is seen to be almost constant and about 9–12 deg for all flow coefficients. The critical flow angle, below which the velocity disturbance is amplified, has been analytically determined for the vaneless diffuser by Senoo and Kinoshita [37] and Tsujimoto et al. [38]. According to their results, the critical flow angle of the present diffuser is 14 deg and 18 deg, respectively, which seems to be consistent with the present experiment. The experiments were, therefore, considered to perform at the vicinity of the critical flow angle, i.e., $\beta_v = 8$ deg, 12 deg, and 16 deg.

3.2 Characteristics of Rotating Stall in the Vaned Diffuser

3.2.1 For Different Vane Setting Angles. The head-capacity curves of the vaned diffusers for three vane setting angles, all of

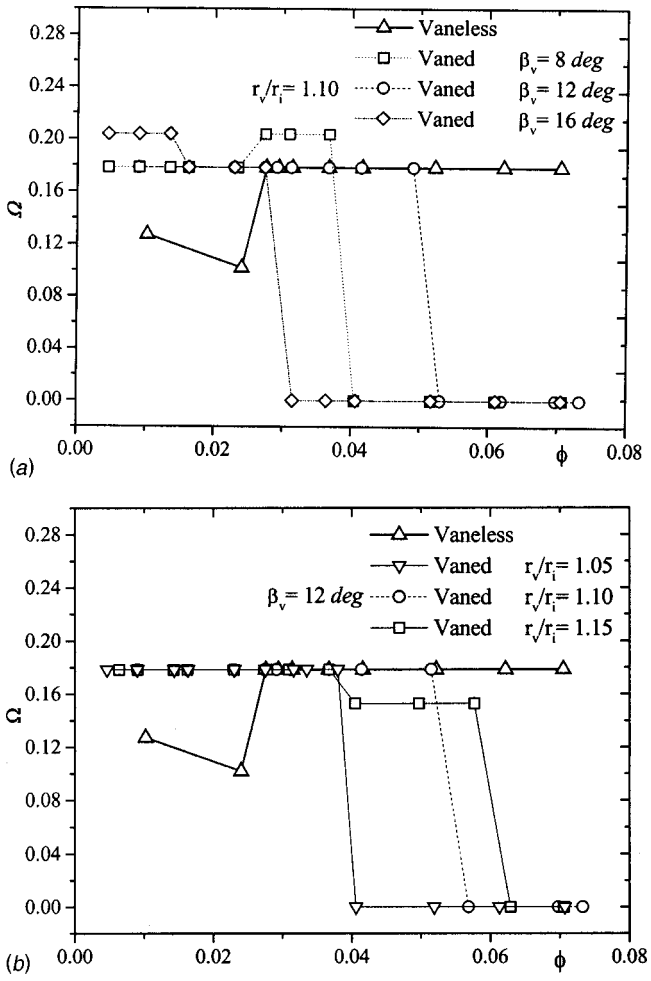

Fig. 5 Rotating stall frequency in vaneless and vaned diffuser. Uncertainty of ϕ is ±1.17 percent. (*a*) For different vane setting angles; (*b*) for different vane setting locations.

them set to $r_v/r_i = 1.10$, are compared in Fig. 4(*a*). The vaneless case is also shown. Arrows in the figure indicate the ϕ, where the inception of rotating stall occurred. Compared with the vaneless case, it can be seen that the insertion of vanes in the diffuser region decreases the stalled flow range. An increase in the vane setting angle yields a low head-coefficient with an increase in stalled flow range, except $\beta_v = 16$ deg. Here stalled flow range means the range of ϕ from stall inception to $\phi = 0$ (no flow). An increase in β_v from 8 deg–12 deg increases the stalled flow range, and a relatively high increase in β_v from 12 deg–16 deg decreases the stalled flow range. The latter phenomenon, an increase in vane angle and a simultaneous decrease in the stalled flow range is also observed by Yoshida et al. [16]. The reason is not clear. However, according to Senoo and Kinoshita [37] and Tsujimoto et al. [38] the critical flow angle for the present vaneless diffuser is 14 deg and 18 deg, respectively. The authors predict that this may have the relation to the present phenomenon though the mechanism of a vaneless diffuser stall is much different from that of a vaned diffuser stall. However, further study is needed. The mass-averaged α in the case of $\phi = 0.05$, Fig. 3(*b*) is calculated as 5.3 deg which relates to the case $\beta_v = 8$ deg, Fig. 4(*a*), where the minimum loss with high pressure coefficient and a significant mass flow reduction at stall inception are realized.

Again in Fig. 4(*a*), the highest rotating stalled flow range is seen in the case of $\beta_v = 12$ deg. Therefore, this case is considered to be good and aimed at suppressing rotating stall for the entire flow range.

3.2.2 For Different Vane Locations. The head-capacity curve of the vaneless and vaned diffuser for three vane setting locations at $r_v/r_i = 1.05$, 1.10 and 1.15 and for a fixed $\beta_v = 12$ deg are compared and shown in Fig. 4(*b*). It can be seen that the head coefficient increases and the stalled flow range decreases when vanes are set closer to the impeller. This means vane setting location largely influence the stalled flow ranges. Similar effects were also observed by Yoshida et al. [17].

3.3 Stall Cell Frequency in the Vaneless and Vaned Diffuser. The rotating stall cell frequency in the vaneless and vaned diffuser for three different vane setting angles and three locations are shown in Fig. 5(*a*) and 5(*b*), respectively. It can be seen that, although rotating stalled flow ranges are different in each figure, their stall frequencies are almost the same, $\Omega = 0.18$. The number of stall cells observed in the vaned diffuser was only one. The stall cell frequencies in the vaned diffuser remain nearly constant for $\phi < 0.03$, which means that stall frequency is independent of ϕ where the flow is highly tangential.

3.4 Suppression of Rotating Stall by the J-Groove

3.4.1 Mechanism of J-Groove. In the vaneless region of a vaned diffuser, the radially outward positive pressure gradient exists due to the centrifugal force. The main flow possesses a strong swirl component and, therefore, large angular momentum when the rotating stall occurs. This swirl flow loses angular momentum when it enters the groove, and experiences no centrifugal force. It therefore flows inward toward the diffuser inlet due to the radial pressure gradient. This radially inward groove flow, called the groove reverse flow, mixes with the main flow at the impeller outlet region and flows together. Theoretical considerations and experimental findings in the case of a vaneless diffuser [33] revealed that the remarkable effect of J-grooves is caused by two mechanisms. The first is a significant decrease in tangential velocity at the diffuser inlet due to mixing between the main flow and the groove reverse flow, and the second is a remarkable increase in radial velocity of the main flow due to the groove reverse flow.

3.4.2 Effect of the Number of J-Grooves. The effect of the number of J-grooves on suppressing rotating stall is shown in Fig. 6(*a*), for the case of $r_v/r_i = 1.10$ and $\beta_v = 12$ deg. Keeping the other groove geometric parameters constant, when the grooves were installed on both walls, n is doubled, and the stalled flow range decreased from $\phi \approx 0.037 - \phi \approx 0.018$. An increase in n increases the groove reverse flow which increases the main flow angle and suppresses the rotating stall. The head-capacity curve for the vaned diffuser without J-grooves is also shown in the same figure. Compared to the ungrooved case, one can see hydraulic loss caused by the grooves in the high flow and very low flow region.

3.4.3 Effect of the Depth of the J-Groove. In Fig. 6(*b*), the effect of depth of the J-groove is shown for the case of $r_v/r_i = 1.10$ and $\beta_v = 12$ deg. Keeping the other groove geometric parameters constant, when d is increased from 1 mm–3 mm, the stalled flow range decreased from $\phi \approx 0.034 - \phi \approx 0.014$. But an increase in depth reduces ψ for the entire flow range. Decrease in ψ is due to the increase in hydraulic loss. Here it can be remarked that the grooves of only 1 mm depth decrease the stalled flow range from $\phi \approx 0.054 - \phi \approx 0.034$ and increase ψ significantly for $\phi < 0.054$ and $\phi > 0.025$. There is also low hydraulic loss for $\phi > 0.054$.

3.4.4 Effect of the Width of the J-Groove. Figure 6(*c*) shows the effect of width of the J-groove for the case of $r_v/r_i = 1.15$ and $\beta_v = 12$ deg. Keeping the other groove geometric parameters constant, when w is increased from 7 mm to 10 mm, no rotating stall is seen for the entire flow range. Increase in w increases the

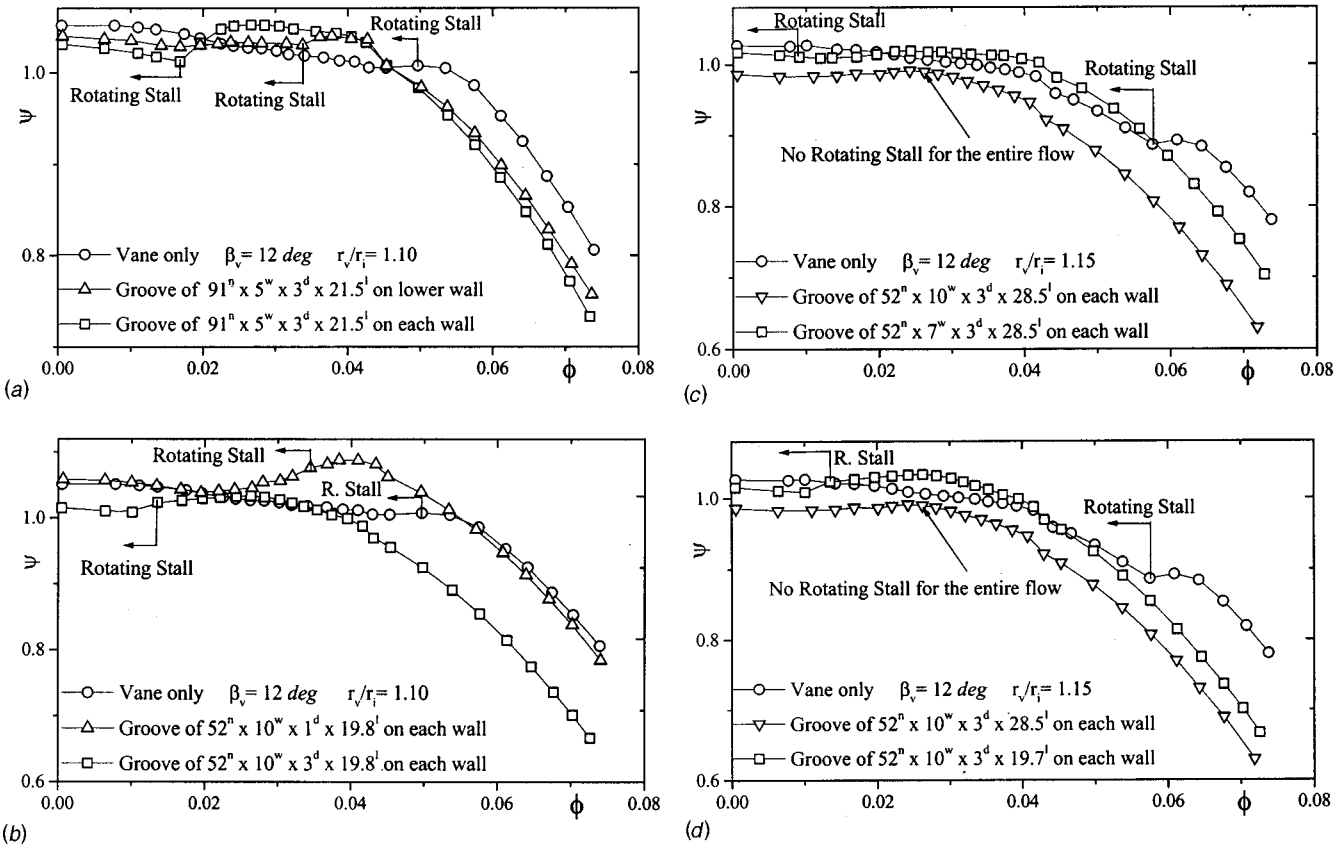

Fig. 6 Suppression of rotating stall by the J-groove. Uncertainties of ψ & ϕ are ±1.5 percent and ±1.17 percent, respectively. (*a*) Effect of number; (*b*) Effect of depth of J-groove; (*c*) Effect of width of J-groove; (*d*) Effect of length of J-groove

groove reverse flow, which increases the main flow angle and suppresses rotating stall. Also, the increase in the width reduces ψ for the entire flow range. [2]

3.4.5 Effect of the Length of the J-Groove. The effect of varying the length of the J-groove is shown in Fig. 6(*d*). Here it can be seen that, when l is increased, the rotating stalled flow range is also decreased. Increase in l increases the groove region and, therefore, the suppression of rotating stall.

3.5 Velocity Distributions for the Vaned Diffuser. Velocity distributions for both the vaned and the vaned with J-grooves

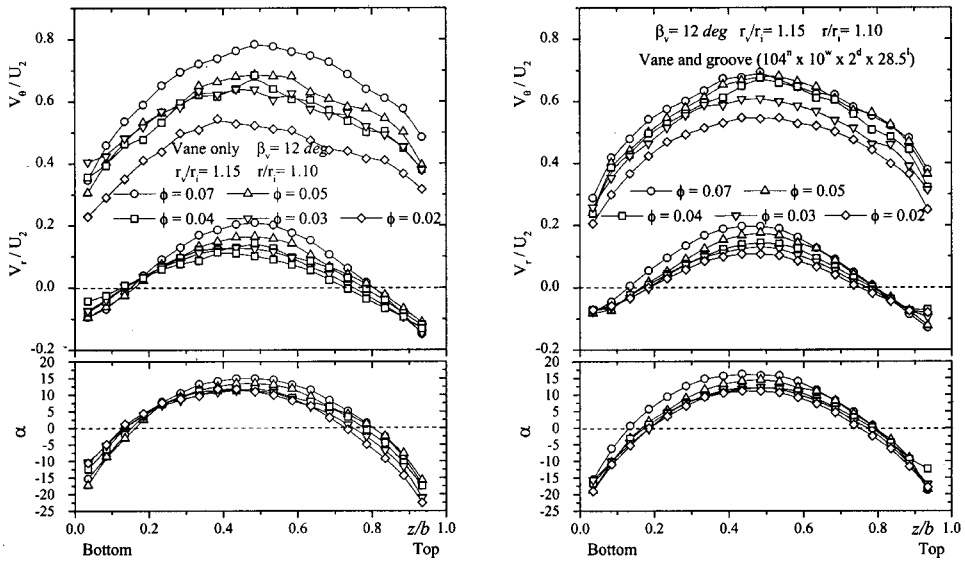

Fig. 7 Velocity distribution for vaned, vane and J-groove at r/r_i=1.10. Uncertainties of V_θ/U_2; V_r/U_2; α&z/b are ±3.23 percent; ±3.23 percent; ±1.5 percent and ±2.24 percent, respectively. (*a*) Velocity distribution (vaned diffuser); (*b*) velocity distribution (vane and J-groove)

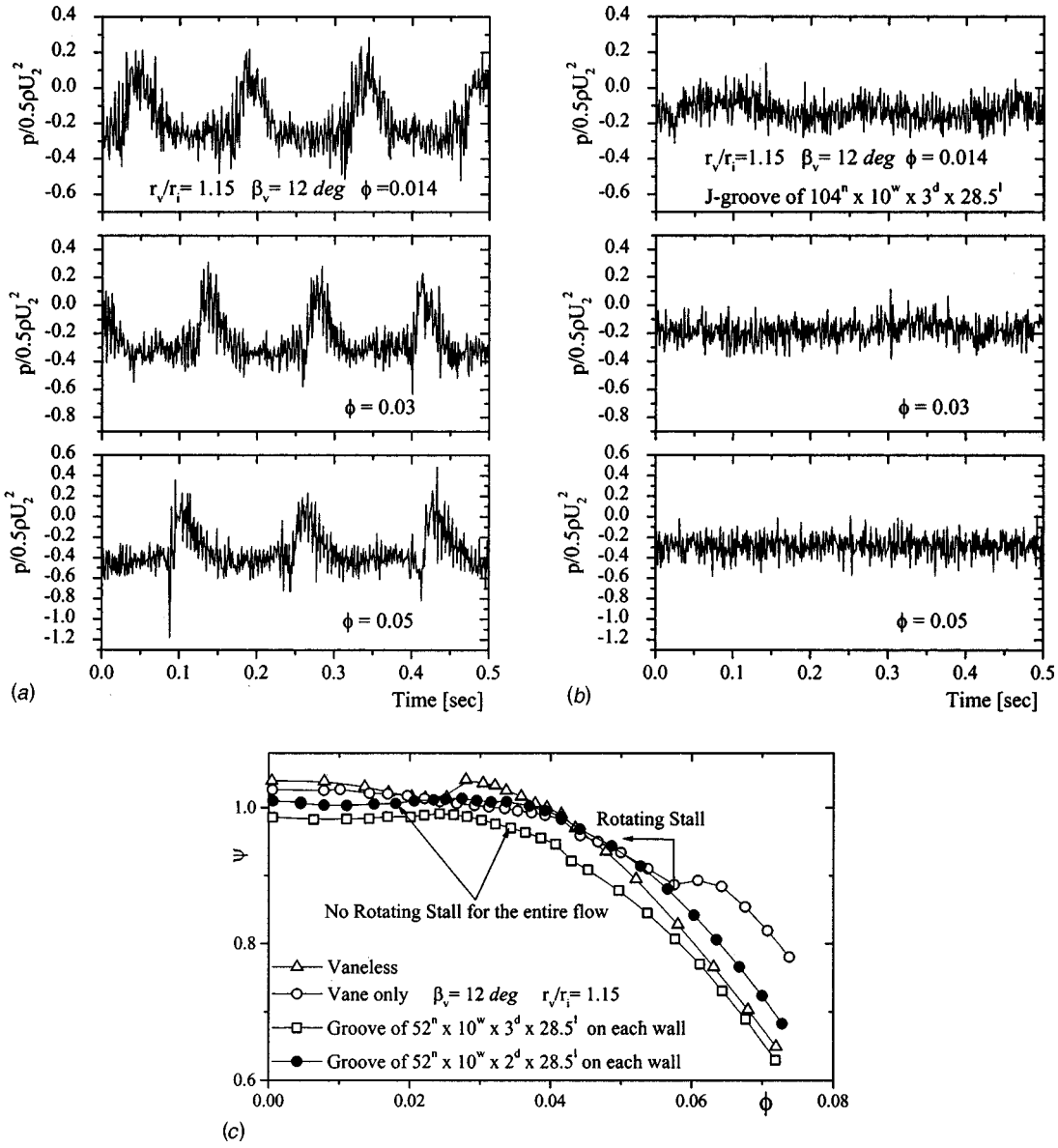

Fig. 8 (*a*) Pressure fluctuation in the vaned diffuser. Uncertainty of $p/0.5\rho U_2^2$ is ±0.73 percent. (*b*) Suppression of pressure fluctuation by J-groove. Uncertainty of $p/0.5\rho U_2^2$ is ±0.73 percent. (*c*) Suppression of rotating stall for the entire flow range. Uncertainties of ψ & ϕ are ±1.5 percent and ±1.17 percent, respectively.

on each wall cases are shown in Figs. 7(*a*) and 7(*b*), respectively. The flow angle was measured at $r/r_i = 1.10$, and at the mid-point between the leading edges of two adjacent vanes, as shown in Fig. 2(*c*). For both cases and all flow coefficients, a significant reduction in the tangential velocity and an increase in the main flow angle are seen, compared to the vaneless case shown in Fig. 3(*b*). The increase in the main flow angle is not significant, although it was expected.

The vane throat flow is complex in between and in the vicinity of the vanes' leading edges, so velocity measured only at a single point may not yield an accurate value. Comparing the two cases of vaned and vaned with J-groove, a tendency toward increased radial velocity near the grooved wall can be seen for the case of vaned with J-groove. Kurokawa et al. [33] deduced that in the vaneless diffuser the groove reverse flow decreases the reverse flow near the diffuser wall. When compared with the vaneless case, the radial velocity near the diffuser walls is indeed more negative for the vaned diffuser, and according to Jansen [4] this

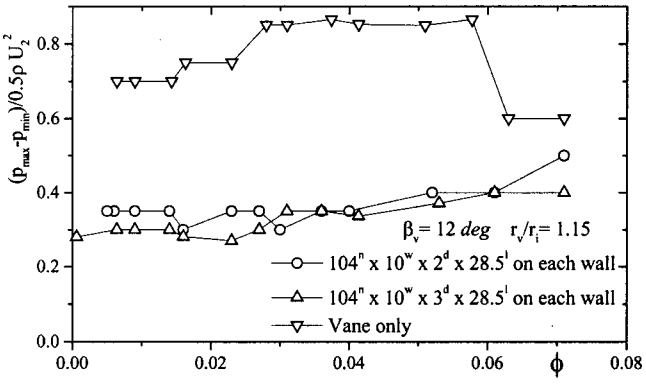

Fig. 9 Suppression of peak-to-peak pressure fluctuation by J-groove. Uncertainties of $(p_{max}-p_{min})/0.5\rho U_2^2$ & ϕ are ±1.0 percent and ±1.17 percent, respectively.

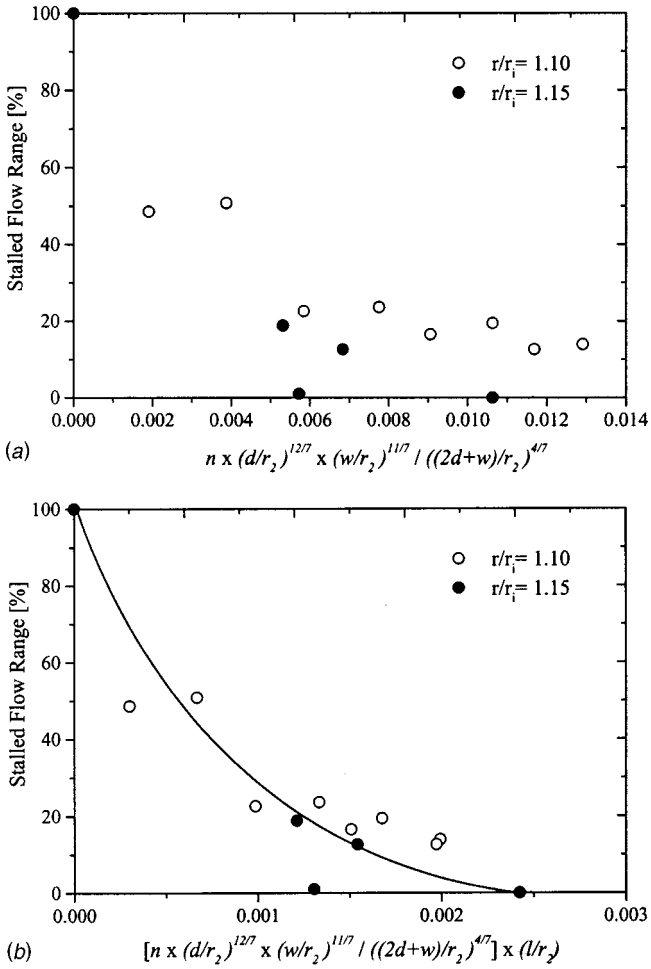

Fig. 10 Criteria of optimum J-groove dimension. Uncertainties of stalled flow range [percent] & JE No. are ±1.65 percent and ±6.63 percent, respectively. (*a*) Without considering length of the J-groove; (*b*) considering length of the J-groove

implies reduced stability. However, rotating stall inception in the vaned diffuser is not caused by the reverse flow near the diffuser wall; rather, it is caused by the velocity perturbation near the vanes' surfaces. Again, velocity is measured only at a single point, the mid-point of two adjacent vane leading edges, and thus is insufficient for a general conclusion.

3.6 Suppression of Rotating Stall for the Entire Flow Range. The pressure fluctuation in the vaned diffuser without grooves is a typical triangular shape oscillation when rotating stall occurs, as shown in Fig. 8(*a*). This can be completely suppressed by the grooves of only $d=3$ mm as shown in Fig. 8(*b*).

During the experiment, the groove geometric parameters were varied widely to measure their effects. But it was not until the grooves of $52^{n}\times10^{w}\times3^{d}\times28.5^{l}$ were formed on both walls for $r_v/r_i=1.15$ and $\beta_v=12$ deg that rotating stall was completely suppressed, as shown in Fig. 8(*c*). It can also be seen that the total pressure loss caused by the grooves is about 11.5 percent of $0.5\rho U_2^2$ in the high flow region. When the groove depth d is increased by 1 mm, the total pressure loss increases significantly and nearly 20.5 percent of $0.5\rho U_2^2$ in the high flow region. This means grooves with larger dimension can also suppress rotating stall for the entire flow range with an increase in hydraulic loss.

The peak-to-peak pressure fluctuation for the ungrooved and two types of grooved cases are shown in Fig 9. It is clear that the grooves cause a decrease in the pressure fluctuation of almost 50 percent of the ungrooved case when rotating stall occurs. It is also clear that the pressure fluctuation decreases a large amount even though the rotating stall does not occur in the range of $\phi>0.06$.

The insertion of radial grooves in the diffuser is inevitably associated with the reduction of the overall efficiency of the turbomachinery, because they decrease the tangential velocity in the diffuser. However, the reduction of tangential velocity also decreases the friction loss in the diffuser, which improves the diffuser performance. Hence the use of the grooved diffuser creates a trade off between stall suppression and loss of pressure in the diffuser.

It can be mentioned that the part load operation of the fan and compressor is generally limited by surge. In this situation it may not be necessary to control the rotating stall for the entire flow range; rather, the stalled flow range only needs to be improved. Thus, the number of grooves can be reduced so the total pressure loss can be minimized. Again by only grinding the diffuser part to form radial grooves on existing turbomachinery, inception of rotating stall can be suppressed completely, or the magnitude of the fluctuating pressure and the range of its occurrence can be improved remarkably.

3.7 Criteria of the Optimum J-Groove Dimension. To decrease the stalled flow range, selection of the optimum groove dimension is required. Kurokawa et al. [33] deduced theoretically that groove flow, Q_G is proportional to the number of groove and groove cross-sectional parameters. That is, $Q_G \propto n(D^{12/7}W^{11/7})/(2D+W)^{4/7}$, where $D=d/r_2$ and $W=w/r_2$. To maximize the groove flow, $dQ_G/dw=0$ yields $w=(22/7)d$, or for simplicity, $w\approx3d$. This gives the optimum groove width-depth ratio. Since the groove reverse flow is related to the increase in the main flow and flow angle, the above relationship is one of the control parameters of rotating stall.

All the experimental data are formulated to deduce a relationship between the inception of stall and the geometry of the J-grooves for the vaned diffuser. The results are shown in Fig. 10(*a*). Here, the percent of stalled flow range is calculated, where the maximum measured stalled flow range in the vaneless case is defined as 100 percent. It can be seen that only groove cross-sectional parameters cannot explain all the experimental results. The other groove geometric parameter is the length of the groove, l, whose effect on suppressing rotating stall is shown in Fig. 6(*d*). By incorporating l, a more reliable dependency between the suppression of rotating stall and the groove geometry can be expressed as

$$\text{JE No.}=n\times(d/r_2)^{12/7}\times(w/r_2)^{11/7}/\{(2d+w)/r_2\}^{4/7}\times(l/r_2)$$

and can be seen in Fig. 10(*b*). It can also be seen that an increase in the JE No. decreases the stalled flow range, and for JE No. $\geqslant0.0024$ there is no rotating stall for the entire flow range.

From the above results it is clear that the control of rotating stall is based on the groove dimensions of width, depth, length and number of grooves. The groove reverse flow is proportional to the square root of the radial pressure gradient [$\tau_o=(A/s)dp/dr$ and $\tau_o\propto Q_G^2 \therefore Q_G\propto\sqrt{dp/dr}$ (Eq. 7 [33])] due to the centrifugal force; therefore, the groove flow becomes stronger with a decrease in the main flow. On the other hand, rotating stall becomes stronger with a decrease in the main flow. Hence it can be realized that the groove flow acts as an automatic control of rotating stall.

4 Conclusions

From the analysis of the above results, the following conclusions can be drawn.

1 J-grooves can suppress rotating stall in the vaned diffuser for the entire flow range.

2 An increase in the number, depth, width, and length of J-groove decreases the stalled flow range but produces hydraulic loss. For a part-load operation, shallow and wide grooves are effective.

3 J-grooves decrease the peak-to-peak pressure fluctuation of the vaned diffuser almost by half. Also, the pressure fluctuation decreases when there is no rotating stall.

4 The insertion of vanes in the diffuser decreases the stalled flow range with a decrease in rotating stall frequency.

5 The vane setting location largely influences the stalled flow range. For a constant vane angle, stalled flow range increases with an increase in radial vane leading edge setting position.

Nomenclature

A = flow area [m^2]
b = impeller/diffuser channel width [mm]
d = depth of J-groove [mm]
f = impeller frequency [Hz]
f_c = rotating stall cell frequency [Hz]
g = acceleration due to gravity [m/s^2]
H = total head [m]
l = average length of J-groove [mm]
n = number of J-groove
n_c = rotating stall cell number
n_s = specific speed [m, m^3/min, rpm]
N = revolution per minute [rpm]
p = pressure [Pa]
Q = flow rate [m^3/s]
r = radius or radial position [mm]
U = impeller speed [m/s]
V = fluid velocity [m/s]
w = width of J-groove [mm]
z = distance from the hub side diffuser wall [mm]
α = flow angle [deg]
β = impeller/diffuser vane angle [deg]
η = efficiency
ν = kinematic viscosity of fluid [m^2/s]
ϕ = flow coefficient [Q/A_2U_2]
ρ = density of fluid [kg/m^3]
ψ = head coefficient [$H/(U_2^2/2g)$]
Ω = nondimensional frequency [f_c/fn_c]

Subscripts

$1,i$ = inlet of impeller and diffuser, respectively
$2,o$ = outlet of impeller and diffuser, respectively
r = radial component
v = diffuser vane
vd = vane design
θ = tangential component

Superscripts

n,w,d,l = number, width, depth, and average length of grooves, respectively
$--^n\times--^w\times--^d\times--^l$ = grooves' combination for one set of experiment

References

[1] Lenneman, E., and Howard, J. H. G., 1970, ''Unsteady Flow Phenomena in Rotating Centrifugal Impeller Passages,'' Trans. ASME, **92**, No. 2, Jan., pp. 65–72.
[2] Kubo, T., and Murata, S., 1976, ''Unsteady Flow Phenomena in Centrifugal Fans,'' Bull. JSME, **19**, No. 135, Sept., pp. 1039–1046.
[3] Mizuki, S., Ariga, I., and Kawashima, Y., 1978, ''Investigation Concerning Rotating Stall and Surge Phenomena Within Centrifugal Compressor Channels,'' ASME Paper No. 78-GT-9.
[4] Jansen, W., 1964, ''Rotating Stall in a Radial Vaneless Diffuser,'' ASME J. Basic Eng., **86**, pp. 750–758.
[5] Senoo, Y., and Kinoshita, Y., 1978, ''Limits of Rotating Stall in Vaneless Diffuser of Centrifugal Compressors,'' ASMA Paer No. 78-GT-19.
[6] Abdelhamid, A. N., Colwill, W. H., and Barrows, J. F., 1979, ''Experimental Investigation of Unsteady Phenomena in Vanelsss Radial Diffusers,'' Trans. ASME, **101**, No. 1, pp. 52–60.
[7] Dutton, J. C., Piemsomboon, P., and Jenkins, P. E., 1986, ''Flowfield and Performance Measurements in a Vaned Fadial Diffuser,'' ASME J. Fluids Eng., **108**, pp. 141–147.
[8] Baghdadi, S., 1977, ''The Effect of Rotor Blade Wakes on Centrifugal Compressor Diffuser Performance—A Comparative Experiment,'' ASME J. Fluids Eng., **99**, pp. 45–52.
[9] Greitzer, E. M., 1981, ''The Stability of Pumping System,'' ASME J. Fluids Eng., **103**, pp. 193–242.
[10] Baghdadi, S., and McDonald, A. T., 1975, ''Performance of Three Vaned Radial Diffusers With Swirling Transonic Flow,'' ASME J. Fluids Eng., **95**, pp. 155–173.
[11] Rodgers, C.,1977, ''Impeller Stalling as Influenced by Diffusion Limitations,'' ASME J. Fluids Eng., **99**, pp. 84–97.
[12] Haupt, U., Seidel, U., Abdel-Hamid, A. N., and Rautenberg, M., 1988, ''Unsteady Flow in a Centrifugal Compressor with Different Types of Vaned Diffusers,'' ASME J. Turbomach., **110**, pp. 293–302.
[13] Stein, W., and Rautenberg, M., 1988, ''Analysis of Measurements in Vaned Diffusers of Centrifugal Compressors,'' ASME J. Turbomach., **110**, pp. 115–121.
[14] Yoshinaga, Y., Gyobu, I., Mishina, H., Koseki, F., and Nishida, H., 1980, ''Aerodynamic Performance of a Centrifugal Compressor With Vaned Diffusers,'' **102**, pp. 486–493.
[15] Hunziker, R., and Gyarmathy, G., 1994, ''The Operational Stability of a Centrifugal Compressor and Its Dependence on the Characteristics of the Subcomponents,'' ASME J. Turbomach., **116**, pp. 250–259.
[16] Yoshida, Y., Tsurusaki, H., Murakami, Y., and Tsujimoto, Y., 1990, ''Rotating Stalls in Centrifugal Impeller/Vaned Diffuser Systems (2nd Report, Comparison between Experiment and Theory),'' in Japanese, Trans. Jpn. Soc. Mech. Eng., Ser. B, **56B**, No. 530, pp. 2999–3006.
[17] Yoshida, Y., Murakami, Y., Tsurusaki, H., and Tsujimoto, Y., 1990, ''Rotating Stalls in Centrifugal Impeller/Vaned Diffuser Systems (1st Report, Experiment),'' in Japanese, Trans. Jpn. Soc. Mech. Eng., Ser. B, , **56B**, No. 530, pp. 2991–2998.
[18] Osborn, W. M., and Moore, R. D., 1990, ''Effect of Casing Treatment on the Overall Performance of Axial Flow Transonic Fan Stage with Pressure Ratio of 1.75 and Tip Solidity of 1.5,'' NASA TMX-3477.
[19] Prince, D. C., Jr., Wisler, D. C., and Hilvers, D. E. 1975, ''A Study of Casing Treatment Stall Margin Improvement Phenomena,'' ASME Paper No. 75-GT-60.
[20] Amann, C. A., Nordenson, G. E., and Skellenger, G. D., 1975, ''Casing Modification for Increasing the Surge Margin of a Centrifugal Compressor in an Automotive Turbine Engine,'' ASME J. Eng. Power, **97**, pp. 329–336.
[21] Takata, H., and Tsukuda, Y., 1977, ''Stall Margin Improvement by Casing Treatment-Its Mechanism and Effectiveness,'' ASME J. Eng. Power, **99,** pp. 121–133.
[22] Greitzer, E. M., Nikkanen, J. P., Haddad, D. E., Mazzawy, R. S., and Joslyn, J. D., 1979, ''A Fundamental Criterion for the Application of Rotor Casing Treatment,'' ASME J. Fluids Eng., **101**, pp. 237–243.
[23] Fujita, H., and Takata, H., 1984, ''A Study on Configurations of Casing Treatment for Axial Flow Compressors,'' Bull. JSME, **27**, pp. 1675–1681.
[24] Smith, G. D. J., and Cumpsty, N. A., 1984, ''Flow Phenomena in Compressor Casing Treatment,'' ASME J. Eng. Gas Turbines Power, **106**, pp. 532–541.
[25] Miyake, Y., Inaba, T., and Kato, T., 1987, ''Improvement of Unstable Characteristics of an Axial Flow Fan by Air-Separator Equipment,'' ASME J. Fluids Eng., **109,** pp. 35–40.
[26] Azimian, A. R., Elder, R. L., and McKenzie, A. B., 1990, ''Application of Recess Vaned Casing Treatment to Axial Flow Fans,'' ASME J. Turbomach., **112**, pp. 145–150.
[27] Epstein, A. H., Ffowcs Williams, J. E., and Greitzer, E. M., 1986, ''Active Suppression of Aerodynamic Instabilities in Turbomachines,'' J. Propul. Power, **5**, No. 2, pp. 204–211.
[28] Day, I. J., 1993b, ''Active Suppression of Rotating Stall and Surge in Axial Compressors,'' ASME J. Turbomach., **115**, pp. 40–47.
[29] Paduano, J. D., Epstein, A. H., Valavani, L., Longley, J. P., Greitzer, E. M., and Guenette, G. R., 1993, ''Active Control of Rotating Stall in a Low-Speed Axial Compressor,'' ASME J. Turbomach., **115**, pp. 48–56.
[30] D'Andrea, R., Behnken, R. L., and Murray, M. R., 1997, ''Rotating Stall Control of an Axial Flow Compressor Using Pulsed Air Injection,'' ASME J. Turbomach., **119**, pp. 742–752.
[31] Gysling, D. L., and Greitzer, E. M., 1995, ''Dynamic Control of Rotating Stall in Axial Flow Compressors Using Aeromechanical Feedback,'' ASME J. Turbomach., **117**, pp. 307–319.
[32] Day, I. J., Breuer, T., Escuret, J., Cherrett, M., and Wilson, A., 1999, ''Stall Inception and the Prospects for Active Control in Four High-Speed Compressors,'' ASME J. Turbomach., **121**, pp. 18–27.
[33] Kurokawa, J., Saha, S. L., Matsui, J., and Kitahoa, T., 2000, ''Passive Control of Rotating Stall in a Parallel-Wall Vaneless Diffuser By Radial Grooves,'' ASME J. Fluids Eng., **122**, Mar., pp. 90–97.
[34] Saha, S. L., Kurokawa, J., Matsui, J., and Imamura, H., 2000, ''Suppression of Performance Curve Instability of a Mixed Flow Pump by Use of J-groove,'' ASME J. Fluids Eng., **122**, Sept., pp. 592–597.
[35] Frigne, P., and Van Den Braembussche, 1984, ''Distinction Between Different Types of Impeller and Diffuser Rotating Stall in a Centrifugal Compressor With Vaneless Diffuser,'' ASME J. Eng. Gas Turbines Power, **106**, pp. 468–474.

[36] Kurokawa, J., Kitahora, T., and Tsutsui, T., 1996, ''Performances of Centrifugal Impellers of Very Low Specific Speed,'' International Symposium on Fluid Machinery and Fluid Engineering, Beijing, China, Sept. 9–12, pp. 276–282.
[37] Senoo, Y., and Kinoshita, Y., 1977, ''Influence of Inlet Flow Conditions and Geometries of Centrifugal Vaneless Diffusers on Critical Flow Angle for Reverse Flow,'' ASME J. Fluids Eng., **99**, pp. 98–103.
[38] Tsujimoto, Y., Yoshida, Y., and Mori, Y., 1996, ''Study of Vaneless Diffuser Rotating Stall Based on Two-Dimensional Inviscid Flow Analysis,'' ASME J. Fluids Eng., **118**, pp. 123–127.

Studies on a Horizontal Axis Wind Turbine With Passive Pitch-Flap Mechanism (Performance and Flow Analysis Around Wind Turbine)

Yukimaru Shimizu
e-mail: shimizu@mach.mie-u.ac.jp

Yasunari Kamada
e-mail: kamada@mach.mie-u.ac.jp

Department of Mechanical Engineering,
Mie University,
1515 Kamihama-cho,
Tsu, Mie 514-8507, Japan

This paper describes the development of a passive system to control the output power of a horizontal axis wind turbine. This pitch-flap coupling mechanism can reduce rotor power above rated wind speed. This mechanism has two kinds of blade motions: the flapping and the pitching motions. In this paper, braking effects are investigated experimentally. It is found that the breaking effect is improved when the ratio of pitch to flap motions is large. Also, the flow pattern around the wind turbine is investigated. It is found that the braking effects are caused by a couple of ring vortices.
[DOI: 10.1115/1.1375817]

Keywords: Fluid Machinery, Horizontal Axis Wind Turbine, Passive Control, Pitching and Flapping Motions, Flow Pattern, Flow Visualization, Vortex Ring

Introduction

With the increase in the size of wind turbines, it becomes more important to secure their safe and reliable control when operating in the harsh natural environment. The authors have developed a passive pitch-flap mechanism that controls excessive output power by horizontal axis wind turbines. The experimental subject of this mechanism is a small size wind turbine (100 kW) that is installed in a problematical site, such as a mountainous area. Prior studies to suppress the excessive output are related to passive pitch control, including flexible rotors [1,2], but there is no application to commercial wind turbines. In our previous paper [3], the behavior of the mechanisms were investigated experimentally with a model wind turbine in a wind tunnel. In this paper, the ratio of pitch to flap angles is varied within a range and the relationship between this ratio and the braking effect on wind turbine is investigated experimentally. Also, the relationship between power suppression and flow patterns around the wind turbine is investigated through velocity distribution measurements and flow visualizations. It is found that at a certain ratio of pitch to flap angles, a couple of vortex rings are generated in the wake of rotor when the wind speed is above rated. The rotor torque is then reduced by these special vortex rings. So far as the authors know, these phenomena are found for the first time in wind turbine rotors. But the vortex ring is known as the unique airflow pattern that occurs in power settling of helicopters [4]. The details are described in the following.

Experimental Apparatus and Methods

Figure 1 shows the experimental apparatus. A three bladed horizontal axis model wind turbine with a diameter of 1.4 m is set at 1 D (D: rotor diameter) downstream from the wind tunnel outlet. The wind tunnel is an open jet type with an outlet diameter of 1.8 m and a maximum wind speed of 15 m/s. The passive pitch-flap mechanism (the details are given in Fig. 2) and a potentiometer for flap angle measurement are set in the boss. A variable speed generator, a torque meter, a rotational speed sensor, and an azimuth angle sensor are positioned in a nacelle. The wind turbine operates at variable speeds within a maximum rotational speed of 950 rpm. The rated wind speed for this model wind turbine is about 11 m/s, so the experiments are carried out with wind speeds ranging from 10-12 m/s. The wind speed is measured by a pitot tube set at 0.5 D upstream of the rotor at the maximum power coefficient. Figure 1(*b*) shows the dimension of the tapered and twisted test blades. The velocity distribution around the rotor is measured with a two-dimensional LDV. Tufted grid and smoke visualization methods are used to investigate the flow pattern around the rotor. The tufted grid and the smoke methods are explained in a later section.

Figure 2 shows the outline of the passive pitch-flap mechanism. When the thrust force acting on the blade overcomes the setting value (initial flapping moment is 20.9 N·m), the blades are inclined in the downstream direction. This is the flapping motion (ζ: flap angle). At the same time, the blade pitch, interlocked to the flapping motion, is changed to the reverse pitch direction. This is the pitching motion (γ: pitch angle). By using these coupled blade motions, the excessive output power of rotor is passively suppressed. Each blade is controlled independently by its own mechanism. In the present experiment, the ratio of pitch to flap angles (γ/ζ) is varied from 1–3 by 0.5 increments.

Velocity Distribution Measurements With LDV. Figure 3 shows the outline of the velocity distribution measurements using a two-dimensional laser Doppler velocity meter. The LDV system is of a backscatter type with a 4 W Ar ion laser. The focal length is 1000 mm. The LDV probe is set in a device that can propel the probe in both axial and radial directions and rotate the probe in the *X-Y* plane. The measuring points are set from 0.8 D upstream to 0.8 D downstream with 0.1 D increments in the axial direction. In the radial direction measurements are made from the rotating axis to 1.0 R with 0.14 R increments in the upstream and from 0.28 R to 1.4 R with 0.14 R increments in the downstream. The axial and tangential velocities are measured. The azimuth angle of the rotor blade is measured by an encoder with a 0.45-degrees resolution. The signals from the LDV probe are stored in a PC through a signal processor. The tracer with a diameter of 1 micrometer is

Contributed by the Fluids Engineering Division for publication in the JOURNAL OF FLUIDS ENGINEERING. Manuscript received by the Fluids Engineering Division September 12, 2000; revised manuscript received March 1, 2001. Associate Editor: Y. Tsujimoto.

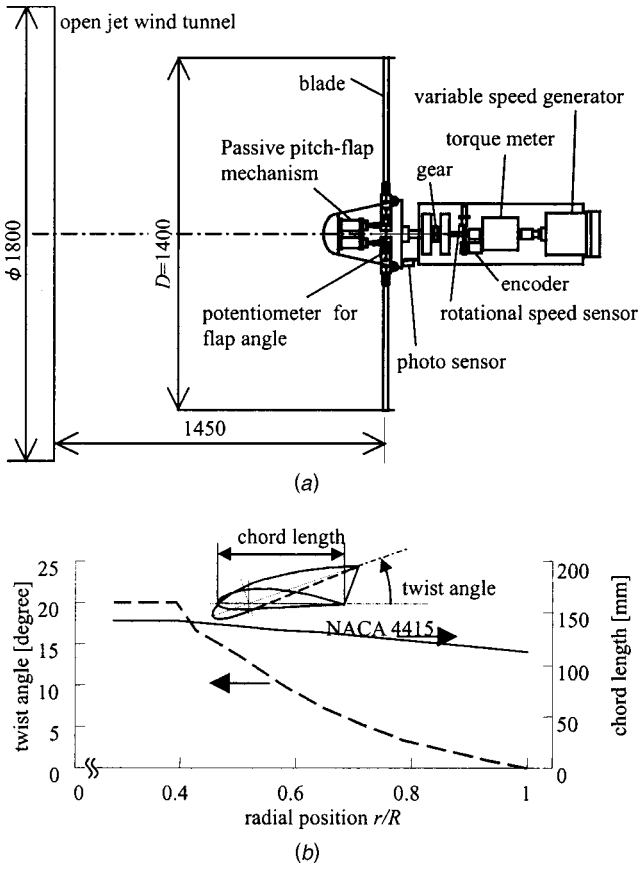

Fig. 1 (*a*) Experimental apparatus; (*b*) dimensions of test blade

poured at the wind tunnel inlet. It is made by a special smoke generator and liquid. The radial velocities are measured with the LDV probe set at two different yaw angles with respect to the rotor plane.

Data Processing Method for the Velocity Measurement Near the Rotor Plane. Figure 4 shows the relationship between axial velocity u and azimuth angle ψ of the rotor plane. The zero azimuth point is set at 60 degrees, before the test blade passes through the measuring plane. The figure shows, as an example, the result of fixed mechanism rotor (normal rotor) at $r/R=0.86$,

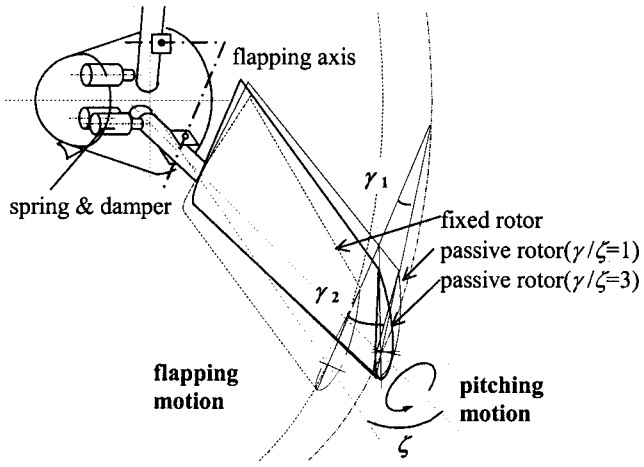

Fig. 2 Overview of pitch-flap mechanism

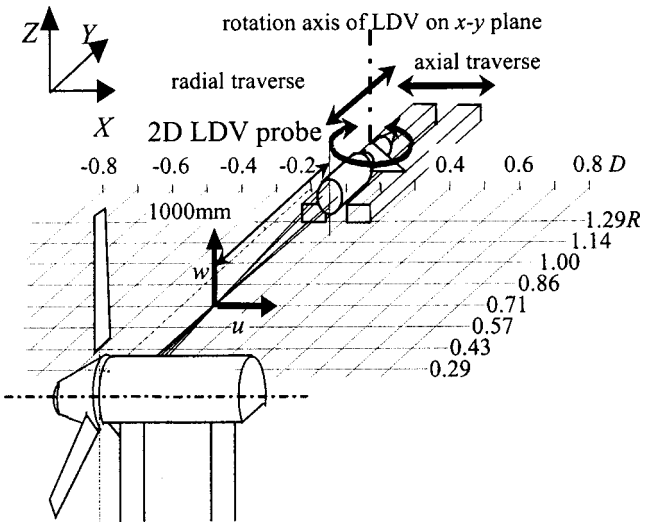

Fig. 3 Schematic diagram of two-dimensional Laser Doppler velocity meter

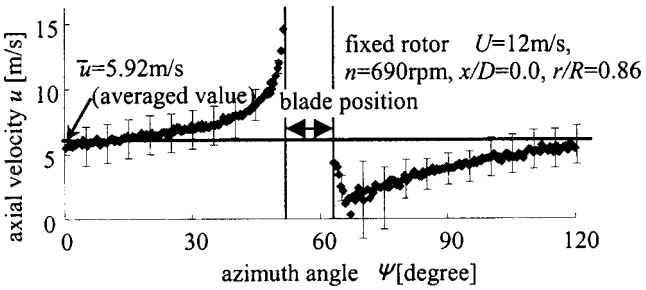

Fig. 4 Relation between axial velocity u and azimuth angle ψ for fixed rotor at $x=0$

$n=690$ rpm and $U=12$ m/s. The number of samples for each measuring point is 2000. The measuring azimuth angle is limited to the range 0–120 degrees. The phase-lock averaged value is made with about 8 data samples for each azimuth angle (0.45 degrees interval). The error bars indicate the scatter in measured values. The blade passes the measuring point at $\psi=60$ degrees; consequently, velocity data cannot be measured there. Therefore, in the following discussion, ''the velocity'' refers to the averaged velocity, calculated from available data.

Experimental Results and Discussions

Performance of the Wind Turbine Which Has Passive Pitch-Flap Mechanism

Performance With Varying Ratios of Pitch to Flap Angles. In our previous paper [3], the performance of this mechanism with a ratio of pitch to flap angles of 1 was investigated. In this paper, the performance of this mechanism with varying ratios of pitch to flap angles from 1–3 by 0.5 increments is investigated experimentally. Figure 5(*a*) shows the power coefficient C_P, and the torque coefficient C_Q as a function of tip speed ratio, λ. Figure 5(*b*) shows the flap angle, ζ, and the pitch angle, γ, as a function of tip speed ratio, λ. The initial pitch angle is 0 degrees. As shown in Fig. 5(*a*), the maximum power coefficient of the fixed rotor is $C_{Pmax}=0.40$ at $\lambda_{opt}=3.5$. In case of the passive rotor with the ratio of $\gamma/\zeta=3$, it is $C_{Pmax}=0.39$ at $\lambda_{opt}=3.1$. For the wind turbine with passive rotor, the mechanism becomes active above the optimum tip speed of the rotor. The output is then lower than that of the fixed rotor. The tip speed ratios for a zero power coefficient

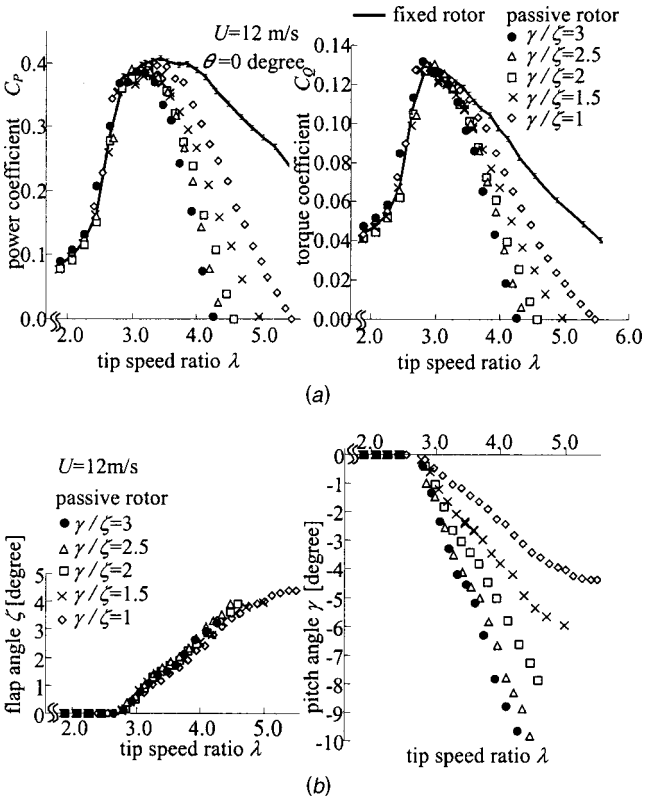

Fig. 5 (*a*) Power coefficient C_P and torque coefficient C_Q as a function of tip speed ratio λ for fixed rotor and passive rotor (uncertainty in C_P: less than ±0.4 percent, in C_Q: less than ±0.3 percent, in λ: less than ±0.2 percent); (*b*) flap angle, ζ, pitch angle, γ, as a function of rotational speed of rotor *n* (Uncertainty in ζ: less than ±0.1 degree, in γ: less than ±0.3 degree)

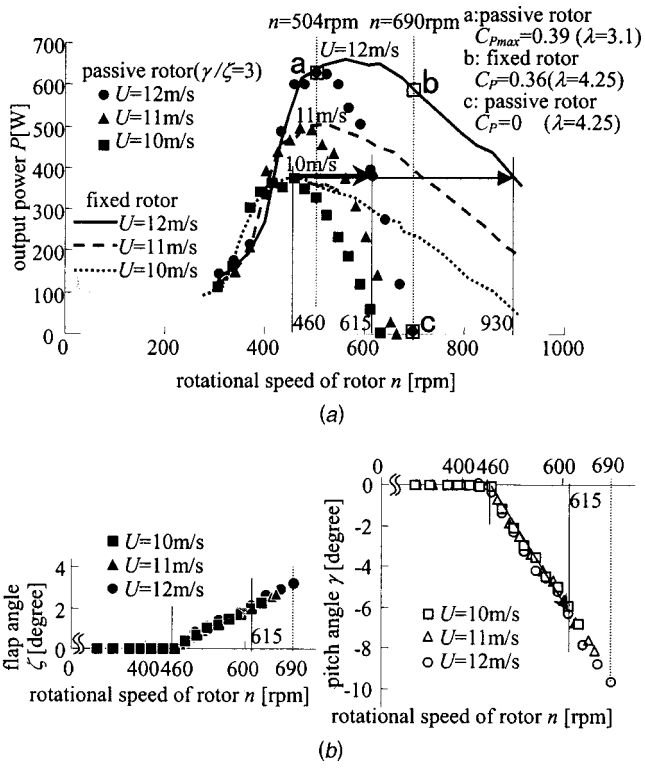

Fig. 6 (*a*) Output power *P* as a function of rotational speed of rotor *n* (Uncertainty in *P*: less than ±3 W, in *n*: less than ±1 rpm); (*b*) flap angle, ζ, pitch angle, γ, as a function of rotational speed of rotor *n* (Uncertainty in ζ: less than ±0.1 degree, in γ: less than ±0.3 degree)

(the no-load operating condition), are $\lambda_{max}=5.5$ for $\gamma/\zeta=1$, $\lambda_{max}=4.5$ for $\gamma/\zeta=2$, and $\lambda_{max}=4.25$ for $\gamma/\zeta=3$. Power suppression above λ_{opt} becomes more pronounced as the ratio of γ/ζ is increased. From Fig. 5(*b*), it can be seen that ζ starts to increase after $\lambda=2.9$, and ζ becomes slightly larger with increasing γ/ζ at fixed λ. The effect of variation of the ratio γ/ζ is very small. On the other hand, $|\gamma|$ becomes larger with increasing γ/ζ at fixed λ. The pitching motion of blade is more effective for power suppression than the flapping motion.

Relationships Between Wind Velocity and Output Suppression. Figure 6(*a*) shows the output power *P*, and Fig. 6(*b*) the flap angle ζ, and the pitch angle γ as functions of the rotational speed of the rotor, *n*, respectively. The maximum power output of the passive rotor for $\gamma/\zeta=3$ is 650 W for 12 m/s, 480 W for 11 m/s and 360 W for 10 m/s. The excessive increase of the rotational speed of the rotor is discussed under the assumption that the output power of a variable speed generator is kept constant while the wind speed is increased from 10 m/s (rated wind speed) to 12 m/s. For the fixed rotor case (shown by lines), the rotational speed of the rotor increases from 460 rpm, which is the optimum for 10 m/s–930 rpm for 12 m/s. The increase in rotational speed is thus 470 rpm. For the passive rotor with $\gamma/\zeta=3$ (shown by markers), the rotational speed of the rotor increases from 460 rpm to 615 rpm. The increase in rotational speed is only 155 rpm. Thus, by applying this mechanism, the excessive increase of rotational speed of the fixed rotor is suppressed to about one-third. In this process, the flap angle increases from 0–2.1 degrees and the pitch angle decreases from 0–6.3 degrees.

In the next chapter, power suppression achieved with this mechanism is discussed from the viewpoint of the flow pattern around the wind turbine. The operating conditions for the flow analysis are at the maximum power coefficient of the passive rotor, point **a** (Fig. 6(*a*)), at $n=690$ rpm for the fixed rotor, point **b** (Fig. 6(*a*)), and at no-load operation, $P=0$W, $n=690$ rpm, for the passive rotor, point **c** (Fig. 6(*a*)).

Flow Analysis Around Wind Turbine Using Velocity Measurements

Velocity Vector Distributions at Maximum Power Coefficient for the Passive Rotor, and at $n=690$ rpm for the Fixed Rotor. Figure 7(*a*) shows the velocity vector distributions and the equal velocity lines of the axial component at the maximum power coefficient ($C_P=0.39$, solid lines) of the passive rotor and at $n=690$ rpm ($C_P=0.36$, dotted lines) with fixed rotor at a wind speed of 12 m/s. For the passive rotor $C_P=0.39$, the flow behind the rotor expands in the radial direction and the axial velocity downstream of the blade tip becomes half the wind speed. This is almost the optimal flow pattern around a wind turbine rotor [5]. In the case of $C_P=0.36$ with the fixed rotor, the axial velocity distribution is almost the same as the passive rotor results, except for the $\overline{u}/U=0.25$ area downstream of the blade tip.

Velocity Vector Distribution With Passive Rotor in Power Suppressed Operation. Figure 7(*b*) shows the velocity vector distribution at a wind speed of 12 m/s, with passive rotor running at $P=0$W ($C_P=0$, $n=690$ rpm) when power is suppressed sufficiently. The flow upstream of the rotor deflects to the outside of the rotor as it approaches the rotor. At the rotor plane, the flow near the center axis flows downstream, while the flow near the tip ($r/R>0.85$) flows upstream with a strong expansion to the outside. Downstream of the blade tip ($0.8<r/R<1.2, 0<x/D<0.5$), there is a reversed flow which has a negative axial velocity component ($\overline{u}/U<0$). The detail of the reversed flow area is discussed together with the results of the flow visualization. In the

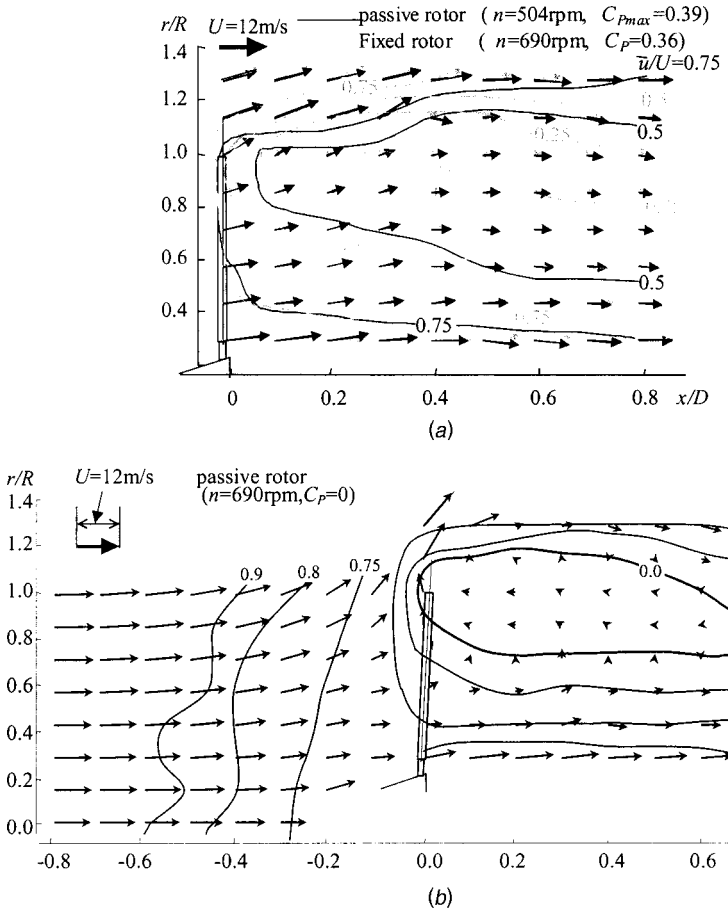

Fig. 7 (*a*) Axial and radial velocity distribution for passive rotor ($n=504$ rpm, C_{Pmax}) and fixed rotor ($n=690$ rpm) (Uncertainty in $\bar{u}/U$: less than ±0.5 percent); (*b*) axial and radial velocity distribution for passive rotor ($n=690$ rpm, $C_P=0$) (Uncertainty in $\bar{u}/U$: less than ±0.5 percent)

next chapter, this power suppression mechanism is discussed based upon the axial velocity distribution at $x=0$ (rotor plane).

Power Suppression Mechanism Explained With Axial Velocity Distribution at Rotor Plane. Figure 8(*a*) shows the distributions of measured axial velocity, u, in the rotor plane at a wind speed of 12 m/s. The attack angle, Fig. 8(*b*), the thrust force dT, Fig. 8(*c*), and the torque dQ, Fig. 8(*d*), which are calculated from u and n are also depicted. The distributions with the passive rotor at optimum operation ($C_P=0.39$, $n=504$ rpm, $\zeta=1$ deg), at $C_P=0.31$, $n=573$ rpm, $\zeta=2$ deg and at sufficiently suppressed operation ($C_P=0$, $n=690$ rpm, $\zeta=3.2$ deg) are depicted by a thin line, a thin broken line, and a thick solid line, respectively. The distributions with fixed rotor $C_P=0.36$, $n=690$ rpm are described by thick broken lines.

Figure 9 shows the relationship between the lift dL, the drag dD, the attack angle α, the initial setting pitch angle θ, the pitching angle γ, and the relative angle of inflow β on a unit element of the rotating blade. The functional relationship between the torque

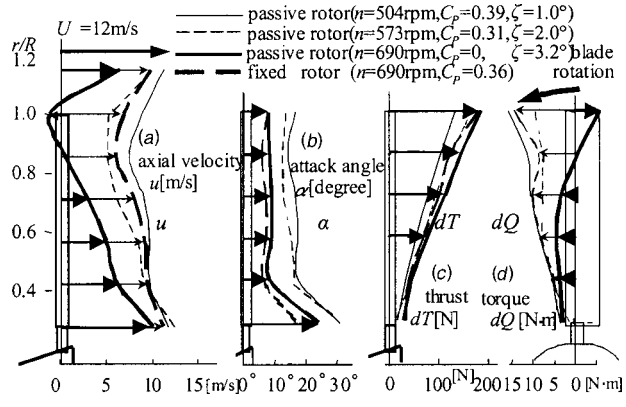

Fig. 8 Relationships among radius r, axial velocity u, attack angle α, thrust dT and torque dQ (Uncertainty in u: less than ±0.06 m/s, in a: less than ±0.4 degree, in dT: less than ±1 N, in dQ: less than ±0.08 N·m)

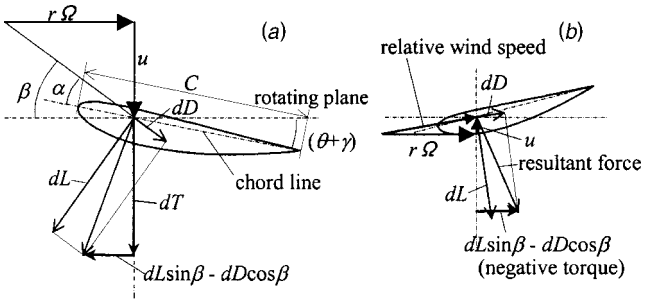

Fig. 9 (*a*) Lift and drag acting on the element of rotating blade at normal state; (*b*) lift and drag acting on the element near the blade tip at braking state

dQ, the thrust force dT, and above values for the considered blade element are expressed in the following equations [6]:

$$\beta=\tan^{-1}(u/r\Omega),\alpha=\beta-(\theta+\gamma) \tag{1}$$

$$dL=1/2\rho\{(r\Omega)^2+u^2\}C_L(\alpha)c$$
$$dD=1/2\rho\{(r\Omega)^2+u^2\}C_D(\alpha)c \tag{2}$$

$$dQ=(dL\sin\beta+dD\cos\beta)r$$
$$dT=(dL\cos\beta+dD\sin\beta) \tag{3}$$

The thrust distributions, Fig. 8(c), calculated from the measured data using Eqs. (1)–(3), become large near the blade tip in all operating conditions. The dT distribution at optimum operation is the smallest, and it increases in order at $C_P=0.31$ ($\zeta=2$ deg), and at $C_P=0$ ($\zeta=3.2$ deg). In the case of the passive rotor, the moment around the flapping axis caused by the thrust force becomes larger as tip speed increases. This makes the blade incline until the moment equivalent to the restoration moment by the spring and damper and inertial forces is achieved. The flap angle is dependent on the magnitude of the moment generated by the thrust force. The thrust force at $C_P=0$ is larger than that with the fixed rotor at the same rotational speed. The reason is that the attack angle with the passive rotor is larger than that with the fixed rotor at 690 rpm.

The dQ distribution at optimum operation becomes large near the blade tip. The dQ distributions at $C_P=0.31$ is a little smaller than in the optimum situation. The dQ distribution at $C_P=0$ has a negative value near the blade tip. Thus the blade elements near the tip work as a brake and power is sufficiently suppressed. Figure 9(b) shows the relationships among the vectors of axial wind speed, rotational speed, and relative wind speed. The reversed flow happens near the blade tip in Fig. 7(b) and, namely, the direction u becomes negative. The resultant force of lift and drag on the blade elements produces the negative torque. On the other hand, the blade elements of the inner part of the rotor generate positive torque, and it is clear that the passive rotor obtains the no-load operation with a torque balance of the inner part and the near tip area. On the contrary, the dQ distribution with the fixed rotor is reduced only a little near the tip compared to the optimum operation.

Flow Analysis Around Rotor by Visualization Method

Flow Visualization by Tufted Grid and Smoke Methods. Figure 10(a) shows the flow visualization method of axial and radial flow by a tufted grid. The tufted grid is set on a horizontal plane (X-Y plane) at the height of rotor axis, and the flow patterns are recorded by a camera which sits above the grid. The tufts are attached radially from 0.3 R–1.4 R in 0.1 R increments on a 0.4 mm wire grid. The grid in downstream is set from 0.1 D–0.5 D downstream in 0.05 D increments and from 0.5 D–0.8 D in 0.1 D increments. The tufts are made from unbound nylon ribbon with adjusted length. Two lights are used for lighting tufts to avoid the shadow area and they are set for lighting tufts only without background. The tufts that are attached at the first three lines from the rotor can rotate around the grid wire to improve the response to flow fluctuations. Furthermore, the fine tufted grid is used for the passive rotor at $C_P=0$, because of the complex flow pattern around the blade tip. The tufted grid for visualization around the blade tip has a tuft length of 30 mm, located every 0.05 R. These tufts are made from unbound silk cord, which can also rotate around the grid wire. Furthermore, the tufts are set upstream of the rotor to investigate the relationship between the outer flow and the tip vortex of the blade. Figure 10(b) shows the setup of the tufted grid for radial and peripheral flow at 0.1 D downstream of the rotor. The tufted grid is set parallel to the rotor plane (Y-Z plane) and the flow pattern is recorded by a camera set behind the rotor. A strobe light, which is synchronized to the rotational speed of rotor, is used for flow visualization according to the azimuth angle of the rotor. The shutter speed of the camera is very slow, about 4 s, so that during the recording the number of rotor revolutions was about 50. Figure 10(c) shows the flow visualization method by smoke [7]. The smoke is poured through an upstream nozzle and lighted by a laser light sheet. The flow pattern is recorded by a camera set downstream. The spread of the laser light sheet is only 20 degrees, so the whole of the rotor cannot be visualized at one time. So the flow is visualized part by part at some angular position of the light sheet and the nozzle, and are afterwards combined to show the whole rotor.

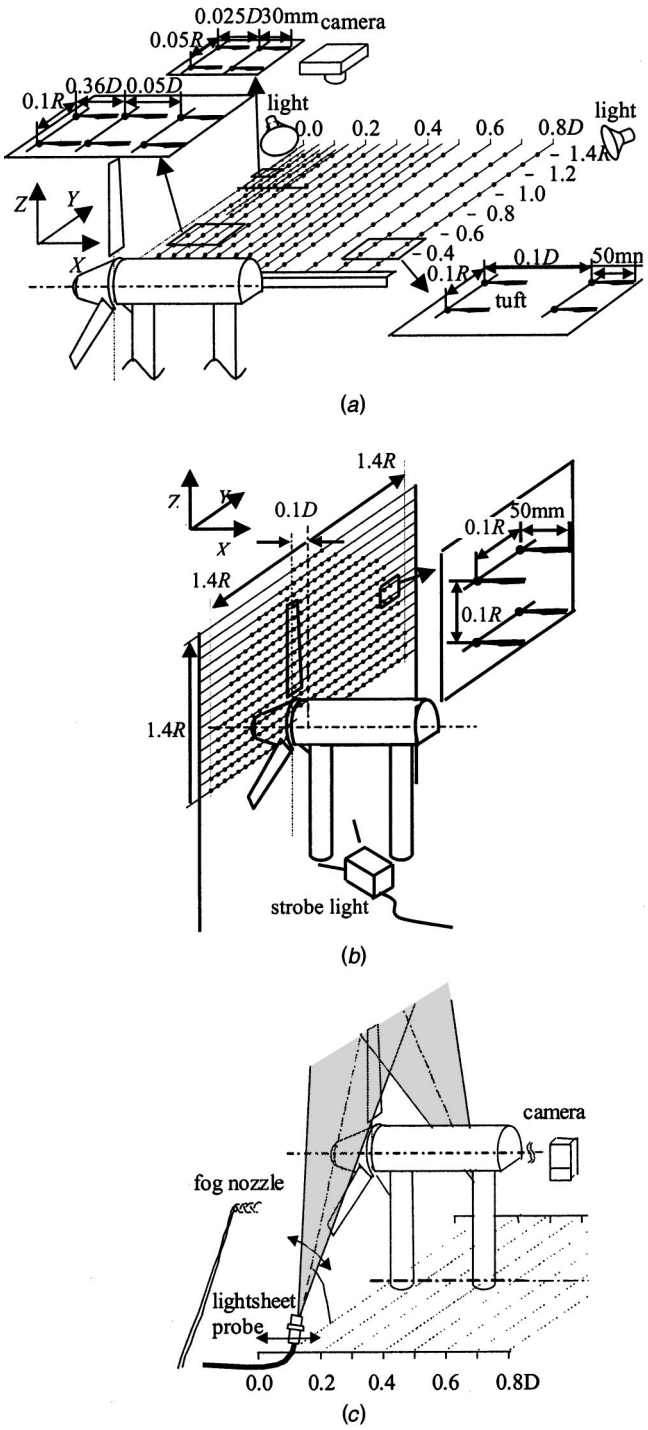

Fig. 10 (a) Schematic outline of tufted grid method at X-Y plane; (b) tufted grid method; (c) smoke method

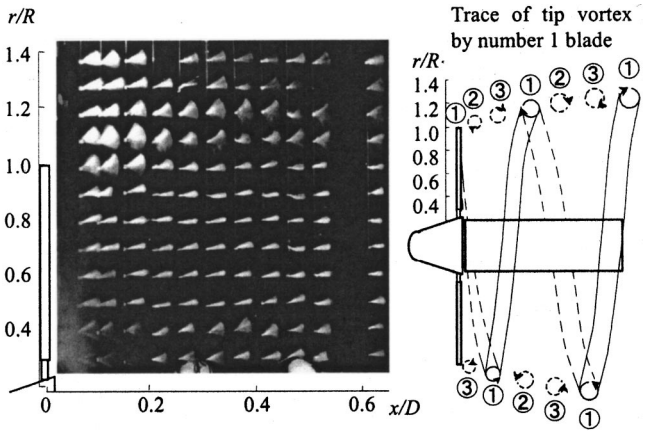

Fig. 11 Flow visualization for passive rotor ($\gamma/\zeta=3$) at $C_{P\max}$

Flow Visualization Results by Tufted Grid Method

Flow Pattern at Maximum Power Coefficient ($C_P=0.39$). Figure 11 shows the flow pattern at maximum power coefficient with the passive rotor. The wind speed is set at 12 m/s, the pitch angle is 0 degrees, and the tip speed ratio is $\lambda_{opt}=3.1$ ($n=504$ rpm). The trace of tip vortex is described on the base of the results of velocity distribution measurements. The tufts behind the rotor become narrowly shaped with a slight inline to outside spread in the radial direction. These tufts show that the flow with rotor energy extraction expands downstream. The tufts downstream and at a radius greater than the blade tip become fan-shaped. It is presumed that the tufts are given a rotational velocity component from tip vortices. The tip vortices flow downstream while drawing a spring-shape trace. The result from the fixed rotor is now shown here, because it has almost the same flow as the passive rotor.

Flow Pattern Downstream of Passive Rotor at Zero Output Power ($C_P=0$). The flow pattern at $C_P=0$, $n=690$ rpm, point **c** (Fig. 6(*a*)) is considered. Figure 12(*a*) shows the flow visualization by tufted grid on *X-Y* plane, $z=0$, which includes the rotational axis. Figure 12(*b*) shows the flow visualization by tufted grid on *Y-Z* plane, $x=0.1$ D, which is set parallel to rotor. The rotor revolution is counterclockwise. White arrows show the tangential velocity distributions at $x=0.1$ D. The wind speed setting is $U=12$ m/s. Figure 13 shows smoke visualization 0.1 D downstream of the rotor. In this visualization, the wind speed is set at $U=4$ m/s, the maximum for visualization by smoke. At $U=4$ m/s the passive mechanism does not work, so the blade angles are set the same as the initial running condition $C_P=0$, $\zeta=3.2$ deg. The tip speed ratio is $\lambda=4.25$ (the same value as 12 m/s) for $C_P=0$. Therefore, it was assumed that the flow pattern for 4 m/s is similar to that of 12 m/s, $C_P=0$. Figure 14 summarizes the results of Figs. 12(*a*), (*b*), and 13. The flow field is rather complex, and therefore Table 1 is set up by pigeonholing the experimental results. The visualizations can be summarized as follows; a vortex ring that has a strong spin and donut shape is formed near the blade tip area. A large-scale vortex ring that has weak counter spin is created inside of the previous vortex ring. Inside of the two vortex rings, a rather strong axial flow is dominant along the boss. It is supposed that the reason the strong vortex ring emerges near the tip of the rotor is that when the rotational speed of rotor increases, the blades begin to incline downstream, as explained in Fig. 5 and Fig. 8. From the axial velocity distribution of Fig. 8(*a*), it can be seen that the axial velocity around the blade tip decreases with the increase of rotational speed from $n=504$ rpm, $C_P=0.39$, $\zeta=1$ deg–$n=573$ rpm, $C_P=0.31$, $\zeta=2$ deg. When the rotational speed of rotor increases further and the flapping angle of blades become $\zeta=3.2$ deg, the tip vortices produced by the three blades join together and make a strong vortex ring. The

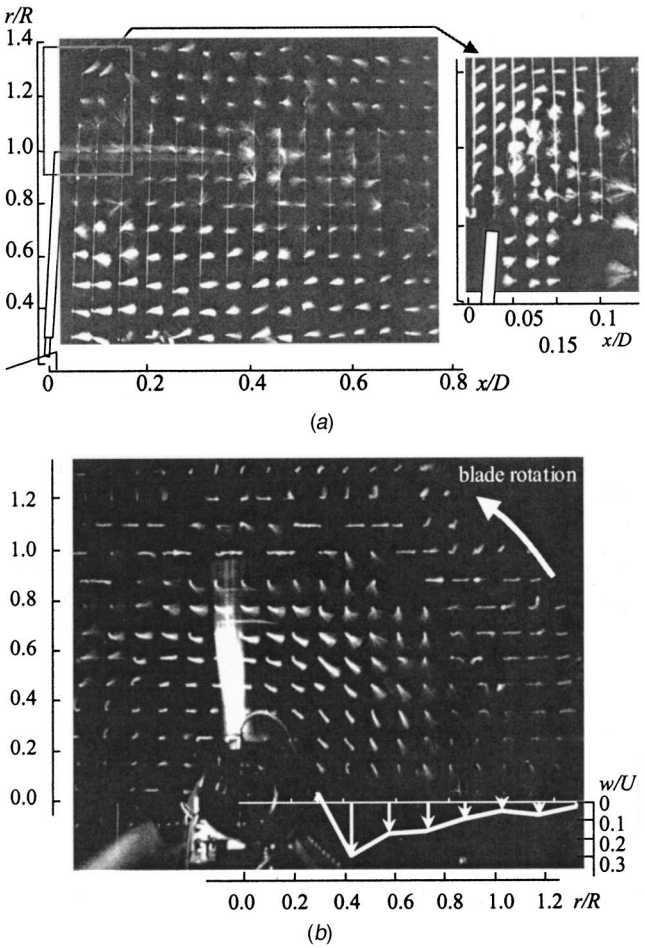

Fig. 12 Flow visualization by tufted grid method on *X-Y* (axial) (*a*) Axial plane (*X-Y*), $z=0$; (*b*) rotor plane (*Y-Z*), $x=0.1D$

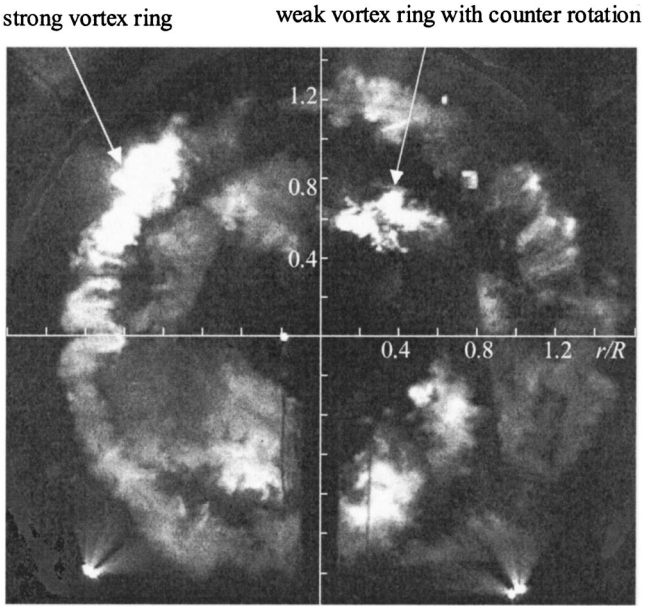

Fig. 13 Flow visualization by smoke method on *Y-Z* (rotor) plane, $x=0.1D$ for passive rotor ($\gamma/\zeta=3$) at $C_P=0$, $U=4$ m/s

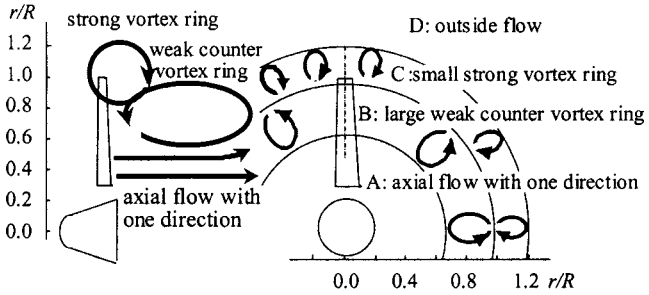

Fig. 14 Flow field around passive rotor at $C_P=0$

Table 1 Flow pattern in the down stream of passive rotor ($C_P=0$)

x/D \ r/R	(X-Y plane) 0.0	0.1	0.2–0.6	0.7	(Y-Z plane) 0.1	
0.3 - 0.5	Non fluttering and downstream direction				Tufts seem to be short.	
0.5 - 0.7	Fluttering and downstream direction		Non fluttering, downstream and slightly outside direction		Fluttering and the counter direction of rotor	Weak and large vorte x ring
0.7 - 0.9	Strongly fluttering and both upstream and downstream directions.			Strongly fluttering and downstream direction.		
0.9 - 1.1	Strongly fluttering and upstream direction.				Coiling around the grid wire	
1.1	Non fluttering and outside direction	Upstream direction	Strongly fluttering and downstream direction.			
1.2		Very strongly fluttering			Strong vortex ring	
1.3		Downstream direction			Tufts seem to be short.	

emergence of a large-scale weak vortex ring with counter spin can be explained by the following: first, a part of the fluid adjacent to the strong vortex ring is pulled upstream by the strong vortex, and second, further inboard the flow is pulled downstream by the inner axial flow.

Conclusion

The following conclusions can be drawn from the above discussions:

1 The pitching motion of blade is more effective for power suppression than the flapping motion. When increasing the ratio of the pitch angle to the flap angle from 2.5–3, the power suppression effect improves in the high tip speed region above the optimum tip speed ratio.

2 When the output power is suppressed sufficiently by this mechanism, a couple of concentric vortex rings emerge in the wake of the rotor. A negative torque at the blade tip which is caused by the reversed flow related to these vortex rings suppresses the rotor torque.

Nomenclature

c = chord length [m]
C_P = power coefficient $=P/((1/2)\rho U^3\pi R^2)$
C_Q = torque coefficient $=Q/((1/2)\rho U^2\pi R^3)$
n = rotational speed of rotor [rpm]
P = output power $=Q\Omega$ [W]
Q = torque [N·m]
r = radial position [m]
R = radius of rotor [m]
U = wind velocity [m/s]
Ω = angular velocity [rad/s]

Additional nomenclature is explained in the text

References

[1] Feuchtwang, J. B., Infiled, D. G., Schmeer, A., and Jeronimidis, G., 1996, ''Development of self-twisting composite blades for passive pitch control of a wind turbine,'' Proc. of 1996 European Union Wind Energy Conference (EUWEC), pp. 293–296.

[2] Infield, D. G., Feuchtwang, J. B., and Fitches, P., 1999, ''Development and testing of a novel self-twisting wind turbine rotor,'' Proc. of 1999 European Wind Energy Conference, pp. 329–332.

[3] Shimizu, Y.et al., 1998, ''Studies on Horizontal Axis Wind Turbine with Passive Teetered Brake & Damper Mechanism,'' JSME International Journal, Series B, **41**, No. 1, pp. 162–169.

[4] Prouty, Raymond W., 1986, *Helicopter Performance, Stability, and Control*, JPWS Engineering, Boston, pp. 102–107.

[5] Shimizu, Y., et al., 1985, ''Studies on Flow Patterns Around Horizontal Axis Wind Turbine and Wind Turbine Performance (Comparison Between the Blade Which is Given Optimum Twist Angle and Non-Twisted Blade),'' Trans. Jpn. Soc. Mech. Eng., Ser. B, **51**, No. 471, pp. 3530–3538.

[6] Shimizu, Y., 1990, *Wind power technology* (in Japanese), Power Corp., Tokyo, pp. 194–201.

[7] Shimizu, Y., et al., 1990, ''Power Augmentation Effects of Horizontal Axis Wind Turbine by Tip Vane (2nd Report, Flow Visualization Around Blade with Tip Vane),'' Trans. Jpn. Soc. Mech. Eng., Ser. B, **56**, No. 522, pp. 502–507.

On Cross-Flow Fan Similarity: Effects of Casing Shape

L. Lazzarotto

A. Lazzaretto

A. D. Martegani

Department of Mechanical Engineering,
University of Padova,
via Venezia, 1 35131 Padova, Italy

A. Macor

Department of Management and Engineering,
University of Padova,
Stradella s. Nicola, 3 36100 Vicenza, Italy

The limited number of experimental investigations on similarity operation in the literature is not sufficient to state the validity of similarity laws for cross-flow fans. This is also due to the operating conditions occurring in practical applications, where the values of impeller size and rotational speed generally result in low Reynolds numbers and, then, in a non-negligible influence of viscous forces on performance. The analysis is further complicated by the high influence of the casing shape on performance, which can lead to induced effects on similarity operation. An experimental test program is presented in this paper, aimed at understanding the influence of Reynolds number on performance for different casing shapes. Five impellers having similar shape and different dimensions were tested, each one matched with five casings at different rotational speed. The results show that similarity laws can be applied with good approximation above critical blade Reynolds numbers of around 4000 to 15,000, depending on the geometrical characteristics of the casing. The strong scale effect, shown by some authors in the literature, is not observed in these tests. [DOI: 10.1115/1.1379033]

1 Introduction

Cross-flow fans are not so widely used in industrial and domestic applications as axial or centrifugal fans. However, they are particularly suitable in applications where the radial room is limited. High mass flow rates can be generated by simply increasing the impeller length without increasing the rotational speed or diameter; this gives the further advantage of less noise. Cross-flow fan operating conditions generally imply low values of Reynolds number, and the influence of flow viscosity on fan performance can be quite important. This fact precludes using the Similarity Laws to predict fan performance in the study of fan operation or design. Only a few discussions on the effects of Reynolds number and fan dimensions have been given by Ilberg and Sadeh [1], Eck [2] and Lajos and Preszler [3–5]. Experimental investigations to verify the validity of Similarity Laws have been made by Tanaka and Murata [6,7]. However, a final conclusion is far from being reached.

Lajos and Preszler [3] cited a doctoral work by W. Engelhardt in which the Similarity Laws are considered to be valid for blade Reynolds numbers higher than 5000, but they did not specify the fan geometrical characteristics. Tanaka and Murata [6,7] presented the most detailed analysis on similarity operation in the literature for cross-flow fans. They carried out experimental investigations on three fans having different dimensions and an approximately constant ratio between homologous geometrical dimensions. They found that fan performance curves are affected by flow viscosity for Reynolds numbers lower than 10,000–15,000. Moreover, they observed that fan performance curves are also influenced by the impeller dimensions. A larger impeller diameter results in an approximately proportional increase in the maximum flow coefficient. The same authors, after studying the flow field within the impeller, concluded that:

- the similarity of the flow field pattern within the impeller is a sufficient but not a necessary condition for obtaining the same values of pressure and flow coefficients; and
- the maximum energy transfer occurs in the flow field zone closest to the vortex periphery. For increasing impeller dimensions this zone becomes proportionally larger, the vortex dimension becomes smaller, and higher flow and pressure coefficients are then obtained.

Thus, according to these authors, the similarity conditions are not fulfilled for either the low Reynolds number operating conditions or for the influence of fan dimensions. On the basis of their experimental findings, Tanaka and Murata [7] suggested it is advantageous to include the Reynolds number and scale effects on the pressure and flow coefficients.

Other studies in the literature (Porter and Markland [8], Murata and Nishihara [9,10], Martegani et al. [11], Lazzaretto et al. [12]) have demonstrated that fan performance curves are strongly affected by the vortex shape and dimension, which, for a given impeller, are influenced by the shape and dimension of the casing walls. These findings suggest further studies of the effects on fan performance of Reynolds number and fan dimensions under varied casing geometrical characteristics.

This is the aim of this work, in which the results of experimental tests on five impellers having similar geometrical characteristics are presented. Each impeller was matched with five different rear casing walls and a flat vortex casing wall. Impeller diameters ranging from 86–200 mm were chosen, because this range covers a wide variety of practical applications, excluding miniature applications such as the cooling of small electronic devices. Particular attention was paid in the fan construction and assembly to accurately produce fan configurations in geometrical similarity. The operating characteristics (pressure, flow rate, power, and efficiency) of each fan configuration were measured while varying the rotational speed from a minimum value to the limit of mechanical resistance. Interesting conclusions on the applicability of Similarity Laws are obtained, often in disagreement with the results of previous experiments in the literature.

2 Test Rig

To test cross-flow fans of variable dimensions and rotational speed, a test rig (Fig. 1) was arranged following the UNI 10531 [13] standard (equivalent to ISO 5801 [14]) on industrial fan test methods and acceptance conditions. The static pressure measurements were performed by means of three water micromanometers, one of which was of differential type for flow rate measurement. The direct current motor includes a tachometric dynamo for measurement of rotational speed. Torque was measured using a load cell arranged in the statoric part of the motor. The arrangement of the test rig allows the test of cross-flow fans having diameters up to 250 mm and lengths up to 400 mm, with different types of casings.

Contributed by the Fluids Engineering Division for publication in the JOURNAL OF FLUIDS ENGINEERING. Manuscript received by the Fluids Engineering Division November 28, 2000; revised manuscript received March 15, 2001. Associate Editor: Y. Tsujimoto.

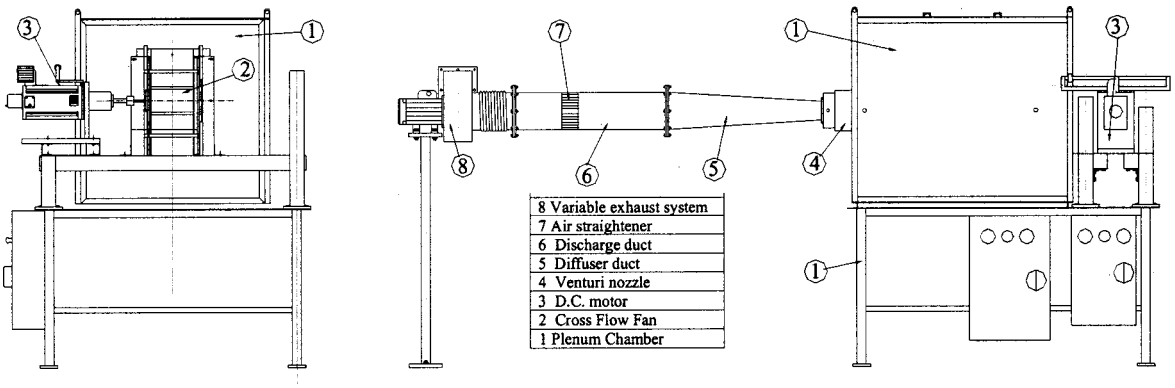

Fig. 1 Schematic of the test rig

2.1 Impellers. The impellers were built in geometrical similarity. A shape similar to the one suggested by Porter and Markland [8] was chosen, because of the high performance of that impeller over a wide range of flow rates (see [8,12]). The outer diameters, equal to 86, 100, 119, 152.4, and 199 mm, were selected to cover the most common dimensional ranges of practical applications.

To guarantee a precise blade geometrical similarity, the 24 blades were constructed by turning steel pipes until the correct inner and outer blade radii were generated. Each blade was then obtained by a longitudinal laser cut. A laser cut was also used to produce the correct stagger angle (γ=14.3 deg in Fig. 2) of the slots on the lateral disks in which blades are fitted. The internal and external blade angles are equal to $\beta_1=70$ and $\beta_2=38$ deg. The other geometrical characteristics (Fig. 2) are $D_2/D_1=0.81$, $L/D_2=1.5$, $Rb/D_2=0.072$, and $s/D_2=0{,}015$.

2.2 Casing Walls. To analyze the influence of the geometrical characteristics of the casing on fan performance, five casing configurations were built for each impeller. To facilitate the construction of the casing walls and to reproduce them in geometrical similarity, high density polystyrene was used, as it can be easily cut using laser technology after drawing the wall shape using a CAD system. This technique had proved to be very satisfactory in the experiments performed earlier [11,12].

Rear Wall. To vary the radial width using a single parameter, a logarithmic spiral rear wall was considered, as already suggested by Porter and Markland [8]. Its profile was obtained by

$$R=R_0e^{\theta/\theta^*}=R_2\left(1+\frac{e_R}{R_2}\right)e^{\theta/\theta^*} \tag{1}$$

where R_0 is the radius at the beginning of the casing rear wall profile at the suction side, θ and R are the angle and radius that define a generic point of this profile, and θ^* is a parameter that defines the radial width. The rear wall profile starts at the angle $\alpha_0=30$ deg measured from the horizontal axis of the impeller (Fig. 3). At this point, the radial clearance between rear wall and impeller (e_R in Eq. (1)) is $0.0413D_2$. The log spiral arc of the rear wall covers the angle $\lambda=135$ deg.

On the basis of the rear wall shapes studied in the literature [2,8,9,12], the value of θ^* was varied in the range 359–139 deg, considering the three following rear walls:

- a *small width rear wall*, having θ^* equal to 359 deg (R1 in Fig. 3), similar to the rear wall patented by Eck [2];
- an *intermediate width rear wall* having θ^* equal to 191 deg; and
- a *large width rear wall*, having θ^* equal to 139 deg.

Two configurations were considered for the rear walls R2 and R3, by varying the type of discharge duct. The first configuration, having a *curved discharge duct* of sinusoidal shape, linked the end of the log spiral profile with the discharge section (Fig. 3) so that, for a fixed position of the vortex wall, the height of the discharge section is the same for both rear walls. These two walls are indicated as R2c and R3c in Fig. 3. The second configuration having a *rectilinear discharge duct*, consequently produces different values for the height of the discharge section. These two walls are indicated as R2r and R3r in Fig. 3. Only the rectilinear discharge duct, having the same height as the discharge section of the two walls R2c and R3c, was used for the rear wall R1.

Vortex Wall. A thin and flat horizontal vortex wall of constant thickness ($S/D_2=0.13$) and having a rounded front edge was selected. This choice was based on the high performances obtained in [11,12] using this vortex wall matched with most of the rear

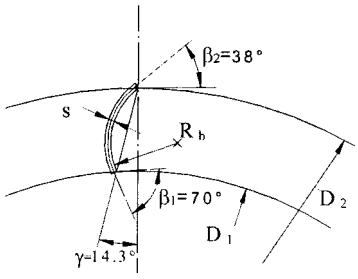

Fig. 2 Detail of the impeller blade

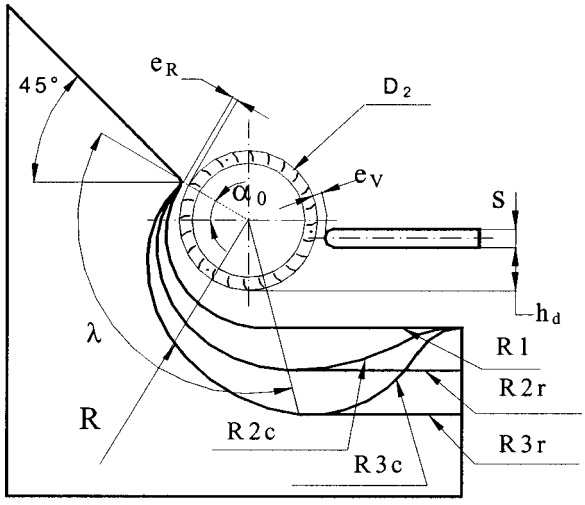

Fig. 3 Geometric configuration of the casing walls

walls selected here. The minimum radial clearance (e_v) between vortex wall and impeller was kept constant at $0.066D_2$ for all the casing configurations.

3 The Test Program

The experimental tests were organized as illustrated by the ''test tree'' in Fig. 4. Each of the five casing rear walls described in Section 2.2 was matched with the vortex wall described in the same section. For a given rear wall, the height of the vortex wall (h_d in Fig. 3) strongly affects fan performance curve [12]. Among the various values of h_d/D_2 tested in that paper, those shown in Fig. 4 were chosen. This resulted in the more stable characteristic curves having the highest value of the total pressure coefficient in the maximum efficiency operating conditions.

The five casing configurations obtained in this way were then tested in conjunction with the five impellers having different diameters (86, 100, 119, 152.4, 199 mm) and similar geometrical shape. The rotational speed of each impeller was varied until the limit of mechanical resistance. The values of rotational speed adopted in the tests and the associated values of Reynolds number, based on the blade chord and rotor tip speed, are shown in Fig. 4.

4 Results of the Experimental Tests

4.1 Effects of Reynolds Number on Fan Performance. To analyze the effects of Reynolds number on fan performance, separate assessments will be made in the following for each different radial width of the casing rear wall, since this variable strongly affects fan performance. The values of the total pressure coefficient (Ψ_t) versus the flow rate coefficient (ϕ) for the casing rear walls R1, R2c, R2r, R3c, and R3r are presented in Figs. 5–9, respectively. The five diagrams in each of these figures are the results obtained from the experiments with the five impellers having similar shape and different diameters. Each diagram includes several curves associated with various rotational speeds, i.e., various Reynolds numbers. Total pressure data were measured under the full spectrum of conditions from fully closed (null flow rate) to fully open (corresponding to null static pressure at the fan discharge section).

Small Width Casing Rear Wall (R1). An unstable trend of the characteristic curves is obtained for low values of the flow rates, when using the small width rear wall (Fig. 5). Moreover, the maximum values of the total pressure coefficient are quite low (1.6–1.7) with respect to those obtained using the other fan configurations. A sudden drop in the total pressure coefficient is observed at Reynolds number ranging between 1000–1700, depending on the fan dimensions. Above these points where the sudden drop occurs, the characteristic curves are very close to each other; they are almost superimposed for Reynolds numbers approximately equal to 4000–5000. Thus, the critical Reynolds number is around these values. These effects are observed within the zone of medium to high values of the flow coefficient (>0.2–0.3), which is the most interesting in practical applications. In the range of lower values of the flow coefficient, the characteristic curves are more separate. In this range, however, a lower reliability of these measurements was obtained due to the unstable operation of the system fan-test chamber.

Intermediate Width Casing Rear Walls (R2c, R2r). The characteristic curves obtained using the intermediate width rear wall with a curved discharge duct (R2c, see Fig. 6) are more regular and flat than those produced by rear wall R1. In fact, a larger width allows the vortex to move along the impeller blades as the flow rate is throttled, as shown in [8,15]. The high values of the pressure and flow coefficient demonstrate the strong influence of the casing's geometrical characteristics on fan performance curves.

For the smaller fans ($D_2=86$, 100) the range of rotational speed considered here (400–2000 rpm) leads to more separate characteristic curves (pressure and flow rate increase with Reynolds) than for the larger ones because of the effects of flow viscosity. These effects tend progressively to disappear as Reynolds approaches 6000–7000.

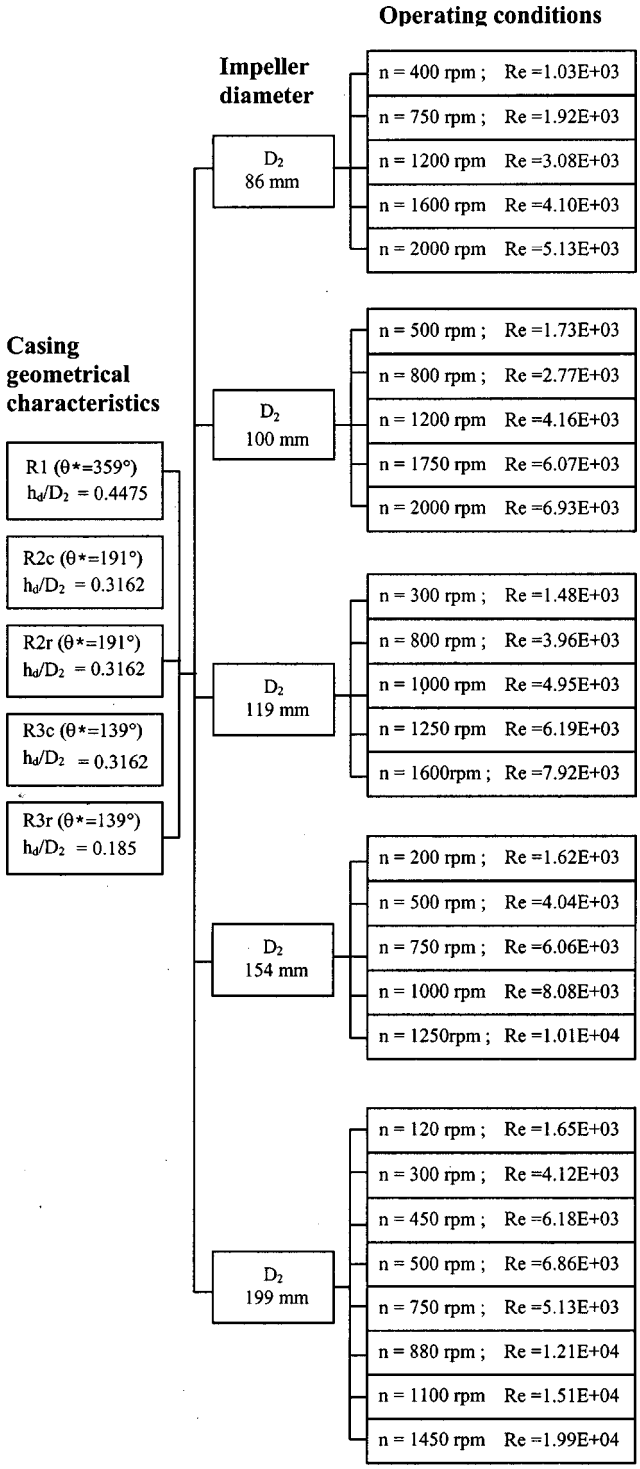

Fig. 4 Test tree

As the fan dimensions increase, under increasing Reynolds number (below its critical value) the characteristic curves become progressively closer to each other. However, the critical Reynolds number remains around 6000–7000, independent of fan dimensions.

Using the rectilinear discharge duct (R2r, see Fig. 7), the pressure coefficient is generally lower and the maximum flow rate is

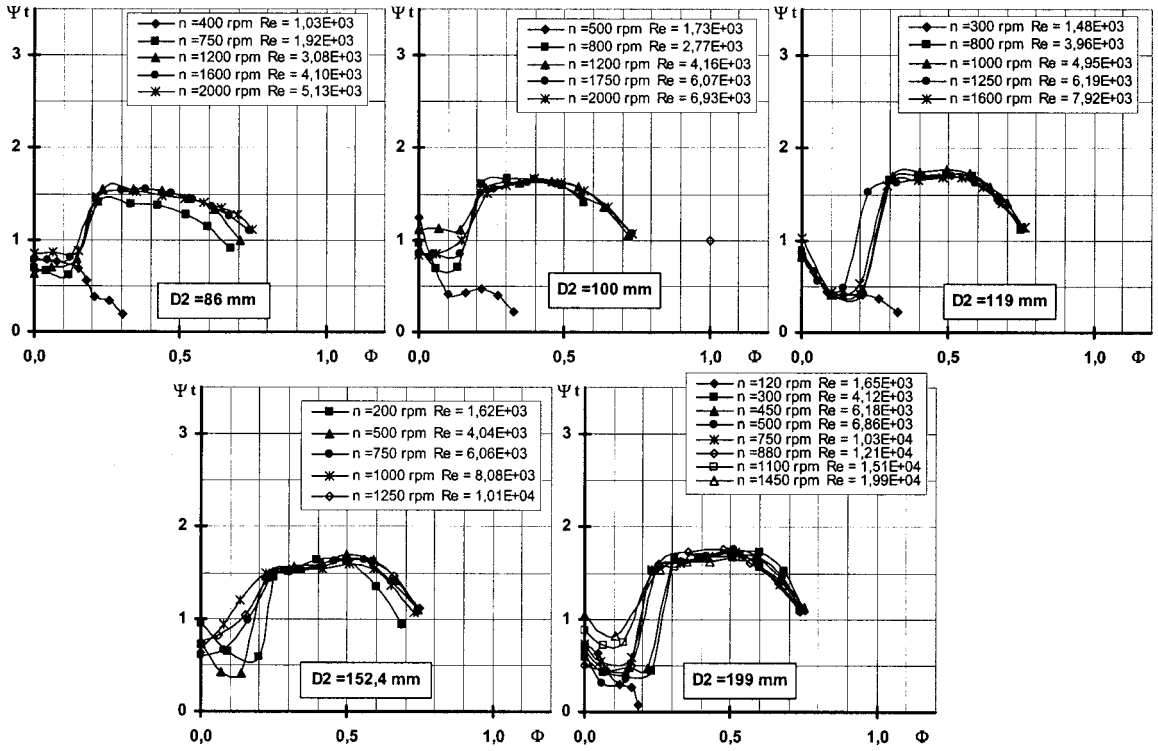

Fig. 5 Casing rear wall R1, having θ^*=359 deg in Eq. (1)

higher. An increase in the Reynolds number (below its critical value) has the effect of increasing the flow rate more than the pressure compared to the curved discharge duct. This effect is stronger for smaller fan dimensions. The critical Reynolds number remains approximately the same (6000–7000) as when using the curved duct.

Large Width Casing Rear Walls (R3c, R3r). As already demonstrated [12], the characteristic curves become very stable when using a large width rear wall (Figs. 8 and 9). At the same Reynolds number, these curves are slightly more divergent than for the intermediate width rear wall. This effect is higher for larger fan dimensions. Accordingly, the critical Reynolds number tends

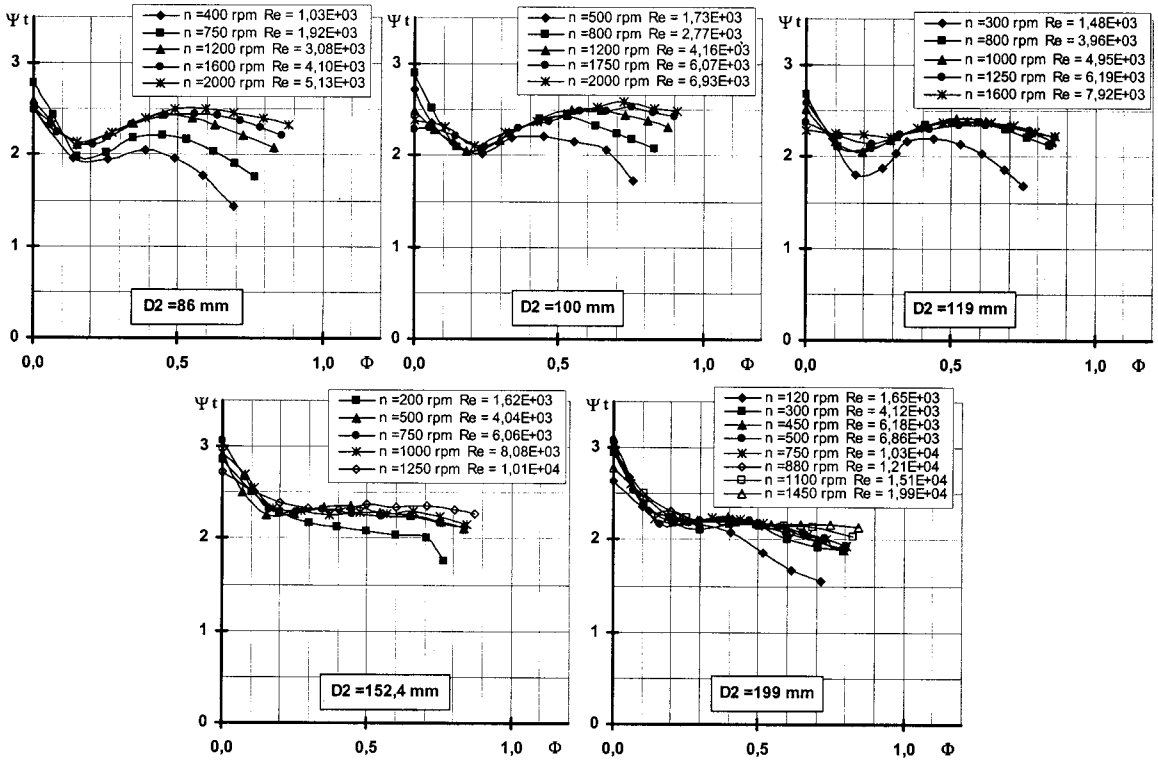

Fig. 6 Casing rear wall R2c, having θ^*=191 deg in Eq. (1) and curved discharge duct

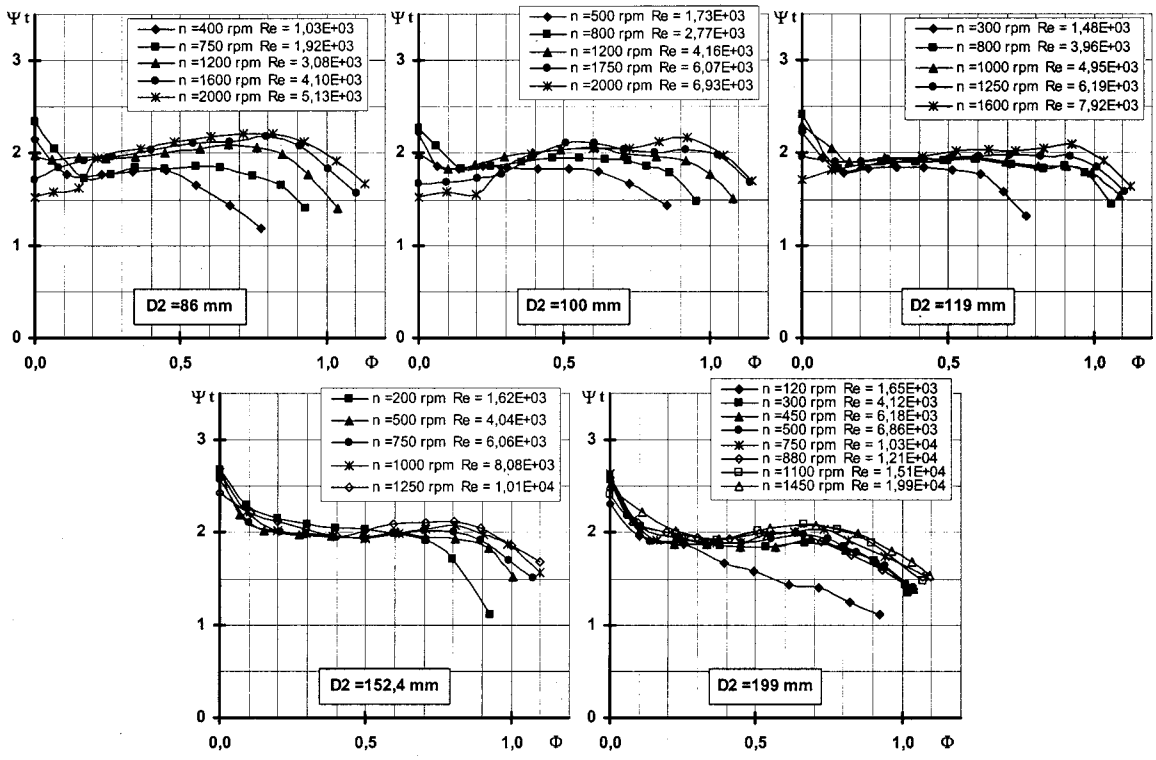

Fig. 7 Casing rear wall R2r, having θ^*=191 deg in Eq. (1) and rectilinear discharge duct

to be higher. For the smaller impellers, an increase in the rotational speed beyond the limits of structural resistance would be needed to reach this value, whereas the characteristic curves are almost superimposed for the bigger ones when Reynolds is around 15,000.

As already seen for the rear wall R2r, the rectilinear discharge duct generally increases the flow rate coefficient. Still, an increase of the Reynolds number (below its critical value) has the effect of increasing the flow rate more than the pressure compared to the curved discharge duct; this effect is observed for all fan dimen-

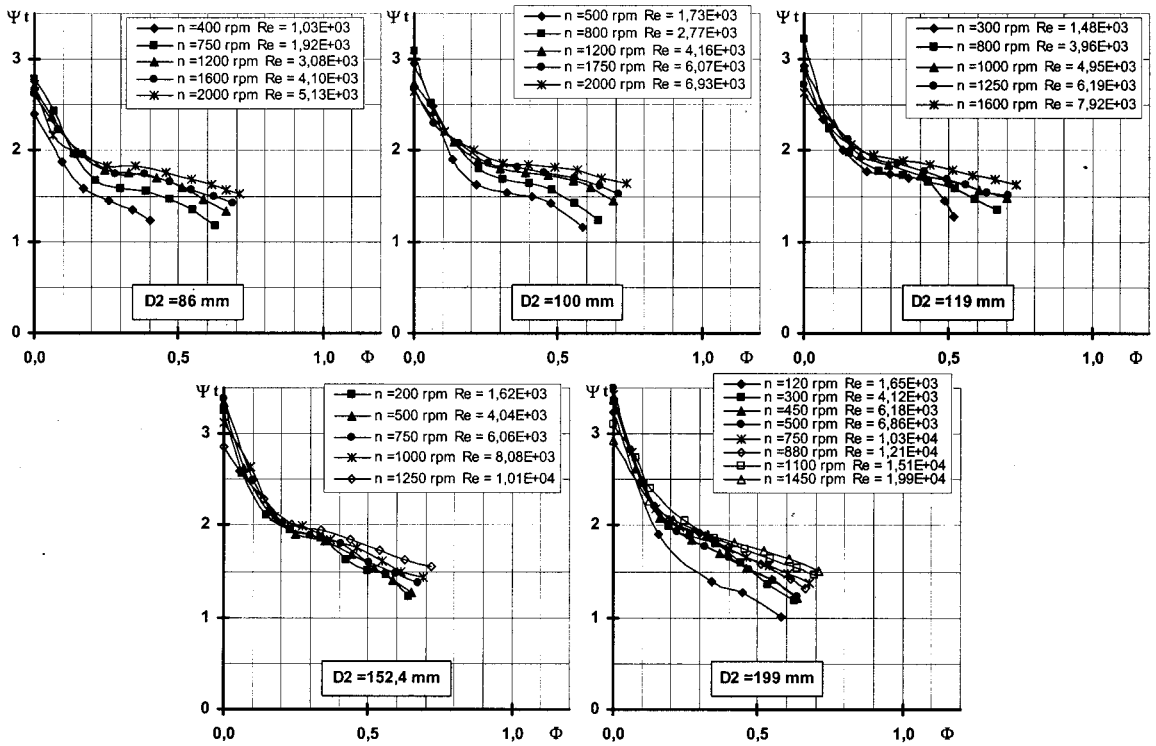

Fig. 8 Casing rear wall R3c, having θ^*=139 deg in Eq. (1) and curved discharge duct

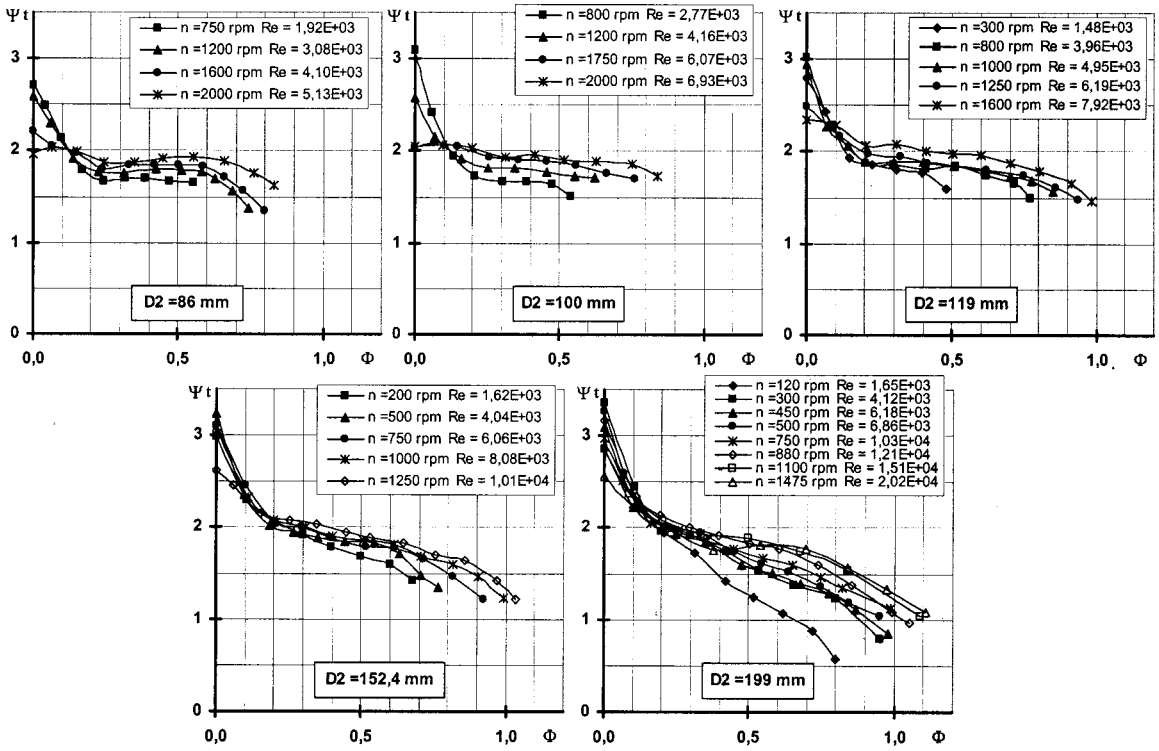

Fig. 9 Casing rear wall R3r, having θ=139 deg in Eq. (1) and rectilinear discharge duct

sions. Although the critical Reynolds number was not reached for the smaller impellers, it seems not to change significantly when using a rectilinear discharge duct. For the bigger diameters (152.4 and 200 mm) it is still around 15,000.

4.2 Effects of the Geometrical Characteristics on Fan Performances at Constant Reynolds Number. By observing the characteristic curves obtained *above or close to the critical Reynolds number* in Figs. 5–9, it is apparent that for casing R1, no

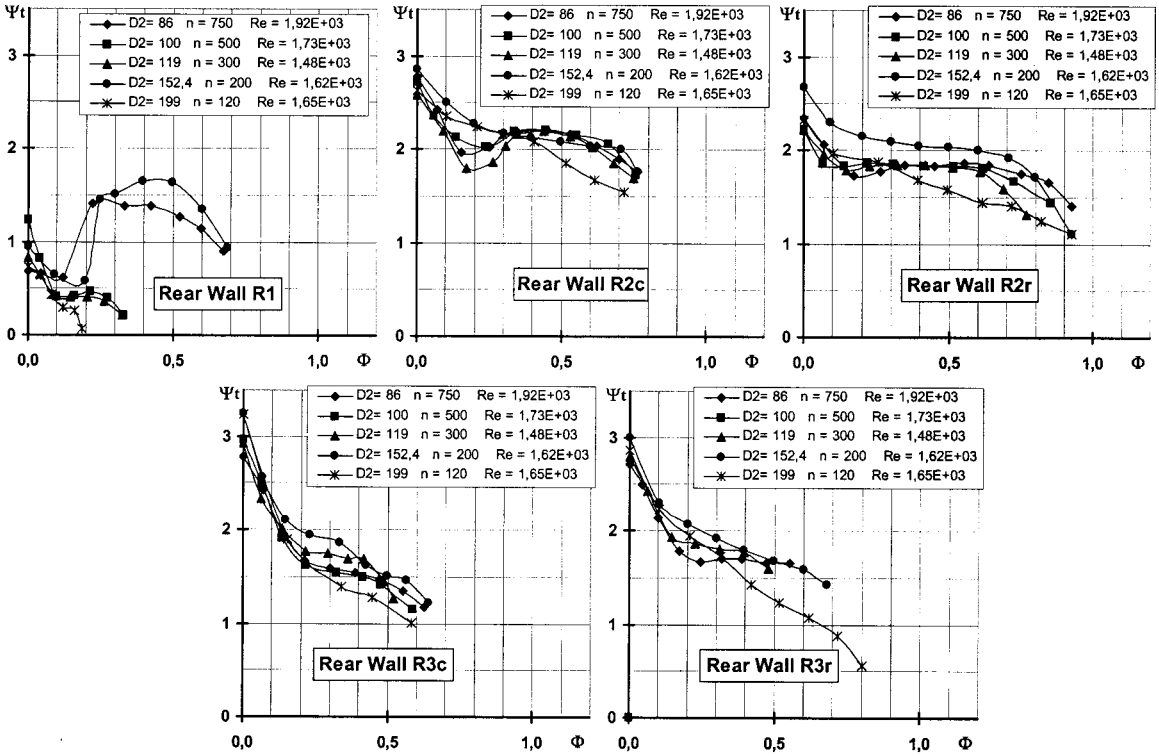

Fig. 10 Reynolds=1.68 E+3

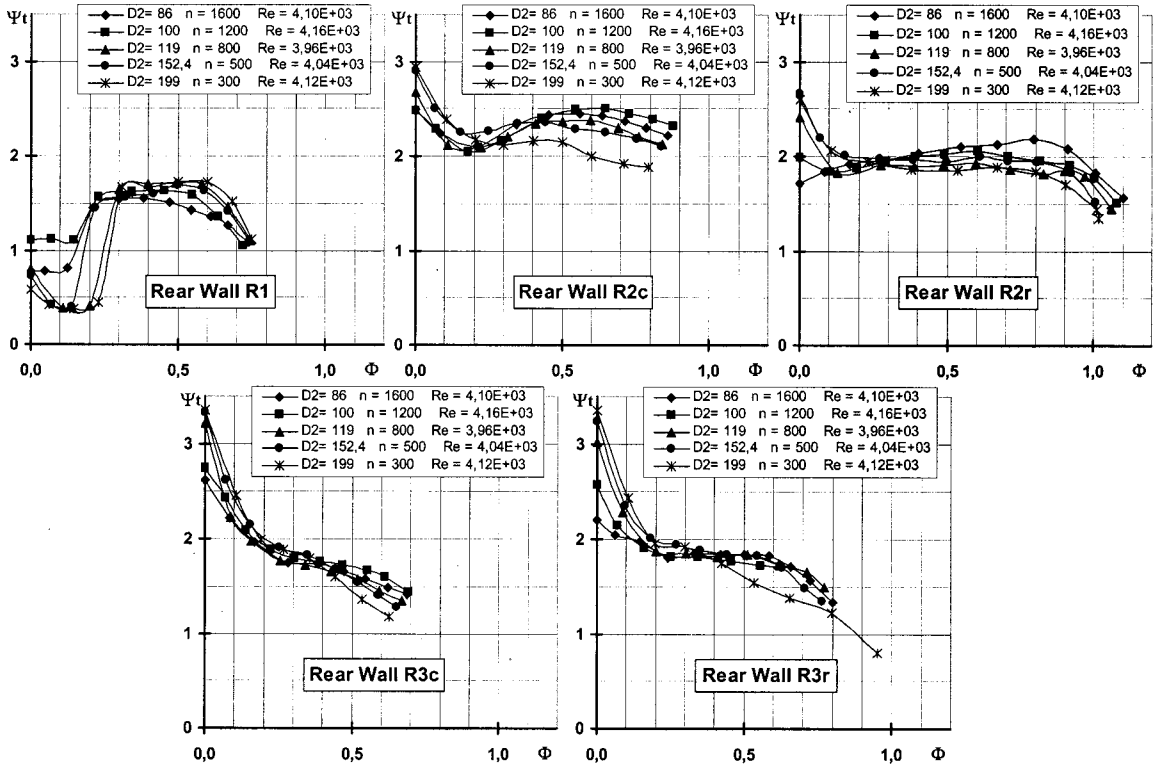

Fig. 11 Reynolds=4.06 E+3

significant scale effects appear. The characteristic curves for Reynolds numbers higher than critical have very similar shapes for different fan dimensions (a slight decrease of the total pressure coefficient is observed only for the smaller fan dimensions). With casing R2c, the characteristic curves become progressively more stable as the fan dimensions increase. With casing R2r, no significant scale effects appear. Finally, with casings R3c and R3r, the characteristic curves become progressively more stable as the fan dimensions increase.

Although the relationships are not extremely clear due to the

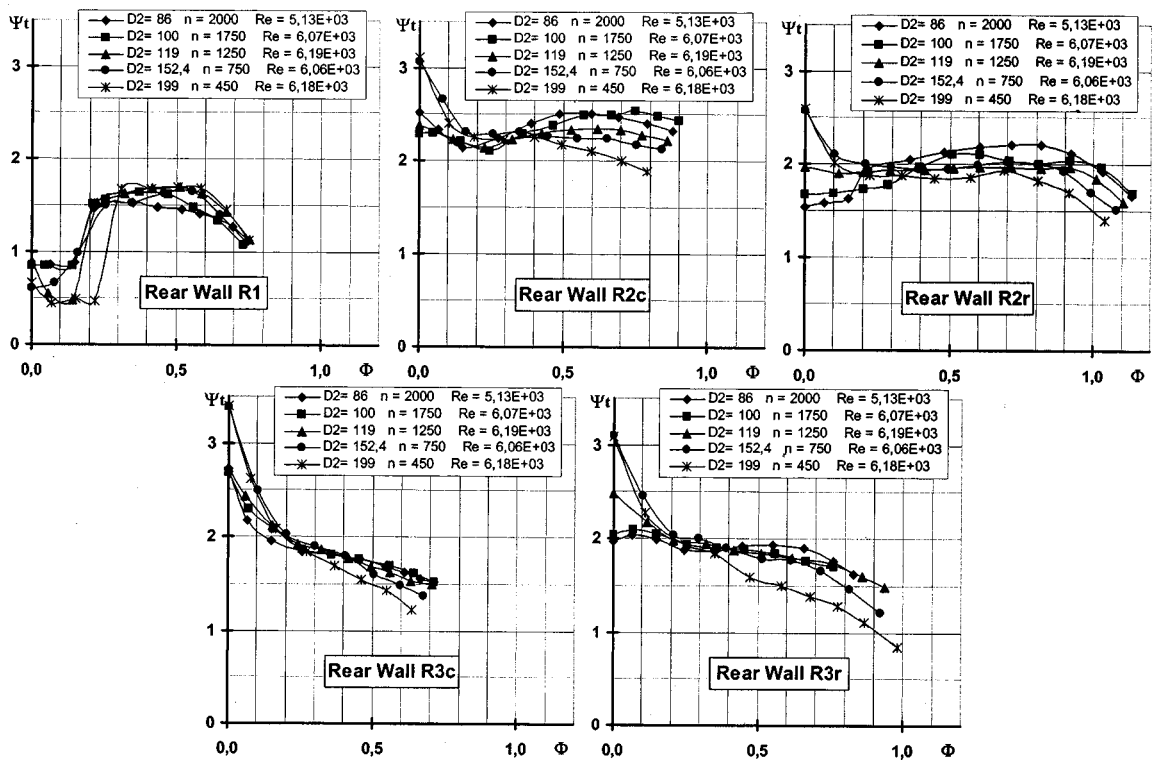

Fig. 12 Reynolds=6 E+3

high number of variables affecting fan performance, it seems that the scale effect has a limited influence on fan performance. This effect is slightly higher for the casing having bigger radial width and curved discharge duct that shows characteristic curves progressively more stable for larger fan dimensions.

For further analysis, characteristic curves obtained for all five casings at constant Reynolds numbers *below the critical value*, approximately equal to 1700, 4000, and 6000, are compared in Figs. 10–12. Conflicting effects were obtained for the small width rear wall (R1), where there is a stronger interaction between the internal vortex and rear wall very close to the impeller. In fact, for very low Reynolds numbers (Fig. 10) when the influence of flow viscosity is high, an increase in the fan dimension leads to a decrease in the total pressure and flow rate coefficients. Conversely, for higher Reynolds numbers (Figs. 11 and 12) the opposite occurs.

On the other hand, a quite clear indication is obtained for the intermediate and large width rear walls. For each of the Reynolds numbers considered here (Figs. 10–12), the slope of the characteristic curve slightly decreases (the curves become more stable) as the impeller diameter increases. As a consequence, in the range of flow rate of practical applications ($\phi > 0.2-0.3$), the total pressure coefficient decreases with an increase in the fan dimensions.

These results conflict with those obtained by Tanaka and Murata [6,7], who tested three impellers having similar dimensions but different shape from those used here. They observed a strong scale effect for Reynolds numbers approximately equal to 4500 and they stated that the same effect occurs also above the critical Reynolds number (10,000–15,000): for larger diameters the characteristic curves are ''stretched,'' i.e., the pressure coefficient remains approximately constant whereas the flow rate progressively increases.

5 Conclusions

The effects of Reynolds number and dimensions on similarity operation of cross-flow fans are investigated in this work. Various fan configurations, characterized by different geometrical characteristics of the casing, dimensions and rotational speed were tested to cover a wide range of practical applications. The following main conclusions can be drawn:

- In the range of dimensions and rotational speed usually met in practical applications, cross flow fans often operate below the critical Reynolds number where fan performance is affected by viscous forces.

- The *critical Reynolds number* varies depending on *the casing shape*. It is then advantageous to make separate conclusions for each radial width of the rear wall, which is the geometric factor of the casing which more greatly affects the operating conditions under similarity. Using a flat horizontal vortex wall of constant thickness, the critical Reynolds number is around 4000–5000 for the rear wall of the casing having smaller radial width, is around 6000–7000 for the intermediate width, and it increases up to 15,000 for the largest radial width. No significant variations in the critical Reynolds number are observed when using a rectilinear discharge duct instead of a curved one for the intermediate and bigger radial width rear walls.

- The drop in fan performance *below the critical Reynolds* is very sudden at Reynolds numbers ranging between 1000–1700 when using the small width rear wall, whereas it is more gradual for the two rear walls having bigger radial width. For these walls the use of a rectilinear discharge duct has the effect of increasing the flow rate more than the pressure compared to the curved discharge duct.

- From the practical point of view, similarity laws cannot be applied when the impeller diameter is lower than 100 mm and the rotational speed is lower than 1500–2000 rpm; below these values, changes in the rotational speed lead to quite important deviations in the characteristic curves.

Although some of the results are quite difficult to interpret due to the high number of variables affecting fan performance, it seems that the *scale effect* has a limited influence on fan performance. *Above the critical Reynolds number*, this effect is slightly higher for the casing having a bigger radial width and curved discharge duct. Thus this configuration shows characteristic curves progressively more stable for higher fan dimensions, which leads to a decrease in the total pressure coefficient within the range of flow rates typical of practical applications. *Below the critical Reynolds number*, conflicting effects were obtained for the small width rear wall. For very low Reynolds numbers, an increase in the fan dimension leads to a decrease in the total pressure and flow rate coefficients; the opposite occurs for higher Reynolds numbers. Clearer indications are obtained for the intermediate and large width rear walls for which the characteristic curves become more stable as the impeller diameter increases (the effect is the same that appears above the critical Reynolds number).

These results are inconsistent with previous experiments of Tanaka and Murata [6,7] who found a strong scale effect on fan performances. Note that this analysis applies only to the impeller shape considered here. A variation in the geometrical characteristics of the impeller might alter the above indications.

Acknowledgments

We would like to acknowledge Dr. Andrea Toffolo for helping us in executing the experimental tests.

Nomenclature

flow coefficient = $\Phi = \frac{q_v}{L \cdot D_2 \cdot u_2}$

total pressure coefficient = $\Psi_t = \frac{p_t}{\frac{1}{2} \cdot \rho \cdot u_2^2}$

blade Reynolds number = $R_e = \frac{u_2 \cdot c_p}{\nu}$ where $u_2 = \frac{2 \cdot \pi \cdot n}{60} \cdot \frac{D_2}{2}$

D_1 = impeller internal diameter [m or mm]

D_2, R_2 = impeller external diameter, radius [m or mm]

R = generic radius of the casing rear wall [m]

R_b = blade internal radius [mm]

h_d = distance between the lower tangent to the impeller and the vortex wall (Fig. 3) [mm]

e_R, e_V = radial clearance between impeller and rear wall, between impeller and vortex wall [mm] (Fig. 3)

α_0 = angle between the beginning of the casing rear wall and the horizontal axis of the impeller [degrees]; (Fig. 3)

γ = blade stagger angle [degrees]

β_2, β_1 = blade external and internal angle [degrees]

λ = rear wall casing angle [degrees]

s = blade thickness [mm]

$\mathbf{S}$ = vortex wall thickness [mm]

q_v = volumetric flow rate [m^3/s]

L = impeller axial length [mm]

p_t = fan total pressure [Pa]

ρ = air density [m^3/Kg]

c_p = blade chord [m]

ν = μ/ρ=air kinematic viscosity [m^2/s]

n = rotational speed [rpm]

References

[1] Ilberg, H., and Sadeh, W. Z., 1965–66, ''Flow Theory and Performance of Tangential Fans,'' *Proc. Instn. Mech. Engrs.*, Vol. 180, Part 1, No 19.

[2] Eck, B. 1973, *Fans*, Pergamon Press, New York.

[3] Lajos, T., and Preszler, L., 1973, ''On the Cross Flow Fan Theory. Part 1: Types of Fans, Operating Principles, Stream Configuration, Velocity Field (In German),'' *Heizung-Lüftung-Haustechnik*, 24 Nr. 5.

[4] Lajos, T., and Preszler, L., 1973, ''On the Cross Flow Fan Theory. Part 2: Calculation of the Blade Circulation and the Flow Field, and Comparison of the Experimental Results With the Theory,'' (in German). *Heizung-Lüftung-Haustechnik*, 24 Nr. 6.

[5] Lajos, T., 1975, ''Investigation of the Flow Characteristics in the Impeller of the Tangential Fan,'' *Proceedings of Sixth Conference on Fluid Machinery*, Budapest.

[6] Tanaka, S., and Murata, S., 1994, ''Scale Effect in Cross-Flow Fans (Effects of Fan Dimension on Performance Curves),'' Bull. JSME, Series B, **37**, No. 4.

[7] Tanaka, S., and Murata, S., 1995, ''Scale Effect in Cross-Flow Fans (Effects of Fan Dimension on Flow Details and the Universal Representation on Performances),'' Bull. JSME, Series B, **38**, No. 3.

[8] Porter, A. M., and Markland, E., 1970, ''A Study of the Cross Flow Fan,'' J. Mech. Eng. Sci., **12**, No. 6.

[9] Murata, S. I., and Nishihara, K., 1976, ''An Experimental Study of Cross Flow-1st Report, Effects of Housing Geometry on the Fan Performance,'' Bull. JSME, **19**, No. 129.

[10] Murata, S. I., and Nishihara, K., 1976, ''An Experimental Study of Cross Flow-2st Report, Movements of Eccentric Vortex inside Impeller,'' Bull. JSME, **19**, No. 129.

[11] Martegani, A. D, Macor, A., and Lazzaretto, A., 1995, ''Theory and Experimental Investigation on Cross Flow Fans. Part II: Testing of a Model (In Italian),'' *Proceedings of 50° Congresso Nazionale ATI*, Vol. 2, pp. 1696–1706, Saint Vincent, 11–15 September. SGEditoriali-Padova.

[12] Lazzaretto, A., Macor, A., Martegani, A. D., and Martina, V., 1997, ''Experimental Optimization of the Casing of a Cross Flow Fan. (In Italian),'' *Proceedings of 52° Convegno Nazionale ATI*, Cernobbio (CO), 22–26 September. SGEditoriali-Padova.

[13] UNI 10531, 1995, ''Industrial Fans-Performance Testing and Acceptance Terms,'' (in Italian), UNI (Italian National Center for Standardization), Milano.

[14] ISO 5801, 1993, ''Industrial Fans-Performance Testing using Standardized Airways,'' International Organization for Standardization.

[15] Martegani, A. D., Navarro, G., Macor, A., Lazzaretto, A., Masi, M., Antonello, M., and De Lorenzi, S., 1999, ''Experimental and numerical analyses of a cross flow fan (In Italian),'' *Proceedings of 54° Congresso Nazionale ATI*, Vol. 2, pp. 1409–1423, L'Aquila, 14–17 September. SGEditoriali-Padova.

Performance Characteristics of a Centrifugal Pump Impeller With Running Tip Clearance Pumping Solid-Liquid Mixtures

Tahsin Engin
Assist. Professor
e-mail: engint@sakarya.edu.tr

Mesut Gur
Professor
e-mail: gur@sakarya.edu.tr

University of Sakarya, Faculty of Engineering,
Department of Mechanical Engineering,
Esentepe Campus 54187, Sakarya, Turkey

This paper presents extensive results on the performance of an unshrouded centrifugal pump impeller handling solid-liquid mixtures. The effect of the clearance between the impeller tip and the casing and of the solid concentration, density and mean diameter on the pump performance characteristics is investigated. The results are discussed and utilized, together with data available in the literature, to establish a correlation allowing the prediction of the head reduction factor for shrouded/unshrouded impeller centrifugal pumps handling solid-liquid mixtures. The predictions made with the proposed correlation show a better agreement with experimental results than previous ones.
[DOI: 10.1115/1.1379034]

1 Introduction

Centrifugal pumps with both shrouded and unshrouded impellers have long been used for hydraulic transportation of fine and coarse-grain solids, such as coal, dirt, and gravel. The advantages of the centrifugal pumps are based, among others, on the high and consistent flow rate, simple and effective controllability and the favorable ratio of flow rate to model, and low manufacturing and maintenance costs. The main disadvantages are the limited head and the low efficiency. Also wear of the impellers and casing from solids leads to additional deterioration of efficiency over the working life.

The flow of solids through the pump has associated hydraulic losses caused by the relative motion of coarse particles (drag effects), which have greater inertia and cannot accelerate as rapidly as the carrier liquid. It is important to realize that, solids suspended in a liquid cannot absorb, store, or transmit pressure energy, which is a property of fluids. Nor can they transmit their kinetic energy to the liquid, since the liquid moves at a higher velocity [1]. Usually, mixtures with a size distribution containing larger particles greater than 0.1 mm approximately are classified as ''settling-mixtures,'' and in such cases the particles and liquid will exhibit their own characteristics. As the liquid passes over the solid particles, the energy given by the impeller to the carrier fluid is dissipated due to ''drag,'' which results in a reduction in pump head and efficiency. The deterioration in performance arises from the energy losses owing to slip between the liquid and the particles as the mixture accelerates or decelerates through the pump, and interactions among the solid particles, as well as between solid particles and internal walls of the pump. However, if the particle sizes are smaller than 0.035 mm such as fine sand, slit and most clays, or the solids concentration is high, the mixture is characterized as ''slow-settling'' or ''nonsettling'' [2]. In such mixtures, there is no hydraulic efficiency loss resulting from slip between solid particles and the carrying liquid. Instead, slow settling mixtures behave as a Newtonian fluid and generally result in increased viscosity, which in turn affects hydraulic efficiency. Slow-settling mixtures are not considered in this study.

Previous studies of the effect of solids on pump performance have shown that the performance of a centrifugal pump with solid-liquid mixtures will be different than with clear water. Several correlations have been proposed to predict the effects of solids on pump performance [3–8]. However, because of the complexity of the problem, none of them is wholly successful in the prediction of these effects.

Both shrouded and unshrouded impellers have long been widely used in centrifugal pumps handling solid-liquid mixtures. Unshrouded impellers are preferable in many practical applications owing to their relatively low disk friction losses, low manufacturing cost and ease of coating of their surfaces to gain high wear resistance. Furthermore, they are suited for pumping suspensions. However, when unshrouded impellers are operated in pumps, tip clearance losses become very important. It is well established that the performance of rotating machines depends strongly on the tip clearance. Tip clearance refers to the clearance between vane tips of a half shrouded impeller and the front casing. In many turbomachines, impellers are not shrouded and the leakage flow through the tip clearance of blades is an unavoidable factor that degrades the machine performance. Although tip clearance effects on pump performance have been studied for many years, and the necessity for reliable information is ever increasing, an exact method for the prediction of these effects currently does not exist. Instead, test data must be relied upon to aid in the development of models to estimate these effects. Several approaches have been presented for modeling tip leakage flow in order to predict tip clearance losses. Loss equations given in the literature have been derived from sparse experimental data and/or based on many assumptions about the loss mechanism [9–14]. On the other hand, most publications in the field are focused either on tip clearance effects with water/gas or on solid effects on pump performance. The operating point of an unshrouded impeller centrifugal pump depends to a high degree, on the value of the tip clearance. Owing to manufacturing and assembly tolerances and clearance enlargements through wear, the designed tip clearance often differs from the actual tip clearance. As a result, the operating parameters do not meet the desired pump performance.

The present experimental study deals with the effects of different solid-liquid mixture properties on the performance characteristics of a centrifugal unshrouded impeller pump, considering the variation of the tip clearance. Although some notable studies [15, 16] have been carried out to investigate the solid-liquid flows through these pumps, understanding of the subject is far from complete. Tip clearance results on the centrifugal pumps handling of solid-liquid mixtures have not been previously reported in the

Contributed by the Fluids Engineering Division for publication in the JOURNAL OF FLUIDS ENGINEERING. Manuscript received by the Fluid Engineering Division August 28, 2000; revised manuscript received April 4, 2001. Associate Editor: Y. Tsujimoto.

literature. Therefore, the secondary objective of this study is to provide primary data needed for the development of new theories and for the validation of numerical methods. Both shrouded and unshrouded impellers were used in the experiments. A new correlation to predict the relative head reduction due to the presence of solids in the pumped water is developed. The validity of the correlation is verified and compared with correlations given in the literature.

2 Experimental Work

2.1 Experimental Apparatus and Instrumentation. The experimental data were obtained by conducting experiments using a specially designed and fabricated experimental facility. The schematic view of the test rig is shown in Fig. 1. The mixture was prepared using a stirrer (10) in a mixing tank (9) by adding required quantities of solids and water. The water required for flushing the test loop before shut-off, was supplied from a flushing tank (8). Two shut-off valves (7) were fitted on the 100 mm diameter suction pipe. The flow rate could be varied over a wide range by operating a third plug valve fitted near the end of the 80 mm delivery pipeline (7). This valve had a servomotor and was remotely controlled by a PC. The suction and discharge pressures were measured by using two pressure transducers (5), with a ± 0.2 percent F.S. accuracy. Pressure transducers with diaphragms were chosen in order to prevent choking of gauges. The calibration of these transducers was periodically checked using a weight-type reference gauge. Flow rate was measured using a Krone electromagnetic flow meter, which was calibrated with water by measuring the rise in the level of water in the flushing tank over a known interval of time. A sampling tube (6) with a valve was provided in the delivery pipe to allow the determination of various mixture properties.

Electrical signals corresponding to the measurement of pressure, flow rate, rotational speed and torque were read by a data acquisition/control unit, which could scan up to 16 channels. The data acquisition/control unit was commanded by the PC. An automatic data processing computer code (Genie 3.02) was used for real-time performance calculations.

The pump (3) is directly coupled to a 5.5 kW-AC motor (2). A typical centrifugal pump having specifications $d_1=134.5$ mm, $d_2=210$ mm, $b_1=31$ mm, $b_2=19$ mm, $\beta_1=40°$, $\beta_2=34°$, and $z=7$ (backward curved) was used in the experiments. Initially, the shrouded impeller was tested, and then the shroud was removed to give an unshrouded impeller with an identical shape to the shrouded one. This unshrouded impeller was then fitted with a new front casing cover having the shroud contour shown in Fig. 2. The running tip clearance (x) between the impeller vanes and the front casing was varied by employing four shroud contours having different thickness. Care was taken to change the clearance without losing the symmetric position of the impeller outlet relative to the casing. A Siemens motor driver (1) (frequency inverter, 0-650 Hz) was employed to measure the pump rotating speed and torque transmitted to the pump shaft. It also allowed the pump speed to be controlled. The meters were checked and calibrated before and after each set of runs.

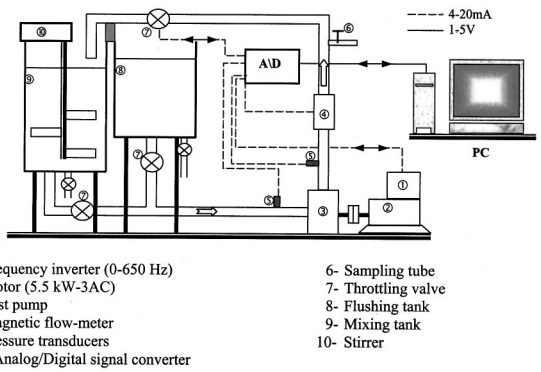

Fig. 1 Experimental test rig and instrumentation (ISO 2548)

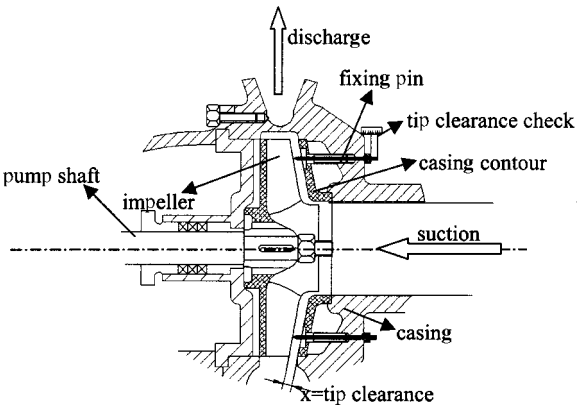

Fig. 2 Meridional profile of the unshrouded impeller with tip clearance arrangement

2.2 Test Method. In order to study the effects of the suspended solids on the centrifugal pump characteristics, tests were conducted with mixtures of four different solid materials, namely casting sand, beach sand, and perlite-A and perlite B. The Physical properties of the materials are shown in Table 1. The particle size distributions of the materials were determined by sieve analysis. A sample of 400 g of solid was used for sieving. The weighted mean diameter (d_w) of different materials was calculated and the mass median diameter (d_{50}) was obtained from the cumulative percentage undersize-particle diameter plot (Fig. 3).

Measurements were made with two different concentrations of each solid material for four different tip clearance settings such as

Table 1 Physical properties of materials used

Materials	Specific gravity S(−)	d_{50} (mm)	d_w (mm)
Casting sand	2.10	0.400	0.400
Beach sand	2.64	0.413	0.440
Perlite-A	2.34	0.270	0.211
Perlite-B	2.34	1.390	1.147

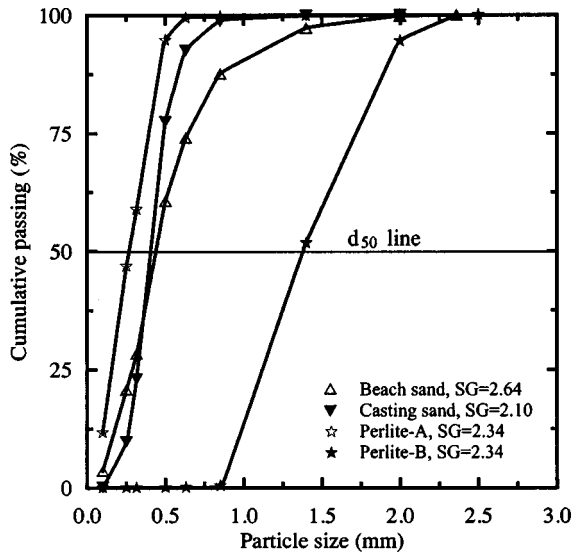

Fig. 3 Particle size distribution of the materials used

1.25 mm, 2.5 mm, 5.5 mm, and 8 mm. Following the completion of the pump test with water, a precalculated amount of solid material was slowly added to water in the mixing tank with the stirrer in operation. The mixture was kept in circulation for approximately 10 minutes for thorough mixing and then the concentration of solids in the circulation was checked before starting any measurements. The delivery valve was opened while the pump was operated at a constant rotating speed. The power input to the motor, the flow rate, the suction and the delivery pressures were recorded. The density of the mixture was determined using a mixture sample collected from the sampling tube. Four samples were taken during each measurement and the average of their densities was used to calculate the concentration of solids. The measurements were repeated for various settings of the delivery valve. Measurements of pump characteristics with clear water were carried out both before and after each mixture test.

3 Results and Discussion

3.1 Effects of Tip Clearance. In order to study the effects of tip clearance on the centrifugal pump performance, tests were conducted for several tip clearances ranging from 1.25 mm–8 mm, and for each mixture of solids at two different concentrations of solids. The results are presented in nondimensional terms. The nondimensional tip clearance, denoted $a=2x/(b_1+b_2)$, is defined as the ratio of the tip clearance to the arithmetic mean of blade inlet and outlet heights, and was varied within the range of 5–32 percent. This range has been widely adopted by most investigators dealing with tip clearance considerations in turbomachines [10,11,14,17]. Performance tests were conducted at a constant shaft speed of 1250 rpm.

The performance of the pump varied with changes in the running tip clearances as indicated in Figs. 4(a–d). The results for clear water are also plotted for direct comparison. Each performance parameter is presented as a percentage ratio of its corresponding value at zero clearance, obtained by extrapolation using Figs. 5(a–c). These indicate the effect of the running tip clearance on the head (uncertainty of $\psi=\pm 0.5$ percent), efficiency (uncertainty of $\eta=\pm 2.2$ percent), capacity (uncertainty of $\phi=\pm 0.3$ percent), and power (uncertainty of $\mu=\pm 2$ percent) at each maximum efficiency point. As seen in these figures, the pump

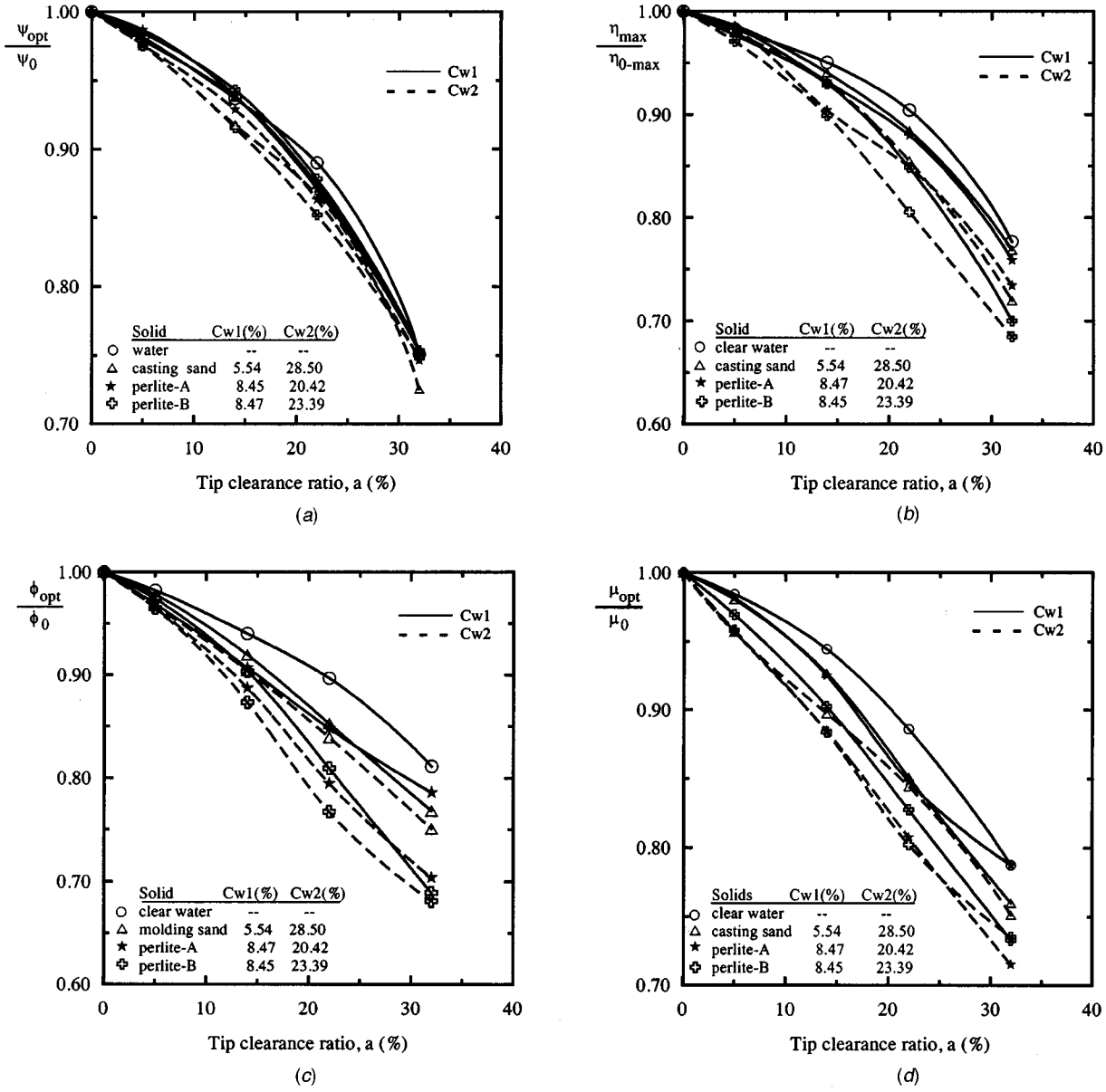

Fig. 4 Effect of tip clearance ratio on the optimal relative performance parameters of the pump

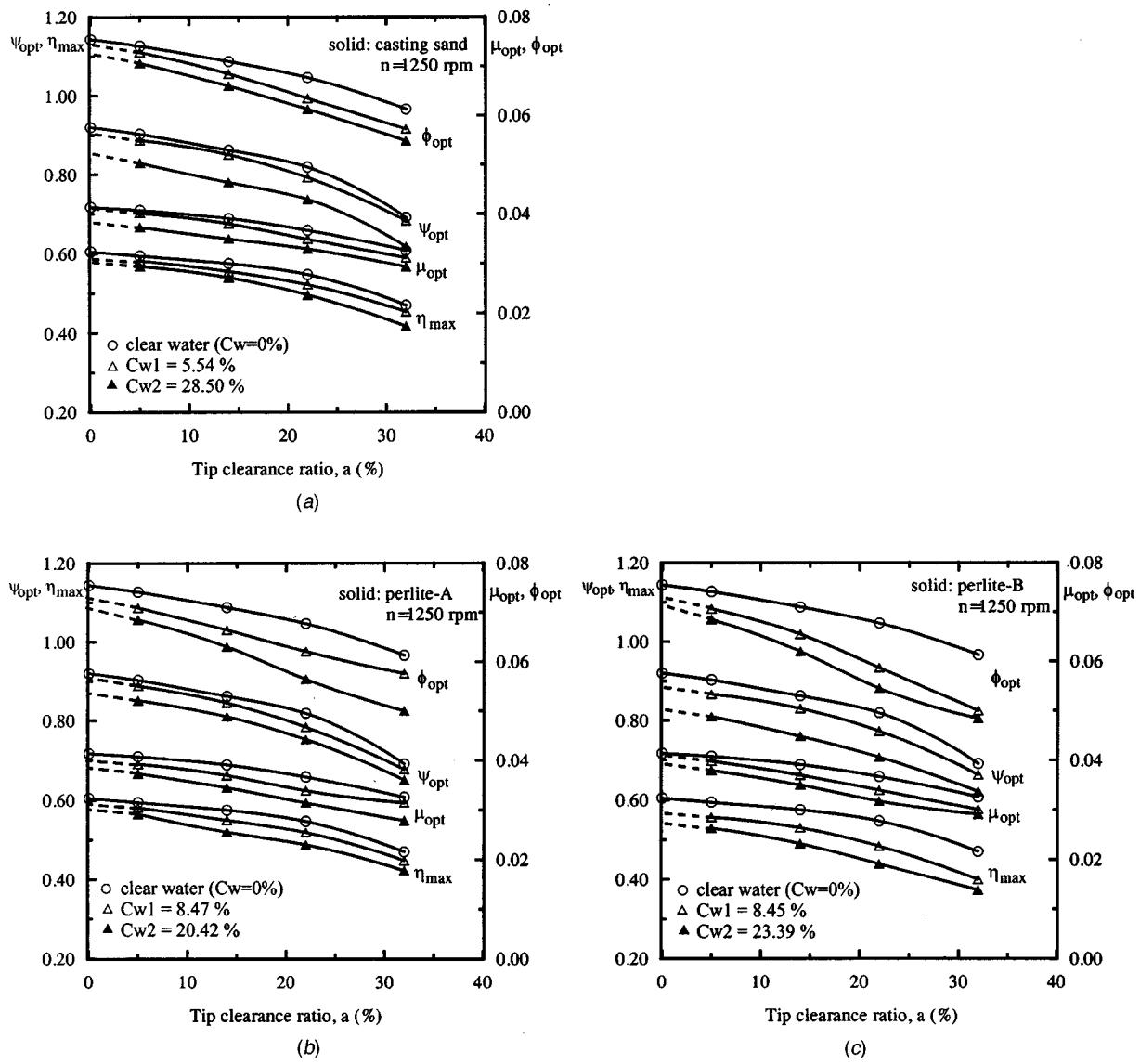

Fig. 5 Effect of tip clearance ratio on the optimal performance parameters of the pump

performance decreases steadily as the tip clearance increases. Such type of tendency is similar to those reported in previous studies [9–14]. Tip leakage loss increases with the increase in tip clearance due to an increase in flow passage.

Figure 5 shows the performance parameters as a function of various tip clearance ratios. All performance parameters decrease with an increase in the concentration of solids by weight. As the tip clearance increases, the decrease in the developed head causes a reduction in the power input to the pump. However, it is well known that the power input to the pump increases as the concentration of solids in the mixture increases. As seen in Fig. 4(*b*) the efficiency also decreases considerably with an increase in the tip clearance. This may be due to the fact that the rate of decrease of developed head is much higher than that of power input to the pump. Therefore, the decrease in the power input, as the tip clearance increases, is heavily limited when the concentration of solids in the mixture increases. As a result, the energy needed to maintain the solid in suspension and motion increases with the increase in concentration of solids. Physical properties of solids also have a significant effect on the deterioration of the pump characteristics. It can be concluded from Figs. 5(*b*) and (*c*) that, the pump shows a better performance while pumping perlite-A than perlite-B under the same test conditions. This could be attributed to the fact that the pump performance parameters decrease as the particle size of the solids increases in suspension.

3.2 Effects of Solids on the Pump Performance. As seen in Fig. 5, a gradual drop in the pump performance parameters occurs for a given tip clearance when solids are introduced into pumped clear water. In this study, the relative reductions in the head and efficiency for a given tip clearance, at any given flow rate have been represented as the head ratio and efficiency ratio, respectively, and are defined as

$$\psi_r = \frac{\psi_{m,a}}{\psi_{w,a}} \tag{1}$$

$$\eta_r = \frac{\eta_{m,a}}{\eta_{w,a}} \tag{2}$$

Another term, known as head reduction factor R_H, is also commonly used and given by

$$R_H = 1 - \psi_r \tag{3}$$

It was observed that both ψ_r and η_r are weakly independent of the pump flow rates [18]. Similar conclusions were drawn by

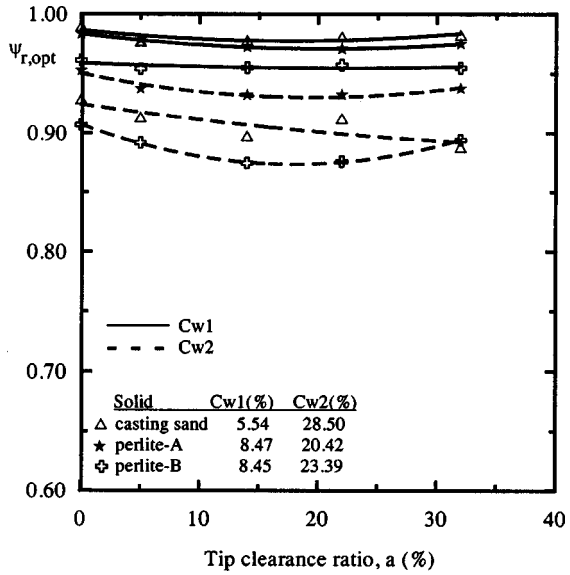

Fig. 6 Effect of tip clearance ratio on the optimal head ratio for different concentrations of solid materials used

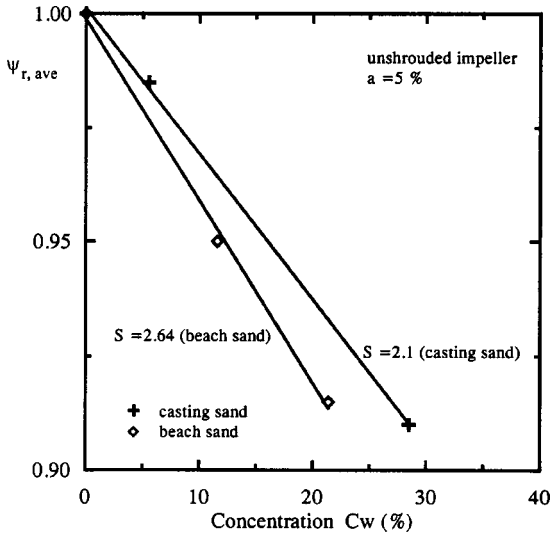

Fig. 8 Effect of specific gravity of solids on the average head ratio

Stepanoff [1]. To study the effect of the running tip clearance on both ratios, the values of ψ_r and η_r at best efficiency point ($\varphi_{opt}=0.06$) were obtained from Fig. 5. Figures 6 and 7 show the variation of ψ_r and η_r, respectively, with the tip clearance ratio for the casting sand, perlite-A and perlite-B samples. As seen in these figures, head ratio appears to be almost independent of the tip clearance ratio. This suggests that nearly the same head reduction occurs for a given tip clearance, whether pumping clear water or a mixture. However, the efficiency ratio shows a slight decrease especially for the perlite-B. Besides, the higher concentrations of solids cause the efficiency ratio to decrease severely. This may be due to the fact that the increased particle size and concentration of solids give rise to additional disk friction loss and therefore to a higher power input to the motor. Also, drag effects near the vane tips due to the tip leakage will increase the power input, leading to lower pump efficiency. Thus it can be concluded that the head reduction factor (R_H) is independent of the tip clearance within the range of this investigation. It is therefore a logical approach to seek a correlation for predicting the head reduction factor in terms of the physical properties and concentration of solids. Although the shape of solids pumped with the water has a slight effect on the head reduction factor, it will not be considered here.

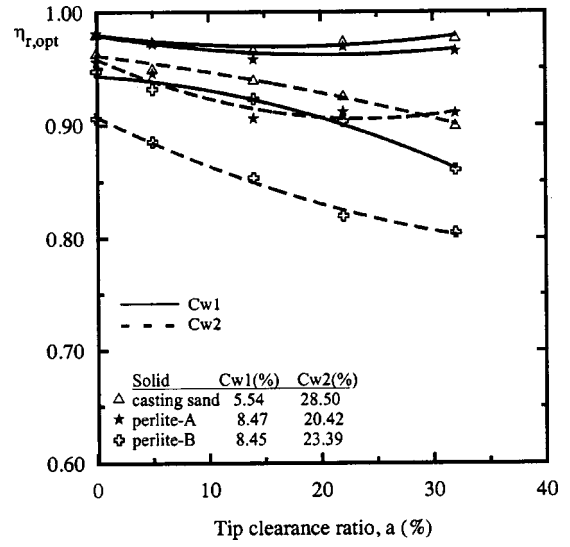

Fig. 7 Effect of tip clearance ratio on the optimal efficiency ratio for different concentrations of solid materials used

In order to ascertain the effect of particle specific gravity and solids concentration on the pump performance, two minerals of nearly identical particle size distribution, beach sand, and casting sand, were used. In Fig. 8, the variations of the average value of ψ_r against the concentration of solids have been compared to determine the effect of solid specific gravity. It is observed that ψ_r decreases linearly with an increase in the concentrations of both beach sand and casting sand. At any given concentration of solids, values of ψ_r for beach sand are lower than that of the casting. This could be attributed to the fact that, the energy needed to maintain and move the solids in suspension increases with an increase in the particle specific gravity. To determine the relationship between R_H and specific gravity of solid (S), it is assumed that ψ_r varies as $(S-1)^{\kappa}$. This assumption has also been adopted by previous studies [3,5,6–8], wherein κ is given in the range of 0.5–1.0. Thus R_H may be expressed in terms of S as follows:

$$R_H \alpha (S-1)^{\kappa} \tag{4}$$

The representative particle diameter (d_{50} or d_w) of two materials, casting sand and beach sand are nearly the same, but have different specific gravity, as given in Table 1. Therefore, a comparison of measured R_H could be made to determine the effect of S on R_H. Consequently, ψ_r values of two minerals have been compared at a given concentration ($C_W=20$ percent), in Fig. 8. The value of R_H for two minerals of different S can be written as

$$\left.\frac{R_H(\text{casting s.})}{R_H(\text{beach s.})}\right|_{\text{Cw}=20\%,x=1.25\text{ mm}} = \frac{1-0.938}{1-0.92} = \frac{(2.1-1)^{\kappa}}{(2.64-1)^{\kappa}} \tag{5}$$

Solving Eq. (5) gives the value for the exponent κ of 0.64. Wilson et al.[19] have shown that the influence of a solid's specific gravity on R_H is approximately proportional to $(S-1)^{0.65}$, which agrees reasonable well with the above calculated value of κ. Hence,

$$R_H \alpha (S-1)^{0.64}. \tag{6}$$

As can be seen from Fig. 8, ψ_r decreases linearly with C_w. Therefore, R_H may be considered proportional to C_w,

$$R_H \alpha C_w \tag{7}$$

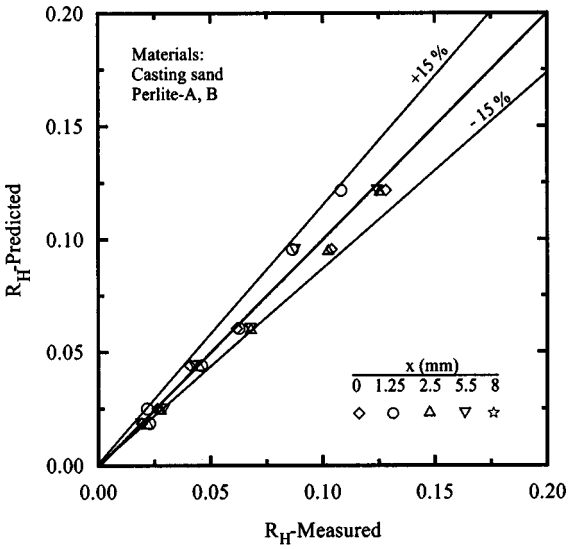

Fig. 9 Accuracy of the proposed correlation (Materials: Table 1)

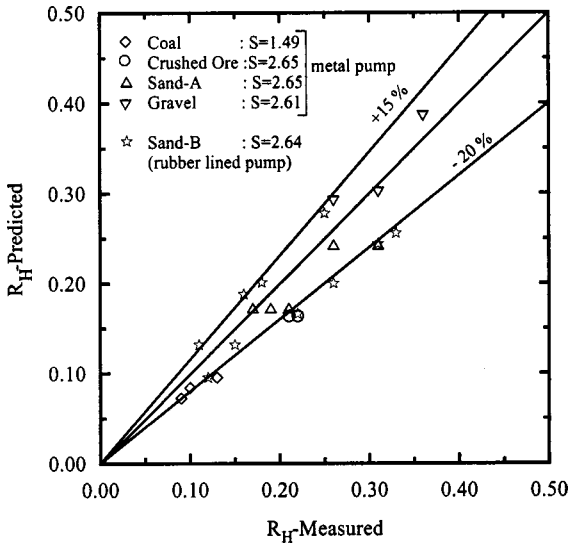

Fig. 11 Accuracy of the proposed correlation (Materials: from Refs. [3, 5])

Similar trends have been observed for various materials used in a previous investigation [18].

Another parameter which has a considerable impact on the R_H is the particle size distribution. Generally, the effect of particle size distribution is represented in terms of a representative particle diameter. For a narrow particle size distribution, either d_{50} (screen size through which 50 percent solids passed) or weighted mean particle diameter d_w may be chosen as the representative particle diameter. However, for a broad size distribution, weighted mean diameter of particles would be a better choice. Kazim et al. [8] concluded that, an identical variation of ψ_r could only be obtained if the weighted mean particle diameters of two solids are equal. It should be noted that, in some cases, considerable changes in the particle size distribution may occur due to recirculation in the closed-loop test rig and interactions between the solid particles and vane tips. To determine the effect of recirculation on the particle size distribution, the efflux samples were taken during the performance tests and analyzed. It has been found that no significant attrition of the solid particles occurred.

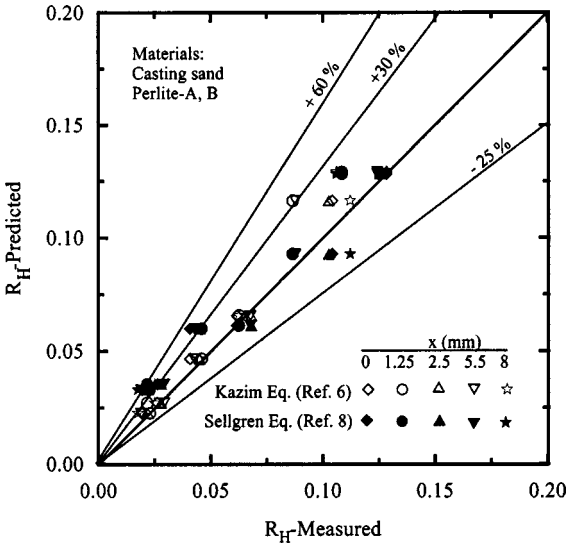

Fig. 10 Comparison between measured and predicted head reduction factors using Eqs. of Refs. [6, 8]

Minemura et al. [20] reported that at the inlet curvature of the impeller passage, just before the impeller inlet, every solid particle moves on a trajectory deviating outward from the streamlines of water, and impinges on the impeller wall at nearly the same radial position of the hub. Within the area of the impeller passage, particles move rectilinearly and the majority of the particles collide again with the shroud contour surface, near the open side of the impeller, just before the impeller exit, and then leave the impeller. According to these observations, an insignificant amount of solid particles having greater inertia might exist in the tip leakage flow, therefore no considerable interaction will likely take place between the particles and vane tip gap.

In order to determine the effect of the particle size on the pump performance, the following functional relationship is formed

$$f(d_w) = \frac{R_H}{C_w(S-1)^{0.64}} \tag{8}$$

where $f(d_w)$ represents a functional dependence on d_w. To determine this relationship, the values of $f(d_w)$ from the present investigation, as well as from published literature [4,13], are plotted on a semi-log plot. The best-fit equation through the data points gives the following relationship:

$$f(d_w) = 0.11 \ln(44 d_w) \tag{9}$$

Combining Eqs. (8) and (9) gives the final form of the correlation as:

$$R_H = 0.11 C_w (S-1)^{0.64} \ln(44 d_w) \tag{10}$$

The predicted head reduction factors for all the mixtures tested in the present study were compared with the measured values in Fig. 9, which shows that the data points are equally distributed on both sides of the ideal line, and the deviations lie within ± 15 percent. This spread appears to be reasonable considering the wide range of parameters investigated and the complexity of the two-phase flow through the unshrouded impeller. In Fig. 9, data points denoted by $a=0$ are obtained from the shrouded impeller tests, in order to make a direct comparison between the unshrouded and shrouded impellers. No considerable distinction is observed for the shrouded impeller. In other words, the test data obtained for the shrouded impeller fall into the same error band.

To gain an insight into the accuracy of some existing correlations that are widely used to predict R_H, a comparison was made between the measured and predicted R_H values, using data obtained from the present study. Here, the correlations proposed by

Sellgren [6] and Kazim et al. [8] are used for the comparison, as illustrated in Fig. 10. The empty marks in the figure represent the predicted values using Kazim's correlation. It is observed that the predicted values using Kazim's correlation are approximately 30 percent higher, whereas Sellgren's correlation gives deviations amounting to $-20-+60$ percent.

In order to ensure the validity of the proposed correlation, a typical comparison of the predicted values of R_H with the experimental data available in the literature is shown in Fig. 11. The data for sand-B were obtained on a rubber lined impeller pump. The errors in the prediction of R_H in Fig. 11 are random and lie within the range of -20 to $+15$ percent band. This is a significant improvement over the existing correlations in the literature.

4 Conclusions

Experiments were conducted to study the effects of solids in an unshrouded centrifugal pump impeller by varying the tip clearance when both handling water and solid-water mixtures. Although tip clearance effects have attracted research interest for many years, clarification of the tip leakage loss mechanism for both single- and two-phase flows through the pumps is far from complete. The present study introduces extensive new results, as a part of continuous investigation of tip clearance effects on a conventional centrifugal pump when handling commercial mixtures or slurries.

According to the results of the present study, tip clearance loss mechanisms while pumping mixtures seem to be similar to those in single phase pumping and a steady deterioration in pump performance for varying tip clearances is observed. Nevertheless, more detailed experiments with different test conditions are necessary to make more definite conclusions on the relationship between performance parameters and the running tip clearance. The head reduction factor (R_H) appears to be almost independent of the variation in the tip clearance, and this allows us to correlate the solids effects on the pump performance regardless of changes in the tip clearance. However, a slight decreasing trend is observed in efficiency ratio when the tip clearance is increased.

A new correlation to predict the head reduction due to presence of solids in pumped water has been developed and examined using data both newly obtained and previously published in the literature. The proposed correlation has given more accurate predictions than existing and widely used correlations. The deviation between the predicted and measured head reduction factor is within a range of -20 to $+15$ percent. In addition to that, the present correlation is found to be applicable to pumps having both metal and rubber-lined, shrouded/unshrouded impellers.

Acknowledgment

This research has been supported by the Research Fund of University of Sakarya, Turkey.

Nomenclature

b = blade height
d = diameter
g = gravitational acceleration
H = pump total head
P = power input to pump
Q = volumetric flow rate
R_H = head reduction factor
S = specific gravity
U = peripheral velocity
x = tip clearance
z = number of blades
β = blade angle
ρ = density
a = $2x/(b_1+b_2)$ = relative tip clearance
η = $\rho g Q H/P$ = overall efficiency
ϕ = $Q/\pi d_2 b_2 U_2$ = flow coefficient
μ = $8P/\pi d_2^2 \rho U_2^3$ = power coefficient
ψ = $2gH/U_2^2$ = pressure coefficient

Subscripts/Superscripts

a = at any tip clearance ratio
ave = average
0 = zero tip clearance
1 = impeller inlet
2 = impeller exit
m = mixture
r = ratio
w = weighted mean, water
50 = mass median
max = maximum
opt = optimal
κ = an exponent

References

[1] Stepanoff, A.J., 1965, *Pumps and Blowers, Two Phase Flow-Flow and Pumping of Solids in Suspension and Fluid Mixtures*, John Wiley, London.
[2] Walker, C.I., and Goulas, A., 1984, ''Performance Characteristics of Centrifugal Pumps When Handling non Newtonian Homogeneous Slurries,'' Proc. Instn. Mech. Engrs., Vol. 198A, No. 1, pp. 41–49.
[3] Vocadlo, J.J., Koo, J.K., and Prang, A.J., 1974, ''Performance of Centrifugal Pumps in Slurry Services,'' Proc. Hydro Transport-3, paper J2, BHRA Fluid Engineering.
[4] Burges, K.E., and Reizes, A., 1976, ''The Effect of Sizing, Specific Gravity and Concentration on the Performance of Centrifugal Pumps,'' Proc. Inst. Mechanical Engineering, Vol. 190-36/76, p. 391.
[5] Cave, I., 1976, ''Effects of Suspended Solids on the Performance of Centrifugal Pumps,'' Proc. Hydro Transport-4, paper H3, BHRA Fluid Engineering.
[6] Sellgren, A., 1979, ''Performance of Centrifugal Pumps When Pumping Ores and Industrial Minerals,'' Proc. Hydro Transport-6, paper G1, BHRA Fluid Engineering.
[7] Gahlot, V.K., Seshadri, V., and Malhotra, R.C., 1992, ''Effect of Density, Size Distribution, and Concentration of Solids on the Characteristics of Centrifugal Pumps,'' ASME J. Fluids Eng., **114**, pp. 386–389.
[8] Kazim, K.A., Maiti, B., and Chand, P., 1997, ''Effect of Particle Size, Particle Size Distribution, Specific Gravity and Solids Concentration on Centrifugal Pump Performance,'' Powder Handling and Processing, **9**, No. 1, pp. 27–32.
[9] Lakshminarayana, B., 1970, ''Methods of Predicting the Tip Clearance Effects in Axial Flow Machinery,'' ASME J. Basic Eng., **92**, p. 467–480.
[10] Senoo, Y., and Ishida, M., 1981, ''On the Pressure Loss Due to the Tip Clearance of Centrifugal Blower,'' ASME J. Eng. Power, **103**, No. 2, pp. 271–278.
[11] Plutecki, J., and Wajda, A., 1975, ''The Influence of an Axial Clearance Between a Semi-Open Impeller and a Casing on a Pump Parameters, By Example of H1-150 Pump,'' Vortrage der Konferenz für Stromungsmaschinen, Budapest, **5**, pp. 833–845.
[12] Wood, G.M., Welna, H., and Lamers, R.P., 1965, ''Tip Clearance Effects in Centrifugal Pumps,'' ASME J. Fluids Eng., **87**, pp. 932–940.
[13] Pfleiderer, C., 1961, *Die Kreiselpumpen*, 5. Auflage, Vol. 99, Springer-Verlag, Berlin.
[14] Engeda, A., Strate, W.P., and Rautenberg, M., 1988, ''Correlation of Tip Clearance Effects to Impeller Geometry and Fluid Dynamics,'' Gas Turbine and Aeroengine Congress, pp. 1–7, Amsterdam, ASME Paper 88-GT-92.
[15] Cader, T., Masbernat, O., and Roco, M.C., 1992, ''LDV Measurements in a Centrifugal Slurry Pump: Water and Dilute Slurry Flow,'' ASME J. Fluids Eng., **114**, pp. 606–615.
[16] Cader, T., Masbernat, O., and Roco, M.C., 1994, ''Two Phase Velocity Distribution and Overall Performance of a Centrifugal Slurry Pump,'' ASME J. Fluids Eng., **116**, pp. 316–323.
[17] Murakami, M., and Minemura, K., 1976, ''Effects of Running Clearance of Semi-Open Impeller Pumps under Air Admitting Conditions,'' Bull. JSME, **19**, No. 136, pp. 1141–1148.
[18] T. Engin, 2000, ''Ph.D. Dissertation,'' Dept. of Mechanical Engineering, University of Sakarya, Sakarya, Türkiye.
[19] Wilson, K.C., Addie, G.R., Sellgren, A., and Clift, R., 1997, *Slurry Transport Using Centrifugal Pumps*, 2nd Edition, Blackie A & P, ISBN 0-7514-0408-X.
[20] Minemura, K., and Murakami, M., 1986, ''Behavior of Solids Particles in a Radial Flow Impeller,'' Bull. JSME, **29**, No. 253, pp. 2101–2108.

Open Channel Boundary Layer Relaxation Behind a Forward Facing Step at Low Reynolds Numbers

Mark F. Tachie
Ram Balachandar
D. J. Bergstrom

College of Engineering,
University of Saskatchewan,
57 Campus Drive,
Saskatoon, Canada

This paper reports laser-Doppler anemometer measurements of mean velocity and turbulence statistics upstream and downstream of a 3-mm forward facing step in a shallow open channel flow. The Reynolds numbers based on the momentum thickness (θ) of the approaching upstream flow and step height (h) are in the range $1010 \leqslant Re_\theta \leqslant 2240$ and $960 \leqslant Re_h \leqslant 1890$, respectively. Measurements are obtained at 50 step heights upstream of the leading edge of the step and $1 \leqslant x/h \leqslant 162$ downstream of the step. The results show that the overlap region develops more slowly than the inner and outer regions. The mean field recovers at $x/h = 50$. Distributions of the turbulence intensity tend to become self-similar for $x/h > 100$ but the profiles do not necessarily collapse onto the upstream profiles. [DOI: 10.1115/1.1383971]

Introduction

Near-wall turbulent flows have received significant attention in the past and in recent years, prompted mainly by their prevalence in engineering and industrial applications. Although smooth wall canonical boundary layers are the most extensively studied near-wall flows, practical engineering flows are relatively more complex. For example, in flow past airfoils and turbine blades, the surfaces might be hydraulically rough, rapid changes in pressure gradients and surface curvature may occur, and blowing and suction may be applied along the airfoil as a form of boundary layer control. Clauser [1] suggested Maxwell's concept of a ''black box'' for the investigation of complex turbulent flows. According to this concept, the physics of the flow can be studied by changing various inputs such as initial and/or boundary conditions and observing the resultant flow outputs [2,3]. Subsequently, a considerable amount of research into complex boundary layers has been undertaken. Many of these flows were studied within a context of perturbation or distortion to a canonical boundary layer. The types of perturbation employed include changes in surface roughness [4–6] forward- and backward-facing steps [7–9] and wake-boundary layer interactions [10–12]. In spite of the considerable (experimental and numerical) research efforts made over the years, our understanding of the physics of complex near-wall flows is not yet complete.

In investigating a distorted boundary layer, the structure of the recovering flow is usually compared to that of a canonical or standard reference boundary layer. According to classical theory, a turbulent boundary layer consists of two regions; an inner layer (i.e., viscous sublayer and a buffer region) where viscous effects dominate, and an inviscid outer layer. In the inner layer, the appropriate velocity and length scales are, respectively, the friction velocity U_τ and viscous length scale ν/U_τ, where ν is the kinematic viscosity of the fluid. In the outer layer, the characteristic length scale is the boundary layer thickness δ. Although classical theories suggest the friction velocity U_τ as the outer velocity scale, the recent boundary layer theory proposed by George and Castillo [13] suggests the freestream velocity U_e. The linear viscous sublayer is described by the following relation:

$$U^+ = y^+ \tag{1}$$

In Eq. (1), $U^+ = U/U_\tau$ and $y^+ = yU_\tau/\nu$, where for a smooth wall, y is the distance measured from the wall. At sufficiently high Reynolds number, the inner and outer layers overlap. According to classical theories, the mean velocity in the overlap region is described by the familiar log-law:

$$U^+ = \frac{1}{k}\ln y^+ + C \tag{2}$$

where κ and C are universal constant that vary slightly from one study to the other. The values adopted for these constants in the present study are: $\kappa = 0.41$ and $C = 5.0$. In the outer part of the flow, the mean velocity deviates from the log-law. Coles [14] proposed a wake function to describe the velocity distribution in this region so that the complete profile becomes:

$$U^+ = \frac{1}{k}\ln y^+ + C + \frac{2\Pi}{\kappa} w\left(\frac{y}{\delta}\right) \tag{3}$$

In Eq. (3), Π is Coles wake parameter which is a measure of the strength of the outer wake component, and $w(y/\delta)$ is a universal function. For a canonical turbulent boundary layer, $\Pi = 0.55$ at sufficiently high Reynolds numbers. In the outer layer, the mean velocity distribution is commonly described in a defect form. Following classical theories, the specific form of the defect profile is given by:

$$U_e^+ - U^+ = \frac{1}{\kappa}\ln\left(\frac{y}{\delta}\right) \tag{4}$$

In assessing the degree of recovery or relaxation of the distorted flow towards the standard form, the structures of the two (i.e., the standard and recovering) flows are compared. In this case, a sense of self-similarity in the log-law and the mean defect profile becomes a useful criterion for the inner and outer regions, respectively. Some investigators implied that a developing turbulent boundary layer is self-preserving if integral parameters such as the profile shape factor H, the momentum thickness θ, and the skin friction coefficient C_f become independent of streamwise distance. The Clauser shape parameter G is, perhaps, the single most important integral parameter to assess the departure of turbulent boundary layer from equilibrium [15]. Here, the Clauser shape parameter is defined as:

Contributed by the Fluids Engineering Division for publication in the JOURNAL OF FLUIDS ENGINEERING. Manuscript received by the Fluids Engineering Division July 7, 2000; revised manuscript received March 20, 2001. Associate Editor: P. Bradshaw.

$$G = \frac{1}{\delta^*}\left(\frac{C_f}{2}\right)^{1/2}\int_0^\infty (U_e^+ - U^+)^2 dy \qquad (5)$$

where, δ^* is the boundary layer displacement thickness

A topic of current debate in investigating the boundary layer recovery process is whether it is the inner layer or the outer layer that relaxes first to the standard form. Some earlier investigators [7,12,16] suggested that the outer layer of the distorted flow recovers more slowly. Castro and Epik [9] argued that because the inner and outer layers are dynamically linked, the inner layer cannot possibly develop normally until the outer layer has become more normal. The eddy structures, being different in the inner and outer layers, will play a dominant role in understanding the recovery process. Bushnell and McGinley [2] indicated that the turbulence production process in wall-bounded flows involve at least three different scales of motion. These are the outer large scales, which are of the order of the boundary layer thickness, δ; intermediate scales with characteristic dimensions of 100 wall units; and near-wall small scale with characteristic dimension of the order of $1\sim10$ wall units. Because of the differences in the characteristic time and velocity scales in each region of the boundary layer, the recovery process will depend on where the distortion is applied. Smits and Wood [3] argued that a step change at the surface (for example, due to roughness element) will localize the disturbance at the wall while a rapid change in pressure gradient will produce a more diffused influence. Note, however, that the dynamic link between the inner and outer layers of the boundary layer is much more complex than assumed hitherto. Recent measurements [4,6] in rough wall turbulent boundary layers provided overwhelming evidence of non-localization of the effects of roughness to the inner region. These studies showed that the effects of surface roughness penetrate deep into the outer layer and do significantly modify the wake strength. Experimental data [17,18] from boundary layer studies at elevated freestream turbulence also showed that the effect of freestream turbulence penetrates deep into the inner layer.

In investigating the recovery of a boundary layer from an imposed distortion, the relaxation length x_R, defined here as the distance beyond which the distorted boundary layer relaxes to the standard form, is an important parameter. Some order of magnitude estimates of the relaxation length are available in the literature. Bradshaw [19] suggested that a suitable response time for the stress-containing eddies must be the ratio of turbulence energy to its rate of production. Based on this assumption, and using the $(1/7)^{\text{th}}$ power law, he estimated $x_R = 10\delta$ in the middle of the layer. Bushnell and McGinley [2] implied that the relaxation process will be completed over a distance on the order of 100 length scales of the affected flow region. Thus, for a flow that is distorted in the outer region, x_R will be on the order of 100δ. For a boundary condition that primarily affects the inner layer (out to $y = 0.2\delta$), x_R will be on the order of 20δ.

The backward- and forward-facing steps are examples of extensively studied near-wall complex flows, perhaps, due to their geometrical simplicity. These flows are also widely used to test the performance of CFD codes. Comprehensive reviews of earlier studies were made by Bradshaw and Wong [7] and Eaton and Johnston [20] and are not repeated here. Subsequent studies include measurements and flow visualization reported by Kiya and Sasaki [21] and Sasaki and Kiya [22] as well as the DNS results reported by Le et al. [23] and Suksangpanomrung [24]. Most of the earlier measurements were made using hot-wires and this precludes accurate measurements in regions of high turbulence levels and flow reversal. With the exception of the study reported by Castro and Epik [9], measurements in earlier forward-facing step studies are limited to 80 step heights downstream of separation.

The present study documents additional measurements upstream and downstream of a forward facing step at low Reynolds numbers in an open channel flow using a laser-Doppler anemometer (LDA). The principal focus is to investigate the recovery of the downstream boundary layers (down to $x/h = 162$). Both the mean velocity and turbulence intensity profiles are examined. The present results will also provide insight into the effects of inappropriate tripping devices on the subsequent downstream development of a turbulent boundary layer. Compared to a typical wind tunnel experiment, the flow structure of an open channel boundary layer may be modified by the moderate background turbulence intensity and free surface effects. These differences notwithstanding, by considering LDA measurements in an open channel flow, some insight can be obtained regarding boundary layer relaxation behind a forward facing step.

Experimental Setup

The experiments were performed in an open channel flume. The channel is 10 m long, 0.8 m wide, and 0.6 m deep. The sidewalls are made of tempered glass. The contraction was preceded with several stilling arrangements to reduce any large scale in the flow. A 3-mm thick, 500-mm wide, and 1500-mm long plate was used to create the test facility (i.e., the forward facing step). The leading edge of the step was placed 5 m downstream of the contraction and on the flume floor. A schematic of the open channel facility and the test body is presented in Fig. 1.

Velocity measurements were made using a single-component fiber-optics LDA (Dantec Inc.). The LDA system is powered by a 300 mW Argon-Ion laser (Ion Laser Technology). The optical elements include a Bragg cell and a 400-mm focusing lens. The LDA system was operated in a backscatter mode. The fiber optic probe was mounted on a three-dimensional traversing mechanism. Each direction of the traversing arrangement was stepper motor driven and controlled by a computer. Sufficient particles were present in the water and no artificial seeding was used in the study. The maximum period of data acquisition at each measurement location was set to 750 seconds. Typical sample size at a measuring point varied from 3000–5000. The Reynolds numbers based on the momentum thickness (θ) of the approaching upstream flow and step height (h) are approximately $1010 \leqslant \mathrm{Re}_\theta \leqslant 2240$ and $960 \leqslant \mathrm{Re}_h \leqslant 1890$, respectively. For each test condition, measurements were obtained at $x/h = -50$ upstream of step and at $x/h = 1$, 10, 20, 50, 100, and 162. The ratios of the plate height h to the upstream boundary layer thickness δ_o were quite low ($h/\delta_o \leqslant 0.1$). Consequently, the present perturbation is considered as weak [7] and would primarily distort the inner region.

Following Schwarz et al. [25], the statistical uncertainty in the mean and turbulence intensity (except for the extremely high turbulence levels near the wall at $x = h$) was estimated to be 1 and 2 percent, respectively. Close to the wall, measurement uncertainty in the turbulence intensity is expected to somewhat higher ($\sim$4 percent) due to lower signal-to-noise-ratio [26]. The mass flow rate was measured using an electronic weighing tank. At least six

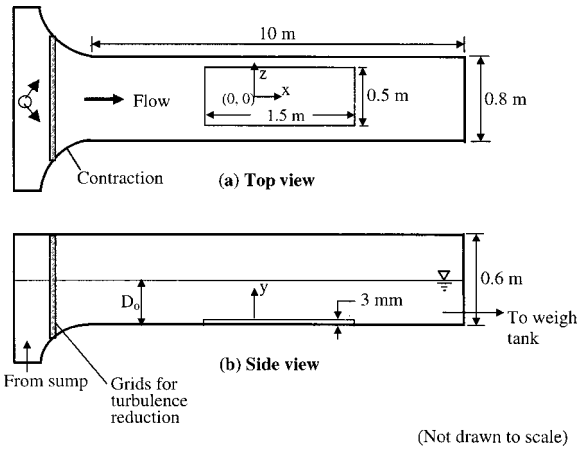

Fig. 1 A schematic of the test facility

Table 1 Summary of upstream flow conditions

Test	U_{eo} (m/s)	D_o (mm)	Tu (%)	δ_o (mm)	θ_o	$(\mathrm{Re}_h)_o$	$(\mathrm{Re}_\theta)_o$	H_o	C_{fo}
Test A	0.32	50	4.4	35	3.14	960	1010	1.32	0.0046
Test B	0.34	90	3.2	42	3.92	1020	1330	1.33	0.0043
Test C	0.63	90	2.9	36	3.55	1890	2240	1.28	0.0042

measurements were obtained for each test condition. The maximum variation in mass flow rate was less than 4 percent. A weir located downstream of the flume kept the variation in the water elevation to ± 1 mm across the test section.

The characteristics of the mean velocity and turbulence statistics obtained upstream of the step are similar to earlier measurements [6,27,28] in open channel flows at similar test conditions. A summary of important parameters of the upstream flow is given in Table 1. Here, U_{eo} is the freestream velocity; D_o is the depth of flow; δ_o is the boundary layer thickness of the upstream flow and is defined as the wall normal location at which the local mean velocity is 99 percent of the maximum value; Tu is the turbulence intensity at the edge of the boundary layer. The momentum thickness and the shape factor are denoted as θ_o and H_o, respectively, C_{fo} is the skin friction coefficient and $(\mathrm{Re}_\theta)_o$ and $(\mathrm{Re}_h)_o$ are the Reynolds numbers based on momentum thickness and step height, respectively. Here, the shape parameter is the ratio of the boundary layer displacement thickness to the momentum thickness.

Results and Discussion

Mean Velocity Profiles. The mean velocity profiles in outer coordinates are shown in Fig. 2. For each test, data are presented for measurements made 150 mm ($x/h=-50$) upstream of step and at $1 \leqslant x/h \leqslant 162$ downstream of the plate. For the purpose of comparison, the upstream profile ($x/h=-50$) is considered as the standard reference profile in each test. Figure 2(*a*) shows the profiles for Test A. Measurements for Test B and Test C are shown in Figs. 2(*b*) and 2(*c*), respectively. At $x/h=1$, negative velocities as high as 20 percent of the freestream value are observed for Test A and Test C. This is comparable to values obtained in backward facing steps at similar locations [20]. For all the test conditions examined, the profiles at this $x/h=1$ deviate significantly from the reference (upstream) profile for $y/\delta<0.5$. At $x/h=10$ and 20, the deviations are considerably reduced. For $x/h \geqslant 50$ the deviations are comparable to measurement uncertainties.

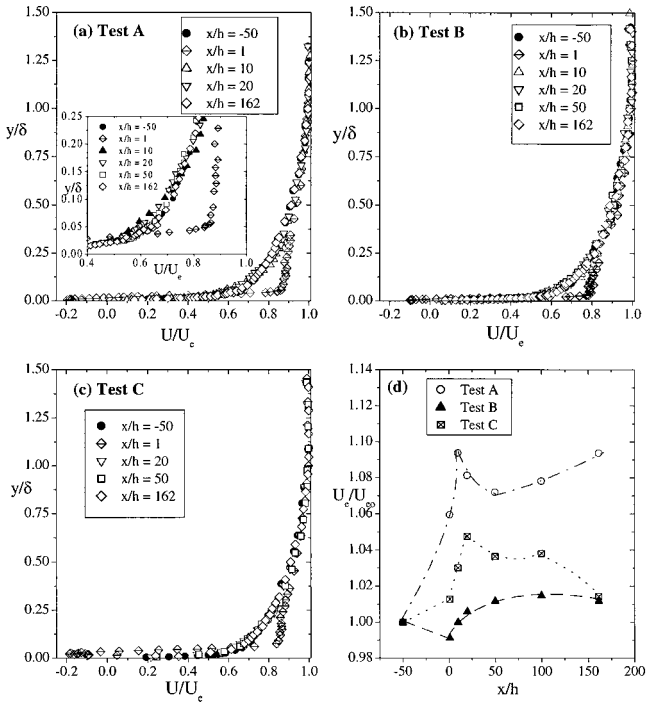

Fig. 2 (*a*), (*b*), and (*c*): Mean velocity profiles in outer variables; (*d*) variation of freestream velocity with streamwise distance (lines are for visual aid only)

In order to examine the distribution more closely in the vicinity of the wall, measurements at $y/\delta \leqslant 0.25$ for Test A are shown as an inset in Fig. 2(*a*). It is observed that deviations among the profiles are greatest for $0.05 \leqslant y/\delta \leqslant 0.15$, which corresponds to the overlap region. Compared to the upstream reference profile, the values of U/U_e at $x/h=1$ are consistently higher at $y/\delta \leqslant 0.15$ while the corresponding values at $x/h=10$ are systematically lower. Farther downstream, i.e., $x/h \geqslant 20$, the profiles relax toward the upstream data. In the measurements reported for another separated flow field, Balachandar and Tachie [12] found that the relaxation process was also non-monotonic. It should also be noted that in the near wall region, $\partial U/\partial y$ is much higher at $x/h \leqslant 20$ than the upstream location and $x/h \geqslant 50$. This may be due to higher entrainment of outer flow into the near-wall region at locations closer to the point of separation.

The variation of the freestream velocity with streamwise distance is shown in Fig. 2(*d*). For each test, the local freestream velocity is normalized by the corresponding upstream value U_{eo}. In all the tests, variation of the local freestream velocities with downstream distance is non-monotonic. The relatively higher values of U_e at $x/h \geqslant 1$, in comparison to the corresponding upstream value U_{eo}, may be due to blockage effects. Consistent with higher values of h/D_o or larger blockage effect, for Test A, the values of U_e/U_{eo} is relatively higher for Test A than Tests B and C. With the exception of the value obtained at $x/h=162$ for Test C, the variations in the freestream values for $x/h \geqslant 20$ are comparable to measurement uncertainty.

The velocity profiles in inner coordinates are shown in Fig. 3. Figures 3(*a*) and 3(*b*) show the data for Test A and Test B, respectively. For these tests, data were obtained in the viscous sublayer and this allowed an estimate of the wall shear stress to be obtained using the velocity gradient at the wall. The uncertainty in the friction velocity U_τ is estimated to be ± 5 percent for Tests A and B. The figures show that the viscous sublayer is not distorted. The data at $x/h=10$ and 20 are in reasonable agreement with the reference profiles for $y^+<20$. The measurements at these locations also show significantly higher wake component, which is consistent with the higher values of $\partial U/\partial y$ observed in Fig. 2(*a*). At $x/h \geqslant 50$, the velocity profiles show a better collapse with the reference profiles over the entire flow. For Test C, the friction velocity could not be obtained from velocity gradient at the wall since adequate measurements could not be obtained in the viscous sublayer. In previous backward- and forward-facing step experiments [9,29], a Clauser technique was used to estimate the skin friction. The present data for Tests A and B also confirmed the applicability of the log-law for $x/h \geqslant 50$. A Clauser method was therefore applied to determine the skin friction for $x/h \geqslant 50$ in the case of Test C. The narrow overlap region at these low Reynolds numbers may compromise the accuracy of a Clauser technique in determining the friction velocity. The uncertainty in the friction velocity for Test C is estimated to be about 7 percent. The velocity profiles for Test C are plotted in Fig. 3(*c*). Except for slightly

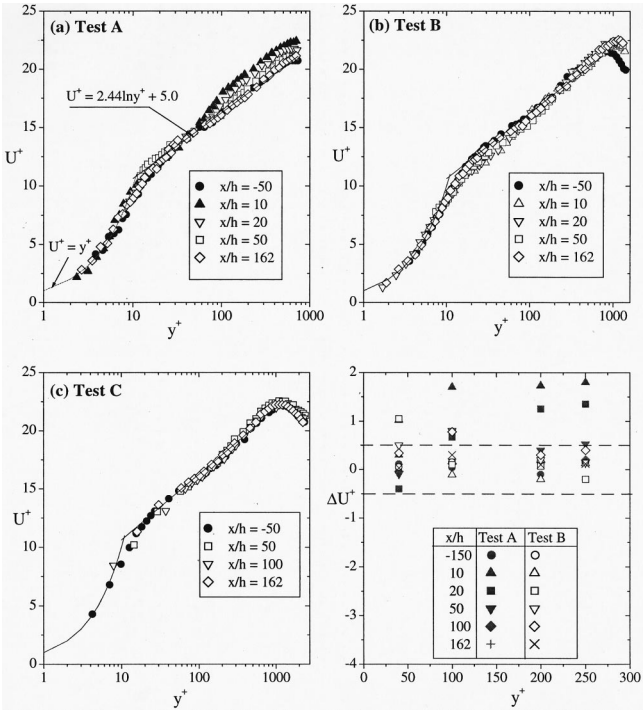

Fig. 3 (*a*), (*b*), (*c*): Velocity profiles in inner variables; (*d*) deviation of measurements (ΔU^+) from the log-law

higher values of U^+ in the outer region at $x=50h$, the collapse of both upstream and the downstream locations is reasonable.

Figure 3(*d*) shows deviations (ΔU^+) of the mean velocity from the log-law profile at $y^+=40$, 100, 200, and 250. For a given axial location, the deviation is greater at larger values of y^+. In general (except at $x/h=10$ and 20 for Test B), the deviation at a given y^+ decreases at larger distances from the leading edge. At $y^+=40$, the log-law (with $\kappa=2.44$ and $B=5.0$) will give $U^+=14.0$ so that $a\pm4$ percent in U^+ is about ±0.56 wall units. An uncertainty of $\pm0.5\Delta U^+$ is indicated by dotted lines in Fig. 3(*d*). Allowing for this level of measurement uncertainty in U^+, it can be concluded from Fig. 3(*d*) that the deviations at $x/h\geqslant50$ are within measurement error.

Figures 4(*a*), 4(*b*), and 4(*c*) show the defect profiles for Tests A, B, and C, respectively. The profiles are normalized by the friction velocity and the boundary layer thickness, which are the proper velocity and length scale according to classical theories. The canonical boundary layer wake law profile (with $\Pi=0.55$) is also included for comparison. It is clear from these figures that the upstream profiles, being typical of open channel defect profiles [6,30], are distinctly different from a canonical boundary layer. Except for $x/h\leqslant20$, the profiles at all measurement locations collapse fairly well onto the upstream profile. For Test B, the agreement among all the downstream profiles is fair across the entire boundary layer. Test C shows that the collapse of the downstream profiles onto the corresponding upstream one is reasonable, especially at the last two measurement stations.

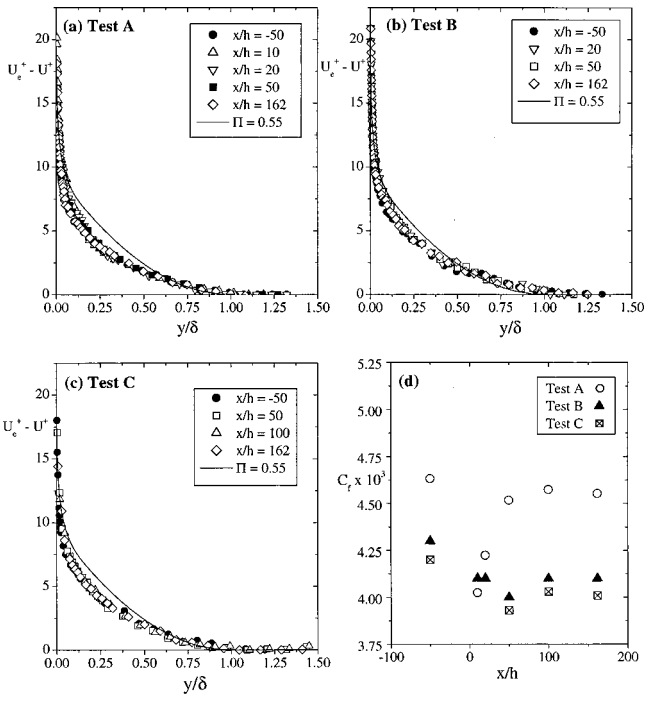

Fig. 4 (*a*), (*b*), (*c*): Velocity defect profiles upstream and downstream of reattachment; (*d*) variations of skin friction coefficient with streamwise distance

Integral Parameters

The values of the skin friction coefficient C_f, evaluated using the local values of U_τ and U_e, are shown in Fig. 4(*d*). The values of C_f at the upstream locations are relatively higher than the values obtained at similar Re_θ in canonical zero-pressure gradient turbulent boundary layers [6,31]. The higher values for open channel flows may be attributed to the higher background turbulence intensity and lower wake parameters compared to canonical turbulent boundary layers. Previous measurements [32] and DNS results [23,24]) indicated negative values of C_f in the recirculation region and a value of $C_f=0$ at the point of reattachment. DNS results [23,24] obtained for backward- and forward-facing steps also indicated that the flow reattaches at $6<x/h<7$. Measurements of C_f in the recirculation region were, however, not obtained in the present study. Immediately downstream of the reattachment location, the present results show a gradual recovery toward the upstream value. The earlier backward-facing study made by Yoo and Baik [29] showed a systematic increase in C_f for $10<x/h<20$. Ruderich and Fernholz [32], Le et al. [23] and Suksangpanomrung [24] also reported a sharp increase in C_f values immediately downstream of flow attachment and a subsequent attainment of a plateau farther downstream. For $x/h\geqslant50$, the variation in C_f for each test condition is comparable to the measurement error. At the last measurement station, the C_f values are within 5 percent of the upstream values. These deviations are similar to a value of 5 percent obtained at $x/h=154$ by Castro and Epik [8].

In Fig. 5(*a*), the boundary layer shape parameter H, at all measurement locations (except for $x=h$) is shown. The values of $H=1.28$ and 1.32 at the upstream locations are typical of the values obtained in many of the previous experiments [6,12,34] made in the present facility and at similar test conditions. Compared to the upstream reference value, H increased in the region immediately downstream of reattachment. This is consistent with the trend shown in Fig. 2(*a*) where the boundary layer profiles closer to the leading edge are less full compared to the upstream value. The relatively higher values of H at lower values of x/h are therefore indicative of deviation from the reference boundary layer profile. Beyond $x/h\geqslant10$, H recovers toward the corresponding upstream values. Figure 5(*b*) shows a plot of the Clauser shape parameter G with streamwise distance. The values of G initially increased from the upstream value to a maximum and decreased thereafter. The non-monotonic variation in G was also noted in the study reported by Balachandar and Tachie [12]. The general trend shown in this figure is qualitatively similar to that observed for H in Fig. 5(*a*). The deviation of G at the last measurement station from the corresponding upstream in each test is less than 6 percent.

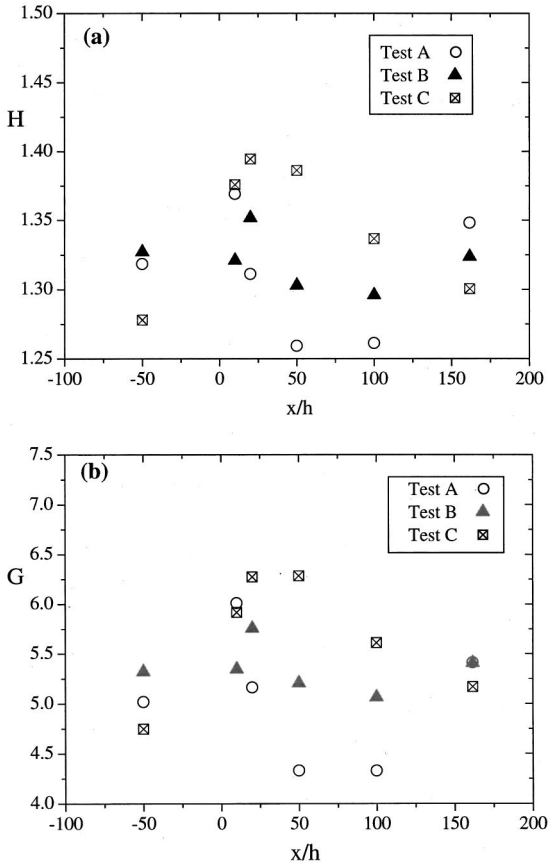

Fig. 5 (*a*) Variation of shape factor with streamwise distance; (*b*) variation of Clauser shape parameter with streamwise distance

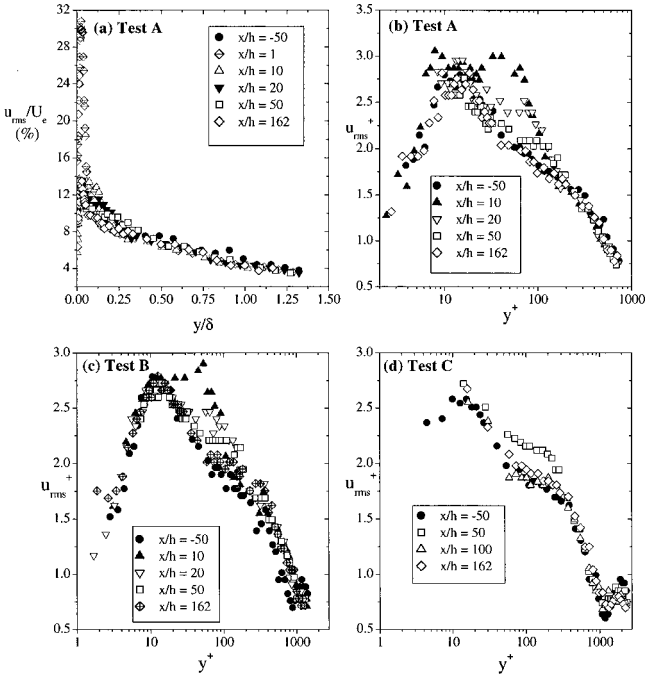

Fig. 6 Distributions of turbulence intensity profiles

Turbulence Intensity

The rms profiles of the streamwise velocity component ($u_{\rm rms}$) is shown in Fig. 6(*a*) for Test A using outer coordinates. The maximum value at $x/h=1$ is about 30 percent. This is substantially higher than the value of 13 percent obtained upstream of the step. The profile at $x=h$ is also consistently higher than the corresponding upstream profile for $y/\delta \leqslant 0.2$. Beyond this location, the profile lies below the standard one. At $x/h=10$ and 20, the $u_{\rm rms}$ profiles exhibit two peaks but the latter is not quite distinct. In outer coordinates, the $u_{\rm rms}$ distributions for Test B and C at $x/h \leqslant 20$ are similar to those observed for Test A. The distributions of rms values in inner coordinates (i.e., $u^+_{\rm rms}=u_{\rm rms}/U_\tau$) are shown in Figs. 6(*b*), 6(*c*), and 6(*d*) for Test A, Test B, and Test C, respectively. The maximum value of $u^+_{\rm rms}\approx 2.78$ at $y^+=15$ for the upstream station is similar to our previous measurements [6,12] at similar Reynolds numbers. For Test A, i.e., Fig. 6(*b*), at $x/h=10$, the value of the two peaks is $u^+_{\rm rms}=3.0$ and these occurred at $y^+=8$ and 41, respectively. At $x/h=20$, the peaks and their corresponding locations are $u^+_{\rm rms}=2.95$ at $y^+=14$ and $u^+_{\rm rms}=2.52$ at $y^+=72$. Similar to the present findings, the DNS and LES results of blunt flat plate [24] as well as the DNS [23] and experimental [33] results for backward-facing step indicate two peaks in the region $10 \leqslant x/h \leqslant 20$. Le et al. [23] remarked that the turbulence structure in the recirculation regions of separated flows is similar that in plane mixing layer. Their DNS results also indicated that in the recirculation region of a backward-facing step, the turbulence transport term removes energy from the shear layer region and delivers it to the near-wall region. The outer peaks at $x/h=10$ and 20 may therefore be an artifact of the mixing layer that develops in the separated region.

Similar to the mean profiles shown in Fig. 2(*a*) deviations from the upstream profile is greatest in the overlap region ($30 \leqslant y^+ \leqslant 200$). The agreement between the upstream profile and at $x/h \geqslant 100$ is reasonable. In Fig. 6(*c*) at $x/h=10$, the two peaks are $u^+_{\rm rms}=2.78$ at $y^+=13$ and $u^+_{\rm rms}=2.9$ at $y^+=52$. The corresponding values at $x/h=20$ are $u^+_{\rm rms}=2.73$ at $y^+=15$ and $u^+_{\rm rms}=2.56$ at $y^+=62$. Note, however, that although the profiles at $x/h=100$ and 162 are self-similar, they are consistently higher than the corresponding upstream profile. For Test C, the profile at $x/h=50$ deviates from the upstream data in the overlap region, otherwise agreement among all the profiles is reasonable. One may conclude that, with respect to the turbulence intensity, the recovery process is complete over the entire flow region for $x/h \geqslant 100$.

Summary and Conclusions

The recovery of the flow downstream of a forward facing step to the undisturbed upstream boundary layer has been examined using various indicators. Although the present flow is somewhat modified by moderate background turbulence levels and free surface effects, the flow structure is qualitatively similar to earlier forward- and backward-facing results obtained from measurements and numerical simulations. The present results show that the viscous sublayer is insensitive to the imposed disturbance or the recovery process, being more rapid closer to the wall than in the overlap region, was complete at $x/h=10$. For each of the test conditions examined, a reasonable agreement between the upstream and downstream mean velocity profile at $x/h \geqslant 50$ is observed. Furthermore, the skin friction coefficient is invariant with downstream location at $x/h \geqslant 50$. We may conclude that as far as the mean field is concerned, the structure of the flow at $x/h \geqslant 50$ is reasonably similar to the corresponding upstream structure.

The streamwise turbulence intensity profiles showed two peaks immediately downstream of the reattachment location. This feature has not been observed in many of the earlier measurements. It is speculated that the outer peak may be an artifact of the complex shear layer in the recirculation region. The recovery of the turbulence intensity is much slower compared to the mean flow. This supports the view that the recovery length depends on the specific

flow parameters being examined. It was observed that although the turbulence intensity profiles become self-similar for $x/h \geqslant 100$, some of these profiles do not collapse satisfactorily on to the corresponding upstream profile. It self-similarity of downstream profiles is used as a criterion, we may conclude that the turbulence statistics recover satisfactorily at $x/h = 100$. If, on the other hand, a complete collapse of downstream profiles onto a standard profile is used to assess complete recovery, as was done in some earlier, then complete recovery may not be achieved in some of the flows.

Acknowledgment

The support of the Natural Sciences and Engineering Research Council of Canada (NSERC) via a postgraduate scholarship to MFT and in the form of equipment grants to RB and DJB is gratefully acknowledged.

Nomenclature

C = additive constant in log law ($=5.0$)
C_f = skin friction coefficient
D_o = depth of flow upstream of the leading edge test plate
G = Clauser shape parameter
H = boundary layer shape parameter
h = thickness of test plate
$\mathrm{Re_h}$ = Reynolds number based on plate thickness
Re_θ = Reynolds number based on boundary layer momentum thickness
x = streamwise distance along the plate relative to the leading edge of the plate
y = wall-normal distance
U_e = Freestream velocity defined as the local maximum mean velocity
u_{rms} = rms value of streamwise velocity component
U_τ = friction velocity
δ = boundary layer thickness at $U = 0.99U_e$
κ = von Karman constant ($=0.41$)
ν = kinematic viscosity
Π = Coles wake parameter
θ = boundary layer momentum thickness

References

[1] Clauser, F. H., 1956, ''The Turbulent Boundary Layer,'' Adv. Appl. Mech., **4**, pp. 1–51.
[2] Bushnell, D. M., and McGinley, C. B., 1989, ''Turbulence Control in Wall Flows,'' Annu. Rev. Fluid Mech., **21**, pp. 1–20.
[3] Smits, A. J., and Wood, D. H., 1985, ''The response of Turbulent Boundary Layers to Sudden Perturbations,'' Annu. Rev. Fluid Mech., **17**, pp. 321–358.
[4] Krogstad, P. A., Antonia, R. A., and Browne, L. W. B., 1992, ''Comparison Between Rough- and Smooth-Wall Turbulent Boundary Layers,'' J. Fluid Mech., **245**, pp. 599–617.
[5] Taylor, R. P., Taylor, J. K., Hosni, M. H., and Coleman, H. W., 1993, ''Relaxation of the Turbulent Boundary Layer After an Abrupt Change From Rough to Smooth Wall,'' ASME J. Fluids Eng., **115**, pp. 379–382.
[6] Tachie, M. F., Bergstrom, D., and Balachandar, R., 2000, ''Rough Wall Turbulent Boundary Layers in Shallow Open Channel Flow,'' ASME J. Fluids Eng., **122**, No. 3, pp. 533–541.
[7] Bradshaw, P., and Wong, F. W. F., 1972, ''The Reattachment and Relaxation of Turbulence Shear Layer,'' J. Fluid Mech., **52**, pp. 113–135.
[8] Castro, I. P., and Epik, E., 1996, ''Boundary Layer Relaxation After a Separated Region,'' Exptl Thermal Sc., **13**, pp. 338–348.
[9] Castro, I. P., and Epik, E., 1998, ''Boundary Layer Development After a Separated Region,'' J. Fluid Mech., **374**, pp. 91–116.
[10] Counihan, J., Hunt, J. C. R., and Jackson, P. S., 1974, ''Wakes Behind Two-Dimensional Surface Obstacles in Turbulent Boundary Layers,'' J. Fluid Mech., **64**, pp. 529–563.
[11] Pal, S., 1981, ''Boundary Layer Behavior on Rough Surfaces in the Presence of Turbulent Wake,'' in *Three Dimensional Turbulent Shear Flows*, ASME, pp. 129–135.
[12] Balachandar, R., and Tachie, M. F., 2001, ''A Study of Boundary Layer-Wake Interaction in Shallow Open Channel Flows,'' Exp. Fluids, **30**, No. 5, pp. 511–525.
[13] George, W. K., and Castillo, L., 1997, ''Zero Pressure Gradient Turbulent Boundary Layer,'' Appl. Mech. Rev., **50**, No. 11, pp. 689–729.
[14] Coles, D., 1956, ''The Law of the Wake in the Turbulent Boundary Layer,'' J. Fluid Mech., **1**, pp. 191–226.
[15] Henkes, R. A. W. M., 1998, ''Scaling of the Turbulent Boundary Layer Along a Flat Plate According to Different Turbulent Models,'' Int. J. Heat Fluid Flow, **19**, pp. 338–347.
[16] Jovic, S., 1993, ''An Experimental Study on the Recovery of a Turbulent Boundary Layer Downstream of Reattachment,'' *Engineering Turbulence Modelling and Experiment*, Rodi, W. and Ganic, E. N., eds., Elsevier, pp. 789–798.
[17] Hancock, P. E., and Bradshaw, P., 1989, ''Turbulence Structure of a Boundary Layer Beneath a Turbulent Freestream,'' J. Fluid Mech., **205**, pp. 45–76.
[18] Thole, K. A., and Bogard, D. G., 1996, ''High Freestream Turbulence Effects on Turbulent Boundary Layers,'' ASME J. Fluids Eng., **118**, pp. 276–284.
[19] Bradshaw, P., 1973, ''Effects of Streamwise Curvature on Turbulent Flow,'' AGARD-ograph 169. NATO.
[20] Eaton, J. K., and Johnston, J. P., 1981, ''A Review of Research on Subsonic Turbulent Flow Reattachment,'' AIAA J., **19**, No. 9, pp. 1093–1100.
[21] Kiya, M., and Sasaki, K., 1983, ''Structure of a Turbulent Separation Bubble,'' J. Fluid Mech., **137**, pp. 83–113.
[22] Sasaki, K., and Kiya, M., 1991, ''Three-Dimensional Vortex Structure in a Leading-Edge Separation Bubble at Moderate Reynolds Numbers,'' ASME J. Fluids Eng., **113**, pp. 405–410.
[23] Le, H., Moin, P., and Mahesh, K., 1997, ''Direct Numerical Simulation of Turbulent Flow Over a Backward-Facing Step,'' J. Fluid Mech., **330**, pp. 349–374.
[24] Suksangpanomrung, A., 1999, ''Investigation of Unsteady Separated Flow and Heat Transfer Using Direct and Large Eddy Simulations,'' Ph.D dissertation, University of Victoria, Canada.
[25] Schwartz, A. C., Plesniak, M. W., and Murthy, S. N. B., 1999, ''Turbulent Boundary Layers Subjected to Multiple Strain,'' ASME J. Fluids Eng., **121**, pp. 526–532.
[26] Ching, C. Y., Djenidi, L., and Antonia, R. A., 1995, ''Low-Reynolds Number Effects in a Turbulent Boundary Layer,'' Exp. Fluids, **19**, pp. 61–68.
[27] Nezu, I., and Nagakawa, H., 1993, ''Turbulence in Open Channel Flow,'' IAHR Monograph Series, Balkema Press, The Netherlands.
[28] Balachandar, R., Blakely, D., and Tachie, M. F., 2001, ''A Study on Turbulent Boundary Layers in Open Channel Flows,'' ASME J. Fluids Eng., **123**, pp. 394–400.
[29] Yoo, J. Y., and Baik, S. J., 1992, ''Redeveloping Turbulent Boundary Layer in the Backward-Facing Step Flow,'' ASME J. Fluids Eng., **114**, pp. 522–529.
[30] Nezu, I., and Rodi, W., 1986, ''Open-Channel Flow Measurements with a Laser Doppler Anemometer,'' J. Hydraul. Eng., **112**, No. 5, pp. 335–355.
[31] Tachie, M. F., Bergstrom, D. J., Balachandar, R., and Ramachandran, S., 2000, ''Skin Friction Correlation for Low Re_θ Open Channel Flows,'' Submitted to the ASME J. Fluids Eng.
[32] Ruderich, R., and Fernholz, H. H., 1985, ''An Experimental Investigation of a Turbulent Shear Flow with Separation, Reverse Flow, and Reattachment,'' J. Fluid Mech., **163**, pp. 53–73.
[33] Jovic, S., and Driver, D. M., 1994, ''Backward-Facing Step Measurements at Low Reynolds Number, $\mathrm{Re_h} = 5000$,'' NASA Tech. Mem. 108807.
[34] Tachie, M. F., Bergstrom, D. J., and Balachandar, R., 2000, ''Mean and Fluctuating Velocity Components in Smooth and Rough Wall Boundary Layers,'' 3rd Symposium on Turbulence, Heat and Mass Transfer, April 2–6, Nagayo, Japan.

Linear and Nonlinear PSE for Stability Analysis of the Blasius Boundary Layer Using Compact Scheme

V. Esfahanian
Associate Professor
e-mail: evahid@chamran.ut.ac.ir

K. Hejranfar
Ph.D. Candidate

Department of Mechanical Engineering,
University of Tehran, Tehran, Iran

F. Sabetghadam
Ph.D. Candidate
Science and Research Faculty,
Azad University, Tehran, Iran

A highly accurate finite-difference PSE code has been developed to investigate the stability analysis of incompressible boundary layers over a flat plate. The PSE equations are derived in terms of primitive variables and are solved numerically by using compact method. In these formulations, both nonparallel as well as nonlinear effects are accounted for. The validity of present numerical scheme is demonstrated using spatial simulations of two cases; two-dimensional (linear and nonlinear) Tollmien-Schlichting wave propagation and three-dimensional subharmonic instability breakdown. The PSE solutions have been compared with previous numerical investigations and experimental results and show good agreement. [DOI: 10.1115/1.1385833]

Introduction

The objective of the present work is the development of an accurate and cost efficient way for investigating the stability and transition computation of incompressible boundary layers on a flat plate. There are several ways for transition predictions such as linear stability theory and direct Navier-Stokes solutions.

The hydrodynamic stability theory is useful in indicating the major dominant effects which hasten or delay transition in a relative sense. Some basic understanding of the transition problem in incompressible boundary layers can be reached using linear stability theory with the assumption of parallel flow. In addition, the transition location can be approximately predicted using an empirical correlation such as the e^N method. The usefulness of linear stability analysis is limited by inaccuracies due to the parallel flow approximation. Also, it is limited by the fact that latter stages of transition are nonlinear.

As a transition prediction tool, the direct numerical simulations (DNS) using full Navier-Stokes equations can accurately model the early stages of transition but require far too much computer power. Moreover, they have been obtained only for very simple geometries such as flat plate. Therefore, it is not appropriate for studying the transition over the complex geometries.

A new methodology for transition prediction which has been proposed by Herbert [1,2], Bertolotti [3] also Chang et al. [4], utilizes the Parabolized Stability Equations (PSE). In spite of linear stability theory, the PSE can be used to study nonparallel as well as nonlinear evolution of convective disturbances in growing boundary layers. In addition, for prediction of the transition location, the PSE do not need an empirical correlation.

The PSE are nonlinear parabolized partial differential equations used to predict the laminar-turbulent transition. Similar to classical stability analysis, the PSE assume that transition process starts with the small disturbances amplifications. Since the PSE are nonlinear equations, they are valid for the finite-amplitude disturbances. But they are limited to flows with slowly varying properties in the streamwise direction.

The PSE are an initial-boundary value problem and they can be solved using a marching procedure. As a result, the computational effort and required storage can be reduced using the PSE. Therefore, these equations are appropriate for a rapid and an accurate prediction of laminar-turbulent transition of incompressible boundary layers.

In this context, the computation of the stability and onset of transition location of incompressible flow over a flat plate based on linear and nonlinear PSE using compact scheme and primitive variables is performed. Two cases are computed by the PSE theory: two-dimensional (linear and nonlinear) Tollmien-Schlichting (TS) wave propagation and three-dimensional subharmonic breakdown. The present computations are compared with available numerical, DNS and experimental results.

Problem Formulation

In this study, the stability of incompressible flow over a flat plate in Cartesian coordinate system is formulated. The Cartesian coordinates are denoted by x, y, and z, where x is the streamwise distance from the leading edge, and y and z are the plate normal and the spanwise coordinates, respectively, as shown in Fig. 1. All quantities are nondimensionalized with the free-stream velocity U_∞ and the fixed length $\delta_o=\delta(x_o)=\sqrt{\nu x_o/U_\infty}$, where x_o is a fixed starting dimensional distance from the leading edge and ν is kinematic viscosity. The resulting nondimensional parameter is the reference Reynolds number $R_o=U_\infty\delta_o/\nu$ at $x=x_o$ (Bertolotti et al. [5]). Then, the three-dimensional incompressible Navier-Stokes equations in nondimensional form are as follows:

$$\nabla\cdot V=0 \tag{1}$$

$$\frac{\partial V}{\partial t}+(V\cdot\nabla)V=-\nabla p+\frac{1}{R_o}\nabla^2 V \tag{2}$$

where $V=(u,v,w)$ is the velocity vector and p is the pressure.

To obtain the disturbance equations, one can split the dependent quantities vector $\phi=(u,v,w,p)^T$ into a steady two-dimensional mean value (basic flow) $\Phi_b=(U_b,V_b,0,P_b)^T$ and an unsteady three-dimensional perturbation quantity $\phi'=(u',v',w',p')^T$

$$\phi(x,y,z,t)=\Phi_b(x,y)+\phi'(x,y,z,t) \tag{3}$$

By substituting the vector ϕ into the Navier-Stokes equations (1) and (2), and subtracting the terms satisfied by the basic flow, one will obtain the governing equations for the disturbances ϕ', which will not be presented here.

Contributed by the Fluids Engineering Division for publication in the JOURNAL OF FLUIDS ENGINEERING. Manuscript received by the Fluids Engineering Division November 22, 1999; revised manuscript received April 12, 2001. Associate Editor: D. R. Williams.

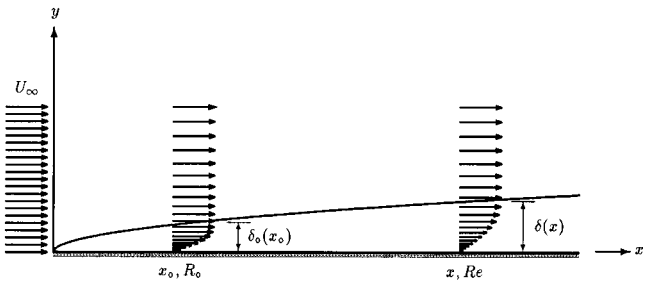

Fig. 1 Flat plat boundary layer model

Basic Flow. For flow over the flat plate the basic flow can be obtained by solving the self-similar boundary layer equations (the Blasius equation):

$$f''' + \frac{1}{2} f f'' = 0 \tag{4}$$

with boundary conditions:

$$f(0) = f'(0) = 0, \quad f'(\infty) = 1$$

where $f(\eta)$ is the Blasius function defined as:

$$\Psi_b = \sqrt{\nu U_\infty x} f(\eta), \quad \eta = y \sqrt{\frac{U_\infty}{\nu x}}$$

and Ψ_b is the stream function of basic flow.

Linear PSE. One way to derive the PSE, as suggested by Herbert and Bertolotti [6], is to decompose a disturbance into rapidly varying wave-like part and a slowly growing shape function. The ellipticity is retained for the wave part while the parabolization is applied to the shape function. For linear PSE, one can assume that the disturbance vector ϕ' for an instability wave with a frequency ω and a spanwise wave number β can be expressed as:

$$\phi'(x,y,z,t) = \hat{\phi}(x,y)\chi(x,z,t) \tag{5}$$

where the shape function vector $\hat{\phi}$ and χ are:

$$\hat{\phi} = (\hat{u}, \hat{v}, \hat{w}, \hat{p})^T$$

$$\chi = \exp\left[i \left(\int_{x_o}^{x} \alpha(s) ds + \beta z - \omega t \right) \right]$$

The shape function $\hat{\phi}$ is a function of both x and y due to the growth of boundary layer and the streamwise wave number α is a function of x to permit the growth of the boundary layer.

The linearized PSE are obtained by substituting the disturbance vector ϕ' into the linear disturbance equations, and with the following essential property; the characteristics of flow such as velocity profiles, wavelengths and growth rates change slowly in the streamwise direction, therefore, the shape function $\hat{\phi}$ along streamwise direction changes such that the second derivatives of $\hat{\phi}$ ($\hat{\phi}_{xx}$) are negligible. Then, the linearized equations that describe the evolution of the shape function $\hat{\phi}$ will be obtained. These equations can be written as a system of first-order differential equations in the y-direction in terms of compact variables F as follows:

$$\mathbf{P} \frac{\partial F}{\partial y} + \mathbf{R} \frac{\partial F}{\partial x} + \mathbf{Q} F = 0 \tag{6}$$

where the new vector F is defined by

$$F = \left(\hat{u}, \hat{v}, \hat{w}, \hat{p}, \frac{\partial \hat{u}}{\partial y}, \frac{\partial \hat{v}}{\partial y}, \frac{\partial \hat{w}}{\partial y} \right)^T$$

Now, a scalar equation is needed to close the system. This equation must resolve the ambiguity created by the dependency of both $\hat{\phi}$ and α on x. This condition is called ''auxiliary'' condition, and in general can be expressed as follows:

$$\int_0^\infty \hat{q}^\dagger \cdot \frac{\partial \hat{q}}{\partial x} dy = 0 \tag{7}$$

where the components of vector $\hat{q}$ are $(\hat{u}, \hat{v}, \hat{w})$ († denotes complex conjugate). The success of a marching solution would require a proper way of updating the wave number. Here, the wave number is updated as follows:

$$\alpha_{\text{new}} = \alpha_{\text{old}} - \frac{i \int \hat{u}^\dagger \frac{\partial \hat{u}}{\partial x} dy}{\int |\hat{u}|^2 dy} \tag{8}$$

In the nonparallel boundary layers, the growth and phase variation of some physical quantity ψ depends on α and $\hat{\phi}$. Therefore, the physical growth rate $\overline{\gamma}$ and the physical wave number $\overline{\alpha}$ for any given flow variable ψ (such as $\hat{u}$, $\hat{v}$, etc.) are defined as:

$$\overline{\gamma}(x) = -\mathcal{I}[\alpha(x)] + \mathcal{R}\left[\frac{1}{\psi} \frac{\partial \psi}{\partial x} \right] \tag{9}$$

$$\overline{\alpha}(x) = \mathcal{R}[\alpha(x)] + \mathcal{I}\left[\frac{1}{\psi} \frac{\partial \psi}{\partial x} \right] \tag{10}$$

According to these equations, the growth rate and the wave number depends upon the wall normal distance. Usually, these quantities are computed at the corresponding location where the fluctuation reaches its maximum value. For incompressible flow, the growth rate and the wave number are computed using the streamwise velocity shape function ($\psi = \hat{u}$).

The solution of linearized PSE equations (6) requires appropriate boundary conditions in the y-direction. At the wall, the components of perturbation velocity satisfy the no-slip condition

$$\hat{u} = \hat{v} = \hat{w} = 0, \quad y = 0 \tag{11}$$

and the Dirichlet conditions are applied in the free-stream

$$\hat{u} = \hat{v} = \hat{w} = 0, \quad y \to \infty \tag{12}$$

For incompressible flows, some residual ellipticity exist that can result in numerical instability in the marching procedure for small stepsizes. Therefore, the marching procedure will remain stable when the stepsize exceeds from the certain minimum value ($\Delta x > \Delta x_{\min}$).

Nonlinear PSE. In the linear PSE, the disturbance amplitude is assumed to be infinitesimally small so that the nonlinear interaction of these waves is negligible. For nonlinear waves, the total disturbance is assumed to be periodic in time and in the spanwise direction. For most problems, it is sufficient to choose a finite number of modes. In these cases, the total disturbance vector $\phi'(x,y,z,t)$ can be expressed as follows:

$$\phi' = \sum_{n=-N}^{N} \sum_{k=-K}^{K} \hat{\phi}_{nk}(x,y) \chi_{nk}(x,z,t) \tag{13}$$

where the shape function vector $\hat{\phi}_{nk}$ and χ_{nk} are:

$$\hat{\phi}_{nk} = (\hat{u}_{nk}, \hat{v}_{nk}, \hat{w}_{nk}, \hat{p}_{nk})^T$$

$$\chi_{nk} = \exp\left[i \left(\int_{x_o}^{x} \alpha_{nk}(s) ds + k\beta z - n\omega t \right) \right]$$

The nonlinear PSE are obtained by substituting the disturbance vector ϕ' into the nonlinear disturbance equations and performing harmonic balance for both linear and nonlinear terms. Finally, the nonlinear PSE equations can be obtained for the shape function

$\hat{\phi}_{nk}$ of a single Fourier mode (n,k), that can be written as a system of first-order differential equations in the y-direction in terms of compact variables F_{nk} as follows:

$$\mathbf{P}_{nk}\frac{\partial F_{nk}}{\partial y}+\mathbf{R}_{nk}\frac{\partial F_{nk}}{\partial x}+\mathbf{Q}_{nk}F_{nk}=H_{nk} \tag{14}$$

where H_{nk} is nonlinear forcing function. The nonlinear PSE for a single Fourier mode is equivalent to the linear PSE with a frequency $n\omega$ and a spanwise wave number $k\beta$ with the additional forcing function H_{nk}.

The procedure for determination of wave number α_{nk} is similar to the linear PSE. For present computation, all modes are assumed to have the same phase speed (phase-locked condition) i.e.,

$$\alpha_{nk}=(n\mathcal{R}(\alpha_F),\mathcal{I}(\alpha_{nk})) \tag{15}$$

where α_F is the fundamental TS wave, which is a function of x. The calculation of α_{nk} is similar to the linear case according to relation (8). For the detuned case the computation procedure is more complicated in the sense that mode bookkeeping become more cumbersome.

The solution procedure of the linear PSE can be applied to the nonlinear PSE, except for the modes with zero frequency ($n=0$). These zero frequency modes are denoted as the mean flow distortion (MFD) ($k=0$) or longitudinal vortex ($k\neq 0$). The boundary conditions (10) and (11) can be applied to the longitudinal vortex mode (zero frequency and non-zero spanwise wave number) without modification. For the MFD mode, the free stream boundary condition for normal velocity is replaced with Neumann condition to allow the mean flow to adjust itself for mass balance:

$$\hat{u}_{00}=\frac{\partial \hat{v}_{00}}{\partial y}=\hat{w}_{00}=0, \quad y\to\infty \tag{16}$$

This would allow the boundary layer to have the correct mass balance (or displacement thickness) due to the modification of mean flow ($U_b+\hat{u}_{00}$) caused by nonlinear mode interactions.

The new mode is generated into the field whenever the maximum magnitude of the corresponding nonlinear term is greater than a threshold (10^{-6}). Similarly, a mode is removed when the corresponding nonlinear term is less than the threshold and has negative growth rate.

Numerical Solution

For accurate numerical solution, the fourth-order compact two-point finite-difference (Euler-Maclaurin formula) (Malik et al. [7])

$$F_{i,j}-F_{i,j-1}=\frac{h_j}{2}\left[\left(\frac{\partial F}{\partial y}\right)_{i,j}+\left(\frac{\partial F}{\partial y}\right)_{i,j-1}\right]-\frac{h_j^2}{12}\left[\left(\frac{\partial^2 F}{\partial y^2}\right)_{i,j}-\left(\frac{\partial^2 F}{\partial y^2}\right)_{i,j-1}\right]+\frac{h_j^5}{720}\left(\frac{\partial^5 F}{\partial y^5}\right)_{i,j} \tag{17}$$

has been used to compute the basic flow and the PSE equations, where F is the solution vector including compact variables and $h_j=y_j-y_{j-1}$ is the variable stepsize in the y-direction. The following relation is used to generate the grid distribution in the wall normal direction

$$y_j=\frac{y_o}{\overline{y}_j}-y_o, \quad \overline{y}_j=\cos\left(\frac{j\pi}{2j_{\max}+1}\right) \tag{18}$$

where $j=0,1,2,\ldots,j_{\max}$ and y_o is a suitable transformation parameter, typically $y_o=4.5$. All the present computations are performed using $j_{\max}=80$ grid points.

The plot of modified wave number for the first derivative approximation of the Euler-Maclaurin method is given in Fig. 2. The traditional fourth-order central finite difference approximation and Hermittion fourth-order method are also presented in this figure.

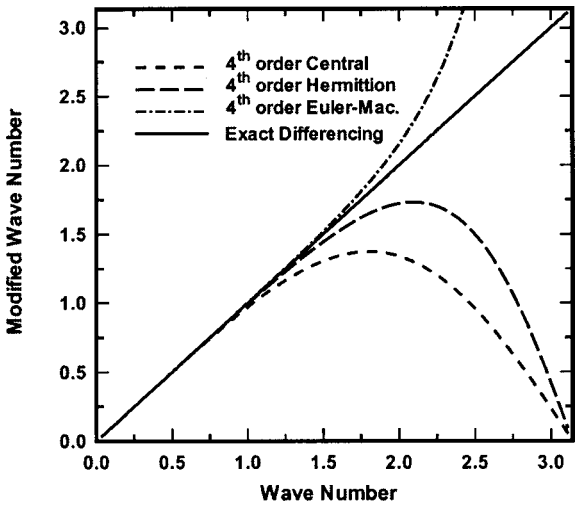

Fig. 2 Comparison of exact and modified wave numbers for the first derivative approximation

The comparison of these methods with the exact wave number indicates that the resolution characteristics of the Euler-Maclaurin scheme is better than the others. This can be also seen from truncation error of finite difference approximation. The additional motivations beside the global accuracy for using the fourth-order Euler-Maclaurin method are:

- This method only involves two grid points and requires no additional relations at boundaries and therefore, the accuracy of method is the same through the whole numerical field.
- Since this formulation involves two grid points, any grid distribution in the physical plane can be used and no mapping is needed.
- Using this method, the first derivatives are automatically computed as a part of numerical solution. Therefore, the computation of nonlinear terms require no intermediate computation of the first derivatives.

The traditional fourth-order central method would require the solution of (4×4) block pentadiagonal system, while the Euler-Maclaurin and Hermitian methods would require the solutions of (7×7) and (11×11) block tridiagonal systems, respectively.

Basic Flow Computation. In order to solve the flow field with the fourth-order compact two-point scheme, the Blasius equation has to be written as a first-order system of equations as follows:

$$F_b=\begin{pmatrix} f \\ v \\ s \end{pmatrix}, \quad F_b'=\begin{pmatrix} v \\ s \\ -fs/2 \end{pmatrix}, \quad F_b''=\begin{pmatrix} s \\ -fs/2 \\ -vs/2+f^2 s/4 \end{pmatrix}$$

where

$$v=f', \quad s=f''$$

Substituting the above vectors into compact relation (17) and linearizing the resulting equations using Newton method, a tridiagonal system obtained which can be solved by the Thomas algorithm. The convergence is quick and it is less than 10 iterations for tolerance of 10^{-12}.

PSE Computation. Numerical solution of PSE equations needs to discretize Eqs. (6) and (14) in both streamwise (x) and wall normal (y) directions. In the streamwise direction, the first and the second order backward difference schemes are used. In the wall normal direction, the fourth-order compact two-point finite-difference is employed.

For linear PSE, the system of first-order differential equations (6) can be rearranged in the following form (Chang et al. [4])

$$\frac{\partial F}{\partial y} = \hat{\mathbf{Q}} F + S \tag{19}$$

provided that $\mathbf{P}^{-1}$ exists. It should be noted that the continuity equation is replaced by its derivative at the wall to avoid $\mathbf{P}$ to be singular ($\mathrm{Det}|\mathbf{P}| = R_o$). In the above equation:

$$\hat{\mathbf{Q}}_{i,j} = -\mathbf{P}_{i,j}^{-1}\left\{\frac{\mathbf{R}_{i,j}}{(1-m)\Delta x} + \mathbf{Q}_{i,j}\right\}$$

$$S_{i,j} = \mathbf{P}_{i,j}^{-1}\mathbf{R}_{i,j}\left\{\frac{(1+m)F_{i-1,j} - mF_{i-2,j}}{(1-m)\Delta x}\right\}$$

where for the first and the second order accuracy m is equal to 0, 1/3, respectively, and Δx is the stepsize in the x-direction. Differentiating Eq. (19) with respect to y and substituting into relation (17) one obtains the following system of equations for the ith streamwise plane:

$$\mathbf{A}_{i,j} F_{i,j-1} + \mathbf{B}_{i,j} F_{i,j} = C_{i,j} \tag{20}$$

where

$$\mathbf{A}_{i,j} = -\mathbf{I} - \frac{h_j}{2}\hat{\mathbf{Q}}_{i,j} - \frac{h_j^2}{12}\left(\frac{\partial \hat{\mathbf{Q}}}{\partial \mathbf{y}} + \hat{\mathbf{Q}}\hat{\mathbf{Q}}\right)_{i,j}$$

$$\mathbf{B}_{i,j} = \mathbf{I} - \frac{h_j}{2}\hat{\mathbf{Q}}_{i,j} + \frac{h_j^2}{12}\left(\frac{\partial \hat{\mathbf{Q}}}{\partial \mathbf{y}} + \hat{\mathbf{Q}}\hat{\mathbf{Q}}\right)_{i,j}$$

$$C_{i,j} = \frac{h_j}{2}(S_{i,j} + S_{i,j-1}) - \frac{h_j^2}{12}\left\{\left[\hat{\mathbf{Q}}S + \frac{\partial S}{\partial y}\right]_{i,j} - \left[\hat{\mathbf{Q}}S + \frac{\partial S}{\partial y}\right]_{i,j-1}\right\}$$

Here $\mathbf{I}$ is the unit matrix. The truncation error for the above scheme is

$$\mathcal{O}[(\Delta x)^{1+3m}, h^4]$$

These equations require seven boundary conditions. Equations (11) and (12) provide six boundary conditions. An additional boundary condition is obtained using the continuity equation at the wall. The above system of equations along with the seven boundary conditions give a block tridiagonal system of equations with a block size of 7×7.

For nonlinear PSE, the above equations can be used for each mode (n,k), except for $S_{i,j}$ that must be modified as follows:

$$S_{i,j} = S_{i,j}|_{\mathrm{linear}} + \mathbf{P}_{i,j}^{-1} H_{i,j}$$

Initial Conditions

The initial conditions for the present computation are obtained by solving the Orr-Sommerfeld equations at the corresponding Reynolds number R_o and nondimensional frequency F ($\omega\nu/U_\infty^2 \times 10^6$). The Orr-Sommerfeld equations in primitive forms can be obtained from the linear PSE equations by setting $\partial/\partial x$ derivatives and V_b equal to zero, i.e.,

$$\left.\frac{\partial F}{\partial y}\right|_{\mathrm{os}} = \hat{\mathbf{Q}} F_{\mathrm{os}}, \quad \hat{\mathbf{Q}} = \hat{\mathbf{P}}^{-1}\mathbf{Q}_{\mathrm{os}} \tag{21}$$

which can be also solved using compact method.

The Orr-Sommerfeld eigenfunctions are normalized such that

$$u'_{\max} = (2\hat{u}\hat{u}^{\dagger})^{1/2} = A^o \tag{22}$$

and

$$\mathrm{Phs} = \tan^{-1}\left\{\frac{\mathcal{I}(\hat{u})}{\mathcal{R}(\hat{u})}\right\}_{\max} = (\mathrm{Phs})^o \tag{23}$$

where A^o and $(\mathrm{Phs})^o$ are initial amplitude and phase which are input parameters to the code.

Results and Discussion

Here, both linear and nonlinear computations are presented for two cases. All calculations initiated at $R_o = 400$ where the shape function and corresponding wave number for the TS wave are provided by the Orr-Sommerfeld (linear quasi-parallel) solutions. All the present computations are performed on 500 MHZ Pentium III with 128 MB RAM.

2-D Linear and Nonlinear PSE. The first test case is the evolution of a two-dimensional TS fundamental wave of frequency F=86 using the linear and nonlinear PSE. The initial amplitude level of the fundamental mode (1F) is chosen to be $A_{1,0}^0 = 0.25$ percent based on $u'_{\max}$. For nonlinear calculations, three Fourier components ($N=2$, $K=0$) with frequencies 0F, 1F, and 2F are used. The stepsize employed in the downstream marching procedure is $\Delta x = 10$ for both the linear and nonlinear PSE. The results are obtained in the interval $400 \leqslant Re \leqslant 1000$. The average CPU times required for linear and nonlinear PSE computations are 40 and 530 seconds, respectively. Figure 3 shows the amplitude curves based on $u'_{\max}$ versus Reynolds number $Re = U_\infty \delta(x)/\nu = \sqrt{U_\infty x/\nu} = \sqrt{Re_x}$ for the fundamental mode (1F) and its first harmonic (2F). The upper curve is the amplitude of the TS wave and the lower one is the amplitude of the 2F harmonic. This figure also shows the TS amplitude curve using linear PSE which compares very well with the Bertolotti results [3]. The present results for nonlinear PSE computations are in good agreement with those of Bertolotti [3] and DNS computed by Bertolotti et al. [5]. The differences between the present solutions and those of the Bertolotti results [3] are due to different approximations used in PSE formulation. Bertolotti used stream function formulation and solved the resulting equation using the spectral method. Here, the primitive form is used and it is numerically solved by the compact method. For the nonlinear PSE, the velocity profiles of u' for the MFD wave (0F), the TS wave (1F) and the first harmonic wave are shown in Fig. 4 at $Re = 796$. These profiles agree very well with the DNS results by Bertolotti et al. [5]. The present computations for nonlinear PSE are also in good agreement with those of DNS computed by Joslin et al. [8], but for clarity these comparisons are not shown in the figures.

3-D Nonlinear PSE. There are different routes to transition depending on the initial conditions. The PSE code developed here

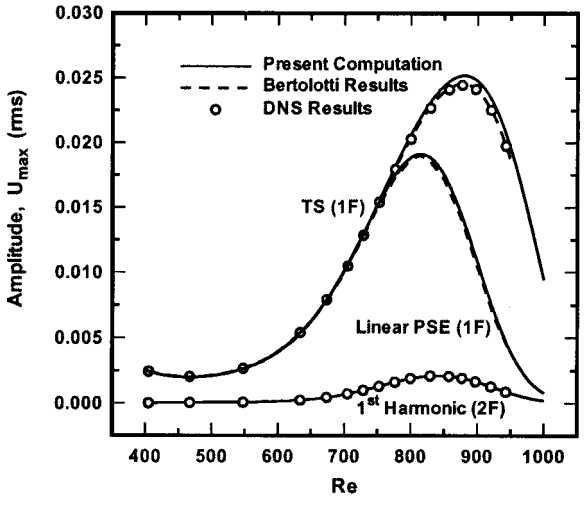

Fig. 3 Comparison of amplitudes based on $u'_{\max}$ versus Reynolds number for the TS wave F=86 using the linear and nonlinear PSE

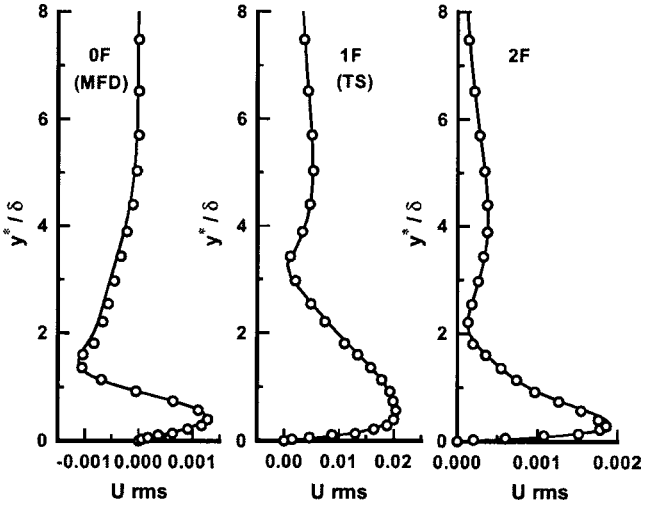

Fig. 4 Comparison of velocity profiles of u' for various modes at $Re=796$ and F=86. Circles denote results from DNS simulation by Bertolotti et al. [5].

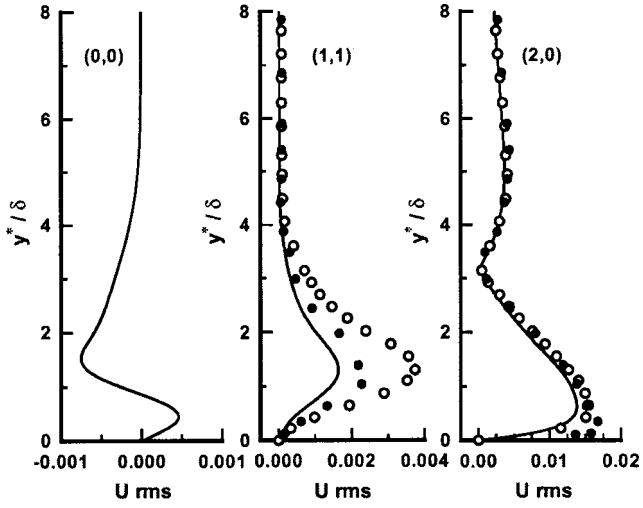

Fig. 6 Comparison of velocity profiles of u' for various modes at $Re=608$ and 2F=124. Circles denote DNS results by Fasel et al. [10] and dots are experimental data [9].

can be used all the way to transition for both fundamental (K-type) and subharmonic (H-type) breakdown. The most dangerous route is expected to be a three-dimensional subharmonic mode interaction. To demonstrate the ability of the PSE in predicting the onset of transition, a nonlinear interaction is considered between a TS fundamental wave (mode (2, 0)) 2F=124 and a pair of subharmonic oblique waves ((1, 1) and (1, −1) modes) for conditions of Kachanov and Levchenko experiment [9]. The initial amplitudes of the TS wave and the subharmonic wave are chosen $A^o_{2,0}=0.46$ percent and $A^o_{1,1}=0.0035$ percent based on $u'_{\max}$, respectively. The spanwise wave number of the subharmonic mode is fixed at $\beta=0.14$. The stepsize for the marching procedure is $\Delta x=15$. The solution is obtained with Fourier series truncated to $N=2$, and $K=1$, and extended from $Re=400$ to $Re=720$. To investigate the effect of initial amplitude of subharmonic mode on the solution, the results are also presented for $A^o_{1,1}=0.01$ percent. For subharmonic breakdown, based on initial amplitudes of subharmonic mode $A^0_{1,1}=0.0035$ percent, 0.01 percent, the average CPU times are 265 and 725 seconds, respectively. Figure 5 shows the PSE results for the amplitudes of three modes (0, 0), (1, 1) and (2, 0) based on $u'_{\max}$ together with experimental data for H-type breakdown. Amplitudes were measured at $\eta=1.3$. The agreement is remarkable for the TS wave (2, 0). The amplitude curve for the subharmonic mode with initial amplitude $A^o_{1,1}=0.01$ percent is in better agreement than $A^o_{1,1}=0.0035$ percent. The results demonstrate that the solution depends on the initial amplitude of subharmonic mode only in the transition region ($Re>630$) where the MFD mode rapidly rises thereafter. The velocity profiles of u' for three modes at $Re=608$ for $A^o_{1,1}=0.01$ percent are shown in Fig. 6. Good agreement in the amplitude profiles are found between the present results and the DNS computed by Fasel et al. [10] and also the experimental data especially for the TS wave. The differences between the PSE and the experimental results for subharmonic mode may come from the initial conditions which are provided by the Orr-Sommerfeld equations. Although not shown here, the present solutions have been compared with those of DNS computed by Joslin et al. [8], and show good agreement. Figure 7 presents the variations of nondimensional displacement thickness and skin friction coefficient versus Reynolds number for the subharmonic breakdown.

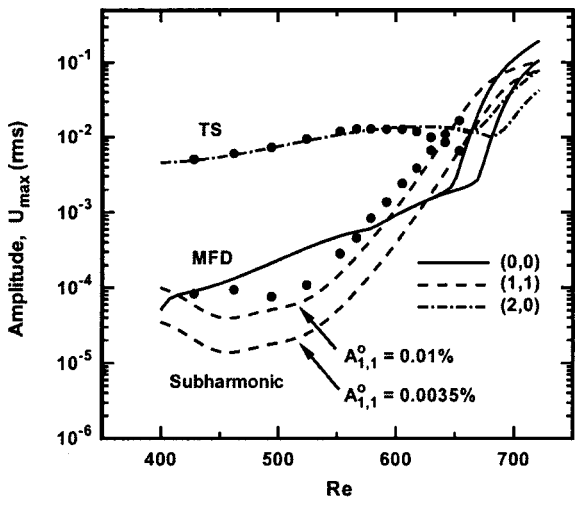

Fig. 5 Comparison of amplitudes based on $u'_{\max}$ versus Reynolds number for subharmonic breakdown (2F=124 and $\beta=0.14$). Dots denote experimental data [9].

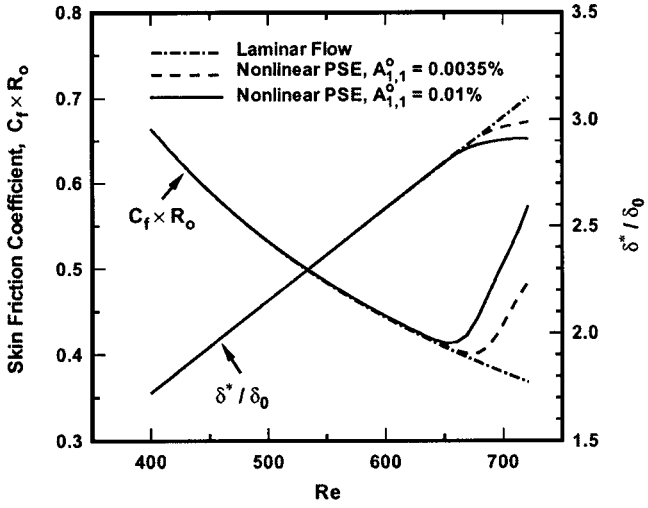

Fig. 7 Variations of nondimensional displacement thickness and skin friction coefficient versus Reynolds number for subharmonic breakdown

This figure shows the results of unperturbed and perturbed flows. As shown in this figure, near the onset of transition the displacement thickness originally increases very little and then decreases. The skin friction coefficient calculated by the nonlinear PSE has a minimum at $Re=670$ for $A^o_{1,1}=0.0035$ percent and is shifted back to $Re=650$ for $A^o_{1,1}=0.01$ percent. The rise of skin friction which is due to the MFD indicates the onset of transition in the sense of operational definition.

Conclusions

The stability analysis of the Blasius boundary layer has been studied using linear and nonlinear PSE. Both linear and nonlinear PSE equations have been solved using compact method and primitive variables. The agreement of the present results with the previous works and the direct numerical solutions and also experiment is very good. The linear and the nonlinear results show that the PSE approach is a powerful tool for the study of boundary layer stability and prediction of transition location.

Acknowledgment

The authors would like to thank University Tehran for financial support of this research.

References

[1] Herbert, Th., 1991, ''Boundary-Layer Transition-Analysis and Prediction Revisited,'' AIAA Paper 91-0737.

[2] Herbert, Th., 1997, ''Parabolized Stability Equations,'' Annu. Rev. Fluid Mech., **29**, pp. 245–283.

[3] Bertolotti, F. P., 1991, ''Linear and Nonlinear Stability of the Boundary Layers with Streamwise Varying Properties,'' Ph.D. thesis, The Ohio State University, Columbus, Ohio.

[4] Chang, C.-L., Malik, M. R., Erlebacher, G., and Hussaini, M. Y., 1991, ''Compressible Stability of Growing Boundary Layers Using Parabolized Stability Equations,'' AIAA Paper 91-1636.

[5] Bertolotti, F. P., Herbert, TH., Spalart, P. R., 1992, ''Linear and Nonlinear Stability of the Blasius Boundary Layer,'' J. Fluid Mech., **242**, pp. 441–474.

[6] Herbert, Th., and Bertolotti, F. P., 1987, ''Stability Analysis of Nonparallel Boundary Layers,'' Bull. Am. Phys. Soc., **32**, p. 2079.

[7] Malik, M. R., Chuang, S., and Hussaini, M. Y., 1982, ''Accurate Numerical Solution of Compressible, Linear Stability Equations,'' Z. Angew. Math. Phys., **33**, 189.

[8] Joslin, R. D., Chang, C.-L., and Streett, C. L., 1993, ''Spatial Direct Numerical Simulation of Boundary-Layer Transition Mechanisms: Validation of PSE Theory,'' Theor. Comput. Fluid Dyn., **3**, pp. 271–288.

[9] Kachanov, Y. S., and Levchenko, V. Y., 1984, ''The Resonant Interaction of Disturbances at Laminar-Turbulent Transition in a Boundary Layer,'' J. Fluid Mech., **138**, pp. 209–247.

[10] Fasel, H. F., Rist, U., and Konzelmann, U., 1990, ''Numerical Investigation of the Three-Dimensional Development in Boundary-Layer Transition,'' AIAA J., **28**, No. 1, pp. 29–37.

InSub Lee
Graduate Student

Hong Sun Ryou
Professor

Department of Mechanical Engineering,
Chung-Ang University,
221 HeukSuk-Dong,
DongJak-Gu, Seoul, 156-756 Korea

Seong Hyuk Lee
Researcher,
Research Institute of Production Engineering,
Chung-Ang University,
221 HeukSuk-Dong,
DongJak-Gu, Seoul, 156-756, Korea

Ki Bae Hong
Professor,
Department of Thermal Engineering,
Choong-Ju University,
Choong-Ju Korea

Soo Chae
Professor,
Department of Automobile,
Kunjang College,
Kunsan, Korea

A Numerical Investigation on the Development of an Embedded Streamwise Vortex in a Turbulent Boundary Layer With Spanwise Pressure Gradient

It is the aim of this article to investigate numerically the effects of spanwise pressure gradient on an embedded streamwise vortex in a turbulent boundary layer. The governing equations were discretized by the finite volume method and SIMPLE algorithm was used to couple between pressure and velocity. The LRR model for Reynolds stresses was utilized to predict the anisotropy of turbulence effectively. The validation was done for two cases: one is the development of a streamwise vortex embedded in a pressure-driven, three-dimensional turbulent boundary layer. The other involves streamwise vortex pairs embedded in a turbulent boundary layer without the spanwise pressure gradient. In the case of the former, the predicted results were compared with Shizawa and Eaton's experimental data. In the latter case, the calculated results were compared against the experimental data of Pauley and Eaton. We performed numerical simulations for three cases with different values of spanwise pressure gradient. As a result, the primary streamwise vortex with spanwise pressure gradients decays more rapidly than the case with no pressure gradients, as the spanwise pressure gradient increases. This indicates that the spanwise pressure gradient may play an important role on mean and turbulent structures. In particular, it can be seen that the increase of pressure gradient enhances a level of turbulent normal stresses. [DOI: 10.1115/1.1378022]

Introduction

Three-dimensional turbulent boundary layers (3DTBLs), with embedded streamwise vortices, are often present in flows of engineering such as aircraft wings, turbomachinery and heat exchanger, etc. Among examples of turbomachinery, the turbine cascade flow is severely complicated by the interaction between several streamwise vortices and the boundary layers forming on the turbine blades and the endwall. In particular, a strong spanwise pressure gradient across the curved passage causes skewing of the endwall boundary layer. In this case, an additional mean-velocity gradient $\partial W/\partial y$ may be caused by a skewing effect of flow due to spanwise pressure gradient. This spanwise pressure gradient plays an important role in evolution of the mean and turbulent flow characteristics because of its contribution to the production of turbulent kinetic energy. Therefore, a better understanding of interactions between a streamwise vortex and turbulent boundary layer with spanwise pressure gradient is very important in engineering design.

During the past decades, a wide variety of research has been performed for junction flows at aircraft wing roots and for ship and submarine appendage-hull junctions. Belik [1] and Shabaka and Bradshaw [2] studied appendage-body junction and the wing-body junction flow, respectively. In addition, Fleming et al. [3] measured the mean and fluctuation velocities on the wing-body junction flow. For an embedded vortex in turbulent boundary layers, Pearcy [4] developed the design rules to determine the optimum configuration of vortex generators. Shabaka et al. [5] and Mehta et al. [6] measured the Reynolds stresses and turbulence triple products in a flow with a single embedded streamwise vortex and with a pair of vortices with common flow upwards and common flow downwards, respectively. Westphal et al. [7] investigated the effect of an adverse pressure gradient on a single embedded vortex. Eibeck et al. [8] conducted experiments on streamwise vortices imbedded in a turbulent boundary layer. Shizawa and Eaton [9] indicated that the development of turbulent flows was very sensitive to the sign of the vortex. Actually, the majority of relevant studies to the present type of flows have been carried out only experimentally; only a few numerical researches were found in the open literature for the type of flows like embedded longitudinal vortices in a turbulent boundary flow.

A principal goal of this paper is to investigate the effects of spanwise pressure gradient on an embedded streamwise vortex in a turbulent boundary layer. According to Lee et al.'s [10] numerical results, all calculations were carried out by using the Reynolds stress model (RSM) including the model of Launder, Reece and Rodi (LRR) [11] to describe the complex flows. For validation, the numerical calculation was first performed for an embedded streamwise vortex in a pressure-driven, three-dimensional boundary layer. The predicted results were compared with the experimental data of Shizawa and Eaton [9]. As another case for assessment, the experiment of Pauley and Eaton [12] was taken for calculating longitudinal vortex pairs embedded in a turbulent boundary layer without spanwise pressure gradient.

In the main numerical simulation of this article, only a clockwise part of vortex pairs was taken as inlet conditions from the data of Pauley and Eaton [12] to effectively investigate the effects of spanwise pressure gradients on an embedded streamwise vortex in a turbulent boundary layer. In the present calculation, three different ducts bended in 0, 15, and 30 degrees were used for

Contributed by the Fluids Engineering Division for publication in the JOURNAL OF FLUIDS ENGINEERING. Manuscript received by the Fluids Engineering Division January 10, 2000; revised manuscript received March 12, 2001. Associate Editor: J. K. Eaton.

taking into consideration the geometry-induced pressure gradient in the spanwise direction. It is thought that these results may increase our understanding of the development of an embedded streamwise vortex while interacting with spanwise pressure gradient.

Mathematical Representation and Boundary Conditions

The Reynolds time-averaged continuity, Navier-Stokes and Reynolds stress transport equations for steady and incompressible flows are used in the computation of this paper. The continuity and momentum equations can be written in conservation as follows.

$$\frac{\partial U_j}{\partial x_j}=0 \tag{1}$$

$$\rho\frac{\partial}{\partial x_j}(U_jU_j)=-\frac{\partial P}{\partial x_i}+\frac{\partial}{\partial x_j}(2\mu S_{ji}-\rho\overline{u_j'u_i'}) \tag{2}$$

The modeled Reynolds-stress transport equations can be written symbolically as follows.

$$U_k\frac{\partial}{\partial x_k}(\overline{u_j'u_i'})=P_{ij}+d_{ij}+\phi_{ij}-\varepsilon_{ij}+\frac{\partial}{\partial x_k}\left(\nu\frac{\partial\overline{u_i'u_j'}}{\partial x_k}\right) \tag{3}$$

where,

$$P_{ij}=-\left[\overline{u_j'u_i'}\frac{\partial U_j}{\partial x_k}+\overline{u_i'u_j'}\frac{\partial U_i}{\partial x_k}\right] \tag{4}$$

$$d_{ij}=\frac{\partial}{\partial x_k}\left[\frac{c_\mu}{\sigma_k}\frac{k^2}{\varepsilon}\frac{\partial\overline{u_i'u_j'}}{\partial x_k}\right] \tag{5}$$

$$\varepsilon_{ij}=\frac{2}{3}\delta_{ij}\varepsilon \tag{6}$$

$$\phi_{ij}=\phi_{ij,1}+\phi_{ij,2}+\phi_{ij,w}^{(1)}+\phi_{ij,w}^{(2)} \tag{7}$$

where P_{ij}, d_{ij}, ϕ_{ij}, and ε_{ij} are the production term, the turbulent diffusion term, the pressure-strain redistribution term, and the dissipation term, respectively. The turbulent diffusion is modeled by Shir [13] and the dissipation term can be determined from the Rotta [14] model. The LRR model is also used for modeling the pressure-strain redistribution term. The LRR model can take into consideration the rapid part as well as the slow part, often referred to as the return-to-isotropy. This model combines the linear Rotta [15] model for the slow part of the pressure strain term with a model of Naot et al. [16] for the rapid part.

$$\phi_{ij,1}=c_1\frac{\varepsilon}{k}\left[\overline{u_j'u_i'}-\frac{2}{3}\delta_{ij}k\right] \tag{8}$$

$$\phi_{ij,2}=-c_2\left[P_{ij}-\frac{1}{3}\delta_{ij}\overline{u_i'u_j'}\frac{\partial U_l}{\partial x_m}\right] \tag{9}$$

Bradshaw [17] has shown that there is an additional contribution to pressure-strain term that has a nontrivial effect close to a solid wall. Near the wall, the pressure-strain term are modified using the wall correction for the slow and rapid parts as follows.

$$\phi_{ij,w}=c_{w1}\frac{\varepsilon}{k}\left[\overline{u_k'u_m'}n_kn_m\delta_{ij}-\frac{3}{2}\overline{u_k'u_i'}n_kn_j-\frac{3}{2}\overline{u_k'u_j'}n_kn_i\right]f+c_{w2}\frac{\varepsilon}{k}\left[\phi_{km,2}n_kn_m\delta_{ij}-\frac{3}{2}\phi_{ik,2}n_kn_j-\frac{3}{2}\phi_{jk,2}n_kn_i\right]f \tag{10}$$

The experimental coefficients used in the LRR model are listed in Table 1 and taken from Gibson and Launder [18]. The dissipation of turbulent kinetic energy can be described as follows.

$$\rho U_j\frac{\partial\varepsilon}{\partial x_j}=c_{\varepsilon1}\frac{\varepsilon}{k}\left(-\rho\overline{u_i'u_j'}\frac{\partial U_i}{\partial x_j}\right)-c_{\varepsilon2}\frac{\rho\varepsilon^2}{k}+\frac{\partial}{\partial x_j}\left(\left(\mu+\frac{\mu_t}{\sigma_\varepsilon}\right)\frac{\partial\varepsilon}{\partial x_j}\right) \tag{11}$$

The incompressible, Reynolds time-averaged Navier-Stokes equations without boundary layer simplifications are solved by a finite volume method on a staggered grid system, with scalar quantities being stored at the center of the scalar control volume and all other quantities are stored at the cell faces. The SIMPLE algorithm is adopted in the present solution procedure in order to provide the solution of pressure field. The inlet conditions for velocity and turbulent stresses can be prescribed using the profiles extracted from the experimental data. At the outlet region, the streamwise derivatives of dependent variables are assumed to be negligible. Meanwhile, in the wall boundary conditions, the possible approach to resolve the region $y^+<50$ is to use a low-Reynolds-number model (Wilcox, [19]), but this approach is too costly in general 3D flows. The alternative is to adopt the wall-function approach of Launder and Spalding [20]. The steep gradient of both mean-flow and turbulence quantities also necessitate modification to the turbulent transport equations. The present approach is based on the two-layers methodology details of which may be found in Launder [21].

Results and Discussion

As mentioned previously, Lee et al. [22] showed that the Reynolds stress model (RSM) with the LRR model performed better than other RSMs for prediction of anisotropy of turbulent normal stresses. Hence, in this article, the RSM with the LRR model was used for the calculation. The present study consists of two parts: one is the preliminary calculations (cases 1 and 2) for assessment of the computer code used in this article, and the other is the numerical simulations (cases 3–5) for investigating how different spanwise pressure gradients influence the flow characteristics of an embedded streamwise vortex in a turbulent boundary layer.

Preliminary Calculation (Cases 1 and 2). To begin with, a preliminary calculation for the flow of the Shizawa and Eaton [9] experiment (case 1) was performed, as listed in Table 2, to assess the computer code used for the present work. They took into consideration two types—counter-clockwise rotating and clockwise rotating vortices. In the present calculation, only a counter-clockwise rotating vortex was treated for validation. As seen in Fig. 1, the test section was designed to turn the initially two-dimensional, turbulent boundary layer producing a skewed three-dimensional boundary layer. The inlet two-dimensional flow is turned by a symmetrical wedge. The computational domain was taken for simulation by selecting a half part of the test section, as seen in Fig. 1. Therefore, the inlet conditions for mean velocities

Table 1 The empirical coefficients of the LRR model

c_1	c_2	c_{w1}	c_{w2}
1.8	0.6	0.5	0.3

Table 2 The test cases for calculation

No. of Case	Vortex Type	Feature	Reference
1	Single vortex	30° bend with pressure effect	Shizawa and Eaton (1992)
2	Vortex Pairs	0° bend without pressure effect	Pauley and Eaton (1988)
3	Single vortex	0° bend without pressure effect	Pauley and Eaton (1988)
4	Single vortex	15° bend with pressure effect	Pauley and Eaton (1988)
5	Single vortex	30° bend with pressure effect	Pauley and Eaton (1988)

and turbulent stresses were given from experimental data at slot 1(x=7.6 cm) for calculation. Both sides in the z direction were treated by wall boundary condition. The cross section x-z plane at $y=0$ consists of two conditions—symmetric and wall conditions. A 67×42×35 grid was used for calculation and the present resolution was found to give adequately grid-independent results in our preliminary test.

Figures 2 compare the predicted mean velocity in the streamwise direction at several locations of slots 2 and 5 with experimental data of Shizawa and Eaton [9]. The predictions for slot 2 are in good agreement with experimental data, whereas the predicted mean velocity of slot 5 is somewhat exaggerated on the whole, especially near the wall. Actually, there may exist nonequilibrium flows when flows are affected by a significant secondary flow due to spanwise pressure gradient. Hence, this discrepancy may result from the fact that the wall-function used in this work is not appropriate for the present type of flow because it is intrinsically based on the assumption of local equilibrium.

From Fig. 3, the predictions of turbulent normal stresses were compared against the experimental data at several y locations of slots 2 and 5. As expected, the RSM used for the present calculation predicted well the anisotropy of normal stresses but it failed to predict the amount of stresses accurately. It may be thought that the predicted results acceptably represent the qualitative trends. On the whole, underestimation of turbulent normal stresses was observed. This indicates that even RSM may not predict the turbulent stresses accurately because the flow presently considered is very complex due to the combined effects of secondary flows such as a vortex with the spanwise pressure gradient. Most of all, it is thought that this failure is mainly due to the conventional wall function used for the calculation.

Meanwhile, as another case for assessment, the experiment of Pauley and Eaton [12] was taken for calculating longitudinal vortex pairs embedded in a turbulent boundary layer without spanwise pressure gradient. Figures 4(*a*) and (*b*) represent the computational grid system for case 2 and the schematic diagram for case 4 as will be referred later. More details for calculation can be seen in the reference (Lee et al. [10]). Figure 5 shows the predicted and measured skin friction coefficient. According to experimental observations (Pauley and Eaton [12]), the skin friction coefficients are high near the place where the normal component of velocity near the surface is negative, resulting from the high-momentum fluid convected downward from above. On the other hand, this value is low when the flow is away from the surface. The predicted skin friction coefficient shows the good agreement with the experimental data. Figure 6 represents comparisons of the turbulent normal stresses with the experimental data at 8 cm in the spanwise direction and at 188 cm in the streamwise direction. Good agreement of predictions can be seen compared to experimental data. In particular, the present calculation shows good predictability of anisotropy of turbulent normal stresses. A high level of turbulent normal stresses is seen near the wall, while a reduced level of stresses can be seen as the distance from the wall increases. There are slightly better predictions for case 2 than those of case 1. This may suggest that the conventional wall function may be as serious problem in predicting the nonequilibrium flows generated by vortex and spanwise pressure gradient. Therefore, this problem of wall function may give us some difficulties in effectively predicting the present type of flows affected by the spanwise pressure gradient.

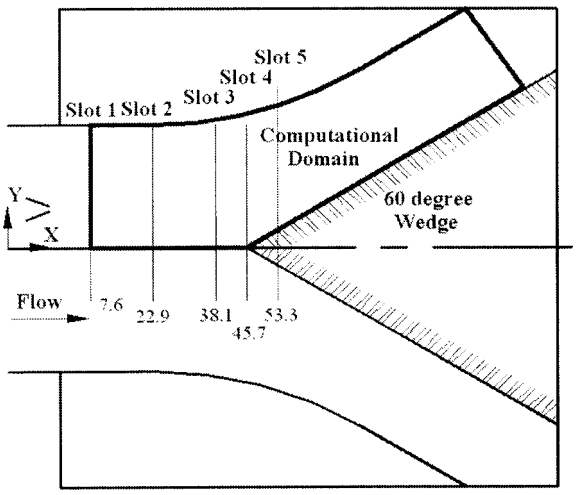

Fig. 1 Schematic diagram for the experiment of Shizawa and Eaton [9]

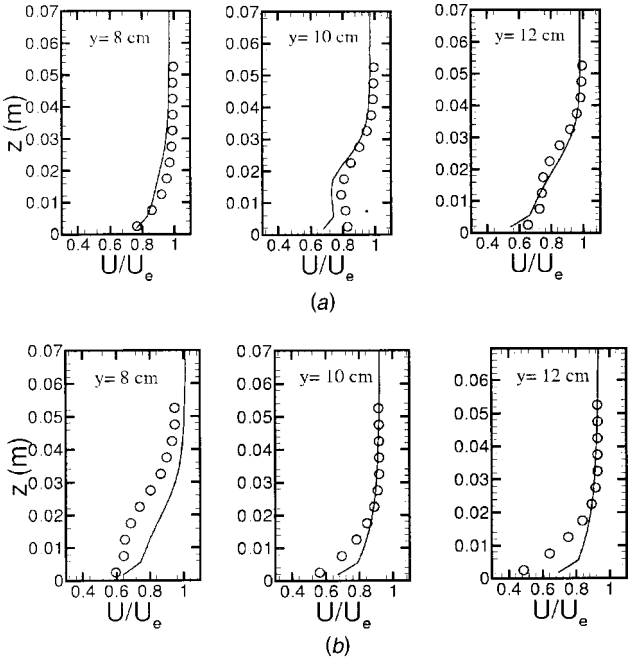

Fig. 2 Comparison between the predictions and the measurements of Shizawa and Eaton [9] for streamwise mean velocity (case 1, Ue=16.5 m/s). (*a*) At slot 2; (*b*) at slot 5

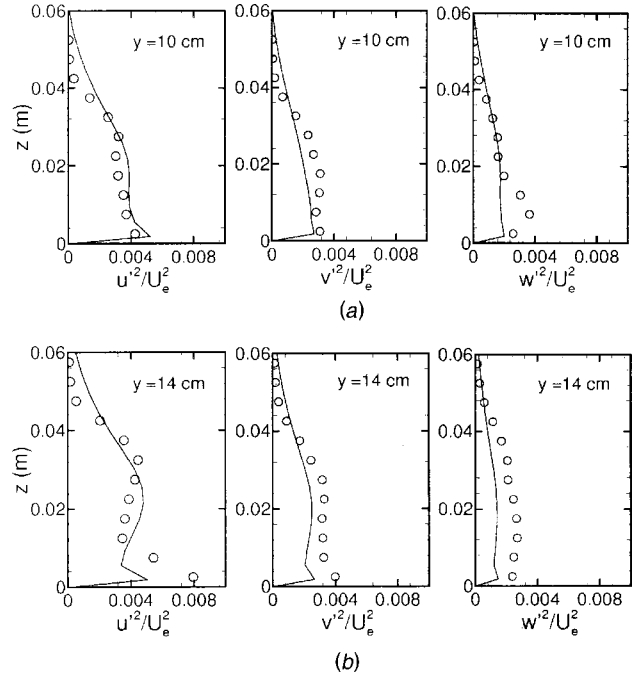

Fig. 3 Comparison of predicted turbulent normal stresses with experimental data of Shizawa and Eaton (1992) (case 1, Ue=16.5 m/s). (*a*) At slot 2; (*b*) at slot 4.

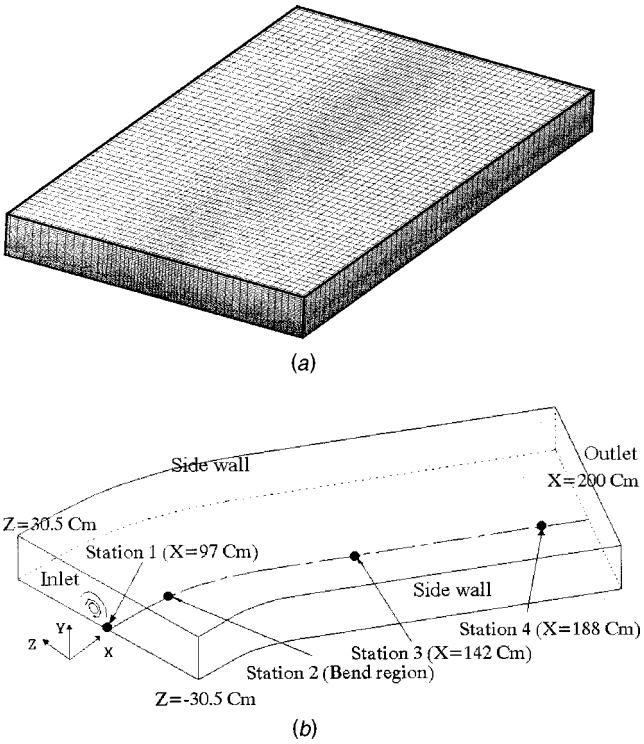

Fig. 4 Schematic diagram for longitudinal vortices with and without the spanwise pressure gradient. (*a*) Grid system for case 2 without spanwise pressure gradient (Pauley and Eaton.); (*b*) schematic diagram for case 4 with turning angle of 15 degree [9].

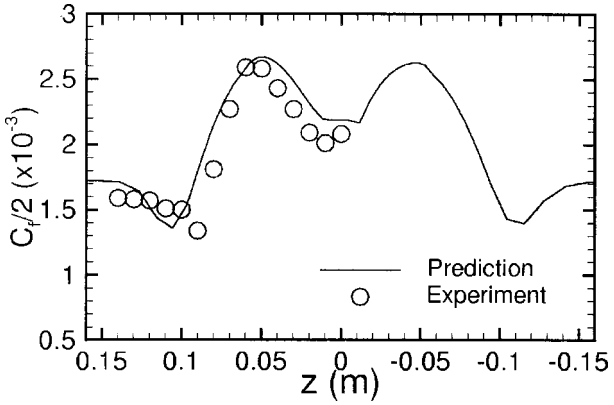

Fig. 5 Comparison of the predicted skin friction coeffcient with experimental data of Pauley and Eaton [11] at station 3 (case 2)

The Influence of Spanwise Pressure Gradient on an Embedded Vortex in a 3DTBL(Cases 3,4,5). As mentioned, an ultimate aim of this article is in examining the mean and turbulent flow characteristics for an embedded streamwise vortex in a turbulent boundary when various pressure gradients are imposed to the flow field in the spanwise direction. In this article, included were three cases set (case 3, 4, 5) arbitrarily on the basis of Pauley and Eaton's [22] experiment. As seen in Fig. 4(*b*), the cross-sectional plane at station 1 was treated as the inlet region for calculation and only a clockwise part of vortex pairs was taken as inlet conditions from the data of Pauley and Eaton [22]. We used the same configuration as Pauley and Eaton [12], except for turning angles such as 0, 15, and 30 degrees for taking into consideration the geometry-induced pressure gradient in the spanwise direction. Hence, in the case of 0 degree, both cases 2 and 3 are of same configuration but in case 3, only a single vortex taken from experiment of Pauley and Eaton [12] is taken into consideration. The plane at station 2 denotes the bend region, which is affected by spanwise pressure gradient for cases 4 and 5. In addition, stations 3 and 4 are the downstream regions where the spanwise pressure gradient is removed and comparisons between predicted and measured results will be presented mainly in stations 2 and 4. The inlet velocities and turbulent quantities were also given from the experimental data of Pauley and Eaton [12]. The calculation was also performed with a $60\times58\times35$ grid and terminated when the convergence criterion of 10^{-5} was satisfied. Using CRAY-T3E, a total time of computation was about 20 hour. As mentioned in the Introduction, it was not easy to find relevant experimental data in the open literature for the present type of flow. Hence, the present article offers the phenomenological trend on the basis of validation from preliminary tests mentioned previously.

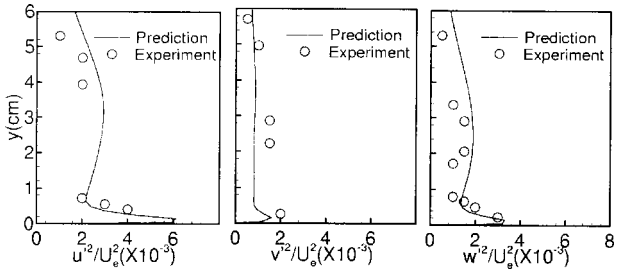

Fig. 6 Comparison of the predicted turbulent normal stresses at Z=8 cm with experimental data of Pauley and Eaton [11] (case 2, Ue=16 m/s)

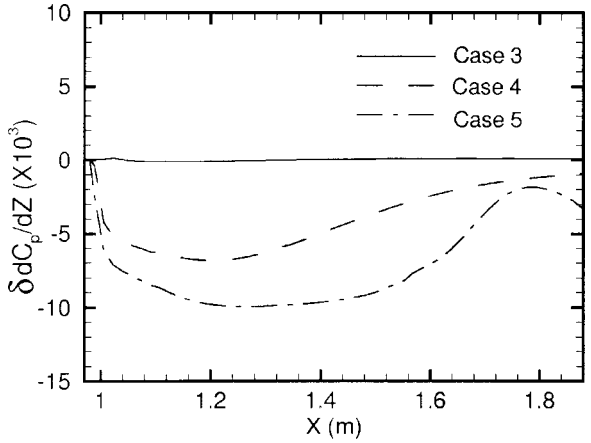

Fig. 7 The predicted spanwise pressure gradients for cases 3, 4, and 5

Figure 7 shows the comparison of spanwise pressure gradients along the streamwise direction. We can see that the spanwise pressure gradient increases with the increase of turning angles. Figures 8(*a*) and (*b*) represent the direction of mean velocity gradient vector for cases 3 and 5, respectively. The direction of velocity gradient vector is defined as follows.

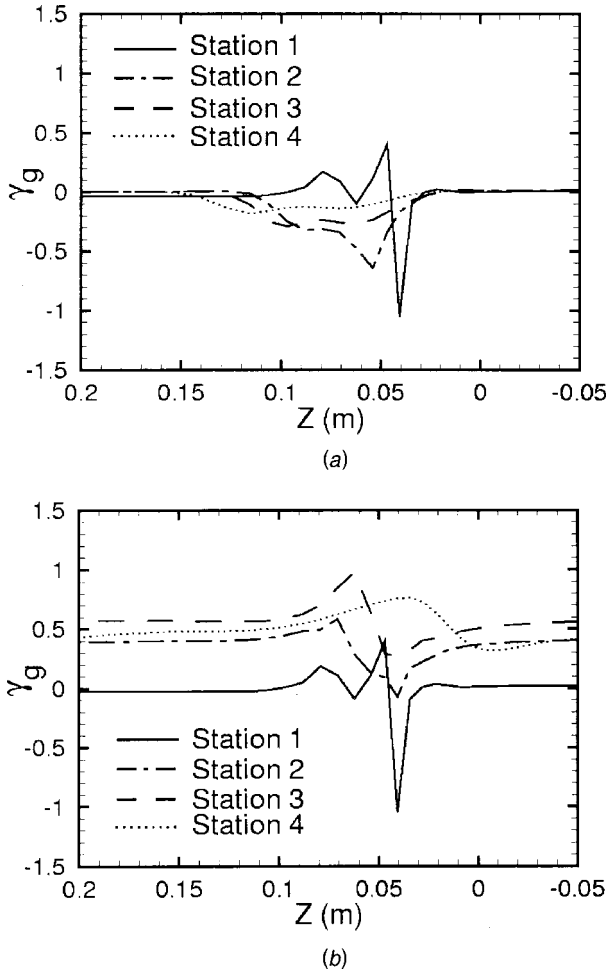

Fig. 8 The calculated direction of velocity gradient vector for cases 3 and 5. (*a*) Case 3; (*b*) case 5.

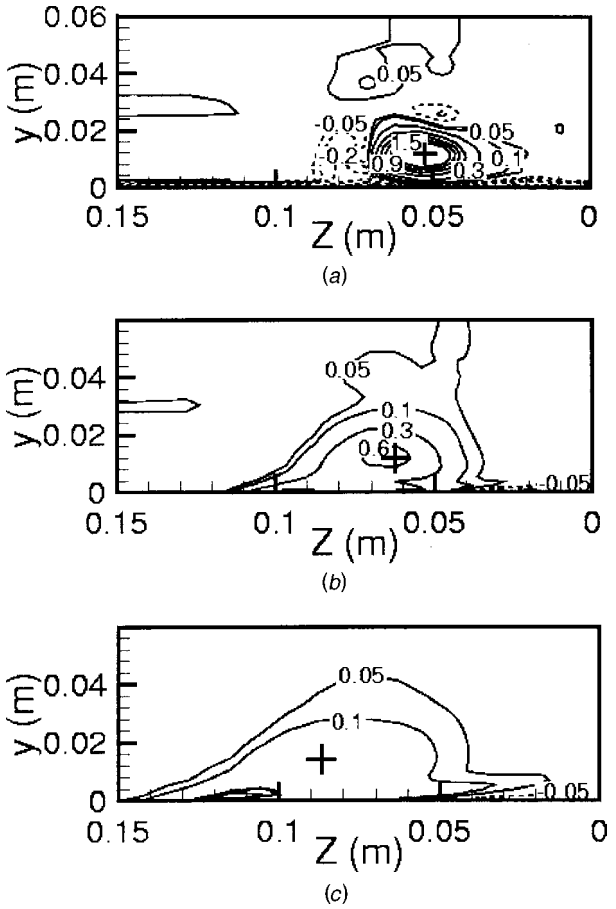

Fig. 9 The contour of normalized streamwise vorticity, Ω_x/U_e, for case 3 at stations 1, 2, and 4. (*a*) Inputs for cases 3, 4, and 5 at inlet region; (*b*) case 3 at station 2; (*c*) case 3 at station 4

$$\gamma_g = \tan^{-1}\left[\frac{\partial W/\partial y}{\partial U/\partial y}\right] \tag{12}$$

This represents the direction of skewed angle between gradients of spanwise and streamwise velocity components. Originally, Schwarz and Bradshaw [23] introduced this parameter in order to explain the lag effect on 3DTBL with spanwise pressure gradient. By using this parameter, we tried to show that there was a skewing effect and a shifting of vortex due to spanwise pressure gradient. In case 3, with turning angle of zero, the velocity gradient vector angle γ_g increases near the vortices, whereas it is nearly zero beyond the region affected by a vortex motion. In the case with turning angle of 30 degrees, it can be seen from Fig. 8(*b*) that there exists some skewing effect even beyond the region affected by the vortex, indicating that the spanwise pressure gradient influences upon the whole region of three-dimensional flow. In case 3, the direction of velocity gradient vector decreases as the flow develops downstream because of decaying vortex due to the effect of turbulent diffusion, as will be discussed later. In case 5, a much higher value of this parameter is found than for case 3 because of the increase of spanwise pressure gradient. In particular, one can see from Fig. 8(*b*) that the position of maximum value is moving from left to right as the vortex develops downstream, compared to case 3. A possible explanation may be that the effect of spanwise pressure gradient is greater than the effect of the image vortex near the wall. From the above results, it is obvious that the spanwise pressure gradient can significantly change the mean structure of flows of the type considered in this article.

Figure 9(*a*) shows the contour of normalized streamwise vor-

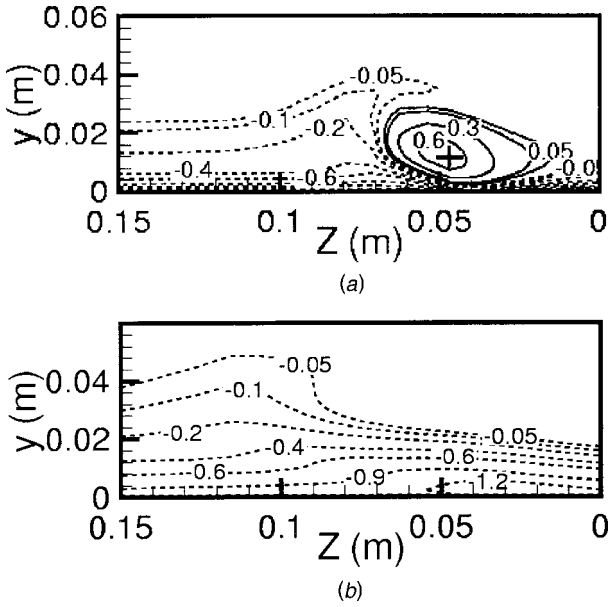

Fig. 10 The contour of normalized streamwise vorticity Ω_x/U_e for case 5 at stations 2 and 4. (*a*) Case 5 at station 2; (*b*) case 5 at station 4.

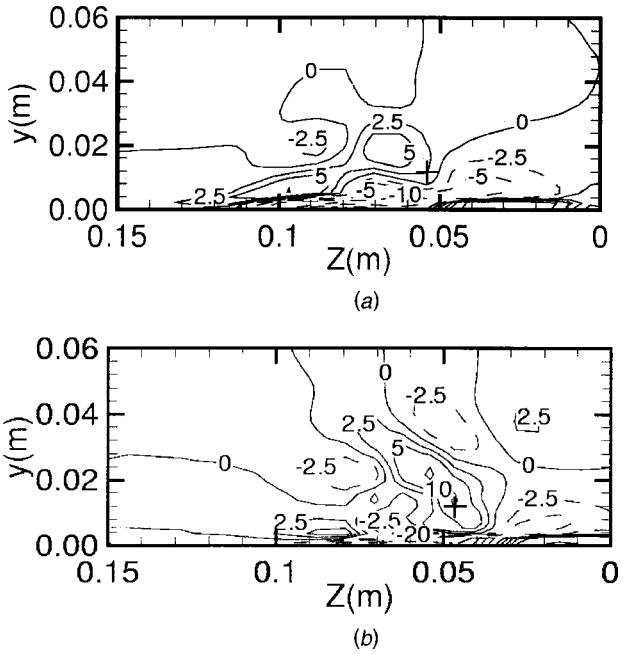

Fig. 11 Normalized contours of turbulent diffusion term. (*a*) Case 2 at station 2; (*b*) case 5 at station 2.

ticity at station 1. This profile taken from the experimental data of Pauley and Eaton [12] was used as inputs for calculation of cases 3–5. The solid and dash lines represent the positive and negative values, respectively, and the cross symbol indicates peak value of primary vorticity. Figures 9(*b*) and (*c*) are the predicted contours for case 3 in bend and downstream regions. Compared to the shape at inlet region, a more elliptic shape can be seen in these regions because of the presence of wall. However, case 5 (Fig. 10) shows quite different shapes from case 3. There exists an enlarged region of negative vorticity due to the spanwise pressure gradient. In other words, this may be because of combined effect, resulting from the fact that the direction of spanwise pressure gradient is of same direction as the spanwise component of negative vorticity near the wall. Consequently, the positive primary vorticity is moving upward due to the enlarged region of negative vorticity and it is decayed gradually due to the turbulent diffusion.

Generally, a way to study the diffusion of vorticity is to examine the vorticity transport equation as follows.

$$U\frac{\partial\xi}{\partial x}+V\frac{\partial\xi}{\partial y}+W\frac{\partial\xi}{\partial z}=\nu\nabla^2\xi+\xi\frac{\partial U}{\partial x}+\eta\frac{\partial U}{\partial y}+\zeta\frac{\partial U}{\partial z}+\frac{\partial}{\partial x}\left(\frac{\partial\overline{u'v'}}{\partial z}-\frac{\partial\overline{u'w'}}{\partial y}\right)+\frac{\partial^2}{\partial y\partial z}(\overline{v'^2}-\overline{w'^2})+\left(\frac{\partial^2}{\partial z^2}-\frac{\partial^2}{\partial y^2}\right)\overline{v'w'} \tag{13}$$

where, ξ, η, and ζ denote the components of vorticity in x, y, and z directions, respectively. As seen in Eq. (13), the mean convection of vorticity on the left-hand side are affected by the gradient in the anisotropy of the normal stresses in the sixth term on the right-hand side. This term is important to the analysis of the turbulent diffusion of vorticity because it is capable of generating or dissipating streamwise vorticity. The effects of this mechanism are present mainly in the vicinity of the vortex and the tongue of induced vorticity in the upwash region. Figure 11 represents the predicted contours of gradient in the anisotropy of the normal stresses. In both cases, the maximum value of this term, $\partial^2(\overline{v'^2}-\overline{w'^2})/\partial y\partial z$, can be found near the wall and in the vicinity of the vortex. In particular, the higher level of this gradient occurs in case 5 with the spanwise pressure gradient. Since the negative values of this term may contribute to the attenuation of vorticity, it can be thought that the vorticity of case 5 may be diffused much more rapidly than that of case 3 with no spanwise pressure gradient.

In Fig. 12, the predicted skin friction coefficients were compared at station 2 in order to show the effects of spanwise pressure gradient. Compared to case 3, the predictions of cases 4 and 5 are shifted to the negative z-direction, showing the movement of vortex due to the spanwise pressure gradient. Generally, similar trends to the case without spanwise pressure gradient can be observed in the upwash and downwash regions for cases 4 and 5, except for the location of peak values.

The predictions of turbulent normal stresses at station 4 are presented in Fig. 13. The turbulent normal stresses increase in cases 4 and 5 with spanwise pressure gradient because the production in Reynolds stress transport equation is increased by additional rates of strain, generated by the spanwise pressure gradient. The increase of the $\overline{v'^2}$ turbulent normal stress without

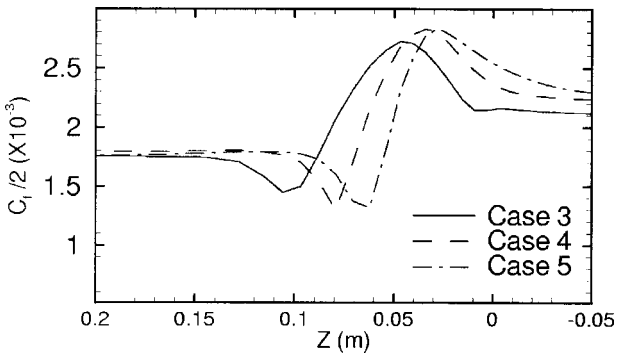

Fig. 12 The predicted skin friction coeffcient for three cases at station 2

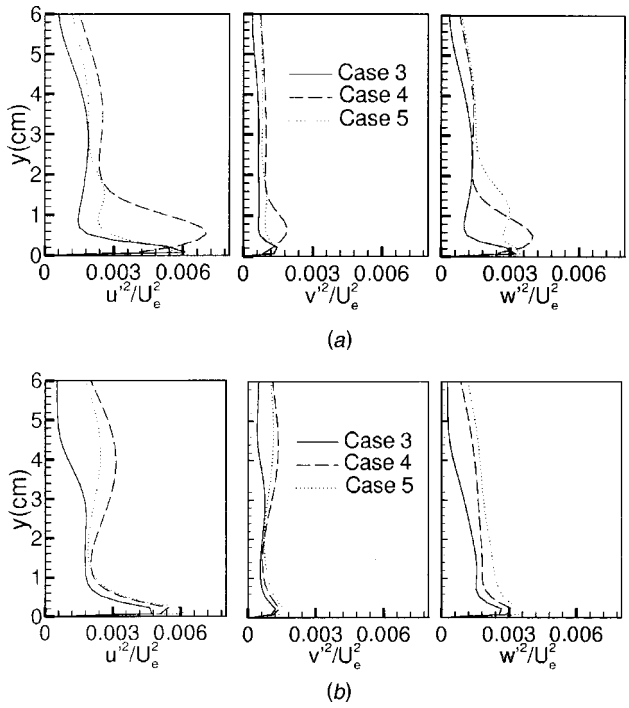

Fig. 13 The calculated turbulent normal stresses for three cases at Z=6 cm and 10 cm. (*a*) At Z=6 cm; (*b*) at Z=10 cm.

production may be due to the increase of the pressure-strain redistribution terms by which the production of $\overline{u'^2}$ and $\overline{w'^2}$ can be increased. In addition, it can be seen that the $\overline{v'^2}$ stress is smaller than the $\overline{u'^2}$ and $\overline{w'^2}$ stresses because the normal component of mean velocity is decreased due to the wall-proximity effect. The overall trends of $\overline{w'^2}$ stress are similar to those of the $\overline{u'^2}$ stress, except for their magnitude. Meanwhile, it can be seen from Fig. 13 that the turbulent normal stresses in case 4 are higher at both locations than that in case 5 with higher spanwise pressure gradient, in spite of the fact that the amount of spanwise pressure gradient of case 5 is greater than that of case 4 as seen in Fig. 7. This may be because the location of the vortex center for each case may be different in the spanwise direction. In other words, the compared location of normal stress is not selected along the center of vortex but at fixed location such as $Z=6$ cm and 10 cm. Therefore, it may be difficult to draw such a conclusion from Fig. 13 for the relation between the spanwise pressure gradient and the turbulent stresses. In addition, higher values of turbulent normal stresses are observed near the wall but in case 4, the peak values of turbulent normal stresses exist at farther locations from the wall relative to other cases. This may be due to the existence of interface between primary and secondary vortices. At this interface, there may be the maximum value of mean velocity gradient because the sign of secondary vortex is opposite to that of primary vortex.

Conclusions

In the present article, numerical simulations were carried out for three cases with different values of spanwise pressure gradient in order to investigate the effects of spanwise pressure gradient on an embedded streamwise vortex in a turbulent boundary layer. The conclusions are as follows.

1 From the preliminary calculations (cases 1 and 2), the predicted results are acceptable in the respect of qualitative trends and the RSM with LRR model accurately predicts the anisotropy of normal stresses. However, there are some discrepancies for the prediction of turbulent normal stresses near the wall. This may be due to the fact that the wall-function used in this work is not appropriate for the present type of flows because it is intrinsically based on the assumption of local equilibrium. Therefore, this problem of wall function may give us some difficulties in effectively predicting the present type of flows affected by the spanwise pressure gradient.

2 In cases with the spanwise pressure gradient (cases 4 and 5), the primary streamwise vorticity decays more rapidly than the case with no pressure effects due to the increases of turbulent diffusion $\partial^2(\overline{v'^2}-\overline{w'^2})/\partial y\partial z$ in the vorticity transport equation. The turbulent normal stresses increase for all of three cases, resulting from the increase of the production of turbulent normal stresses due to the spanwise pressure gradient.

Actually, the present paper only offers the qualitative trend for the effects of spanwise pressure gradient on an embedded streamwise vortex in a turbulent boundary layer. For greater accuracy, it is thought that more sufficient experimental data for the present type of flows in this article should be provided.

Acknowledgments

This work was funded by Chung-Ang University Grant in 1998. Also, we wish to express our gratitude to Professor John K. Eaton of Stanford University for his assistance.

References

[1] Belik, L., 1973, ''The Secondary Flow about Circular Cylinders Mounted Normal to a Flat Plate,'' Aero. Quarterly, **24**, pp. 47–54.
[2] Shabaka, I. M. M. A., Bradshaw, P., 1981, ''Turbulent Flow Measurements in an Idealized Wing/Body Junction,'' AIAA J., **19**, No. 2, pp. 131–312.
[3] Fleming, J. L., Simpson, R. L., Cowling, J. E., and Devenport, W. J., 1993, ''An Experimental Study of a Turbulent Wing-Body Junction and Wake Flow,'' Exp. Fluids, **14**, pp. 336–378.
[4] Pearcy, H. H., 1961, ''*Boundary Layer and Flow Control*, G. V. Lachmann, Vol. IV.
[5] Shabaka, I. M. M. A., Mehta, R. D., and Bradshaw, P., 1985, ''Longitudinal Vortices Imbedded in Turbulent Boundary Layer. Part I. Single Vortex,'' J. Fluid Mech., **155**, pp. 37–57.
[6] Mehta, R. D., and Bradshaw, P., 1988, ''Longitudinal Vortices Imbedded in Turbulent Boundary Layer,'' J. Fluid Mech., **188**, pp. 529–546.
[7] Westphal, R. V., Eaton, J. K., and Pauley, W. R., 1987, ''Interaction Between a Vortex and a Turbulent Boundary Layer in a Streamwise Pressure Gradient,'' *Turbulent Shear Flows 5*, Springer-Verlag, Vol. 3, pp. 266–277.
[8] Eibeck, P. A., and Eaton, J. K., 1987, ''Heat Transfer Effects of a Streamwise Vortex Imbedded in a Turbulent Boundary Layer,'' ASME J. Heat Transfer, **109**, pp. 16–24.
[9] Shizawa, T., and Eaton, J. K., 1992, ''Turbulence Measurements for a Longitudinal Vortex Interaction with a Three-Dimensional Turbulent Boundary Layer,'' AIAA J., **30**, No. 1, pp. 49–55.
[10] Lee, S. H., Ryou, H. S., and Choi, Y. K., 1999, ''Heat Transfer in a Three-Dimensional Turbulent Boundary Layer with Longitudinal Vortices,'' Int. J. Heat Mass Transf., **42**, pp. 1521–1534.
[11] Launder, B. E., Reece, G. J., and Rodi, W., 1975, ''Progress in the Development of a Reynolds-Stress Turbulence Closure,'' J. Fluid Mech., **68**, pp. 537–566.
[12] Pauley, W. R., and Eaton, J. K., 1988, ''The Fluid Dynamics and Heat Transfer Effects of Streamwise Vortices Embedded in a Turbulent Boundary Layer,'' Report MD-51, Department of Mechanical Engineering, Stanford University.
[13] Shir, C. C., 1973, ''A Preliminary Study of Atmospheric Turbulent Flow in the Idealized Planetary Boundary Layer,'' J. Atmos. Sci., **30**, pp. 1327–1339.
[14] Rotta, J. C., 1951, ''Statistischer Theorie Nichthomogener Turbulenz,'' Z. für Physik,'' **129**, pp. 543–572.
[15] Rotta, J. C., 1979, ''A Family of Turbulence Models for Three-Dimensional Boundary Layers,'' *Turbulent Shear Flows I*, Springer-Verlag, New York, pp. 267–278.
[16] Naot, D., Shavit, A., and Wolfshtein, M., 1970, ''Interaction Between Components of the Turbulent Velocity Correlation Tensor,'' Isr. J. Technol., **8**, p. 259.
[17] Bradshaw, P., 1973, ''The Strategy of Calculation Methods for Complex Turbulent Flows,''Imperial College Aero. Report, No. 73-05.
[18] Gibson, M. M., and Launder, B. E., 1978, ''Ground Effects on Pressure Fluctuations in the Atmospheric Boundary Layer,'' J. Fluid Mech. **86**, pp. 491–511.

[19] Wilcox, D. C., 1993, Turbulence Modeling for CFD, DCW Industries, Inc. La Canada, CA.
[20] Launder, B. E., and Spalding, D. B., 1974, ''The Numerical Computation of Turbulent Flow,'' Comput. Methods Appl. Mech. Eng., **3**, pp. 269–289.
[21] Launder, B. E., 1986, ''Low-Reynolds-Number Turbulence Near Walls,'' Rep., TFD/86/4, Department of Mechanical Engineering, UMIST.
[22] Lee, I., Ryou, H. S., Lee, S. H., and Soo, C., 2000, ''Comparison of Two-Equation Model and Reynolds Stress Models with Experimental Data for the Three-Dimensional Turbulent Boundary Layer in a 30 Degree Bend,'' KSME International Journal, **14**, No. 1, pp. 93–102.
[23] Schwarz W. R., and Bradshaw, P., 1992, ''Three-Dimensional Turbulent Boundary Layer in a 30 Degree Bend: Experiment and Modeling,'' Rept. MD-61, Thermosciences Division, Stanford University.

Effects of Bulk Flow Pulsations on Phase-Averaged and Time-Averaged Film-Cooled Boundary Layer Flow Structure

I.-S. Jung
Graduate Student,
Turbo and Power Machinery Research Center,
Department of Mechanical Engineering.
Seoul National University, Seoul 151-742, Korea

P. M. Ligrani
Fellow ASME
Professor,
Convective Heat Transfer Laboratory,
Department of Mechanical Engineering,
50 S. Central Campus Drive, University of Utah,
Salt Lake City, UT 84112

J. S. Lee
Mem. ASME
Professor,
Turbo and Power Machinery Research Center,
Department of Mechanical Engineering,
Seoul National University, Seoul 151-742, Korea

Flow structure in boundary layers film cooled from a single row of round, simple angle holes, and subject to bulk flow pulsations, is investigated, including phase-averaged streamwise velocity variations, and alterations of time-averaged flow structure. The bulk flow pulsations are in the form of sinusoidal variations of velocity and static pressure, and are similar to flow variations produced by potential flow interactions and passing shock waves near turbine surfaces in gas turbine engines. Injection hole length to diameter ratio is 1.6, time-averaged blowing ratio is 0.50, and bulk flow pulsation frequencies range from 0–32 Hz, which gives modified Strouhal numbers from 0–1.02. Profiles of time-averaged flow characteristics and phase-averaged flow characteristics, measured in the spanwise/normal plane at $x/d=5$ and $z/d=0$, show that effects of pulsations are larger as imposed pulsation frequency goes up, with the most significant and dramatic changes at a frequency of 32 Hz. Phase shifts of static pressure (and streamwise velocity) waveforms at different boundary layer locations from the wall are especially important. As imposed pulsation frequency varies, this includes changes to the portion of each pulsation phase when the largest influences of static pressure waveform phase-shifting occur. At a frequency of 32 Hz, these phase shifts result in higher instantaneous injectant trajectories, and relatively higher injectant momentum levels throughout a majority of each pulsation period. [DOI: 10.1115/1.1383972]

Introduction

Interest in the effects of large-scale bulk flow pulsations on film cooling as applied to the turbine surfaces of gas turbine engines has been increasing in recent years. Such bulk flow pulsations result from the relative motion of adjacent blade rows because of potential flow interactions in subsonic and transonic turbines, and because of passing shock waves in transonic turbines. Flow unsteadiness in turbines is also present due to passing wakes, as well as freestream turbulence generated in the combustion chamber. Because of the detrimental influences of these modes of unsteadiness on surface heat transfer and the protection provided by film cooling, detailed experimental data illustrating the influences of these phenomena are needed for the design of gas turbine blade components, as well as for the development of more widely applicable numerical models and prediction schemes.

One of the earliest studies on flow pulsation influences on film cooling is described by Rigby et al. [1], who examine the effects of simulated nozzle guidevane shock waves and wakes on an array of turbine blades placed in a linear cascade. Significant effects of unsteadiness are apparent on film cooling from two separate rows of holes placed on a blade suction surface. However, the film cooling from holes placed on the pressure surface are only slightly affected by the imposed unsteadiness. Abhari and Epstein [2] describe rotor heat transfer results from a short-duration blow-down turbine test facility. The authors indicate that families of passing shock waves and potential flow interactions cause the time-averaged heat transfer rate to increase by 12 percent on the suction surface downstream of two rows of holes (compared with values measured with no pulsations). Five percent increases are observed on the pressure surface downstream of three rows of holes. Later studies [3–6] provide additional data on the dramatic influences of shock waves and/or potential flow interactions on film cooling. In one case [5], reductions of adiabatic film effectiveness by as much as 64 percent are predicted on the pressure surface of a rotor blade. These are connected to time-averaged magnitudes of unsteady surface heat flux which are 230 percent greater than steady-state predictions.

Other recent work considers the influences of different forms of flow unsteadiness on surface heat transfer, temperature fields, and film cooling performance in two-dimensional cascades [7–10], and annular cascades [11,12]. Of these studies, Nix et al. [7] show a maximum increase of heat flux of 60 percent due to passing shock waves when data are averaged over a single blade passing event. In contrast, Popp et al. [8] present measurements from the suction sides of transonic rotor blades, which show that film effectiveness and heat transfer coefficient data are not affected appreciably by passing shock waves. A later study by the same authors [10] indicates that unsteady heat transfer fluctuations are due mostly to temperature fluctuations from passing shock waves, rather than significant alterations to heat transfer coefficients and film effectiveness magnitudes by the passing shock waves.

Another recent study [13] includes flow visualization results obtained downstream of round, simple angle $l/d=4$ film cooling holes on a flat plate over a range of blowing ratios when bulk flow pulsations are imposed. Two distinct types of injectant flow behavior are observed, quasi-steady, and non-quasi-steady, which are separated by magnitudes of Sr_c less than or greater than 1–2. According to follow-up studies [14–16], the largest changes to surface film effectiveness distributions, and to time-averaged film cooled boundary layer structure are often present with higher-frequency non-quasi-steady behavior. Other recent investigations examine the effects of bulk flow pulsations on film cooling from different length injection holes [16], from two rows of holes [17], from spanwise oriented holes [18], from holes with different blowing ratios [19], and from holes with different density ratios

Contributed by the Fluids Engineering Division for publication in the JOURNAL OF FLUIDS ENGINEERING. Manuscript received by the Fluids Engineering Division August 31, 2000; revised manuscript received March 5, 2001. Associate Editor: K. Zaman.

[20]. Of these studies, Bell et al. [19] and Ligrani and Bell [20] provide correlations which give film and freestream conditions when cooling protection is reduced due to bulk flow pulsations. According to these correlations and the data presented, acceptable levels of protection are present over wider ranges of imposed pulsation frequency n as either density ratio ρ_c/ρ_∞, length-to-diameter ratio l/d, or time-averaged blowing ratio $\overline{m}$ become larger.

In the present paper, attention is on the effects of pulsations of static pressure and streamwise velocity induced throughout the flow field as they alter the flow structure in boundary layers film cooled using a single row of holes. These pulsations are arranged to model similar variations which exist in the first turbine stages of operating engines, especially ones due to potential flow interactions, and to a lesser extent, to passing families of shock waves. New experimental data and information are presented on: (i) the variations of phase-averaged streamwise velocity which occur through the period of each pulsation, and (ii) time-averaged flow structure at different experimental conditions (including profiles of all three velocity components $\overline{u},\overline{v},\overline{w}$, three normal Reynolds stresses $\overline{u'^2},\overline{v'^2},\overline{w'^2}$, and two Reynolds shear stresses $-\overline{u'v'},\overline{u'w'}$). Unlike results presented in an earlier paper [15], these data are given for different flow pulsation frequencies at one time-averaged blowing ratio $\overline{m}$ of 0.5. Of particular interest are the effects of different phase-shifts of pulsating streamwise velocity (and pulsating static pressure) on flow structure. This is because these phase shifts not only have a large effect on the behavior of the film and the surrounding flow field, but also because they provide insight into flow field alterations due to the imposed pulsations. The new data presented, which contain this flow field information, are then also useful for the development of numerical prediction schemes.

Experimental Apparatus and Procedures

The present experiment is conducted on a large scale with a flat plate test section, low speeds, and constant properties to allow detailed probing of flow features, and to isolate the interactions between the film cooling, imposed pulsations, and boundary layer. Important parameters are scaled so that nondimensional forms match transonic turbine operating conditions.

Wind Tunnel. The wind tunnel is open-circuit and subsonic, with a 6.25 to 1 contraction ratio nozzle. The nozzle leads to the test section which is a rectangular duct 3.0 m long and 0.4 m wide. At a freestream velocity of 10 m/s, flow at the test section inlet shows excellent spatial uniformity, freestream streamwise velocity variations less than 0.5 percent, and a freestream turbulence level less than 0.2 percent. A schematic of the test section, including the coordinate system and injection hole geometry, is shown in Fig. 1. A boundary layer trip is located on the test plate just downstream of the nozzle exit.

The center of the injection holes is located 24 hole diameters downstream of the trip. Injection hole diameter d is 25 mm. The five film cooling holes are placed in a single row with spanwise spacing of 3 hole diameters. Each hole is oriented in a streamwise/normal plane (i.e., with a simple angle orientation) inclined at 35 degrees angle from the test surface. The air used for the injectant first flows through an orifice followed by a heat exchanger and a plenum chamber. Pressure drops across the orifice plate are measured to deduce injectant mass flow rates. The heat exchanger provides means to heat the injectant above ambient temperature, but is not used to obtain any of the results presented in this paper. The interior dimensions of the plenum chamber, which supplies injectant to the film holes, are 0.58 m by 0.48 m by 0.12 m. Film hole entrances are located on the side of the plenum with the largest surface area, located on the top.

The freestream mean velocity is fixed at 10 m/s and the Reynolds number (based on measured distance from the leading edge of the trip) at the hole center is 614,000. Ratios of boundary layer thickness to hole diameter δ/d, displacement thickness to hole diameter, and momentum thickness to hole diameter at the same location are 1.02, 0.12 and 0.08, respectively. The time-averaged blowing ratio $\overline{m}$ is 0.5. Corresponding injectant Reynolds number (based on hole diameter and average injectant velocity) is 7800. The ratio of injectant to freestream density is 1.0.

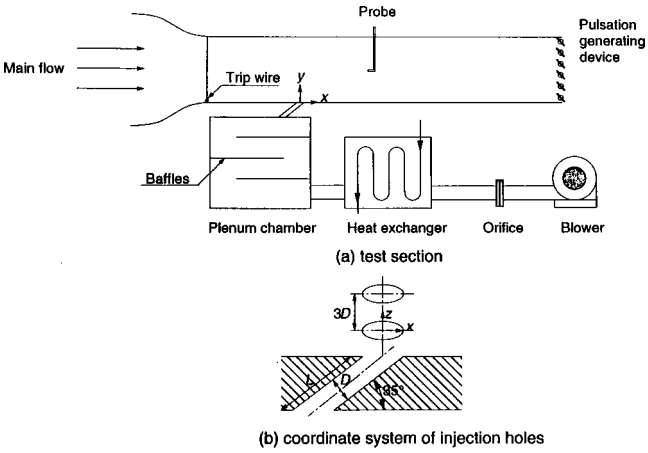

Fig. 1 Schematic drawings of (*a*) test section and coordinate system and (*b*) injection hole geometry and coordinate system

Velocity Component Measurements. A crossed hot-wire probe, with 5 μm diameter and 1.25 mm long sensing wires, and driven using constant temperature anemometer bridges is used to measure instantaneous magnitudes of all three velocity components. Different components are measured by orienting the crossed-hot wire probe in different measurement planes. These hot-wire probes are calibrated in the wind tunnel freestream, including yaw calibrations used to determine effective angles of the two sensors in the probe. The frequency response of the electronic components of these constant temperature anemometry systems is about 20 kHz. Time-averaged quantities are obtained using a multimeter with a resolution of 10 nV which corresponds to a measurement error of ± 0.05°C. Time varying velocities are recorded using a digital data acquisition system, which includes a multiplexer and an analog-to-digital converter.

Phase-averaged quantities are deduced from instantaneous velocity time records using a decomposition based on the three different types of timewise variations experienced by the flow. With imposed periodic flow, the instantaneous streamwise velocity is given by $u=\overline{u}+\tilde{u}+u'$, where $\overline{u}$ is the time-averaged streamwise velocity, $\tilde{u}$ is the phase-averaged periodic velocity component, and u' is the fluctuating velocity component. The time period used in the determination of phase-averaged values is based on the angular speed of the encoder of the motor used to drive the rotating shutter blades which are used to pulsate the flow. One motor rotation corresponds to two flow pulsation periods. Signals from more than 500 flow pulsation periods are ensemble-averaged to obtain each phase-average. Data are sampled digitally to obtain 500 data points over each flow pulsation period. Individual phase-averaged wave forms are determined at 100 equally spaced times through each flow pulsation period.

Uncertainty Magnitude Estimates. Uncertainty estimates are based on 95 percent confidence levels, and determined using the methods described by Kline and McClintock [21] and by Moffat [22]. The uncertainty of the phase-averaged velocity $\tilde{u}$ is about 2.5 percent, and the uncertainty of $\overline{u}$ is about 1.5 percent. Uncertainty of $\overline{u'^2}$ is typically 4 percent. Uncertainties of $\overline{v'^2}$, $\overline{w'^2}$, $-\overline{u'v'}$, and $\overline{u'w'}$ are each about 10 percent.

Generation of Bulk Flow Pulsations. Static pressure pulsations are produced by an array of six shutter blades, which are driven by a DC motor and a timing belt, and extend across the span of the exit of the wind tunnel test section. Periodic blockage is produced by the shutter blades as they rotate. Their sizes relative to the cross-sectional area of the test section exit set the amplitudes of the imposed flow pulsations. Each shutter has 25.0 mm width (which, when perpendicular to the flow gives maximum blockage), and 1.5 mm thickness (for minimum blockage) across the 0.28 m high by 0.4 m wide exit area. This gives a ratio of maximum blockage area to the total open test section area of 0.53. This arrangement is advantageous because the static pressure changes without significant total pressure variations, and reasonably high frequencies of pulsation can be produced, often in a sinusoidal form [16].

With the arrangement employed here, freestream pulsation amplitudes, $(\tilde{u}_{\infty\,\max}-\tilde{u}_{\infty\,\min})/2\overline{u}_{\infty}$, range from 18 percent at a pulsation frequency of 2 Hz, to about 6 percent at a pulsation frequencies of 16 Hz and 32 Hz. At higher imposed frequencies, the amplitude thus stays about constant. These magnitudes depend upon wind tunnel test section dimensions as well as the variations of flow blockage which are produced as pulsation vanes rotate. Lower amplitudes at higher imposed pulsation frequencies result because of flow inertia, which also causes timewise variations of the streamwise velocity to lag behind the static pressure pulsations imposed at the test section outlet [15].

Results and Discussion

Bulk Flow Pulsation Characteristics. For the results which follow, magnitudes of the coolant Strouhal number Sr_c range from 0–10, compared to values from 0.2–6.0 in the first stages of operating transonic turbines. Ligrani and Bell [20] present a modified Strouhal number Sr_x, given by

$$\mathrm{Sr}_x = \mathrm{Sr}_c/[\overline{m}^{0.6}(\rho_c/\rho_\infty)^{2.0}(l/d)^{2.0}] \tag{1}$$

which provides better correlation of film cooled pulsation data, than given by the coolant Strouhal number Sr_c alone. According to these authors, significant reductions in film protection due to the pulsations are present when Sr_x exceeds .055–.070 (note that Sr_x ranges from 0–0.30 in the present study). This means that acceptable levels of protection ($\mathrm{Sr}_x < .055-.070$) are present over smaller ranges of imposed pulsation frequency f as either $\overline{m}$, ρ_c/ρ_∞, or l/d becomes smaller. This is a consequence of complicated flow physics, and because the protection provided by film cooling *generally* (but not always) degrades as the pulsation frequency f increases.

From Ligrani et al. [15] and Seo et al. [16], instantaneous freestream velocity variations are strongly sinusoidal at lower frequencies, but then become more sawtooth shaped at higher frequencies from 20 Hz–32 Hz. Such behavior is evidenced from measured waveforms and associated spectra of instantaneous streamwise velocity at imposed pulsation frequencies from 2 Hz [15]–32 Hz [16]. The shapes of velocity waveforms associated with the pulsations are also affected by the resonant frequency of the wind tunnel. According to Al-Asmi and Castro [23], wave forms at frequencies which are multiples of the wind tunnel resonant frequency are more likely to be sinusoidal than waveforms at other frequencies.

Also important are phase shifts of boundary layer flow properties. These occur in turbulent boundary layers subject to imposed pulsations, even without film cooling, where wall shear stress (and near-wall streamwise velocity) are phase-shifted by larger amounts relative to pulsating freestream velocity as the imposed pulsation frequency increases [24]. With film cooling added, the phase shifts between static pressure and streamwise velocity at different points in the flow are even more complex.

Of particular importance are phase shifts between instantaneous static pressure at the exits of the film cooling holes p_c, and the instantaneous freestream static pressure at the same streamwise location p_∞. As a result of such activity, phase shifts also occur between the pulsating components of the instantaneous injectant velocity u_c and instantaneous freestream velocity u_∞. The importance of such variations is illustrated by the traces presented in Fig. 2. The hypothetical data in this figure show that, as the phase of the injectant velocity shifts relative to the phase of the freestream velocity, the amplitude and waveform of the instantaneous velocity ratio u_c/u_∞ changes significantly. For example, the ''phase 0'' distribution (i.e., no phase shift between u_c and u_∞) in Fig. 2 gives constant instantaneous velocity ratio u_c/u_∞. In contrast, the ''phase 1'' and ''phase 2'' distributions give velocity ratios u_c/u_∞ with important timewise variations (which are different from each other because phase shifts between u_c and u_∞ are different). Note that the peak-to-peak amplitude of each u_c waveform shown in Fig. 2(*b*) is the same.

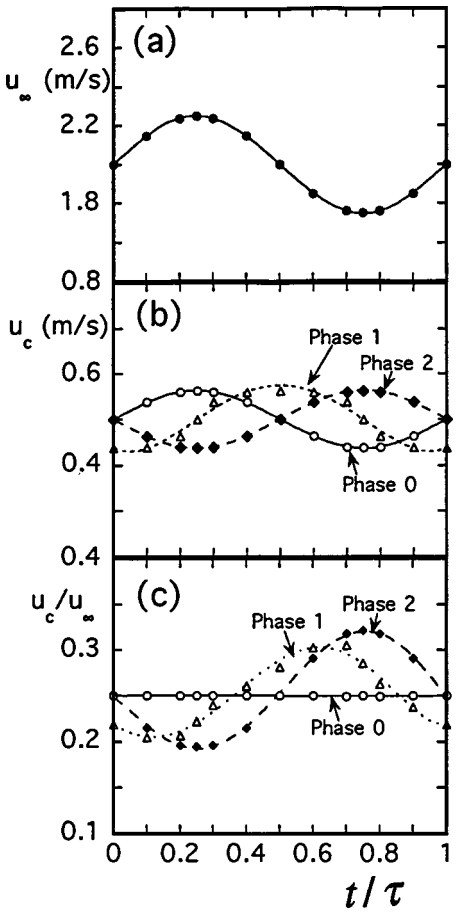

Fig. 2 Typical timewise variations of: (*a*) freestream velocity, (*b*) injectant velocity, and (*c*) injectant to freestream velocity ratio, as the injectant velocity waveform is phase-shifted relative to the freestream velocity waveform. Phase 0: 0 degrees or 0 π phase shift. Phase 1: 90 degrees or $\pi/2$ phase shift. Phase 2: 180 degrees or π phase shift.

Phase shifts between u_c and u_∞ are thus important because, without them, u_c/u_∞ is generally about constant in the pulsating flow field. Such phase shifts of velocity waveforms are due to shifts of the static pressure waveform through the turbulent boundary layer, which are further altered by the presence of the film cooling. In Fig. 2(*c*), both the phase and amplitude of the different velocity ratio signals changes as u_c is phase-shifted relative to u_∞. Data presented by Seo et al. [16] provide evidence of larger phase shifts between instantaneous p_c and p_∞ (and hence, also between instantaneous injectant velocity u_c and instantaneous freestream velocity u_∞) as pulsation frequency increases. Such variations result in changes to the injectant flow rate and velocity

ratio u_c/u_∞ over one pulsation period, and hence, to alterations of both instantaneous and time-averaged injectant trajectories, coverage, and overall protection.

Effects of Pulsation Frequency on Phase-Averaged Streamwise Velocity Profiles. The effects of phase-shifts on injectant trajectories and on phase-averaged boundary layer structure are illustrated by results presented in Figs. 3, 4, and 5 for $\overline{m}=0.5$, $l/d=1.6$, $x/d=5$, and $z/d=0$. Presented are profiles of streamwise velocity, determined at different phases through pulsation cycles, for imposed pulsation frequencies of 2 Hz, 16 Hz, and 32 Hz, respectively. Note that each phase-averaged velocity value (at each boundary layer location) is determined from an ensemble-average over more than 500 flow pulsation periods.

The results presented in Fig. 3 for $f=2$ Hz correspond to $\mathrm{Sr}_c=.094$, $\mathrm{Sr}_\infty=.032$, and $\mathrm{Sr}_x=.064$. Such low coolant Strouhal number values generally give quasi-steady film cooling behavior [13,15]. When the flow is quasi-steady at all times (which is not entirely the case for the Fig. 3 results), the film trajectory and distribution at each instant in time are then similar to the steady trajectory and distribution which would exist at the same instantaneous flow condition. As a result, the film follows a continuous stream away from the film cooling holes (at each instant in time) as it pulsates in time. As the bulk pulsations are imposed, static pressure then varies such that high values correspond to low streamwise velocities in the freestream and outer parts of the boundary layer, and low static pressure values correspond to high streamwise velocities in the freestream and outer parts of the boundary layer (relative to time-averaged velocity magnitudes). Low static pressures at the exits of the film cooling holes also correspond to instantaneously high values of injectant trajectory, momentum, mass output, and blowing ratio (all relative to time-averaged values). High near-wall static pressures then produce opposite relative magnitudes of these injectant quantities relative to time-averaged values.

Now, consider phase shifts of static pressure through the film cooled boundary layer. If there are *no* such *phase shifts*, then high streamwise velocities in the freestream and outer boundary layer correspond with high values of injectant velocity and relatively high injectant trajectories (through a part of each pulsation cycle). Low freestream values then correspond to low magnitudes of injectant velocity and relatively low injectant trajectories. Examining Fig. 3 for $f=2$ Hz indicates that relative magnitudes of $\tilde{u}/\overline{u}_\infty$ in the outer parts of the boundary layer (at $y/d>0.6$–0.7) *generally* correspond with the same relative magnitudes of $\tilde{u}/\overline{u}_\infty$ nearer to the wall (at $y/d<0.6-0.7$) where the film makes the biggest impression on the flow field. Exceptions are evident at t/τ of 0.7, 0.8, 0.9, and 0 since trends of velocities near the wall are different from trends observed at other t/τ. In particular, streamwise velocities at these four t/τ values are higher than many other values present near the wall for the same y/d.

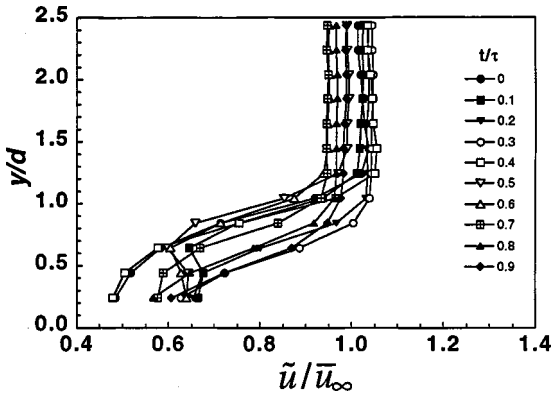

Fig. 4 Phase-averaged streamwise velocity profiles at $x/d=5$ and $z/d=0$ for $\overline{m}=0.5$, $l/d=1.6$, and $f=16$ Hz

These alterations are thus due to phase-shifts in streamwise velocity waveforms and static pressure waveforms through the film-cooled boundary layer. They are indicated by minima in phase-averaged velocities in the outer parts of the boundary layer ($y/d>0.6$-0.7, where the freestream dominates), which are occurring at a different part of the pulsation period compared to minima in phase-averaged velocities in near wall regions ($y/d<0.6-0.7$, where the film cooling is most influential). The largest phase shifts are occurring in the part of pulsation periods where streamwise velocities in the freestream are lowest and static pressures in the freestream are near maximum values. Such phase-varying velocity profile distortion evidences nonlinear flow behavior, especially in the film dominated region of the boundary layer near the wall. In this case, because of the low imposed frequency employed ($f=2$ Hz), the most significant phase-shifts are limited only to about 40 percent of each overall pulsation period. Such behavior also means that the film coolant is not quasi-steady 100 percent of the time. Instead, parts of the flow are quasi-steady only over portions of each pulsation period.

According to Fig. 4, such phase-shifts become more significant and occur over larger portions of each pulsation period (and over larger portions of the boundary layer) when the imposed pulsation frequency is 16 Hz ($\mathrm{Sr}_c=.75$, $\mathrm{Sr}_\infty=.26$, and $\mathrm{Sr}_x=.51$). In this case, the relative qualitative magnitudes in the freestream are out of phase with variations through most of the boundary layer over about 70 percent of each pulsation period. This is evident in Fig. 4 at t/τ values from 0–0.6. This is a much larger percentage than observed in Fig. 3 even though the pulsation amplitude at 16 Hz is

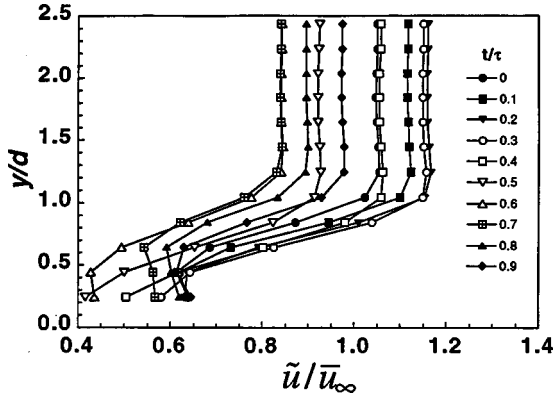

Fig. 3 Phase-averaged streamwise velocity profiles at $x/d=5$ and $z/d=0$ for $\overline{m}=0.5$, $l/d=1.6$, and $f=2$ Hz

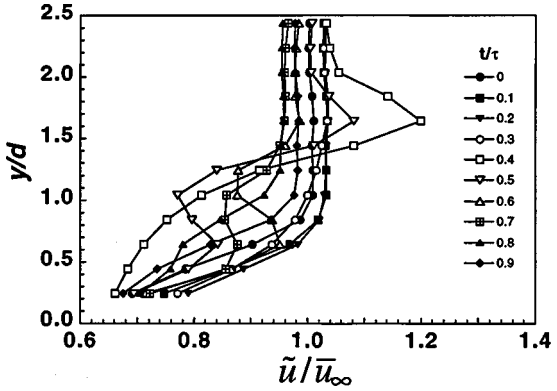

Fig. 5 Phase-averaged streamwise velocity profiles at $x/d=5$ and $z/d=0$ for $\overline{m}=0.5$, $l/d=1.6$, and $f=32$ Hz

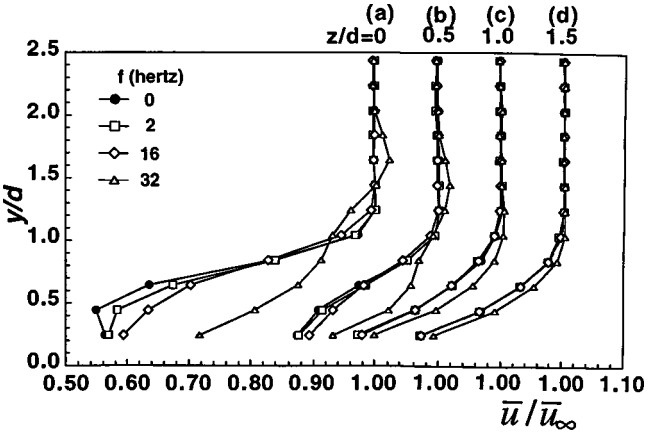

Fig. 6 Time-averaged streamwise velocity profiles at $x/d=5$, $\overline{m}=0.5$, $l/d=1.6$, and bulk flow pulsation frequencies f of 0 Hz, 2 Hz, 16 Hz, and 32 Hz. (*a*) $z/d=0$, (*b*) $z/d=0.5$, (*c*) $z/d=1.0$, (*d*) $z/d=1.5$.

about 70 percent of the magnitude at 2 Hz. With the higher frequency, variations of $\tilde{u}/\overline{u}_\infty$ profiles are also more complex. This is illustrated by the trace at $t/\tau=0.5$, which is in the middle of the profiles at other t/τ in the freestream, lower than other profiles at $y/d=0.7-1.2$, and then in the middle with relatively higher values at lower y/d. Such trends evidence highly nonlinear, complex film-cooled boundary layer behavior when $\overline{m}=0.5$, $l/d=1.6$, and the bulk flow pulsation frequency is 16 Hz.

Figure 5 then shows that this nonlinearity and complexity grow even more when the imposed pulsation frequency reaches 32 Hz, and $\mathrm{Sr}_c=1.50$, $\mathrm{Sr}_\infty=.52$, and $\mathrm{Sr}_x=1.02$. Thus, the changes from Fig. 4–Fig. 5 (where f changes from 16 Hz to 32 Hz) are much larger than the changes from Fig. 3–Fig. 4 (where f changes from 2 Hz to 16 Hz). In Fig. 5, the phase-averaged velocity profiles change by larger amounts as t/τ varies through each pulsation period. Profiles are especially distorted due to phase-shifts of static pressure waveforms at t/τ from 0.4–0.8. This is particularly evident for the $t/\tau=0.4$ and $t/\tau=0.5$ profiles since these show magnitudes which are both larger and smaller than all of the other profiles at $y/d=1.4-2.3$ and $y/d<1.4$, respectively. These t/τ times thus correspond to the portions of the pulsations with the highest magnitudes of streamwise velocity, and injectant trajectories which are farthest from the surface. These times also coincide with the portions of each phase when the largest influences of static pressure waveform phase-shifting are felt. Because this occurs when static pressures in the freestream are *minimum* (instead of maximum), behavior is then opposite to that observed when the pulsation frequency is 2 Hz. Such differences for $f=32$ Hz (in Fig. 5) are partially due to non-quasi-steady behavior of the film at higher frequencies and higher values of coolant Strouhal numbers. Non-quasi-steady films are influenced by multiple flow pulsations over the time interval required for the film to enter and exit each film hole. This produces a wavy instantaneous film trajectory when viewed from the side, as well as larger, overall changes to film structure, and film distributions which are spread over larger volumes as they are advected downstream [13].

Time-Averaged Streamwise Velocity Profiles at Different Spanwise Locations. The influences of bulk flow pulsations on streamwise velocity magnitudes are also evident when these profiles are time-averaged. Such profiles are given for z/d of 0, 0.5, 1.0, and 1.5 in Figs. 6(*a*)–(*d*). The profiles presented in Figs. 3–5 are time-averaged to obtain the profiles given in Fig. 6(*a*) for $z/d=0$. Film cooling flow conditions in this figure as well as Figs. 6(*b*)–(*d*) thus correspond to the same ones employed to obtain the results in Figs. 3–5: $\overline{m}=0.5$, $l/d=1.6$, and imposed pulsation frequencies are 0 Hz, 2 Hz, 16 Hz, and 32 Hz.

At each z/d, the time-averaged streamwise velocity profiles at f of 2 Hz and 16 Hz are relatively close in magnitude to the profile measured at $f=0$ Hz. This is especially so when z/d is 1.0 and 1.5. At z/d of 0 and 0.5, these profiles are higher than the $f=0$ Hz profile at $y/d<0.8$, and in some cases, somewhat lower than the $f=0$ Hz profile at $0.8<y/d<1.5$.

Substantial differences between time-averaged velocity profiles measured at an imposed pulsation frequency of 32 Hz and ones measured at 0 Hz in Figs. 6(*a*)–(*d*) evidence dramatic changes to instantaneous and time-averaged structure within the film-cooled boundary layers. For all four z/d of 0, 0.5, 1.0, and 1.5, the $f=32$ Hz *time-averaged* profile is higher, and in many cases, significantly higher than the profiles at other pulsation frequencies at most all y/d locations. This is consistent with results in Figs. 3–5, where *phase-averaged* velocities throughout the pulsation period at 32 Hz are also much higher than profiles of phase-averaged velocity measured throughout the film cooled boundary layers at f of 2 Hz and 16 Hz. This is due to the influences of the pulsations at boundary layer locations just downstream of the film holes, at the film hole exits, and within the holes. Associated variations of static pressure with time and spatial location at $f=32$ Hz are quite complex, and result in higher instantaneous injectant trajectories, and higher injectant momentum levels throughout a majority of each pulsation period.

Another important feature of the streamwise velocity profiles in Fig. 6(*a*) is the large gradient of velocity which is present at y/d between 0.5 and 1.0. At $x/d=5$ and $z/d=0$, this location corresponds to the outer portion of the largest film concentrations. The gradient then develops due to a shear layer which develops at the interface between fluid with low streamwise momentum (below) and fluid with high streamwise momentum (above). When the pulsations are imposed, the same shear layer gradient is present, and in many cases, it extends over a larger vertical portion of the boundary layer. This is because the imposed pulsations produce periodically unsteady static pressure fields at the exits of the injection holes which result in pulsating coolant flow rates. In addition, the pulsating static pressure and velocity fields in the boundary layer just downstream from the injection holes result in complex variations with time of the trajectories, distributions, as well as the coverage of the injectant along the surface. The film thus instantaneously changes its momentum and position in the boundary layer when bulk flow pulsations are imposed. The mean injectant trajectory with pulsations is also somewhat different, and the same amount of injectant is spread over a larger volume compared to nonpulsating flow, especially when the pulsation frequency f is 32 Hz.

Comparing the results in Figs. 6(*a*)–6(*d*) also gives information on the influences of spanwise location on time-averaged structure when $f=32$ Hz. The differences between these profiles and the ones measured at $f=0$ Hz are much larger at z/d of 0 and 0.5 than when z/d is 1.0 and 1.5. This means that the largest effects of the pulsations on time-averaged structure are present at and near the middle of the highest film concentrations.

Time-Averaged Profiles of Spanwise and Normal Component Velocities. The profiles of the time-averaged normal component of velocity in Fig. 7 are again given for $z/d=0$, $\overline{m}=0.5$, and $l/d=1.6$. The $f=0$ Hz time-averaged profile in this figure shows that the normal velocity component becomes progressively larger as the wall is approached and y/d decreases to 0. Profiles at pulsation frequencies of 2 Hz and 16 Hz are qualitatively similar, with only small quantitative deviations. Such behavior, of course, is due to the upward motion of the fluid from the film cooling holes, and the upwash region between the vortex pair created as the film emerges from each hole. Large changes are then apparent when the imposed pulsation frequency reaches 32 Hz, just like the streamwise velocity component profiles in Figs. 6(*a*)–(*d*). In this case, normal velocity component magnitudes (for $f=32$ Hz) are significantly larger at most all y/d examined, compared to those measured at the other three pulsation frequencies studied.

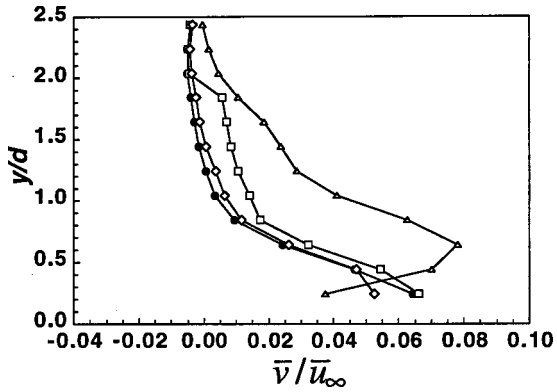

Fig. 7 Time-averaged normal component velocity profiles at $x/d=5$ and $z/d=0$, for $\overline{m}=0.5$, $l/d=1.6$, and bulk flow pulsation frequencies f of 0 Hz, 2 Hz, 16 Hz, and 32 Hz. Symbols defined in Fig. 6.

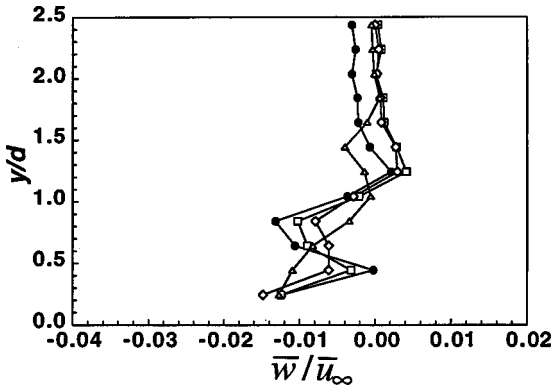

Fig. 8 Time-averaged spanwise component velocity profiles at $x/d=5$ and $z/d=0$, for $\overline{m}=0.5$, $l/d=1.6$, and bulk flow pulsation frequencies f of 0 Hz, 2 Hz, 16 Hz, and 32 Hz. Symbols defined in Fig. 6.

Another feature of the results in Fig. 7 is the decrease of magnitudes of the normal velocity component as one moves upwards and through the shear layer, mentioned earlier. For f equal to 0 Hz, 2 Hz, and 16 Hz, this shear layer is located at y/d between 0.5 and 1.0. For $f=32$ Hz, it is located farther from the wall at y/d between 0.8 and 1.3.

Time-averaged profiles of the spanwise velocity component are given for the same overall experimental conditions in Fig. 8. Note that velocity magnitudes measured with $f=0$ Hz are first positive and then negative as y/d increases from 0. Such variations are due to the vortex structures produced by the film as it emerges from the holes and enters the boundary layer. Magnitudes of $\overline{w}/\overline{u}_\infty$ then become progressively closer to $\overline{w}/\overline{u}_\infty=0$ as pulsation frequency goes up. This means that alterations with pulsation frequency in Fig. 8 evidence changes in vortex strength, with smaller vorticity magnitudes as f increases from 0 Hz–32 Hz. Measurements from another source [15] show similar behavior. Important are different levels of vorticity diffusion with unsteadiness, and time-averaging quantities in structures which are changing position with time. As the each pulsation is imposed on the film cooled boundary layer, the two horseshoe vortex legs oscillate toward and away from the wall. As a result, vorticity regions associated with each vortex cover a larger volume, and each oscillating vortex appears somewhat weaker and more spread out in the time-averaged surveys.

Time-Averaged Reynolds Normal Stress Profiles. Time-averaged profiles of the streamwise, normal, and spanwise components of the Reynolds normal stress are given in Figs. 9, 10, and 11, respectively. These are given for the same locations and experimental conditions mentioned earlier: $x/d=5$, $z/d=0$, $\overline{m}=0.5$, and $l/d=1.6$.

The changes with pulsations are due mostly to different levels of turbulent diffusion as the pulsations are imposed, time-averaging of flow structures which are changing position temporally, and the dramatic alterations to film behavior and structure which become larger as pulsation frequency increases. Thus, the largest changes relative to the $f=0$ Hz profile occur when the imposed pulsation frequency f is 32 Hz. Here, the influences of higher injectant trajectories and smearing of magnitudes of the time-varying trajectories are particularly apparent since magnitudes of $(\overline{u'^2})^{1/2}/\overline{u}_\infty$, $(\overline{v'^2})^{1/2}/\overline{u}_\infty$, and $(\overline{w'^2})^{1/2}/\overline{u}_\infty$ are increased by very large amounts (relative to the 0 Hz profile) at y/d from 0.8 to 2.5. In contrast, profiles of the normal stresses at 2 Hz and 16 Hz are very similar to the 0 Hz profile over the same y/d range. At smaller y/d, quantitative variations between profiles at different pulsation frequencies are apparent. In addition, profile magnitudes are generally smaller than the 0 Hz profile (for $y/d<0.8$), which generally has the highest local value. Peaks for all three normal Reynolds stress components are present within the strong shear layers (discussed earlier), because this is where three-dimensional production terms are highest, and where the pressure-strain correlation is most effective in transferring energy between the three normal stress components. Further note that the magnitudes of the normalized peaks of all three components in Figs. 9, 10, and 11 for $z/d=0$ are roughly the same, as each is in the vicinity of 0.10. Also notice that the data in Fig. 9 are also given

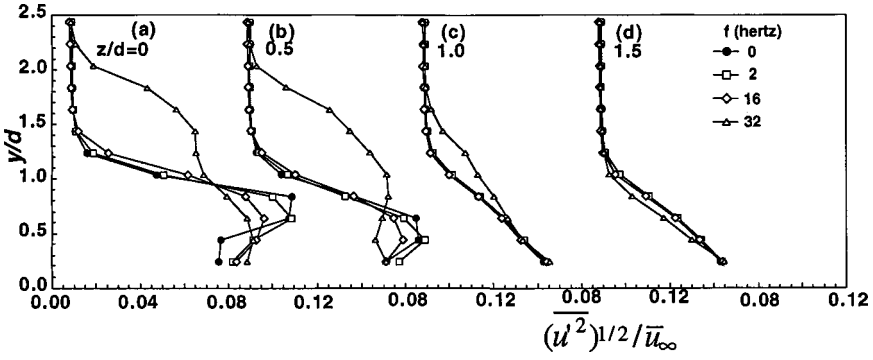

Fig. 9 Time-averaged, normalized profiles of the longitudinal Reynolds normal stress at $x/d=5$, $\overline{m}=0.5$, $l/d=1.6$, and bulk flow pulsation frequencies f of 0 Hz, 2 Hz, 16 Hz, and 32 Hz. (*a*) $z/d=0$, (*b*) $z/d=0.5$, (*c*) $z/d=1.0$, (*d*) $z/d=1.5$.

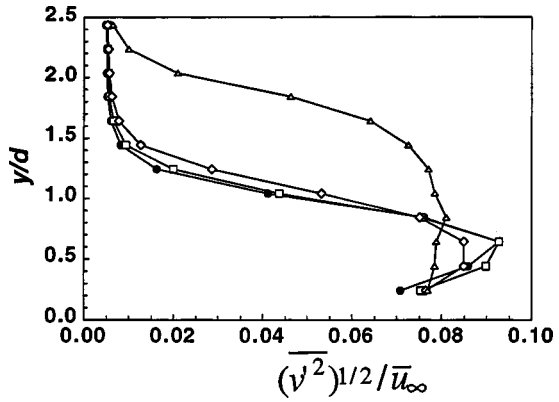

Fig. 10 Time-averaged, normalized profiles of the normal component of Reynolds normal stress at $x/d=5$ and $z/d=0$, for $\overline{m}=0.5$, $l/d=1.6$, and bulk flow pulsation frequencies f of 0 Hz, 2 Hz, 16 Hz, and 32 Hz. Symbols defined in Fig. 9.

for z/d values of 0.5, 1.0, and 1.5. The variations of these data with z/d provide additional evidence that the pulsations have the largest effects on the central parts of the largest film concentrations.

Time-Averaged Reynolds Shear Stress Profiles. Time-averaged profiles of $\overline{u'v'}/\overline{u_\infty}^2$ and $\overline{u'w'}/\overline{u_\infty}^2$ are presented in Figs. 12 and 13, respectively, for imposed pulsation frequencies of 0 Hz, 2 Hz, 16 Hz, and 32 Hz, and the same experimental conditions and location $(z/d=0)$ mentioned previously.

Each profile of $\overline{u'v'}/\overline{u_\infty}^2$ in Fig. 12 shows an important local minimum located about $0.65d$ from the wall for f of 0 Hz, 2 Hz, 16 Hz, and about $1.25d$ from the wall for f of 32 Hz. Values of normalized three-dimensional shear stress $\overline{u'w'}/\overline{u_\infty}^2$ in Fig. 13 show positive peaks at roughly the same locations relative to the surface. The shear layer (mentioned earlier) at the interface between fluid with low streamwise momentum below and fluid with much higher streamwise momentum above is responsible. This is partially because the region of high negative $\overline{u'v'}/\overline{u_\infty}^2$ is bounded by regions above and below (just outside of the shear layer) where the normalized Reynolds shear stress is sometimes of opposite sign and significantly lower in absolute magnitude.

As the imposed pulsation frequency increases, the most important factor affecting shear stress magnitudes are then the periodic alterations of the y positions of the shear layer and the highest film concentrations. As this shear layer oscillates to and from the wall

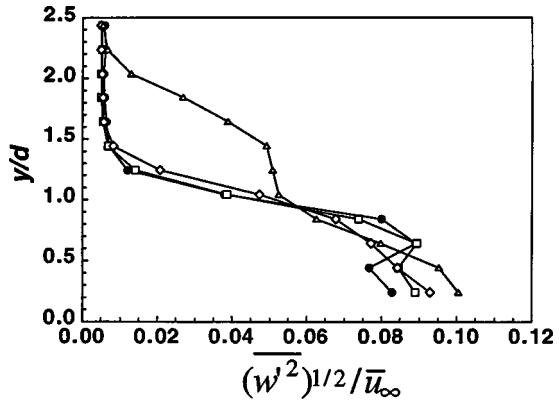

Fig. 11 Time-averaged, normalized profiles of the spanwise component of Reynolds normal stress at $x/d=5$ and $z/d=0$, for $\overline{m}=0.5$, $l/d=1.6$, and bulk flow pulsation frequencies f of 0 Hz, 2 Hz, 16 Hz, and 32 Hz. Symbols defined in Fig. 9.

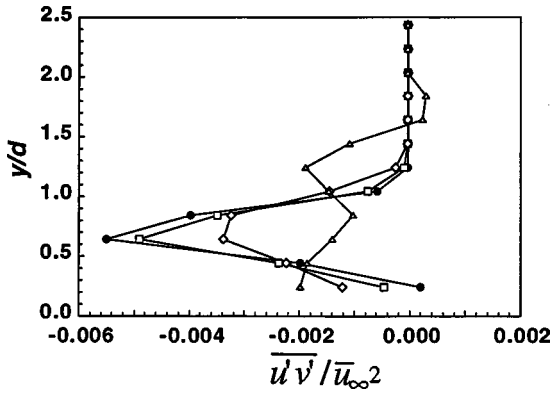

Fig. 12 Time-averaged, normalized profiles of the Reynolds shear stress $\overline{u'v'}$ at $x/d=5$ and $z/d=0$, for $\overline{m}=0.5$, $l/d=1.6$, and bulk flow pulsation frequencies f of 0 Hz, 2 Hz, 16 Hz, and 32 Hz. Symbols defined in Fig. 9.

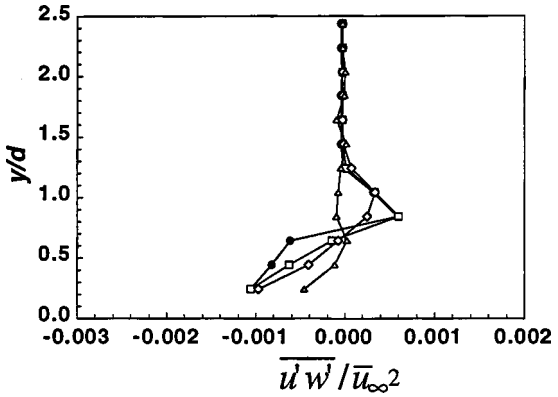

Fig. 13 Time-averaged, normalized profiles of the Reynolds three-dimensional shear stress $\overline{u'w'}$ at $x/d=5$ and $z/d=0$, for $\overline{m}=0.5$, $l/d=1.6$, and bulk flow pulsation frequencies f of 0 Hz, 2 Hz, 16 Hz, and 32 Hz. Symbols defined in Fig. 9.

with each pulsation, the fluid containing the highest values of stress is more spread out spatially which gives lower *time-averaged* magnitudes of maximum Reynolds shear stress (as mentioned earlier). Consequently, Figs. 12 and 13 show peak magnitudes of the normalized, time-averaged shear stresses, $\overline{u'v'}/\overline{u_\infty}^2$ and $\overline{u'w'}/\overline{u_\infty}^2$, which decrease in absolute magnitude continually as the imposed pulsation frequency f increases.

Summary and Conclusions

Flow structure in boundary layers film cooled from a single row of round, simple angle holes, and subject to bulk flow pulsations, is investigated. Of particular interest are phase-averaged streamwise velocity variations, and alterations of time-averaged flow structure (streamwise velocity, normal velocity, spanwise velocity, three Reynolds normal stresses, and two Reynolds shear stresses) at bulk flow pulsation frequencies f of 0 Hz, 2 Hz, 16 Hz, and 32 Hz. Coolant Strouhal numbers Sr_c then range from 0–1.5, freestream Strouhal numbers Sr_∞ range from 0–.52, and modified Strouhal numbers Sr_x (Ligrani and Bell [20]) range from 0 to 1.02. Injection hole length to diameter ratio l/d is 1.6, and the time-averaged blowing ratio $\overline{m}$ is 0.50. These values are chosen for investigation because of the relatively large influences of bulk flow pulsations on flow structure at these experimental conditions, as indicated by several studies [16,19,20], which show that pulsation effects generally become larger with increasing f, as either l/d or $\overline{m}$ decreases.

Profiles of time-averaged flow characteristics and phase-averaged flow characteristics, measured in the spanwise/normal plane at $x/d=5$ and $z/d=0$, show that important alterations to film-cooled boundary layer flow structure are present when pulsations are imposed compared to distributions measured with no pulsations. Effects are larger as imposed pulsation frequency goes up, with the most significant and dramatic changes at $f=32$ Hz. As z/d is changed and x/d is held constant at 5, the largest changes occur just downstream of the hole centerlines where film concentrations are largest. In phase-averaged streamwise velocity profiles, such changes are due to different phase shifts of static pressure (and streamwise velocity) waveforms at different boundary layer locations from the wall. They result in distributions which can be vastly different from time-averaged distributions at the same overall flow conditions, and for $f=32$ Hz, higher instantaneous injectant trajectories, and relatively higher injectant momentum levels throughout a majority of each pulsation period. Also indicated, as imposed pulsation frequency varies, is a change of the portion of each phase when the largest influences of static pressure waveform phase-shifting are felt. At $f=32$ Hz, this occurs when static pressures in the freestream are near minimum values, and at $f=2$ Hz, this occurs when static pressures in the freestream are near maximum values.

The changes with pulsations are mostly due to: (i) spreading of injectant concentrations over larger volumes, compared to steady distributions, as the pulsations are imposed; (ii) time-averaging of these flow structures as they change position temporally; (iii) the dramatic alterations to film behavior and structure which become larger as pulsation frequency increases; and (iv) different levels of turbulent diffusion. In addition to the alterations to boundary layer structure described, the effects mentioned are also expected to result in changes to magnitudes of film cooling protection (in most cases, to decreased levels).

Acknowledgment

The portions of this effort conducted at the University of Utah were sponsored by the National Science Foundation, Grant number CTS-9615196.

Nomenclature

d = injection hole diameter
f = imposed bulk flow pulsation frequency
l = injection hole length
$\overline{m}$ = time-averaged blowing ratio $=\rho_c \overline{u}_c / \rho_\infty \overline{u}_\infty$
p = instantaneous static pressure
Sr_c = injectant Strouhal number $=2\pi f l/\overline{u}_c$
Sr_∞ = freestream Strouhal number $=2\pi f \delta/\overline{u}_\infty$
Sr_x = modified Strouhal number, Eq. (1)
t = time
u = instantaneous streamwise or injectant velocity
v = instantaneous normal component of velocity
w = instantaneous spanwise component of velocity
x = streamwise coordinate, measured from downstream edge of film holes
y = normal coordinate, measured from test surface
z = spanwise coordinate, measured from test surface spanwise centerline
δ = boundary layer thickness
ρ = density
ν = kinematic viscosity
τ = pulsation period

Superscripts

$\overline{\ }$ = time-averaged
$\tilde{\ }$ = phase-averaged
$'$ = fluctuating component
min = minimum value
max = maximum value

Subscripts

c = injectant at the exit planes of the holes
∞ = freestream

References

[1] Rigby, M. J., Johnson, A. B., and Oldfield, M. L. G., 1990, ''Gas Turbine Rotor Blade Film Cooling With and Without Simulated NGV Shock Waves and Wakes,'' *International Gas Turbine & Aeroengine Congress & Exposition*, Paper No. 90-GT-78, Brussels.
[2] Abhari, R. S., and Epstein, A. H., 1994, ''An Experimental Study of Film Cooling in a Rotating Transonic Turbine,'' ASME J. Turbomach., **116**, pp. 63–70.
[3] Juhany, K. A., and Hunt, M. L., 1994, ''Flowfield Measurements in Supersonic Film Cooling Including Effect of Shock-Wave Interaction,'' AIAA J., **32**, pp. 578–585.
[4] Kanda, T., Ono, F., Takahashi, M., Saito, T., and Wakamatsu, Y., 1996, ''Experimental Studies of Supersonic Film Cooling With Shock Wave Interaction,'' AIAA J., **34**, pp. 265–271.
[5] Abhari, R. S., 1996, ''Impact of Rotor-Stator Interaction On Turbine Blade Film Cooling,'' ASME J. Turbomach., **118**, pp. 103–113.
[6] Garg, V. K., and Abhari, R. S., 1996, ''Comparison Of Predicted And Experimental Nusselt Number For A Film-Cooled Rotating Blade,'' *International Gas Turbine & Aeroengine Congress & Exposition*, Paper No. 96-GT-223, Birmingham.
[7] Nix, A. C., Reid, T., Peabody, H., Ng, W. F., Diller, T. E., and Schetz, J. A., 1997, ''Effects of Shock Wave Passing on Turbine Blade Heat Transfer in a Transonic Cascade,'' AIAA Paper No. AIAA-97-0160.
[8] Popp, O., Smith, D. E., Bubb, J. V., Grabowski, H. C. III, Diller, T. E., Schetz, J. A., and Ng, W. F., 1999, ''Steady and Unsteady Heat Transfer in a Transonic Film Cooled Turbine Cascade,'' *International Gas Turbine & Aeroengine Congress & Exposition*, Paper No. 99-GT-259, Indianapolis.
[9] Smith, D. E., Bubb, J. V., Popp, O., Grabowski, H. C. III, Diller, T. E., Schetz, J. A., and Ng, W. F., 2000, ''Investigation of Heat Transfer in a Film Cooled Transonic Turbine Cascade, Part I: Steady Heat Transfer,'' *International Gas Turbine & Aeroengine Congress & Exposition*, Paper No. 2000-GT-202, Munich.
[10] Popp, O., Smith, D. E., Bubb, J. V., Grabowski, H. C. III, Diller, T. E., Schetz, J. A., and Ng, W. F., 2000, ''Investigation of Heat Transfer in a Film Cooled Transonic Turbine Cascade, Part II: Unsteady Heat Transfer,'' *International Gas Turbine & Aeroengine Congress & Exposition*, Paper No. 2000-GT-203, Munich.
[11] Dunn, M. G., Haldeman, C. W., Abhari, R. S., and McMillan, M. L., 2000, ''Influence of Vane/Blade Spacing on the Heat Flux for a Transonic Turbine,'' *International Gas Turbine & Aeroengine Congress & Exposition*, Paper No. 2000-GT-206, Munich.
[12] Bergholz, R. F., Dunn, M. G., and Steuber, G. D., 2000, ''Rotor/Stator Heat Transfer Measurements and CFD Predictions for Short-Duration Turbine Rig Tests,'' *International Gas Turbine & Aeroengine Congress & Exposition*, Paper No. 2000-GT-208, Munich.
[13] Ligrani, P. M., Gong, R., Cuthrell, J. M., and Lee, J. S., 1996, ''Bulk Flow Pulsations and Film Cooling: Part 1, Injectant Behavior,'' Int. J. Heat Mass Transf., **39**, pp. 2271–2282.
[14] Ligrani, P. M., Gong, R., Cuthrell, J. M., and Lee, J. S., 1996, ''Bulk Flow Pulsations and Film Cooling: Part 2, Flow Structure and Film Effectiveness,'' Int. J. Heat Mass Transf., **39**, pp. 2283–2292.
[15] Ligrani, P. M., Gong, R., Cuthrell, J. M., and Lee, J. S., 1997, ''Effects of Bulk Flow Pulsations on Film-Cooled Boundary Layer Structure,'' ASME J. Fluids Eng., **119**, pp. 56–66.
[16] Seo, H. J., Lee, J. S., and Ligrani, P. M., 1998, ''The Effect of Injection Hole Length on Film Cooling With Bulk Flow Pulsations,'' Int. J. Heat Mass Transf., **41**, No. 22, pp. 3515–3528.
[17] Sohn, D. K., and Lee, J. S., 1997, ''The Effects of Bulk Flow Pulsations on Film Cooling From Two Rows of Holes,'' *International Gas Turbine & Aeroengine Congress & Exposition*, Paper No. 97-GT-129.
[18] Jung, I.-S., and Lee, J. S., 1998, ''Effects Of Bulk Flow Pulsations on Film Cooling From Spanwise Oriented Holes,'' *International Gas Turbine & Aeroengine Congress & Exposition*, Paper No. 98-GT-211, Stockholm.
[19] Bell, C. M., Ligrani, P. M., Hull, W. A., and Norton, C. M., 1999, ''Film Cooling Subject to Bulk Flow Pulsations: Effects of Blowing Ratio, Freestream Velocity, and Pulsation Frequency,'' Int. J. Heat Mass Transf., **42**, pp. 4333–4344.
[20] Ligrani, P. M., and Bell, C. M., 2001, ''Film Cooling Subject to Bulk Flow Pulsations: Effects of Density Ratio, Hole Length-to-Diameter Ratio, and Pulsation Frequency,'' Int. J. Heat Mass Transf., **44**, No. 10, pp. 2005–2009.
[21] Kline, S. J., and McClintock, F. A., 1953, ''Describing Uncertainties in Single Sample Experiments,'' Mech. Eng. (Am. Soc. Mech. Eng.), **75**, pp. 3–8.
[22] Moffat, R. J., 1988, ''Describing the Uncertainties in Experimental Results,'' Exp. Therm. Fluid Sci., **1**, No. 1, pp. 3–17.
[23] Al-Asmi, K., and Castro, I. P., 1993, ''Production of Oscillatory Flow in Wind Tunnels,'' Exp. Fluids, **15**, pp. 33–41.
[24] Menendez, A. N., and Ramaprian, B. R., 1989, ''Experimental Study of a Periodic Turbulent Boundary Layer in Zero Mean Pressure Gradient,'' Aeronaut. J., **93**, pp. 195–206.

Robert F. Kunz[1]
e-mail: rfk@wt.arl.psu.edu

Stephen W. D'Amico

Peter F. Vassallo

Michael A. Zaccaria

Lockheed Martin,
Schenectady, NY 12301

LDV Measurement of Confined Parallel Jet Mixing

Laser Doppler Velocimetry (LDV) measurements were taken in a confinement, bounded by two parallel walls, into which issues a row of parallel jets. Two-component measurements were taken of two mean velocity components and three Reynolds stress components. As observed in isolated three-dimensional wall bounded jets, the transverse diffusion of the jets is quite large. The data indicate that this rapid mixing process is due to strong secondary flows, transport of large inlet intensities, and Reynolds stress anisotropy effects. [DOI: 10.1115/1.1383970]

Introduction

Three-dimensional bounded jets are important in a variety of engineering applications including turbine blades, gas turbine combustors and microcircuit cooling, thrust vectoring nozzles, airfoil boundary layer control, and ventilation system exhaust. Mixing of bounded jets with adjacent jets or with their surroundings (i.e., transverse and boundary normal momentum and heat transfer), plays a crucial role in the effectiveness of the injected flow in these applications. A considerable body of research has been performed which studies different classes of bounded jets. These include: jets bounded by free surfaces and solid walls, planar and three-dimensional wall jets, jets bounded by one plane wall, two parallel plane walls and axisymmetric walls (pipe and diffuser geometries), and systems with multiple interacting jets of various configurations.

The authors investigated the mixing characteristics of confined parallel turbulent jets. A large body of experimental research has been performed on related flows, which suggests that some of the physical mechanisms present in such Parallel Confined Jet (hereafter PCJ) mixing are important in rapid transverse mixing in other bounded jet flows. Specifically, isolated three-dimensional wall bounded turbulent jets have been studied by numerous researchers. Measurements by Newman et al. [1], and many others, on three-dimensional isolated wall bounded jets have shown that transverse jet growth rates in these flows are substantially larger than the growth rates normal to the wall. Physical mechanisms to which this anisotropic jet growth have been attributed include increased turbulence transport (i.e., $\partial(\overline{u'v'})/\partial y > \partial(\overline{u'w'})/\partial z$, see coordinate convention in Fig. 1), and secondary flows of the first and second kind (Launder and Rodi [2]). Also, Davis and Winarto [3] took velocity and Reynolds stress measurements in an isolated three-dimensional wall bounded jet and observed larger effective momentum diffusion transverse to the jet than normal to the bounding wall.

An isolated three-dimensional wall jet bounded on two sides by a confinement has been studied by Holdeman and Foss [4]. Their mean flow measurements showed strong secondary motions (streamwise vorticity) and large jet spreading rates.

Several nondimensional geometric scales can be adopted to characterize PCJ flows. The ratio of inlet nozzle hydraulic diameter to confinement height and jet spacing D_H/h, D_H/L (see Fig. 2) and the nozzle aspect ratio (AR) are relevant and serve to distinguish the geometries investigated by others. The configuration investigated here is characterized by closely confined, closely coupled and low aspect ratio jets (i.e., D_H/h, D_H/L and AR all of order 1).

PCJ configurations have been studied by Krothapalli et al. [5]. They found that the spreading rates of a multiple rectangular jet configuration was not significantly affected by the presence of a partial confinement. However, the configuration considered in this paper differs significantly from that of Krothapalli and his coworkers in that the aspect ratio of their rectangular jets was $AR \cong 20$ (versus $\cong 1$ for the present geometry) and the normalized distance between their jets was $D_H/L \cong 5$ (versus $\cong 1$ for the present geometry). Accordingly, the presence of a confinement in their experiments has significantly less influence on parallel jet mixing than observed in this study.

The purpose of the present PCJ measurement program was to take mean flow and Reynolds stress data of sufficient detail to improve the understanding of the physics in PCJ flows, and for turbulence model development and CFD analysis verification. An adequately verified CFD tool will provide the ability to optimize the flow rates and jet size/position to maximize mixing rates. The present experimental program contributes to the available measurements of bounded jet flows, with the configuration investigated being characterized by the presence of multiple parallel jets, bounding surfaces on two sides, low aspect ratio jet cross-sections and close proximity of adjacent jet centerlines (relative to jet di-

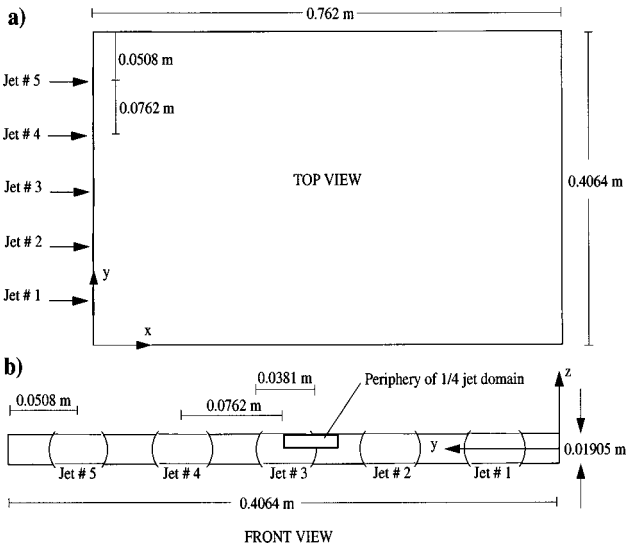

Fig. 1 (a) Top view, (b) front view sketches of parallel confined jet test section

[1]Corresponding Author, Current Address: Applied Research Laboratory, The Pennsylvania State University, P. O. Box 30, University Park, PA 16804.

Contributed by the Fluids Engineering Division for publication in the JOURNAL OF FLUIDS ENGINEERING. Manuscript received by the Fluids Engineering Division October 7, 1998; revised manuscript received July 12, 2000. Associate Editor: S. Banerjee.

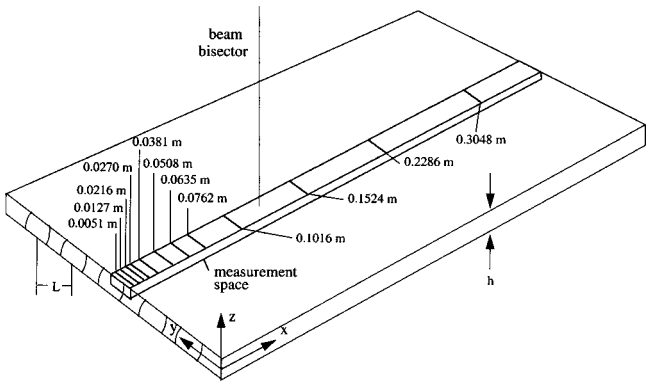

Fig. 2 Sketch of probe orientation and 12 scan locations

ameters). The purposes of this paper are to present and interpret the experimental measurements taken in the PCJ configuration.

Configuration and Measurement Program

Figures 1 and 2 show sketches of the test section and optical configuration used for the measurement program. The coordinate convention utilized throughout is also presented in Fig. 1. Five pipes of diameter $D=0.0381$ m and 22 diameters long issue into a confinement. The confinement is 0.01905 m in height, 0.4064 m wide, and 0.7620 m long. The flat walls of the confinement give rise to very good optical access. The axis of the third pipe is coincident with the centerline of the confinement. The pipe centerlines are spaced 0.0762 m apart. The end walls ($y=0.0$ and 0.4064 m) were located 0.0508 m from the centerline of the outermost jets.

The dynamics of the parallel confined jet flow can be qualitatively characterized as follows. As the water flowing through each of the five inlet pipes nears the inlet to the confinement, it accelerates because the cross-sectional areas at the inlet to the confinement are smaller than the pipe cross-sectional area (Fig. 1). As the jets issue into the confinement, they decelerate due to a step increase in flow area, and begin to diffuse in the transverse (y) direction. Recirculation zones appear between each pair of jets. The jets mix out quite rapidly; the centerline axial velocity of jet 3, normalized by confinement bulk velocity, decreases from 2.7–1.6 within approximately 5 confinement heights downstream from the inlet. As the jets mix out, the region of the flow well away from the endwalls approaches that of a fully developed two-dimensional turbulent duct flow.

A 40 hp variable speed centrifugal pump was used to control flow. The test section flow rate was measured to $\pm 1/2\%$ of reading using a turbine flow meter in the supply line to the test section. Flow rates through the five inlet pipes were controlled and measured to an accuracy of 2.5×10^{-5} m^3/s using rotometers in the individual pipe inlet lines. The volume flow rate of water through the facility was 6.31×10^{-3} m^3/s. The flow split was controlled via valves downstream from the rotometers. This flow split was optimized through trial and error to yield near periodicity of the three middle jets as discussed below. Loop temperature was controlled using resistance heaters located on the pump suction piping and chilled water through a heat exchanger as necessary. The loop temperature was held constant at 38°C. The Reynolds number of the inlet pipe flows based on pipe bulk velocity and diameter was approximately 60,000.

The test section was designed using clear cast acrylic. To minimize distortion of the beams through the test section walls, the cast acrylic was milled to a 0.13 mm tolerance on thickness and polished to retain optical clarity.

A four-beam backscatter laser Doppler fiber optic velocimetry system was used to take the velocity measurements. A 122 mm focal length lens was utilized with the probe, producing a measurement volume 0.32 mm long and 0.06 mm wide in water. The fiberoptic probe was supported above the test section with a beam mounted to a milling machine which controlled traversing, with an estimated maximum positional error of ±0.25 mm. Neutrally buoyant latex seed particles (5 μm) were used for the LDV measurements. Water added to the loop was deaerated to minimize the presence of bubbles in the flow stream. In all cases the beam powers were maintained between 30 and 60 mW for the green (514 nm wavelength) beams and between 10 and 20 mW for the blue (488 nm wavelength) beams. A 4 W Argon laser generated the beams.

A digital burst correlator was used to process the LDV data. This processor discriminates signal from noise using autocorrelation instead of amplifying detection. A total of 256 digital samples per Doppler burst were analyzed to calculate a single velocity measurement. A 40 MHz Bragg shift was applied to one beam of each of the beam pairs to enable measurement of zero and negative velocities. Coincidence between the two velocity components was achieved by requiring the two measurements be within a specified time interval. For this experiment, the coincidence interval specified was 100 μs. The coincidence data rate varied between approximately 10 Hz and 300 Hz, depending on the proximity of the measurement volume to the wall. Three-thousand samples were taken at each point to maximize statistical certainty. A transit time weighting scheme was used to correct the velocity data from biases due to turbulent fluctuations (Barnett and Bentley [6]).

Considerable effort was made to generate a nearly periodic jet field in the central part of the test section. Predesign Navier-Stokes analyses indicated that using five jets would provide reasonable periodicity in the three central jets. The near periodicity of the jet field, reduced the total amount of data to be obtained, since three planes of symmetry could be exploited, as indicated in Figs. 1 and 2. Additionally, CFD analysis of the flow can be simplified by reducing the required computational domain size. Near periodicity in the central three jets, and the x-y and x-z symmetries afforded by the geometry were realized, as verified by measurements presented below. Accordingly, relatively high resolution data was taken in a 1/4 jet section at twelve axial locations shown in Fig. 2. Scans were taken at all twelve locations. Figure 3 shows a typical cross sectional measurement scan grid. For the

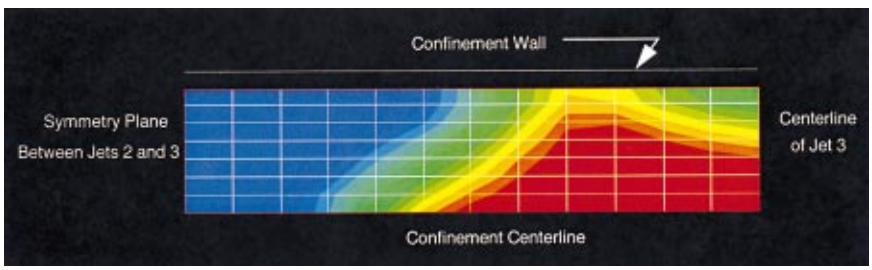

Fig. 3 Contours of measured axial velocity 0.027 m downstream from confinement inlet, illustrating the cross-stream resolution of scans in the measurement space

first 9 axial scan locations ($x \leqslant 0.1016$ m), a 13×8 traverse grid was used as shown in Fig. 3. Superposed in this figure are contours of measured axial velocity at $x = 0.0279$ m downstream from the confinement inlet. As the jets mixed more thoroughly, well downstream from the inlet ($x \geqslant 0.1524$ m), a coarser traverse grid of 10×5 was utilized.

Experimental Results and Interpretation

Experimental Errors. LDV measurements are subject to numerous errors, most of which can be quantified. The total uncertainty can be found by combining precision and bias errors as: $U_{\text{total}} = \pm(B + tP)$, where B is the bias error, P is the precision error, and $t = 1.96$ for a 95% confidence level (for a sample size greater than 50). Patrick [7] states the bias errors include errors from laser beam geometry, signal processor errors and seeding bias errors. Most of the bias errors are very small compared to precision errors (discussed below) and are thus neglected. The bias errors which can be of the same order of magnitude as the precision errors are velocity and angle bias. As mentioned above, the velocity bias error is corrected using transit time weighting, while frequency shifting was used to minimize angle bias. Thus the bias errors can be neglected.

The precision errors in LDV measurement are data processing errors which result from averaging a finite number of data samples per data point. In LDV measurements, the velocity does not remain constant during the sampling period, but fluctuates due to turbulence. Thus the precision error in the mean velocity, assuming a normal distribution of velocity samples, is:

$$\frac{S_{\overline{V}}}{\overline{V}} = \frac{1}{\sqrt{N}}\left(\frac{V'}{\overline{V}}\right) \tag{1}$$

where $\overline{V}$ is the sample mean velocity, and $V'/\overline{V}$ is the local intensity. Patterson [8] states that the mean square turbulence intensity has a chi-square distribution. For a large sample size ($N > 50$), the precision error of the turbulence intensity measurement can be found from:

$$\frac{S_{v'}}{v'} = \frac{1}{\sqrt{2N}} \tag{2}$$

For the LDV measurements taken here, 3000 axial and tangential coincident samples were taken at each measurement position. This gives an uncertainty of approximately $\pm 2\%$ inside the jet, $\pm 4\%$ in between the jets for both U and V and $\pm 2\%$ for $\sqrt{\overline{u'u'}}$ and $\sqrt{\overline{v'v'}}$ (these errors based on normalization with respect to U_{bulk}).

Flow Field Characterization. Several initial characterization studies of the flow field were performed to verify the absence of large scale unsteady motions, to verify the desired symmetry and periodicity characteristics of the five jet flows and to characterize the flows well upstream and downstream from the confinement inlet.

Figure 4(*a*) shows an energy spectrum of axial velocity measured at the center of jet 3, 2.67 confinement heights downstream from the confinement inlet ($x = 0.0508$ m, $y = 0.0$ m, $z = 0.0$ m). The plot shows a Fast Fourier Transform (FFT) of the 500,000 data points taken at a average random acquisition rate of approximately 525 Hz. For the geometric length and mean velocity scales of the present configuration a turbulence scale range of approximately 100 Hz to 10,000 Hz is anticipated. Clearly, the spectrum only captures the larger scales of turbulence (the energy content of the smaller scales being aliased to lower frequencies). The spectrum exhibits no indication (peak) associated with long time scale quasi-unsteadiness associated with the ''mean'' flow (as may be manifested in jet ''flapping'').

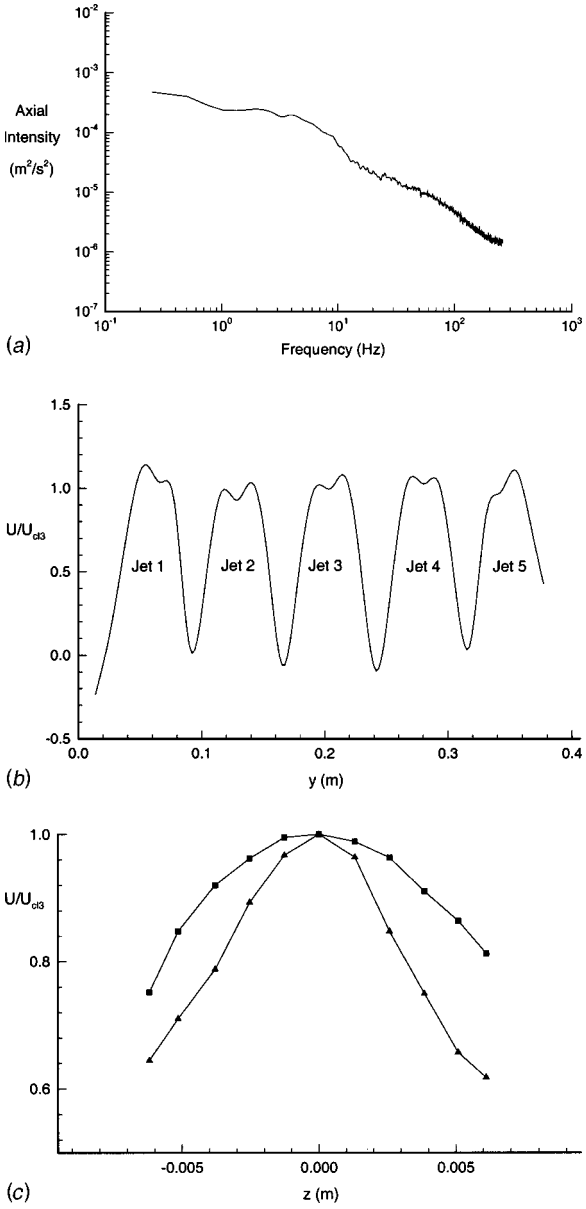

Fig. 4 (*a*) Energy spectrum of axial velocity taken at x = .0508 m, y = 0.0 m, z = 0.0 m; (*b*) Measured axial mean velocity versus y at x = .0508 m, z = 0.0 m; (*c*) Measured axial mean velocity versus z for jet 3 at y = .2032 m for x = .0508 m (triangles) and .1016 m (squares)

Several transverse scans ($\overline{U}$ versus y) were taken along the centerline of the confinement ($z = 0.0$ m). These served to provide guidance in adjusting the flow rate through the outer jets to maximize the periodicity of the center three jets. Figure 4(*b*) shows the data from the $x = 0.0508$ m scan, and illustrates the near periodicity achieved. The flow rate splits through jets 1–5, were 19.7, 20.2, 20.2, 20.2, and 19.7%, respectively, of the total test section flow rate of 6.31×10^{-3} m^3/s. The axial momentum defect which appears at the centerline of each jet in this plot will be discussed below.

Figure 4(*c*) shows the nearly symmetrical scans of U/U_{jcl} versus z along the centerline of jet 3 ($y = 0.2032$ m) at $x = 0.0508$ and $x = 0.1016$ m. Figures 4(*b*) and 4(*c*) serve to justify the use of the three symmetry planes exploited in the detailed measurement program pursued and in Navier-Stokes analysis (details of CFD computations appear in Kunz et al. [9]).

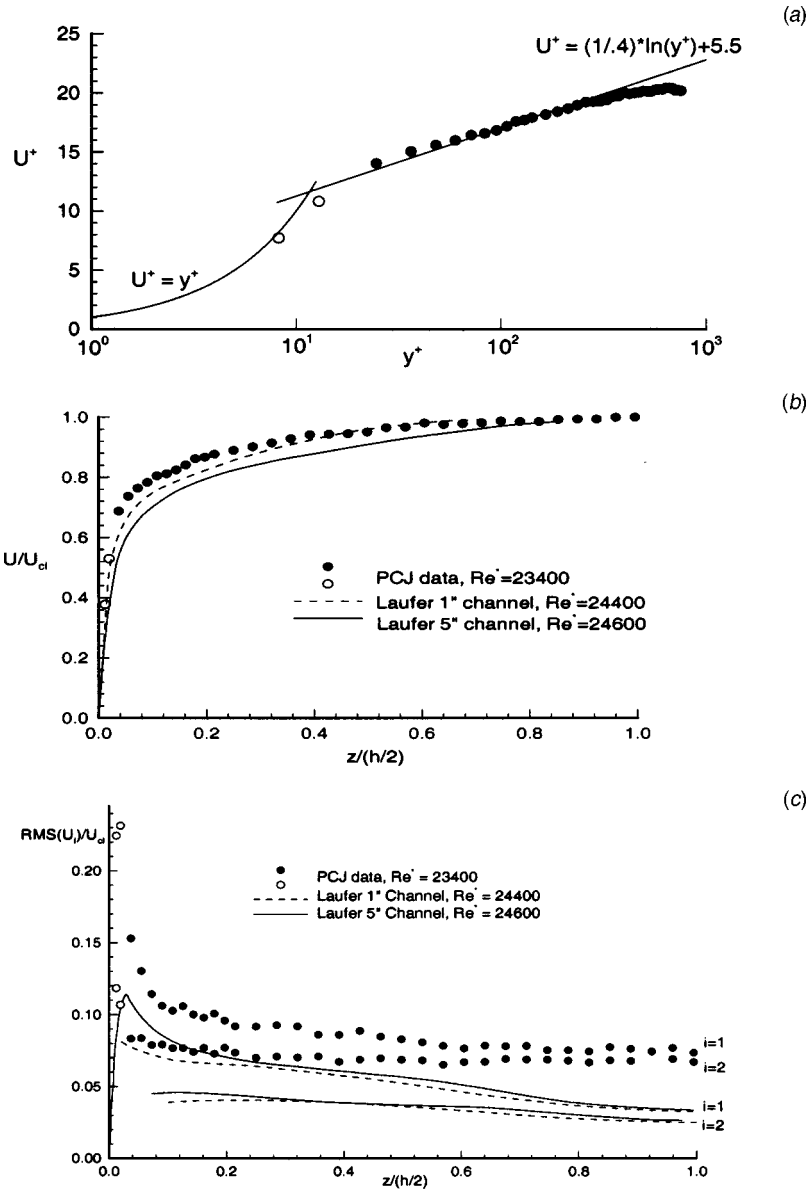

Fig. 5 Measurements of axial velocity and normal stresses versus z at x = 0.6604 m, y = 0.2032 m. (a) Comparison of axial velocity with law-of-the-wall; (b) comparison of axial velocity with data due to Laufer [10]; (c) comparison of normal stresses with data due to Laufer [10].

As the jets mix, the confinement flow approaches that of a fully developed two-dimensional turbulent duct flow, since three-dimensional effects become negligible (aspect ratio of confinement = 21.3). A detailed scan was performed in the z direction near the confinement outlet, 34.67 confinement heights downstream from the inlet station ($x = 0.6604$ m, $y = 0.2032$ m). Figures 5(*a*) and (*b*) show the measured axial velocity profile versus z at this location. (Measured transverse velocity was no more than $0.007\,U_{cl}$). The open symbols in Figs. 5(*a*-*c*) correspond to data obtained very close to the confinement wall (z-$z_{wall} = 0.12, 0.19$ mm).[2] A normalized wall shear stress of $C_f = 2\tau_w/\rho U_{cl}^2 = 0.0065$ collapses the axial velocity reasonably well to a logarithmic law-of-the-wall profile as seen in Fig. 5(*a*). (A spline fit through the first two data points yielded $C_f = 0.0057$). Laufer [10] investigated several nearly fully developed channel flows including two of very similar Reynolds number to the PCJ configuration ($R_e^* = 24{,}400$, 24,600 versus 23,400 for PCJ). Laufer reported wall stress values of $C_f = 0.0036$ and 0.0038 for these two channels, significantly lower than the values deduced for the PCJ configuration. Consideration of this difference and of the mean velocity and turbulence intensity data in Figs. 5(*b*) and 5(*c*) suggest that the Reynolds normal and shear stresses in the PCJ confinement flow are significantly higher than in Laufer's channels. This is consistent with results to follow which indicate that the turbulence levels in the PCJ configuration are still decaying from their large near-inlet values at this near-outlet location.

Figure 6 shows a plot of measured axial mean velocity in the inlet pipe to jet 3, 1.75 pipe diameters upstream of the confinement inlet ($x = -0.0667$ m). The profile is seen to be very close to symmetric, and compares well with a 1/7 power law distribu-

[2]The measurement volume length of 0.32 mm in water indicates that the probe volume partially intersects the wall for these two measurement locations. Though the measured values of mean velocity appear reasonable, the normal stresses appear to be unrealistically high. Accordingly, the uncertainty associated with these two points was deemed significantly higher than the uncertainty estimated below for all the other top scan data.

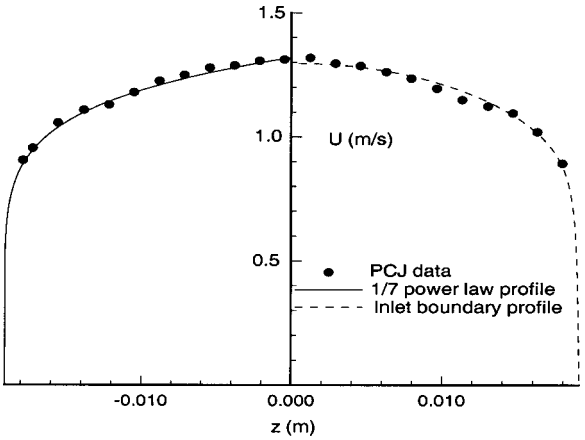

Fig. 6 Comparison of measured axial mean velocity in the jet 3 inlet pipe at x=−0.0667 m, with 1/7 power law profile

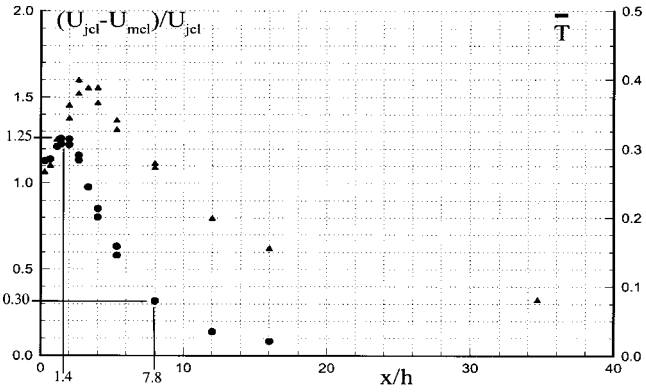

Fig. 8 Measured axial distributions of jet 3 axial velocity decay (circles) and mass weighted average axial turbulence intensity (triangles)

tion. Some evidence of the approaching confinement area step change is discernible in slight symmetric inflections near $z=\pm 0.01$ m ($z/h \equiv \pm 0.5$).

Detailed Scans. Figures 7 and 8 present axial and transverse mean velocity data at the first 10 scan locations. Figures 7(*a-j*) show front view contour plots of U and V. Figure 7(*k*) shows a plot of the $x=0.0381$ m scan. Clearly, the data are quite smooth, and both mean velocity components were found to be repeatable to within 0.02 m/s.

Several important features of the mean flow are obtained from the data in Fig. 7. Flow issuing into the confinement from the inlet pipe encounters a variable height ''forward step'' contraction, the maximum height of which occurs at the pipe/jet centerline. This gives rise to a large axial momentum defect at the jet centerlines.

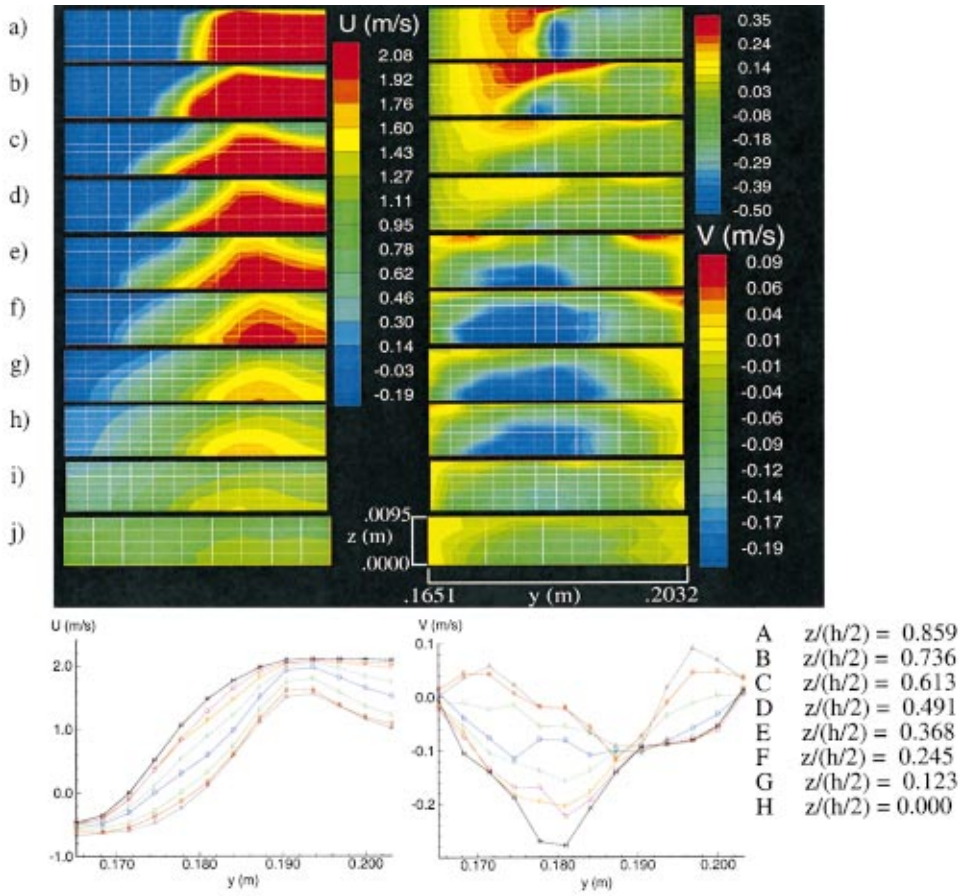

Fig. 7 Measured mean velocities, U and V. (a)–(j) are contour plots at x=0.0051, 0.0127, 0.0216, 0.0270, 0.0381, 0.0508, 0.0635, 0.0762, 0.1016, 0.1524 m, respectively. Experimental scan location grid is overlaid on contour plots. Two contour level bars for V velocity correspond to top four and bottom six scans, respectively. Figure 3 shows relative position of confinement wall and symmetry planes for these plots; (k) shows carpet plots of these data at x =0.0381 m.

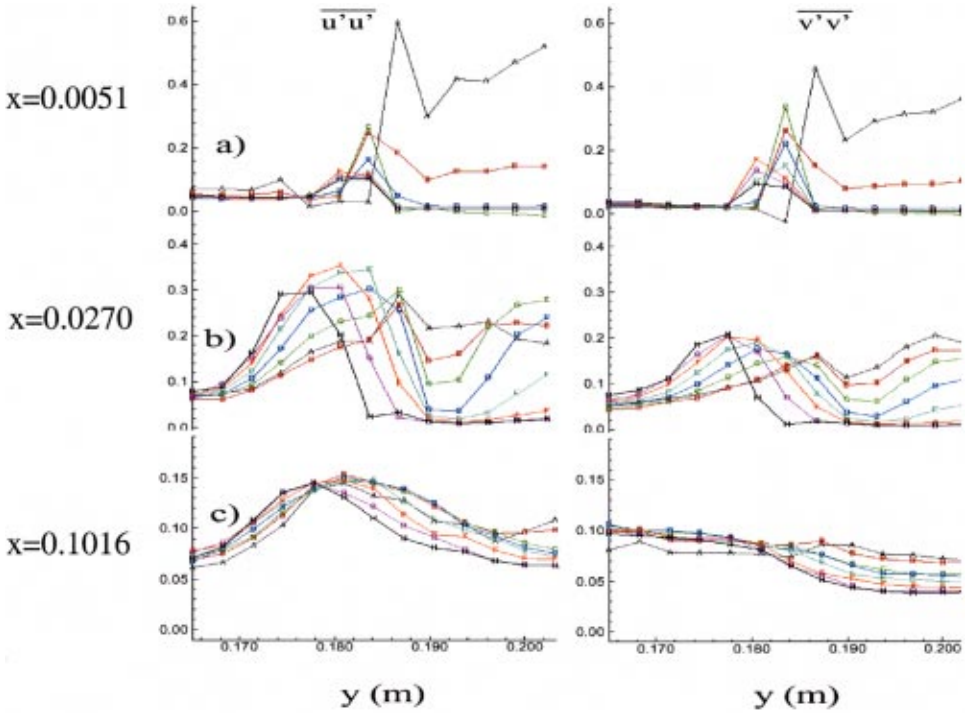

Fig. 9 Carpet plots of measured axial and transverse intensities (m^2/s^2). Left column: $\overline{u'u'}$, right column: $\overline{v'v'}$. (a)–(c) at x=0.0051, 0.027, 0.1016 m. Refer to Fig. 7 for key.

This defect is observed only very near the confinement wall at $x = 0.00508$ m (Fig. 7(*a*)). The size of this defect region grows in z and y over the first several scan locations. This is due in part to turbulence diffusion. Secondary flows which develop near the inlet likely also play a role in this transport of low momentum fluid. The peak jet centerline velocity is seen to increase due to this blockage (see also Fig. 8). The region of diminished axial velocity reaches the confinement centerline at $x = 0.0270$ m. This may be considered the axial extent of the near potential flow core at the jet centerline. This centerline defect is observed all across the confinement from $x = 0.0270$ m to $x \cong 0.15$ m (Fig. 7(*j*)) where its influence is seen to wash out.

As the parallel jets issue into the confinement, a large recirculation appears between adjacent jets. This recirculation zone is seen to be wider (Δy) and longer (Δx) near the confinement wall than at the confinement centerline (Figs. 7(*a-g*)). Specifically, at the confinement centerline, $x_{\text{reattach}} \cong 0.063$ m, compared to $x_{\text{reattach}} \cong 0.069$ m at the scan location closest to the wall ($z/(h/2) = 0.859$). Maximum magnitudes of reversed flow velocities are larger near the confinement wall than at the confinement centerline: $|\overline{V}|_{\text{max,recirc}} \cong 0.67$ m/s versus 0.51 m/s.

Downstream from the recirculation zones between the jets ($x > 0.07$ m) significant negative V velocities were measured across the jet due to jet spreading (streamline divergence). Near the confinement inlet ($x = 0.0127, 0.0216, 0.0270, 0.0381$ m), however, relatively large transverse velocities near the wall are positive (towards jet centerline) and near the confinement centerline negative. The magnitudes of these transverse velocities reach nearly 0.4 m/s, compared to the cross-section bulk velocity of 0.82 m/s. This suggests significant streamwise vorticity, arising from streamline divergence and secondary flows. Transverse velocities eventually diminish towards zero as the jets decay.

In Fig. 8, the axial jet decay along the confinement centerline is presented as a plot of normalized difference between measured axial velocity at the jet 3 centerline ($y_{\text{jcl}} = 0.2032$ m) and at the symmetry plane between jets 2 and 3 ($y_{\text{mcl}} = 0.1651$ m). (Two velocity difference values appear at several axial locations since repeated measurements were performed there.) The difference between U_{jcl} and U_{mcl} increases near the inlet as discussed above, reaching a maximum of $(U_{\text{jcl}} - U_{\text{mcl}})/U_{\text{jcl}} \cong 1.25$ at $x = 0.027$ m. The jets then mix out quite rapidly, falling to $(U_{\text{jcl}} - U_{\text{mcl}})/U_{\text{jcl}} \cong 0.3$ at $x = 0.152$ m.

Also presented in Fig. 8 is mass weighted average axial turbulence intensity, defined as:

$$\overline{T} = \frac{1}{U_{\text{bulk}}} \sqrt{\int_{A_{xs1/4}} \overline{u'u'}\, U\, dA_{xs1/4} \Big/ \int_{A_{xs1/4}} U\, dA_{xs1/4}} \quad (3)$$

plotted versus x. This intensity is seen to increase rapidly near the inlet, reaching approximately 0.40 at $x = 0.0508$ m. The turbulence intensity then decays exponentially. At $x = 0.6604$ m the average turbulence intensity is approximately 0.08, and still apparently decaying (see Fig. 5(*c*) and discussion).

Figure 9 shows selected comparison of measured axial and transverse turbulence intensities at three axial locations. The three selected scans are located: (a) very near the confinement inlet ($x = 0.0051$ m), (b) approximately halfway along the axial extent of the recirculation zones ($x = 0.027$ m), and (c) approximately two confinement heights downstream of reattachment ($x = 0.1016$ m). Very near the confinement inlet, turbulence intensities are quite small except near the wall and at the interface between the incoming jet and the recirculation region between jets, where maximum local intensities, $\sqrt{u'u'}/U_{\text{local}}$, of approximately 25% are observed. At $x = 0.027$ m, intensities grow quite large in the vicinity of the jet-recirculation zone interface. The location of peak intensity shifts towards the jet centerline as the confinement wall is approached, consistent with the cross-sectional shape of the inlet (Fig. 1). Turbulence levels at the confinement centerline remain small near the jet centerline, since flow at this location has primarily been subject to relatively small normal strains.

Transverse intensities exhibit the same trends as axial intensities at these first two scan locations, though the magnitudes of $\overline{u'u'}$ are nominally 50% higher. Downstream of reattachment, $\overline{u'u'}$ and $\overline{v'v'}$ exhibit significantly different character. Specifi-

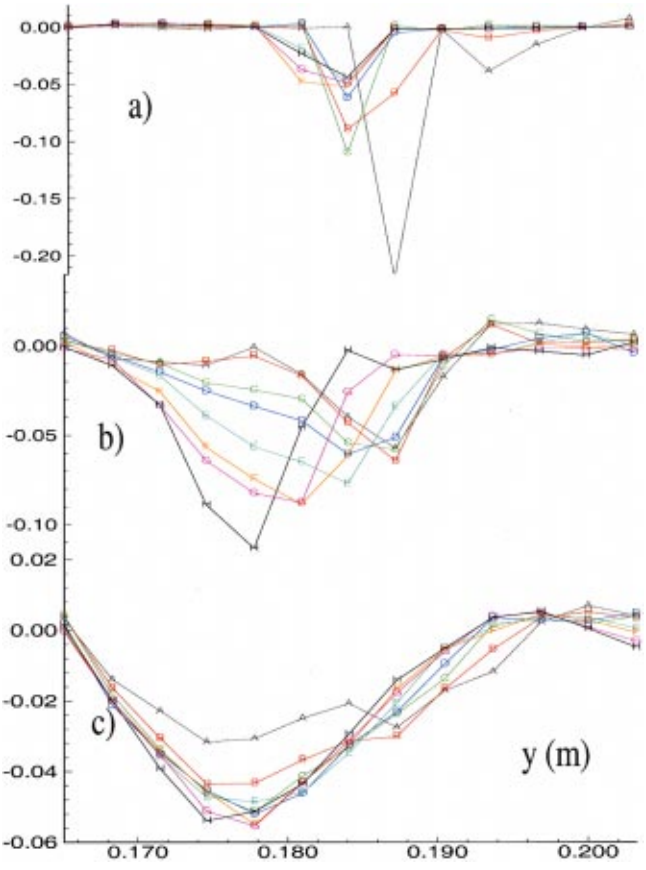

Fig. 10 Carpet plots of measured Reynolds stress, $\overline{u'v'}$ (m^2/s^2). (a)–(c) at x=0.0051, 0.027, 0.1016 m. Refer to Fig. 7 for key.

cally, in the defect region between the jets $\overline{v'v'}$ is larger than $\overline{u'u'}$, and diminishes monotonically toward the jet centerline. $\overline{u'u'}$ retains its upstream character of maximum magnitude near the location of maximum transverse shear ($\partial U/\partial y$).

The Reynolds shear stress data, $\overline{u'v'}$, are plotted in Fig. 10 at the same three representative axial locations. Qualitatively, these shear stresses follow gradient diffusion trends, as comparison with Fig. 7 affirms.

Conclusions

Detailed LDV measurements were taken in a parallel confined jet configuration. Two components of mean velocity and three Reynolds stresses were obtained. Several conclusions were drawn from the measurements:

Test section design and tuning the flow rates in the outermost jets gave rise to a nearly periodic flow so that three planes of symmetry could be exploited in the measurement program. This also, of course, facilitates Navier-Stokes analysis efforts.

Detailed resolution of the development of quantities obtained from the measurements provided insight into the complex mean flow and turbulence physics of this flow.

Mean flow measurements characterized important features including rapid jet decay, large recirculation zones between jets, strong secondary motions and peak axial velocities away from the jet centerline.

Turbulence intensities near the confinement inlet are quite high due to abrupt geometry change and dump diffusion there.

Significant anisotropies in the axial and transverse intensities appear near the symmetry plane between jets. This persists well downstream. The Reynolds shear stresses were observed to qualitatively follow gradient diffusion trends.

Nomenclature

A_{xs} = cross-sectional area of test section (m^2)
$A_{xs1/4}$ = area of 1/4 jet cross section
h = confinement height (=0.0195 m)
L = distance between adjacent jet centerlines (=0.0762 m)
N = number of samples taken
Q = volume flow rate through facility (m^3/s)
$Q_{1/4}$ = volume flow rate through 1/4 jet cross section
R_e = Reynolds number based on h and U_{bulk}
R_e^* = Reynolds number based on h and U_{cl}
U, V, W = mean cartesian velocity components
U_{bulk} = bulk velocity in confinement ($=Q/A_{xs}=0.815$ m/s)
u, v, w = fluctuating cartesian velocity components
x, y, z = Cartesian coordinates as defined in Fig. 1

Subscripts

cl = confinement centerline ($z=0.0$ m)
jcl = centerline of jet 3 ($y=0.2032$ m, $z=0.0$ m)
mcl = midpoint between jets 2 and 3 ($y=0.1651$ m, $z=0.0$ m)

References

[1] Newman, B. G., Patel, R. P., Savage, S. B., and Tjio, H. K., 1972, ''Three-Dimensional Wall Jet Originating from a Circular Orifice,'' Aeronaut. Q., **23**, p. 188.
[2] Launder, B. E., and Rodi, W., 1983, ''The Turbulent Wall Jet-Measurements and Modelling,'' Annu. Rev. Fluid Mech., **15**, p. 429.
[3] Davis, M. R., and Winarto, H., 1980, ''Jet Diffusion From a Circular Nozzle Above a Solid Plane,'' J. Fluid Mech., **101**, Part 1, p. 201.
[4] Holdeman, J. D., and Foss, J. F., 1975, ''The Initiation, Development, and Decay of the Secondary Flow in a Bounded Jet,'' ASME J. Fluids Eng., **97**, Sept., p. 342.
[5] Krothapalli, A., Baganoff, D., and Karamcheti, K., 1981, ''Partially Confined Multiple Jet Mixing,'' AIAA J., **19**, No. 3, p. 324.
[6] Barnett, D., and Bentey, H., 1974, ''Statistical Biasing of Individual Realization Laser Velocimeters,'' Proceedings of the Second International Workshop on Laser Velocimetry, Purdue University, p. 428.
[7] Patrick, R. W., 1987, ''Flowfield Measurements in a Separated and Reattached Flat Plate Turbulent Boundary Layer,'' NASA CR-4052, March.
[8] Patterson, R. W., 1982, ''Turbofan Forced Mixer-Nozzle Internal Flowfield, I-Benchmark Experimental Study,'' NASA CR-3492, April.
[9] Kunz, R. F., D'Amico, S. W., Vassallo, P. F., Zaccaria, M. A., Aksoy, H., and So, R. M. C., 1995, ''LDV Measurement and Navier-Stokes Computation of Parallel Jet Mixing in a Rectangular Confinement,'' AIAA Paper 95-2147.
[10] Laufer, J., 1950, ''Investigation of Turbulent Flow in a Two-Dimensional Channel,'' NACA Report 1053, p. 1247.

Numerical Simulation of Unsteady Turbulent Flow in Axisymmetric Sudden Expansions

Baoyu Guo

Tim A. G. Langrish

David F. Fletcher

Department of Chemical Engineering,
University of Sydney, NSW 2006, Australia

This paper is concerned with the numerical simulation of unsteady turbulent flows behind sudden expansions without inlet swirl. Time dependent simulations have been carried out using the VLES approach with the standard k-ε model. The expansion ratio investigated is in the range from 1.96–6.0. The simulations show that the flows in axisymmetric sudden expansions are inherently unstable when the expansion ratio is above a critical value. The precessing phenomenon, which features self-sustained precession of the global flowfield around the expansion centerline, is predicted successfully using CFD, with simulated oscillation frequencies that are in general agreement with reported data. For the case of expansion ratios from 3.5–6.0, a combination of a precession motion and a flapping motion in a rotating frame of reference is predicted in terms of the jet movement. Large-scale structures are identified in the downstream flowfield. Other important phenomena, such as the transition of the oscillation patterns, have also been predicted.
[DOI: 10.1115/1.1374441]

Introduction

Incompressible flows in sudden expansions are classical examples of many aspects of fluid flow phenomena (e.g., boundary layer development, shear layers, recirculation zones). They are fundamental to many engineering applications, such as burners and spray dryers. The flow phenomenon, known as a Precessing Vortex Core (PVC), has been observed mostly in swirling flows, such as cyclone separators (Yazdabadi et al. [1]) and swirl burners (Fick et al. [2]; Dellenback et al. [3]), all of which involve sudden expansion of the flow. However, the imparted swirl has proved not to be a prerequisite for the generation of a precessing flow instability. It has also been found to occur in a nonswirling axisymmetric sudden expansion flow (Hill et al. [4]; Nathan et al. [5]).

A fundamental study of the effect of jet precession on combustion has shown that it can be used to increase flames luminosity in, and reduce global NO_x emissions from, open natural-gas flames (Nathan et al. [6]). However, while preferred in burners and mixing vessels as it encourages the large-scale mixing process, the oscillations arising from such precessions within a large expansion should be avoided in spray dryers because they tend to cause undesirable back-mixing and particle deposition on walls, thus ruining the quality of products (Southwell and Langrish [7]). The PVC in swirl flows can also cause many other problems in process equipment by resonating with other system instabilities.

Lawson and Davidson [8] demonstrated a flapping oscillatory flow in a 1/3 scale water model of a casting mould by LDA measurements. In their model, as shown in Fig. 1, the jet was introduced from a tube into a rectangular chamber. A range of Reynolds number up to the order of 10^4 (at the inlet tube) was used. The crossflow time series recorded were found to be roughly sinusoidal in appearance with a relatively stable oscillation frequency. Two feedback pathways were considered responsible for the self-sustaining oscillation, namely, the crossflow region near the nozzle and crossflow through the gap between the nozzle and the cavity wall, with the former being the primary mechanism.

The investigations of the two-dimensional situation have highlighted the mechanism of the asymmetry and the oscillation of the flow. The restrictions in a two-dimensional sudden expansion do not necessarily exist in its three-dimensional, axisymmetric counterpart. For the three-dimensional sudden expansion from a circular tube or pipe, the recirculation vortex behind the expansion face is toroidal, with the pressure being continuous in the entire toroidal region. The early studies of the axisymmetric sudden expansion flows, including Durrett et al. [9] and Back et al. [10], were mainly concerned with the measurement of the reattachment location for a small expansion ratio (2.7 or less) and a low Reynolds number relative to those in most industrial flows (4,200 or less). Although the shear layer instability was experienced that causes the transition from laminar to turbulent flow, the mean flowfield remained axisymmetric and steady. On the other hand, Moon et al. [11] and Gould et al. [12] made measurements of the mean velocity and turbulent quantities with a Reynolds number of about 10^5. In the results of Gould et al. [12], some behavior of the turbulent triple products seemed to indicate the passage of large eddy structures or that the central core region was oscillating at some resonant frequency. They noted that this unidentified oscillation might be a fundamental characteristic of axisymmetric sudden expansion flow, but they did not investigate it further.

The precession phenomenon was initially observed in swirling flows. Experiments were performed by Hallett and Gunther [13] on swirling airflow in a sudden expansion with an expansion ratio of 2.22. For the highest swirl tested, a central recirculation zone (or vortex breakdown) was formed, while at swirl intensities below the critical value required for central back flow, a precession of the flow was discovered. This precession was strongest and most regular for low swirl, while at higher swirl the motion became increasingly irregular, until the advent of vortex breakdown damped out the precession completely. In addition, the shedding of large irregular eddies from the step downstream of the throat was observed, with an estimated frequency of between five and ten times that of the precession.

Dellenback et al. [3] made measurements in turbulent swirling flows through an abrupt axisymmetric expansion with an expansion ratio of 1.94, and examined the influence of the swirl number. The measurements of mean and RMS velocities were performed in a water flow using a laser Doppler anemometer (LDA). In the upstream tube, the Reynolds number was varied from 30,000–100,000 and the swirl number from zero to 1.2 (see Table 1). They noted that the PVC occurs for low swirl levels, and the PVC precesses with the mean swirl for larger swirl numbers, and against the mean swirl for low swirl numbers. The frequency in-

Contributed by the Fluids Engineering Division for publication in the JOURNAL OF FLUIDS ENGINEERING. Manuscript received by the Fluids Engineering Division October 12, 1999; revised manuscript received March 2, 2001. Associate Editor: U. Ghia.

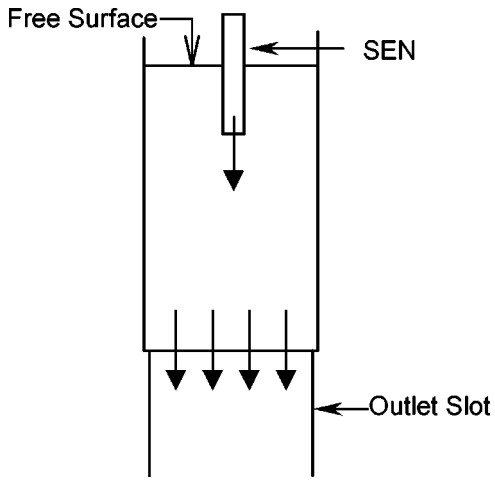

Fig. 1 A schematic representation of the geometry of the experiment by Lawson and Davidson [8]

formation was converted to a set of Strouhal numbers (fD^3/Q, where f is the precession frequency, D is the downstream diameter, and Q is the volumetric flow rate), which is shown in Fig. 2.

It was shown by the work of Hill et al. [4] that upstream swirl is not a prerequisite for precession provided that the expansion ratio is sufficiently large. They visualized the precession of a reattachment point in a large expansion into a long axisymmetric pipe without inlet swirl. Their observations suggest that any model in which the flow is constrained to be axisymmetric for a sudden expansion will be of limited relevance. The precessing frequency, f_p, was presented for the expansion ratio from 3.75–14.0 over a range of Reynolds numbers from 5000–65,000 at the inlet. The Strouhal number, defined as $\mathrm{St}=f_p\sqrt{\rho}D^2/\sqrt{M}$, was approximately constant (0.07–0.1), where M is a point source of axial momentum located on the centerline of a long axisymmetric duct of diameter D.

Nathan et al. [5] experimentally investigated a continuously unstable precessing flow within a short cylindrical chamber following a large sudden expansion without inlet swirl. They discovered that, with certain expansion ratios of the nozzle inlet orifice and for sufficiently large flow rates, an asymmetric precessing jet flow developed, which has proved beneficial in combustion applications. Two flow modes, i.e., an instantaneously highly asymmetric ''precessing jet'' (PJ) and a quasi-symmetric ''axial jet'' (AJ), were identified, with the temporal probability (proportion of time) of the PJ mode increasing with the Reynolds number. Their careful measurements excluded the possibility that the phenomenon was an artifact of some asymmetry within the inlet flow or the apparatus. As a variation to the precessing jet, a quasiplanar, naturally flapping jet has also been developed (Mi et al. [14]). Due to the complexity of the phenomenon, the precessing instability was very difficult to study at the fundamental level and was sometimes decomposed into its component features, which were investigated separately (Mi et al. [15], Schneider et al. [16]).

There have been relatively few simulations of this type of instability. Two cases from the work of Honeyands et al. [17], who made measurements in a series of rectangular blind (two-dimensional) cavities into which a jet is introduced, were studied numerically using the standard k-ε model and were compared with the experimental results, at jet Reynolds numbers of 35,000 and 45,000. The calculated oscillation frequencies were shown to be 12–18 percent lower than those measured. Gebert et al. [18] studied a jet oscillation observed in thin slab continuous casting. In their model, the fluid was injected from a small solid into the domain via an internal inlet, as shown in Fig. 3. The effect of the Submerged Entry Nozzle (SEN) volume was accounted for by exerting a resistance force in that region as the function of the velocity. A consistent cyclic jet oscillation was obtained when the resistance was below a critical value.

The oscillatory behavior in spray dryers is the primary concern of the current work. As discussed above, there have been several experimental studies of these flow instabilities in axisymmetric sudden expansions, which feature self-sustained precession of the global flowfield around the expansion centerline. However, the fundamental understanding has thus far remained rather incomplete. Here, a numerical study of these instabilities has been carried out using Computational Fluid Dynamics, in order to explore

Table 1 Summary of flow regions (Dellenback et al. [3])

Re=30,000	Remarks	Re=100,000
0<S<0.18	Vortex precesses in direction opposite to the mean swirl	0<S<0.12
S≈0.18	Precession frequency goes to zero	S≈0.12
0.18<S<0.37	Vortex precesses in same direction as the mean swirl	0.12<S<0.40
S≈0.37	PVC vanishes	S≈0.40
0.37<S<0.50	Bubble-type vortex breakdown	0.40<S<0.57
S≈0.50	Transition from recirculating bubble to strong on-axis tube of recirculating flow	S≈0.57
S>0.50	Strong on-axis recirculation	S>0.57

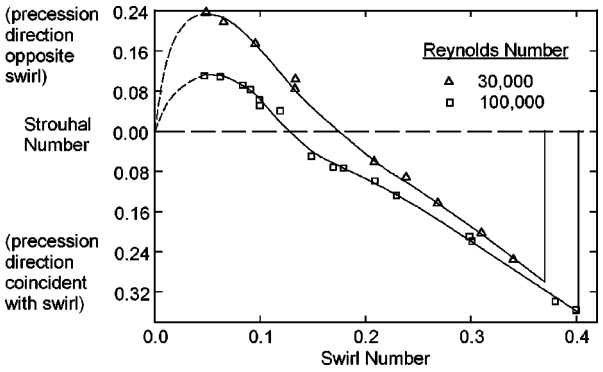

Fig. 2 Variation of Strouhal number with swirl number (Dellenback et al. [3])

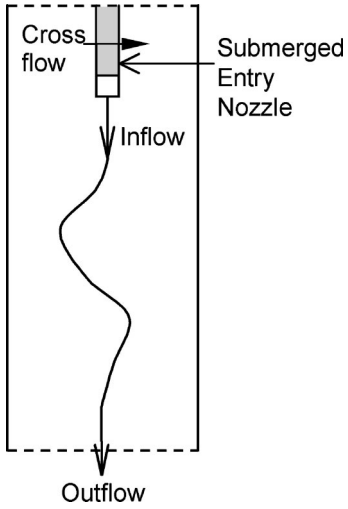

Fig. 3 A schematic diagram of the geometric model used by Gebert et al. [18]

the underlying phenomena. This current work uses the commercial CFD package CFX4 (CFX, [19]) to simulate the three-dimensional, time-dependent flow numerically in axisymmetric sudden expansions. When no swirl is present, a sustained precession and a flapping motion are found to exist simultaneously for the turbulent mean flow. The good agreement between frequencies measured and predicted by the numerical simulation gives confidence in the procedures used in the simulation, and further results on a swirling flow, which again reproduce experimental data very well, have been presented in another paper (Guo et al. [20]).

Mathematical Equations

Turbulent flows are extremely complex and time-dependent, but they are present in most engineering situations. Most fluid flows can be described by the full Navier-Stokes equations, which comprise equations for conservation of mass and momentum and, in a nonisothermal flow, energy. Nevertheless it is still infeasible to solve these directly via Direct Numerical Simulation (DNS) to the required accuracy using current technology, except for low Reynolds numbers in simple geometries. Therefore, in most engineering applications, a Reynolds averaging (time-averaging) method (RANS) is usually used to solve for the mean quantities rather than for all details of the turbulence. In this case, a turbulence model has to be used in order to close the system equations, which addresses the unknown correlation terms of the velocity fluctuations (Reynolds stresses).

There are more sophisticated methods, such as the Large Eddy Simulation (LES) approach, in which only the small-scale turbulent fluctuations are modeled and the larger-scale fluctuations are computed directly. A discussion of RANS and LES has been given by Spalart [21] and Speziale [22]. While LES is known to be able to predict more details of the flowfield, it requires considerably more computer resources than the RANS approach. Apart from the cost consideration, intense efforts are currently focused on devising a satisfactory subgrid-scale stress model, which is the primary deficiency of the method at this time. A great deal of research is required before it will be known how widely the method can be used (Rodi et al. [23]). Spieziale [22] has introduced an intermediate approach, known as Very Large Eddy Simulation (VLES), in which a mesh sufficiently fine to resolve the key transient flow features is used and a RANS model is used to model the small scale dissipative features. He studied some test cases using a nonlinear k-ε model as the RANS model. Therefore it seems worthwhile to test this simpler type of model for this flow, as it is infeasible to use the LES approach for routine engineering applications in the complex, high Reynolds number flows like the current case. This is particularly true for some applications, such as in a spray dryer, which has a wide range of eddy scales and the largest scale is of most interest.

Detailed descriptions of RANS turbulence models can be found in Wilcox [24]. The most commonly used turbulence models can be put into two broad classes, viz., eddy viscosity models and second order closure models. The two-equation k-ε model, an eddy viscosity model, is the simplest complete model of turbulence, and it is the most popular model, with what have become the ''standard'' constants being used:

$$C_\mu = 0.09,\ C_{\varepsilon 1} = 1.44,\ C_{\varepsilon 2} = 1.92,\ \sigma_k = 1.0,\ \sigma_\varepsilon = 1.3$$

This model is more reliable with a high Reynolds number. To avoid using a large number of grid points in a wall boundary layer, wall functions are usually employed. Several low Reynolds number versions of the two equation eddy viscosity model, such as the k-ω model, have been developed, but they are difficult to implement in the boundary layer for three-dimensional problems due to the requirement of very fine grids.

Another often-used high Reynolds number model, the Differential Reynolds stress model (a second moment closure model), solves differential transport equations for Reynolds stresses, in which higher-order correlations are retained and have to be modeled in terms of known lower-order ones. However, this model is much more computationally expensive than the k-ε model, and has undergone much less validation. These models have been applied mostly to some simple flows, such as mixing layers and channel flow, with varying degrees of success. Therefore validation is usually required for each application. To compare the effect of the turbulence model on the flow instability induced oscillation, several models were applied to a two-dimensional problem (Guo et al. [25]) which is closely related to the problem considered here. The standard k-ε model proved to be satisfactory in capturing the essence of the instability and is thus used in the simulation of the axisymmetric expansion flows presented here.

Numerical Considerations

The simulations used the Computational Fluid Dynamics (CFD) program CFX4 which uses a structured mesh and a finite volume formulation to discretize the Navier-Stokes equations. A discussion of various schemes and turbulence models was given in Shore et al. [26]. This study showed that the high-order schemes implemented in CFX4 could reproduce the swirl flow velocity fields obtained using orthogonal grids aligned with the flow using nonorthogonal, non-flow aligned grids. Based on this work, the discretizing scheme used for the convective term is the QUICK scheme (Leonard [27]) for velocities. The Van Leer limiter (see Hirsch [28]) was implemented for the turbulence quantities k and ε. This scheme is almost second-order accurate and maintains monotonicity across computational cells, hence preventing numerical oscillations in the solution domain. It has also been used for velocity components, and this change was found not to influence the results. The PISO algorithm (Issa [29]) was used for pressure correction. In this algorithm, a second pressure-correction equation is solved in order to improve the solution of momentum equations while maintaining continuity and thus reducing the number of global iterations for convergence. This algorithm was found to produce the same results (in terms of the dynamical behavior reported) as the SIMPLEC algorithm. The quadratic (second-order), fully implicit scheme has been used for time discretization. The diffusion terms are represented using a second order scheme, so that the entire scheme is second order accurate in both space and time. The equation solvers were Stone's method for velocities and algebraic multigrid for the pressure.

The working fluid was chosen as incompressible and Newtonian. A time-dependent calculation was usually started from a steady calculation, in which a global mass balance had been enforced and residuals of other variables had been considerably reduced. Although the results appeared to be chaotic and varied from case to case for an initial period of time after the time-dependent calculation was started, the final solution was independent of the initial conditions in most cases. However, there were exceptions in which multiple solutions existed, or a transition of flow patterns occurred from one mode to another.

As a convergence criterion, the sum of the absolute mass source residuals over all cells was less than 0.1 percent of the total flowrate. This resulted in a sufficient number of iterations being carried out for each time step so that the changes in the monitoring point values were indiscernible with further iterations (Guo et al. [20]). Further reduction of mass source residual by one order of magnitude had no discernible effect on the oscillation frequencies. However, since the convergence rate can be affected by other factors, such as the time step, the size and quality of the grid, the variation of residual values with iterations was checked to ensure that the residuals for all the equations were consistently decreasing and approaching their limit of the accuracy for single precision. This minimized the chance of error accumulation over successive time steps.

Geometric Model and Boundary Conditions

The geometry shown in Fig. 4 consists of two pipes of diameter d and D. The ratio of the larger diameter D to the inlet tube diameter is defined as the expansion ratio E. The x-axis of the Cartesian coordinates is on the axis of the pipes and the origin is at the center of the expansion face. There are several reasons to choose Cartesian coordinates instead of cylindrical coordinates: (1) The physics of interest is asymmetric and time dependent despite the axisymmetric nature of the geometry. (2) There is a singularity on the axis in cylindrical coordinates where zero radial and azimuthal velocities do not allow the transient flow to pass through the axis. (3) It is comparatively flexible to adjust the grid distribution as needed. The simulation regime has been taken as $l=5\sim10d$ and $L>16D$. U_i and U_0 denote the axial bulk velocities for the inlet and outlet.

A fully three-dimensional structured grid (as shown in Fig. 5) has been used and constructed to have small orthogonality deviations. At the center of the larger cylinder it consists of five blocks, which when viewed in the axial direction show four blocks making an O-grid around an H-grid (a so-called butterfly mesh). In the annular region, a refining structure has been used to avoid over concentration of cells at the center. Unlike cases with cylindrical grids, the solution with this model is able to vary smoothly across the center axis of the geometry and resolves the full flowfield of the whole domain rather than part of it. The cell density along the axis is nonuniform, and increases as the expansion plane is approached, with the neighboring cells varying in size by no more than 10 percent.

The velocity at the inlet was parallel to the inlet tube axis without any cross-stream components, with the mass flux being specified. Except where the sensitivity to inlet conditions was examined, Neumann boundary conditions were imposed for both the inlet and the outlet, which meant that the velocity components and turbulence quantities were assumed to be fully developed for the inflow but had a zero normal gradient for the outflow. The relative pressure was set to zero at the outlet. A universal log-law wall function was applied for all walls. To ensure the validity of the wall function treatment, the y^+ value of the near wall nodes was verified after the simulations and was confirmed to lie in the range of 10–500. The maximum value usually occurred at the tip of the expansion throat due to the high local velocity, thus adequate grid refinement needed particular care in that region.

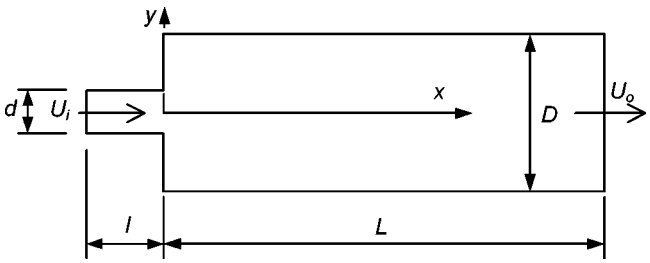

Fig. 4 A schematic diagram of the geometry

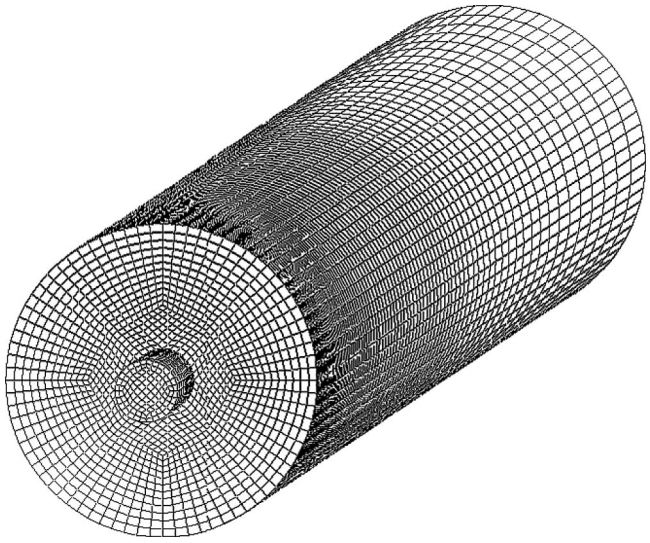

Fig. 5 A typical grid used in the calculations

Steady-State Simulation

Usually a steady simulation was attempted at the initial stage, but it was extremely difficult to achieve convergence even using very small under-relaxation factors in the iteration scheme. As the physics of the flow are unstable, the instability can be easily triggered by numerical oscillations introduced by the truncation errors and iterative solution procedures. After a sufficient number of iterations, the residuals for each equation reduced to a certain level, and then they neither converged nor diverged but oscillated with further iterations. On the other hand, the values of the variables at a monitoring point fluctuated constantly. This implied that a time-dependent solution may exist, therefore it was sensible to switch to a transient calculation.

It is also noted that an unsteady flow can be distinguished from a steady one in an unsteady simulation, because the solution tends to develop toward time independence if a steady-state exists as the calculation proceeds, regardless of initial disturbances. This has been demonstrated in the simulation of a swirl flow for a smaller expansion ratio (Guo et al. [20]).

Time Variation of the Flow Variables

A time-dependent simulation was carried out first with an expansion ratio of five (l=10d, $L=20$ D) for a Reynolds number of 10^5. All the Reynolds numbers used in the current simulations are based on the inlet diameter and average inflow velocity (bulk flow velocity at the inlet). Velocities and pressure were recorded at several locations during the course of the transient calculation, producing a time series for each flow quantity. After a period of chaotic transition, coherent oscillations of the variables at the monitoring points have been observed, as shown in Fig. 6, regardless of the initial conditions. In the graph, the time, t, is normalized as $U_i t/d$. The velocity components have been normalized by U_i and the pressure has been normalized by the dynamic pressure of the bulk flow at the inlet, $\frac{1}{2}\rho U_i^2$. As can be seen, the velocity components V in the y direction and W in the z direction oscillate intensely. However, the variations of V and W velocities look alike except that there is a phase difference between them. Moreover, there is an oscillation of higher frequency superimposed on a fundamental oscillation. It is possible to identify the frequencies of the two apparent oscillations. Due to the axisymmetric nature of the geometry, it is sensible to analyze the velocity component in the cross-stream plane or transverse velocity (with the amplitude of $(V^2+W^2)^{0.5}$ and the direction expressed by a phase angle

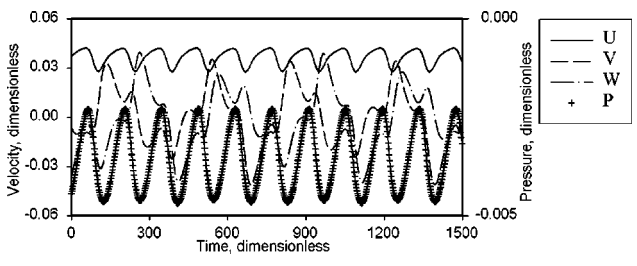

Fig. 6 Flow variables at the monitoring point 4D downstream from the expansion on the center-line ($E=5$, Re=10^5)

$\tan^{-1}(W/V)$). In polar coordinates, the amplitude indicates the motion in the radial direction, while the phase angle represents the motion in the tangential direction. It can be seen from Fig. 7 that the amplitude appears more regular and oscillates periodically about a fixed value (~0.025). The above phenomena indicate that there are two different motions (swinging and precession or rotation) of the jet which occur simultaneously at that point.

In Fig. 8, the phase of the transverse velocity runs from $-\pi$ to $+\pi$ (or $+\pi$ to $-\pi$, depending on the precessing direction) in a cycle (the corresponding time interval is defined as the precession time period), so that the existence of the precession is evident. A periodic function of higher frequency is superimposed on the straight lines from $-\pi$ to $+\pi$ (or $+\pi$ to $-\pi$). This periodic function corresponds to the oscillation of the amplitude in Fig. 7. Therefore the plane of the swinging motion also rotates with the precessing motion. This means that a higher-order oscillation occurs relative to a moving coordinate frame that rotates at the fundamental frequency of the precession. Thus, in this fashion, a relatively complex time series can be decomposed into two regular periodic oscillation curves.

The behavior can be described as a jet precession that is generated by the flow instability downstream from a sudden expansion. As distinct from a swirling motion, it refers to the rotation of the jet about an axis other than its own axis. Figure 9 shows a time series of variables at an off centerline monitoring point. The positive peaks of the axial velocity (U) correspond to the moments when the jet passes the point.

The variation of the flowfield with time is often expressed in this paper via a ''limit cycle,'' which is obtained from the cross-stream velocity components V and W at a fixed point on the geometric center-line. The limit cycle is a mathematical term that is sometimes used to describe the complicated behavior of nonlinear dynamical systems. Here it is meant to facilitate the identification of the global motion of the flowfield. By processing the velocity components at the central monitoring points in this way, the patterns of the jet movement are qualitatively indicated in Fig. 10. At the point close to the expansion, the values on the axes are proportional to the deflection angle of the jet. The animation of the flow field in a cross-sectional slice indicates that the limit cycle as in Fig. 10 can essentially represent the pattern of the jet movement in the corresponding plane. Therefore, the ''bouncing-around'' path can be interpreted as a combination of two or more simple functions, typically a global precession and a quasi-flapping (as we define it) in a rotating frame of reference that corresponds to the precession (as sketched in Fig. 11). Quasi-flapping is so called because the jet moves, relative to the rotating frame of reference, along a nearly straight line or a curve other than a circle and may in fact be at an angle (θ) to the radial direction. In terms of the jet

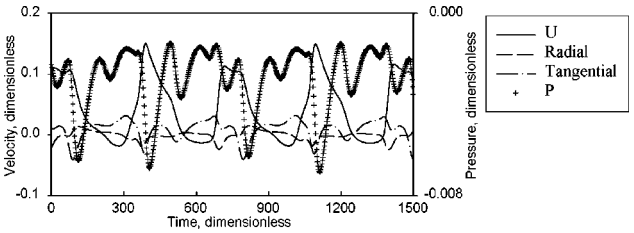

Fig. 9 Flow variables at the monitoring point 0.4 D from center-line and 4D downstream from the expansion (conditions as in Fig. 6)

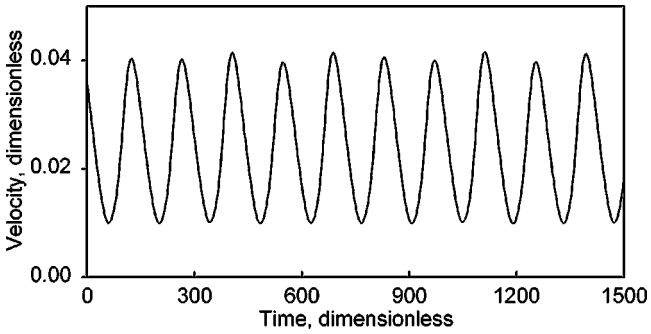

Fig. 7 Amplitude of transverse velocity (conditions as in Fig. 6)

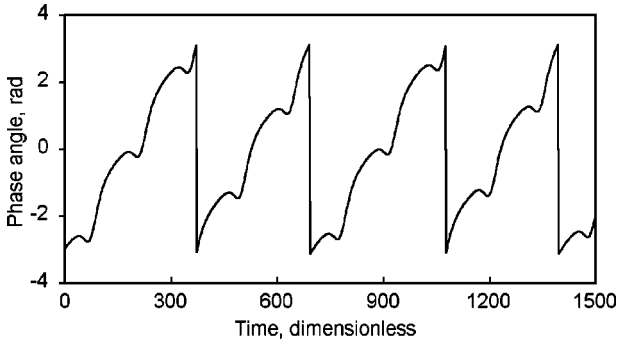

Fig. 8 Direction angle of transverse velocity (conditions as in Fig. 6)

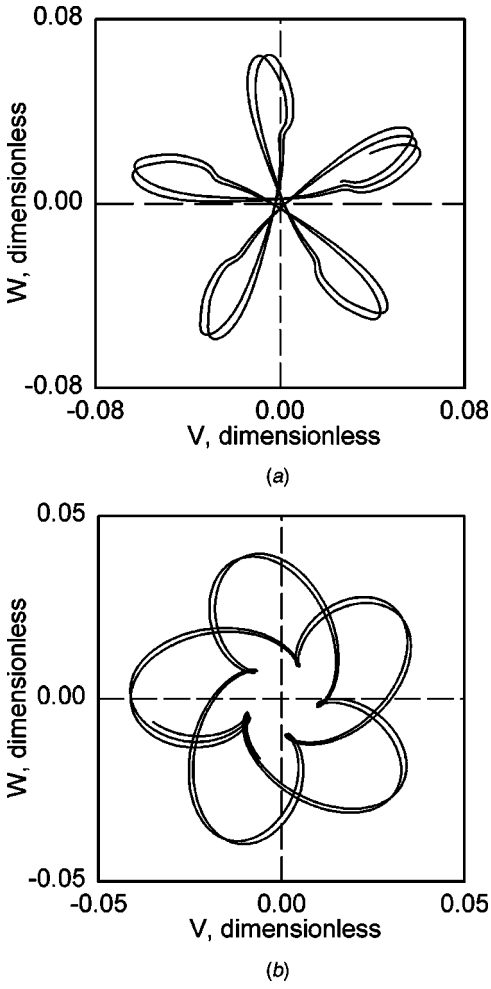

Fig. 10 Limit cycles at different axial locations (conditions as in Fig. 6) (*a*) 0.2D from the expansion; (*b*) 4D from the expansion

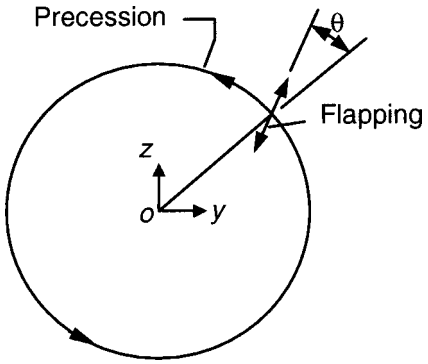

Fig. 11 A schematic diagram showing a jet precessing and flapping

motion, while the jet rotates around the centerline, its location with respect to the centerline (or the distance to the centerline) constantly changes due to the flapping. The flapping amplitude is prominent in the proximity of the expansion throat relative to the precession, but becomes smaller in scale than the precession as the fluid proceeds downstream. As can be seen, the centers of these limit cycles are on the center-axis, implying that the flow field is globally symmetric over a long time period about the centerline in spite of instantaneous asymmetry.

Sensitivity Checks

Time Step. The pressure variation is denoted in Fig. 6 and Fig. 9 by symbols corresponding to each time step, which shows that the chosen time step resolved the oscillation adequately and the flow variables changed smoothly. Typically, there were about 180 time steps in each precession. This time step was small enough that the oscillation frequency was insensitive to further reduction. For instance, halving the time step from this value varied the precession frequency by less than 2 percent.

Grid Sensitivity. Table 2 lists the periods of oscillations for a series of different grid sizes. The fundamental feature, i.e., a combination of a precession and a flapping relative to a rotating reference, has been predicted in all these cases. Refining the grid by over 50 percent in both the axial and the diametrical direction (corresponding to a four times increase from 52,875–217,625 in the total number of cells in the larger pipe) resulted in a difference of 6 percent for the time periods of oscillations. The final grid used in this case has about 150,000 cells.

Inlet Conditions. Flow simulations have indicated that, except at the bifurcation point, the initial flow fields are not critical. However, this is not true for the boundary conditions if the simulation domain is not carefully specified. In the previous calculations, a mass flow boundary for inflow has been implemented so that all velocities and turbulence quantities have zero gradients, so it is not necessary to set any profiles as these are determined as a part of the solution. The resulting profiles at the inlet are typical of a fully developed pipe flow.

In order to check the sensitivity to the variation of the inflow quantities, Neumann boundary conditions have been replaced by the Dirichlet boundary conditions so that the values of flow variables were explicitly assigned at the inlet. When a length of inflow pipe is included within the simulation domain, if a nonequilibrium value is set at the inlet, it may be dissipated in the inflow pipe. Any disturbance may also decay away before reaching the expansion. Therefore, significant influence only appears within the inflow tube, and the solution in the downstream pipe is less sensitive to the inlet condition with an inlet pipe than without it. On the other hand, the conditions upstream of the expansion can be affected by the downstream oscillation. For the case of an expansion ratio $E=4.87$ and a Reynolds number $\mathrm{Re}=10^5$, the flow deflection angle at the expansion is about one degree, and the influence extends about one diameter upstream from the expansion plane. This further shows the importance of the inflow tube.

Table 2 Period of oscillations for different grid sizes ($E=5.0$, $Re=10^5$)

Number of cells in the larger pipe			Time period of oscillations, dimensionless	
Axial	Diametric	Total	Flapping	Precession
75	35	52,875	148	365
85	42	88,740	143	353
90	52	152,280	140	355
125	53	217,625	139	343

Visualization of the Flow Field

Although the instantaneous flowfield changes with time, the fundamental features remain the same. Figure 12 shows a picture of instantaneous streaklines originating from an upstream plane for the case of $E=5.0$, and Fig. 13 is the interpretation of the corresponding streaklines. The fluid emanating from the inflow tube separates at the expansion, departs from the central axis and moves toward the large cylindrical wall. It reattaches to the wall at around 1.5D. This point may vary with time due to the flapping oscillation. The reattachment occurs over a length of about 3D. Then the jet separates from the wall and bends inward toward the other side of the wall. While a smaller proportion of the jet fluid moves downstream, most of the fluid reattaches to the opposite side of the wall and then flows upstream along the wall, thus creating a significant reverse flow. In this way a large structure is formed by the reverse flow together with the main jet, which looks like a skewed elliptical ring (or recirculation ring). This recirculation ring is essentially different from the central recirculation zone that appears with a vortex breakdown in a strong swirling flow, in which the time mean flow reverses at the center-axis. The length scale of this ring-like recirculation in the present simulation is 1D in the cross-stream direction and about 4D in the streamwise direction. The jet is gradually dispersed and becomes very weak after the recirculation zone. The downstream flow has a specific time lag due to the flow inertia, thus the jet spirals in the opposite

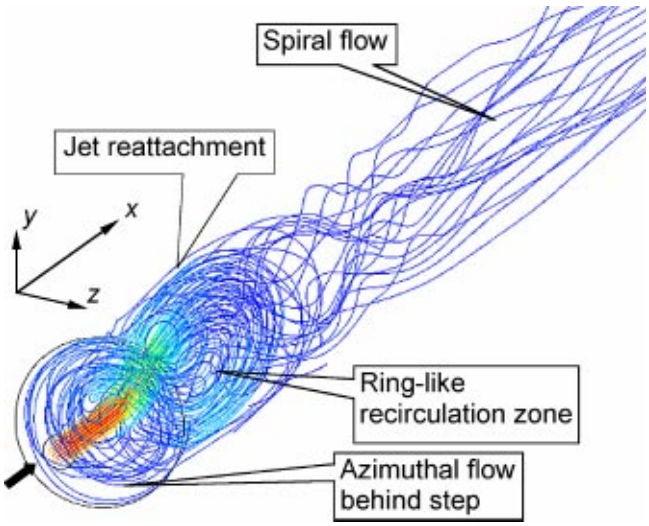

Fig. 12 Instantaneous streaklines calculated for precessing flow in an axisymmetric sudden expansion ($E=5.0$, $\mathrm{Re}=10^5$)

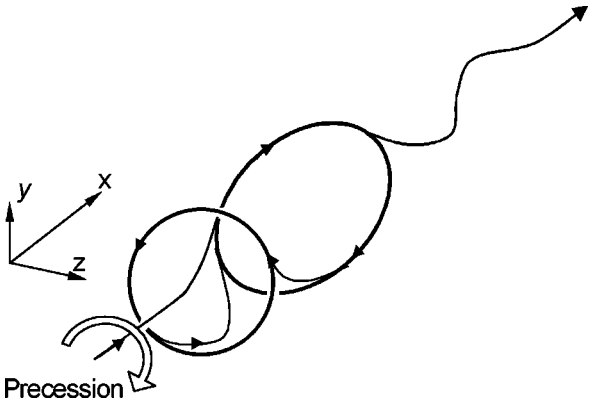

Fig. 13 A schematic interpretation of the instantaneous streaklines

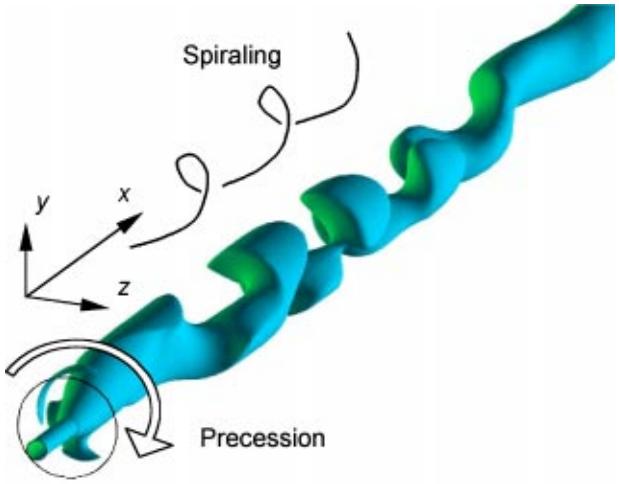

Fig. 14 An iso-surface for axial velocity ($E=5.0$, $Re=10^5$). The spiraling direction relative to the precession is indicated schematically.

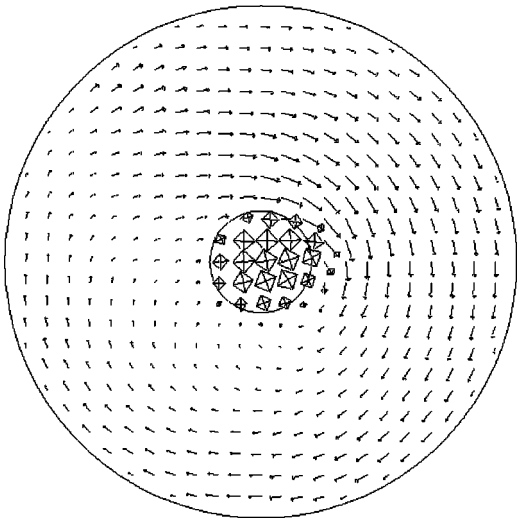

Fig. 15 Instantaneous velocity vectors in a cross-stream plane 0.2D downstream from the expansion ($E=5.0$, $Re=10^5$)

direction to the precession, as can be seen in an iso-surface of the axial velocity in Fig. 14. This spiral nature of the jet is important for the jet precession as it produces a nonzero tangential momentum to the jet, which is well balanced by the remaining fluid motion so that the sum of the angular momentum remains insignificant.

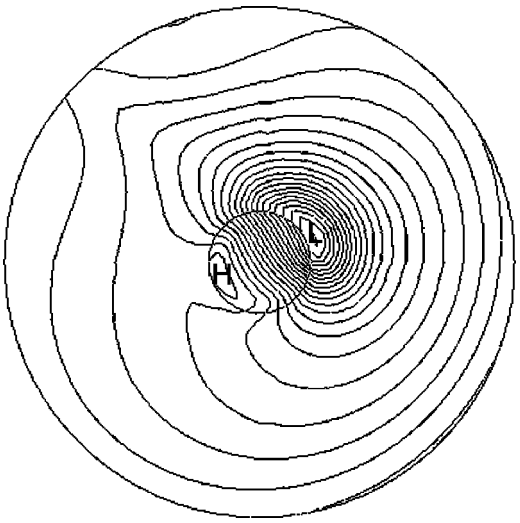

Fig. 16 Instantaneous pressure contours in a cross-stream plane 0.2D downstream from the expansion ($E=5.0$, $Re=10^5$)

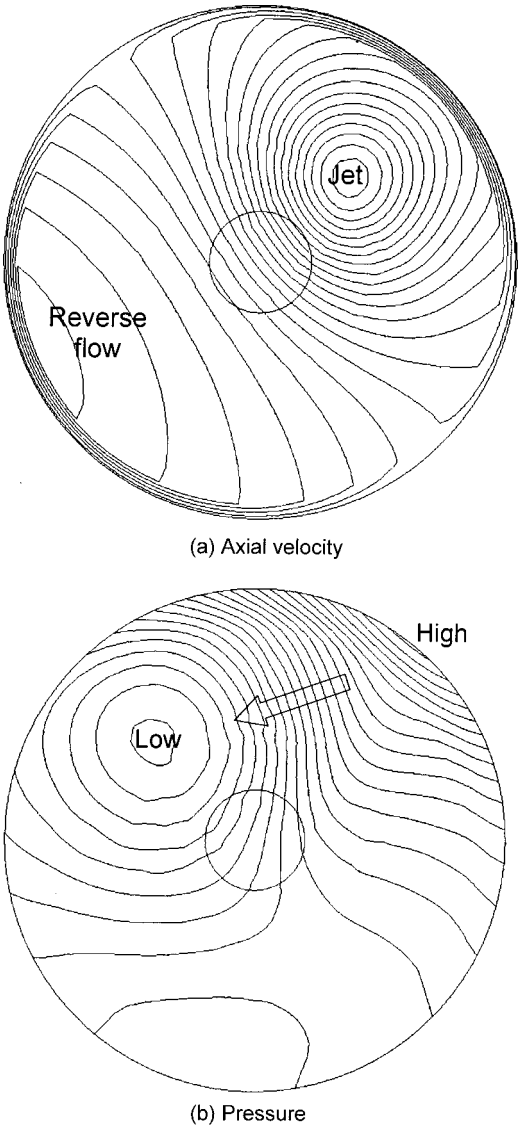

Fig. 17 Contour plot in a cross sectional plane 1.6D from the expansion ($E=5.0$, $Re=10^5$)

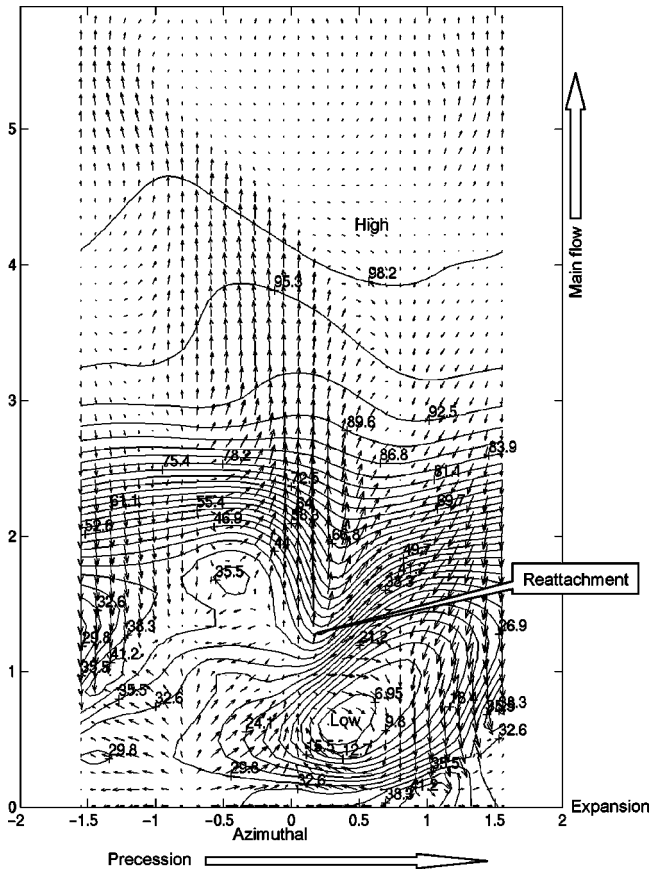

Fig. 18 Wall velocity vectors and static pressure contour map ($E=5.0$, $\mathrm{Re}=10^5$). The pressure contour values are relative pressure, which are scaled up by a factor of 10^3.

Just behind the expansion face, a tangential flow moves in the opposite direction to the precession. This tangential flow is fed by the central recirculation flow, and is partly entrained into the main jet. Figure 15 shows the velocity vectors in a cross-stream plane near the expansion, which indicates that the tangential flow is not uniform in the circumferential direction. In spite of the tangential flow and precessing motion being induced, the net angular momentum over any cross-sectional plane remains low (it is two orders of magnitude smaller than the axial momentum). However, significant mixing between the upstream and downstream flows, as well as tangential mixing, would be expected.

Figure 16 shows an instantaneous pressure contour map. At this moment, a low-pressure core has departed from the center-line and created a pressure difference across the jet that drives the jet away from the center-line toward the wall. Figure 17 shows the contour maps at a point in time on a cross-sectional plane that cuts through the larger recirculation zone. The positions of the jet and reverse flow on the axial velocity contour map (Fig. 17(*a*)) indicate that the recirculation ring is not perfectly symmetric about an axial cutting plane. It can be seen, from the corresponding pressure contour map (Fig. 17(*b*)), that the highest pressure occurs on the wall where the jet reattaches. There exists a low-pressure zone, which creates a pressure gradient across the jet. This gradient may drive the jet to move towards the other side of the wall at an oblique angle, and the jet appears to ''bounce'' off the wall (see further discussion later).

Figure 18 shows instantaneous near-wall velocity vectors and pressure contours in the upstream section of the chamber, with the circular wall being mapped to a planar surface. The horizontal axis represents the tangential location along the circumference, and the vertical axis is the axial distance from the expansion. The distance has been normalized by the downstream diameter and the pressure has been normalized by the dynamic pressure at the inlet, i.e., $\frac{1}{2}\rho U_i^2$. The precession in this case is from left to right. The static pressure increases significantly along the stream within four diameters from the expansion. In this region, complicated processes of momentum transfer take place and most of the kinetic energy is transformed into pressure energy. It can be seen that the pressure at the impingement point of the jet, which can be identified (marked as ''Reattachment'') on the near-wall surface vector map, is relatively higher than any other point at the same axial position. The configuration of the reattachment region is not aligned with the center-axis, confirming that the jet is spiralling when moving down in the direction opposite to the precession. The three-dimensional nature of the jet produces tangential momentum. There is a low-pressure zone (marked as ''Low'') near the reattachment point, due to which a pressure gradient is formed across the jet at an oblique angle to the stream direction. This is a driving force for the precessing movement of the jet reattachment point.

Flow Regime Map

In the above sections, a regular precessing flow has been discussed in detail. By ''regular precession'' we mean that there are no significant variations in the period and the direction reversal among consecutive cycles. This is the case with an expansion ratio between 4.0 and 6.0 (with high Reynolds numbers). In this region, the precession is induced in either the clockwise or the counter-clockwise direction and does not change direction once established. However, different behavior has been found by changing the expansion ratio. Figure 19 shows the extended results with the flow pattern as a function of expansion ratio and Reynolds number.

The patterns of oscillations produced by the instability can be qualitatively divided into several regions. At the smallest expansion ratio (below about three), the flow tends to be stable due to the smaller extent of the shear layer. In this region, the substantial viscous force at a low Reynolds number, in relation to a high Reynolds number, serves to damp out any disturbances, and flow thus remains steady (laminar or turbulent). However, the increase of the expansion ratio causes stronger disturbances and thus encourages an early transition to unsteadiness, thus the boundary is qualitatively represented by a sloping line.

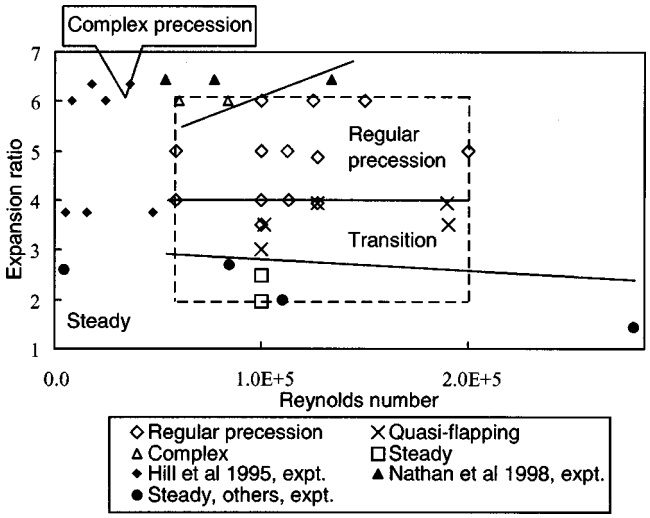

Fig. 19 Schematic map of flow patterns in axisymmetric sudden expansions. The data marked ''others'' in the legend are for steady conditions from Durrett et al. [9], Back et al. [10], Gould et al. [12], and Moon et al. [11].

The region between the regular precession and steady flow is called the transition region, with the expansion ratio being about 3.0–4.0. In this region, due to either a bifurcation or hysteresis, two different modes can develop: one is related to the regular precession and the other is called quasi-flapping. For the latter mode, the smaller space surrounding the jet limits the extent of the interaction in the tangential direction, thus the jet may be unable to complete a precessing cycle around the centerline. The simulation in this region also gives a periodic (regular) time series at every monitoring point.

For a larger expansion ratio above 6.0, the Reynolds number plays a role. At a low Reynolds number, the flow pattern exhibits a complex behavior. However, when the Reynolds number increases above a certain value, the oscillations regain a regular pattern. In this case, a minimum Reynolds number is necessary to maintain the regular state.

Most of our calculation results fall into the rectangular region marked by a dashed line, with the expansion ratio $E=1.96-6.0$, and high Reynolds numbers between 50,000–200,000. Some reported experimental data with similar expansions are also shown here for comparison. In the steady state region, the simulation result for the case of $E=1.96$ indicates that the reattachment occurs at approximately 8 step heights downstream of the expansion, which agrees with the published results from many earlier studies (Gould et al. [12]).

For the case of precession, the geometries used in the literature differ from the geometry used in the current simulations. For example, Hill et al. [4] used a smooth contraction inlet to a sudden expansion, whereas the nozzle used by Nathan et al. [5] had a sharp-edged inlet orifice and a contracted exit. The alternation of PJ and AJ modes observed by Nathan et al. [5] possesses similar features to the complex oscillation discussed here. It was found that, although the percentage of time spent in the PJ mode is strongly dependent upon the nozzle geometry details, the stability of the PJ mode increases with Reynolds number. Their results qualitatively support the present predictions. Nevertheless, their observation suggests a transition from the complex patterns to the regular ones in a gradual way rather than an abrupt change.

Uncertainty is possible at the regime boundaries. The flow patterns at the transition region may be sensitive to the geometry details, external disturbances, and initial conditions, just like the transition from laminar flow to turbulence, so the boundaries of the regimes may therefore not be clear-cut.

The visualization by Hill et al. [4] showed an intermittent precession and the Reynolds numbers used for the expansion ratios from 3.75–6.36 were in a range between 5000 and 37,000, which is much lower than those used here. Due to the limited capability of turbulence models for low Reynolds number flows, no predictions have been attempted in this region. In the transition region, however, no experimental data about the quasi-flapping behavior have been found for the axisymmetric geometry.

Strouhal Number

The oscillation frequency (or period) is important because it represents the real timescale of the self-sustained transient problem. It is normalized in terms of a Strouhal number, in order to establish a dynamic similarity between different cases, i.e., geometry and Reynolds number. The instability is induced downstream of the expansion by the momentum transfer between the jet and confining wall. Visualization shows that both the recirculation vortex formed and the extent of the jet movement have a length scale of the downstream chamber dimension. Therefore it is physically sensible to define a Strouhal number in terms of a downstream characteristic length D and the jet momentum flux M. According to dimensional analysis, the Strouhal number can be defined as

$$\mathrm{St}=\frac{f\sqrt{\rho}D^2}{\sqrt{M}} \tag{3}$$

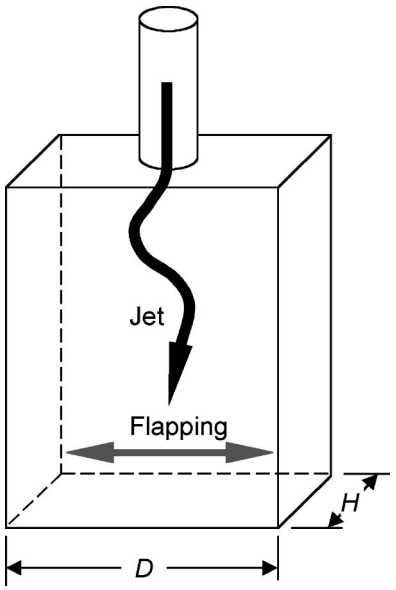

Fig. 20 Schematic diagram of the dimensions in the definition of Strouhal number for a non-circular chamber

This formula was used by Hill et al. [4] and was found to give a common curve with the experimental data for the precession frequencies in axisymmetric sudden expansions. In these cases, the downstream diameter is chosen as the characteristic length, and the jet momentum flux is calculated by

$$M=\frac{\pi}{4}d^2\rho U_i^2 \tag{4}$$

Equation (3) thus becomes

$$\mathrm{St}=\frac{2}{\sqrt{\pi}}\frac{fd}{U_0}=\frac{2}{\sqrt{\pi}}E^2\frac{fd}{U_i} \tag{5}$$

where f can be the flapping frequency f_s or the precessing frequency f_p.

To extend to the cases where the downstream geometry is other than circular and/or a flapping oscillation occurs in a specific direction in a quasi two-dimensional fashion, Eq. (3) is modified as

$$\mathrm{St}=\frac{f\sqrt{\rho}D^2}{\sqrt{M}}\left(\frac{H}{D}\right)^{0.5} \tag{6}$$

to accommodate the numerous geometric variations. Here both D and H refer to the cross-stream dimensions of the downstream chamber, as indicated in Fig. 20 for a noncircular chamber. D is the width in the flapping direction and H is the dimension in the

Table 3 Coefficients and exponents for the Strouhal number

	C	n
Nathan *et al.* [5]	1	0
Current and Hill *et al.* [4]	$2/\sqrt{\pi}$	2
Hallett and Gunther [13], Dellenback *et al.* [3]	$4/\pi$	3

normal direction to the flapping. For a real two-dimensional problem, the results obtained using Eq. (6) are independent of H.

Different parameters have been used to normalize the precession frequency by other researchers. In spite of slightly different definitions, Strouhal numbers used in the literature can be expressed in a general form, $\mathrm{St}=CE''fd/U_i$, where the coefficient and exponent are listed in Table 3. The exponent n represents the sensitivity of the precession frequency to the expansion ratio.

Effect of Reynolds Number

Since the k-ε model is most reliable when the Reynolds number is high (of the order of 10^4 or above), the Reynolds number was set only within the range 50,000–200,000 to examine this effect. The Strouhal number as shown in Fig. 21, although increasing considerably with the expansion ratio, is insensitive to the Reynolds number. For cases of the expansion ratio $E=5.0$, the Strouhal number changes by only 3 percent within the Reynolds number range considered. As this is within the limits of numerical error, the Strouhal number is considered to be constant with Reynolds number for a specific expansion ratio. On the other hand, the data of Hill et al. [4] and Nathan et al. [5] have relatively low Reynolds numbers and a wider range of expansion ratios from 3.75–14. They show that the Strouhal number tends to decrease with the Reynolds number, but this dependence seems to become weaker as the Reynolds number increases. It was suggested by Nathan et al. [5] that the compressibility effects are the probable cause of the Reynolds number dependence. This was not examined here since the present simulations assumed incompressible flow.

This situation is different when the expansion ratio is increased. For the case of $E=6.0$, a minimum Reynolds number of about 10^5 is necessary to sustain the regular oscillations, otherwise a complex oscillation occurs.

Effect of Expansion Ratio

A well-defined Strouhal number provides a basis for further quantifying each region. For axisymmetric sudden expansion flows, the Reynolds number at the inlet is larger than that at the outlet by a factor equal to the expansion ratio. The difference in Reynolds numbers increases as the expansion ratio increases. Most researchers use the Reynolds number defined at the inlet for convenience. However, when the expansion ratio is large, the downstream Reynolds number becomes so small that the flow may fall into the transitional region. The expansion ratio has thus been limited to values less than six.

For the range of expansion ratios considered from 3.0 to 6.0, two modes of oscillations were observed. Figure 22 presents the effects of expansion ratio on the Strouhal number defined in Eq. (5). For cases between $E=3.95$ and 6.0, a combination of a regular precession and a flapping motion in a rotating frame of reference has always been identified. In this case, two separate Strouhal numbers can be determined, which correspond to the precession and the flapping frequencies. This state is named the regular precession mode (PJ mode for short), since the precession dominates over the flapping motion in most of the domain.

When the expansion ratio was further reduced to be between 3.0 and 3.95, both the regular precession and a quasi-flapping oscillation were predicted but in separate runs. The time series looked regular (Fig. 23) and approximately sinusoidal. Thus only one single frequency was obtained. In this case, the oscillation is called ''quasi-flapping'' because the limit cycle is biased from the geometry center and does not rotate with time, though its appearance may vary slightly from case to case. Further downstream this bias quickly becomes weak and the jet moves in a two-dimensional fashion, with no sign of precession being observed in the downstream flow.

As an example, two modes of oscillations have been achieved in the case of $E=3.95$ by using different initial flow-fields, even with the same grid and boundary conditions. The difference of jet motions for the two modes is shown by the limit cycles in Fig. 24. One mode is the precession mode similar to the case of $E=5.0$. The other is a mode in which only the quasi-flapping oscillation takes place. The precession mode exhibits a stronger oscillation intensity of flow variables than the flapping mode in the whole field. Due to the presence of multiple modes, a bifurcation point appears to occur around the expansion ratio of 3.95, across which another mode arises, or the precession motion ceases, as the expansion ratio decreases.

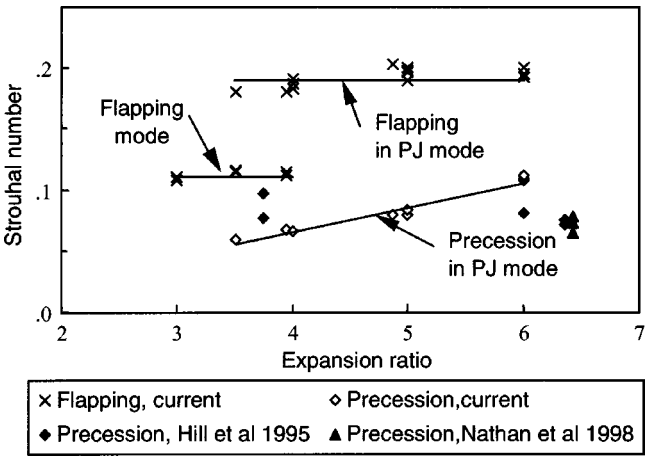

Fig. 22 The effect of expansion ratio on Strouhal number for oscillations in axisymmetric sudden expansion. PJ denotes the regular precession mode.

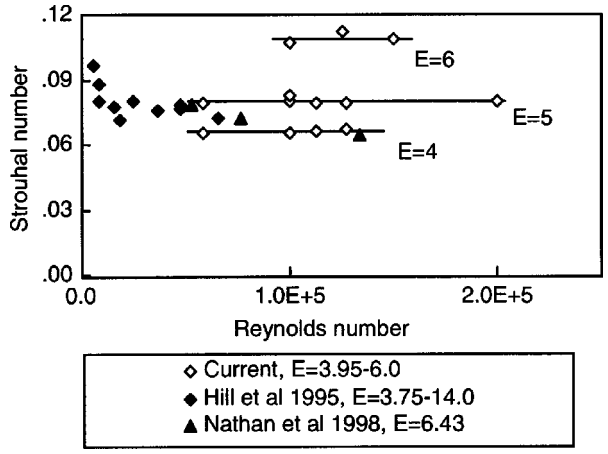

Fig. 21 A plot of Strouhal number for precession against Reynolds number

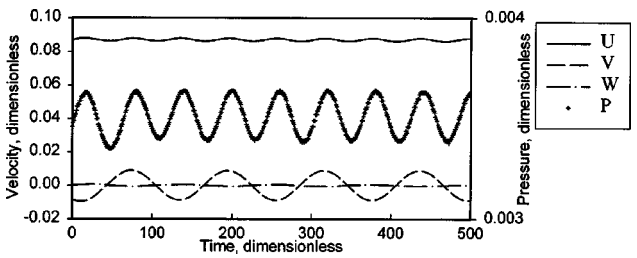

Fig. 23 Flow variables at the monitoring point 4D downstream from the expansion on the center-line, indicating a flapping mode ($E=3.5$, $\mathrm{Re}=10^5$)

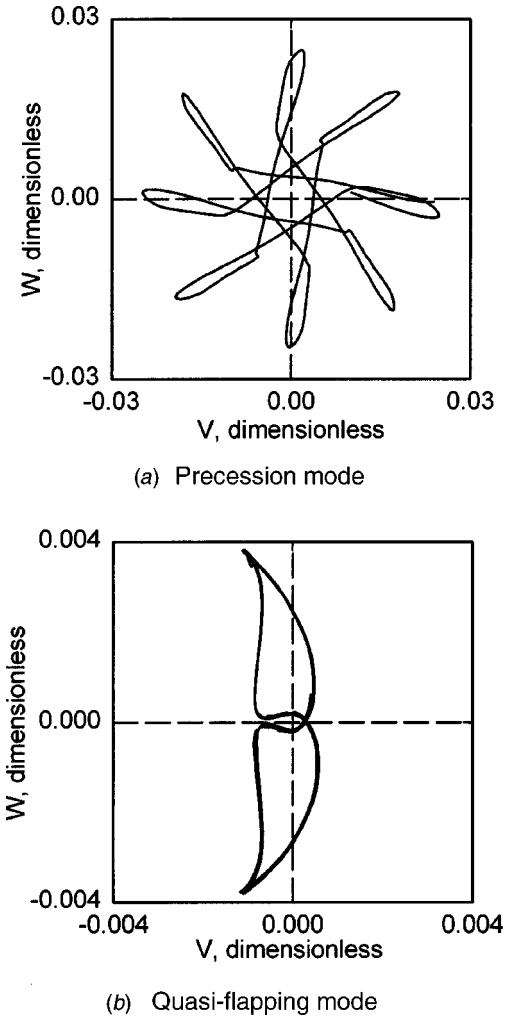

Fig. 24 Two modes of oscillations expressed by the limit cycles for $E=3.95$, $Re=1.27\times10^5$ (monitored at the center of the expansion)

For the quasi-flapping mode the Strouhal number is constant (St=0.11) over a range of expansion ratios from 3.0–3.95. In the regular precession mode, the Strouhal number for the flapping frequency is weakly dependent on the expansion ratio, varying by 6 percent about St=0.19 over a range of expansion ratios from 3.5–6.0. However, the Strouhal number for the precessing frequency is approximately proportional to the expansion ratio in the range from 3.5–6.0. It is noted that the Strouhal number, if defined based on the inflow velocity and outflow diameter, will be nearly constant for these simulations.

The data shown in Fig. 22 are only for the cases of regular oscillations in the current simulations. In comparison with the experimental data, despite the geometric variations, the predicted frequencies of the precession are of the same order of magnitude as those in the experiments, suggesting that they are closely related. The difference is that the Strouhal number in the current simulations clearly shows an increasing trend with the expansion ratio, while this trend is not apparent in the experiments. As can be noted, the current precession results show a nearly linear trend with expansion ratio. This suggests that the Strouhal number will be nearly constant if defined using the inflow diameter.

Regarding the flapping oscillation, the observation of video images by Nathan et al. [5], that the exit angle varies from cycle to cycle relative to the nozzle axis, appears to be consistent with the prediction here, but they did not provide quantitative information on the frequency. No other reported data on the flapping frequencies have been found for the axisymmetric sudden expansion flow. Some experimental and numerical data on flapping oscillations in rectangular cavities are presented in Table 4 for comparison, with Reynolds numbers varying widely between 100–200,000. The geometries used are different in terms of the direction of the outflow and/or the form of the jet (inlet). The numerical simulations reported in Table 4 are two-dimensional ones, while the experiments are, strictly speaking, three-dimensional. However, it can be seen that the flapping frequencies normalized by Eq. (6) are brought into close proximity of 0.1, in spite of the variations of geometric configurations and a wide range of Reynolds numbers. This suggests that the flapping oscillations predicted in the current simulations are closely related to the instability observed in these situations and that the chosen Strouhal number is an appropriate parameter for normalizing the oscillation frequencies.

Table 4 Comparison of the Strouhal number for the flapping oscillations

Source	Strouhal number	Reynolds number	Comments
Current, regular flapping mode	0.113	100,000-190,000	Numerical
Current, regular precession mode	0.192	50,000-200,000	Numerical
Battaglia *et al.*, [30]	0.084-0.197	100-1,000	Numerical
Lawson *et al.*, [8]	0.121	30,000	Experimental
Honeyands *et al.*, [17]	0.106-0.116	35,780-44,100	Experimental
Honeyands *et al.*, [17]	0.0945	35,780-44,100	Numerical

For the case of $E=6.0$, the regularity of the oscillation curves was found to be sensitive to the Reynolds number. With a high Reynolds number above 10^5, the oscillations appear to be regular. However, when the Reynolds number is less than 10^5, the monitoring point values look more complex, although the flapping and precessing modes can still be identified. In this case, the periods of oscillation are difficult to determine as they change from cycle to cycle. Based on this trend, the oscillations in a large expansion above 6.0 would be expected to have a complex behavior.

Complex Flow Patterns

A large expansion ratio with a low Reynolds number is also a possible cause of the complex oscillation. When the expansion ratio is 6.0 or above, a higher Reynolds number is necessary to maintain the regular jet motion. For example, for the case of $E=6.0$, when Re is 8.34×10^4 or less, the flow variables show a complex pattern. Figure 25 shows the time series of the pressure at a central point in the downstream pipe (dimensionless), and Fig. 26 and Fig. 27 are the corresponding amplitude and phase angle of the cross-flow velocity. Although both the flapping and precession of the jet still exist, the flow variables oscillate intermittently, and there is a short time breakdown of the flapping oscillation. During each duration of the oscillation, both the amplitude and the frequencies vary from cycle to cycle. At the same time the pressure builds up with each cycle and finally stops the flapping motion. The phase angle in Fig. 27 shows that the direction of the precession switches, with the jet precessing in alternate directions between two breakdowns. Therefore, a critical Reynolds number occurs which is correlated with the expansion ratio. Above this Reynolds number a regular pattern of oscillation remains permanently.

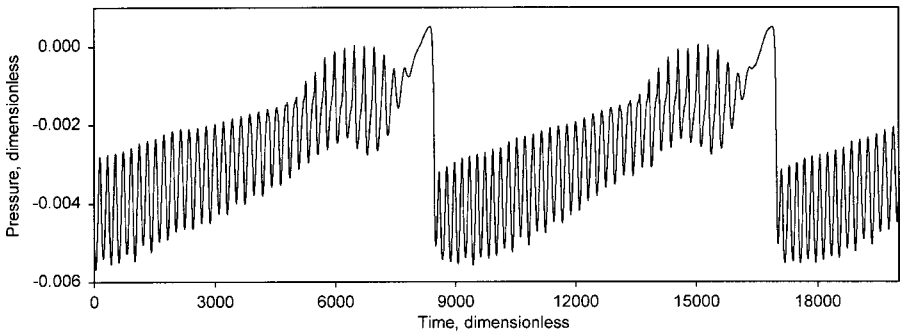

Fig. 25 Time series of pressure for the case of complex oscillations ($E=6.0$, monitoring point at 3.7D from the expansion, $Re=8.34\times10^4$)

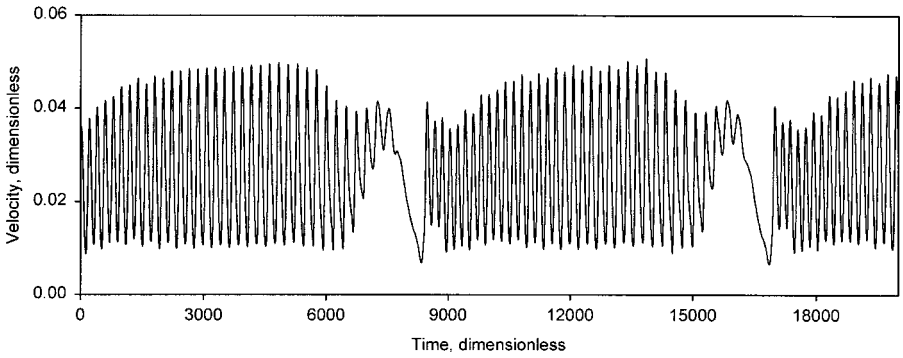

Fig. 26 The amplitude of the transverse velocity component (corresponding to Fig. 25)

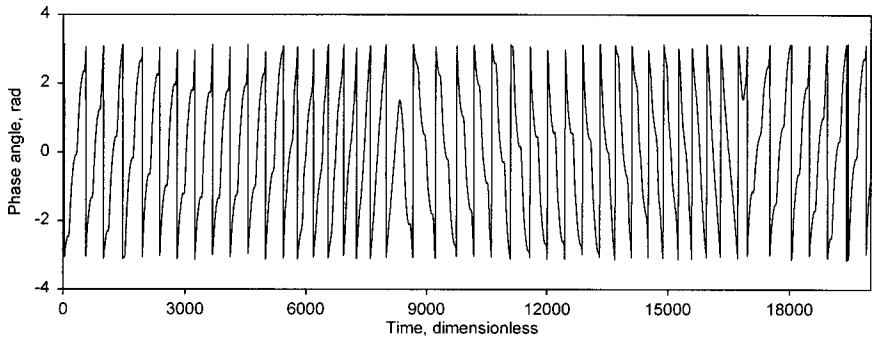

Fig. 27 The phase angle of the transverse velocity component (corresponding to Fig. 25)

Mechanism

For the two-dimensional problem, the flapping oscillation is produced by a dynamic balance between the pressure difference across the jet and the transverse momentum of the jet. The cross-flow is essential for the sustained flapping oscillation. For the three-dimensional case of precession, a cross flow may exist in the annular space between the central jet and surrounding wall, so the flapping oscillation is not difficult to understand. The pressure contours discussed earlier partly reflect the driving force of the jet motion. As the momentum transfer between the jet and wall through the recirculating vortex is extremely complex, we may explain the formation of stable jet oscillation in terms of the jet movement as a solid body. When the flapping jet deflects from the centerline (as in Fig. 28), the jet moves toward the wall so that it hits the wall at an oblique angle, and a tangential component of momentum arises. The flapping jet appears as if the wall reflects it. A coupling between the two patterns of motions arises and a sustained precession results. Therefore, the interaction between the flapping and precessing motions of the jet is necessary for retaining the precession. In this sense the persistence of the precession is dependent on the flapping oscillation.

For the expansion ratio from 3.95–6.0, the precession frequency increases relative to the flapping frequency. In order to explain this relationship in a simple way, based on the limit cycle of the jet deflection, it is assumed that the flapping of the jet is essential and the precession momentum is produced by the reflection of flapping momentum from the wall. The displacement of the flapping plane is assumed to remain the same from the centerline. When the downstream pipe diameter (or E) increases, the momentum is reflected by a larger angle ($\alpha_2>\alpha_1$) as shown in Fig. 28, and this leads to a larger angular step (α) corresponding to a larger frequency of precession.

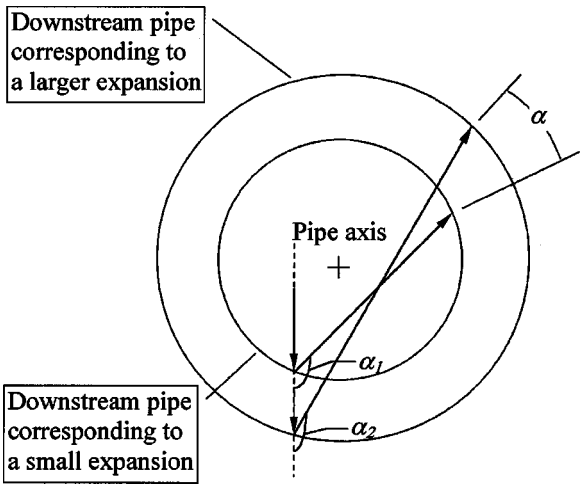

Fig. 28 A schematic diagram of the reflection of the jet motion with different expansion ratios, explaining how a large expansion ratio produces a higher precession frequency. (The arrows indicate the direction of the jet motion.)

Conclusions

By solving the three-dimensional, unsteady, Reynolds-averaged Navier-Stokes equations, the turbulent flows in axisymmetric sudden expansions for purely axial flow conditions were simulated using the VLES approach and the standard k-ε model. The performance of the k-ε model is reasonable for the problem in capturing the fundamental features as a whole. It is believed that this is because the mesh is sufficiently fine to resolve the key transient flow features and that the k-ε model is acting simply to provide dissipation at small scales. The range of Reynolds number used was from 50,000–200,000 and a fully developed velocity profile was imposed at the inlet. The global flow pattern can be divided into several regimes depending on the expansion ratio and Reynolds number. Strong self-sustained oscillations can be induced in the downstream pipe above a critical expansion ratio. The simulations demonstrate that the asymmetry and subsequent oscillations are inherently physical phenomena within an expansion flow rather than originating from any possible imperfection of the geometry or asymmetry from upstream.

In the expansion ratio range of 3.5–6.0, both a precessing oscillation and a flapping oscillation, in a rotating frame of reference, of high regularity were predicted. In the expansion ratio range of 3.0–4.0, however, two oscillation modes were identified, i.e., a regular precession and a quasiflapping oscillation. A lower Reynolds number and higher turbulence intensity at the inlet may cause the oscillations to develop complex flowfields. For the quasi-flapping oscillation, the Strouhal number (based on the inflow momentum flux and downstream diameter) is basically independent of the Reynolds number, but increases linearly as the expansion ratio increases in the range of 3.5–6.0 examined. While the dependence on the expansion ratio seems to have been overpredicted, the calculated values of the Strouhal number are of the same order as the reported data.

It seems that the flapping motion is fundamental in all the range of expansions considered. It may either coexist with the precession for a high expansion ratio or occur separately without the presence of the precession for a smaller expansion ratio. Although no relevant information has been reported for the case of axisymmetric expansion flows, the flapping frequencies are comparable with those in two-dimensional or quasi-two-dimensional problems.

The visualization of the flow field and wall surface pressure distribution for the expansion ratio of five suggests that a pressure gradient arises across the jet in both the radial and tangential directions, which may be the driving force for both the flapping and the precessing motions. Large-scale coherent structures, i.e., a large ring-like recirculation zone and a significant swirling flow behind the expansion face have been identified, which enhance streamwise and cross-sectional mixing. Further downstream, the jet, while spreading gradually, exhibits a spiral nature with a direction opposite to the precession.

Acknowledgments

This work is supported by an Australian Research Council Large Grant. Regarding this phenomenon, discussions between T. A. G. Langrish and Dr. K. R. Morrison, of the University of Canterbury, New Zealand, are gratefully acknowledged.

Nomenclature

d = diameter of upstream pipe, m
D = diameter of downstream pipe, m
E = expansion ratio of diameter D/d
f = oscillation frequency, l/s
k = turbulent kinetic energy, m^2/s^2
L,1 = length of the pipes, m
M = jet momentum flux, $kg.m/s^2$
P = pressure, Pa
Re = Reynolds number at the inlet
St = Strouhal number
t = time, s
U,V,W = Reynolds-averaged velocity components, m/s
U_i, U_0 = bulk velocity at the inlet and exit, m/s
ε = turbulence dissipation rate, m^2/s^3
ρ = density, kg/m^3
μ = laminar viscosity, Pa.s
θ = angle of flapping relative to the radial direction

References

[1] Yazdabadi, P. A., Griffiths, A. J., and Syred, N., 1994, ''Characterization of the PVC Phenomena in the Exhaust of a Cyclone Dust Separator,'' Exp. Fluids, **17**, No. 1/2, pp. 84–95.
[2] Fick, W., Syred, N., Griffiths, A. J., and O'Doherty, T., 1996, ''Phase-Averaged Temperature Characterized in Swirl Burners,'' Journal of Power and Energy, **210**, No. 5, pp. 383–395.
[3] Dellenback, P. S., Metzger, D. E., and Neitzel, G. P., 1988, ''Measurement in Turbulent Swirling Flow Through an Abrupt Axisymmetric Expansion,'' AIAA J., **26**, No. 6, pp. 669–681.
[4] Hill, S. J., Nathan, G. J., and Luxton, R. E., 1995, ''Precession in Axisymmetric Confined Jets,'' *Proceedings of 12th Australasian Fluid Mechanics Conference*, Bilger, R. W., ed., Sydney, Dec. 10–15, pp. 135–138.
[5] Nathan, G. J., Hill, S. J., and Luxton, R. E., 1998, ''An Axisymmetric 'Fluidic' Nozzle to Generate Jet Precession,'' J. Fluid Mech., **370**, pp. 347–380.
[6] Nathan, G. J., Turns, S. R., and Bandaru, R. V., 1996, ''The Influence of Jet Precession on NO_x Emissions and Radiation from Turbulent Flames,'' Combust. Sci. Technol., **112**, pp. 211–230.
[7] Southwell, D. B., and Langrish, T. A. G., 2000, ''Observations of Flow Patterns in a Spray Dryer,'' Drying Technol., **18**, No. 3, pp. 661–685.
[8] Lawson, N. J., and Davidson, M. R., 1999, ''Crossflow Characteristics of an Oscillating Jet in a Thin Slab Casting Mould,'' ASME J. Fluids Eng., **121**, pp. 588–595.
[9] Durrett, R. P., Stevenson, W. H., and Thompson, H. D., 1988, ''Radial and Axial Turbulent Flow Measurements with an LDV in an Axisymmetric Sudden Expansion Air Flow,'' ASME J. Fluids Eng., **110**, pp. 367–372.
[10] Back, L. H., and Roschke, E. J., 1972, ''Shear-Layer Flow Regimes and Wave Instabilities and Reattachment Lengths Downstream of an Abrupt Circular Channel Expansion,'' ASME J. Appl. Mech., **39**, pp. 677–681.
[11] Moon, L. F., and Rudinger, G., 1977, ''Velocity Distribution in an Abrupt Expanding Circular Duct,'' ASME J. Fluids Eng., **99**, pp. 226–230.
[12] Gould, R. D., Stevenson, W. H., and Thompson, H. D., 1990, ''Investigation of Turbulent Transport in an Axisymmetric Sudden Expansion,'' AIAA J., **28**, No. 2, pp. 276–283.
[13] Hallett, W. L. H., and Gunther, R., 1984, ''Flow and Mixing in Swirling Flow in a Sudden Expansion,'' The Canadian Journal of Mechanical Engineering, **62**, Feb. pp. 149–155.
[14] Mi, J., Nathan, G. J., and Luxton, R. E., 1995, ''Precessing and Axial Flows Following a Sudden Expansion in an Axisymmetric Nozzle,'' *Proceedings of 12th Australasian Fluid Mechanics Conference*, Bilger, R. W., ed., Sydney, Dec. 10–15, pp. 119–122.
[15] Mi, J., Luxton, R. E., and Nathan, G. J., 1998, ''The Mean Flow Field of a Precessing Jet,'' *Proceedings of 13th Australasian Fluid Mechanics Confer-*

ence, Thompson, M. C., and Hourigan, K., eds., Melbourne, Dec. 13–18, pp. 325–328.
[16] Schneider, G. M., Nathan, G. J., and Luxton, R. E., 1992, ''An Experimental Study of a Precessing, Deflected Jet,'' *Proceedings of 11th Australasian Fluid Mechanics Conference*, Davis, M. R., and Walker, G. J., eds., Hobart, Dec. 14–18, pp. 1105–1108.
[17] Honeyands, T. A., and Molloy, N. A., 1995, ''Oscillations of Submerged Jets Confined in a Narrow Deep Rectangular Cavity,'' *Proceedings of 12th Australasian Fluid Mechanics Conference*, Bilger, R. W., ed., Sydney, Dec. 10–15, pp. 493–496.
[18] Gebert, B. M., Davidson, M. R., and Rudman, M. J., 1998, ''Computed Oscillations of a Confined Submerged Liquid Jet,'' Appl. Math. Model., **22**, pp. 843–850.
[19] CFX, Solver Manual, CFX International, AEA Technology, 1997, Harwell, Didcot, Oxon, UK.
[20] Guo, B., Langrish, T. A. G., and Fletcher, D. F., 2001, ''Simulation of Turbulent Swirl Flow in an Axisymmetric Sudden Expansion,'' AIAA J., **39**, No. 1, pp. 96–102.
[21] Spalart, P. R., 2000, ''Strategies for Turbulence Modelling and Simulations,'' International Journal of Heat and Fluid Flow, **21**, No. 3, pp. 252–263.
[22] Speziale, C. G., 1998, ''Turbulence Modeling for Time-Dependent RANS and VLES: a Review,'' AIAA J., **36**, No. 2, pp. 173–184.
[23] Rodi, W., Ferziger, J. H., Breuer, M., and Pourquie, M., 1997, ''Status of Large Eddy Simulation: Results of a Workshop,'' ASME J. Fluids Eng., **119**, pp. 248–262.
[24] Wilcox, D. C., 1994, *Turbulence Modeling for CFD*, DCW Industries, Inc.
[25] Guo, B., Langrish, T. A. G., and Fletcher, D. F., 2001, ''An Assessment of Turbulence Models Applied to the Simulation of a Two-Dimensional Submerged Jet,'' Appl. Math. Model, **25**, No. 8, pp. 635–653.
[26] Shore, N. A, Haynes, B. S., Fletcher, D. F., and Sola, A. A., 1995, ''Numerical Aspects of Swirl Flow Computations,'' *Proceedings of the Seventh Biennial Conference on Computational Techniques and Applications: CTAC95*, May, R. L., and Easton, A. K., eds., Melbourne, July 3–5, pp. 693–700.
[27] Leonard, B. P., 1979, ''A Stable and Accurate Convective Modelling Procedure Based on Quadratic Upstream Interpolation,'' Comput. Methods Appl. Mech. Eng., **9**, No. 1, pp. 59–98.
[28] Hirsch, C., 1990, *Numerical Computation of Internal and External Flows*, Vol. 2, Wiley, New York, pp. 536–545.
[29] Issa, R. I., 1985, ''Solution of the Implicitly Discretised Fluid Flow Equations by Operator Splitting,'' J. Comput. Phys., **62**, No. 1, pp. 40–65.
[30] Battaglia, F., Kulkarni, A. K., Feng, J., and Merkle, C. L., 1997, ''Simulations of Planar Flapping Jets in Confined Channels,'' *AIAA Paper 97–1992*, pp. 1–11.

Laminar Flow of a Herschel-Bulkley Fluid Over an Axisymmetric Sudden Expansion

Khaled J. Hammad[1]
Adjunct Assistant Professor

George C. Vradis
Associate Professor

M. Volkan Ötügen
Associate Professor

Mechanical, Aerospace and Manufacturing Engineering,
Polytechnic University,
Six Metrotech Center,
Brooklyn, NY 11201

The steady flow of non-Newtonian Herschel-Bulkley fluids over a one-to-two axisymmetric sudden expansion was studied numerically. Finite difference numerical solutions of the governing continuity and fully-elliptic momentum equations were obtained within the laminar flow regime for a range of Reynolds numbers, yield numbers, and power-law index values. The Reynolds number, based on the upstream pipe diameter and bulk velocity, was varied between 50 and 200, while the yield number was varied between 0 and 2. The power-law index values mapped the 0.6–1.2 range, allowing for the investigation of both shear-thinning and shear-thickening effects. Two distinct flow regimes are identified. One is associated with a combination of low yield numbers, high Reynolds numbers, and high power-law indexes, and exhibits a recirculating flow region at the step corner which is similar to that seen in Newtonian flows. The other flow regime, however, is characterized by a dead-zone behind the step corner, and is obtained for a combination of high yield numbers, low Reynolds numbers, and low power-law indexes. The yield number appears to be the dominant parameter affecting the shape and extent of the corner flow region as well as flow redevelopment further downstream. In general, the influence of the power-law index on the flow structure is stronger when the yield number is small. A flow character that is an exception to this general trend is the recirculating corner vortex intensity which decreases substantially with decreasing power-law index values for all investigated yield numbers. [DOI: 10.1115/1.1378023]

Introduction

The laminar flow through an axisymmetric sudden expansion has received the attention of researchers for a long time because of its fundamental as well as practical importance. The geometry can be found in numerous equipment, such as heat exchangers, combustion chambers, mixing vessels, reactors, as well as many other fluid processing, handling, and transport equipment. Flows through axisymmetric expansions have also been studied to shed light on the physics of wall-bounded separated and reattached flows. Additionally, the circular sudden expansion geometry has been used to model physiological flows by Feurstein et al. [1]. The simplicity of the geometry, on the one hand, and the intrinsic complexity of the flow field (*i.e.*, flow separation, reversal, and reattachment) on the other, resulted in its acceptance as a benchmark problem for testing computational codes.

The earliest and most comprehensive computational and (qualitative) experimental study of laminar Newtonian flow in an axisymmetric sudden expansion was carried out by Macagno and Hung [2]. In their report, they presented results for a Reynolds number range, $\mathrm{Re}_d \leqslant 200$ in a one-to-two axisymmetric expansion (based on pipe diameters). Flow visualization experiments revealed information related to the shape and extent of the recirculation zone. In the computational simulation of their experiment, they imposed a fully developed velocity profile as a boundary condition of the incoming fluid. A good qualitative agreement was obtained between the experimental results and those obtained using a finite difference numerical approximation for the streamlines-vorticity formulation of the governing Navier-Stokes equations. Furthermore, it was shown that the shear layer reattachment length, L_r, increased linearly with inlet Reynolds number, Re_d. Most of the research work that followed concentrated on the effects of the Reynolds number, the expansion ratio, and the inlet velocity profile on the onset of shear layer instability and transition to turbulence, reattachment length, and the intensity of the recirculating eddy, e_i. Through additional studies it has been established that shear layer instability and the accompanying unsteady effects do not exist for $\mathrm{Re}_d < 200$ for a fully developed inlet profile (see, for example, Badekas and Knight [3]).

Studies focusing on the laminar fluid flow of non-Newtonian fluids through axisymmetric sudden expansions are more limited compared to those dealing with Newtonian fluids. Halmos et al. [4] carried out a numerical study of the flow of a power-law fluid over a one-to-two axisymmetric sudden expansion geometry. Additionally, they presented flow visualization-based experimental results that were in agreement with their computed results. Some of these studies, such as that of Ponthieux et al. [5], were motivated by the desire to acquire detailed knowledge of the pressure losses which arise due to geometric variations, and the usually high apparent viscosity displayed by these fluids. Inertia effects on laminar flows of Bingham plastics through suddenly expanding geometries have also been studied in the past. Scott et al. [6] presented results for the flow of Bingham and Casson fluids through both planar and axisymmetric expansions and stenosis, while Vradis and Ötügen [7] reported on numerical solutions to the problem of a Bingham plastic through an axisymmetric expansion.

Recently, Hammad et al. [8] carried out an experimental study of the laminar axisymmetric sudden expansion flow of a Herschel-Bulkley fluid using the optical technique particle image velocimetry (PIV). The study revealed the complicated nature of this flow with features not encountered in Newtonian flows. However, due to the difficulty in obtaining optically transparent fluids for a wide range of rheological parameters, it was not possible to systematically investigate the effect of these parameters. Apart from the experimental approach, no systematic computational study of the laminar flows of Herschel-Bulkley fluids covering a wide range of Reynolds, yield numbers, and the power-law index have been reported in the literature. Currently, the detailed understanding of the effect of these parameters on the flow structure is far from

[1]Presently, with Dantec Measurement Technology.

Contributed by the Fluids Engineering Division for publication in the JOURNAL OF FLUIDS ENGINEERING. Manuscript received by the Fluids Engineering Division April 1, 1999; revised manuscript received March 5, 2001. Associate Editor: J. Katz.

being complete. The Herschel-Bulkley constitutive equation can adequately describe the flow behavior of numerous non-Newtonian fluids. Despite the considerable importance of Herschel-Bulkley fluids from a fundamental point of view and their diverse applications, studies of internal flows of such fluids have so far received little attention from fluid mechanics researchers, partially due to the complexity involved in their analysis. The present work, therefore, is a comprehensive computational study geared toward expanding our limited knowledge of complex and confined flows of nonlinear viscoplastic non-Newtonian fluids whose behavior can be approximated by a Herschel-Bulkley constitutive model. In the present computations, a finite-difference formulation of the governing continuity and fully-elliptic momentum conservation equations is used along with a coupled-variables technique to solve the resulting system of nonlinear equations, which are linearized by employing an iterative marching solution technique.

The Governing Equations. The nondimensionalized governing elliptic equations for the steady, laminar, incompressible flow of a Herschel-Bulkley non-Newtonian fluid in cylindrical coordinates are

$$\frac{\partial u}{\partial x}+\frac{1}{r}\frac{\partial r\nu}{\partial r}=0 \tag{1}$$

$$u\frac{\partial u}{\partial x}+\nu\frac{\partial u}{\partial r}=-\frac{\partial p}{\partial x}+\frac{1}{\mathrm{Re}}\left[\frac{\partial}{\partial x}\left[2\mu_{\mathrm{eff}}\frac{\partial u}{\partial x}\right]+\frac{1}{r}\frac{\partial}{\partial r}\left[\mu_{\mathrm{eff}}r\left[\frac{\partial u}{\partial r}+\frac{\partial \nu}{\partial x}\right]\right]\right] \tag{2}$$

$$u\frac{\partial \nu}{\partial x}+\nu\frac{\partial \nu}{\partial r}=-\frac{\partial p}{\partial r}+\frac{1}{\mathrm{Re}}\left[\frac{1}{r}\frac{\partial}{\partial r}\left[2r\mu_{\mathrm{eff}}\frac{\partial \nu}{\partial r}\right]+\frac{\partial}{\partial x}\left[\mu_{\mathrm{eff}}\left[\frac{\partial u}{\partial r}+\frac{\partial \nu}{\partial x}\right]\right]-2\mu_{\mathrm{eff}}\frac{\nu}{r^2}\right] \tag{3}$$

In the case of a Herschel-Bulkley fluid the relationship between the stress tensor τ_{ij} and the rate of deformation tensor Δ_{ij} is given by the following formula:

$$\tau_{ij}=\left[K\left(\frac{1}{2}\Delta_{ij}\Delta_{ij}\right)^{(n-1)/2}+\frac{\tau_y}{\left(\frac{1}{2}\Delta_{ij}\Delta_{ij}\right)^{1/2}}\right]\Delta_{ij} \quad \text{for} \quad \frac{1}{2}\tau_{ij}\tau_{ij}>\tau_y^2 \tag{4a}$$

$$\Delta_{ij}=0 \quad \text{for} \quad \frac{1}{2}\tau_{ij}\tau_{ij}\leqslant\tau_y^2 \tag{4b}$$

Here $\Delta_{ij}=\partial u_i/\partial x_j+\partial u_j/\partial x_i$ and $\Delta_{ij}\Delta_{ij}$ is the second invariant of Δ_{ij}. In cylindrical coordinates the function $(1/2)\Delta_{ij}\Delta_{ij}$ is given by:

$$\frac{1}{2}(\Delta_{ij}\Delta_{ij})=2\left[\left[\frac{\partial \nu}{\partial r}\right]^2+\left[\frac{\nu}{r}\right]^2+\left[\frac{\partial u}{\partial x}\right]^2\right]+\left[\frac{\partial \nu}{\partial x}+\frac{\partial u}{\partial r}\right]^2 \tag{4c}$$

As a result, the nondimensional effective viscosity is defined as:

$$\mu_{\mathrm{eff}}=\left(\frac{1}{2}\Delta_{ij}\Delta_{ij}\right)^{(n-1)/2}+\frac{Y}{\sqrt{\frac{1}{2}\Delta_{ij}\Delta_{ij}}} \quad \text{for} \quad \frac{1}{2}\tau_{ij}\tau_{ij}>\tau_y^2 \tag{5a}$$

and

$$\mu_{\mathrm{eff}}=\infty \quad \text{for} \quad \frac{1}{2}\tau_{ij}\tau_{ij}\leqslant\tau_y^2 \tag{5b}$$

where, the yield number, Y, is a nondimensional yield stress.

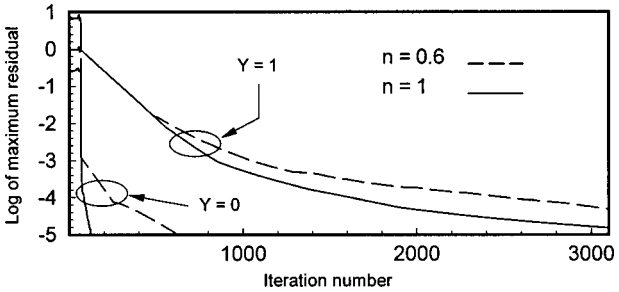

Fig. 1 Convergence history for Y=0, 1; n=0.6,1

Solution Technique. The finite-difference numerical technique used in the present study is described in detail by Hammad [9] and Vradis and Hammad [10]. Fully second-order accurate approximations are used for the derivatives appearing in the governing equations. Centered differences are used in all cases with the exception of the convective streamwise derivatives which are upwinded using first order approximations, to ensure stability. The resulting system of algebraic equations for mass conservation and momentum is solved by employing an iterative marching technique in which the linearized equations are solved simultaneously along lines in the radial direction using an efficient block-tridiagonal matrix inversion technique. The linearization of the equations is accomplished by using the convective coefficients at the previous iteration level. The convergence parameter employed in the present analysis is the magnitude of the maximum residual in the difference equations. The discretization is made in such a way that the continuity equation is always satisfied to ''machine accuracy'' at any stage of the solution procedure. Therefore, convergence is checked for the two momentum equations and the iterative procedure is terminated when the residual becomes less than 10^{-6}. The convergence history for the Herschel-Bulkley fluid as a function of yield number and the power-law index are shown in Fig. 1. The residual corresponds to the maximum of the two momentum equations. For a fixed grid size, the number of iterations required, prior to convergence, increases significantly with the yield number and is, in general, higher when the fluid is shear-thinning, with or without a yield stress. An initial rapid decline in the residual is always obtained followed by a much smaller rate of reduction. In the core regions of the flow the effective viscosity, μ_{eff}, attains an infinite value since $\Delta_{ij}=0$ in such regions. Large values of μ_{eff} create convergence problems since the coefficient matrix becomes very ''stiff'' due to large differences in the magnitude of its elements. In order to avoid such problems, μ_{eff} is ''frozen'' at a relatively high value of μ_0 when the value of $\sqrt{1/2\Delta:\Delta}$ drops below a certain preset level thus, guaranteeing convergence.

The same approach was adopted by other researchers in the past (O'Donovan and Tanner [11] and Lipscomb and Denn [12]). The modified nondimensional effective viscosity expression for a Herschel-Bulkley rheology becomes:

$$\mu_{\mathrm{eff}}=\min\left(\mu_0,\left(\frac{1}{2}\Delta_{ij}\Delta_{ij}\right)^{(n-1)/2}+\frac{Y}{\sqrt{\frac{1}{2}\Delta_{ij}\Delta_{ij}}}\right) \tag{6}$$

The ''min'' operator in Eq. (6) selects the lowest of the two viscosity values appearing between parenthesis. The result of such an approximation is that the rheological behavior of a yield stress fluid is altered from that of a Herschel-Bulkley fluid to one with two different viscosities, i.e., a high viscosity of μ_0 at low rates of deformation, and a lower value (still shear-rate dependent) at higher rates of deformation. To accurately simulate the yield stress behavior a very high μ_0 value should be utilized. Extensive numerical experimentation led to the establishment of $\mu_0=1000$

as high enough to obtain an accurate solution yet low enough to obtain convergence. In previous work by O'Donovan and Tanner [11] and Beverly and Tanner [12] a $\mu_0 = 1000$ was adopted after extensive numerical experimentation.

Due to the sharp variations in the values of effective viscosity, in order to obtain convergence very strong under-relaxation of the effective viscosity is necessary from one iteration level to the next, especially in the earlier stages of the iterative procedure.

Discussion of Results

The geometry and the boundary conditions of the flow problem are shown in Fig. 2. The flow at the inlet ($x=0$) is assumed to be fully developed with $u=u(r)$ and $v=0$. At the exit plane of the computational domain, the flow is assumed fully developed. Thus, the streamwise derivative of the velocity components are zero, while the pressure is uniform. The length of the computational domain depends on the Reynolds and yield numbers as well as the power-law index and is not known a priori. For each case, it has to be adjusted individually, sometimes through multiple trial runs. After each computational run, it is always verified that the downstream boundary is located far enough to allow a completely fully developed flow at the exit. Along the solid walls, the velocity satisfies the no-slip condition ($u=v=0$). The grid used for obtaining the results presented is 97×80 grid, which is variable in the streamwise (97) direction and uniform in the transverse (80) direction. It is finer closer to the step and becomes increasingly coarser as the exit plane is approached. Extensive numerical experimentation established the grid-independent nature of the results with the grid defined above. Figure 3 displays the development of the centerline velocity downstream of the expansion plane for various grids. Results are shown for both 70×60 and 97×80 grids when the fluid is Newtonian, i.e., $Y=0$, and when $Y=1$. The figure shows the grid independent nature of the numerically obtained results. Further details on the effect of grid refinement on the results of problems involving the flow and heat transfer of viscoplastic fluids in this and other similar geometries can be found in the works of Vradis and Ötügen [7] and Vradis and Hammad [10].

The fully developed velocity profiles at the inlet plane used throughout this parametric study are presented in Fig. 4. Each velocity profile at the inlet is obtained numerically by solving the problem of the fully developed flow of such a fluid in a straight pipe. As clearly seen in Figs. 4(*b*)–4(*d*), the profile is characterized by the existence of a plug-flow region around the centerline. The radial extent of this plug region increases with an increase in yield number and a decrease in power-law index. Outside the plug-flow region the velocity decreases rapidly to zero. The velocity gradient close to the wall is greater for smaller power-law exponents and higher yield numbers as clearly demonstrated in Fig. 4.

Some characteristics of the suddenly expanding internal pipe flow are indicated in Fig. 2. Upon reaching the plane of the step, the flow of a Newtonian fluid separates and then reattaches and forms a recirculation zone whose size and intensity depends only on the Reynolds number. In the laminar flow regime, the reattachment length has been shown to vary linearly with the Reynolds number (Macagno and Hung [2] and Vradis and Ötügen [7]). After reattachment, the flow evolves until fully developed conditions are attained. The redevelopment length increases with increasing Reynolds numbers. In the case of a Bingham fluid, Vradis and Ötügen [7] have shown that, for a fixed yield number, the reattachment length is also a linear function of the Reynolds number. However, the reattachment length decreases rapidly with increasing yield numbers. The redevelopment length is also a strong function of the yield number, decreasing rapidly with increasing yield numbers.

In the present study, a more complex flow structure is revealed, whose details depend on the combination of Reynolds and yield numbers and power-law index values. Figure 5(*a*) shows the effective viscosity distribution for selected Re, *Y*, and *n* combinations. In Fig. 5(*a*) the Reynolds number is Re=50, the yield number is $Y=1$ and the power-law index is $n=1$. The small values of effective viscosity at the edge of the step are associated with the large rates of deformation within the shear layer developing at the

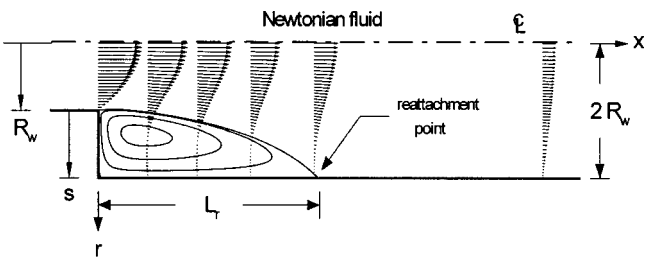

Fig. 2 Schematic of the confined flow geometry and the boundary conditions

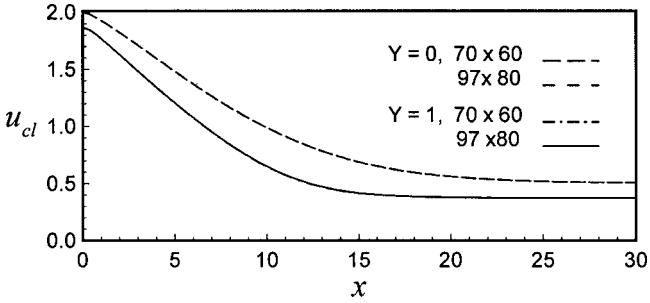

Fig. 3 Centerline velocity evolution for two sets of grids

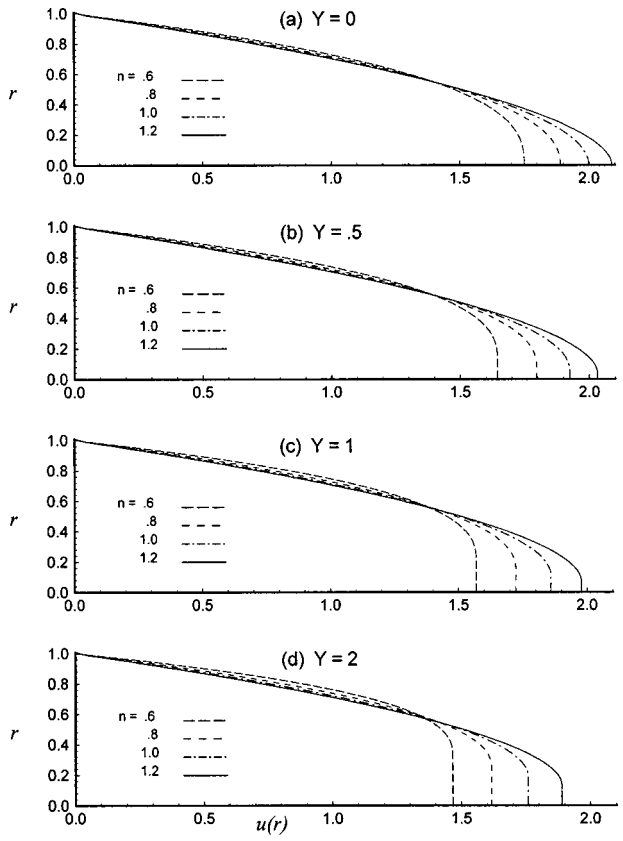

Fig. 4 Inlet velocity profiles for Y=0, .5, 1, 2; n=.6, .8, 1, 1.2

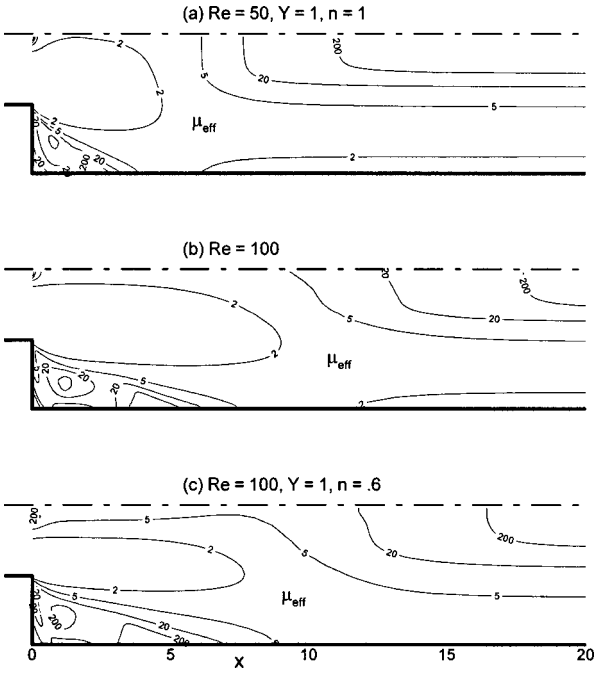

Fig. 5 Effective viscosity contours for Y=1 and (*a*) Re=50, n =1; (*b*) Re=100, n=1; (*c*) Re=100, n=0.6

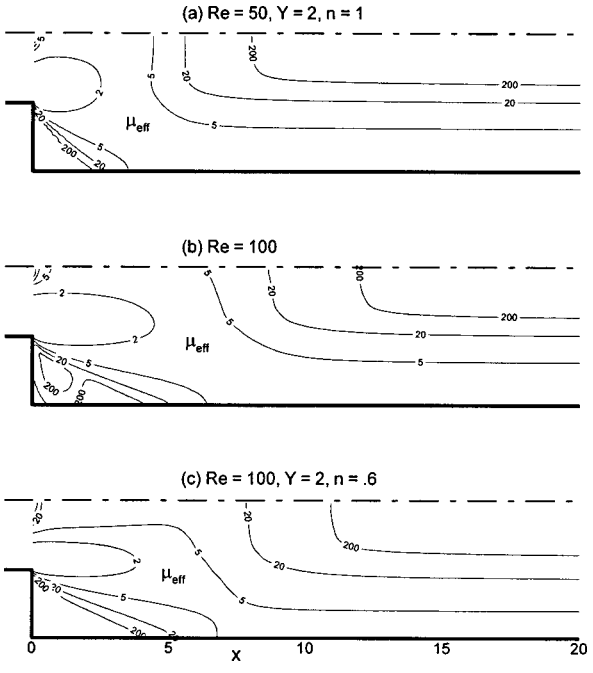

Fig. 6 Effective viscosity contours for Y=2 and (*a*) Re=50, n =1; (*b*) Re=100, n=1; (*c*) Re=100, n=0.6

step's corner. Further downstream, close to the centerline, μ_{eff} starts increasing again as the conditions for a new core flow region start developing. At the corner, the flow is characterized by very high values of the effective viscosity, i.e., the existence of a small ''dead-zone.'' This zone exists due to the low stress levels in that region and, therefore, the lack of deformation of the fluid elements. Given the condition for kinematic continuity and the no-slip condition at the wall, this region is one characterized by zero velocities. Downstream of this dead-zone, there exists a region of weak recirculation (as will be demonstrated next), within which appreciable levels of deformation rates are present making the effective viscosity values moderate. Further downstream, there is another ''dead'' (or no-flow) zone which, in the present flow, plays the role that the reattachment point does in the case of a Newtonian fluid. Therefore, it is seen that the reattachment point is replaced here by a reattachment dead-zone. It should be stated here that both the corner dead zone and the reattachment dead zone were observed earlier by Hammad et al. [8] in their experimental study. The center of the recirculating zone is also characterized by large values of the effective viscosity, again, due to the lower rates of deformation there. Downstream of the reattachment zone, the flow starts to redevelop. As this happens, a plug-flow region starts forming along the centerline, characterized by high effective viscosities, while along the wall a boundary layer starts forming indicated by the low effective viscosity values. Increasing the Reynolds number from 50–100, while keeping $Y=1$ and $n=1$, as shown in Fig. 5(*b*), increases the intensity of the recirculation, evidenced from the overall decrease in the effective viscosity distribution throughout the corner region. Increasing the Reynolds number also shifts the reattachment region location further downstream but the reattachment dead-zone is still present as indicated by the $\mu_{\text{eff}}=200$ contour. The effect of the power-law index at Re=100, and $Y=1$, can be observed by comparing Figs. 5(*b*)–5(*c*). At a lower power-law index of $n=0.6$ (shown in Fig. 5(*c*)), an overall increase in the effective viscosity values throughout the flowfield is obtained. The strongest impact of the reduction in n is seen adjacent to the step. The overall lower rates of deformation lead to an increase in the size of nonmoving reattachment region and a weakening of the recirculation intensity. The redevelopment length is decreased as the plug zone along the centerline forms at a shorter distance from the step.

Figure 6 shows the behavior of μ_{eff} for the case of $Y=2$. As the yield number is increased from 1–2 (with Re=50 and $n=1$), the basic features of the flow field change fairly significantly, as discerned form Fig. 6(*a*). Comparing Fig. 6(*a*)–Fig. 5(*a*), we see that the recirculation zone is replaced by a fairly extensive dead-zone at the step's corner effectively forming a ramp (defined by the $\mu_{\text{eff}}=200$ contour) extending to about $x\cong 2$. The surface of this dead-zone has a slight concave curvature and serves as a solid surface over which the moving fluid is sheared as it expands. This type of corner flow structure was first observed experimentally by Hammad et al. [8]. No flow reversals, and hence, separation and reattachment zones are observed in this flow case. The flow expands over this zone and redevelops even faster than in the previous case of $Y=1$, given the higher effective viscosities associated with the higher yield number. Also observed is the reduction of μ_{eff} near the wall for $Y=2$ (Fig. 6(*a*)) as compared to $Y=1$. (Fig. 5(*a*)). As the radial extent of the plug zone increases for $Y=2$, the developing boundary layer underneath sustains larger shear rates and, hence, exhibits smaller effective viscosities. As for the effect of Reynolds numbers, increasing this parameter from Re=50 to Re=100, for a fixed yield number of $Y=2$, leads to a change in the shape of the corner dead-zone. Observing the centerline evolution of μ_{eff} in Fig. 6(*b*), one also notes that the initial destruction of the plug zone and its subsequent reappearance takes a longer axial distance for the higher Reynolds number. Reducing the power-law index from $n=1$ to $n=0.6$, while maintaining Re=100 and $Y=2$, increases the effective viscosity values throughout, as explained earlier. This, in turn, leads to a drop in rates of deformation throughout the corner region as shown in Fig. 6(*c*). Again, this reduction in the power-law index is significant enough that an extensive corner dead-zone reappears.

The impact of both fluid rheology and flow inertia on the characteristics of the corner flow region is summarized in Figs. 7, 8, and 9. The axial extent of the corner region downstream of the expansion plane is represented here in terms of the length, L_r, which is normalized with the step height, S, ($l_r=L_r/S$). The length L_r represents the reattachment length in the case of zero

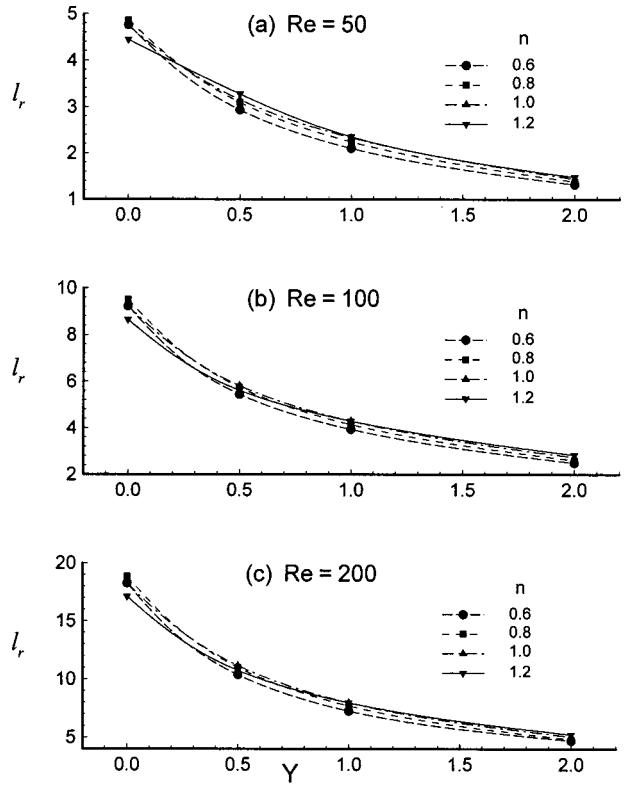

Fig. 7 Reattachment length versus yield number at n=0.6, 0.8, 1 and 1.2 for (*a*) Re=50; (*b*) Re=100; (*c*) Re=200

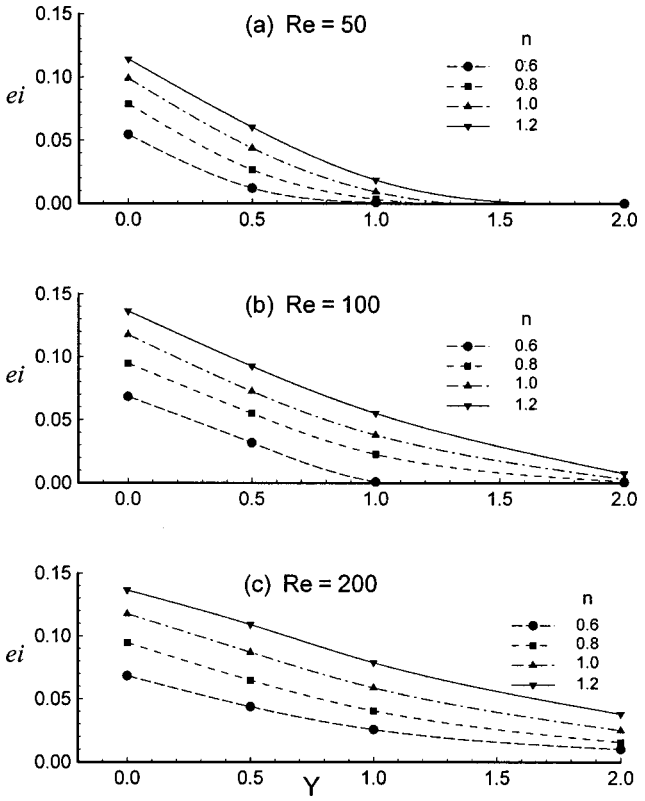

Fig. 9 Relative eddy intensity versus yield number at n=0.6, 0.8, 1 and 1.2 for (*a*) Re=50; (*b*) Re=100; (*c*) Re=200

yield stress fluids and either the center of the reattachment region or the extent of the corner dead-zone for the yield stress fluids. As shown in Fig. 7, the extent of this corner region decreases with increasing yield numbers and increases with increasing Reynolds numbers. The dependence of l_r on the power-law index, however, is more complex. For moderate to high yield numbers ($Y=1-2$), modest increases in the length l_r with increasing n are observed. In the case of zero yield stress fluids, increasing the power law exponent from $n=1$ to $n=1.2$ (shear-thickening fluid), leads to approximately a 10 percent drop in the reattachment length, while varying the power-law index between 0.6 and 1 leads to a much smaller variation in the obtained reattachment length (less than 5 percent). This small variation in the reattachment length for power-law fluids with the power-law index values within the range 0.6–1.0 is in agreement with the computational predictions of Halmos et al. [4] and experimental findings of Halmos et al. and [14] reported on shear-thinning fluid flows over a two-to-one axisymmetric flows covering the $n=0.65-1.0$ range and Reynolds number values between Re=7 and 159. In general, the influence of the power-law index on the length, l_r, is more pronounced at low Reynolds numbers but remains small relative to that of the yield number.

To further establish the validity of the present results, computations representing the dependency of the reattachment length on the Reynolds number for a Newtonian fluid are compared to both quantitative PIV and qualitative flow visualization results obtained earlier. As shown in Fig. 8, the agreement between computations and experimental results is very good.

The corner vortex strength is represented in Fig. 9 in terms of the relative eddy intensity, e_i, which is plotted against the yield number for all power-law exponents and Reynolds numbers. The relative eddy intensity is defined as the maximum amount of back flow in the vortex region relative to the inlet flow rate or $-\Psi_{\min}/\Psi_{\max}$. Unlike l_r, e_i displays a strong dependence on both the power-law index as well as the yield number. e_i increases with the power-law index while it decreases with the yield number for all Reynolds numbers. For zero yield stress fluids, the dependence of the relative eddy intensity on the Reynolds number weakens at high Reynolds numbers, hinting at the existence of an asymptotic limit. For a Reynolds number of 50 and all studied power-law index values, as shown in Fig. 9(*a*), a yield number of $Y=2$ is sufficient to bring the corner vortex to a total halt and thus creating a corner dead-zone as demonstrated earlier in Fig. 5. The combined effect of increasing the yield number and reducing n would always lead to a reduction in the vortex intensity. This is expected since smaller shear-thinning exponents and larger yield numbers increase the viscosity values throughout the vortex region, thus lowering rates of deformation and, hence, circulation intensity. The monotonic and rather significant increase of e_i with

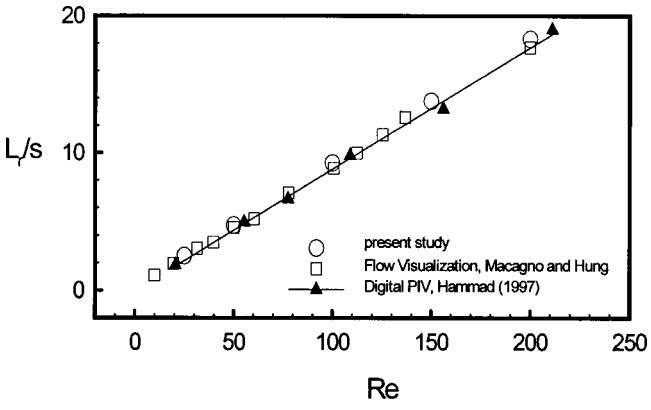

Fig. 8 Reattachment length versus Reynolds number for a Newtonian fluid: a comparison between present computations and available experimental results

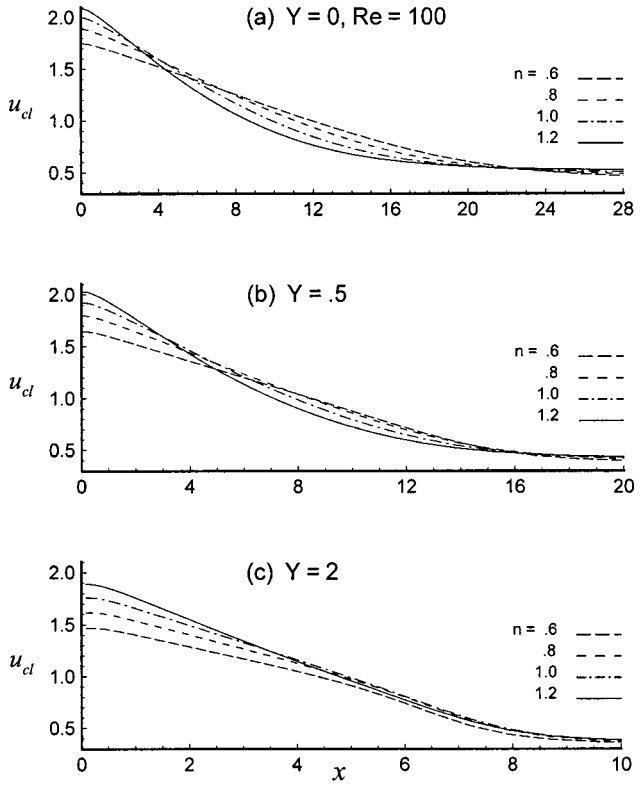

Fig. 10 Centerline velocity evolution at Re=100, n=0.6, 0.8, 1 and 1.2 for (*a*) Y=0; (*b*) Y=1; (*c*) Y=2

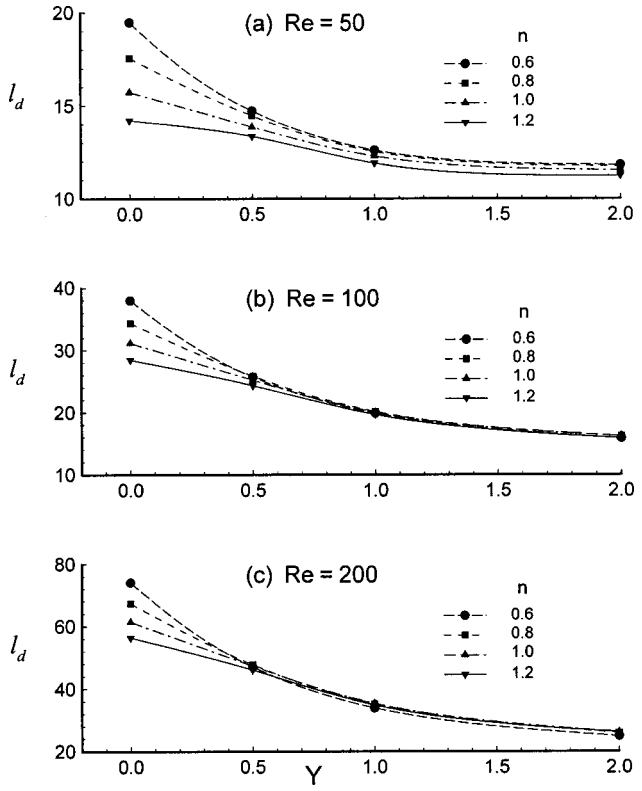

Fig. 11 Redevelopment length versus yield number at n=0.6, 0.8, 1 and 1.2 for (*a*) Re=50; (*b*) Re=100; (*c*) Re=200

n is a trend consistent with that reported by Halmos and Boger [14] for shear-thinning fluids. For a fixed yield number and power-law index, higher Re values lead to increased momentum transfer into the corner region and thus increase the recirculation intensity.

The effect of the fluid rheology on flow development is further investigated in Fig. 10 which shows the centerline velocity distributions for a range of yield numbers and power-law indexes at Re=100. A quick look at Fig. 10 reveals that the centerline velocity at the expansion plane ($x=0$) decreases with increasing yield numbers and decreasing power-law index values. The presence of yield stress and the shear-thinning effect lead to a more blunt fully developed velocity profile in the upstream pipe as previously demonstrated in Fig. 4. This, in turn, reduces the fully developed maximum centerline velocity. In general, the evolution of the centerline velocity is slower at smaller yield numbers, leading to shorter overall redevelopment lengths for larger yield numbers. It is also noted that the fully developed values of the downstream centerline velocities are decreasing with increasing yield numbers, again, as a result of the larger plug-flow regions characteristic of such cases.

Figure 10 reveals that the effect of the power-law index on the evolution of the centerline velocity depends on the yield number value. In the case of $Y=0$ and 0.5, the evolution of the centerline velocity has a simple dependence on the power-law index. Higher power-law index values lead to smaller plug-flow regions, and hence, a larger centerline velocity in the fully developed flow zones. This is clearly seen both at the step and in the fully recovered region further downstream (Figs. 10(*a*) and 10(*b*)). In addition to this, the flow develops faster for larger *n* values which results in the two crossovers of u_{cl} curves in the same two figures. However, for $Y=2$ case presented in Fig. 10(*c*), the rate of evolution of u_{cl} for the different *n* values are too close to make a clear determination. Clearly, the introduction of a yield stress modifies the trends. For the case of $Y=2$, the power-law index no longer plays a significant role in the centerline velocity development.

A clearer insight into the effects of inertia and fluid rheology on flow redevelopment can be gained by using the centerline velocity curves shown in Fig. 10 to extract the axial distances downstream of the expansion plane beyond which fully developed conditions are considered established, (i.e., the redevelopment length, l_d). Here the flow is considered fully developed at an *x* location where $u_{cl}/u_{cl,fd}=1.01$. The $u_{cl,fd}$ values used here correspond to the numerically predicted values of u_{cl} at the furthest downstream location which were within less than 1 percent of the analytical ones. The information is presented in Fig. 11 in terms of l_d against *Y* for all Reynolds numbers and power-law exponents. As concluded earlier and clearly displayed here in Fig. 11, the impact of variations in the power-law index on the redevelopment length is most significant for zero yield stress (or simple power-law) fluids. For the yield numbers of $Y=0$ and $Y=0.5$, the redevelopment length always decreases with increasing power-law index. The effect, however, is much weaker for $Y=1$ and $Y=2$, indicating the dominance of the yield stress parameter over the power-law index in this region.

Conclusions

Finite difference numerical solutions have been obtained for the governing equations describing the flow of Herschel-Bulkley fluids through an axisymmetric sudden expansion for a range of yield numbers and power-law exponents in the laminar flow regime. The detailed parametric study was undertaken to explore the effects of fluid rheology and flow inertia on the characteristics of the corner flow region and flow redevelopment. The results show that there is a strong dependence of the flow field on the yield number and a weak one on the power law index for larger values of the yield number. For lower values of the yield number, both the yield number and the power law index have a significant effect on the flow field. The results establish the yield number as a parameter greatly affecting the structure of the flow field and its evolution. At low yield numbers, a recirculating flow exists at the

edge of the step that is bounded by a very small dead-zone attached to the corner of the step. In addition, the reattachment point that is characteristic of Newtonian fluids, is replaced here by a ''reattachment zone,'' which is also a stagnant-zone of zero velocity. As the yield number increases the recirculating flow disappears and the flow remains attached to the wall throughout the expansion. Instead, a backward-facing ramp of nonmoving fluid forms over the expansion corner.

Acknowledgments

This project was partially funded by Exxon Education Foundation. The authors gratefully acknowledge this support.

Nomenclature

d = diameter of upstream pipe
e_i = corner eddy intensity, ratio of the maximum amount of backflow in the recirculation region to the inlet flow rate, $-\Psi_{\min}/\Psi_{\max}$
K = consistency index
l_d = redevelopment length, $l_d = x$ corresponding to $u_{cl}/u_{cl,fd} = 1.01$
l_r = reattachment length
n = power-law index
P = pressure
p = nondimensional pressure, $P/\rho U_i^2$
R = radial coordinate
R_w = radius of upstream pipe
r = nondimensional radial coordinate, R/S
Re = Reynolds number, $\rho d^n U_i^{2-n}/K$
S = step height, here $S = R_w$
U = streamwise velocity
U_i = inlet streamwise bulk velocity
u = normalized streamwise velocity, U/U_i
u_{cl} = normalized centerline velocity, U_{cl}/U_i
$u_{cl,fd}$ = normalized fully developed centerline velocity in the downstream pipe, $U_{cl,fd}/U_i$
V = radial velocity
v = normalized radial velocity, V/U_i
X = streamwise coordinate from step
x = nondimensional streamwise coordinate, X/S
Y = yield number, $\tau_y d^n/KU_i^n$
$\Psi_{\max}$ = maximum value of stream function
$\Psi_{\min}$ = minimum value of stream function
Δ_{ij} = rate of deformation tensor
μ = effective viscosity
μ_{eff} = nondimensional effective viscosity
ρ = density
τ_{ij} = stress tensor
τ_y = yield stress

References

[1] Feurstein, I. A., Pike, G. K., and Rounds, G. F., 1975, ''Flow in an abrupt expansion as a model for biological mass transfer experiments,'' J. Biomech., **8**, pp. 41–51.
[2] Macagno, E. O., and Hung, T. K., 1967, ''Computational and Experimental Study of a Captive Eddy,'' J. Fluid Mech., **28**, pp. 43–64.
[3] Badekas, D., and Knight, D. D., 1992, ''Eddy correlations for laminar axisymmetric sudden expansion flows,'' ASME J. Fluids Eng., **114**, pp. 119–121.
[4] Halmos, A. L., Boger, D. V., and Cabelli, A., 1975, ''The Behavior of a Power-Law Fluid Flowing Through a Sudden Expansion: Part I. A Numerical Solution,'' AIChE J., **21**, No. 3, pp. 540–549.
[5] Ponthieux, G., Devienne, R., and Lebouche, M., 1992, ''Energy losses associated with sudden expansions and conical divergents for different pseudoplastic fluids,'' Eur. J. Mech., B/Fluids, **11**, No. 6.
[6] Scott, P. S. and Mizra, F., 1988, ''Finite-Element Simulation of Laminar Viscoplastic Flows With Regions of Recirculation,'' J. Rheol., **32**, pp. 387–400.
[7] Vradis, G. C., and Ötügen, M. V., 1997, ''The Axisymmetric Sudden Expansion Flow of a Non-Newtonian Viscoplastic Fluid,'' ASME J. Fluids Eng., **119**, pp. 193–200.
[8] Hammad, K. J., Ötügen, M. V., Vradis, G., and Arik, E., 1999, ''Laminar Flow of a Nonlinear Viscoplastic Fluid Through an Axisymmetric Sudden Expansion,'' ASME J. Fluids Eng., **121**, pp. 488–495.
[9] Hammad, K. J., 1997, ''Experimental and Computational Study of Laminar Axisymmetric Recirculating Flows of Newtonian and Viscoplastic Non-Newtonian Fluids,'' Ph.D. dissertation, Polytechnic University, New York.
[10] Vradis, G., and Hammad, K. J., 1998, ''Strongly Coupled Block-Implicit Solution Technique for Non-Newtonian Convective Heat Transfer Problems,'' Numer. Heat Transfer, Part B, **33**, pp. 79–97.
[11] O'Donovan, E. J., and Tanner, R. I., 1984, ''Numerical Study of the Bingham Squeeze Film Problem,'' J. Non-Newtonian Fluid Mech., **15**, pp. 75–83.
[12] Beverly, C. R., and Tanner, R. I., 1992, ''Numerical Analysis of Three-Dimensional Bingham Plastic Flow,'' J. Non-Newtonian Fluid Mech., **42**, pp. 85–113.
[13] Lipscomb, G. G., and Denn, M. M., 1984, ''Flow of a Bingham Fluid in Complex Geometries,'' J. Non-Newtonian Fluid Mech., **14**, pp. 337–346.
[14] Halmos, A. L., Boger, D. V., and Cabelli, A., 1975, ''The Behavior of a Power-Law Fluid Flowing Through a Sudden Expansion: Part II. Experimental Verification,'' AIChE J., **21**, No. 3, pp. 550–553.

Two-Dimensional Study of the Turbulent Wake Behind a Square Cylinder Subject to Uniform Shear

A. K. Saha

G. Biswas

K. Muralidhar

Department of Mechanical Engineering,
Indian Institute of Technology, Kanpur,
Kanpur, 208 016 UP India

The flow past a square cylinder at a Reynolds number of 20,000 has been simulated through direct calculations and through the calculations using turbulence model. The present investigation highlights significant differences between the two approaches in terms of time-averaged flow, Strouhal number, and aerodynamic forces. The time-averaged drag coefficient and the rms fluctuations due to the direct calculations are higher than those due to the turbulence model. However, Strouhal number is underpredicted in the direct calculations. The effect of shear on the flow has also been determined using the turbulence model. The time-averaged drag coefficient is found to decrease with the increase in shear parameter up to a certain value. Then it increases with the further increase in the shear parameter. On the other hand, lift coefficient increases with the increase in shear parameter. Strouhal number shows a decreasing trend with the increase in shear parameter whereas the rms values of drag and lift coefficients increase with the shear parameter. The Kármán vortex street, mainly comprising clockwise vortices due to shear, decays slowly compared to the uniform flow condition. [DOI: 10.1115/1.1383549]

Introduction

Unsteady flow past bluff bodies is of direct relevance to structural engineering, where flow induced vibration is one of the most important considerations in designing the massive structures. The wake of bluff objects is unsteady, the near-wake being strongly periodic and driven by the shed vortices. The nuances of the wake structure depend on the incoming flow and its quality. The analysis of wake with incoming uniform velocity is complex and the nonuniformity of the velocity makes the study more difficult. The shear may be of three types namely, (1) pure transverse shear, (2) pure axial shear and (3) combination of transverse and axial shear. Out of the above three, the study of the third one seems to be more difficult. The applications of flows with nonuniform upstream velocity are plenty. The approaching flow of a curved river against the bridge pier is one such example. The pipeline laid above the ground experiences a nonuniform stream since it is within the boundary layer formed due to earth surface. The effect of inlet shear at high Reynolds number at which the flow becomes turbulent may be severe. Kiya et al. [1] investigated experimentally the effect of transverse shear on critical Reynolds number beyond which the vortex shedding starts. They considered the case of flow past a circular cylinder and found that the shear parameter influenced Strouhal number. Kwon et al. [2] have presented experimental results for the effect of shear parameters on the drag coefficient and Shrouhal number for the case of flow past a circular cylinder. Ayukawa et al. [3] have reported results showing the influence of shear on the wake structure for a square cylinder at moderate Reynolds number. They have observed that at high shear rates, the Kármán vortex street breaks down and the flow pattern downstream tends to be similar at any instant. Saha et al. [4] have reported the influence of shear for a wide range of Reynolds numbers (500–1250). Their results show that the mean drag coefficients and the rms values of lift and drag coefficients initially decrease until certain values of shear rate and then increase with increase in shear parameter. Their findings also reveal that the Strouhal number decreases uniformly with increase in shear parameter. They showed that at higher shear rates, the Kármán vortex street comprising of alternate vortices breaks and the wake shows clockwise vortices. However, they have not considered high Reynolds number turbulent flow in their study.

The geometry of the present flow model is nominally two-dimensional. But the flow past a square cylinder is highly three-dimensional at high Reynolds number. The flow becomes three-dimensional beyond a Reynolds number of 175 (Williamson [5] and Saha [6]). The flow turns out to be chaotic and possibly turbulent at a Reynolds number of 500 (Saha et al. [7]). Flows above a Reynolds number of 500 require to be computed by solving the three-dimensional unsteady Navier-Stokes equations using very fine grids. However, computation of three-dimensional Navier-Stokes equations at higher Reynolds number is computationally quite expensive. To economize computation, engineering applications are being computed at high Reynolds numbers in two-dimensions using various eddy viscosity models of turbulence (Hadid et al. [8]). In such simulations, energetic interactions with respect to the third component of velocity are effectively set to zero. Hence, the occurrence of shedding and the prediction of the nuances of shedding depend significantly on the turbulence model used and the details of the numerical technique. This is revealed from the numerical studies of Hadid et al. [8] and Franke and Rodi [9].

The flow past a square cylinder beyond a Reynolds number of 175 is three-dimensional (Saha [6]). Therefore, the computation of such flow using three-dimensional equations takes into account proper magnitude of diffusion and dissipation mechanism, which is an inherent feature of the third dimension of the flow. However, the two-dimensional model of such flow does not take into account the proper diffusion phenomenon of the flow due in absence of the third dimension. The vortex stretching in three-dimensional flow field can be represented as the diffusion mechanism (Saha [9]). The energy transfer from large to small scale (or eddies) is also dependent on the dimensionality of the model equations representing the flow. If two-dimensional model equations are solved for a physically three-dimensional flow, then there is an increase in the in-plane velocity fluctuations. The unrealistic higher fluctuations can be reduced if the modeling of the fluctuations is done in such a way that the additional diffusion due to the third com-

Contributed by the Fluids Engineering Division for publication in the JOURNAL OF FLUIDS ENGINEERING. Manuscript received by the Fluids Engineering Division July 31, 2000; revised manuscript received May 1, 2001. Associate Editor: P. W. Bearman.

ponent of velocity fluctuations is incorporated. The two-dimensional model can represent the two-dimensional (spanwise averaged) flow structures if the physical diffusion and dissipation mechanism are incorporated and the model becomes equivalent to the three-dimensional simulation as far as the energy cascading or diffusion mechanism is concerned. The incorporation of the k-ϵ model adds diffusion into the two-dimensional model equation through the eddy viscosity. The eddy viscosity is deployed to model the velocity fluctuations of the three-dimensional flow field and capture the nuances of the large scale activities of the flow.

At higher Reynolds numbers, three-dimensional random turbulent fluctuations are superimposed on the unsteady periodic motion. The random motion represents small scales of turbulence and can be simulated by a stochastic model. In the wake of a bluff-body flow, the time varying component ϕ (for example, velocity and pressure) may be written as the combination of global mean component $\overline{\phi}$, a periodic component $\tilde{\phi}$ and a random component ϕ' (Hussain [10]). This can be written mathematically as

$$\phi(x_i,t)=\overline{\phi}(x_i)+\tilde{\phi}(x_i,t)+\phi'(x_i,t)=\langle\phi\rangle(x_i,t)+\phi'(x_i,t) \tag{1}$$

where $\langle\phi\rangle$ refers to a phase average quantity. Based on this idea, one can adopt the following viewpoint (Saha et al. [11]): The Reynolds averaged Navier-Stokes equations determine the phase-averaged velocity and pressure (quantities inside '$\langle\ \rangle$' in Eq. (1)). The eddy viscosity arising from the Boussinesq approximation can now be associated with the random fluctuations (quantities marked by $'$ in Eq. (1)). The eddy viscosity in turn can be determined by the transport equations: one for the turbulent energy level k and one for the rate of energy dissipation ϵ. This has come to be called the k-ϵ family of models.

Okajima et al. [12] have carried out a detailed study for rectangular cylinders with round and square leading edges while the trailing edge is square in all the cases. They have simulated flows over a range of Reynolds numbers ($1\times10^3-7\times10^3$) using the standard k-ϵ model. Though they were able to capture some of the aspects of bluff body aerodynamics, they found significant differences between experiments and numerical predictions. Franke and Rodi [9] have shown that the occurrence of shedding past a square cylinder and its characteristics depend on the turbulence model used. They have also reported that the physically meaningful predictions are modulated by the details of the numerical technique used. Hadid et al. [8] have reported turbulent simulation past a square cylinder using two different approaches, namely, the standard k-ϵ model and an anisotropic k-ϵ model. They have found that the anisotropic k-ϵ model resolves the anisotropy of the Reynolds stresses and predicts the mean energy distribution closer to the experiments vis-a-vis the standard k-ϵ model. Rodi [13] has reviewed calculations performed on vortex shedding past long cylinders of various shapes at high Reynolds numbers using different k-ϵ models, the Reynolds Stress Equations (RSE) model and the Large Eddy Simulation (LES). The RSE model and the LES simulation have emerged superior in his review. Bosch and Rodi [14] have reported experimental as well as numerical results for the flow past a square cylinder at a Reynolds number of 22,000 placed at various distances from the adjacent wall. Their observation reveals that vortex shedding and the consequent unsteadiness in the flow field are suppressed when the cylinder is placed very close to the wall. Saha et al. [11] have carried out RANS (Reynolds-Averaged Navier-Stokes) computations past a square cylinder using three different models and captured all the nuances of the unsteady wake and found good match with experiments. The conclusion of the study is that the Kato-Launder model is the best among the three as it can handle the stagnation zone properly.

The aim of the present study is to compare the performances of the two-dimensional direct (model-free) and the k-ϵ model calculations. The influence of the inlet shear on the aerodynamic forces and the wake structures past a square cylinder has also been studied. The models deployed to account for the random fluctuations is based on the Kato-Launder modification (Kato-Launder [15]) of the standard k-ϵ paradigm. The Reynolds number considered is 20,000, based on the cylinder width and the average incoming velocity. Two nondimensional parameters, which govern the flow around a square cylinder with uniform inlet shear, are the Reynolds number, Re and the shear parameter, K. These are defined as

$$\mathrm{Re}=\frac{u_{av}B}{\nu}\quad\text{and}\quad K=\frac{GB}{u_{av}}$$

where the uniform shear at the inflow plane is given as

$$u(y)=u_{av}+Gy$$

Here the transverse velocity gradient on the inflow plane is G, the width of the obstacle is B, the average velocity is u_{av} and H is the transverse dimension of the domain of interest.

Phase-Averaged Flow Equations

At high Reynolds numbers, the wake of a square cylinder can be visualized as the superposition of the three-dimensional (3D) turbulent fluctuations over a two-dimensional (2D) flow field. This can also be viewed as a three-dimensional unsteady periodic flow field. An instantaneous quantity ϕ can be, therefore, described by the summation of the phase-averaged value and the stochastic fluctuation as expressed in Eq. (1). Assuming incompressible flow, the phase-averaged continuity and momentum equations can be written as (Saha et al. [11])

$$\frac{\partial\langle u_i\rangle}{\partial x_i}=0 \tag{2}$$

$$\frac{\partial\langle u_i\rangle}{\partial t}+\frac{\partial[\langle u_j\rangle\langle u_i\rangle]}{\partial x_i}=-\frac{1}{\rho}\frac{\partial\langle p\rangle}{\partial x_i}+\frac{\partial}{\partial x_j}\left[\nu\frac{\partial\langle u_i\rangle}{\partial x_j}-\langle u_i'u_j'\rangle\right] \tag{3}$$

In the above equations the velocities are nondimensionalized with the average axial velocity u_{av} at the inlet, all lengths are nondimensionalized with the cylinder width B and the pressure with ρu_{av}^2.

To enforce closure, the Reynolds stress tensor, $\langle u_i'u_j'\rangle$ in the momentum equations are to be suitably modeled. The alternatives available for evaluating $\langle u_i'u_j'\rangle$ are far greater compared to the choices for the numerical procedure. The Kato-Launder k-ϵ model has been taken up for the closure in the present investigation.

Turbulence Models

The present simulation has been carried out using two-equations model of Kato-Launder [15]). The model can be referred as KaLa model here onwards. The model relate the turbulent viscosity $\langle\nu_t\rangle$ to the turbulent kinetic energy $\langle k\rangle$ and its rate of dissipation $\langle\epsilon\rangle$. In the KaLa model, the transport equations for $\langle k\rangle$ and $\langle\epsilon\rangle$ are

$$\frac{\partial\langle k\rangle}{\partial t}+\frac{\partial[\langle u_i\rangle\langle k\rangle]}{\partial x_i}=\frac{\partial}{\partial x_i}\left[\frac{\langle\nu_t\rangle}{\sigma_k}\frac{\partial\langle k\rangle}{\partial x_i}\right]+P_k-\langle\epsilon\rangle \tag{4}$$

$$\frac{\partial\langle\epsilon\rangle}{\partial t}+\frac{\partial[\langle u_i\rangle\langle\epsilon\rangle]}{\partial x_i}=\frac{\partial}{\partial x_i}\left[\frac{\langle\nu_t\rangle}{\sigma_\epsilon}\frac{\partial\langle\epsilon\rangle}{\partial x_i}\right]+C_{\epsilon1}P_k\frac{\langle\epsilon\rangle}{\langle k\rangle}-C_{\epsilon2}\frac{\langle\epsilon\rangle^2}{\langle k\rangle} \tag{5}$$

where the production term is

$$P_k=C_\mu\langle\epsilon\rangle S\Omega,\quad \Omega=\frac{\langle k\rangle}{\langle\epsilon\rangle}\sqrt{\frac{1}{2}\left[\frac{\partial\langle u_i\rangle}{\partial x_j}-\frac{\partial\langle u_j\rangle}{\partial x_i}\right]^2},$$
$$S=\frac{\langle k\rangle}{\langle\epsilon\rangle}\sqrt{\frac{1}{2}\left[\frac{\partial\langle u_i\rangle}{\partial x_j}+\frac{\partial\langle u_j\rangle}{\partial x_i}\right]^2} \tag{6}$$

Table 1 Model parameters

C_μ	$C_{\epsilon 1}$	$C_{\epsilon 2}$	σ_κ	σ_ϵ
0.09	1.44	1.92	1.0	1.3

The quantity Ω is related to the average rotation of a fluid element. In the simple shear flow context, S and Ω are equal. However, in stagnation flows, such as impinging jets, $\Omega=0$ and $S>0$. This leads to the desired reduction of the production of kinetic energy near the forward stagnation point of the bluff objects. This has an important effect of lowering eddy viscosity in the boundary layers and permitting vortices to be shed from the rear side.

The eddy viscosity $\langle \nu_t \rangle$ is determined from the expression

$$\langle \nu_t \rangle = C_\mu \frac{\langle k \rangle^2}{\langle \epsilon \rangle} \tag{7}$$

The parameters for the model appearing in Eqs. (4)–(7) are given in Table 1. The recommendation of Kato-Launder model is that $12 \leqslant y^+ \leqslant 60$. However, effort was made (grid size was so chosen) to retain y^+ closer to 12 in most of the computations.

Numerical Method

The two-dimensional Navier-Stokes equations, along with the continuity constraint, have been solved for direct calculations using the similar procedure as that of k-ϵ model described below.

For k-ϵ model calculations, the differential equations (2) and (3) have been solved on a staggered grid by using a modified version of the MAC algorithm of Harlow and Welch [16] (also see Hoffman and Benocci [17]). The important factor in the choice of the spatial differencing strategy is the formal order of accuracy. The order of accuracy has to be balanced against the global conservation properties of the numerical scheme. The order of accuracy relates to the accuracy of the solution whereas the conservative property improves the stability of the scheme. In the present study, diffusion terms have been approximated by second-order central differencing. For the advection terms, a hybrid scheme employing a balance between upwinding and central differencing has been used. A more accurate spatial differencing could have been used but it was found that most higher-order schemes did not satisfy the global conservation property. Very fine grids have been used in the present simulations. Hence it was possible to reduce the fraction of upwinding to 0.1, and yet eliminate spurious oscillations associated with central differencing of the advection terms. In addition, a very fine mesh has been used in the present simulation in order to offset the local inaccuracy, if any.

When the flow is incompressible, the pressure and velocity are to be solved simultaneously, since the pressure field has to be compatible with the continuity equation. This has been implemented by a two-step procedure, namely (a) a predictor step using current values of pressure (p^n) that is fully explicit and (b) a corrector step in which the correction to velocity and pressure are obtained by ensuring compatibility with the continuity equation. An explicit second order in time, Adams-Bashforth differencing scheme has been used for the time advancement of the convection and diffusion terms. The complete numerical algorithm is summarized below.

The momentum equation is written using as a space operator, g containing the convection and diffusion terms as

$$\frac{\partial u_i}{\partial t} = g(u_i, u_j) - \frac{\partial p}{\partial x_i} \tag{8}$$

Thus the predictor step for the time advancement takes the form

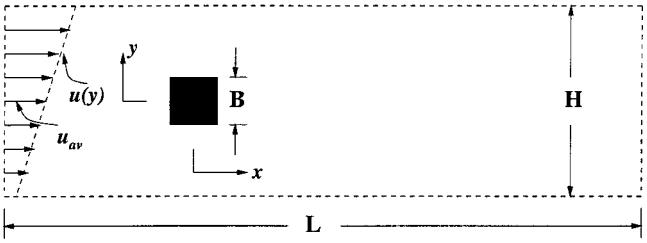

Fig. 1 Two-dimensional channel flow with built-in obstacle

$$\frac{u_i^* - u_i^n}{\delta t} = \frac{3}{2} g(u_i, u_j)^n - \frac{1}{2} g(u_i, u_j)^{n-1} - \frac{\partial p^n}{\partial x_i} \tag{9}$$

This is followed by the corrector step

$$p' = -r_0 \frac{\partial u_i^*}{\partial x_i} \Bigg/ \left[2\delta t \left\{ \frac{1}{(\delta x)^2} + \frac{1}{(\delta y)^2} \right\} \right] \tag{10}$$

The final solution for velocity and pressure are given as

$$p^{n+1} \leftarrow p^n + p' \tag{11}$$

$$u_i^{n+1} \leftarrow u_i^* + \frac{\delta t}{\delta x_i} p' \tag{12}$$

The corrector step is solved by point-wise Gauss-Seidel iterations with r_0 as an over-relaxation factor to accelerate the pressure correction process. A typical value of r_0 used in all the simulations is 1.8.

Computational Domain and Boundary Conditions

The physical problem considered is flow past a cylinder of square cross-section, placed centrally in a channel. The computational domain for this geometry is presented in Fig. 1. The dimensions of the channel are $H=8.0$, $B=1.0$, and $L=32.0$. The cylinder is placed at a distance of 8.0 unit from the inlet. A uniform mesh with sufficient cells has been used. The obstacle surfaces are treated as no-slip boundaries. The free-slip boundary conditions have been applied at the top and bottom surfaces. At the inlet, the flow enters with a velocity $u(y)$ and the prescribed turbulence intensity ($I=\sqrt{\overline{u_i'^2}}/2/u_{av}$) at the inlet is set to 10 percent. For all the computations, the eddy viscosity is specified as $\nu_t/\nu=10$ at the inflow plane (Bosch and Rodi [14]). The value of $\langle \epsilon \rangle$ is specified using the Eq. (7). Wall function treatment has been used at all the solid boundaries. During wall function treatment, the first grid points from the wall have fallen in the range of $12 \leqslant y^+ \leqslant 60$. Most of the cases y^+ value have been closer to 12. At the outlet, the convective boundary condition due to Orlanski [18]) has been used. This condition may be stated as

$$\frac{\partial \psi}{\partial t} + u_c \frac{\partial \psi}{\partial x} = 0$$

where ψ can take the values of u_i, k and ϵ, and u_c, the convective velocity is the streamwise celerity of the vortices leaving the outflow plane.

The time-step used in the present simulation for the direct calculation and for the k-ϵ model is 4 percent of the time period of vortex shedding. For the cases with inlet shear, the time-steps have been same as those of the cases without shear. The time steps have been kept constant. However, the time steps satisfy the conditions necessary to prevent numerical instability. The conditions concerning the numerical instabilities are determined from the Courant-Friedrichs-Lewy (CFL) condition and the restriction on the grid-Fourier numbers. Each cycle of vortex shedding took

Table 2 Comparison of engineering parameters for direct and model calculations for a Reynolds number of 20,000

Type of calculation	St	$\overline{C_D}$	$\overline{C_L}$	C_D'	C_L'	l_r
Direct	0.122	2.41	0.063	0.116	1.729	1.28
Model	0.142	1.93	0.003	0.022	0.604	2.07
Lyn et al. [19]) (Re=21400)	0.132	2.05	-	-	-	1.38

about 100 minutes of CPU time on a DEC-Alpha machine having a processor speed of 125 MHz and 32 MB RAM. The time-averaged quantities have been obtained by integrating the instantaneous field over a long period of not less than 40 shedding cycles, but without including the initial transients.

Spatial Grid Independence

In order to establish a grid independent solution for both direct and model calculations, computations have been performed for two different meshes with 496×122 and 332×82 grids. The time-averaged drag coefficient (C_D) for the k-ϵ model on a 496×122 grid was found to be 1.983. On a 332×82 grid the value for the k-ϵ model was 1.935, a difference of less than 3 percent. Similarly, the difference in mean drag between the two grids due to direct calculation was found to be 6 percent. The rms values of the lift coefficient during the calculations using k-ϵ model are 0.724 and 0.70 on the grid-meshes of 332×82 and 496×122, respectively. The time averaged drag coefficient for the k-ϵ model on a 386×98 grid was found to be 1.971. Hence all computational results were obtained on the 332×82 grid mesh for the both direct (model-free) and k-ϵ model computations.

Code Validation

The present code has been validated thoroughly with the published results due to Lyn et al. [19]) in an earlier study (Saha et al. [11]). The time-averaged aerodynamic forces and Strouhal number show good match with the experiments and are shown in Table 2. There are good agreements between the time-averaged experimental flow fields and the present numerical results. The kinetic energy distribution also reveal close comparison with the experimental counterpart.

Results and Discussions

Flow past a square cylinder has been computed by solving two-dimensional Navier-Stokes equations directly as well as using k-ϵ turbulence model. The turbulence model has been used to account for the contribution due to random fluctuations. It has been established that the two-dimensional calculations for the flow past square cylinder is doubtful beyond a Reynolds number of 175 (Saha [6]). At the same time two-dimensional calculation can predict the engineering parameters closely if the proper turbulence model is used to account for the random fluctuations (Saha [6]). Therefore, one of the aims of the present study is to quantify the difference between the two sets of calculations, namely direct (model-free) and k-ϵ model calculations.

Comparison of Direct and k-ϵ Model Calculations. The differences in the results between the two calculations have been presented using the time-averaged and instantaneous flow field.

Engineering Parameters. Table 2 shows the Strouhal number, time-averaged and rms values of lift and drag coefficients for flow past a square cylinder subject to uniform parallel flow at inlet. The predicted vallue of the Strouhal number is higher for the case of calculations with the k-ϵ model and gives a closer estimation to the experimental value of 0.132 (Lyn et al. [19]). The time-averaged drag coefficient is lower in the case of k-ϵ model calculation. The rms fluctuations are greater in the direct calculation as the k-ϵ model calculation damps down the fluctuations owing to excess diffusion.

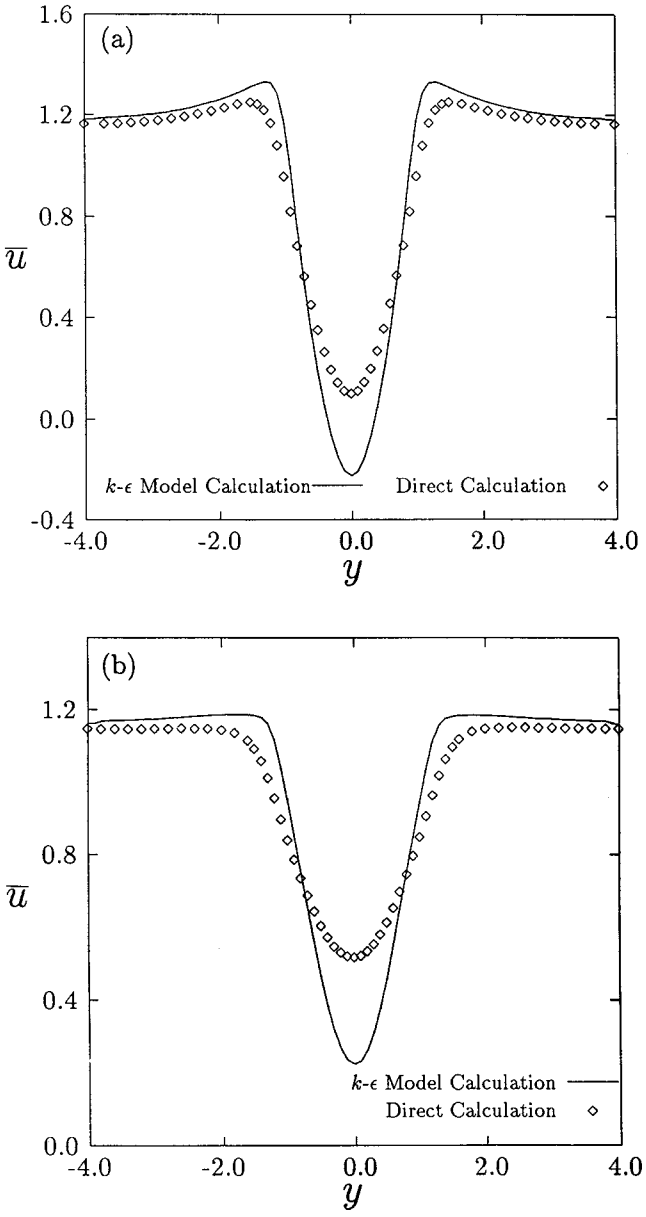

Fig. 2 Comparison of time-averaged streamwise velocity profiles due to direct calculation and k-ϵ model calculation at (*a*) $x=1.5$ and (*b*) $x=2.5$, for a Reynolds number of 20,000

Time-Averaged Flow Field. Figure 2 shows the time-averaged streamwise velocity at two different locations, namely $x=1.5$ and $x=2.5$. The time-averaged quantities have been obtained by integrating the instantaneous field over a long duration, with a minimum of 20 shedding cycles. Figure 2 reveals that the recovery of velocity is faster in case of direct calculation at both the locations. The velocity deficit is more due to k-ϵ model calculation. The additional diffusion in the phase-averaged Navier-Stokes equations makes the shear layer elongated. The velocity recovery becomes slow due to this elongated shear layer which in turn affects the entrainment across the transverse direction. The comparison of the time-averaged streamwise velocity profiles due to k-ϵ with the experimental data of Lyn et al. [19] has already been presented by Saha et al. [11]. The comparison is very good except very near the obstacle surface.

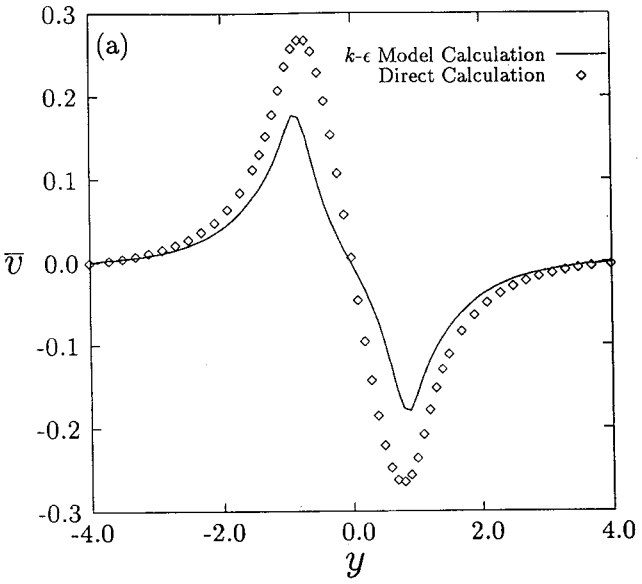

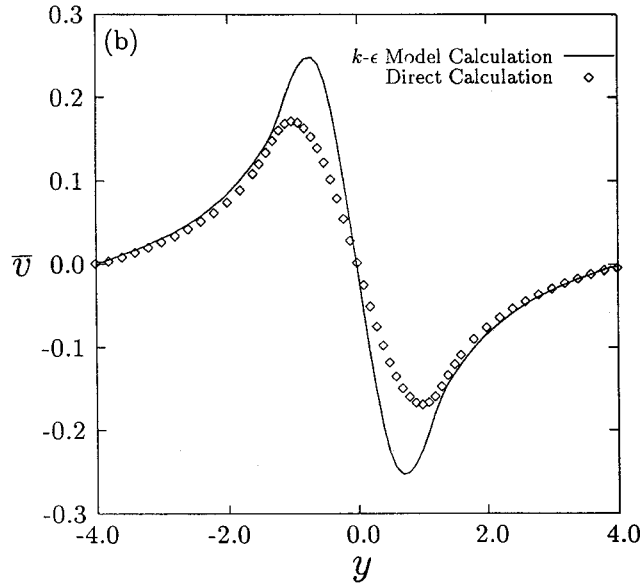

Fig. 3 Comparison of time-averaged transverse velocity profiles due to direct calculation and *k-ε* model calculation at (*a*) $x=1.5$ and (*b*) $x=2.5$, for a Reynolds number of 20,000

The profiles of the transverse component of velocity in the *y*-direction have been depicted in Fig. 3. It is interesting to note that the entrainment due to *k-ε* model and direct calculations show opposite trend between the two locations, namely $x=1.5$ and $x=2.5$. The comparison of predicted time-averaged transverse velocity profiles with the experimental results at different downstream locations has been accomplished by Saha et al. [11]. The entrainment due to direct calculation decreases with the increased downstream distance while it increases in case of *k-ε* model. The extent of entrainment of fluid into the wake (for $x \geq 2.5$) differs between two simulations. The phase-averaged *k-ε* model is contemplated to capture, at least partly, the nuances of large scale activities of a three-dimensional flow. The mean recovery length for a three-dimensional simulation is more than that for a two-dimensional case. Hence, the entrainment due to the *k-ε* model calculation is more (for $x \geq 2.5$) than that of the direct two-dimensional calculation. Furthermore, it can be stated that the transverse entrainment increases initially with the increase in streamwise direction up to a certain distance and then starts decreasing and goes to zero in the far downstream. The mean circulation lengths for the direct and the *k-ε* model calculations are 1.28 and 2.07, respectively. Therefore, at the location $x=1.5$, the entrainment is more for the direct calculation due to the fact that it reaches a very high value. On the contrary, the entrainment for the *k-ε* model calculation does not reach its peak at the same location ($x=1.5$) owing to the higher recirculation length. Similarly, at $x=2.5$, the entrainment is more for the *k-ε* model as the location ($x=2.5$) is very close to the wake stagnation point (full length of the recirculation bubble) due to the *k-ε* model calculation. The location $x=2.5$ is far behind the location of the wake stagnation point due to the direct calculation and the entrainment due to the direct calculation is eventually set on a decreasing trend. Figure 4 presents the centerline recovery of the streamwise component of velocity. The direct calculation shows faster recovery and lower back flow compared to the *k-ε* model. However, there is negligible difference in the recovered value of the streamwise velocity in both the cases. The time-mean recirculation length in direct and model calculations are found to be 1.28 and 2.07, respectively. In one of the earlier investigations, Saha et al. [11] have shown that the *k-ε* model due to Kato-Launder [15] displays a reasonably good centerline recovery of the streamwise component of velocity when compared with the experimental values of Lyn et al. [19] downstream of the obstacle.

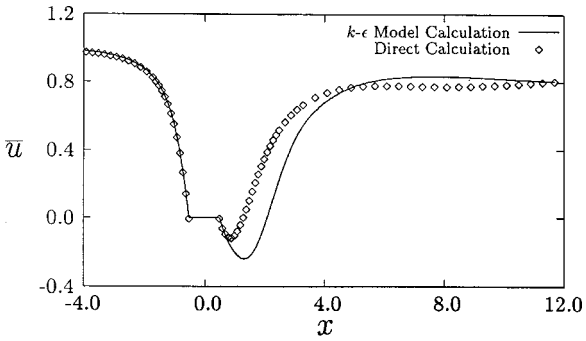

Fig. 4 Comparison of time-averaged streamwise velocity recovery due to direct calculation and *k-ε* model calculation along the centerline ($y=0$), for a Reynolds number of 20,000

The time-averaged vorticity contours have been shown in Fig. 5. Figures 5(*a*) and 5(*b*) clearly show that the shear layers due to the *k-ε* model elongate more in the streamwise direction compared to that due to the direct calculation. Present contour plots have striking similarity with those of Mittal and Balachandar [20]. Mittal and Balachandar [20] have analyzed flow past a circular cylinder. They showed that the shear layers due to three-dimensional calculations elongated more in the streamwise direction as compared to two-dimensional calculations. As we have mentioned earlier, the phase-averaged *k-ε* model is believed to capture some aspects of large scale activities of three-dimensional simulation. Hence, the present simulation is quite consistent. The longer shear layer in the case of *k-ε* model calculation is caused by the higher diffusion in the streamwise direction (Saha [4]).

Instantaneous Flow Field. The instantaneous vorticity contours for the two cases (Fig. 6) show similar pattern formation of the Kármán vortex street. It is to be noted that the contour plots in Fig. 6 have been plotted at the same phase, namely at an instant when the local lifts are positive maximum. Figure 6(*a*) shows the instantaneous vorticity contours due to the direct calculation. The lift coefficient or any of the flow variables in the direct calculation does not show constant periods over the cycles. In other words, it can be said that the direct calculation suffers from phase jitter. Therefore, phase-averaging of the flow field due to direct calculation at the phase of positive maximum lift has been carried out over 20 cycles. Phase-averaging has been done to compare the instantaneous and phase-averaged flow field. The phase-averaged

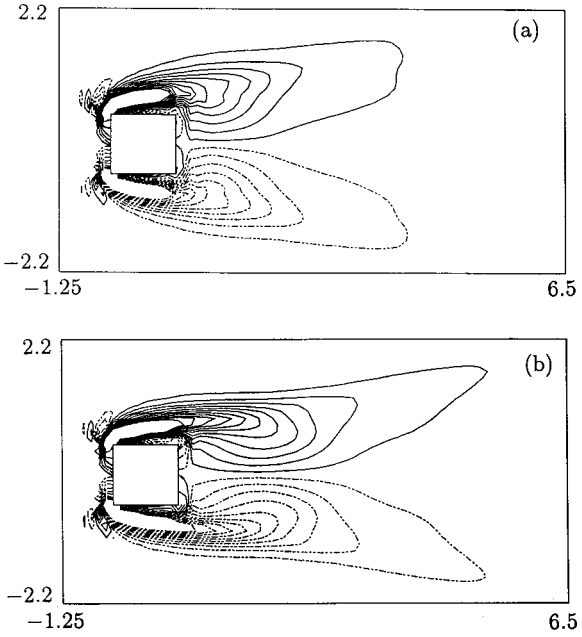

Fig. 5 Time-averaged vorticity contours due to the (*a*) direct calculation and (*b*) *k-ε* model calculation, for a Reynolds number of 20,000

vorticity contours have been presented in Fig. 6(*b*). Comparison of Figs. 6(*a*) and 6(*b*) reveal that the near-wake ($x \leqslant 3$) shows no significant changes whereas the intermediate- and far-wake have been affected due to phase-averaging. The vortices in the wake ($x \geqslant 3$) smear out as a result of increased phase jitter with the downstream direction. Figure 6(*c*) depicts the instantaneous vorticity contours at the same phase due to the *k-ε* model. The shear layer in the *k-ε* model is longer in the streamwise direction and rolls up symmetrically from top and bottom of the square cylinder over a cycle. The interesting point to be noted that the number of

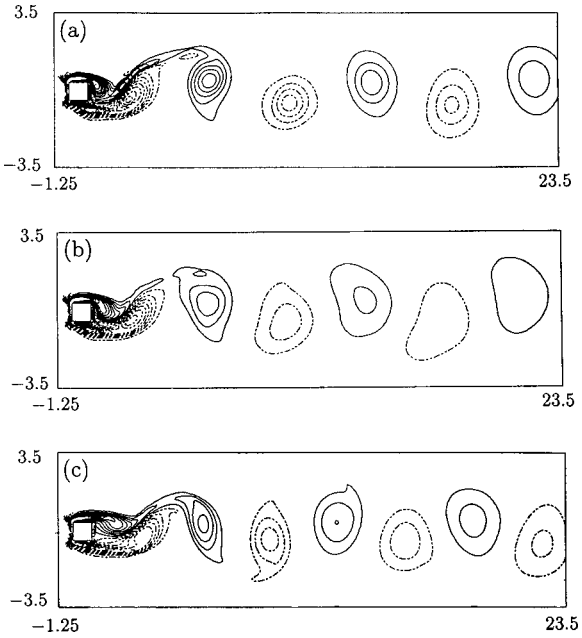

Fig. 6 (*a*) Instantaneous vorticity contours due to direct calculation, (*b*) phase-averaged vorticity contours due to direct calculation and (*c*) instantaneous vorticity contours due to *k-ε* model calculation, for a Reynolds number of 20,000

Table 3 Effect of shear on Strouhal number and aerodynamic forces for a Reynolds number of 20,000

K	St	$\overline{C_D}$	$\overline{C_L}$	C_D'	C_L'
0.0	0.142	1.93	0.003	0.022	0.604
0.125	0.140	1.90	0.055	0.043	0.606
0.1875	0.137	1.88	0.073	0.063	0.696
0.250	0.135	1.89	0.075	0.099	0.812

detached vortices is more in *k-ε* model than those in direct calculation. This particular phenomenon is in agreement to the higher Strouhal number in the case of *k-ε* model calculation. It is to be noted that the model calculation gives constant period over the cycles for any variables and the instantaneous field itself is the phase-averaged flow field. The decay rate of vortices with the downstream distance is faster in the case of direct calculation as compared to the *k-ε* model. This particular feature is clear from the Figs. 6(*b*) and 6(*c*).

Effect of Shear on Vortex Dynamics. It has already been shown that the *k-ε* model performs better when two-dimensional calculation is carried out at a higher Reynolds number for flow past a square cylinder. Saha et al. [11] have shown that the KaLa *k-ε* model is a better choice among different variants of the *k-ε* model as far as the flow past a square cylinder is concerned. Therefore, KaLa model has been used for the present model calculations. Attempts have been made to show the effect of shear of the incoming flow on the vortex dynamics in the present study. The following part of the investigation is the study of flow past a square cylinder with inlet shear. The KaLa *k-ε* model has been used to study this objective. The aerodynamic forces, time-averaged and instantaneous flow fields have been chosen to show the effect of shear.

Engineering Parameters. Table 3 shows the effect of shear on the aerodynamic forces and their rms fluctuations. Strouhal number has been found to decrease with the increase in shear parameter. However, the time-averaged drag coefficient shows that it decreases up to a shear parameter of $K=0.1875$ and then increases with the further increase in shear parameter. The time-averaged lift and rms fluctuations of the aerodynamic forces increase with the increase in shear parameter. The cylinder experiences a positive lift as a consequence of sheared approach velocity and the magnitude of which increases with the increase in shear parameter. The possible reasons for the positive lift and its increase with the increase in shear parameter are as follows. The inlet shear influences the separated shear layers on either side of the leading edge of the cylinder. The flow always separates at the leading edge of the cylinder. For higher Reynolds numbers, the recirculation regions elongate and the reattachment point moves past the trailing edge over part of the shedding cycle (Robichaux et al. [21]). The broadening of wake is brought about by the higher Reynolds numbers. The width of the wake region in the transverse direction indicates the size of the shear layer. These shear layers on top and bottom side of the cylinder are of different sizes, if there is an imposed shear at the inflow plane. The shear layer on higher free stream velocity side is larger than that on the other side. This causes a pressure difference in the transverse direction, and culminates in a positive lift. The increase in shear increases this difference in pressure as the size of the shear layer on higher free stream velocity side increases and the shear layer on other side decreases.

Time-Averaged Flow Field. The time-averaged velocity field during the flow past a square cylinder, exposed to uniform shear at inlet, shows significant differences at higher shear parameters. Figure 7 shows the time-averaged streamwise velocity profiles at two different locations, namely $x=1.5$ and $x=2.5$. Both the figures reveal that the velocity at the wake edges vary considerably with the variation in shear parameters. The centreline velocity

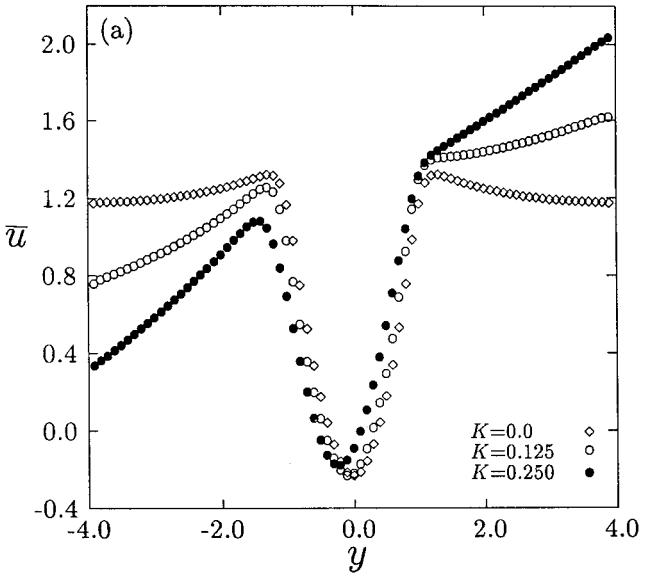

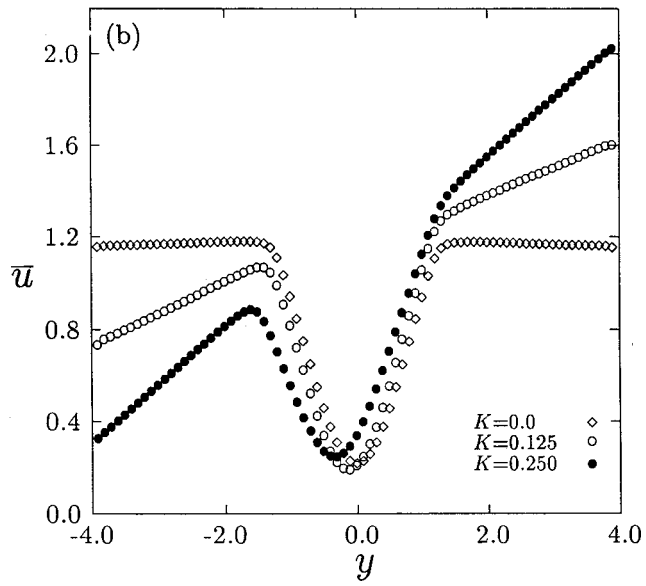

Fig. 7 Time-averaged streamwise velocity profiles at different locations for a Reynolds number of 20,000 and various shear parameters: (*a*) $x=1.5$ and (*b*) $x=2.5$

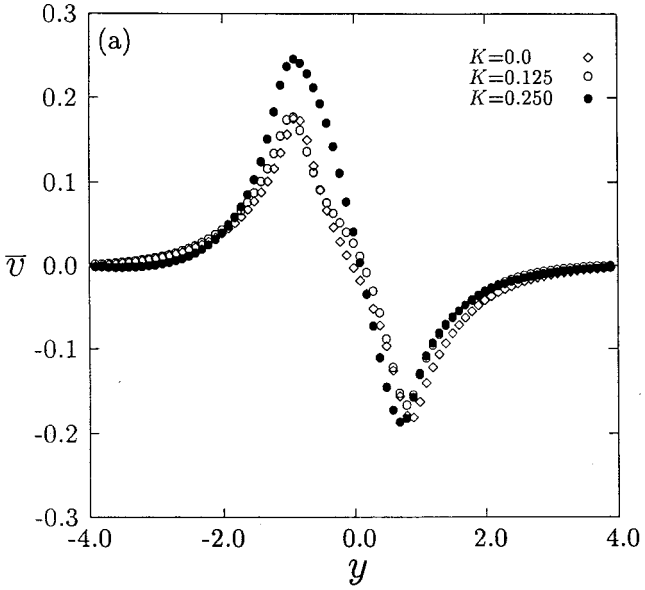

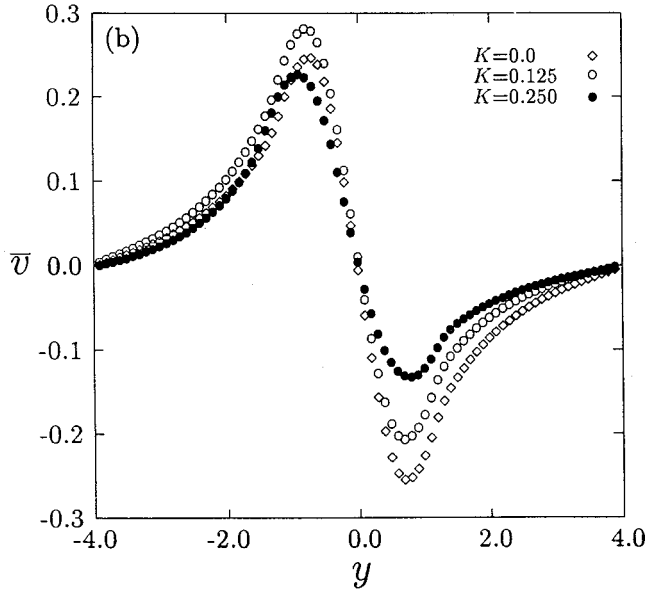

Fig. 8 Time-averaged transverse velocity profiles at different locations for a Reynolds number of 20,000 and various shear parameters: (*a*) $x=1.5$ and (*b*) $x=2.5$

does not show significant susceptibility to shear parameter. Another point to be noticed is that the wake centreline shifts towards the lower free stream velocity side. The transverse offset of the wake centreline from the cylinder center has been found to increase with the increase in shear parameter. The same trend is observed in the downstream direction. Figure 8 depicts the time-averaged transverse velocity at the two locations. The entrainment of fluid is more on the side of lower free stream velocity. The entrainment increases with the increase in the downstream distance for lower value of shear parameters, namely for $K=0.0$ and 0.125. However, the entrainment decreases with increasing downstream distance at a higher shear parameter ($K=0.25$).

Instantaneous Flow Field. The effect of shear can be well understood if the instantaneous flow field is compared and provides the explanation of the variations in the engineering parameters.

The instantaneous vorticity contours for the three shear parameters have been depicted in Fig. 9. Two distinct changes are seen with the increasing shear parameter. In the first place, the number of clockwise vortices (negative) decreases with the increase in shear parameter which is in agreement with the decrease in shedding frequency with the increasing shear parameter. The size of the vortices also grows with the increase in shear parameter. The second change is that the counterclockwise or positive vortices decay faster with the increase in shear parameter and only negative or clockwise vortices prevail.

The instantaneous contours of turbulent kinetic energy reveal total correlation with the instantaneous vorticity field (see Figs. 9 and 10). Figure 10 depicts the instantaneous contour plots of turbulent kinetic energy. The kinetic energy shows higher generation where there is substantial shear in the flow field. It is interesting to note that the flow with inlet shear shows less decay of the kinetic energy with downstream distance as compared to the case of uniform flow.

Figure 11 presents the instantaneous dissipation contours at three different shear parameters. The maximum value of dissipa-

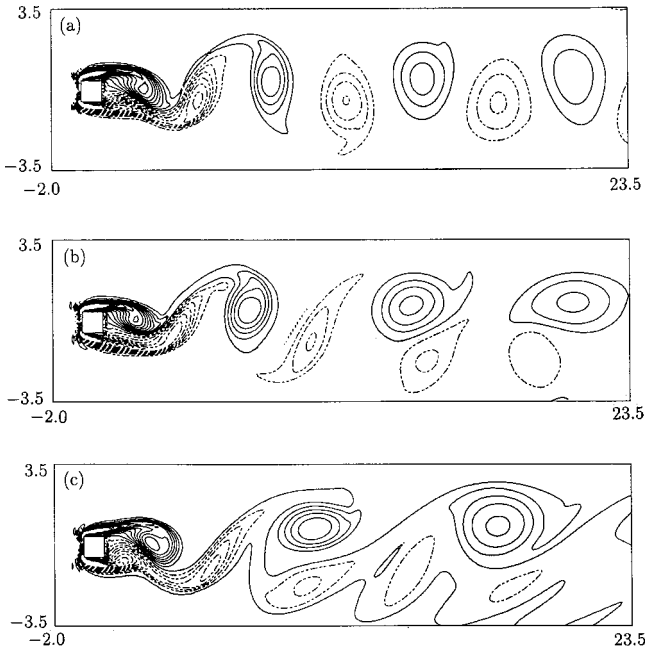

Fig. 9 Instantaneous vorticity contours for a Reynolds number of 20,000 and different shear parameters: (*a*) $K=0$, (*b*) $K=0.125$, and (*c*) $K=0.25$

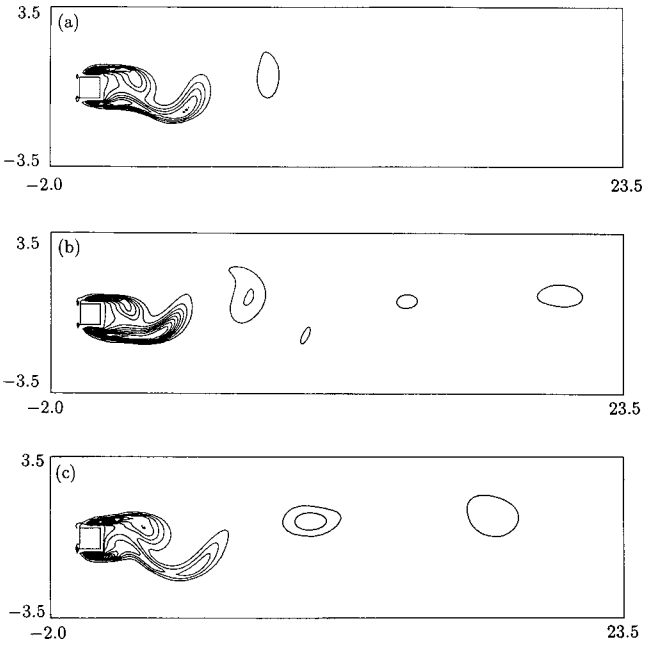

Fig. 11 Instantaneous turbulent dissipation contours for a Reynolds number of 20,000 and different shear parameters: (*a*) $K=0$, (*b*) $K=0.125$, and (*c*) $K=0.25$

tion decreases with the increasing shear parameters. This trend is commensurate with the contour plots of turbulent kinetic energy. However, the intermediate wake and the far wake region experience dissipation with the increases in shear parameter.

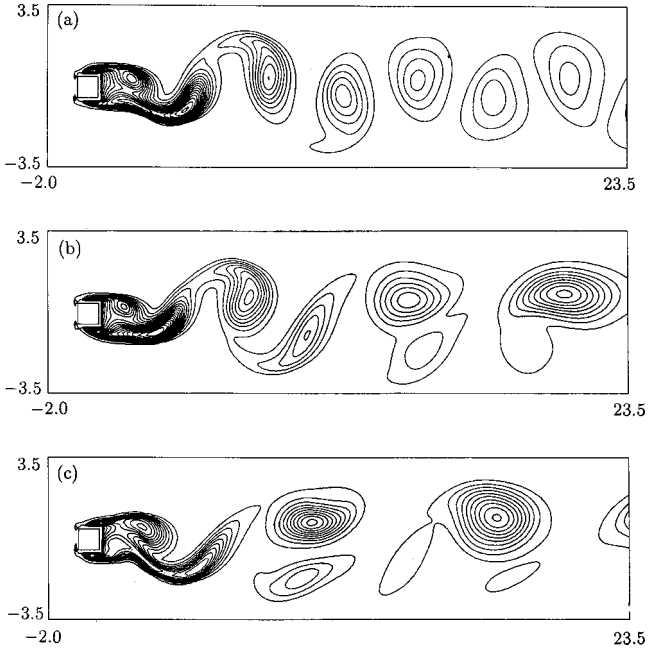

Fig. 10 Instantaneous turbulent kinetic energy contours for a Reynolds number of 20,000 and different shear parameters: (*a*) $K=0$, (*b*) $K=0.125$, and (*c*) $K=0.25$

Conclusions

The flow past a square cylinder has been simulated using both direct method and k-ϵ turbulence model. The effect of shear at inlet on the vortex dynamics has also been one of the aims of the present study. The following conclusions have been drawn out of the present study.

1 Significant differences in the terms of time-averaged flow field and the instantaneous flow field have been observed between the direct calculation and the calculation based on k-ϵ model.

2 The time-averaged drag coefficient and rms fluctuations due to direct calculation are higher as compared to their counterparts due to k-ϵ model, whereas Strouhal number is underpredicted by the direct calculation.

3 The time-averaged drag coefficient decreases with the increase in shear parameter up to a certain value but then it increase with further increase in the shear parameter. However, the time-averaged lift coefficient always increases with the increase in shear parameter.

4 The rms values of the drag and lift coefficients increase with increasing shear parameter. Strouhal number is found to decrease with the increase in the shear parameter.

5 Under the influence of shear, the Kármán vortex street mainly consists of clockwise vortices whose decay is very slow compared to the uniform flow condition.

Acknowledgments

The research was supported by the AR & DB grant RD/134/100/10/99-2000/1032.

Nomenclature

B = obstacle width
C_D = drag coefficient, $\mathcal{D}/(1/2\rho u_{av}^2 B)$
$\mathcal{D}$ = drag force on the square cylinder, $\Sigma_1 \tilde{P}\,\delta y - \Sigma_2 \tilde{P}\,\delta y$
C_L = lift coefficient, $\mathcal{L}/(1/2\rho u_{av}^2 B)$
$\mathcal{L}$ = lift force on the square cylinder, $\Sigma_3 \tilde{P}\,\delta x - \Sigma_4 \tilde{P}\,\delta x$
C_D' = RMS value of drag coefficient
C_L' = RMS value of lift coefficient

f = frequency of vortex shedding
G = transverse velocity gradient on the inflow plane
H = channel width
k = turbulent kinetic energy due to random fluctuations of velocities
K = shear parameter
l_r = mean recirculation length
p = static pressure
$\tilde{P}$ = pressure distribution on the square cylinder surface
r_0 = relaxation factor
Re = Reynolds number, $\rho u_{av} B/\mu$
S = strain parameter in Eq. (6)
St = Strouhal number, fB/u_{av}
T = time period of oscillation, $1/f$
t = time
u, v = streamwise and transverse components of velocity
$\overline{u}, \overline{v}$ = time-averaged streamwise and transverse components of velocity
u_c = convective velocity at the outlet
$\tilde{u}, \tilde{v}$ = streamwise and transverse components of velocity
u', v' = streamwise and transverse components of velocity fluctuations
x, y = streamwise and transverse coordinates
ϵ = dissipation of turbulent kinetic energy
μ = dynamic viscosity of the fluid
ν = kinematic viscosity of fluid
ν_t = eddy viscosity
ρ = density of the fluid
ω = instantaneous vorticity of the flow field ($\partial u/\partial y - \partial v/\partial x$)

Subscripts

1,2 = forward and rear sides of the cylinder
3,4 = top and bottom sides of the cylinder

References

[1] Kiya, M., Tamura, H., and Arie, M., 1980, ''Vortex Shedding from a Circular Cylinder in Moderate-Reynolds-Number Shear Flow,'' J. Fluid Mech., **101**, pp. 721–735.
[2] Kwon, S., Sung, H. J., and Hyun, J. M., 1992, ''Experimental Investigation of Uniform-Shear Flow Past a Circular Cylinder,'' ASME J. Fluids Eng., **114**, pp. 457–460.
[3] Ayukawa, K., Ochi, J., and Hirao, T., 1993, ''Effects of Shear Rate on the Flow around a Square Cylinder in a Uniform Shear Flow,'' J. Wind. Eng. Ind. Aerodyn., **50**, pp. 97–106.
[4] Saha, A. K., Biswas, G., and Muralidhar, K., 1999, ''Influence of Inlet Shear on Structures of Wake behind a Square Cylinder,'' J. Eng. Mech., **125**, No. 3, pp. 359–363.
[5] Williamson, C. H. K., 1996, ''Vortex Dynamics in the Cylinder Wake,'' Annu. Rev. Fluid Mech., **28**, pp. 477–539.
[6] Saha, A. K., 1999, ''Dynamical Characteristics of the Wake of a Square Cylinder at Low and High Reynolds Numbers,'' PhD Thesis, IIT Kanpur India.
[7] Saha, A. K., Muralidhar, K., and Biswas, G., 2000, ''Transition and Chaos in Two-Dimensional Flow Past a Square Cylinder,'' J. Eng. Mech., **126**, pp. 523–532.
[8] Hadid, A. H., Sindir, M. M., and Issa, R. I., 1992, ''Numerical Study of Two-Dimensional Vortex Shedding from Rectangular Cylinders,'' Compt. Fluid Dyn. J., **2**, pp. 207–214.
[9] Franke, R. and Rodi, W., 1993, ''Calculation of vortex Shedding Past a Square Cylinder with Various Turbulence Models,'' *Turbulent Shear Flows 8*, F. Durst et al., eds., Springer, New York, pp. 189–204.
[10] Hussain, A. K. M. F., 1983, ''Coherent Structures-Reality and Myth,'' Phys. Fluids, **26**, No. 10, pp. 2816–2850.
[11] Saha, A. K., Biswas, G., and Muralidhar, K., 1999, ''Numerical Study of the Turbulent Unsteady Wake behind a Partially Enclosed Square Cylinder using RANS,'' Comput. Methods Appl. Mech. Eng., **178**, pp. 323–341.
[12] Okajima, A., Ueno, H., and Sakai, H., 1992, ''Numerical Simulation of Laminar and Turbulent Flows around Rectangular Cylinders,'' Int. J. Numer. Methods Fluids **15**, pp. 999–1012.
[13] Rodi, W., 1993, ''On the Simulation of Turbulent Flow Past Bluff Bodies,'' J. Wind. Eng. Ind. Aerodyn., **46 and 47**, pp. 3–19.
[14] Bosch, G., and Rodi, W., 1996, ''Simulation of Vortex Shedding Past a Square Cylinder Near a Wall,'' Int. J. Heat Fluid Flow, **17**, pp. 267–175.
[15] Kato, M., and Launder, B. E., 1993, ''The Modeling of Turbulent Flow around Stationary and Vibrating Square Cylinders,'' *Proc. 9th Symposium on Turbulent Shear Flows*, Kyoto, Japan, Vol. 10-4.
[16] Harlow, F. H., and Welch, J. E., 1965, ''Numerical Calculation of Time-Dependent Viscous Incompressible Flow of Fluid with Free Surfaces,'' Phys. Fluids, **8**, pp. 2182–2188.
[17] Hoffman, G., and Benocci, C., 1994, ''Numerical Simulation of Spatially-Developing Planer Jets,'' AGARD, CP-551, pp. 26.1–26.6.
[18] Orlanski, I., 1976, ''A Simple Boundary Condition for Unbounded Flows,'' J. Comput. Phys., **21**, pp. 251–269.
[19] Lyn, D. A., Einav, S., Rodi, W., and Park, J.-H., 1995, ''A Laser-Doppler Velocimetry Study of Ensemble-Averaged Characteristics of Turbulent Near Wake of a Square Cylinder,'' J. Fluid Mech., **304**, pp. 285–319.
[20] Mittal, R., and Balachandar, S., 1995, ''Effect of three-dimensionality on the lift and drag on nominally two-dimensional cylinders,'' Phys. Fluids, **7**, pp. 1841–1865.
[21] Robichaux, J., Balachandar, S., and Vanka, S. P., 1999, ''Three-dimensional Floquet instability of the wake of a square cylinder,'' Phys. Fluids, **11**, pp. 560–578.

Kazuyuki Fujimura
Graduate Student

Hiroaki Yoshizawa
Graduate Student

Reima Iwatsu
Associate Professor

Hide S. Koyama
Professor

Department of Mechanical Engineering,
Tokyo Denki University,
2-2 Kanda-Nishikicho, Chiyodaku,
Tokyo 101-8457, Japan

Jae Min Hyun
Professor
Department of Mechanical Engineering,
Korea Advanced Institute of Science
and Technology,
400, Kusong-dong, Yusong-gu,
Taejon 305-701, Korea

Velocity Measurements of Vortex Breakdown in an Enclosed Cylinder

Experimental measurements were carried out of three-component velocity fields inside a cylindrical container. Flow was driven by the rotation of the top endwall disk. The purpose of the precision laser-Doppler velocimetry measurements was to describe the velocity characteristics pertinent to the vortex breakdown phenomenon. A turntable experimental apparatus was fabricated. Extensive laser-Doppler measurements, as well as flow visualizations, were made for the aspect ratio 1.50 and 2.50, and the Reynolds number ranges 0.99×10^3–2.20×10^3. *The measured meridional velocities were found to be consistent with the prior visualization studies. The characteristic changes in swirling motions in the vicinity of vortex breakdown bubble are depicted. Detailed flow patterns near the rotating disk are constructed by using the experimental data.*
[DOI: 10.1115/1.1385834]

1 Introduction

Flow inside an enclosed cylindrical container, with one endwall disk (say, the top endwall in the present paper) rotating steadily about the longitudinal axis, has served as a paradigmatic model to study vortex breakdown phenomena. The other endwall disk and the cylindrical sidewall are stationary. For convenience, a cylindrical coordinate frame (r,θ,z), with the corresponding velocity components (u,v,w), is attached at the center of the bottom endwall. In general, the fluid close to the top endwall acquires angular momentum and is propelled radially outward, and near the cylindrical sidewall the fluid flows downward. The swirling fluid reaches the stationary bottom endwall disk and moves radially inward along the bottom endwall. In the vicinity of the axis, the swirling fluid flows upward toward the top endwall, thus completes the circuit in the meridional plane. This global three-component flow picture has been documented (see, e.g., Pao [1,2]), and the overall flow pattern is characterized by two nondimensional parameters, i.e., the Reynolds number $\mathrm{Re}\equiv R^2\Omega/\nu$ and the cylinder aspect ratio $\mathrm{Ar}\equiv H/R$, where R, H, Ω, and ν denote the cylinder radius, the cylinder height, the angular velocity of the top endwall and the kinematic viscosity of fluid, respectively.

It is important to note that, for a given Ar, as Re increases beyond a certain threshold value Re_t, the vortical flow along the axis undergoes a dramatic change. This gives rise to axial stagnation points with a closed stream surface, which is interpreted as axisymmetric vortex breakdown. The distinctive features are the emergence of separation bubble(s) on the axis, in which recirculating flow regions are formed. This separation bubble should be distinguished from the wall flow separation (Brown and Lopez [3]). These celebrated phenomena were succinctly captured by the pioneering visualization studies of Escudier [4]. The occurrence of vortex breakdown bubbles was charted in the Re-Ar parameter space by Escudier's visualizations (see Fig. 2), and numerical efforts were made to establish the qualitative validity of the above regime diagram of Escudier (e.g., Lugt and Haussling [5], Lugt and Abboud [6], Daube and Sorensen [7], Lopez [8], Brown and Lopez [3], Tsitverblit [9], Lee and Hyun [10]).

Offering a convincing explanation for the physical mechanism of vortex breakdown, however, remains an elusive issue. Lugt [11] summarized three major theories on the nature of vortex breakdown: a kind of flow separation within a rotating fluid; a consequence of instability; a process which depends on the existence of a critical state. However, no universally accepted theory appears to prevail at this moment. As observed by Lopez [8], a precise description of swirling flows, equipped with improved theoretical tools, is needed for a more elucidating rationalization of this complex and intriguing problem.

As remarked earlier, the classical visualization experiments of Escudier [4] and Spohn et al. [12] yielded pictures of the meridional flows, which provided the bases to determine the formation of breakdown bubble(s). It is clear now that, in order to achieve an enhanced level of understanding, comprehensive and accurate velocity data are essential to supplement the visualized meridional flow structure. The purpose of the present endeavor is to supply such quantitative experimental data of the three-component flow field by employing the laser-Doppler veolcimetry(LDV) measurement techniques. A survey reveals that full velocity data are not available in the literature. It is anticipated that the present data, which cover broad ranges of Re and Ar, will give baseline information to be exploited by theoreticians as well as numerical modelers. It is emphasized that, in the present experiments, the axial and radial variations of swirling flow are portrayed in detail. In addition to the LDV measurements, flow visualizations were performed. The results of these exercises yield high-quality data on meridional flows. The objective is to gain a depiction of three-dimensional flows in the cylinder, which will be the key to a proper documentation of vortex breakdown phenomenon.

It appears that full-scale numerical computations, for instance, a direct numerical simulation approach, may prove to be effective in analyzing these types of flow. A parallel effort is underway to conduct such numerical exercises. The results of these numerical endeavors will be reported in forthcoming publications.

Contributed by the Fluids Engineering Division for publication in the JOURNAL OF FLUIDS ENGINEERING. Manuscript received by the Fluids Engineering Division February 1, 2000; revised manuscript received April 17, 2001. Associate Editor: M. R. Hajj.

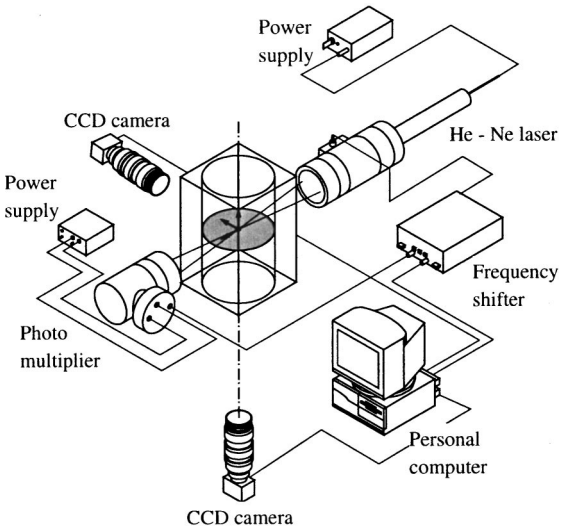

Fig. 1 Schema of the overall experimental apparatus

2 Experiment

A high-precision turntable apparatus was fabricated, which was capable of encompassing extended ranges of Re and Ar. The major components are two sets of rotating turntable-drive gears, rotation-controllers, a closed cylinder and LDV system. A schema of the experimental apparatus is shown in Fig. 1.

The power drive was connected to the motor by using a timing belt. The maximum rotation rate was 1000 rpm, which far exceeded the limit used in Escudier's original experiment [4]. The rotation rate was regulated to an accuracy of 0.2 percent. An angular-roll bearing unit was employed for the turntable axis to suppress eccentric motions and vertical vibrations. A bearing set of JIS P4 class, together with forced-circulation lubrication, was used. An AC-servo motor, with a built-in rotary encoder, of 7.5 kW rating was deployed for power drive. These permit a precision digital-control of the rotation rate.

A cylindrical container was mounted to the flange of the turntable. The material of the container was pyrexglass, and the inner radius $R=71.35\pm0.05$ mm, and the thickness of the container wall was 3.5 mm. The vertical location ($z=H$) of the top endwall disk was variable, accurate to ±0.02 mm; the range of Ar in the present experiment was $1.3\sim3.3$. As is well understood, when the interior fluid motions are viewed, the objects appear distorted due to the lens effect of the curved cylindrical sidewall. To reduce this effect, a square-shaped outer tank, made of 7.5 mm acrylic resin, was installed, which surrounded the cylinder. The working fluid used was a water-glycerin mixture (80 percent glycerin by weight). The refractive indices of 80 percent water-glycerin mixture, water, pyreglass, and acrylic resin are 1.456, 1.474, 1.333, and 1.492, respectively.

The dependence of kinematic viscosity ν on temperature is appreciable (approximately 5 percent per degree centigrade); therefore, ν was measured in strict accordance with the established procedure (JIS Z8803). In actual experimental runs, the working fluid was poured into the cylinder. A constant-temperature water (at 25.0 ± 0.1°C) was forced to circulate inside the outer tank to attain a thermal equilibrium between the interior working fluid and the outer circulating water. The overall uncertainty in the value of Re was less than ±1 percent.

For flow visualizations, fluorescein sodium was selected as dye. In the preparation stage, a small amount of dye was mixed with the working fluid. A tiny quantity of this dye-mixed working fluid was injected into the main body of fluid in the cylinder through a hole of 1 mm diameter at the center of the bottom endwall. The injection was made by using a constant-volume pump (Tokyo Rikakikai Co., MP-3). The meridional plane of the cylinder is illuminated by a sheet beam of about 1 mm width, which was produced from the light of a slide projector. An auto-driven camera photographed the visualized flow patterns. Also, the images were monitored by two CCD cameras (Sony Co., XC-77RR), which were aligned perpendicular to and parallel to the rotation axis. In particular, a zoom lens was attached to the CCD camera, which enabled the identification of precise locations of stagnation points and the size of vortex breakdown bubble.

The LDV (TSI Inc., Model 9100 series) of two-beam one-component system was employed. A 5-mW He-Ne laser with 632.8 nm lines was used. The diameter and length of the measuring volume were 0.17 mm and 1.75 mm, respectively. The entire LDV system was mounted on a traversing mechanism, positioned with 0.01 mm resolution. To measure the velocities in the recirculation bubble(s), the frequency shift was 100 kHz (Edwards [13], Liou et al. [14]). To measure the swirl and radial velocities, the plane including two beams of laser was oriented perpendicular to the cylinder axis. For axial velocities, the plane was aligned parallel to the axis. A small quantity of water-based paint was introduced as light-scattering particles, with a nominal diameter of 1 μm. An FFT-type processor (KANOMAX Inc., Model 8007) was used to process the Doppler signal. For typical runs, a total of 8192 data samples were assembled, and the arithmetic-mean velocity was calculated. Depending on the location of the measuring volume, typical data rates were 200–500 s^{-1}. It should be noted that the refractive index difference has a subtle effect on the LDV measuring volume. To consider the position changes of the laser beams due to five layers of different refractive index, the crossing point and the angle of two laser beams were measured by a CCD camera. A personal computer, which was interfaced with a video-capture board, calculated the precise position of the measuring volume and the conversion into the velocity data. To estimate the present procedure, a relatively stationary state ($u=0$, $v=r\Omega$, $w=0$) in a rotating cylindrical container at a constant angular velocity Ω was examined by the LDV. Discrepancies between the measured and theoretical swirl velocities were found to be within ±3 percent except near the side wall of the cylindrical container.

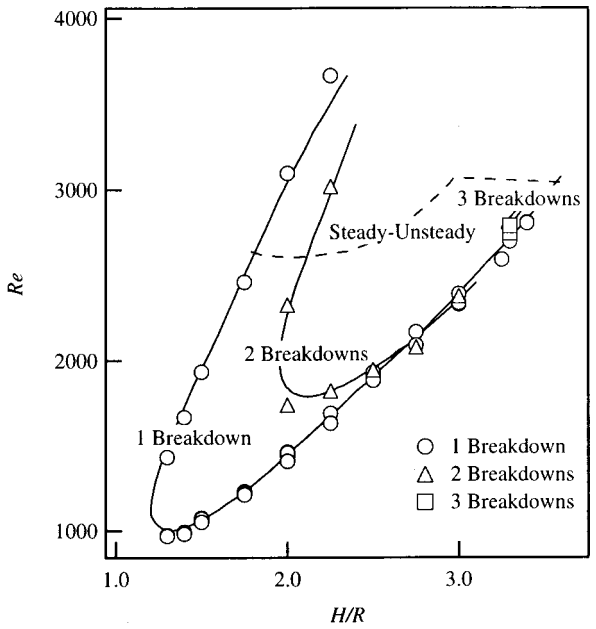

Fig. 2 (Re-Ar) regime diagram of vortex breakdown. The solid lines and dashed line represent the results of Escudier, and symbols denote the present data. (Uncertainty in Ar: less than ±0.5 percent; in Re: less than ±1 percent.)

The mass-balance error from the direct integration of the mean axial velocity profiles at axial stations was found to be within ±4.7 percent.

3 Experimental Results

First, in an effort to establish the validity of the present experimental setup, a series of experiments were conducted to verify the (Re-Ar) regime diagram on vortex breakdown, as displayed in Fig. 2. Clearly, the present results are in close agreement with the original reports of Escudier [4]. In addition to the regime diagram of Fig. 2, the vertical location of the lower stagnation point h/H was measured. The measured variation of h/H as Re and Ar were altered was highly consistent with the results of Escudier.

As ascertained explicitly in the original experiment of Escudier [4], the global flow pattern of present concern was found to be highly axisymmetric. Thorough inspections of flow visualizations were made, and the results were consistent with the basic assumption of axisymmetry.

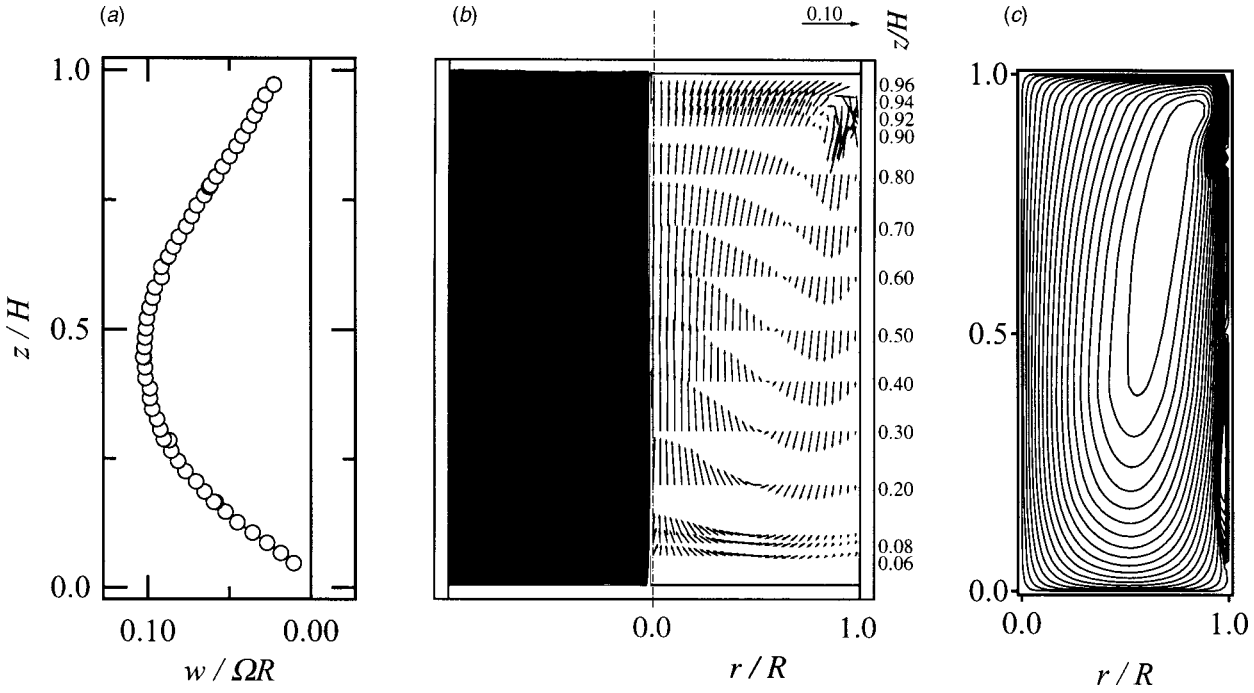

Fig. 3 Distributions of (*a*) axial velocity component w on the axis, (*b*) flow visualization and velocity vector plots in the meridional plane and (*c*) contour plots of stream function ψ. Ar=2.50 and Re=1.01×10³. Contour values for ψ are $\psi = \psi_{max}(i/10)^3$, $i=0,1,\ldots,10$, $\psi_{min}(i/20)^3$, $i=0,1,\ldots,20$. (Uncertainty in each velocity component: less than ±3 percent.)

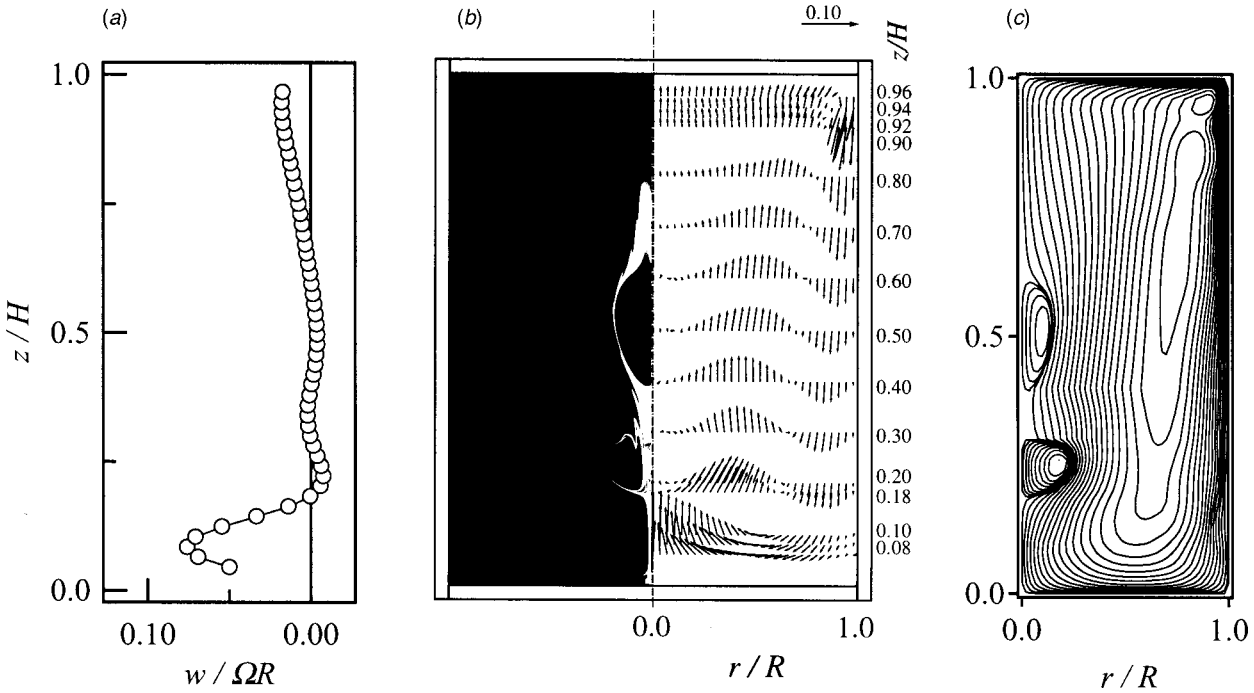

Fig. 4 Same as in Fig. 3. Ar=2.50 and Re=2.20×10³. (Uncertainty: see Fig. 3 caption.)

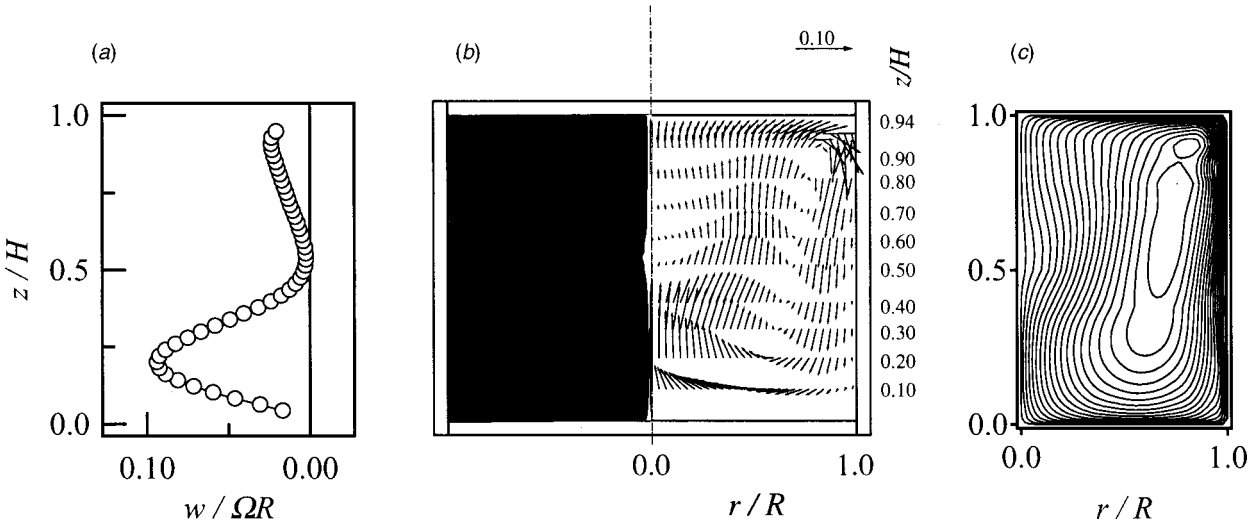

Fig. 5 Same as in Fig. 3. Ar=1.50 and Re=0.99×10³. (Uncertainty: see Fig. 3 caption.)

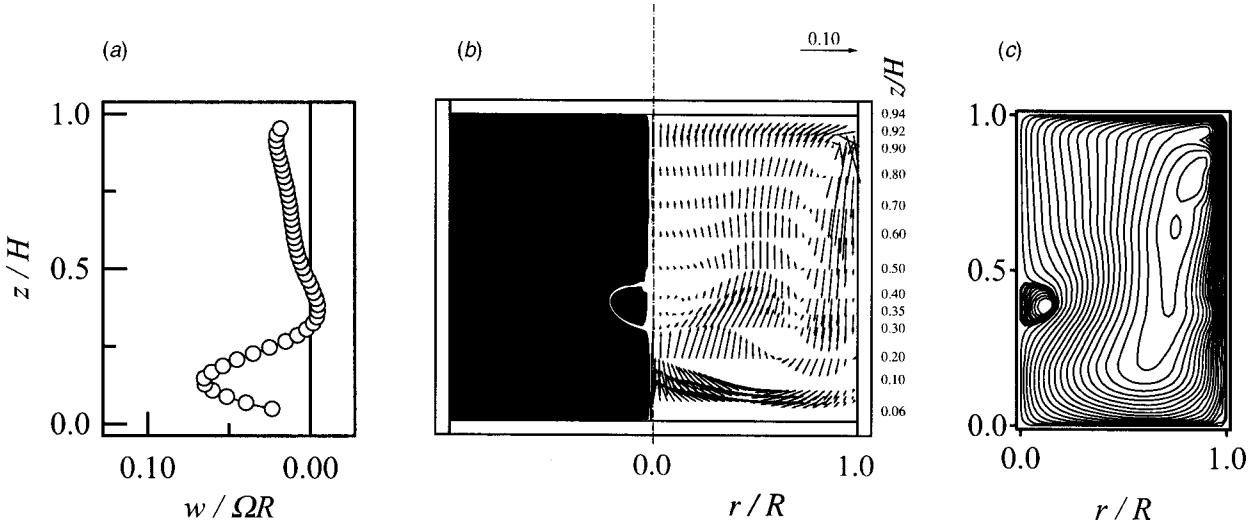

Fig. 6 Same as in Fig. 3. Ar=1.50 and Re=1.29×10³. (Uncertainty: see Fig. 3 caption.)

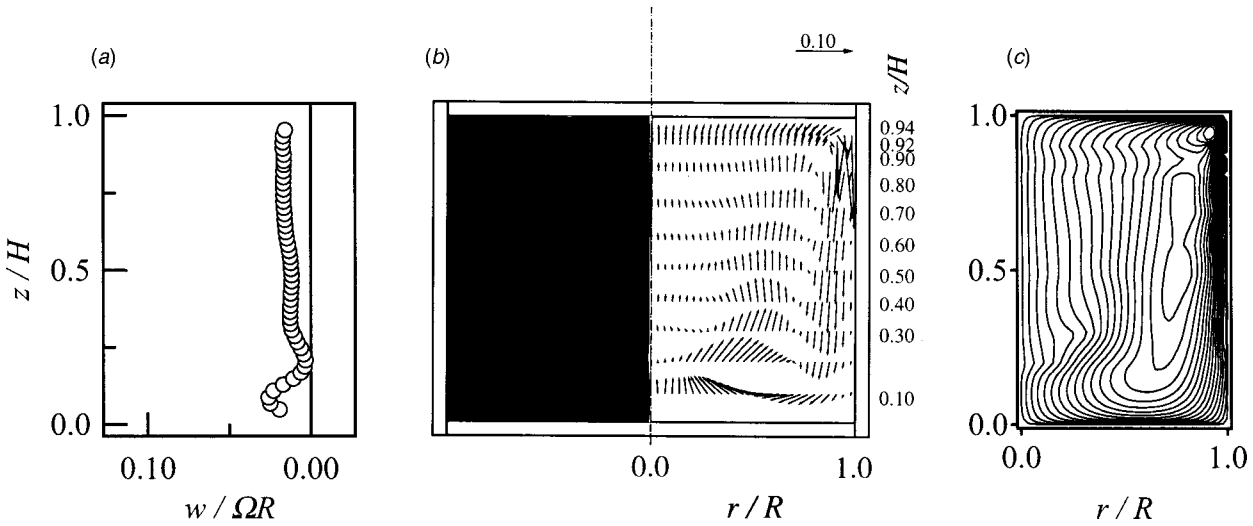

Fig. 7 Same as in Fig. 3. Ar=1.50 and Re=2.18×10³. (Uncertainty: see Fig. 3 caption.)

Detailed velocity measurements were carried out for two sets of conditions: (1) Ar=2.50, Re=1.01×10^3 and 2.20×10^3; (2) Ar=1.50, Re=0.99×10^3, 1.29×10^3 and 2.18×10^3. The laser measurement points were at an interval of $z/H=0.10$ within the interior region $0.10\leqq z/H\leqq0.90$. In the neighborhoods of the endwalls, i.e., $z/H\leqq0.10$ and $z/H\geqq0.90$, the interval between measurement points was $z/H=0.02$. To cover the radial and azimuthal variations, the laser arrangement was moved by means of a traverse mechanism. In the vicinities of the axis and the sidewall, measurements were made at an interval of 2.5 mm, and in the interior region, the traverse interval was 5.0 mm.

Meridional Flow. It is advantageous to use the axisymmetric stream function ψ, which is defined as $u=1/r\partial\psi/\partial z$ and $w=-1/r\cdot\partial\psi/\partial r$. In actual computation, ψ was calculated by $\psi(r,z)=-\int_{r_0}^{r}rw(r,z)dr+\int_{Z_0}^{Z}ru(r_0,z)dz$, where r_0 and z_0 are an arbitrary constant. In the course of data processing, when the measuring points for u and w do not coincide, interpolations were employed for u and w to obtain ψ.

Plots (a), (b), and (c) of Figs. 3 and 4 show the results of laser measurements of the meridional flows, together with the flow visualization pictures for Ar=2.50. It is evident that the velocity measurements are substantially consistent with the visualizations in terms of the location and size of the vortex breakdown bubbles. In the present visualizations, detailed structures of flow in the corner areas are not clearly captured. The emphasis is placed on depicting the behavior along the centerline. For Re=1.01×10^3 (see Fig. 3(*a*)), the axial velocity at the axis is maximum near the mid-height. Note that, at this combination of Re and Ar, no breakdown bubbles are seen. However, for Re=2.20×10^3 (see Fig. 4(*a*)), the *w*-velocity at the axis is largest near the bottom endwall, and *w* at the axis cross the zero mark four times, indicating the presence of two breakdown bubbles (see Fig. 4(*c*)).

The flow behavior in the meridional plane is exemplified in Figs. 5–7 for Ar=1.50. When Re is slightly below the critical value (see Fig. 5 for Re=0.99×10^3), no breakdown bubbles are visible. At this particular parameter setting, the behavior of *w* is very close to the borderline of two flow regimes. Therefore, by relying only on the present visualization pictures, no definitive statement can be made as to the qualitative character of flow pattern. The *w*-velocity at the axis has a maximum close to the bottom endwall. The *z*-variation of the *w*-velocity at the axis is appreciable. As Re increases beyond the critical value (see Fig. 6 for Re=1.29×10^3), a single bubble is noticeable, which is discernible in the zero-crossings of *w* at the axis. As can be inferred from the regime diagram of Fig. 2, for Ar=1.50, when Re is larger than approximately 1.95×10^3, no breakdown bubbles are seen, as demonstrated in Fig. 7. The *w*-velocity at the axis is generally very weak, and in much of the vertical region away from the bottom endwall (say $z/H\geqq0.3$), *w* is largely uniform with height. The axial gradient of *w* at the axis, $\partial w/\partial z|_{r\to0}$, provides useful information on the qualitative behavior of *u*. The continuity equation near the axis can be rewritten as $\partial w/\partial z|_{r\to0}=-1/r\cdot\partial(ru)/\partial r|_{r\to0}$. In the region in which $\partial w/\partial z|_{r\to0}>0$, $\partial(ru)/\partial r|_{r\to0}<0$. In view of the fact that $u\to0$ as $r\to0$, the above relation implies the flow is directed radially-inward in the neighborhood of the axis. It follows that, if $\partial w/\partial z|_{r\to0}<0$, the flow is radially-outward. These observations are in accord with the measurement data of Figs. 3–7.

Azimuthal Flow. Figure 8 illustrates the radial profiles of azimuthal velocity $v/\Omega R$ at selected vertical levels for Ar=2.50 and 1.50. Furthermore, based on the compilations of measured v-data, contour plots of circulation $rv/\Omega R^2$, in the entire cylinder are constructed in Fig. 9. Comparison of Figs. 9(*a*) and 9(*c*) reveals the effect of Ar on the azimuthal flow patterns at a similar value of Re($\fallingdotseq$1000). In the case of Ar=2.50 (see Fig. 9(*a*)), no distinctive boundary layer is seen on the stationary bottom endwall. On the contrary, for Ar=1.50 (see Fig. 9(*d*)), the existence of boundary layer on the bottom endwall is apparent.

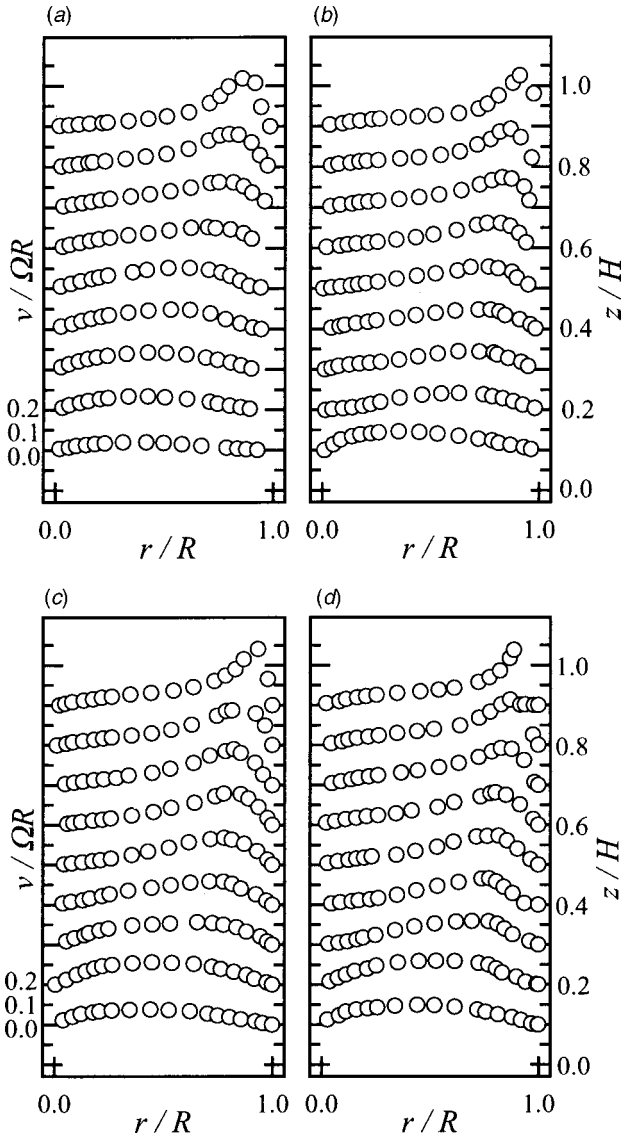

Fig. 8 Radial profiles of azimuthal velocity component v/ΩR at selected vertical levels. (*a*) Ar=2.50 and Re=1.01×10^3, (*b*) Ar=2.50 and Re=2.20×10^3, (*c*) Ar=1.50 and Re=0.99×10^3 and (*d*) Ar=1.50 and Re=1.29×10^3. (Uncertainty in v/ΩR: less than ±3 percent.)

Cross-comparisons of Figs. 9(*b*), 9(*d*) and the meridional-flow plots of Figs. 3–7 disclose that, in the lower zone of the stagnation point, large radial gradients of v are visible. This points to the presence of strong azimuthal velocities. Also, in this area, appreciable radial gradients of meridional flows are in evidence. Above the bubble, the gradients of v are substantially smaller than in the lower zone. These are characteristic of vortex breakdown in other flow geometries (e.g., delta wing, swirling flow in a pipe). The present results are in support of the contention that a strong swirling motion undergoes the aforesaid characteristic changes from the lower region, and through the breakdown bubble, and to the above region.

It is stressed that the experimental data of v have not been available in the literature. The present measurements of v, displayed in Fig. 9, are in broad agreement with the numerical computational results of Lopez [8].

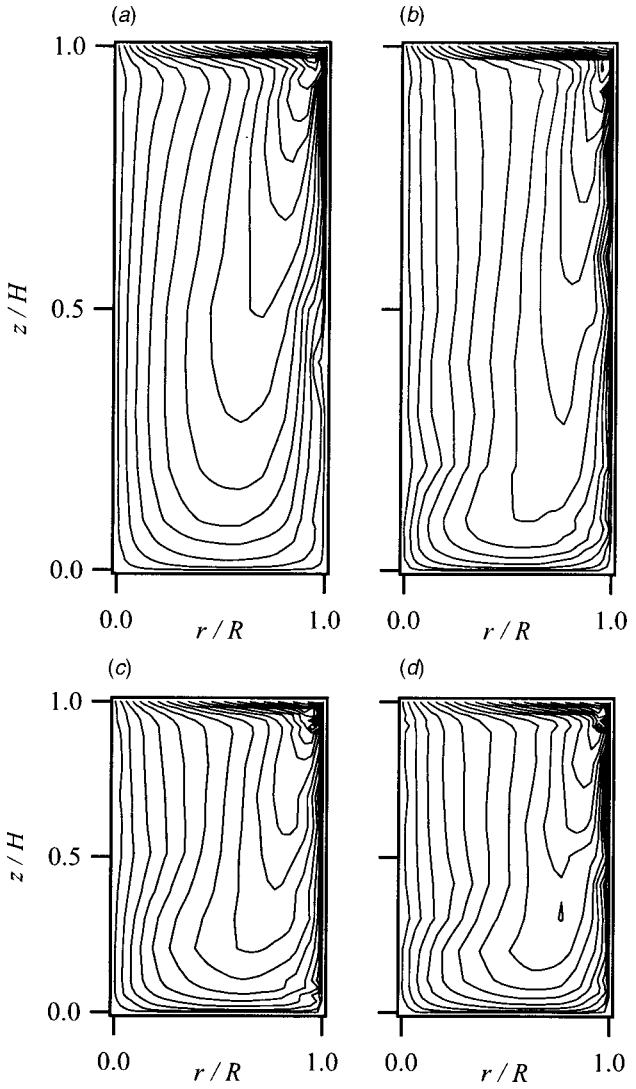

Fig. 9 Contour plots of circulation ($rv/\Omega R^2$). (*a*) Ar=2.50 and Re=1.01×10³, (*b*) Ar=2.50 and Re=2.20×10³, (*c*) Ar=1.50 and Re=0.99×10³ and (*d*) Ar=1.50 and Re=1.29×10³. (Uncertainty in $rv/\Omega R^2$: less than ±3 percent.)

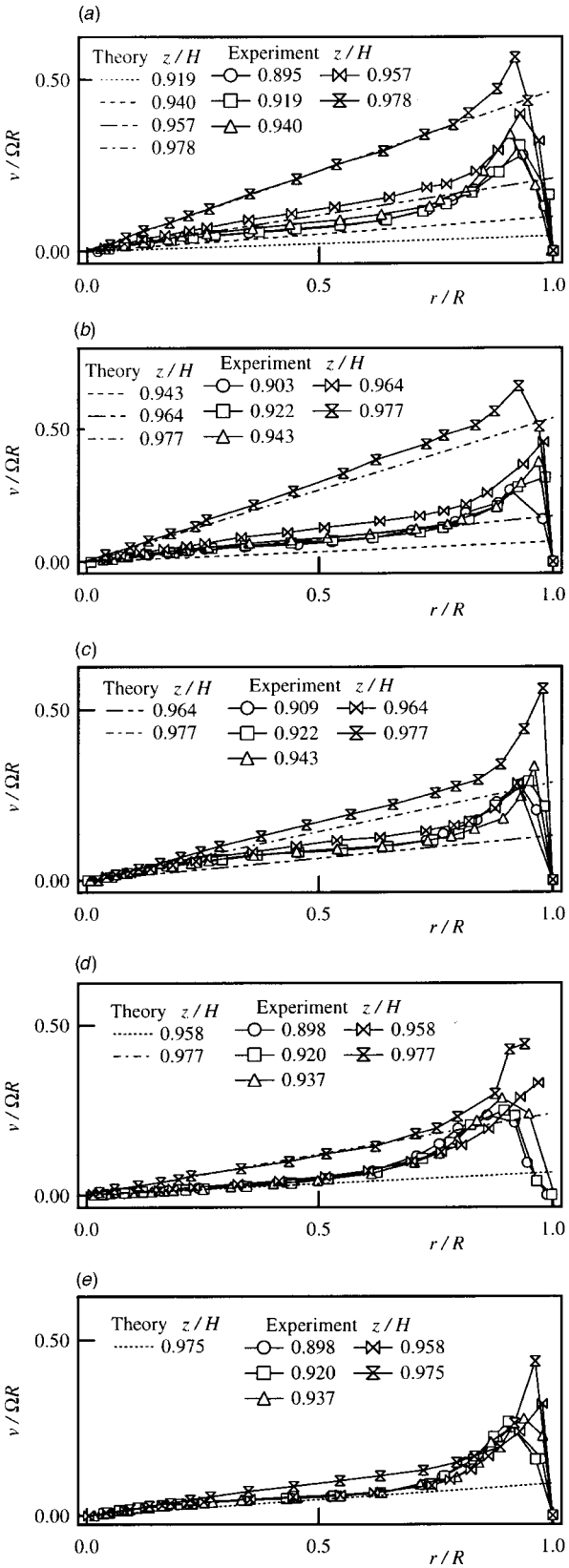

Fig. 10 Radial profiles of azimuthal velocity component $v/\Omega R$ near the rotating disk. (*a*) Ar=2.50 and Re=1.01×10³, (*b*) Ar=2.50 and Re=2.20×10³, (*c*) Ar=1.50 and Re=0.99×10³, and (*d*) Ar=1.50 and Re=1.29×10³ and (*e*) Ar=1.50 and Re=2.18×10³. Similarity solutions are shown in dashed lines. (Uncertainty in $v/\Omega R$: less than ±3 percent.)

Flow Near the Rotating Disk. Of interest are the measurement data near the rotating top endwall, $z/H \geqq 0.9$. The velocity structure close to the finite shrouded rotating disk is now delineated. It should be pointed out that a similarity solution was given by von Karman [15] for an infinite disk rotating steadily in an infinite expanse of fluid at rest.

Figures 10–12, respectively, describe the azimuthal (v), radial (u), and axial (w) velocity profiles as obtained by the present LDV measurements. The v-velocity is generally proportional to the radial distance r, with the exception of the near-sidewall region. In the bulk of interior, the degree of departure of v-profile from that of similarity solution depends on the precise axial location. The present results indicate that in the central axis region, the similarity solution provides an adequate approximation to the v-structure. The observations on the u- and v-profiles lead to similar conclusions. The sidewall effect is noticeable in the region $r/R \geqq 0.8$.

4 Concluding Remarks

The aim has been to present the results of accurate LDV measurements of three-component velocity field.

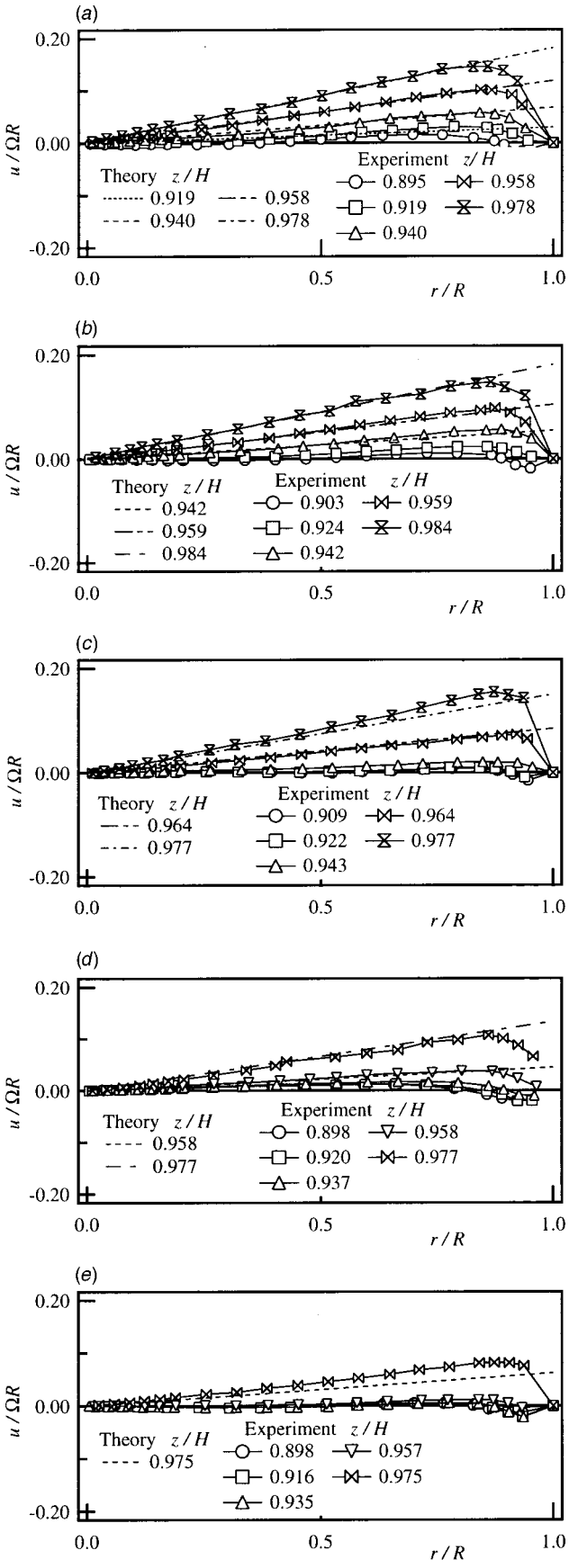

Fig. 11 Radial profiles of radial velocity component u/ΩR near the rotating disk. The values of Ar and Re are the same as in Fig. 10. Similarity solutions are shown in dashed lines. (Uncertainty in u/ΩR: less than ±3 percent.)

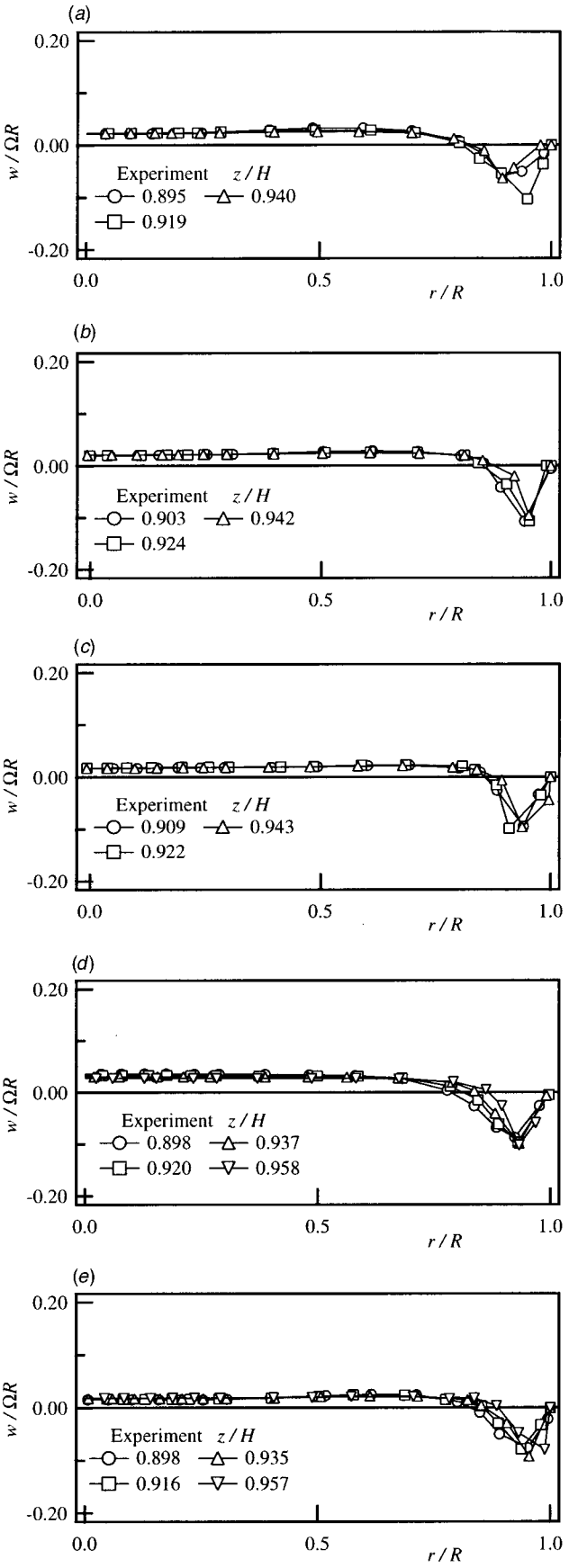

Fig. 12 Radial profiles of axiall velocity component w/ΩR near the rotating disk. The values of Ar and Re are the same as in Fig. 10. (Uncertainty in w/ΩR: less than ±3 percent.)

The meridional velocity vector plots and stream functions, which were secured by using the velocity data, were highly consistent with the flow visualizations in terms of the position and size of breakdown bubbles. The overall structure of the sidewall boundary layer in the meridional plane is found to be qualitatively similar as Re varies. The thickness of the sidewall boundary layer is principally a function of Re and less of Ar. The structure of the sidewall boundary layer has not been explicitly discussed in the present text. The depictions of the sidewall layer call for a substantial research effort. Programs are being undertaken to secure pertinent data for this challenging problem.

Meaningful interpretations of flow features may be aided by introducing the parameter Re/Re_t. As Re/Re_t increases, the location of free shear layer in the meridional plane moves closer to the sidewall. Also, with increasing Re/Re_t, in the lower region of the breakdown bubble, the radial gradients of the swirl angle become large in the central axis region.

Acknowledgment

Appreciation is extended to the referees for explicit and useful comments. Their suggestions led to improvements in the revised version.

References

[1] Pao, H.-P., 1970, ''A Numerical Computation of a Confined Rotating Flow,'' ASME J. Appl. Mech., **37**, pp. 480–487.
[2] Pao, H.-P., 1972, ''Numerical solution of the Navier-Stokes equations for flows in the disk-cylinder system,'' Phys. Fluids, **15**, No. 1, pp. 4–11.
[3] Brown, G. L., and Lopez, J. M., 1990, ''Axisymmetric Vortex Breakdown. Part 2. Physical mechanisms,'' J. Fluid Mech., **221**, pp. 553–576.
[4] Escudier, M. P., 1984, ''Observations of the flow produced in a cylindrical container by a rotating endwall,'' Exp. Fluids, **2**, pp. 189–196.
[5] Lugt, H. J., and Haussling, H. J., 1982, ''Axisymmetric Vortex Breakdown in Rotating Fluid within a Container,'' ASME J. Appl. Mech., **49**, pp. 921–923.
[6] Lugt, H. J., and Abboud, M., 1987, ''Axisymmetric Vortex Breakdown with and without Temperature Effects in a Container with a Rotating Lid,'' J. Fluid Mech., **179**, pp. 179–200.
[7] Daube, O., and Sorensen, J. N., 1989, ''Simulation numerique de l'ecoulement periodique axisvmetrique dans une cavite cylindrique,'' Computes Rendus Academy de Science, **II**, pp. 463–469.
[8] Lopez, J. M., 1990, ''Axisymmetric Vortex Breakdown. Part 1. Confined Swirling Flow,'' J. Fluid Mech., **221**, pp. 533–552.
[9] Tsitverblit, N., 1993, ''Vortex Breakdown in a Cylindrical Container in the Light Continuation of a Steady Solution,'' Fluid Dyn. Res., **11**, pp. 19–35.
[10] Lee, C. H., and Hyun, J. M., 1999, ''Flow of a stratified fluid in a cylinder with a rotating lid,'' Int. J. Heat Fluid Flow, **20**, pp. 26–33.
[11] Lugt, H. J., 1983, *Vortex Flow in Nature and Technology*, Wiley, New York.
[12] Spohn, A., Mory, M., and Hopfinger, E. J., 1993, ''Observations of vortex breakdown in an open cylindrical container with a rotating bottom,'' Exp. Fluids, **11**, pp. 70–77.
[13] Edwards, R. V., 1987, ''Report of the Special Panel on Statistical Particle Bias Problems in Laser Anemometry,'' ASME J. Fluids Eng., **109**, pp. 89–93.
[14] Liou, T.-M., Chang, Y., and Hwang, D.-W., 1990, ''Experimental and Computational Study of Turbulent Flows in a Channel With Two Pairs of Turbulence Promoters in Tandem,'' ASME J. Fluids Eng., **112**, pp. 302–310.
[15] von Karman, T., 1921, ''Laminare und turbulente Reibung,'' Z. Angew. Math. Mech., **1**, p. 233.

Sahjendra N. Singh
Department of Electrical and Computer Engineering,
University of Nevada,
Las Vegas, NV 89154-4026

James H. Myatt

Gregory A. Addington

Siva Banda

James K. Hall

Airforce Research Laboratory (AFRL/VACA),
2210 Eighth St., Bldg. 146,
Wright-Patterson AFB, OH 45433-7531

Optimal Feedback Control of Vortex Shedding Using Proper Orthogonal Decomposition Models

This paper treats the question of control of two-dimensional incompressible, unsteady wake flow behind a circular cylinder at Reynolds number Re=100. Two finite-dimensional lower order models based on proper orthogonal decomposition (POD) are considered for the control system design. Control action is achieved via cylinder rotation. Linear optimal control theory is used for obtaining stabilizing feedback control systems. An expression for the region of stability of the system is derived. Simulation results for 18-mode POD models obtained using the control function and penalty methods are presented. These results show that in the closed-loop system mode amplitudes asymptotically converge to the chosen equilibrium state for each flow model for large perturbations in the initial states. [DOI: 10.1115/1.1385513]

I Introduction

Feedback control of fluid flows is a problem of considerable importance and currently is an active field of research. However, despite significant progress in control theory, the control of fluid flow remains unresolved. The difficulty lies in the inherent nonlinearity of the Navier-Stokes equations which govern the flow dynamics. General studies of the optimal control of viscous incompressible flows have been made [1–5]. Considerable experimental research has been also done to address the flow control problem [6–11].

To avoid the complexity of infinite-dimensional flow dynamics, finite dimensional approximate models are often obtained. These approximate models are still of large order which create numerical difficulties for control system design. As such, low order models which capture essential flow dynamics and reduce computational burden are of practical value.

Proper orthogonal decomposition (POD) (which is also known as the Karhunen-Loeve decomposition [12,13]) provides a reduction method which can be used to obtain low dimensional models of distributed parameter systems. The advantage of low order POD models is that the well-developed control theory for finite dimensional systems can be applied for flow control design. However, it must be noted that any POD model is only an approximation of the Navier-Stokes equations. As such, the success of design using POD models rests on their ability to capture the dynamics of Navier-Stokes equations closely.

Recently, the POD method has been used to derive low order flow models for various applications [14–18]. Graham et al. [19,20] have considered the development of POD models for flow past a circular cylinder and designed a control system for ameliorating the effect of vortex shedding. This approach requires the iterative solution of the associated two-point boundary value problem. These results show the usefulness of POD models for the analysis and design. However, further research in closing the gap between the POD model and Navier-Stokes equations remains to be done.

In this paper, control of a two-dimensional flow past a circular cylinder is considered. The POD models derived by Graham et al. [19,20] using the control function and penalty methods are used for the design of feedback control systems. Linear optimal control theory is used for the design of control laws. In the closed-loop system, asymptotic regulation of the mode amplitudes to the chosen equilibrium state is accomplished. An analytical expression for the region of stability is also obtained. For the synthesis of the control systems, it is assumed that all the mode amplitudes are available for feedback. An estimate of state variables can be obtained by constructing an observer; however the design of an observer is not treated here. Simulation results for 18-mode nonlinear POD models are obtained which show that in the closed-loop system mode amplitudes asymptotically converge to the chosen equilibrium point by rotating the cylinder appropriately.

The organization of the paper is as follows. The models of the flow dynamics are given in Section II. Section III presents the design of controllers. A region of stability is derived in Section IV, and simulation results are given in Section V.

II Mathematical Model: Flow Past A Cylinder

Two-dimensional, incompressible flow of a fluid with density ρ past a circular cylinder of diameter D_c (Fig. 1) is governed by the Navier-Stokes and continuity equations. In nondimensional form, these are described by

$$\partial u/\partial t + (u\cdot\nabla)u = -\nabla p + (1/\mathrm{Re})\nabla^2 u \tag{1}$$

$$\nabla\cdot u = 0 \tag{2}$$

where the velocity $u=(u_1,u_2)$ has been nondimensionalized by the inflow velocity U, the pressure p by the ρU^2, time by D_c/U, and spatial variables by D_c. The Reynolds number Re is defined as $\mathrm{Re}=\rho U D_c/\mu$, where μ is the fluid's dynamic viscosity.

The boundary conditions are [19,20]

$$\begin{gathered}(u_1,u_2)=(1,0),(x,y)\in\Gamma_1\\ \partial u_1/\partial y=0, u_2=0,(x,y)\in\Gamma_2,\Gamma_4\\ p=0,(x,y)\in\Gamma_3\\ (u_1,u_2)=(-\gamma y,\gamma x),(x,y)\in\Gamma_c\end{gathered} \tag{3}$$

where γ is the angular velocity of the cylinder which is the control input variable. The assumption that the pressure is zero on Γ_3 is reasonable, provided that this boundary is placed at a sufficient distance downstream of the cylinder. Indeed, the flow solution of

Contributed by the Fluids Engineering Division for publication in the JOURNAL OF FLUIDS ENGINEERING. Manuscript received by the Fluids Engineering Division October 28, 2000; revised manuscript received May 1, 2001. Associate Editor: P. Bradshaw.

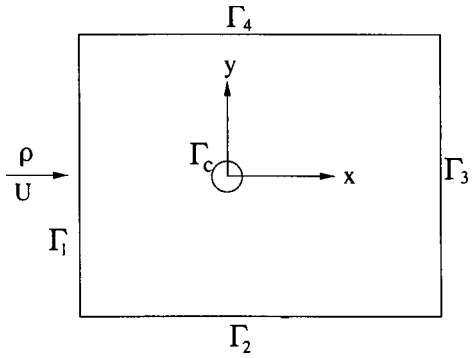

Fig. 1 Simulation domain for flow past circular cylinder (diameter of cylinder=1; upstream and downstream boundaries from center of cylinder=10, 15; width=20)

Graham et al. [19,20] for the model under consideration at Reynolds number 100 show vortex street behind the cylinder, and no spurious reflections from downstream boundary appear. Thus the boundary condition given in Eq. (3) is acceptable.

In this study, low order finite dimensional models derived by Graham et al. [19,20] using proper orthogonal decomposition are considered. Readers may refer to [19,20] for the details of derivation and the numerical results obtained using POD models. Authors first solved Eqs. (1) and (2) by discretization in time via a three step projection method [21] and in space using a Galerkin finite element approximation [22], and used the computed flow field to obtain POD basis functions by solving an eigenvalue problem. They used these POD modes to obtain a finite dimensional models via Galerkin projection of the Navier-Stokes equations. Now these two models of Graham et al. [19,20] obtained using the control function and penalty methods are briefly described.

A1 Control Function Method (Model I). For the control function method, one expands the velocity as

$$u(x,y,t)=u_m(x,y)+\gamma(t)\Phi_c(x,y)+\sum_{i=1}^{N} q_i(t)\Phi_i(x,y) \quad (4)$$

where N is the number of modes chosen for approximation, $u_m(x,y)$ is the mean velocity, $q_i(t)$ is the mode amplitude, $\Phi_i(x,y)$ is the ith basis function which is obtained using the POD approach, and $\Phi_c(x,y)$ is a suitable divergence-free control function. The basis functions $\Phi_i(x,y)$ have zero velocity on the cylinder surface. In Eq. (4), the control function $\Phi_c(x,y)$ has been introduced to satisfy the inhomogenous boundary condition on the surface of the cylinder.

Then substituting (4) in the Navier-Stokes equation Eq. (1) and using Galerkin projection, one obtains

$$\dot{q}_i=a_i+\sum_{j=1}^{N} b_{ij}q_j+\sum_{j=1}^{N}\sum_{k=1}^{N} c_{ijk}q_jq_k+d_i\dot{\gamma}+\left(e_i+\sum_{j=1}^{N} f_{ij}q_j\right)\gamma+g_i\gamma^2 \quad (5)$$

where a_i, b_{ij}, c_{ijk}, d_i, e_i, f_{ij}, and g_i are constant parameters.

A2 Penalty Method (Model II). In this approach, the velocity is expanded in a series form as

$$u(x,y,t)=u_m(x,y))+\sum_{i=1}^{N} q_i(t)\Phi_i(x,y) \quad (6)$$

Since the basis functions Φ_i have nonzero velocity on the cylinder surface, there is need for the boundary condition to be enforced via the penalty method. For enforcing the essential boundary condition in an integral, ''weak'' fashion, the velocity on the cylinder surface is taken to be

$$u=\gamma(D_c/2)\hat{e}_\theta-\epsilon\partial u/\partial n \quad (7)$$

where ϵ is a small parameter and $\hat{e}_\theta$ is the unit tangent vector.

Then performing Galerkin projection, one obtains the set of differential equations describing the evolution of mode amplitudes given by

$$\dot{q}_i=a_i+\sum_{j=1}^{N} b_{ij}q_j+\sum_{j=1}^{N}\sum_{k=1}^{N} c_{ijk}q_jq_k+d_i\gamma \quad (8)$$

Note that these parameters a_i, b_{ij}, c_{ijk}, and d_i differ from those used in Eq. (5).

It is seen that the control function method yields state equations which depend on the angular acceleration $\dot{\gamma}$, but the equation derived using the penalty method does not contain $\dot{\gamma}$. As such, one must treat $\dot{\gamma}$ as the control input variable and γ as a state component for the purpose of control system design using model I. For the design of a controller, one can treat γ as the control input for model II. Of course one can introduce the angular acceleration as a control variable even for model II by introducing γ as an additional state variable.

The equilibrium point of the uncontrolled system is obtained by solving the set of equations obtained from Eq. (5) or Eq. (8) by setting $\gamma=0$ and $\dot{q}=0$. For the nonlinear model there are multiple equilibrium points which may be asymptotically stable or unstable. Furthermore, this system exhibits periodic solutions as well. In view of the velocity expansions given in Eqs. (4) and (6), one observes that by controlling the mode amplitudes one can modify the velocity field in the span of the basis functions (modes). For avoiding flow separation in the neighborhood of a point on the surface of the cylinder, one may like to control q_i $(i=1,\ldots,N)$ such that $\partial u_\theta/\partial n>0$ at the selected point. In general, a large order POD model may not be controllable with few control inputs. In such a case one may simply like to suppress the wake unsteadiness caused by the dominant modes as much as possible.

In this study, we shall be interested in regulating the state vector to an equilibrium point. For this purpose, a linearized model of each nonlinear flow model is obtained, and using linear quadratic optimal control theory stabilizing control systems for both models are designed.

III Control Law Design

In this section, first an optimal control system for the model I obtained using the control function method is designed. Define $q=(q_1,\ldots,q_N)^T\in R^N$, the vector of mode amplitudes and $u_c=\dot{\gamma}$ (T denotes matrix transposition). Then a state variable representation of Eq. (5) can be written in a compact form as

$$\begin{pmatrix}\dot{q}\\ \dot{\gamma}\end{pmatrix}=\begin{pmatrix}A+Bq+(q^TC_1^Tq,\ldots,q^TC_N^Tq)^T+(E+Fq)\gamma+G\gamma^2\\ 0\end{pmatrix}+\begin{pmatrix}D\\ 1\end{pmatrix}u_c \quad (9)$$

where $A=(a_1,\ldots,a_N)^T$; B and F are matrices whose elements in the ith row and jth column are b_{ij} and f_{ij}, respectively; $D=(d_1,\ldots,d_N)^T$ is part of the input matrix, C_i has its $j-k$th element c_{ijk}; $E=(e_1,\ldots,e_N)^T$; and $G=(g_1,\ldots,g_N)^T$.

Let q^* be an equilibrium point of the unforced system Eq. (9) with $\gamma=0$. Then q^* is a solution of

$$A+Bq^*+[q^{*T}C_1^Tq^*,\ldots,q^{*T}C_N^Tq^*]^T=0$$

Linearizing the system (9) about the equilibrium point $q_a^*=(q^{*T},0)^T\in R^{N+1}$ gives

$$\dot{\tilde{q}}_a = \begin{pmatrix} B+C^* & E+Fq^* \\ 0 & 0 \end{pmatrix} \tilde{q}_a + \begin{pmatrix} D \\ 1 \end{pmatrix} u_c \doteq A_a \tilde{q}_a + D_a u_c \quad (10)$$

where $\tilde{q}_a = ((q-q^*)^T, \gamma)^T \in R^{N+1}$ denotes the deviation of the state $q_a = (q^T, \gamma)^T$ from the equilibrium point q_a^*, 0 denotes null matrices of appropriate dimensions, matrices A_a and D_a are defined in Eq. (10), and the $N \times N$ matrix C^* is given by

$$C^* = \begin{pmatrix} q^{*T}(C_1 + C_1^T) \\ \vdots \\ q^{*T}(C_N + C_N^T) \end{pmatrix}$$

Since we are interested in regulating the vector q_a to q_a^*, consider a performance index for minimization of the form

$$J = \int_0^\infty (\tilde{q}_a^T Q \tilde{q}_a + R u_c^2) dt \quad (11)$$

where Q is a positive definite symmetric weighting matrix and R is a positive real number. It is assumed that the matrix pair (A_a, D_a) is controllable, that is, the rank of the controllability matrix $(D_a, A_a D_a, \ldots, A_a^N D_a)$ is $N+1$, the dimension of the state space. Then the optimal control law [23]

$$u_c = -R^{-1} D_a^T S \tilde{q}_a \doteq -K \tilde{q}_a \quad (12)$$

exists where S is the positive definite symmetric matrix which is the solution of the matrix Riccati equation [23]

$$S A_a + A_a^T S - S D_a R^{-1} D_a^T S + Q = 0 \quad (13)$$

Then the closed-loop matrix $A_c = (A_a - D_a K)$ is a Hurwitz matrix. The weighting matrix Q and R are chosen properly to obtain desirable response characteristics of the mode amplitudes.

The optimal feedback control law for the model II is similarly designed. If one introduces γ as an additional state variable, the design procedure used for model I can be exactly followed. However, one may as well treat γ as the control input u_c and consider the linearized system

$$\dot{\tilde{q}} = (B + C^*) \tilde{q} + D u_c \quad (14)$$

for design. In this case the feedback law takes the form

$$u_c = \gamma = -K \tilde{q} \quad (15)$$

Here we have considered two state space models of the flow dynamics. To this end, one may like to explore the equivalence of these two state space representations. For this we must first introduce an additional state variable γ for the flow model II, and include $\dot{\gamma} = u_c$ in Eq. (5). In general, it seems rather difficult to find a nonlinear state transformation between the two nonlinear models. But then it is of interest to examine similarity at least locally in neighborhoods of certain equilibrium points of the two models. If there exists a similarity transformation for the linearized models, their local stability behavior must be topologically similar. The two linearized models considered in Section V are controllable. If any similarity transformation T_r for the linearized model exists then one must have $q_{a2} = T_r q_{a1}$, and system matrices must satisfy $A_{a2} = T_r A_{a1} T_r^{-1}$, and $D_{a2} = T_r D_{a1}$, where q_{ai}, A_{ai}, and D_{ai} denote the state vectors and the system matrices (A_a, D_a) of the two models $(i = I, II)$. The matrix A_{a2} of model II is obtained by replacing $E + Fq^*$ by D, and D_a by $(0,1)^T$ in Eq. (10). Furthermore, their controllability matrices must be related as $M_2 = T_r M_1$, where M_1, M_2 are the controllability matrices of model I and II, respectively [24]. Thus the required matrix T_r is $M_2 M_1^{-1}$. In the neighborhood of the chosen equilibrium points of Section V, the systems are not equivalent. Thus the question remains: Are there other equilibrium points for which state equivalence can be established? One may yet like to explore a measure of closeness of the two models if they are not locally equivalent. Answers to these questions are important but are considered beyond the scope of this paper.

IV Region of Stability

The design has been performed using linear optimal control theory. Therefore, this control system guarantees only local asymptotic stability of the equilibrium point q_a^* of the nonlinear model. However, a conservative region of stability can be obtained using the Lyapunov approach [25]. In the following, the derivation of a region of stability for the model I is considered. One can similarly derive a region of stability for the model II.

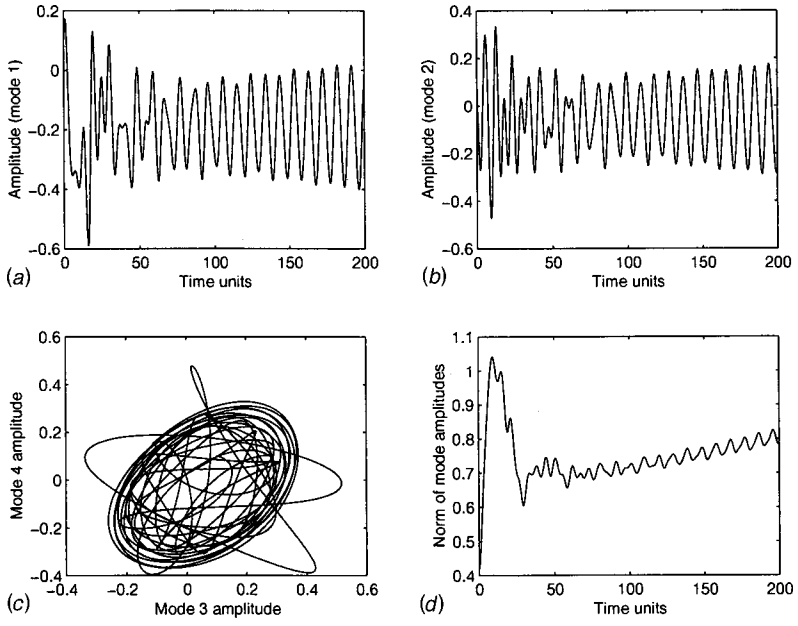

Fig. 2 Open-loop response of Model I: (2a) Amplitude (mode 1); (2b) amplitude (mode 2); (2c) amplitude phase plot (mode 3, mode 4); (2d) norm of mode amplitudes

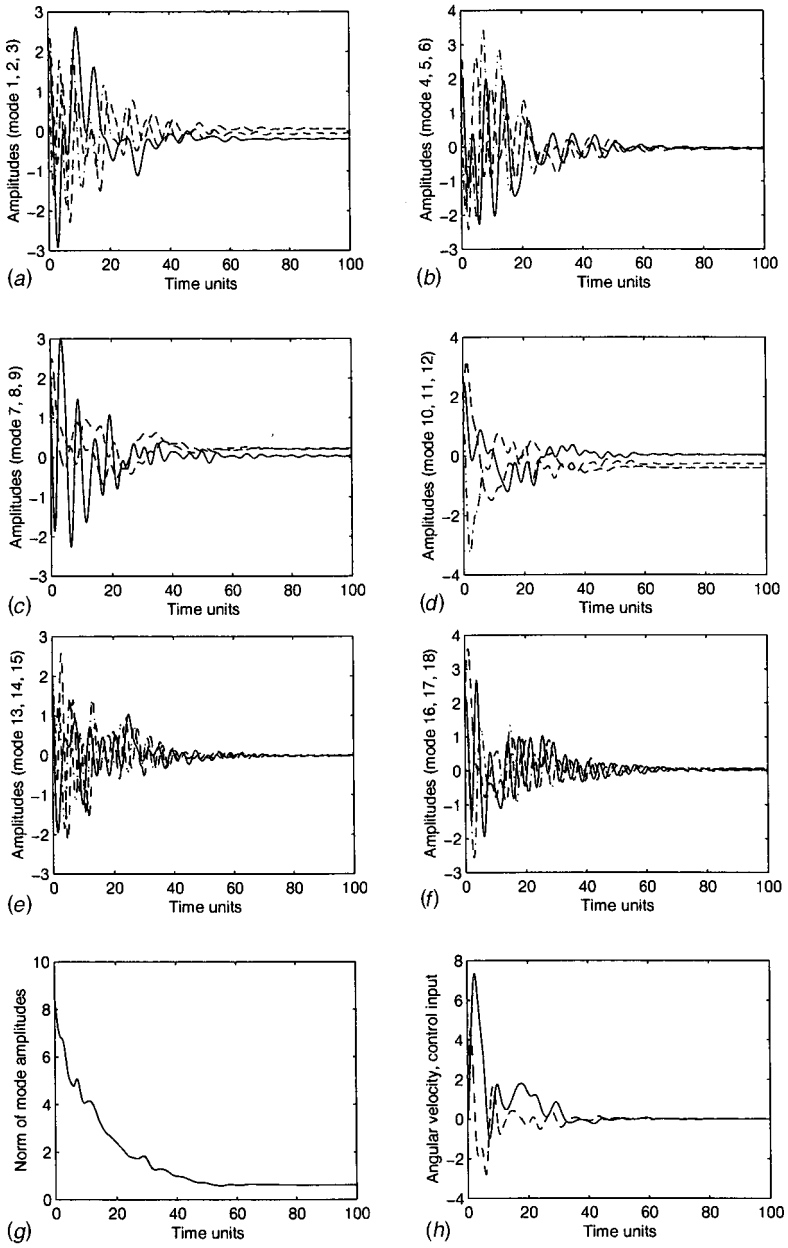

Fig. 3 Closed-loop control (Model I): (3a) Amplitude mode 1 to 3 (solid; —·—·—·—; — — —); (3b) amplitude mode 4 to 6 (solid; —·—·—·—; — — —); (3c) amplitude mode 7 to 9 (solid; —·—·—·—; — — —); (3d) amplitude mode 10 to 12 (solid; —·—·—·—; — — —); (3e) amplitude mode 13 to 15 (solid; —·—·—·—; — — —); (3f) amplitude mode 16 to 18 (solid; —·—·—·—; — — —); (3g) norm of mode amplitudes; (3h) angular velocity and control input (solid; — — —)

Substituting $q=q^*+\tilde{q}$ in the closed-loop system including model I and the control law Eq. (12) and simplifying the equation gives

$$\dot{\tilde{q}}_a = A_c\tilde{q}_a + [\tilde{q}_a^T L_1^T \tilde{q}_a, \ldots, \tilde{q}_a^T L_N^T \tilde{q}_a, 0]^T \tag{16}$$

where $A_c=(A_a-D_aK)$ and the $N+1\times N+1$ matrices L_i $(i=1,\ldots,N)$ are given by

$$L_i = \begin{pmatrix} C_i & F_i^T/2 \\ F_i/2 & g_i \end{pmatrix}$$

Here F_i denotes the ith row of the matrix F_i. Since the closed-loop system matrix A_c is Hurwitz, there exists a positive definite matrix P which is the unique solution of the Lyapunov equation [25]

$$PA_c + A_c^T P = -W \tag{17}$$

where W is any positive definite symmetric matrix. Now for obtaining a region of stability, consider a quadratic positive definite Lyapunov function [25]

$$V = \tilde{q}_a^T P \tilde{q}_a \tag{18}$$

Its derivative along the trajectory of the system Eq. (16) is given by

$$\dot{V}=\tilde{q}_a^T[PA_c+A_c^TP]\tilde{q}_a+2\tilde{q}_a^TP[\tilde{q}_a^TL_1^T\tilde{q}_a,\ldots,\tilde{q}_a^TL_N^T\tilde{q}_a,0]^T \tag{19}$$

Using Eq. (19), one has

$$\dot{V}\leq-\tilde{q}_a^TW\tilde{q}_a+\|\tilde{q}_a\|\|P\|\left[\sum_{i=1}^{N}\{\tilde{q}_a^T(L_i+L_i^T)\tilde{q}_a\}^2\right]^{1/2}$$

$$\leq-\lambda_{\min}(W)\|\tilde{q}_a\|^2+\lambda_{\max}(P)\left[\sum_{i=1}^{N}\lambda_{\max}^2(L_i+L_i^T)\right]^{1/2}\|\tilde{q}_a\|^3 \tag{20}$$

In view of Eq. (20), it follows that $\dot{V}<0$ if

$$\|\tilde{q}_a\|<\frac{\lambda_{\min}(W)}{\lambda_{\max}(P)[\Sigma_{i=1}^{N}\lambda_{\max}^2(L_i+L_i^T)]^{1/2}}=\mu^* \tag{21}$$

Define an ellipsoid $E_r\subset R^{N+1}$ by

$$E_r=\{\tilde{q}_a\in R^{N+1}:\|\tilde{q}_a^TP\tilde{q}_a\|=r\} \tag{22}$$

and the ball $B_r=\{\tilde{q}_a\in R^{N+1}:\|\tilde{q}_a\|=r\}$. It is easily seen that the largest ellipsoid contained in the ball B_{μ^*} is E_{r^*} where $r^*=\lambda_{\min}(P)\mu^{*2}$, and this ellipsoid encloses any ball of radius

$$k^*<\{\lambda_{\min}(P)/\lambda_{\max}(P)\}^{1/2}\mu^* \tag{23}$$

Then any trajectory beginning in B_{k^*} cannot escape the set E_{r^*} since in E_r^* one has $\dot{V}\leq 0$. Then it follows from the Lyapunov stability theory that the trajectory asymptotically converges to the origin $\tilde{q}_a=0$, and B_{k^*} lies in the region of stability [25].

V Simulation Results

In this section simulation results for the two flow models at Reynolds number Re=100 are presented. The numerical values of system parameters (Eqs. (5) and (8)) obtained by Graham et al. [19,20] are used for obtaining responses. Graham et al. [19,20] obtained solutions of Eqs. (1) and (2) when the cylinder had imposed oscillatory motion of varying frequency as well resulting in adequate excitation of modes, and selected snapshots for constructing the basis functions. Interestingly, authors found that 18 basis functions capture around 97 percent of the snapshot energy. Readers may refer to Graham et al. [19,20] which provide details of approximation results using the POD models. Here we consider 18th order models (Eqs. (5) and (8)) for the design of the optimal control law and simulation using MATLAB and Simulink software. First the flow model obtained using the control function method is considered.

A1 Stabilization of Flow Model I. The open-loop flow model is simulated. A variety of responses are obtained which depend on the initial conditions. For the initial condition $q_i(0)=0.1$ $(i=1,\ldots,18)$ close to the origin and $\gamma(0)=0$, responses are shown in Fig. 2. A bounded oscillatory but slowly diverging response for each mode is observed.

With the objective of suppressing the unsteady wake, an equilibrium point close to the origin $(q=0)$ is considered. A perturbed initial state away from the equilibrium point is assumed for which the norm of the mode amplitudes is $\|q(0)\|=8.42$, but at the equilibrium point, one has $\|q^*\|=0.62$. This gives a relatively large perturbation in the mode amplitudes from the chosen equilibrium value. This initial state differs from that of Fig. 2. Note that the linearized model about the equilibrium point has two unstable complex poles $(0.0052+0.6601j, 0.0052-0.6601j)$, and the remaining 8 pairs of poles associated with the modes are lightly damped. For the purpose of regulating the trajectories to the equilibrium point, the controller is designed using the weighting matrix Q as $10I_{19\times 19}$ and R is set to 50, where I denotes an identity matrix of indicated dimension.

Selected responses for the nonlinear model I are shown in Fig. 3. It is seen that the mode amplitudes converge to the equilibrium point in about 60 nondimensional time units. During the transient period an oscillatory mode amplitude responses are observed. As the trajectory tends to the equilibrium point, the angular velocity and angular acceleration of the cylinder also converge to zero as predicted.

A2 Stabilization of Flow Model II. The selected open-loop mode amplitude responses of model II are shown in Fig. 4. For the

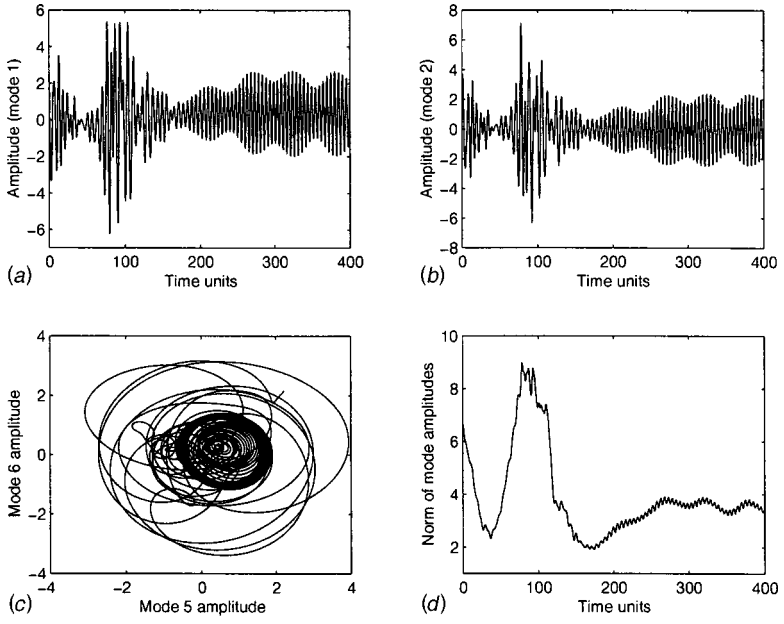

Fig. 4 Open-loop response of Model II: (4a) Amplitude (mode 1); (4b) amplitude (mode 2); (4c) amplitude phase plot (mode 5, mode 6); (4d) norm of mode amplitudes

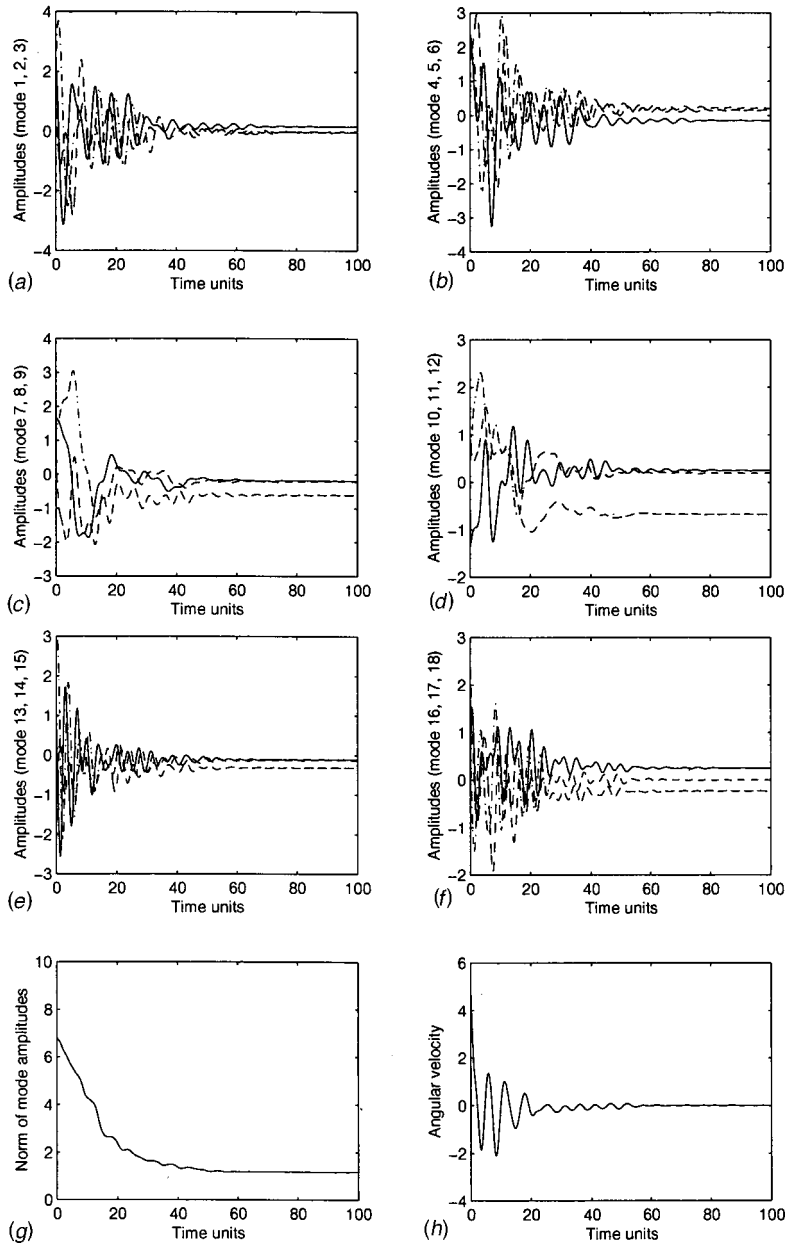

Fig. 5 Closed-loop control (Model II): (5a) Amplitude mode 1 to 3 (solid; —·—·—·—; — — —); (5b) amplitude mode 4 to 6 (solid; —·—·—·—; — — —); (5c) amplitude mode 7 to 9 (solid; —·—·—·—; — — —); (5d) amplitude mode 10 to 12 (solid; —·—·—·—; — — —); (5e) amplitude mode 13 to 15 (solid; —·—·—·—; — — —); (5f) amplitude mode 16 to 18 (solid; —·—·—·—; — — —); (5g) norm of mode amplitudes; (5h) angular velocity

chosen initial condition, periodic oscillatory responses in the steady-state are observed.

Similar to model I, stabilization of the mode amplitudes about an equilibrium point which is in the vicinity of the origin is considered. For simplicity it is assumed that the angular velocity instead of the angular acceleration is the control input. For the chosen equilibrium point, one has $\|q^*\| = 1.17$. For simulation, the initial state is set to a value such that $\|q(0)\| = 8.22$. This is a relatively large perturbation in mode amplitudes. For the chosen equilibrium point, the linearized open-loop model is unstable.

For suppressing the unsteady components of the mode amplitudes, a feedback K is obtained for $Q = 4I_{18\times 18}$ and $R = 30$. Selected responses are shown in Fig. 5. We observe convergence of each mode amplitude response to the desired equilibrium value following initial oscillations in the transient period. The response time is of the order of about 60 nondimensional time units. Cylinder rotation rate also tends to zero as the state reaches the equilibrium point.

Extensive simulation for both models has been performed. Faster responses are obtained by increasing the value of the weighting matrix Q or reducing the parameter R, but this requires larger control magnitude. It is found that the linear controller can regulate the state from an even larger perturbed initial state $q(0)$, however, this too requires a larger cylinder angular rate.

Low order POD models for design and simulation show good responses. However, since the Navier-Stokes equations are of in-

finite dimension, these finite dimensional models can only provide an approximate solution. It is reasonable to expect that if the POD modes are generated using sufficiently rich flow field by adequate excitation of modes to capture most of the energy, a finite dimensional model can be constructed which can predict the solution with accuracy. Of course, there remains much research to be done related to the choice of imposed excitation of the cylinder, selection of good snapshots which give POD modes, the dimension of low-order models yielding better approximation capability, and the spillover effect of designed controllers on the neglected uncontrolled modes. However, answers to these questions are beyond the scope of this paper, in which our focus is to demonstrate ability to control vortex shedding using a simple rotation (one input) of POD models of having a large number of state variables, and examine the region of stability in the closedloop system.

VI Conclusions

Feedback control of unsteady flow past a circular cylinder was considered. Two kinds of flow dynamics derived using the control function and penalty methods were considered. Linear optimal control theory was used for the derivation of feedback control laws for the stabilization of the mode amplitudes. It was assumed that all the mode amplitudes are derivable from measurements for feedback. Simulation results were presented which showed that in the closed-loop system asymptotic regulation of mode amplitudes to the desired equilibrium state can be accomplished by judiciously rotating the cylinder. Interestingly, the linear controller is capable of suppressing large unsteady mode amplitude perturbations in spite of the nonlinearity in the flow dynamics of the two models.

While both models have somewhat qualitatively similar flow dynamics, the control design for model II is relatively simple. Model I includes nonlinear functions of the angular velocity, but model II has only linear angular velocity dependent terms. In a quantitative sense, it seems rather difficult to derive a state space equivalence relationship for these two models, although it has been shown numerically in the literature that these two models give comparable flow dynamics. Further research is needed to establish a connection between the two models in control system design.

System theory provides several analysis and design tools for finite dimensional systems which one can apply to POD models. But any design using approximate POD models of Navier-Stokes equations provides only an approximate control system. One can design adaptive and robust control systems for flow control using POD models which can compensate uncertainties and neglected dynamics due to truncation of modes to a certain extent. However, a question remains: How well the control system will perform when Navier-Stokes equations are used for validation? It is hoped that POD models of sufficient order capturing the most of the energy of snapshots obtained by adequate excitation of the flow dynamics can provide good controllers for controlling the flow. Indeed even the suppression of dominant modes using POD models can provide good control of vortex shedding. It must be noted that final success can be measured only by experimental results. Further research is needed to examine the relative merits of two (POD) models and to evaluate the performance of the designed optimal controllers using Navier-Stokes equations for simulation.

Acknowledgment

The authors would like to sincerely thank Professor W. R. Graham of the University of Cambridge for making the flow data from his published articles available and for his useful suggestions on flow dynamics.

References

[1] Hou, L. S., and Ravindran, S. S., 1997, ''A Penalized Neuman Control Approach for Solving an Optimal Dirichlet Control Problem for Navier-Stokes Equations,'' SIAM J. Control Optim., **36**, pp. 1795–1814.

[2] Ito, K., and Ravindran, S. S., 1998, ''A Reduced Order Method for Simulation and Control of Fluid Flows,'' J. Comput. Phys., **143**, pp. 403–425.

[3] Burns, J. A., and Ou, Y. R., 1994, ''Feedback Control of the Driven Cavity Problem Using LQR Design,'' Proc. 33rd IEEE Conf. on Decision and Control, Florida, pp. 289-284.

[4] Joslin, R. D., Gunzburger, M. D., Nicolaides, R., Erlebacher, G., and Hussaini, M. Y., 1997, ''A Self-Contained, Automated Methodology for Optimal Flow Control Validated for Transition Delay,'' AIAA J., **35**, pp. 816–824.

[5] Sritharan, S. S., 1992, ''An Optimal Control Problem in Exterior Hydrodynamics,'' Proceedings of the Royal Society of Edinburgh, Vol. 121A, pp. 5–32.

[6] Seifert, A., Darabi, A., and Wyganski, I., 1996, ''Delay of Airfoil Stall by Periodic Excitation,'' J. Aircr., **33**, No. 4.

[7] Modi, V. J., Mokhtarian, F., Fernando, M., and Yokomizo, T., 1991, ''Moving Surface Boundary-Layer Control as Applied to Two-Dimensional Airfoils,'' J. Aircr., **28**, pp. 104–112.

[8] Roussopoulos, K., 1993, ''Feedback Control of Vortex Shedding at Low Reynold's Numbers,'' J. Fluid Mech., **248**, pp. 267–296.

[9] Maddlon, D. V., Collier, F. S., Montoya, F. S., and Land, C. K., 1989, ''Transition Flight Experiments on a Swept Wing with Suction,'' AIAA Paper 89-1893.

[10] Smith, B. L., and Glezer, A., 1997, ''Vectoring and Small Scale Motions Effected in Free Shear Flows Using Synthetic Jet Actuators,'' AIAA Paper 97-0213.

[11] Rediniotis, O. K., Ko, J., Yue, X., and Kurdila, A. J., 1999, ''Synthetic Jets, their Reduced Order Modeling and Applications to Flow Control,'' AIAA Paper 99-1000.

[12] Karhunen, K., 1946, ''Zur Spectral Theorie Stochasticher Prozesse,'' Annales Academiae Scientiarum Fennicae, Mthematica-Physica, **37**.

[13] Loeve, M., 1945, ''Functiona Aleatoire de Second Ordre,'' Comptes Rendus Academie des Sciences, Paris.

[14] Aubry, N., Holmes, P., Lumley, J. L., and Stone, E., 1988, ''The Dynamics of Coherent Structures in the Wall Region of a Turbulent Boundary Layer,'' J. Fluid Mech., **192**, pp. 115–173.

[15] Berkooz, G., Holmes, P., and Lumley, J. L., 1993, ''The Proper Orthogonal Decomposition in the Analysis of Turbulent Channel Flow,'' Annu. Rev. Fluid Mech., **25**, No. 5, pp. 539–575.

[16] Rajaee, M., Karlson, S. K., and Sirovich, L., 1994, ''Low Dimensional Description of Free Shear Flow Coherent Structures and their Dynamic Behavior,'' J. Fluid Mech., **258**, pp. 1401–1402.

[17] Rempfer, D., 1996, ''Investigations of Boundary Layer Transition via Galerkin Projections on Empirical Eigen Functions,'' Phys. Fluids, **8**, No. 1, pp. 175–188.

[18] Ravindran, S. S., 1999, ''Proper Orthogonal Decomposition in Optimal Control of Fluids,'' NASA/TM-1999-209113.

[19] Graham, W. R., Peraire, J., and Tang, K. Y., 1999, ''Optimal Control of Vortex Shedding Using Low Order Models, Part I: Open-loop Model Development,'' Int. J. Numer. Methods Eng., **44**, No. 7, pp. 945–972.

[20] Graham, W. R., Peraire, J., and Tang, K. Y., 1999, ''Optimal Control of Vortex Shedding Using Low Order Models, Part II: Model Based Control,'' Int. J. Numer. Methods Eng., **44**, No. 7, pp. 9973–990.

[21] Donea, J., Giuliani, S., Laval, H., and Quartapelle, L., 1982, ''Finite Element Solution of the Unsteady Navier-Stokes Equations by a Fractional Step Method,'' Comput. Methods Appl. Mech. Eng., **30**. pp. 53–73.

[22] Zienkiewicz, O. C., Szmelter, J., and Peraire, J., 1990, ''Compressible and Incompressible Flow; An Algorithm for all Seasons,'' Comput. Methods Appl. Mech. Eng., **78**, pp. 105–121.

[23] Chen, C-T., 1999, *Linear Systems Theory and Design*, Oxford University Press, New York, pp. 151-152.

[24] Athans, M., and Falb, P., 1966, *Optimal Control*, McGraw-Hill, New York.

[25] Vidyasagar, M., 1993, *Nonlinear Systems Analysis*, Prentice-Hall, Englewood Cliffs, NJ.

Dynamic Subgrid-Scale Modeling for Large-Eddy Simulations in Complex Topologies

Stephen A. Jordan
Naval Undersea Warfare Center,
Newport, RI 02841

The dynamic eddy-viscosity relationship is a suitable choice for modeling the subgrid-scales (SGS) in a large-eddy simulation (LES) of complex turbulent flows in irregular domains. This algebraic relationship is easy to implement and its dynamic coefficient will give negligible turbulent viscosity contributions in the flow regions that are irrotational or laminar. Its fine-scale turbulence predictions can be qualitatively reasonable if the local grid resolution maintains the SGS field predominantly within the equilibrium range of turbulent energy spectra. This performance is given herein by two curvilinear coordinate forms of the dynamic Smagorinsky model that are formally derived and a-priori tested using the resolved physics of the cylinder wake. The conservative form evaluates the dynamic coefficient in the computational (transformed) space whereas its non-conservative counterpart operates in the physical domain. Although both forms equally captured the real normal SGS stress reasonably well, the real shear stress and dissipation rates were severely under-predicted. Mixing the eddy-viscosity choice with a scale-similarity model can ease this latter deficiency. [DOI: 10.1115/1.1374215]

1 Introduction

The large-eddy simulation (LES) methodology is now firmly acknowledged by the general fluid dynamic community as a viable means for numerically capturing the salient physics of complex turbulent flows. This acceptance has recently sparked numerous practical applications of the LES technique that have appeared in various articles and conference proceedings. The methodology itself rests on the fact that the larger energy-bearing structures are resolved (computed) while the finer turbulent eddies are characterized by a physics-based model. Demarcation between the resolved and modeled fields is distinct and formally instituted by a spatial filter in the LES formulation. In practical applications, however, this separation varies locally and is given by the respective grid spacing of the discretized domain. The spatial filter in these cases is denoted as the grid filter. The corresponding turbulence model represents those length scales lying beneath the grid's resolution, which must properly communicate with the finest local scales of the resolved field. These subgrid-scales (SGS) typically embody most of the equilibrium range of the turbulent energy spectra and tend toward homogeneous and isotropic conditions. Based on published *a-priori* testing (see for example O'Neil and Meneveau [1]), the SGS field should not extend beyond the inertial subrange of the local turbulent energy spectra. This requirement insures satisfactory performance of the SGS model. Unfortunately, maintaining this essential criterion during a LES computation in a complex domain is a difficult task.

Formal derivation of a SGS model for practical topologies and understanding its role in the predicted turbulence statistics remains largely unknown. Ghosal and Moin [2] proved that the filter operation does not commute with the differentiation when implemented over variable grid spacing. Nonuniform filtering introduces a second-order error into the LES solution that precludes the use of high-order-accurate schemes. Beaudan and Moin [3] applied a SGS model over nonuniform gridding and reported the turbulent stress distributions at several radii downstream of a circular cylinder. They also showed reasonable circumferential distributions of the turbulent eddy viscosity within the cylinder near wake. However, no formal treatment was given of the SGS model derivation nor its global contributions relative to the resolved stresses. Jordan and Ragab [4] later performed LES computations of the circular cylinder wake using their curvilinear coordinate form of the dynamic SGS model. They illustrated the significance of the model's contributions relative to the artificial dissipation produced by an upwind scheme applied to the convective term of the resolved field. After examining their model, Armenio and Piomelli [5] questioned their contraction procedure for determining the local dynamic coefficient in view of its rotational invariance in the physical domain. Notably, neither of these near wake applications studied the dynamic model's accuracy for representing the real SGS stress field.

The present objective aims to formally derive a dynamic eddy-viscosity SGS model for complex topologies and then illustrate its narrow band fidelity relative to the inertial subrange of the turbulent energy spectra. The concept of dynamic SGS modeling was formally conceived by Germano et al. [6]. It is a welcomed improvement over Smagorinsky's original eddy-viscosity model (Smagorinsky [7]) where the constant coefficient was user-defined. The improved model samples the spectral content of the finest resolved scales to dynamically regulate its single coefficient. This procedure is well suited for practical LES applications because the resultant SGS stress field correctly responds to the instantaneous flow conditions. Negligible stress contributions are sustained in the potential and laminar flow regimes of the flow and the correct asymptotic behavior will take place near solid walls bounding the turbulent regimes. The dynamic coefficient will take on both positive and negative values that signify forward scatter or backscatter in the turbulent energy spectra, respectively. Piomelli et al. [8] first recognized this latter behavior in their *a-priori* tests of a turbulent channel flow. Physically, backscatter denotes the reversal of kinetic energy across the cut-off wavenumber from the model to the finest resolved scales of the turbulent field.

The present SGS model derivation orders the sequence of spatial operations according to the procedure recommended by Jordan [9]. Jordan demonstrated that the fundamental LES formulation and discrete filter definition are both ill-conditioned if the initial equation system is filtered before transformed (traditional approach). By reversing the operations, the filter definition is correctly oriented along the curvilinear lines and its operation commutes with the differentiation in the transformed space (alternate approach). Like the resolved-field terms, the model's Cartesian

Contributed by the Fluids Engineering Division for publication in the JOURNAL OF FLUIDS ENGINEERING. Manuscript received by the Fluids Engineering Division October 6, 2000; revised manuscript received March 15, 2001. Associate Editor: I. Celik.

form also requires transformation to a curvilinear coordinate framework for application over the boundary-fitted grid lines. Evaluating the dynamic coefficient, in particular, formally involves three spatial operations; two filters and a coordinate transformation. Accordingly, starting with the Navier-Stokes (N-S) equations the extended sequence of spatial operations to evaluate the SGS model coefficient) proceeds as

$$\underset{\text{(Cartesian)}}{\text{N-S}} \Rightarrow \textbf{Transform} \Rightarrow \underset{\text{(curvilinear)}}{\text{N-S}} \Rightarrow \textbf{Filter}_{\text{(grid)}} \Rightarrow \textbf{Filter}_{\text{(test)}}$$

$$\Rightarrow \underset{\text{(curvilinear)}}{\text{Model Coefficient}}$$

The second filter tests the finest scales of the resolved field to locally extract a representative dynamic coefficient for the model. Depending on the final formulation, this explicit operation can occur in either the physical domain or the transformed space. Jordan [9] showed that box filtering in either the physical or transformed space yields identical damping of the quantity's spectral components. But if the physical domain is chosen, one must recognize the inherent commutation error in the formulation due to the nonuniform spacing.

The fully-resolved turbulent physics by direct numerical simulation (DNS) of the immediate wake of a circular cylinder will serve herein as a testbed to evaluate the transformed forms of the dynamic SGS model. This dataset is an excellent choice because the real and model stresses can be directly compared over a broadband range of wavenumbers. In particular, the spatial resolution emanating normally from the cylinder surface decays exponentially with downstream distance. The Reynolds number (Re) of the present dataset is 3900; based on the cylinder diameter. At this Re, the inertial subrange in wavenumber space is broadband (approximately one-half of a decade) and consistent throughout the far wake in Kolmorgorov units.

II Smagorinsky's SGS Model: Curvilinear Coordinate Formulation

As noted earlier, execution of the spatial filter dictates the resolved turbulent scales separate from the modeled ones. This spatial operation should be instituted after the transformation phase to acquire the proper SGS field for irregular topologies. The filter itself is sensibly directed along the curvilinear lines where the independent spatial variables are the curvilinear coordinates (ξ,η,ζ). In the physical domain, we assumed that the filter width is synonymous with the grid's resolution $(\Delta=\Delta_g)$, which eliminates a Leonard-type term in the final formulation. In the transformed space, the filter width is unity.

Following the alternative approach, the conserved real (exact) SGS stress field (σ_i^k) of an incompressible flow in the computational domain is defined as

$$\sigma_i^k=\overline{U^k}\,\overline{u_i}-\overline{U^k u_i} \tag{1}$$

where the grid-filtered contravariant velocity components $\langle \overline{\mathbf{U}},\overline{\mathbf{V}},\overline{\mathbf{W}}\rangle$ are evaluated in terms of their physical velocities $\langle \overline{u},\overline{v},\overline{w}\rangle$ by $\overline{\mathbf{U}^\mathbf{k}}=\sqrt{\tilde{\mathbf{g}}}\tilde{\xi}^k_{x_j}\overline{\mathbf{u}_\mathbf{j}}$. The overbar denotes the grid-filter operation and the tilde symbolizes implicit filtering of the metric coefficients $(\tilde{\xi}^k_{x_j})$ through their numerical approximation (see Jordan [9]). Because these coefficients are smooth quantities, they have been removed from the grid-filter operation.

Transforming Smagorinsky's eddy-viscosity relationship to the curvilinear lines gives

$$\sqrt{\tilde{\mathbf{g}}}\tilde{\xi}^k_{x_j}\tau_{ij}-1/3\sqrt{\tilde{\mathbf{g}}}\tilde{\xi}^k_{x_j}\delta_{ij}\tau_{ll}=2\mathbf{C}\overline{\Delta}^2|\overline{S}|\sqrt{\tilde{\mathbf{g}}}\tilde{\xi}^k_{x_j}\overline{\mathbf{S}_\mathbf{ij}} \tag{2}$$

or in terms of the conserved contravariant densities.

$$\sigma_i^k-1/3\tilde{\zeta}^k_{x_j}\tau_{ll}=2\mathbf{C}\overline{\Delta}^2|\overline{\mathbf{S}}|\overline{\mathbf{S}}^k_i \tag{3}$$

where the coefficient C is considered as the model coefficient in either space and the filtered metric term $(\tilde{\zeta}^k_{x_j})$ transforms the trace of the Cartesian stress tensor (τ_{ll}). The turbulent eddy-viscosity (υ_T) is defined as

$$\upsilon_\mathbf{T}=\mathbf{C}\overline{\Delta}^2|\overline{\mathbf{S}}| \tag{4}$$

where the magnitude of the resolvable strain-rate tensor is $|\overline{\mathbf{S}}|=\sqrt{2\overline{\mathbf{S}_\mathbf{ij}}\overline{\mathbf{S}_\mathbf{ij}}}$ and $\overline{\Delta}$ is the respective grid-filter width. In the physical domain, Δ is defined in terms of the covariant metric tensors as $\overline{\Delta}=\sqrt[6]{\tilde{\mathbf{g}}}=\sqrt[6]{\tilde{\mathbf{g}}_{11}\tilde{\mathbf{g}}_{22}\tilde{\mathbf{g}}_{33}}$ for orthogonal grids.

III Dynamic Model Coefficient

Properly evaluating the dynamic model coefficient along the curvilinear lines is a critical ingredient to the successful use of Smagorinsky's eddy-viscosity relationship for complex topologies. This aspect of the computation demands explicit filtering of the resolved field by a correctly designed test filter. The derivation must orient the test filter along the curvilinear lines and yield a unique expression for determining the model coefficient in either a conservative or nonconservative form. The pertinent form depends on whether filtering is performed in the physical domain or the transformed space. In the interest of brevity, the derivation will center on a fully conservative formulation. However, this section will close with a brief description of the nonconservative form and its error-free application in the physical domain.

A. Conservative Form. The present derivation follows the procedure developed by Germano et al. [6] for Cartesian coordinate systems, but with the introduction of the contravariant velocities as well as special treatment given to the metric coefficients. Keeping in mind that the metric coefficients are smooth variables, test filtering the momentum equation according to the alternate approach introduces a modified contravariant Reynolds stress and a modified contravariant Leonard stress into the curvilinear formulation that are defined as

$$\mathbf{T}^\mathbf{k}_\mathbf{i}=\overline{\overline{\mathbf{U}^\mathbf{k}}}\,\overline{\mathbf{u}_\mathbf{i}}-\overline{\overline{\mathbf{U}^\mathbf{k}\mathbf{u}_\mathbf{i}}} \quad \text{(Reynolds stress)} \tag{5a}$$

$$\mathbf{L}^\mathbf{k}_\mathbf{i}=\overline{\overline{\mathbf{U}^\mathbf{k}}}\,\overline{\mathbf{u}_\mathbf{i}}-\overline{\overline{\mathbf{U}^\mathbf{k}}\,\overline{\mathbf{u}_\mathbf{i}}} \quad \text{(Leonard stress)} \tag{5b}$$

The second overbar denotes the second filter operation $(\bar{\overline{\Delta}}/\overline{\Delta}\geqslant 2)$. Note that both these stress tensors require test filtering the Cartesian as well as the contravariant velocity components of the resolved field in the transformed space. The Germano identity for Cartesian coordinate systems has a similar form in the computational space

$$\mathbf{L}^\mathbf{k}_\mathbf{i}=\mathbf{T}^\mathbf{k}_\mathbf{i}-\overline{\boldsymbol{\sigma}^\mathbf{k}_\mathbf{i}} \tag{6}$$

where the single overbar shows test filtering the contravariant SGS stress tensor. This identity clearly illustrates the contravariant resolved stress tensor $(\mathbf{L}^\mathbf{k}_\mathbf{i})$ as representing those turbulent scales lying between the grid and test filter operations in the computational domain. Assuming that the wavenumber cut-off from the test filter still lies within the equilibrium range of the turbulent energy spectra (scale-invariance), the modified Reynolds stress can also be expressed by an eddy-viscosity relationship as

$$\mathbf{T}^\mathbf{k}_\mathbf{i}-\mathbf{1/3}\tilde{\bar{\boldsymbol{\zeta}}}^\mathbf{k}_{\mathbf{x_j}}\mathbf{T}_{ll}=\mathbf{2C}\bar{\bar{\boldsymbol{\Delta}}}^\mathbf{2}|\bar{\mathbf{S}}|\bar{\mathbf{S}}^\mathbf{k}_\mathbf{i} \tag{7}$$

with the same model coefficient as used for the SGS field. Furthermore, assuming that $\boldsymbol{\sigma}^\mathbf{k}_\mathbf{i}$ and $\mathbf{T}^\mathbf{k}_\mathbf{i}$ behave statistically scale-similar, Eqs. (3) and (7) can be substituted into the new identify (Eq. (6)). If the model coefficient is then removed from the test filter operation, the eddy-viscosity expression for the modified Leonard stress in the transformed space becomes.

$$\mathbf{L}^\mathbf{k}_\mathbf{i}-1/3\bar{\tilde{\zeta}}^k_{x_j}\mathbf{L}_{ll}=2\mathbf{C}\overline{\boldsymbol{\Delta}}^\mathbf{2}\mathbf{M}^\mathbf{k}_\mathbf{i} \tag{8a}$$

The contravariant model stress density ($\mathbf{M_i^k}$) in this relationship is defined as

$$\mathbf{M_i^k}=\alpha^2|\bar{\bar{S}}|\bar{\bar{S}}_i^k-\overline{|\bar{S}|\bar{S}_i^k} \tag{8b}$$

with the filter width ratio $\alpha=\bar{\bar{\Delta}}/\bar{\Delta}$. For moderate to high-Re turbulent flows, M_i^k essentially models the instantaneous scales of the inertial subrange that lie between the grid and test filters. This tensor and L_i^k are known resolvable quantities in Eq. (8*a*) with the only unknown being the local coefficient *C*.

To find a unique expression for the model coefficient while concurrently circumventing a singular evaluation, Lilly [10] executed a least-squares procedure that is equivalent to contracting the Cartesian form of Eq. (8*a*) with M_{ij}. But by following Lilly's procedure in the computational space, one must be careful to insure rotational invariance of *C* in the physical domain as well. This concern was ignored in the model coefficient definition given by Jordan and Ragab [4]. The contraction should be performed such that the contravariant error density E_i^k is defined with the transformation metrices of L_{ij} and M_{ij} not summed independently

$$\mathbf{E_i^k}=\sqrt{\bar{\bar{\mathbf{g}}}}\bar{\bar{\xi}}^k_{x_j}\mathbf{L_{ij}}-1/3\bar{\bar{\xi}}^k_{x_j}\mathbf{L}_{ll}-2\mathbf{C}\bar{\Delta}^2\sqrt{\bar{\bar{\mathbf{g}}}}\bar{\bar{\xi}}^k_{x_j}\mathbf{M_{ij}} \tag{9}$$

Minimizing this error along the curvilinear lines using the least-squares approach gives

$$C=\frac{G^{kk}L_{ij}M_{ij}}{2\bar{\Delta}^2G^{kk}M_{mn}M_{mn}}=\frac{L_i^k\cdot M_i^k}{2\bar{\Delta}^2M_m^k\cdot M_m^k} \tag{10}$$

where $\mathbf{G^{kk}}=\nabla\xi^k\cdot\nabla\xi^k$. The second expression for *C* indicates the inner product of the Cartesian tensor components of $\mathbf{L_i^k}$ and $\mathbf{M_i^k}$ that are evaluated in the computational space. Note that while Lilly minimized five independent relationships, 27 equations are minimized in the generalized curvilinear coordinate framework (i.e., $\mathbf{E}_1^2\neq\mathbf{E}_2^1$). We will see that although the modeled SGS field retains the correct behavioral characteristics, the correlation between the contravariant real and model stresses degrades as compared to their Cartesian analogue.

B. Nonconservative Form. The above sequence applied to a nonconservative form of the LES equations differs primarily in interpreting the result. One must realize that transforming the SGS stress gradients after their numerical evaluation along the curvilinear lines implies filtering in the physical domain. Although the metric coefficients can be uncoupled from the filtered transformed quantity, the filter operation itself does not exactly commute with the differentiation. For example, test filtering the conservative SGS term can be easily reformulated to a nonconservative form

$$\overline{\frac{1}{\sqrt{\bar{g}}}\frac{\partial\sigma_i^k}{\partial\xi^k}}=\bar{\bar{\xi}}^k_{x_j}\overline{\frac{\partial\tau_{ij}}{\partial\xi^k}}=\bar{\bar{\xi}}^k_{x_j}\frac{\partial\bar{\tau}_{ij}}{\partial\xi^k}+O(\Delta)^2 \tag{11}$$

where $\bar{\tau}_{ij}=\bar{\bar{u}}_i\bar{\bar{u}}_j-\overline{\bar{u}_i\bar{u}_j}$. This form characterizes test-filtering τ_{ij} in the physical domain with a nonuniform filter width as determined locally by the grid spacing. The key point is that if the numerical accuracy of the chosen differencing scheme (or filter kernel) is second-order, explicit filtering in the physical domain will not degrade the nonconservative results of the LES computation. However, second-order approximation schemes commonly difference the cell flux vectors to insure conservation throughout the physical domain. Thus, the nonconservative form not only nullifies the accuracy gained by higher-order-accurate approximations, but also violates a telescopic collapse of the SGS stress vectors when summed over the entire discretized domain.

Given this perception, the Cartesian forms of Smagorinsky eddy-viscosity model with Lilly's dynamic evaluation of the respective coefficient replace Eq. (3) and Eq. (10), respectively, in the nonconservative form of the governing LES equation system. Note that the commutation error can be avoided in the model coefficient expression by carefully test filtering its physical elements over nonuniform spacing. For example, the strain-rate should be reformulated to a conservative framework and numerically approximated prior to test filtering. The approach differs slightly from Lilly's sequence, but circumvents the commutation error by denoting the first-order derivatives as the test-filtered quantities.

IV DNS Database for the SGS Model Evaluations

The resolved turbulent physics of the immediate wake of a circular cylinder provide an excellent testbed for *a-priori* comparisons between the real and modeled SGS stress fields. Inasmuch as the wake can be resolved with variable grid spacing that is normal to the cylinder surface and uniform spacing near the wake centerline, the model's performance is easily explored over a broadband range of wave numbers. The upper limit depicts the finest dissipation scales as found in the vortex formation region while the energy range cut-off can be easily established many diameters downstream in the vortex street.

A suitable DNS computation of this canonical flow was described in detail by Jordan [9] at a subcritical Reynolds number of 3400; based on the cylinder diameter (D). The impetus for constructing his DNS dataset was to study several filtering schemes and the relative importance of the Leonard term in the resolved-field component of the LES formulation in curvilinear coordinates. Since the wake physics are statistically self-similar beyond closure of the mean vortex formation region ($\sim$1.5 diameters downstream), Jordan truncated the vortex exit boundary at 12 diameters. To insure numerical stability in the coarse grid regions (near the vortex exit boundary) and inhibit aliasing within the finely resolved formation region, the convective terms were differenced using a third-order-accurate upwind scheme (ξ, η lines). In the spanwise direction (*z* or ζ lines), these terms were approximated for a fourth-order compact scheme where the turbulent physics were assumed to be homogeneous and periodic. The diffusion terms in all directions were differenced by a three-point conservative scheme thereby giving second-order spatial accuracy to the overall DNS solution. Further details of the computational procedure as well as the grid generation and flow boundary conditions can be found in Jordan [9] and Jordan and Ragab [11].

The present DNS dataset mimics the same computational procedure just described. However, as shown in Fig. 1 the grid housed 321×241×64 points in the circumferential (ξ lines), radial (η lines), and spanwise (ζ lines) directions, respectively, and the Reynolds number was increased to 3900. This Reynolds number was specifically chosen to verify the spatial resolution against the recent experimental evidence taken directly from Ong and Wallace [12] in the immediate near wake. The grid holds uniform point spacing throughout the viscous wake in the circumferential and spanwise directions, and exponentially decays radially. Scal-

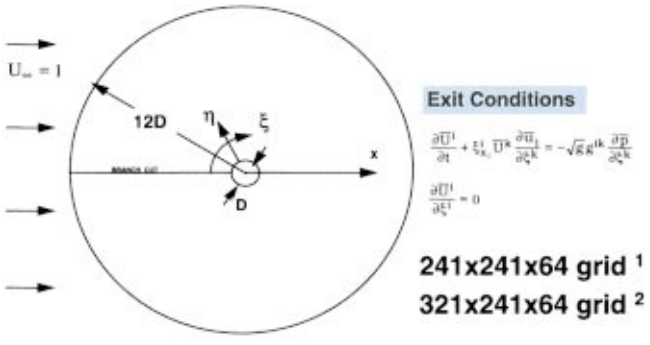

Fig. 1 Topology and flow conditions for the direct numerical simulation of the cylinder wake flow; [1]Jordan [9], Re=3400; [2]present computation, Re=3900

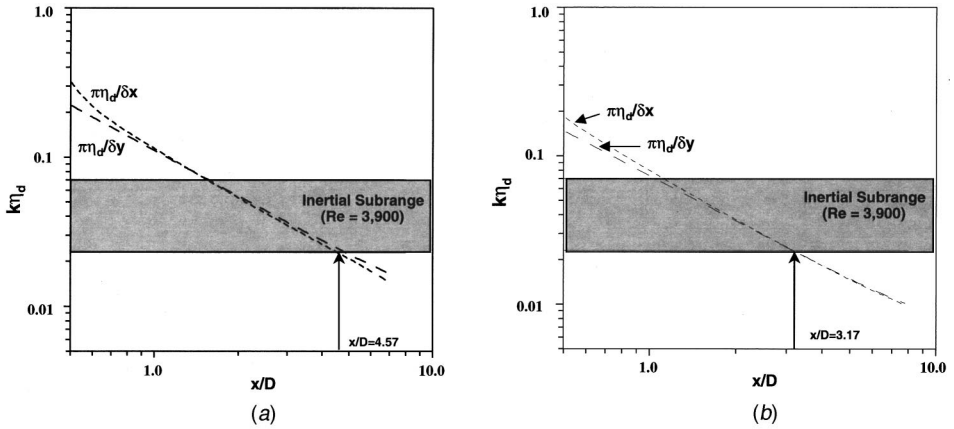

Fig. 2 Downstream grid spacing $\pi\eta_d/\delta x$ and $\pi\eta_d/\delta y$ for the present computations referenced to the inertial subrange (Ong and Wallace [3]) of the cylinder vortex street region; Re=3900

ing the spatial resolution of the DNS grid along the wake centerline by the respective time-averaged experimental values of Kolmogorov's microscale (Ong and Wallace [12]) is illustrated in Fig. 2(*a*). This comparison shows an unbiased spatial resolution after approximately 3/4's diameter downstream (referenced to the cylinder center). Notice that the equilibrium range of the near wake is well resolved up to about five diameters downstream. Finally, a spanwise resolution of 64 points over π length was chosen to adequately capture the periodic disturbances as measured by Mansey et al. [13]. Specifically, each disturbance was resolved by at least seven computational points.

One must remember that since the instantaneous flow constitutes three components (global mean, periodic mean, and random), the resolved random scales must be acquired through phase averaging. Heren, proof of sufficient DNS resolution for properly evaluating both model forms is carried out over three datasets. Each dataset is in-phase according to the Strouhal number ($S_t = 0.21$) as reported by Ong and Wallace [12], $S_t = fU/D$ where U is the freestream velocity and f is the shedding frequency of the large-scale vortices. Three phase-averages were necessary to attain a statistical dissipation rate having a relative 2 percent periodic error. Besides phase averaged, the turbulent statistics as well as the model's predictions are spanwise averaged with a 50 percent overlap. The spanwise averaging follows the procedure of Choi and Moin [14] where each computational point is treated as a separate realization. With a 50 percent overlap, three instantaneous datasets produce over 300 spanwise realizations.

A comparison of the turbulent energy spectra is shown in Fig. 3*a*, which includes experimental data taken from Uberoi and Freymuth [15] for the far wake. The agreement indicates the correct cascade of turbulent energy as resolved by the DNS computation in the immediate near wake region ($0.5 \leqslant x/D \geqslant 5.0$). According to the discussion by Beaudan and Moin [3], the cut-off wave numbers over this range are adequate to resolve the dominant turbulent scales that encapsulate most of the wake's energy. By computing the correct energy spectra, we can easily identify a reasonable downstream limit for truncating the model evaluations. The dissipation spectra in Fig. 3*b* clearly show that the peak dissipation rate is properly captured up to 5 diameters downstream. This fact gives reason for realizing the correct forward scatter of the turbulent spectral energy at the finest resolved scales (Fig. 3*a*). In particular, the computed spectra do not indicate tailing nor excessive damping of the turbulent energy at the grid-scale wave number. However, the downstream cut-off typifying sufficient DNS resolution should show tailing off of the dissipation rate at the finest resolved scales. With this understanding, the resolved immediate wake physics lying between $0.5 \leqslant x/D \leqslant 3.0$ should provide fair evaluations of both SGS model's performance.

V Explicit Filtering

Direct comparisons between the real and model SGS fields require proper preparation of the DNS dataset into a symbolic LES form. This process demands a relevant choice of conservative grid filtering. Knowing that the present DNS solution accuracy as well as the commutation error of nonuniform filtering are both second-order, discrete volume averaging as given by the box filter kernel over 2Δ spacing should suffice. In wavenumber space, the attenuation effects of box filtering are equivalent to a second-order, finite-volume solution methodology of the convective flux vectors along the curvilinear lines. Choosing a higher-order filter kernel would indeed minimize the level of damped resolved energy, but the filtering error is untraceable in the SGS model performance. Herein, the resultant resolved LES field houses the damped spectral physics over $161 \times 121 \times 32$ points in the ξ, η, ζ directions, respectively (again assuming homogeneous turbulence spanwise). The field to be modeled is bounded by the resolved LES scales and the original DNS solution. The resultant LES spatial resolution, referenced to the wake's inertial subrange, is illustrated in Fig. 2(*b*).

One can choose to explicitly filter the DNS data in either the physical domain or computational space to produce the LES resolved field where the model is applied. The resultant damped spectral energy components are identical regardless of the choice. The only notable distinction between the two filter operations is the CPU cost, which bears no relevance to the present need. Understanding the important difference between each domain rests solely upon when to test filter. Since the partial differentiation and filter operations commute in the transformed space, the test filter should yield equal values for the model coefficient whether it's done before or after discretizing the participating matrices. Conversely, the commutation error associated with the filter operation in the physical domain can only be avoided if the respective matrices (or their first-order components) are computed prior to test filtering. Furthermore, each component should be formulated in a conservative structure, flux-differenced, then test-filtered in the physical domain to guarantee a dynamic model coefficient that possess resolved physics which are inherently conserved and error-free.

The box filter attenuates all Fourier components of the physical quantity except at wavenumber $k=0$. In three-dimensions, the local filter width $2\Delta_{\xi^k}$ along the curvilinear lines operates on 26 neighboring points (or eight grid volumes). For the present explicit filter operations, a physical quantity $\Phi_{k,j,k}$ was box-filtered according to

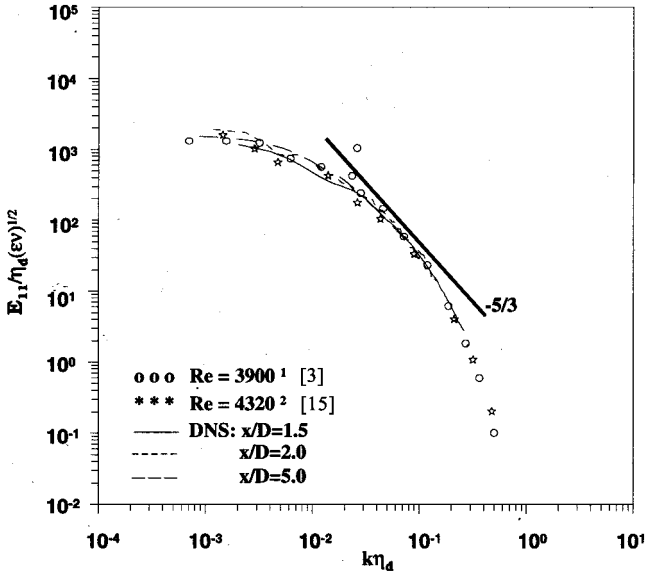

(*a*)

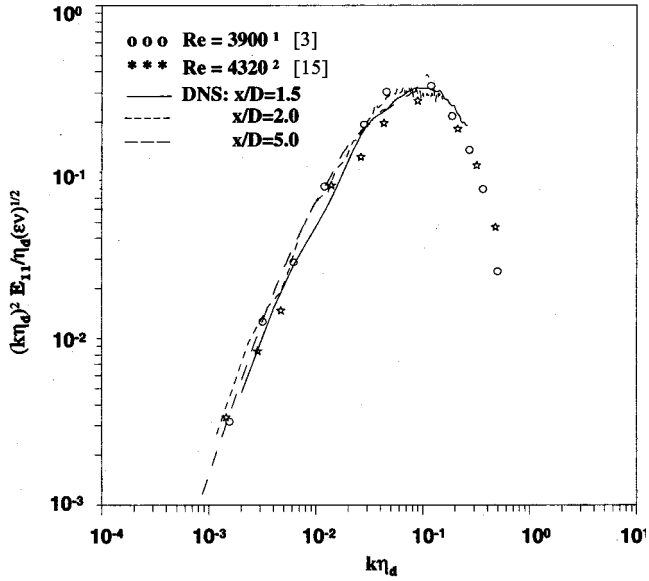

(*b*)

Fig. 3 Comparison of the present DNS computations (Re =3900) and the experimental velocity power and dissipation spectra in Kolmorgorov units for the cylinder vortex street; Ong and Wallace [3], x/D=5 and Uberoi and Freymuth [15] x/D=200

$$\begin{aligned}\bar{\Phi}_{i,j,k} = {} & \mathbf{C_1}\lfloor(1+\alpha)(\Phi_{i,j+1,k}+\beta\Phi_{i,j-1,k})+(1+\beta)\\ & \times(\Phi_{i+1,j,k}+\alpha\Phi_{i-1,j,k})\rfloor\\ & +\mathbf{C_2}\lfloor(1+\alpha)(\Phi_{i,j+1,k\pm1}+\beta\Phi_{i,j-1,k\pm1})+(1+\beta)\\ & \times(\Phi_{i+1,j,k\pm1}+\alpha\Phi_{i-1,j,k\pm1})\rfloor\\ & +\mathbf{C_2}\lfloor\Phi_{i+1,j+1,k}+\alpha\Phi_{i-1,j+1,k}+\beta\Phi_{i+1,j-1,k}\\ & +\alpha\beta\Phi_{i-1,j-1,k})\rfloor+\mathbf{C_3}\\ & \times\lfloor\phi_{i+1,j+1,k\pm1}+\alpha\Phi_{i-1,j+1,k\pm1}+\beta\Phi_{i+1,j-1,k\pm1}\\ & +\alpha\beta\Phi_{i-1,j-1,k\pm1})\rfloor+\mathbf{C_4}\Phi_{i,j,k\pm1}+\mathbf{C_5}\Phi_{i,j,k}\end{aligned} \tag{12}$$

where

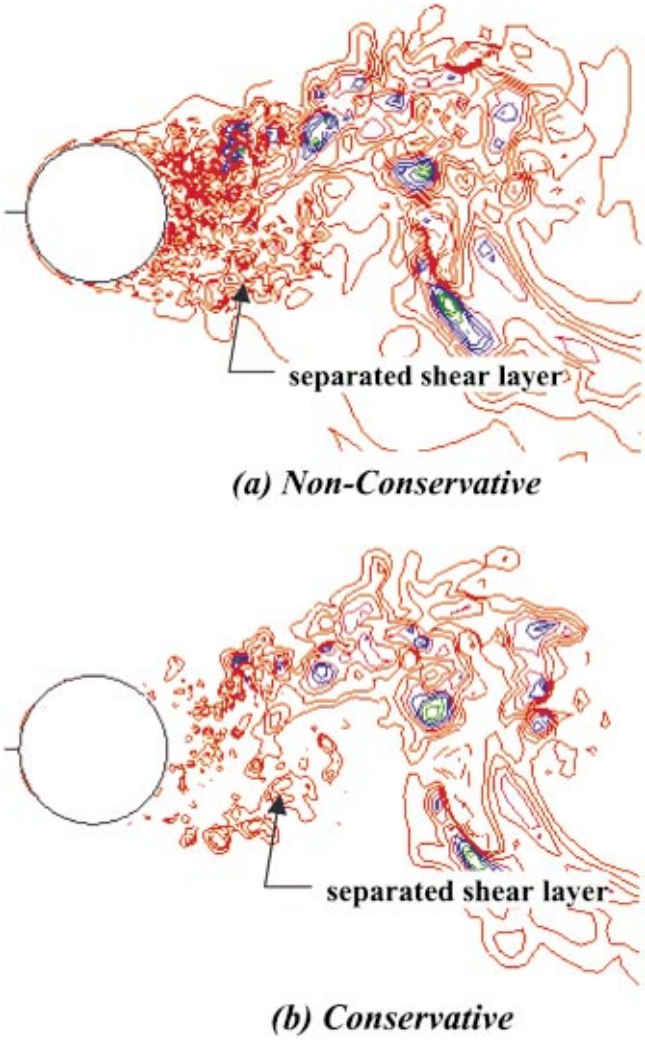

Fig. 4 Snapshots of the turbulent eddy viscosity distribution (ν_T/ν) in the cylinder immediate wake as predicted by the nonconservative and conservative forms of the curvilinear dynamic model; (*a*) contours max. 12.0, min. −13.0, incr. 0.5 and (*b*) contours max. 16.0, min −11.0, incr. 0.5

$$\mathbf{C}=(1+\alpha)(1+\beta),\quad \mathbf{C_1}=\mathbf{S}(1-\mathbf{S})^2/2\mathbf{C},$$

$$\mathbf{C_2}=\mathbf{S}^2(1-\mathbf{S})/2\mathbf{C},\quad \mathbf{C_3}=\mathbf{S}^3/2\mathbf{C},$$

$$\mathbf{C_4}=\mathbf{C}\mathbf{C_1},\quad \mathbf{C_5}=1-8\mathbf{C}[\mathbf{C_1}+1/2\mathbf{C_2}+1/4\mathbf{C_3}]$$

In the physical domain, the weighting parameters α and β hold description of the grid's nonuniformity in the ξ and η directions, respectively; $\alpha=\sqrt{\mathbf{g}_{11}^{+}/\mathbf{g}_{11}^{-}}$ and $\beta=\sqrt{\mathbf{g}_{22}^{+}/\mathbf{g}_{22}^{-}}$ where + and − denote the corresponding forward and backward grid spacing. One should be aware that grids possessing severe nonuniformity strongly damp the high-wavenumber quantities as reflected by the magnitude of the weighting parameters. By default, α and β are unit-valued in the computational space. Note that this particular box filter indicates no weighting parameter in the z, ζ direction because the spanwise spacing is uniform throughout.

VI Curvilinear Dynamic Smagorinsky Model (CDSM) Evaluations

Given that the spatial resolution of the DNS grid is homogeneous, we can now conduct a consistent evaluation of the nonconservative and conservative forms of the dynamic curvilinear SGS model. This statistical review includes local regions within the vortex formation regime where the finest turbulent scales are

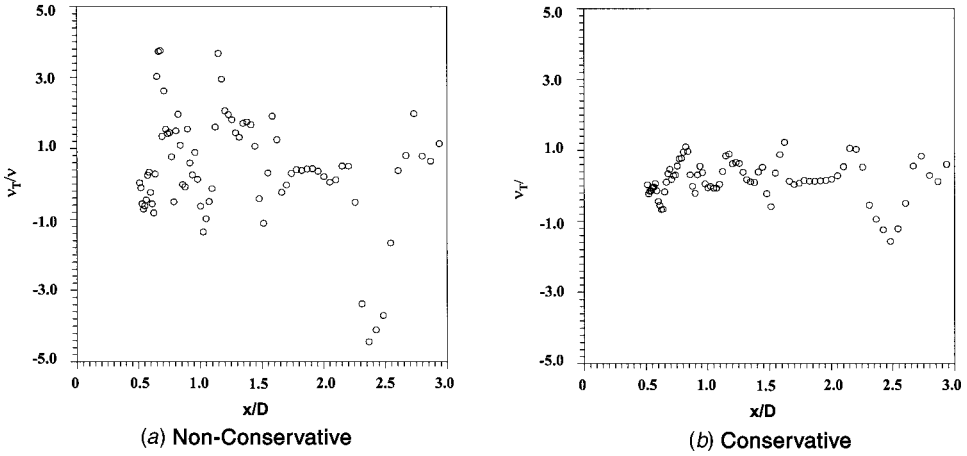

Fig. 5 Instantaneous turbulent eddy viscosity (ν_T/ν) along the wake centerline as predicted by the nonconservative and conservative forms of the curvilinear dynamic model

moderately consistent as well as within the immediate vortex street where local regions of small scales reside. Outside the near wake, we anticipate negligible contributions of turbulent eddy viscosity. Moreover, this same response is expected inside the early growth regions of the separated free shear layers that bound the formation regime. Separation at this Re is laminar (subcritical), and the resultant free shear layer instabilities support only a gradual transition to turbulence. Thus, the inherent complexity of the cylinder near wake physics provides a natural testbed for an effective investigation of the SGS model performance.

One should note that the performance statistics presented below are *a-priori*, meaning that the SGS model's *a-posteriori* response will differ in an actual LES simulation. *A-posteriori* studies have shown that the resolve field locally adheres and adjusts itself to the SGS model's presence. Also, the model's backscatter contributions typically have long correlation times that demand *ad hoc* measures to control diverging solutions. Nevertheless, the relative model behaviors are both qualitatively and quantitatively similar, which justifies indulging into *a-priori* testing.

Snapshots showing the scaled turbulent eddy viscosity distribu-

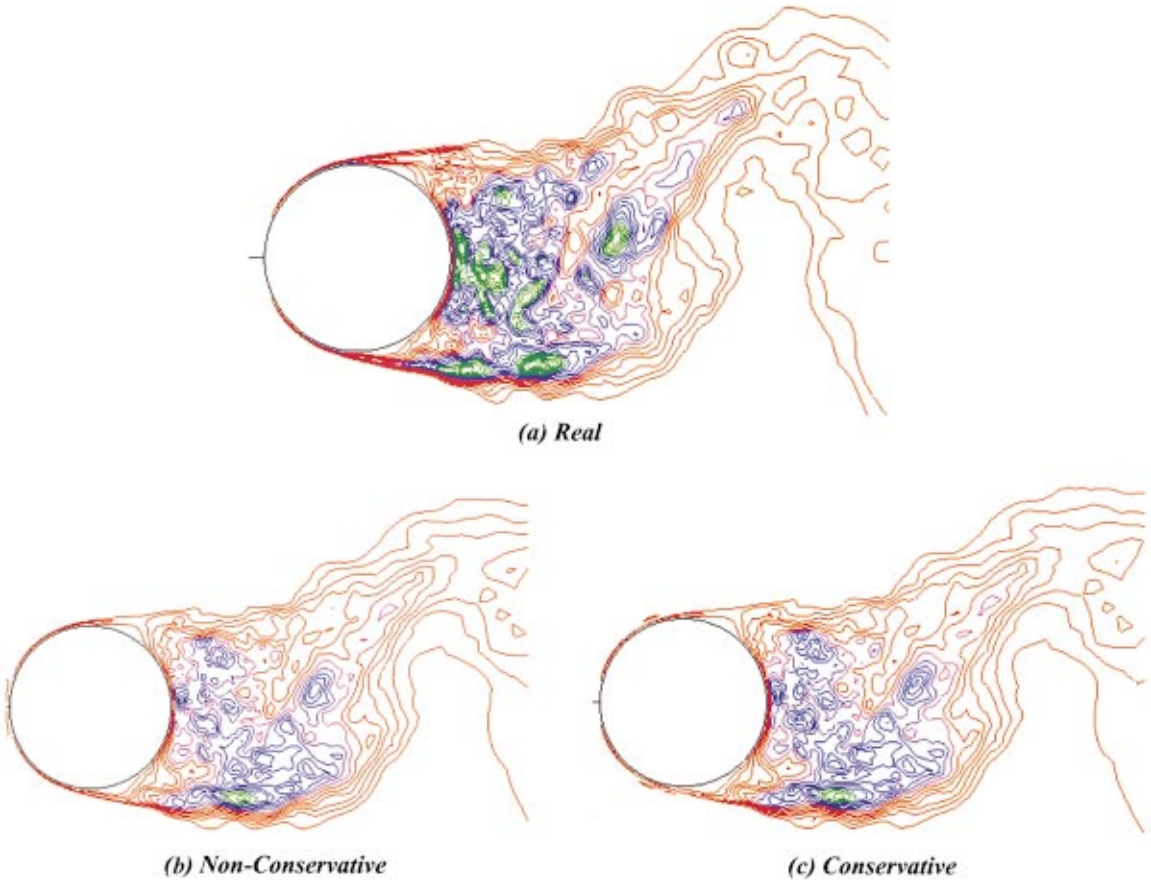

Fig. 6 Phase-averaged and spanwise averaged distributions of the real, nonconservative and conservative normal stress τ_{11} within the immediate wake; contours max 0.008, min, −0.08, incr. 0.004

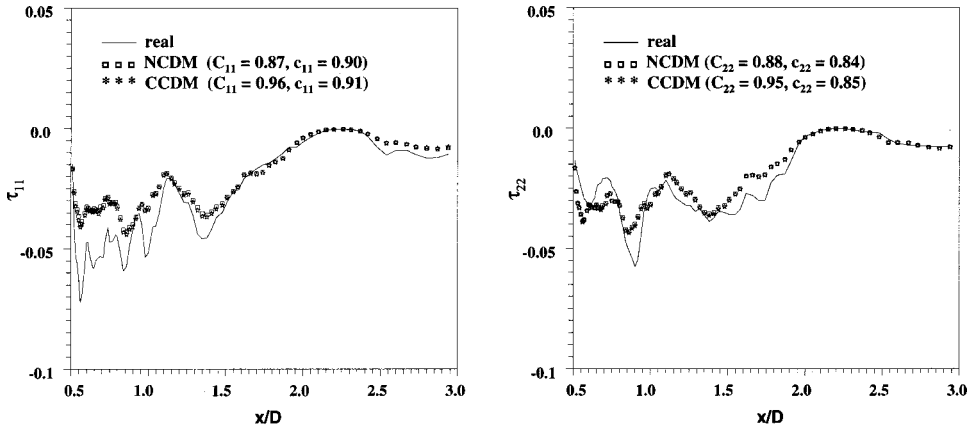

Fig. 7 Comparisons of the real and modeled normal SGS stresses (τ_{11} and τ_{22}) along the wake centerline; nonconservative (NCDM) and conservative (CCDM)

tions (ν_T/ν) for both CDSM forms are plotted in Fig. 4 using the three LES datasets. These applications gave the correct response within the irrotational regions of the flow as well as the upstream boundary layers. The separated shear layers display contours of ν_T/ν correlating well with transition to turbulence within these layers. However, while the maxima and minima of each curvilinear form are comparable, their predominant distributions differ most notably in the vortex formation region. Profiles of the LES grid resolution shown in Fig. 2(*b*) suggest that the CDSM contributions should be minimal immediately downstream of the cylinder. Only test filtering in the computational space gave this performance. This observation is emphasized further in Fig. 5 where ν_T/ν is plotted along the downstream centerline. Both models suggest increased magnitudes of ν_T/ν with degradation of the grid's resolution capacity, but test filtering in the physical domain gave significant contributions ($-3>\nu_T/\nu>3$) in the formation region where the turbulent scales are still considered well resolved.

Contours illustrating the spatial distribution of the real and model SGS normal stress τ_{11} within the immediate near wake are shown in Fig. 6. Each contour constitutes τ_{11} values that were phased-averaged and spanwise-averaged up through 3.5 diameters downstream. Both models distinguish cleanly the turbulent wake from the laminar and inviscid regions of the downstream flow. Highest concentrations of τ_{11} are predicted within the free-shear layer approximately one diameter downstream from separation. This location coincides with transition to turbulence according to Bloor [16]. Given the same spatial resolution, both models failed to capture the pockets of highest τ_{11} within the formation zone as indicated by their real counterpart. This deficiency is emphasized in Figs. 7(*a*) and 7(*b*), which compare the averaged real and modeled normal SGS stresses (τ_{11} and τ_{22}) along the wake centerline. Two correlation coefficients are given in these figures. The upper case notation denotes global correlation while the lower case depicts centerline values averaged along $0.5<x/D<3.0$. Collectively, both models suggest good global correlation, but respond poorly in the immediate turbulent vortex formation region. This latter shortcoming is a near-wall response that was expected, because the respective turbulent physics typify strong anisotropy and inhomogeneity of which the fidelity of an eddy viscosity built model breaks down. Beyond the vortex formation regime, both models correlate well with the real field even into the near vortex street ($x/D>1.5$).

Although this behavior is somewhat encouraging, the real shear stress distribution and magnitudes were regularly under-predicted by both SGS models. This fact surfaces in Fig. 8 where the predictions of the leading deviatoric component τ_{12} are especially poor throughout the vortex formation zone; which typically house

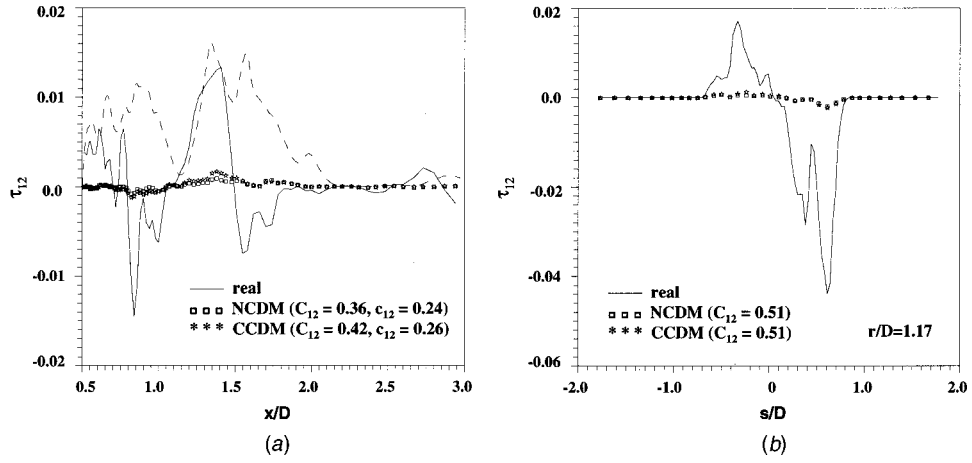

Fig. 8 Comparisons of the real and modeled Reynolds stress τ_{12} along (*a*) the wake centerline and (*b*) the circumferential line (r/D=1.17); nonconservative (NCDM) and conservative (CCDM)

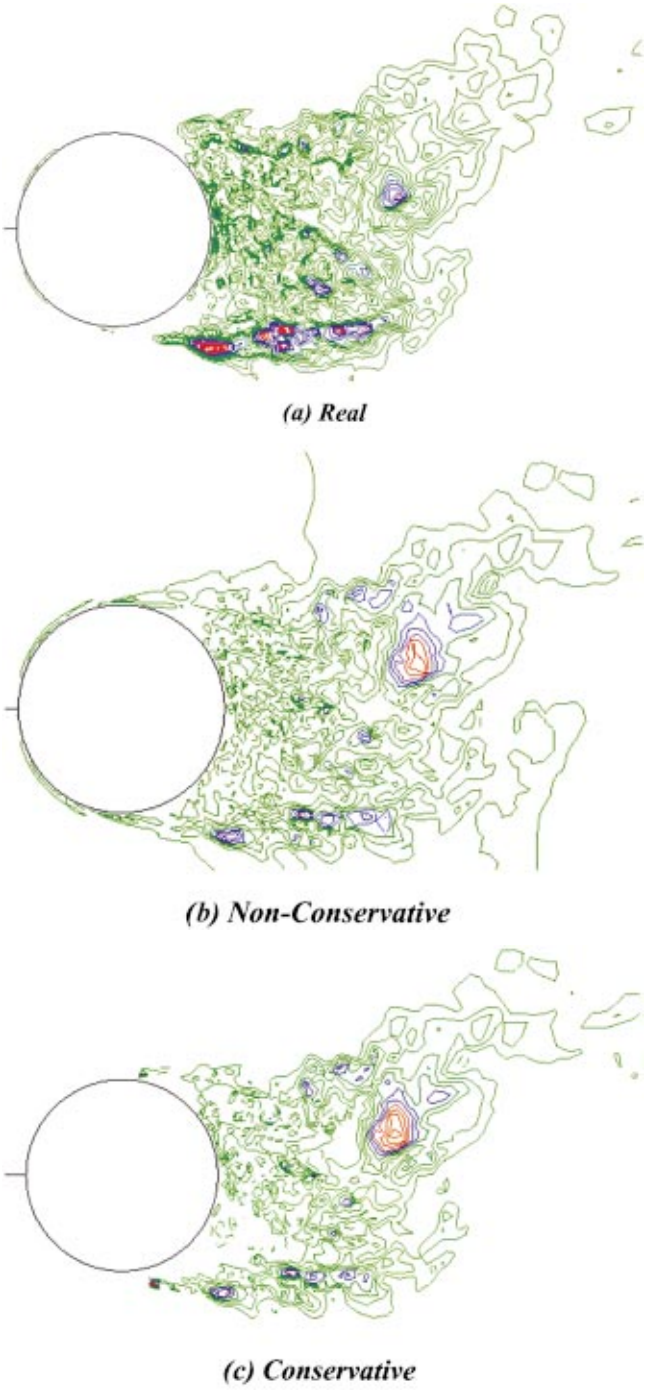

Fig. 9 Phase-averaged and spanwise averaged distributions of the SGS dissipation within the immediate wake; real: max 0.38, min. −0.018, incr. 0.018; nonconservative and conservative: max 0.11, min. −0.11, incr. 0.011

many pockets of dominant rates-of-strain. The *a-priori* predictions shown in Fig. 8(*b*) are taken along the circumferential line $r/D=1.17$ that passes through the lower separated shear layer as well as several clusters in the formation regime that possess high levels of real shearing stress. Both models respond correctly outside the formation zone. But comparisons within this zone indicate that both forms grossly under-predict τ_{12}. The conservative form gives only slightly better correlation with the real stress τ_{12} as listed in Fig. 8(*a*).

The dashed line in Fig. 8(*a*) denotes the centerline distribution of the $u'v'$ component of the total SGS shear stress. Note that its magnitude is of the same order as τ_{12}, which is unlike the much lower values seen in turbulent boundary layers. Commonly, we would require an eddy-viscosity model to capture at least this pure contribution. But as clearly demonstrated in the figure, the Smagorinsky model does not fulfill this expectation even when improved by dynamically evaluating its coefficient.

The dissipation rate of the SGS field discloses the direction of energy transfer at the cut-off wavenumber. This term is defined by $\varepsilon_{SGS}=\boldsymbol{\tau}_{ij}\overline{\mathbf{S}}_{ij}$, where positive values imply forward scatter (or removal of turbulent energy from the resolved field) and negative values signify the reverse. Distribution of the real and model predictions of ε_{SGS} inside the cylinder immediate wake are shown in Fig. 9. In this figure, backscatter is denoted by the dashed contours. Qualitatively, both model forms predict the correct distribution of the dissipation rate. Highest values appear in the separated shear layers after transition to turbulence whereas negligible dissipation is predicted in the irrotational field and upstream boundary layers. The present sampling domain of the immediate wake gives 75% of positive real ε_{SGS} that averaged 0.043, while backscatter values averaged −0.005. Comparatively, both models predicted similar percentages, but again like the Reynolds stress comparisons discussed above, each form under-predicted the dissipation rate magnitudes throughout the immediate wake. The conservative model averages are 0.014 (58%) and −0.002 (42%) whereas the nonconservative form gave 0.012 (60%) and −0.003 (40%) for the forward scatter and backscatter of turbulence energy, respectively.

We can further evaluate the quantitative model performance by comparing the real and predicted SGS dissipation rate along the wake centerline as well as along the selected circumferential line ($r/D=1.17$). Figure 10 indicates both models grossly underpredicting the forward scatter characteristic inside the vortex formation regime. Notably, near the downstream cylinder walls the models predictions of ε_{SHS} were opposite of the true energy transfer.

VII Final Remarks

The evidence presented herein indicates that both forms of the curvilinear dynamic model showed high global correlation coefficients. This favorable statistic reflects primarily their performance outside the near wake region. Inside the near wake, local comparisons reveal neither form giving good predictions. Away from the downstream cylinder surface, the real normal SGS stress components were reasonably captured, but not the Reynolds shear stressed (an analogously the contravariant SGS stress components). Two factors contribute to this poor performance apart from understanding the model's fundamental capabilities and limitations. These factors center on the discrete test filter and the grid's cut-off wavenumber.

Because the box filter dampens the turbulent spectral energy over all wave numbers except the zeroth, the dynamic model coefficient is expected to embody resolved physics extracted from the energy range. Minimizing contributions from this range can be accomplished by using a higher-order test filter, but only in conjunction with the conservative form of the CDSM where filtering is done in the computational space. As proven earlier, the conservative form preserves commutation between the filter operation and the partial differentiation so that implementing a high-order test filter is permissible.

Approaching optimum success of the SGS model's performance is aided by knowing the smallest local resolved grid-scale relative to the energy spectra. Controlling this important factor was demonstrated after comparing profiles of the modeled contravariant SGS stresses with their real counterpart. Given the broadband range of cut-off wavenumbers by the cylinder wake gridding, we saw the CDSM performance degrading significantly when expected to mimic the energy-dominant scales of turbulence.

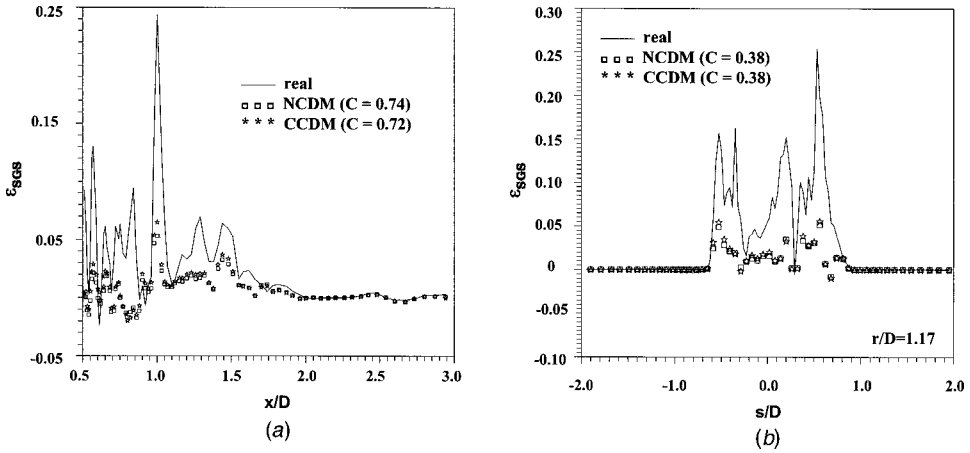

Fig. 10 Comparisons of the real and modeled SGS dissipation rates using the nonconservative and conservative forms of the curvilinear dynamic model; (*a*) along wake centerline (C indicates global correlation coefficient) and (*b*) along circumferential line r/D=1.17 in vortex formation regime

Keeping these conditions in mind, we can improve at least the near-wall SGS field predictions by coupling the dynamic model with a similarity relationship. For example, the similarity model conceived by Bardina et al. [17] correlates well with the real SGS field if the local stresses are consistent over variable filter widths. This observation can be realized in the vortex formation region of the cylinder near wake where the CDSM performance was poorest. For example, Armenio and Piomelli [5] mixed Bardina similarity with a dynamic eddy-viscosity relationship and transformed the resultant model to a curvilinear coordinate framework according to the alternate approach (Jordan [9]). By implementing Lagrangian averaging to evaluate the model coefficient, they demonstrated the similarity counterpart as the dominant contributor to the total SGS stress in a turbulent channel flow. Likewise, Liu et al. [18] showed that a dynamic version of the similarity SGS model mixed with the dynamic eddy viscosity relationship insures sufficient mean dissipation to stabilize the computation. For complex topologies, proper contraction of the two model coefficients would lead to a rather CPU intensive mixed form. But this particular formulation should perform well in local regions of the wake that are characterized by high rates-of-strain, and ease an attempt to grid the flow domain such that the finest resolved wavenumbers are maintained within the equilibrium range of turbulence.

Finally, knowing that both dynamic SGS eddy-viscosity models under-predict the dissipation rate (or even predict opposite sign), use of conservative high-order approximations (such as compact schemes) for the convective derivative is a noteworthy problem in an *a-posteriori* LES computation. Control of the model backscatter compounds this issue because these physics strongly correlate over long execution times. One should expect the excess energy to be redistributed throughout the flow domain including the inviscid regions, which can potentially destabilize the computation. Coupling the dynamic model with an upwind scheme seems like a reasonable remedy, but a careful balance must be insured between the spatial resolution and the dissipative truncation error to entertain useful model contributions.

Acknowledgments

This author gratefully acknowledges the support of the Office of Naval Research, Contract Number N0001400AF00002 (Dr. L. Patrick Purtell, Program Officer) and the In-house Laboratory Independent Research Program (Mr. R. Philips, Coordinator) at the naval Undersea Warfare Center Division Newport.

References

[1] O'Neil, J., and Meneveau, C., 1997, ''Subgrid-Scale Stresses and Their Modeling in a Turbulent Plane Wake,'' J. Fluid Mech. **349**, pp. 253–293.
[2] Ghosal, S., and Moin, P., 1995, ''The Basic Equations for the Large Eddy Simulation of Turbulent Flow in Complex Geometry,'' J. Comput. Phys. No. **118**, pp. 24–37.
[3] Beaudan, P., and Moin, P., 1994; ''Numerical Experiments on the Flow Past a Circular Cylinder at Sub-Critical Reynolds Number,'' Report No. TF-62, Stanford, University, Stanford, CA.
[4] Jordan, S. A., and Ragab, S. A., 1998, ''A Large-Eddy Simulation of the Near Wake of a Circular Cylinder,'' ASME J. Fluids Eng. **120**, pp. 243–252.
[5] Armenio, V., and Piomelli, U., 2000, ''A Lagrangian Mixed Subgrid-Scale Model in General Coordinates,'' Flow, Turbulence and Combustion, **65**, No. 1, pp. 51–81.
[6] Germano, M., Piomelli, U., Moin, P., and Cabot, W. H., 1991, ''A Dynamic Subgrid-Scale Eddy Viscosity Model,'' Phys. Fluids A **3**, pp. 1760–1765.
[7] Smagorinsky, J., 1963, ''General Circulation Experiments with the Primitive Equations, I. The Basic Experiment,'' Mon. Weather Rev. **91**, pp. 99–164.
[8] Piomelli, U., Cabot, W. H., Moin, P., and Lee, S., 1991, ''Subgrid-Scale Backscattering Turbulent and Transitional Flows,'' Phys. Fluids A **3**, pp. 1766–1772.
[9] Jordan, S. A., 1999, ''Large-Eddy Simulation Methodology in Generalized Curvilinear Coordinates,'' J. Comput. Phys. **148**, pp. 322–340.
[10] Lilly, D. K., 1992, ''A Proposed Modification of the Germano Subgrid-Scale Closure Method,'' Phys. Fluids A **4**, pp. 633–635.
[11] Jordan, S. A., and Ragab, S. A., 1996, ''An Efficient Fractional-Step Technique for Unsteady Incompressible Flows Using a Semi-Staggered Grid Strategy,'' J. Comput. Phys. **127**, pp. 218–225.
[12] Ong, L., and Wallace, J., 1996, ''The Velocity Field of the Turbulent Very Near Wake of a Circular Cylinder,'' Exp. Fluids **40**, pp. 441–453.
[13] Mansy, H., Yang, P., and Williams, D. R., 1990, ''Quantitative Measurements of the Three-dimensional Structures in the Wake of a Circular Cylinder,'' J. Fluid Mech. **270**, pp. 277–296.
[14] Choi, H., and Moin, P., 1994, ''Effects of the Computational Time Step on Numerical Solutions of Turbulent Flow,'' J. Comput. Phys. **113**, pp. 1–4.
[15] Uberoi, M. S., and Freymuth, P., 1969, ''Spectra of Turbulence in Wakes Behind Circular Cylinders,'' Phys. Fluids **12**, No. 7, pp. 1359–1363.
[16] Bloor, M. S., 1964, ''The Transition of Turbulence in the Wake of a Circular Cylinder,'' J. Fluid Mech. **19**, pp. 290–304.
[17] Bardina, J., Ferziger, J., and Reynolds, W. C., 1980, ''Improved Subgrid-Scale Model for Large-Eddy Simulation,'' AIAA Paper 80-1357.
[18] Liu, S., Meneveau, C., and Katz, J., 1995, ''Experimental Study of Similarity Subgrid-Scale Models of Turbulence in the Far-Field of a Jet,'' Appl. Sci. Rev. **54**, pp. 177–188.

Mingde Su
Senior Post-Doctoral Fellow

Qingyan Chen
Associate Professor
e-mail: qchen@mit.edu

Building Technology Program, Massachusetts Institute of Technology, Cambridge, MA 02139-4307

Che-Ming Chiang
Professor,
Department of Architecture, National Cheng-Kung University, Tainan, 701, Taiwan

Comparison of Different Subgrid-Scale Models of Large Eddy Simulation for Indoor Airflow Modeling

The Smagorinsky subgrid-scale model, a dynamic subgrid-scale model, and a stimulated subgrid-scale model have been used in a large eddy simulation (LES) program to compute airflow in a room. A fast Fourier transformation (FFT) method and a conventional iteration method were used in solving the Poisson equation. The predicted distributions of indoor air velocity, temperature, and contaminant concentrations show that the three subgrid-scale models can produce acceptable results for indoor environment design. The dynamic and stimulated models performed slightly better than the Smagorinsky model. The use of FFT can significantly reduce the computing time. LES is a tool of the next generation of indoor air distribution design. [DOI: 10.1115/1.1378294]

1 Introduction

Computational Fluid Dynamics (CFD) can be used to determine turbulent fluid flow, heat transfer, and the transport of chemical species for indoor environment design, allowing for the determination of thermal comfort parameters and indoor air quality (Chen [1]). The numerical simulation of turbulent flow in an indoor space can be divided into three types: direct numerical simulation (DNS), Reynolds Averaged Navier-Stokes (RANS) equation modeling, and Large Eddy Simulation (LES).

DNS solves the Navier-Stokes equations for flow motion numerically without using a turbulence model, producing a very reliable simulation. Turbulent flow consists of vortices with various scales, where the ratio between the largest scale and the smallest scale is approximately equal to $Re^{3/4}$ (Lesieur [2]). In order to describe the various scales of the vortices, the grid number used to solve turbulent flow should be larger than $Re^{9/4}$. Since the Reynolds number for a typical indoor airflow is 10^4, the grid number required is on the order of one billion. Currently, a supercomputer is capable of handling a grid number of up to 10^8. If such a large-capacity computer necessary for modeling indoor airflow were to become available, the computing time required to reach a useful solution would be a few months. It is therefore impractical at the present time to use DNS as a tool for indoor environment design.

Most of the current indoor airflow designs solve the RANS equations, because this numerical simulation can be performed on a PC. Since the RANS equations require a coarse grid system and calculate averaged flow properties (air velocity, temperature, and species concentrations, etc.), the computing time requires is a only a few hours for most indoor environment designs. However, the RANS equations contain unknown Reynolds stresses that have to be modeled by a turbulence model. At present, no generic turbulence models are available. Most of the developed turbulence models, such as the mixing length theory, one-equation models, two-equations models, and second moment models, may perform reasonably well in one case, but poorly in another [1]. Therefore, the accuracy of the numerical results is not guaranteed, and the designers have difficulties in choosing a suitable turbulence model. In addition, RANS equation modeling cannot provide instantaneous information concerning turbulent flows, which is important for thermal comfort design. Therefore, RANS modeling has severe limitations in building environmental design.

LES divides flow motion into two parts: large-scale and small-scale motions. LES directly calculates large-scale motions. Small-scale motions, with sizes normally smaller than the numerical grid size, are modeled with subgrid scale models. When the grid size is sufficiently small, the impact from the subgrid scale models on the flow motion will be small. Furthermore, the subgrid scale models will become general, because the turbulent flow at very small scales is nearly isotropic. Therefore, the subgrid scale models generally contain fewer empirical coefficients and artificial factors than those used in the turbulence models of the RANS equations. Since the flow information at small scales may not be important for engineering applications, LES is becoming an important and powerful tool in studying turbulence (Piomelli [3], Lesieur and Metais [4]). However, questions still remain as to how accurate LES is, and how much computing time LES requires for indoor environment design. The accuracy is related to the approximations used in the subgrid scale models, while the computing time is influenced by the numerical technique used in solving the transport equations.

Various subgrid scale models have been developed in the last twenty years. Most of them are eddy viscosity models, which use the Boussinesq hypothesis to calculate eddy viscosity. The most popular models used in engineering can be mainly divided into the Smagorinsky model and the dynamic models. Our study focuses on these two types of eddy-viscosity subgrid scale models as well as on one noneddy viscosity model. The Smagorinsky model uses a constant eddy viscosity coefficient for the entire flow domain. This model is not suitable for complex flows, where the coefficient may vary over time and location. The dynamic models calculate the eddy viscosity coefficient according to local flow characteristics. The dynamic models are more appropriate than the Smagorinsky model. On the other hand, Shah and Ferziger [5] developed a noneddy viscosity model, the stimulated small-scale subgrid (SSSS) model, which calculates small-scale motion by using a stimulated method based on the operation. Since this model has a strong mathematical and physical background, it deserves further attention. However, performing LES needs more demanding time than RANS modeling.

Among the computing time used by LES, solving the Poisson equation with the conventional iteration method would consume 90 percent of the time. In order to reduce the computing cost, the

Contributed by the Fluids Engineering Division for publication in the JOURNAL OF FLUIDS ENGINEERING. Manuscript received by the Fluids Engineering Division October 27, 2000; revised manuscript received March 15, 2001. Associate Editor: G. Karniadakis.

fast Fourier transformation (FFT) method is used. In the present paper, the FFT method is used for both periodic and Neumann boundary conditions.

The effort of this investigation is to systematically examine the performance of the Smagorinsky subgrid scale (SSGS) model (Smagorinsky [6]), the Dynamic Sub-Grid Scale (DSGS) model (Germano et al. [7]), and the SSSS model for indoor airflow simulation. This investigation also compares the computing time required by the conventional iteration method and by the FFT method to solve the Poisson equation.

2 Governing Equations and Subgrid Scale Models

Using a spatial filter, LES divides turbulence flow into large-scale and small-scale (grid-scale) motions. The filtered flow parameters for large-scale motions can be obtained by solving the following filtered Navier-Stokes equations:

$$\left.\begin{aligned}
&\frac{\partial \overline{v_i}}{\partial x_i}=0\\
&\frac{\partial \overline{v_i}}{\partial t}+\frac{\partial \overline{v_i}\,\overline{v_j}}{\partial x_j}=-\frac{1}{\rho}\frac{\partial p}{\partial x_i}+\nu\frac{\partial^2 \overline{v_i}}{\partial x_i \partial x_j}-\frac{\partial \tau_{ij}}{\partial x_i}\\
&\frac{\partial \overline{T}}{\partial t}+\frac{\partial \overline{T}\,\overline{v_i}}{\partial x_i}=\kappa\frac{\partial^2 \overline{T}}{\partial x_i \partial x_j}-\frac{\partial T_{Tj}}{\partial x_i}\\
&\frac{\partial \overline{C}}{\partial t}+\frac{\partial \overline{C}\,\overline{v_i}}{\partial x_i}=\kappa_c\frac{\partial^2 \overline{C}}{\partial x_i \partial x_j}-\frac{\partial D_{Cj}}{\partial x_i}+q_c
\end{aligned}\right\} \tag{1}$$

where

$$\tau_{ij}=\overline{v_i v_j}-\overline{v_i}\,\overline{v_j} \tag{2}$$

$$T_{Ti}=\overline{T v_i}-\overline{T}\,\overline{v_i} \tag{3}$$

$$D_{Ci}=\overline{C v_i}-\overline{C}\,\overline{v_i} \tag{4}$$

The variables, τ_{ij}, T_{Tj}, and D_{Cj}, are unknown, and should be calculated by subgrid scale models. This study uses three subgrid scale models, the SSGS, DSGS, and SSSS models, in order to compare their performance for indoor airflow simulation. The following section discusses how τ_{ij} is modeled. The same concept can be applied to T_{Tj}, and D_{Cj}.

2.1 Eddy-Viscosity Models. The SSGS and DSGS models are eddy viscosity models that have a common form:

$$\tau_{ij}-\frac{\delta_{ij}}{3}\tau_{kk}=-2\nu_T\overline{S}_{ij} \quad \text{with} \quad S_{ij}=\frac{1}{2}(\overline{v}_{i,j}+\overline{v}_{j,i}) \tag{5}$$

The eddy-viscosity models are used to determine the eddy-viscosity, ν_T. Using the equilibrium assumption (that the turbulence in a grid with small scale eddies is in equilibrium, and the dissipated energy is implemented from the large scale eddies), the following algebraic model can be used to calculate the eddy-viscosity:

$$\nu_T=C_M\Delta^2|\overline{S}|\overline{S}_{ij}, \quad |\overline{S}|=(2\overline{S}_{ij}\overline{S}_{ij})^{1/2} \tag{6}$$

where Δ is the grid scale and is equal to the cubic root of a cell volume, if the grid cell is anisotropic. C_M is a parameter in the model. The SSGS and DSGS models are separately discussed below.

(a) Smagorinsky subgrid-scale model (SSGS): The widely used Smagorinsky model is the simplest subgrid-scale model. The model uses $C_M=C_s^2$, where C_s is the Smagorinsky coefficient. Normally, C_s is a constant in the range of 0.12–0.2. This coefficient must be decreased (Piomelli et al. [8]) for shear flows (e.g., flows near solid boundaries or transitional flows) by using the van Driest damping function or the intermittency function.

(b) Dynamic subgrid-scale model (DSGS): Although the ad hoc modification on the Smagorinsky coefficient can be used for transitional and turbulent flows, Germano et al. [7] concluded that it is impossible to find a single, universal constant for different flows. In some cases, the ad hoc modifications are far from desirable. In addition, the Smagorinsky model cannot account for the energy transfer from small-scale eddies to large-scale eddies (backscatter), which can be significant in many flows. The development of the DSGS model reflects significant progress in the subgrid-scale modeling of nonequilibrium flows. The DSGS model calculates the model coefficient from the energy of the smallest resolved scale, rather than by setting a priori parameters like the Smagorinsky model.

The DSGS model defines a grid filtering scale, $\overline{\Delta}$, and a test filtering scale, $\widetilde{\Delta}$ (Germano et al. [7]). Two filtering functions, $\overline{G}$ and $\widetilde{G}$, are used over $\overline{\Delta}$ and $\widetilde{\Delta}$, respectively. By applying $\widetilde{\overline{G}}$ $(=\widetilde{G}\overline{G})$ to the Navier-Stokes equations, the subgrid scale stresses on the test filter can be obtained as:

$$T_{ij}=\widetilde{\overline{v_i v_j}}-\widetilde{\overline{v_i}}\,\widetilde{\overline{v_j}} \tag{7}$$

The first term on the right side of Eq. (7) cannot be directly determined, like the one in Eq. (2). However, by applying the basic assumptions of eddy viscosity models, the following is true:

$$\begin{aligned}
&\tau_{ij}=-\frac{\delta_{ij}}{3}\tau_{kk}\cong m_{ij}=-2C\overline{\Delta}^2|\overline{S}|\overline{S}_{ij}\\
&T_{ij}-\frac{\delta_{ij}}{3}T_{kk}\cong M_{ij}=-2C\widetilde{\Delta}^2|\widetilde{\overline{S}}|\widetilde{\overline{S}}_{ij}
\end{aligned} \tag{8}$$

where C is the same for both filters. As a result, the following is obtained:

$$L_{ij}\overline{S}_{ij}\equiv(T_{ij}-\widetilde{\tau}_{ij})\overline{S}_{ij}=-2C(\widetilde{\Delta}^2|\widetilde{\overline{S}}|\widetilde{\overline{S}}_{ij}\overline{S}_{ij}-\overline{\Delta}^2|\overline{S}|\overline{S}_{ij}\overline{S}_{ij}) \tag{9}$$

Averaging the equation along a homogeneous or periodical direction of the flow produces

$$C=-\frac{1}{2}\frac{\langle L_{ij}\overline{S}_{ij}\rangle}{\langle\widetilde{\Delta}^2|\widetilde{\overline{S}}|\widetilde{\overline{S}}_{ij}\overline{S}_{ij}-\overline{\Delta}^2|\overline{S}|\overline{S}_{ij}\overline{S}_{ij}\rangle} \tag{10}$$

The symbol $\langle\ \rangle$ stands for an average over the homogeneous or periodical direction. Therefore, the model is only suitable for homogeneous turbulence. Lilly [9] suggested that the coefficient can be determined by the least square method. This method uses the following equation as an object function:

$$Q=(2CM_{ij}-(\widetilde{\Delta}^2|\widetilde{\overline{S}}|\widetilde{\overline{S}}_{ij}\overline{S}_{ij}-\overline{\Delta}^2|\overline{S}|\overline{S}_{ij}\overline{S}_{ij}))^2\equiv(2CM_{ij}-L_{ij})^2 \tag{11}$$

From this, the optimal coefficient becomes

$$C=\frac{L_{ij}M_{ij}}{2M_{ij}M_{ij}} \tag{12}$$

The DSGS model can be applied to various turbulent flows. For better numerical stability, it is necessary to smooth the C distribution (Zhang and Chen [10]), and set C to be greater than zero. Since the backscatter can only be described with a negative C, there is a contradiction between the backscatter and the numerical stability.

2.2 Noneddy Viscosity Model. By filtering, LES divides unfiltered flow parameters, such as velocity, pressure, temperature, and species concentrations, into resolved (large-scale) parameters and unresolved (small-scale) parameters. A noneddy viscosity model attempts to obtain the unresolved parameters by using mathematical and/or physical methods based on statistical theory or DNS data. With both the large-scale and small-scale velocities known, the Reynolds stress can be calculated.

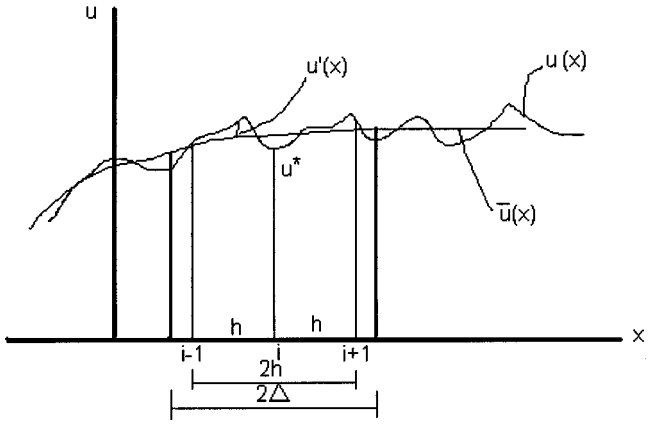

Fig. 1 Relationship between the filtered and unfiltered velocities

A simple method used to generate the unfiltered parameter distribution is the Taylor expansion series. By letting u^* stand for $u(x)$ at x_i, and $u'(x)=u(x)-\overline{u}(x)$ (refer to Fig. 1), the Taylor expansion produces

$$u(x)=u_i^*+(x-x_i)\left(\frac{du}{dx}\right)_i^*+\frac{(x-x_i)^2}{2}\left(\frac{d^2u}{dx^2}\right)_i^*+\cdots\cdots \quad (13)$$

By neglecting the third-order and higher-order terms and replacing the derivatives with central differencing ones, this equation becomes

$$u(x)=u_i^*+(x-x_i)\frac{u_{i+1}^*-u_{i-1}^*}{2h}+\frac{(x-x_i)^2}{2}\frac{u_{i+1}^*-2u_i^*+u_{i-1}^*}{h^2} \quad (14)$$

By filtering $u(x)$ over 2Δ through the use of a box-filter, the filtered velocity is:

$$\overline{u}_i=u_i^*+\frac{\Delta^2}{6}\frac{u_{i+1}^*-2u_i^*+u_{i-1}^*}{h^2} \quad (15)$$

Then, by letting $\Delta=h/2$,

$$\overline{u}_i=\frac{u_{i+1}^*}{24}+\frac{11u_i^*}{12}+\frac{u_{i-1}^*}{24} \quad (16)$$

For a nonuniform grid distribution, this equation becomes

$$\overline{u}_i=au_{i-1}^*+bu_i^*+cu_{i+1}^* \quad (17)$$

where

$$a=\frac{h_i^2(m^2-3m)+h_ih_{i-1}(3m-m^2)+h_{i-1}^2m^2}{12h_{i-1}(h_i+h_{i-1})},\quad m=\frac{\Delta_i+\Delta_{i-1}}{h_i+h_{i-1}}$$

$$b=1-a-c \quad (18)$$

$$c=\frac{h_i^2m^2+h_ih_{i-1}(3m-m^2)+h_{i-1}^2(m^2-3m)}{12h_{i-1}(h_i+h_{i-1})}$$

with $h_i=x_{i+1}-x_i$. This can then be rewritten in a simple operator form:

$$L_x(u_i^*)=\overline{u}_i \quad (19)$$

For a three-dimensional case,

$$L(u_{i,j,k}^*)=\overline{u}_{i,j,k}\quad L=L_xL_yL_z \quad (20)$$

The Reynolds stresses can then be calculated from

$$\tau_{ij}=\overline{u_i^*u_j^*}-\overline{u_i^*}\,\overline{u_j^*} \quad (21)$$

This model is identical to the SSSS model developed by Shah and Ferziger [5]. This paper has mathematically explained the SSSS model. In addition, T_{Ti} and D_{Ci} can be determined with the same method. The procedure to calculate the Reynolds stresses and other second order correlations are as follows (let f and g be two variables where f can be a velocity component [u, v, or w] while g can be a velocity component, temperature, or species concentration):

(a) Calculate f^* and g^* from $\overline{f}$ and $\overline{g}$, respectively, at all interior cells by using Eq. (20). This procedure solves a series of tridiagonal algebraic equation systems in the x-, y- and z-directions. Since, according to Eq. (18), the coefficients in every row satisfy $a+b+c=1$, the tridiagonal coefficient matrix of the operator L_x is nonsingular, and there are no instability problems.

(b) Determine the product f^*g^* at all the interior cells.

(c) Computer $\overline{f^*g^*}$ by using Eq. (17). This is a series of simple algorithm operations.

(d) Calculate $\overline{f^*g^*}-\overline{f^*}\,\overline{g^*}$ in order to obtain the Reynolds stresses and other correlations.

In the implementation of the SSSS model, we solve a series of tridiagonal equation systems and complete simple arithmetic operations. It does not demand more computing time than the DSGS models.

3 Numerical Method

3.1 Difference Scheme in Time and Space. The present investigation studied indoor airflows, which have relatively low Reynolds numbers. The numerical oscillation or instability is not significant. However, this oscillation or instability can be problematic when simulating airflow around buildings. A solution to avoid this problem is the use of the third order upwind scheme for the convection terms. Since numerical instability was not significant for this indoor airflow study, the second order Adams-Bashforth scheme was used.

3.2 Projection Method. The equations that need to be solved numerically for indoor airflow are the continuity, momentum, energy, and species concentration equations. The indoor air can be considered to be incompressible. The buoyancy resulting from air density variations produced by a temperature difference is added to the momentum equation via the Boussinesq assumption. The continuity equation of incompressible flow has no derivative term over time and cannot be directly solved simultaneously with the momentum equation. In the projection method (Chorin [11]), however, the continuity and momentum equations can be related through pressure. The projection method is described below.

The filtered Navier-Stokes equations are written in following form:

$$\left.\begin{aligned}\frac{\partial\overline{v_i}}{\partial x_i}&=0\\ \frac{\partial\overline{v_i}}{\partial t}+\overline{v_j}\frac{\partial\overline{v_i}}{\partial x_j}&=-\frac{1}{\rho}\frac{\partial p}{\partial x_i}+\frac{\partial}{\partial x_j}\left(\nu\frac{\partial\overline{v_i}}{\partial x_j}+\tau_{ij}\right)\end{aligned}\right\} \quad (22)$$

The projection method solves the momentum equation without the pressure term:

$$\frac{\partial\overline{v_i^*}}{\partial t}+\overline{v_j^*}\frac{\partial\overline{v_i^*}}{\partial x_j}=\frac{\partial}{\partial x_j}\left(\nu\frac{\partial\overline{v_i^*}}{\partial x_j}+\tau_{ij}\right) \quad (23)$$

where $\overline{v_i^*}$ is the predicted velocity. The predicted velocity does not normally satisfy the continuity equation. However, by using a pressure correction, the predicted velocity can be modified to obtain the true velocity. A Poisson equation of pressure can be established by subtracting Eq. (24) from the momentum equation,

Eq. (22). Then, by taking the divergence of both sides of the obtained equation, and by considering the continuity equation, we obtain a Poisson equation of pressure:

$$\frac{1}{\Delta t}\frac{\partial \overline{v_i}}{\partial x_i} = -\frac{1}{\rho}\frac{\partial^2 p}{\partial x_i \partial x_i} \tag{24}$$

By solving this Poisson equation, we obtain the pressure p, which is used to modify the predicted velocity using the following equation:

$$\overline{v_i}^{n+1} = \overline{v_i}^{*} - \frac{1}{\rho}\Delta t \frac{\partial p}{\partial x_i} \tag{25}$$

This modified velocity now satisfies the continuity equation, and is therefore the true velocity.

When applying the Fourier transformation to the Navier-Stokes equations, the pressure term is translated in the direction normal to the velocity plane. Therefore, ignoring the pressure term in the physical space is equivalent to projecting the Navier-Stokes equations onto the velocity plane in the spectral space. This is the reason this method is called the projection method (Lesieur [2]).

3.3 Differencing Scheme. In order to numerically solve the partial differential equations, the present study uses the staggered grid system and the second-order central-differencing scheme. For the time term, this investigation uses the second order Adams-Bashforth scheme.

3.4 Poisson Equation and Its Solvers. If the Poisson equation were to be solved by the iteration method, it would consume about 90 percent of the overall computing time. Therefore, it is very important to develop an efficient solver for the Poisson equation. The present study uses FFT to improve the efficiency, accuracy, and speed of solving the Poisson equation.

FFT is used in both periodic and Neumann boundary conditions. In the case of Neumann boundary conditions, the Gauss-Chebyshev transformation is found to be acceptable. After reorganizing the coefficients (Su [12]), FFT can also be used in place of the discrete Gauss-Chebyshev transformations without decreasing the accuracy and efficiency. In the presented numerical examples, a nonuniform grid system is allowed in only one direction when using the FFT method to solve the Poisson equation of pressure.

Note that if all boundary conditions for the pressure are either periodic or homogeneous Neumann ones, the Poisson equation will have either no solution, or multiple solutions due to the singularity of the differencing-equation system. To ensure a unique solution, the sum of $q_{i,j,k}$ in the differencing equations over $i=1,2,\ldots,$ IM, $j=1,2,\ldots,$ JM, and $k=1,2,\ldots,$ KM should be zero (or should have a numerical error less than 10^{-6}). The pressure at a reference point or the average pressure in the whole flow domain should be set to zero.

When the flow domain contains obstacles in a room, such as occupants, computers, and furniture, the above-mentioned methods cannot be directly used due to the no-flux conditions on the surfaces of these obstacles. Therefore, it is necessary to ensure that the normal velocity at the surfaces, v_n, be equal to zero. The present study introduces an additional term, $-\beta v_n - \alpha v_n|v_n|$, into the momentum equation at the surfaces (McGrattan et al. [13], Peskin [14], Goldstein et al. [15]):

$$\frac{\partial v_n}{\partial t} + \text{Conv} = -\frac{1}{\rho}\frac{\partial p}{\partial n} + \text{Diss} - \beta v_n - \alpha v_n|v_n| \tag{26}$$

Note that $\partial v_n/\partial t = -\beta v_n - \alpha v_n|v_n|$ is an ordinary differential equation. When solving this ordinary differential equation, v_n will quickly approach a small value if $\beta>0$ and $\alpha>0$ (this study uses $0.8/\Delta t$ for β and 10 for α). Therefore, the additional term seems to be a damping term and Eq. (26) can be approximated as:

$$\text{Conv} = -\frac{1}{\rho}\frac{\partial p}{\partial n} + \text{Diss} \tag{27}$$

This approach is used at the obstacle surfaces for all three components of velocity. In fact, this method exploits the relatively small changes in pressure from one time step to the next in order to enforce the no-flux condition on the obstacle surfaces, because the pressure at the current time step is unknown until the Poisson equation is solved.

Our experience shows that v_n changes from 10^{-4} to 10^{-6} very quickly, and remains unchanged afterwards. Since v_n is normally several orders smaller than the mean velocity in the flow domain, v_n can be considered to be zero, which implies a successful simulation of a solid surface. This approximation method does not need to specify pressure boundary conditions on an obstacle surface, and the corresponding grids can be treated as a normal internal one. Therefore, the Poisson equation can still be solved by using the above-mentioned FFT algorithm.

4 Results

The above-mentioned subgrid scale models and numerical algorithms have been used to study indoor airflow. Indoor airflow consists of forced convection, natural convection, and mixed convection (which is a combination of forced and natural convection). This section will examine the performance of the subgrid scale models in predicting these three convection flows in a room.

4.1 Forced Convection. This study used forced convection flow in a room with measured air velocity profiles from Restivo [16]. The room geometry is shown in Fig. 2, where $H=3$ m. The velocity at the inlet was uniform and equal to 0.455 m/s. The flow Reynolds number was 5000, based on the inlet height and air velocity. The inlet height was 0.168 m. The air velocity was measured by a laser Doppler anemometer.

The computations used a uniform air velocity profile at the inlet, and a zero gradient condition for the air velocity at the outlet. Our computation applied a uniform mean velocity profile using six points across the jet. This was rather inconsistent with

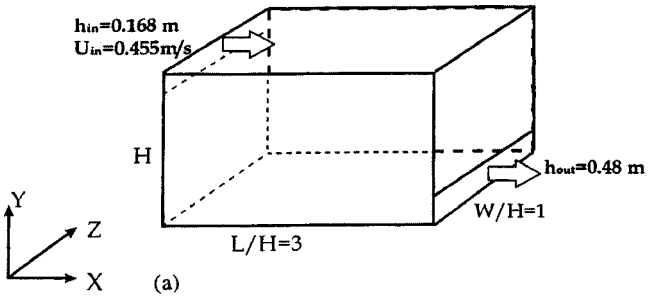

Fig. 2 The schematic of the room with forced convection

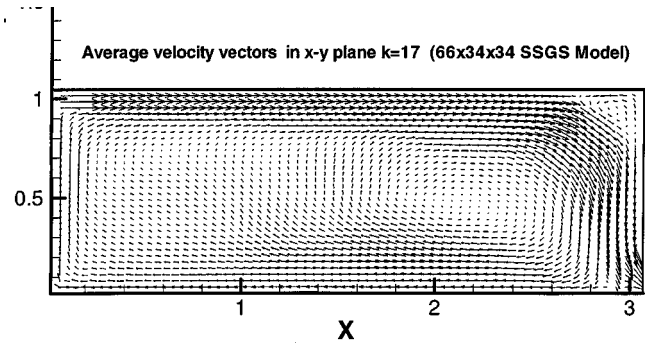

Fig. 3 Mean airflow pattern in the middle plane of the room

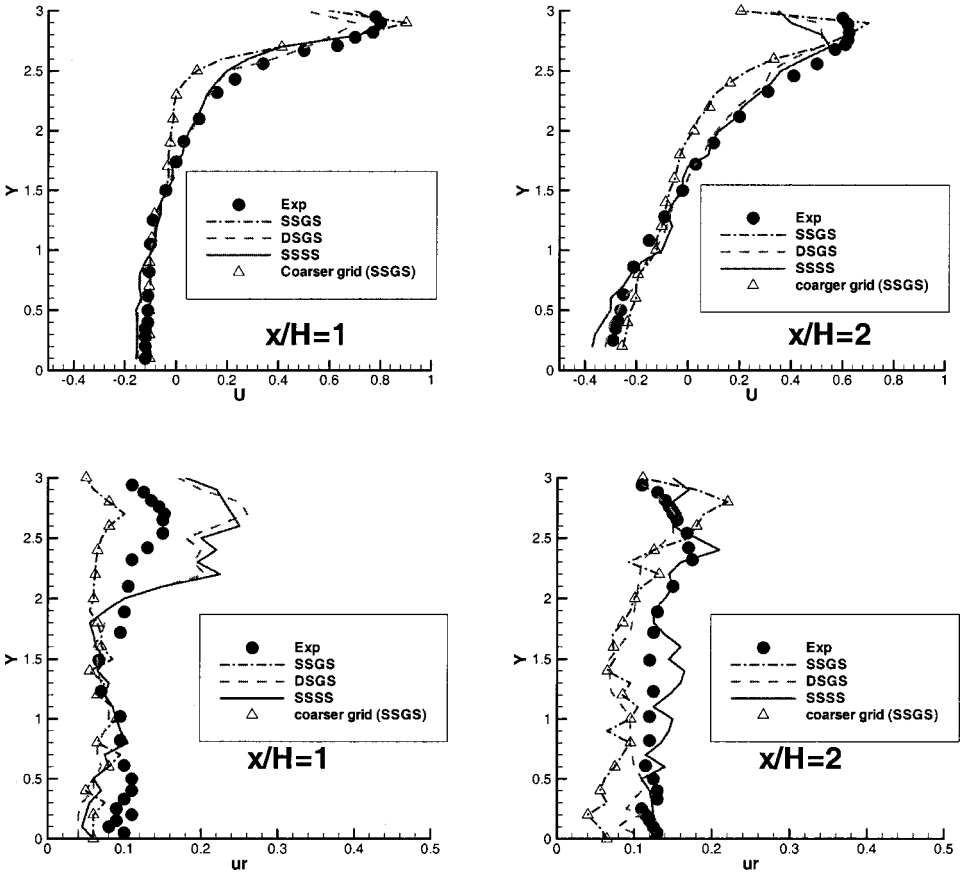

Fig. 4 Comparison of the computed mean and fluctuation velocity profiles with the experimental data at x=H and 2H sections

the experimental data. The experiment measured a small perturbation, which was neglected in the computation. All of these considerations were added in the revision. The log-law wall function was used for the walls (Wilcox [17]). The computational meshes employed were $66\times18\times34$ and $66\times34\times34$ corresponding to the length (x), height (y), and width (z) directions. The grid distribution was uniform in the x and z directions, and nonuniform in the y direction. The numerical results show a very small difference between the two meshes as compared in Fig. 4. The results in this paper are from the finer mesh, for $t=400$ to 800 s. Figure 3 shows the computed airflow pattern. Aside from the large vortex in the center of the room, there was a small eddy in the upper right corner, which was observed in the experiment.

The dimensionless time step used in this calculation was $\Delta t=0.01$ s, which was much larger than the 0.002 s time step normally used for the iteration method in solving the Poisson equation. Therefore, the high accuracy of the FFT algorithm greatly improved the numerical stability.

Figure 4 compares the computed mean dimensionless air velocity ($U=u/u_{in}$) and the computed dimensionless velocity fluctuation (u_r = [mean square-root fluctuate velocity in x direction] $/u_{in}$) with the corresponding experimental data from the middle section of the room at both $x=H$ and $2H$. The Smagorinsky coefficient used in the SSGS model was 0.16, which was recommended for indoor airflow by Murakami [18]. The results show that the DSGS and SSSS models performed slightly better than the SSGS model in calculating the mean air velocity. The underprediction by the SSGS model may be attributed to the large viscosity computed. The calculated air velocities by the DSGS and the SSSS models are almost identical. The DSGS model calculated the turbulence viscosity coefficient according to the local flow type, and the SSSS model calculated the quasi-Reynolds stress by using the stimulated small-scale velocity. Therefore, these two models described the flow better than the SSGS model. For velocity fluctuations, none of the three models produced satisfactory results. The SSGS model generally under-predicted the velocity fluctuation, while the other two models over-predicted this velocity fluctuation in the area near the air inlet. The discrepancies among the results of the three models are large in the area where there is a large gradient in mean velocity. The SSSS model computed the small-scale velocity according to the mean velocity gradient. The larger the mean velocity gradient is, the higher the stimulated small-scale velocity becomes. Therefore, the velocity fluctuation was also high.

Table 1 Computing time needed by different numerical schemes

Computer	Alpha Workstation		Cray T90 (one Processor)	Cray T90 (14 Processors)
Time steps	100	250	60,000	
Grid number	130×34×34	130×34×34	130×34×34	130×34×34
Conventional iteration code	796 s	1800 s	160 h	
FFT code	240 s	600 s	16 h	1.5 h

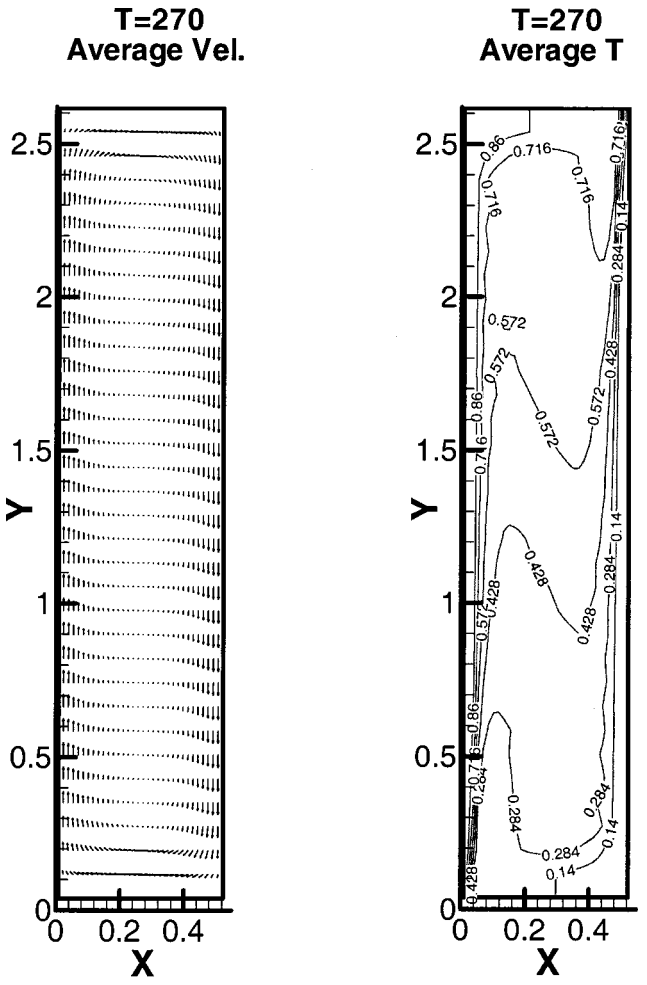

Fig. 5 The mean airflow pattern and dimensionless air temperature distribution in the middle section of the cavity. ($T=(t-t_c)/(t_h-t_c)$, where t_h and t_c are the temperatures of the hot wall and cold wall, respectively.)

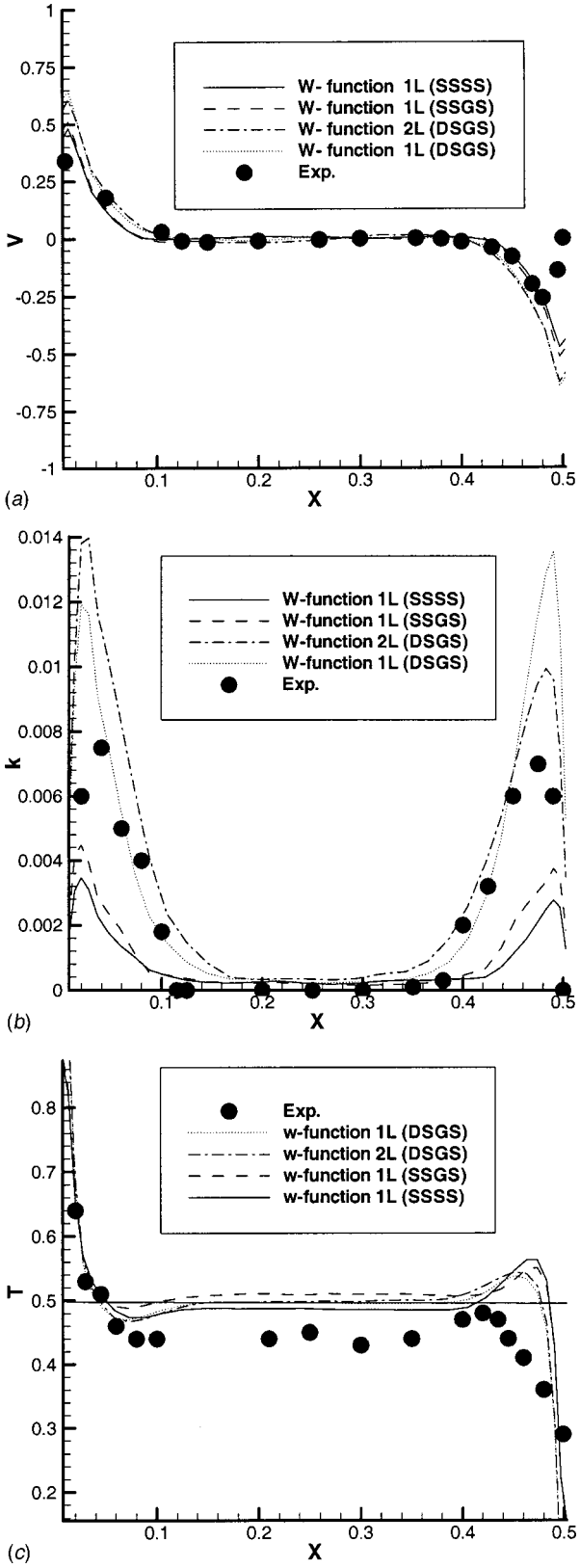

Fig. 6 The computed mean profiles of (*a*) mean air velocity, (*b*) turbulent kinetic energy, and (*c*) dimensionless temperature in the mid-height of the cavity and the corresponding experimental data

Table 1 compares the computational time used by the conventional iteration method with the time used by the FFT method for the case with a total grid number of $130\times34\times34$. These computations were carried out on an Alpha workstation and a Cray-T90 supercomputer. The results produced from the Cray supercomputer show that the FFT method is ten times faster than the iteration method. When comparing the FFT method results between the Alpha workstation and the Cray supercomputer, the computing time per time step per grid cell was 2×10^{-5} s on the workstation, and 8×10^{-6} s on the single-processor supercomputer. However, for the iteration method results, it was 6×10^{-4} s on the workstation, and 8×10^{-5} s on the supercomputer. Since FFT uses double precision on the workstation, the computing speed of the FFT method is only three times faster than the iteration method. Since double precision is default on the supercomputer, computation with the FFT can reduce the computing time more significantly than that with the iteration method.

4.2 Natural Convection. This investigation also studied natural convection flow in a cavity, as shown in Fig. 5. Cheesewright et al. [19] measured the air velocity, temperature, and turbulent energy in the cavity. Their experimental data were used to compare with our numerical results. The cavity was 2.5 m high, 0.5 m wide, and 0.5 m deep. The left wall was heated to 68.0°C, and the right wall was kept at 22.2°C. All the other walls were insulated. Cheesewright et al. [19] noted that the cavity was not well insulated.

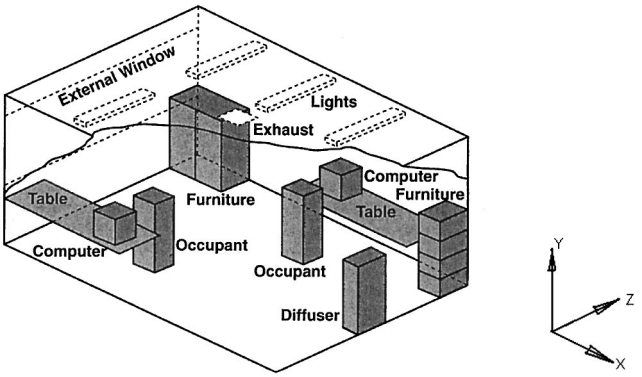

Fig. 7 The schematic of a two-person office with displacement ventilation

The computations used only one nonuniform grid distribution in the *x*-direction. This nonuniform grid distribution is very important in obtaining the correct results, due to the sharp temperature gradient near the hot and cold walls. However, a limited computer memory prevented the use of a uniform grid system in *x*-direction since this would require many grids. The smallest grid size close to the walls in the *x*-direction was only 0.005 m. The *y*- and *z*-directions used uniform grids, since the air velocity, temperature, and turbulent kinetic energy varied only slightly in these two directions, as shown in Fig. 5. Periodic boundary conditions were applied in the *z*-direction. In addition, the computation used the Boussinesq approximation to consider the buoyancy effect. Surprisingly, two grid meshes ($34\times34\times18$ and $66\times66\times34$) used in the computations yielded the same results. Figure 5 shows the computed mean airflow pattern and air temperature distribution in the middle section of the cavity, using the finer grid mesh. The air temperature distribution is given for the dimensionless temperature, T, which is defined as $T=(t-t_c)/(t_h-t_c)$. In order to identify the impact of the grid scale and the wall function on the mean flow distribution, this investigation used two different wall functions: the one-layer log-law wall function (1L), and the two-layer wall function (2L) from Wilcox [17]. Our results do not show any significant difference between these two wall functions.

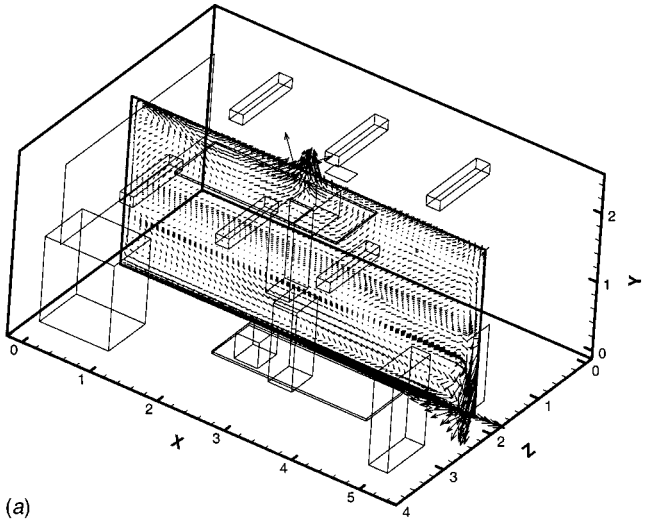

Fig. 8 The (*a*) mean and (*b*) instantaneous airflow patterns in the middle section of the office

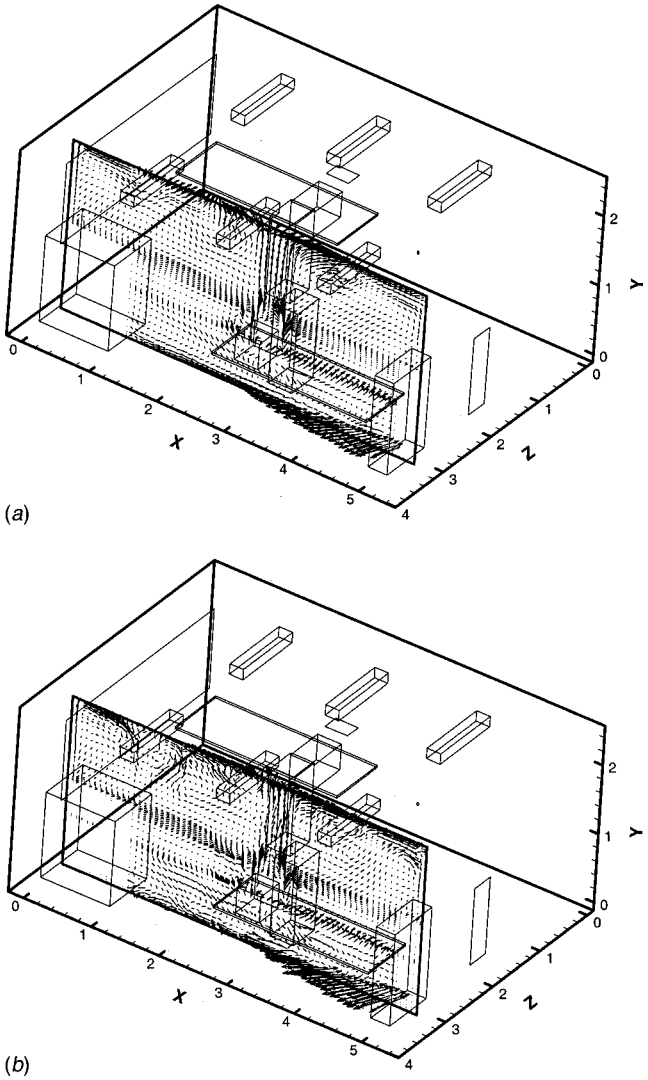

Fig. 9 The (*a*) mean and (*b*) instantaneous airflow patterns at the section near the side wall of the office

Figure 6 compares the computed mean profiles of air velocity, turbulent kinetic energy, and air temperature with the measured data at the mid-height of the cavity. In Fig. 6, the units of velocity and turbulent kinetic energy are m/s and m^2/s^2, respectively. In the LES simulations with the DSGS model, both wall functions were used.

The results confirm that the three models produced similar mean air velocity and temperature profiles. These results show

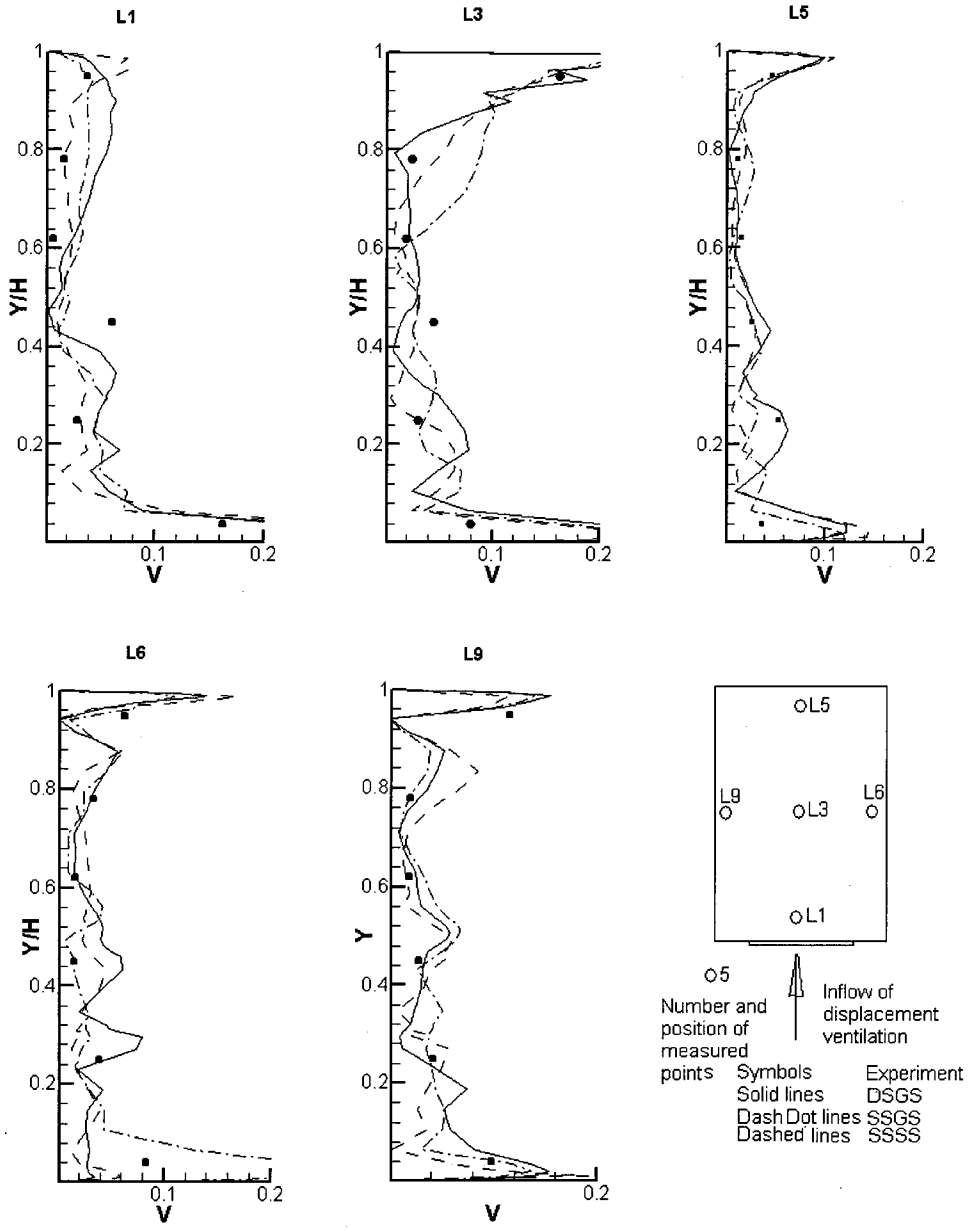

Fig. 10 Comparison of the computed mean air velocity profiles with the experimental data at five different locations in the room (m/s)

that the wall functions had a small influence on the profiles of mean temperature and velocity. The notable difference was found in the vicinity of the walls, seen in the velocity and turbulent kinetic energy profiles of Fig. 6. The mean velocity values calculated in the vicinity of the hot and cold walls were much greater than the measured data, although the grid scale was very small, and the computations used both wall functions. It seems that there are some unknown reasons influencing the values of velocity in this region. Further investigation is therefore necessary. In addition, Fig. 6(*b*) shows that the turbulent kinetic energy values obtained by the DSGS model in the vicinity of the wall were greater than the measured data. However, these values were closer to the measured data in all other regions than those results obtained by the SSGS and SSSS models. From these results, it can be concluded that the damping of the DSGS model is smaller than that of the SSGS and SSSS models. Therefore, the results of the DSGS model were the best among the three subgrid scale models.

The computed mean air temperature was much higher than the experimental data. The reason for this discrepancy is that the poor insulation used in the cavity led to a significant heat loss in the experiment. This condition also induced the asymmetry of the measured mean air velocity. Therefore, the measured data was not asymmetric due to the poor insulation on the cavity, and it was incorrect.

4.3 Mixed Convection. The mixed convection study used a displacement ventilation case that supplied cold air through the diffuser in the lower part of a room, and exhausted warm air at the ceiling level, as shown in Fig. 7. This is a practical case of ventilation system design for a room. The room was 5.16 m long, 3.65 m wide, and 2.43 m high. This case presents a real scenario of a two-person office with many heated and unheated objects, such as the occupants, lighting, computers, and furniture. Yuan et al. [20] measured the air temperature, air velocity, and tracer-gas (SF_6) concentration for the case. The tracer-gas was used to simulate CO_2 emissions from the two occupants. The temperature

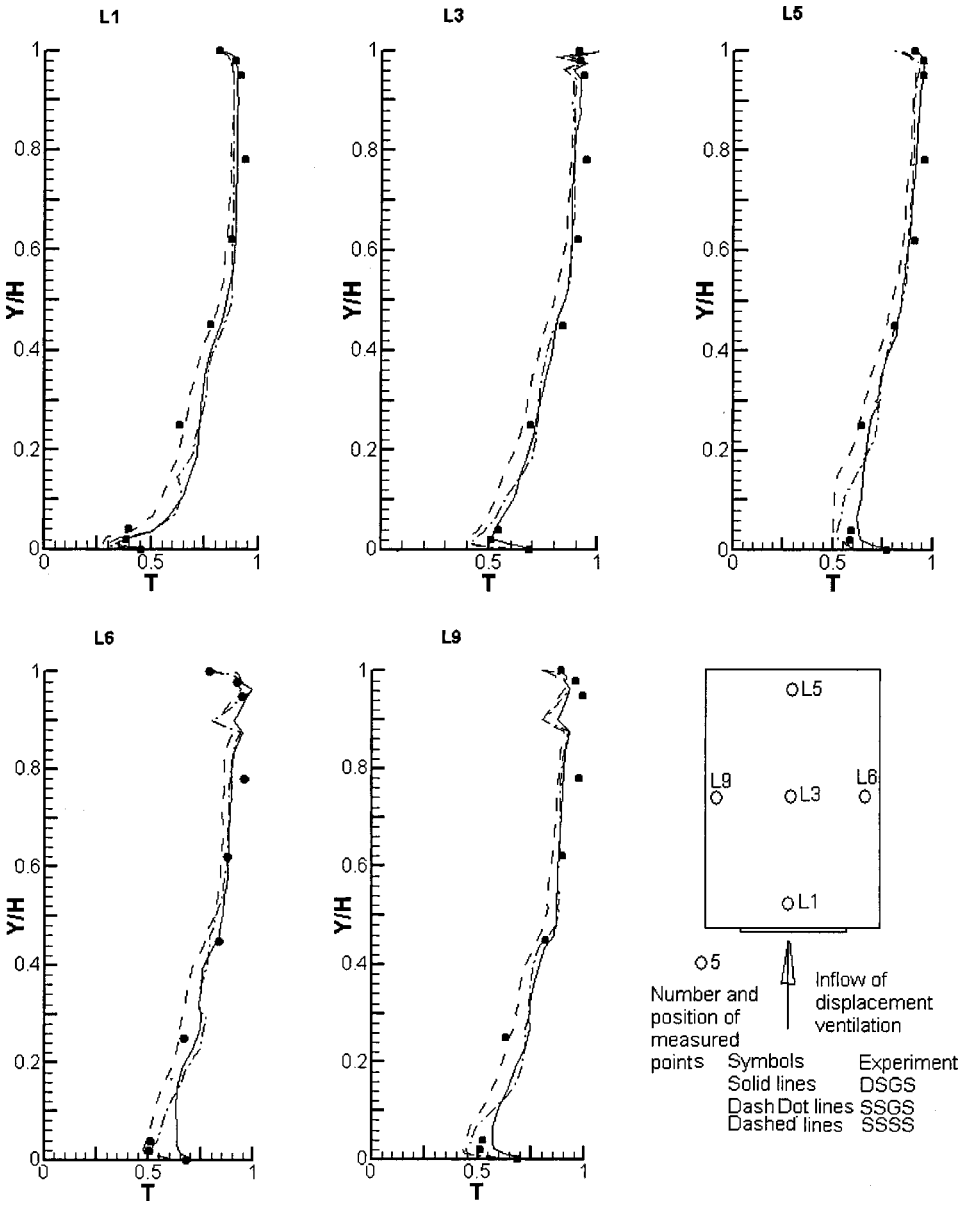

Fig. 11 Comparison of the computed mean air temperature with the experimental data at five different locations in the room ($T=(t-t_s)/(t_{exh}-t_s)$, $t_s=17.0°C$, $t_{exh}=26.7°C$, where t_s and t_{exh} are the temperatures of the supply and exhaust, respectively.)

of the inlet airflow from the diffuser was $t_{sup}=17.0°C$, and the ventilation rate was 183 m^3/h. The total heat sources in the room were 636 W. The measured data were used here to validate the LES results.

According to the studies of forced and natural convection cases, a very fine grid resolution did not provide more accurate results. The coarse grid distributions are acceptable for engineering applications. In addition, this mixed convection case had smaller temperature and velocity gradients in the flow domain so that it did not need a very fine grid resolution. Hence, the current study used a grid distribution of $66\times46\times34$. The grid is quite coarse for such a complex geometry. The grid distribution is nonuniform in the *y*-direction, and uniform in the other two directions. The time step used was 0.005 s over a 300 s period. With such a grid resolution and time step, it is possible to calculate the mixed convection case on an Alpha workstation with a single 21264 processor. The total computing time was about 30 hours.

The boundary conditions used in the study were as follows. The log-law wall functions were used for all the solid surfaces. The thermal boundary conditions for the surfaces were set as either fixed temperatures or heat fluxes. At the air supply inlet, a uniform velocity and temperature profile was assumed and the turbulence intensity was estimated to be 10 percent. The boundary conditions for the exhaust were zero pressure and zero gradient for all other variables.

Figure 8 shows the mean and instantaneous airflow pattern at the middle section of the office. The cold air from the diffuser moved downwards rapidly along the floor due to the buoyancy effect. The mean airflow pattern showed a large and weak recirculation in the lower part of the room. In the upper part of the room, there were some areas of recirculation caused by the thermal plumes from the heated objects, such as the computers, occupants, and overhead lights. The airflow pattern computed was similar to that observed with the smoke visualization (Yuan et al. [20]).

The computed results shown in Fig. 8 illustrate a significant difference between the mean and instantaneous flow patterns. The

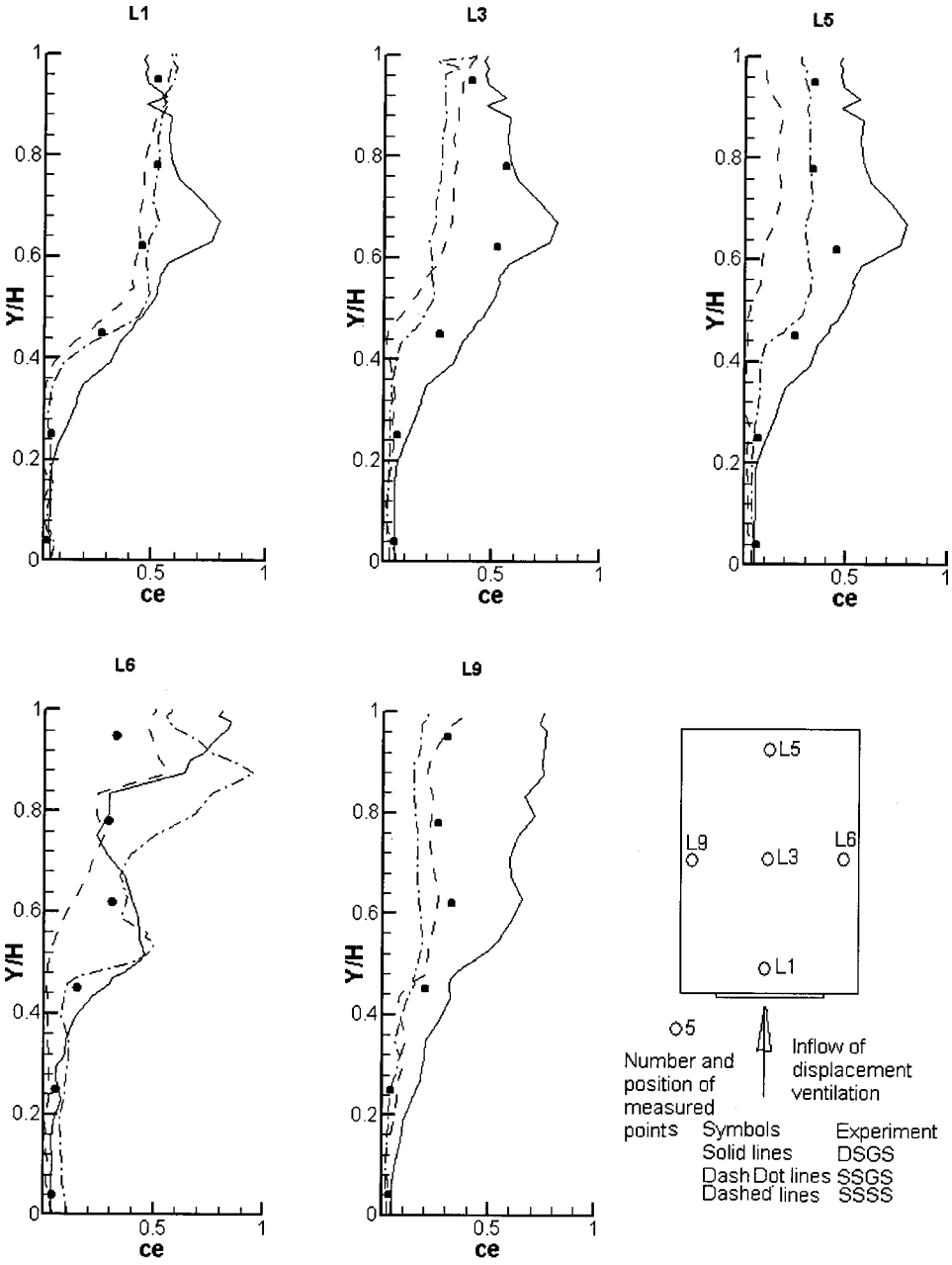

Fig. 12 Comparison of the computed mean tracer-gas (SF_6) concentration distributions with the experimental data at different locations in the room ($ce=(c-c_s)/(c_e-c_s)$, $c_e=0$ ppm, $c_s=0.42$ ppm, where c_s and c_e are the tracer gas concentrations of the source and environment, respectively)

instantaneous flow is unstable, and the flow appears to be very chaotic. This phenomenon can be found in another cross section through the computer, as shown in Fig. 9. Note that the velocity fluctuation in the office can be very high, even though the mean velocity is very small. This is especially evident in the upper part of the room. This information, which is normally not available from turbulence modeling, is very important for thermal comfort design.

In addition, the experiment has also measured the mean air velocity with omni-directional anemometers. Figure 10 compares the computed mean air velocity with the experimental data at five locations in the office. $Y/H=0$ corresponds to the floor surface, and $Y/H=1$ to the ceiling surface. The bottom right figure shows a floor plan where the five measuring locations are labeled. The experiment observed a low frequency oscillation (2–5 minutes per cycle). The data were averaged in the measurements over a period of a few seconds. Therefore, the experimental data appears rather smooth. The three subgrid-scale models of LES predicted very similar velocity distributions, except in the area close to the floor at location 6. This difference can be attributed to the constant coefficient used in the Smagorinsky model. Since the anemometers are not suitable for low velocity measurements, the comparison is not conclusive. Nevertheless, the trend and the magnitude of the velocity distributions are the same between the computed results and the measured data.

Figure 11 shows the profiles of the mean air temperature at the five positions in the room. All the computed results agree well with the experimental data. The differences among the three subgrid-scale models are generally small, although the SSSS model seems to perform the best. The SSSS model estimated the

small-scale temperature from the heat fluxes and the temperature distribution. Since the temperature variation over time and location was found to be not significant, these results suggest that the air temperature is not very sensitive to the turbulence viscosity.

One important objective in studying indoor airflow is to predict contaminant concentration distributions. Carbon dioxide is often considered to be a contaminant. The experiment conducted by Yuan et al. [20] used tracer-gas to simulate the carbon dioxide from the two occupants. Figure 12 presents the computed tracer-gas concentration distributions and the corresponding experimental data at five different positions in the room. The agreement between the experimental data and computational results is poor. This is because the diffusion process is very slow for this case. The average of the results should be made over a long period of time in order to obtain more accurate mean results. Our calculation for a total of 500 s is too short. Nevertheless, the three subgrid-scale models are able to predict the trend and magnitude of the concentration distributions.

5 Conclusion

This investigation used three subgrid-scale models of LES to study forced, natural, and mixed convection flows in a room. The three subgrid-scale models are the Smagorinsky (SSGS) model, a dynamic model (DSGS), and a stimulated small-scale SGS (SSSS) model (also referred to as the deconvolution model in some literature, such as [21]). The LES used fast Fourier transformation (FFT) as its numerical algorithm. The experimental data from the three cases are used to validate the numerical results. This study leads to the following conclusions:

1 The SSGS, DSGS, and SSSS models can be used for the prediction of indoor airflow. The performance of the DSGS and SSSS models was slightly better than that of the SSGS model. The differences between the DSGS and SSSS models are small. For building design, the LES models produce results with reasonable accuracy.

2 Because the SSSS model has a solid mathematical and physical background, it deserves further attention. In the present paper, the use of this model has been extended through the LES calculation of temperature and concentration.

3 The LES provides not only the mean flow parameters, but also instantaneous airflow information. The instantaneous flow information is an important thermal comfort parameter, and it cannot be easily obtained through turbulence modeling. Therefore, LES is a promising tool for the next generation of building environmental design.

All results show that the computational profiles of velocity and turbulent kinetic energy in the vicinity of the wall are far different from the measured data. Therefore, further investigation of this problem is necessary.

Acknowledgment

This work is supported by the U.S. National Science Foundation under grant CMS-9877118 and by the Archilife Research Foundation, Taiwan. We would like to thank Dr. Kevin McGrattan of the National Institute of Standards and Technology for many useful discussions.

Nomenclature

a = coefficient in the difference Poisson equation
a,b,c = coefficients of stimulated
= operator (see Eq. (18))
C = species concentration; coefficient of dynamic model
C_M = parameter in the eddy-viscosity model
C_s = Smagorinsky coefficient
Conv = convection term in the momentum equation
D_{Cj} = $\overline{Cv_i}-\overline{C}\,\overline{v_i}$ species concentration flux
Diss = dissipation term in the momentum equation
G = filtering function
H = height
h_i = $x_{i+1}-x_i$
h = for the case of uniform grid
I = unit matrix
IM,JM,KM = total numbers of nodes in the x-, y-, and z-directions
n = normal direction
i = $\sqrt{-1}$
L_{ij} = $T_{ij}-\tilde{\tau}_{ij}$
L_x; L_y; L_z = stimulated operator in the x-, y-, and z-directions
L = $L_xL_yL_z$
M_{ij} = $T_{ij}-\frac{\delta_{ij}}{3}T_{kk}=-2C\tilde{\Delta}^2|\tilde{S}|\tilde{S}_{ij}$
m = see Eq. (18)
m_{ij} = $\tau_{ij}-\frac{\delta_{ij}}{3}\tau_{kk}=-2C\overline{\Delta}^2|\overline{S}|\overline{S}_{ij}$
p = pressure
S = source
Q = object function
q_c = source term of concentration
S = tensor of deformation rate
S_{ij} = component of S, $=\frac{1}{2}(\overline{v}_{i,j}+\overline{v}_{j,x})$
T = dimensionless temperature
T_{Tj} = $\overline{Tv_i}-\overline{T}\,\overline{v_i}$ heat flux
T_{ij} = $\widetilde{v_iv_j}-\tilde{v}_i\tilde{\theta}_j$ heat flux
T_{kk} = $\sum_{i=1}^{3}T_{ii}$
t = time; temperature
U = dimensionless mean velocity
u = a general flow parameter; component of velocity in x direction
u_r = dimensionless fluctuate velocity
$u(x)$ = A function of x
u_i^* = value of $u(x)$ at x_i
$\overline{u}(x)$ = filtered function of $u(x)$
$u'(x)$ = $u(x)-\overline{u}(x)$
$\overline{u}_i$ = value of $\overline{u}(x)$ at x_i
v = component of velocity in y direction; scale of velocity
$\overline{\theta}_i$, $\overline{\theta}_j$ = velocity components in the x_i- and x_j-directions
$\overline{v}_{i,j}$ = $\partial\overline{v}_i/\partial x_j$
x_i = x coordinate of ith node; $x_1=x$; $x_2=y$; $x_3=z$
x,y,z = Cartesian coordinates

Greek letters

α,β = selected parameters in Eq. (39)
Δ = grid scale, filtering scale
Δt = time step
δ_{ij} = Kronecker symbol, if $i=j$, it is 1, else 0
κ = thermal diffusivity
κ_c = species diffusivity
ρ = air density
ν = kinetic viscosity of fluid
ν_T = eddy-viscosity
τ_{ij} = Reynolds stresses

Subscripts

c = cold wall
e = environment
exh = exhaust
h = hot wall
i = component in x_i direction

m,n = indexes in the x-, y-phase space
n = normal component
s = supply or source

Superscripts

$*$ = value of original function at node (see Fig. 1); imaginative velocity in projection method
n = time level
$\overline{(\ )}$, = filtered value with scale $\overline{\Delta}$
$(\ )\sim$ = and $\tilde{\Delta}$
$(\ )'$ = small scale value

References

[1] Chen, Q., 1997, ''Computational fluid dynamics for HVAC: successes and failures,'' ASHRAE Trans., **103**, Part 1, pp. 178–187.
[2] Lesieur, M., 1997, *Turbulence in Fluids* (third revised and enlarged edition), Kluwer Academic Publishers, Dordrecht.
[3] Piomelli, U., 1999, ''Large Eddy simulation: achievements and challenges,'' Prog. Aerosp. Sci., **35**, pp. 335–362.
[4] Lesieur, M., and Metais, O., 1996, ''New trends in large eddy simulations of turbulence,'' Annu. Rev. Fluid Mech., **28**, pp. 45–82.
[5] Shah, K. B., and Ferziger, J. H., 1995, ''A new non-eddy viscosity subgrid-scale model and its application to channel flow,'' Center for Turbulence Research Annual Research Briefs.
[6] Smagorinsky, J., 1963, ''General circulation experimental with the primitive equations,'' Mon. Weather Rev., **91**, pp. 99–164.
[7] Germano, M., Piomelli, U., Moin, P., and Cabot, W. H., 1991, ''A dynamic subgrid-scale eddy viscosity model,'' Phys. Fluids A, **3**, pp. 1760–64.
[8] Piomelli, U., Cabot, W. H., Moin, P., and Lee, S., 1991, ''Subgrid scale backscatter in turbulent and transitional flows,'' Phys. Fluids A, **3**, No. 11, pp. 1766–71.
[9] Lilly, D. K., 1992, ''A proposed modification of the Germano subgrid-scale closure method,'' Phys. Fluids A, **4**, No. 3, pp. 633–635.
[10] Zhang, W., and Chen, Q., 2000, ''Large eddy simulation of natural and mixed convection airflow indoors with two simple filtered dynamic subgrid scale models,'' Numer. Heat Transfer, Part A, **37**, No. 5, pp. 447–463.
[11] Chorin, A. J., 1968, ''Numerical solution of incompressible flow problem,'' Studies in Numerical Analysis 2, Society for Industrial and Applied Mathematics, Philadelphia, PA, pp. 64–70.
[12] Su, M. D., 1993, ''LES of turbulent flow in straight/curve duct,'' Ph.D. thesis, Techinesche Universitaet Muenchen, Germany.
[13] McGrattan, K. B., Baum, H. R., Rehm, R. G., Hamins, A., and Forney, G. P., 1999, ''Fire dynamics simulator: technical reference guide,'' National Institute of Standards and Technology (NIST).
[14] Peskin, C. S., 1972, ''Flow patterns around heart valves: a numerical method,'' J. Comput. Phys. , **10**, pp. 252–271.
[15] Goldstein, D., Handler, R., and Sivovich, L., 1995, ''Direct numerical simulation of turbulent flow over a modeled riblet covered surface,'' J. Fluid Mech., **302**, pp. 333–376.
[16] Restivo, A., 1979, ''Turbulent flow in ventilated rooms,'' Ph.D. thesis, University of London, UK.
[17] Wilcox, D. C., 1988, *Turbulence modeling for CFD* (second edition), DCW industries, La Canada, CA.
[18] Murakami, S., 1998, ''Overview of turbulence models applied in CWE, 1997,'' J. Wind. Eng. Ind. Aerodyn. , **74-76**, pp. 1–24.
[19] Cheesewright, R., King, K. J., and Ziai, S., 1986, ''Experimental data for validation of computer codes for prediction of two-dimensional buoyant cavity flows,'' ASME Winter Annual Meeting, HTD-60, Anaheim, pp. 75–81.
[20] Yuan, X., Chen, Q., Glicksman, L. R., Hu, Y., and Yang, X., 1999, ''Measurements and computations of room airflow with displacement ventilation,'' ASHRAE Trans., **105**, No. 1, pp. 340–352.
[21] Stolz, S., and Adams, N. A., 1999, ''An approximate deconvolution procedure for large-eddy simulation,'' Phys. Fluids, **11**, No. 7, pp. 1699–1701.

Two-Equation Turbulence Modeling for Impeller Stirred Tanks

Raymond M. Jones
Louisiana State University,
Baton Rouge, LA 70803

Albert D. Harvey III
The Dow Chemical Company,
Plaquemine, LA 70765

Sumanta Acharya
Louisiana State University,
Baton Rouge, LA 70803

In this study, the predictive performance of six different two-equation turbulence models on the flow in an unbaffled stirred tank has been investigated. These models include the low Reynolds number k-ϵ model of Rodi, W., and Mansour, N. N., ''Low Reynolds Number k-ϵ Modeling With the Aid of Direct Simulation Data,'' J. Fluid Mech., Vol. 250, pp. 509–529, the high and low Reynolds number k-ω models of Wilson, D. C., 1993, Turbulence Modeling for CFD, DCW Industries, La Canada, CA., the RNG k-ϵ model, and modified k-ω and k-ϵ models which incorporate a correction for streamline curvature and swirl. Model results are compared with experimental laser Doppler velocimetry (LDV) data for the turbulent velocity field in an unbaffled tank with a single paddle impeller. An overall qualitative agreement has been found between the experimental and numerical results with poor predictions observed in some parts of the tank. Discrepancies in model predictions are observed in the anisotropic regions of the flow such as near the impeller shaft and in the impeller discharge region where the model overpredicts the radial velocity component. These results are discussed and a strategy for improving two-equation models for application to impeller stirred tanks is proposed.
[DOI: 10.1115/1.1384568]

Introduction

Computation of turbulent flow in an impeller stirred tank reactor (STR) can be a considerable challenge for existing turbulence models. Factors contributing to this difficulty include the nonisotropic nature of the flow in a stirred tank, the complex geometry of rotating impellers and the large disparity in geometric scales present. In addition, the flow and turbulence encountered and produced by each blade are further complicated due to the fact that the blade itself is riding in the wake of another blade.

Past work with modeling turbulent flow in STRs has been focused primarily on simplified computational analyses. This is not surprising since the problem is quite complex geometrically and the flow is unsteady. By far, the most popular simplified analysis has been to use experimentally measured velocity and kinetic energy profiles at the impeller tip as boundary conditions to approximate the impeller. In this approach, the tank wall is the only solid surface modeled. This simplified approach neglects the impeller geometry and models the impeller region as a fictitious disk where transport variables are input as inflow/outflow boundary conditions. A multitude of applications employing this technique have been reported in the literature. A few include Harvey and Greaves [1], Ranade and Joshi [2], Ju et al. [3], Kresta and Wood [4], Bakker et al. [5], and Ducoste and Clarke [6]. Many other numerical results obtained using the technique have been reported throughout the literature in the past few years.

Past attempts to eliminate the experimental (or empirical) input in the CFD calculation have been primarily through the solution of the high Reynolds number (Re) k-ϵ transport equations and the use of wall functions to model turbulent boundary layers on the impeller and tank surfaces. Use of this technique eliminates the numerical difficulties associated with the low-Re k-ϵ models where the k and ϵ equations are integrated all the way through the viscous sublayer to the surface of a solid wall. Typical industrial sized STRs are large and often contain multiple impeller configurations. The grid resolution required for the application of low-Re turbulence models can be excessive and therefore high-Re turbulence models with wall functions are typically used in simulations performed by industry.

While wall functions in the high-Re models alleviate the problems with grid resolution, their applicability may be questioned under certain flow conditions. As an example, at impeller surfaces, boundary layers are not fully developed before trailing edge separation occurs, and the use of wall functions in these regions of the tank is clearly questionable. Dong et al. [7], presents results using a popular commercial CFD package (FLUENT) and the standard k-ϵ model with wall functions to model the flow resulting from a paddle impeller in an unbaffled tank. The model predicts the overall features of the flow satisfactorily. However, the tangential velocities are underpredicted near the shaft and the impeller discharge velocities are significantly overpredicted.

Harvey et al. [8] have focused exclusively on modeling laminar flow in STRs. Their approach is to represent the geometry precisely using a generalized coordinate system, eliminating the need for experimental input of boundary conditions. Wechsler et al. [9], have extended this technique to turbulent flows and it is used in the present work. Six two-equation turbulence models are applied to the flow generated by a paddle impeller in an unbaffled tank and investigated experimentally by Dong et al. [10]. The experimental configuration consists of a single set of eight blades with a rotation speed of 100 rpm. This corresponds to a Reynolds number (based on impeller diameter and the mean velocity at the tip of the impeller) of 3273. The goal of this study is to provide a detailed investigation of the predictive capabilities of two-equation turbulence models to predict the flow in STRs. The flow field and turbulence quantities have been computed throughout the tank and ad hoc models for the impeller region have not been used. As a first step, an unbaffled tank is tank considered to avoid the complexities induced by side wall baffles.

Note that only the Reynolds-averaged Navier-Stokes equations are solved to provide predictions of the time-averaged velocity and turbulence quantities. The effect of velocity fluctuations due to turbulence or large scale unsteady structures on the time-averaged quantities, is essentially represented by the turbulence model for the Reynolds stresses. The accuracy of the predictions

Contributed by the Fluids Engineering Division for publication in the JOURNAL OF FLUIDS ENGINEERING. Manuscript received by the Fluids Engineering Division March 16, 1999; revised manuscript received March 5, 2001. Associate Editor: P. E. Raad.

of the mean statistics depends on how well these models capture the effect for the flow fluctuations (over the entire spectrum of scales).

The turbulence models considered in this study include the low Reynolds number (LKW) and high Reynolds number (HKW) k-ω models of Wilcox [11], a low Reynolds number k-ϵ model (LKE), an RNG k-ϵ model (RNG), and modified k-ω (MKW) and k-ϵ (MKE) models which use a correction for streamline curvature and swirl.

The LKW, HKW, and the MKW models consist of transport equations for turbulent kinetic energy, k, and specific turbulent dissipation, ω. The low Reynolds number k-ϵ model (LKE), modified k-ϵ model (MKE), and the RNG k-ϵ (RNG) consist of transport equations for turbulent kinetic energy, k, and turbulent dissipation ϵ. The values of k and ω or ϵ are then used to compute the eddy viscosity, ν_t. Low Reynolds number models require ad hoc damping functions at a solid boundary to insure the correct profile for the eddy viscosity near the boundary. The LKE, LKW, and MKE models integrate the transport equations for turbulence quantities all the way to the impeller surfaces. Thus, the boundary layer and its spatial growth rate are computed as part of the solution. The value of y^+ at the first grid point off the wall was less than 1.0 for all of the computations. The RNG k-ϵ model uses a two-layer zonal model for computing ϵ near solid boundaries.

It should be noted that the present study is the first comparative study of the application of low-Reynolds number turbulence models (LKE, LKW, MKE, MKW) to STRs. Further, in the MKE and MKW models we have investigated the effect of adding specific swirl and curvature corrections and their application to STRs in the low-Reynolds formulation are also unique.

In the next section, a brief overview of the time-averaged Navier-Stokes equation solver is presented followed by an overview of each of the turbulence models. In the Results section, the models are tested for the flow in the unbaffled stirred tank studied experimentally by Dong et al. [10].

Mean Flow Equations

The mean flow equations are the steady incompressible Navier-Stokes equations written in a generalized coordinate system. These equations are solved in a rotating frame of reference, and therefore, centrifugal and Coriolis force terms appear in the momentum equations.

The coupling between the velocity and pressure fields is accommodated through the use of the pseudocompressibility technique (Rogers et al. [12]) which introduces a pseudo-time derivative of pressure in the continuity equation. Solutions to the resulting hyperbolic equation set are obtained by marching in pseudo-time and driving the pressure derivative to zero. Details on the flow equations and their numerical solutions can be found in Rogers et al. [8].

Turbulence Models

k-ϵ model (LKE). The k-ϵ model is the most popular of the two-equation models and has produced qualitatively satisfactory results for a number of complex flows. The low Reynolds number k-ϵ (LKE) model solves a transport equation for turbulent kinetic energy k and a transport equation for the isotropic part of dissipation $\tilde{\epsilon}$ which, unlike ϵ, goes to zero at the wall. Damping functions f_μ, f_1, f_2, and f_3 of Rodi and Mansour [13] are used to account for the near-wall effects. Note that Rodi and Mansour [13] used Direct Numerical Simulation (DNS) data to curve-fit the model coefficients and expressions, and have presented their model as an improvement over other competing models. This model has not been used for predicting STR flows in the past. The incompressible form of the equations is:

$$\nu_t = C_\mu f_\mu \frac{k^2}{\tilde{\epsilon}}$$

$$\frac{Dk}{Dt} = \tau_{ij}\frac{\partial u_i}{\partial x_j} - \epsilon + \frac{\partial}{\partial x_j}\left[(\nu + \sigma_k \nu_t)\frac{\partial k}{\partial x_j}\right]$$

$$\frac{D\tilde{\epsilon}}{Dt} = C_{\epsilon 1} f_1 \frac{\tilde{\epsilon}}{k}\tau_{ij}\frac{\partial u_i}{\partial x_j} - C_{\epsilon 2} f_2 f_3 \frac{\tilde{\epsilon}^2}{k} + \frac{\partial}{\partial x_j}\left[(\nu + \sigma_\epsilon \nu_t)\frac{\partial \tilde{\epsilon}}{\partial x_j}\right]$$

with $\tilde{\epsilon} = \epsilon - D$, δ_{ij} is the Kronecker delta function and

$$\tau_{ij} = \nu_t\left(\frac{\partial u_i}{\partial x_j} + \frac{\partial u_j}{\partial x_i}\right) - \frac{2}{3}k\delta_{ij}$$

The near-wall damping functions and model constants are defined by:

$$f_\mu = 1 - \exp(-0.0002\,\mathrm{Re}_y - 0.00065\,\mathrm{Re}_y^2), \quad f_1 = 1.0, \quad \sigma_\epsilon = 1.0,$$

$$f_2 = 1 - 0.3\exp(-\mathrm{Re}_t^2), \quad \sigma_k = 1.3, \quad C_{\epsilon 1} = 1.44,$$

$$f_3 = \exp(2R_p^3), \quad C_{\epsilon 2} = 1.92, \quad C_\mu = 0.09,$$

$$R_p = \frac{P/\epsilon}{0.3\sqrt{\mathrm{Re}_t}}, \quad \mathrm{Re}_t = k^2/\nu\epsilon, \quad \mathrm{Re}_y = k^{1/2}y/\nu$$

where P is the production of turbulence and Re_t and Re_y are turbulence Reynolds numbers. The functions E and D represent near-wall effects and are defined by:

$$E = 2\nu\nu_t\left(\frac{\partial u_i}{\partial x_j}\right)^2, \quad D = 2\nu\left(\frac{\partial k^{1/2}}{\partial x_j}\right)^2$$

Note that in this model the introduction of the function f_3 and the curve-fitted expression for f_μ are based on DNS data, and according to Rodi and Mansour [13] represent improvements over the conventional low Re k-ϵ models. The constant 0.3 appearing in the expression was based on a sensitivity study and appeared to be the best choice.

Modified k-ϵ Model (MKE). The modified k-ϵ (MKE) model is similar to the above LKE model except that the ϵ equation has been modified using the gradient Richardson number correction. The new ϵ equation becomes:

$$\frac{D\tilde{\epsilon}}{Dt} = C_{\epsilon 1} f_1 \frac{\tilde{\epsilon}}{k}\tau_{ij}\frac{\partial u_i}{\partial x_j} - C_{\epsilon 2} f_2 (1 - C_{gs}\mathrm{Ri}_{gs})\frac{\tilde{\epsilon}^2}{k} + \frac{\partial}{\partial x_j}\left[(\nu + \sigma_\epsilon \nu_t)\frac{\partial \tilde{\epsilon}}{\partial x_j}\right]$$

where

$$C_{gs} = 0.02 \quad \mathrm{Ri}_{gs} = \frac{k^2}{\epsilon^2}\frac{u_\theta}{r^2}\frac{\partial (r u_\theta)}{\partial r}$$

and u_θ is the tangential component of velocity.

The gradient Richardson number represents the ratio of an apparent body force acting on a fluctuating, or displaced fluid element, to a typical inertial force Sloan et al. [14]. A positive gradient will tend to produce a positive Richardson number which will increase the dissipation rate and decrease the kinetic energy and eddy viscosity. A negative gradient will tend to produce a negative Richardson number and increase the kinetic energy and eddy viscosity.

RNG k-ϵ Model (RNG). The RNG-based k-ϵ (RNG) model follows the same framework as other two equation models but uses Renormalization Group methods, Yakhot [15]. The model is said to provide improved predictions of near-wall flows and flows with high streamline curvature. The RNG model along with a two-layer zonal wall function approach was recommended by FLUENT [16] for predicting the flow in STRs. The governing equations and the two-layer wall function model are:

$$\mu_{\text{eff}} = \mu_{mol}\left[1+\sqrt{\frac{C_\mu}{\mu_{mol}}}\frac{k}{\sqrt{\epsilon}}\right]^2$$

$$\frac{Dk}{Dt} = \tau_{ij}\frac{\partial u_i}{\partial x_j} - \epsilon + \frac{\partial}{\partial x_j}\left[(\sigma_k \mu_{\text{eff}})\frac{\partial k}{\partial x_j}\right]$$

$$\frac{D\epsilon}{Dt} = C_{\epsilon 1}\frac{\epsilon}{k}\tau_{ij}\frac{\partial u_i}{\partial x_j} - C_{\epsilon 2}\frac{\epsilon^2}{k} + \frac{\partial}{\partial x_j}\left[(\sigma_\epsilon \mu_{\text{eff}})\frac{\partial \epsilon}{\partial x_j}\right] - R$$

where R in the ϵ equation is given by:

$$R = \frac{C_\mu \eta^3\left(1-\frac{\eta}{\eta_0}\right)}{1+\beta\eta^3}\frac{\epsilon^2}{k}$$

with $\eta = Sk/\epsilon$, and S is the modulus of the mean rate-of-strain tensor, $\eta_0 = 4.38$, $\beta = 0.012$. The model constants are:

$$C_{\epsilon 1} = 1.42, \quad C_{\epsilon 2} = 1.68, \quad \sigma_k = 1.393, \quad \sigma_\epsilon = 1.393$$

The two-layer zonal model splits the domain into a viscosity-affected region and a fully turbulent region. The two regions are divided by the turbulent Reynolds number, Re_y. In the viscosity-affected region ($\text{Re}_y < 200$), the one equation model of Wolfstein [17] is used. In the one-equation model the momentum and k equations are solved but ϵ and the eddy viscosity ν_t are computed using the following expressions.

$$\epsilon = \frac{k^{3/2}}{l_\epsilon}, \quad \nu_t = C_\mu \sqrt{k} l_\mu$$

The length scales l_ϵ and l_μ are defined as:

$$l_\epsilon = c_l y\left[1-\exp\left(-\frac{\text{Re}_y}{A_\epsilon}\right)\right]$$

$$l_\mu = c_l y\left[1-\exp\left(-\frac{\text{Re}_y}{A_\mu}\right)\right]$$

$$c_l = \kappa C_\mu^{-3/4} \quad A_\mu = 70 \quad A_\epsilon = 2c_l$$

k-ω Model (LKW), (HKW). Unlike the k-ϵ model, it is easier to prescribe the boundary conditions in the k-ω model. We know that $k = 0$ on solid boundaries, and ω can be specified at the first few grid points away from the wall as $\omega = 6\nu/\beta y^2$ Wilcox [11]. The resulting equations for k, ω, and ν_t are:

$$\nu_t = \alpha^* \frac{k}{\omega}$$

$$\frac{Dk}{Dt} = \tau_{ij}\frac{\partial u_i}{\partial x_j} - \beta^* \omega k + \frac{\partial}{\partial x_j}\left[(\nu + \sigma_k \nu_t)\frac{\partial k}{\partial x_j}\right]$$

$$\frac{D\omega}{Dt} = \frac{\sigma}{\nu_t}\tau_{ij}\frac{\partial u_i}{\partial x_j} - \beta_2 \omega^2 + \frac{\partial}{\partial x_j}\left[(\nu + \sigma_\omega \nu_t)\frac{\partial \omega}{\partial x_j}\right] + 2\sigma_{\omega_2}\frac{1}{\omega}\frac{\partial k}{\partial x_j}\frac{\partial \omega}{\partial x_j}$$

The model constants for the HKW model are:

$$\sigma_k = 0.5, \ \sigma_\omega = 0.5, \ \beta = 0.075, \ \beta^* = 0.09, \ \kappa = 0.41, \ \alpha = \frac{5}{9},$$

$$\alpha^* = 1.0, \ \sigma_{\omega_2} = 0.75$$

For the LKW model the constants are:

$$\beta^* = \frac{9}{100}\frac{\frac{5}{18}+\left(\frac{\text{Re}_t}{R_\beta}\right)^4}{1+\left(\frac{\text{Re}_t}{R_\beta}\right)^4}$$

$$\alpha^* = \frac{\alpha_0^* + \frac{\text{Re}_t}{R_k}}{1+\frac{\text{Re}_t}{R_k}}, \quad \alpha = \frac{5}{9}\frac{\alpha_0 + \frac{\text{Re}_t}{R_\omega}}{1+\frac{\text{Re}_t}{R_\omega}}(\alpha^*)^{-1}$$

$$\beta = 0.075, \ \alpha_0 = 0.1, \ \sigma_k = 0.5, \ \sigma_\omega = 0.5, \ R_\beta = 8,$$

$$R_k = 6, \ \alpha_0^* = \frac{\beta}{3}, \ R_\omega = 2.7$$

The HKW and LKW models both integrate the transport equations for k and ω all the way to the wall, but the HKW model has been shown to be asymptotically inconsistent with the expected behavior of k and dissipation, $\epsilon = \beta^* \omega k$, approaching a solid boundary Wilcox [11]. Also the HKW model, like most two-equation models, predicts transition from laminar to turbulent at a critical Reynolds number, $\text{Re}_c \approx 8100$, which is much lower than the minimum critical Reynolds number, $\text{Re}_c \approx 90{,}000$, which Wilcox derived using linear-stability theory of a Blasius boundary layer. The LKW model tries to remedy these problems by using functional closure coefficients instead of constant coefficients.

Modified k-ω Model (MKW). The modified k-ω (MKW) model is similar to the above LKW model except that the ω equation has been modified using the gradient Richardson number and a correction formulated by Bardina (cited in Reynolds [18].) Both of these corrections are designed to enhance dissipation in the presence of stabilizing curvature. A more detailed discussion of these corrections will be given in the next section. The new ω equation becomes:

$$\frac{D\omega}{Dt} = \frac{\gamma 2}{\nu_t}\tau_{ij}\frac{\partial u_i}{\partial x_j} - \beta_2(1-C_{gs}Ri_{gs})\omega^2 + \frac{\partial}{\partial x_j}\left[(\nu+\sigma_\omega \nu_t)\frac{\partial \omega}{\partial x_j}\right] + 2\sigma_{\omega_2}\frac{1}{\omega}\frac{\partial k}{\partial x_j}\frac{\partial \omega}{\partial x_j} - C_B k\omega\zeta$$

where

$$C_B = 3$$

$$\zeta = \left[\left(\frac{\partial u_\theta}{\partial z}\right)^2 + \left(\frac{\partial u_\theta}{\partial r} + \frac{u_\theta}{r}\right)^2 + \left(\frac{\partial u_r}{\partial z} - \frac{\partial u_a}{\partial r}\right)^2\right]$$

In the above expression u_r and u_a are the radial and axial components of velocity.

The Bardina correction is based on the assumption that rotation appears to trap the energy in the large scales, organize the fluctuations into more coherent eddies, and decrease the cascade of energy transfer to the small eddies. The correction is defined as ζ and is the square root of the scalar product of the mean vorticity vectors contracted with itself. Third-order upwind differencing was used for the convective terms and second-order central differencing used for the viscous terms. The k and ϵ or (ω) equations were solved in a coupled manner using a GMRES solution procedure.

Results and Discussion

Reactor Geometry and Operating Conditions. The flow investigated experimentally by Dong et al. [10] is chosen in the present work to study the performance of the turbulence models for flow in stirred tanks. These experiments are chosen primarily due to the absence of baffles in the experiments, which greatly simplifies the computational problem. Thus, the turbulence models can be evaluated without the need for simulations involving sliding meshes.

Detailed measurements of all three components of the mean velocity and the rms velocity is reported in the paper by Dong et al. [10] for two different configurations in an unbaffled stirred tank with a diameter/height ratio of 1. In case 1, a 2.5 cm diameter

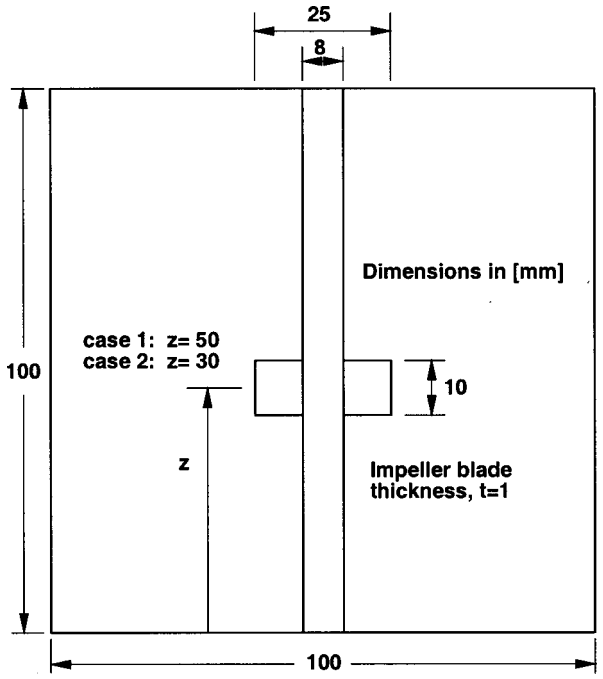

Fig. 1 Experimental setup of Dong

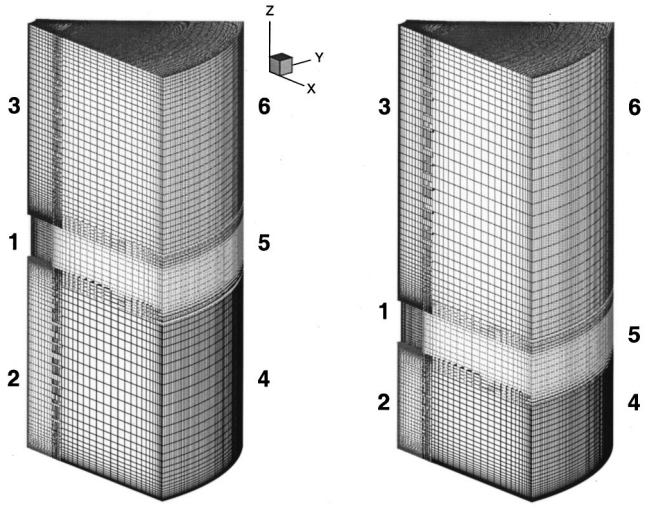

Fig. 2 Topology and computational grid for case 1 (left) and case 2 (right)

paddle impeller is positioned at mid-height in the tank. In case 2, the impeller is positioned at 1/3 of the tank height from the bottom of the tank. These configurations, along with the remaining dimensions, are shown schematically in Fig. 1. In both cases the impeller rotational speed is 100 rpm and the kinematic viscosity, $\nu = 10^{-6}$ m^2/s. This corresponds to a Reynolds number, Re $=3273$.

The computational results were circumferentially averaged and compared with the time averaged data of Dong [10]. In the experiments, measurements of mean and fluctuating velocity were taken using a sampling rate which was much greater than the frequency of a blade passage time. Circumferential averaging is equivalent to time averaging in STR flows without baffles since each circumferential location represents the blade location at some instant in time.

The calculations were performed on a three-dimensional computational domain using a fixed grid consisting of an overlapping multi-block grid topology. The grids used for case 1 and case 2 are shown in Fig. 2. The computational domain consists of one of the eight regions between neighboring blades of the impeller. This $\pi/4$ circumferential slice is discretized into 6 different grid zones, each of which overlaps with its neighboring zones using a Chimera approach. Zone 1 describes the region directly between the two impeller blades. Zones 2 and 3 sit directly underneath and overhead, respectively, of the impeller zone (zone 1). Zone 5 represents the discharge region of the impeller and is made finer than the surrounding zones. Zones 4 and 6 extend from the impeller blade tips out to the tank wall and sit underneath and overhead, respectively, of zone 5.

Boundary conditions for faces of zones, which are not physical boundaries of the domain, are obtained using a trilinear interpolation procedure from points interior to neighboring zones. The trilinear interpolation is applied at the Chimera interfaces to update the solution.

A primary reason for the selection of this particular grid topology is that clustering of the grid at all solid surfaces can take place efficiently without the need for propagating the clustering into the far-field. In addition, specific regions of the grid can be made finer than other regions. This topology can be stacked end-on-end for multiple impeller applications.

A grid independence study was performed using the MKE model for case 1. The tangential and radial velocity profiles are presented in Fig. 3 for coarse, medium, and fine grid solutions and indicate that the computed results are grid independent. Note that in going from the coarsest grid to the finest grid, the number of grid points has been increased nearly four times (94,500–338,000 points). Different levels of grid refinement have been implemented in different zones, with the highest refinement in the regions with the largest gradients. The results in this study are based on the fine grid computations.

Numerical Results. Kresta [19] has given a clear overview of the turbulence characteristics and some modeling challenges associated with STRs. Papers by Kresta and Wood [20], Fort and Makovsky [21], Zhou et al. [22], and Jaworski et al. [23] show that all three time averaged rms velocity components are approximately equal close to the blades, and the assumption of local isotropy is valid. Experiments by Hockey and Nouri [24] show that in the outer impeller region away from the blade this is not the case. Experiments by Brodkey [25] indicate that local isotropy may exist if the local Reynolds number Re_λ (based on the turbulent length scale λ and the fluctuating velocity) is greater than 800, while Sreenivasan [26] indicates that local isotropy may exist for $\mathrm{Re}_\lambda = 50$. Kresta [19] also indicates that in the impeller region Re_λ is approximately 200–400 for typical experimental conditions. In the remainder of the tank, Re_λ is approximately 60–150. Thus, regions of the flow near the impeller blades may exhibit isotropy, while other regions may be anisotropic, and the present results will shed light on the ability of the two equation models to accurately predict such a flow field. It is also uncertain if conventional two-equation models can capture the dynamics associated with the vortex shedding from the blades. Stoots and Calabrese [27] have shown that for a Rushton blade these vortices are well defined and have a diameter of order $D/10$, where D represents the diameter of the impeller. The current blade configuration is a paddle blade which produces similar flow characteristics as the Rushton impeller. It is believed these vortices have a large influence on the turbulence energy and dissipation in the impeller region. Since traditional turbulence models are calibrated against simpler flows, their performance in more complex flows have been mixed.

Large scale, low-frequency motions in the flow have also been investigated by Kresta et al. [28]. The experiments show that the pitch-blade turbines are more susceptible to these low-frequency motions than are Rushton blade turbines. As stated before, the present tank configuration is a paddle blade which exhibits flow

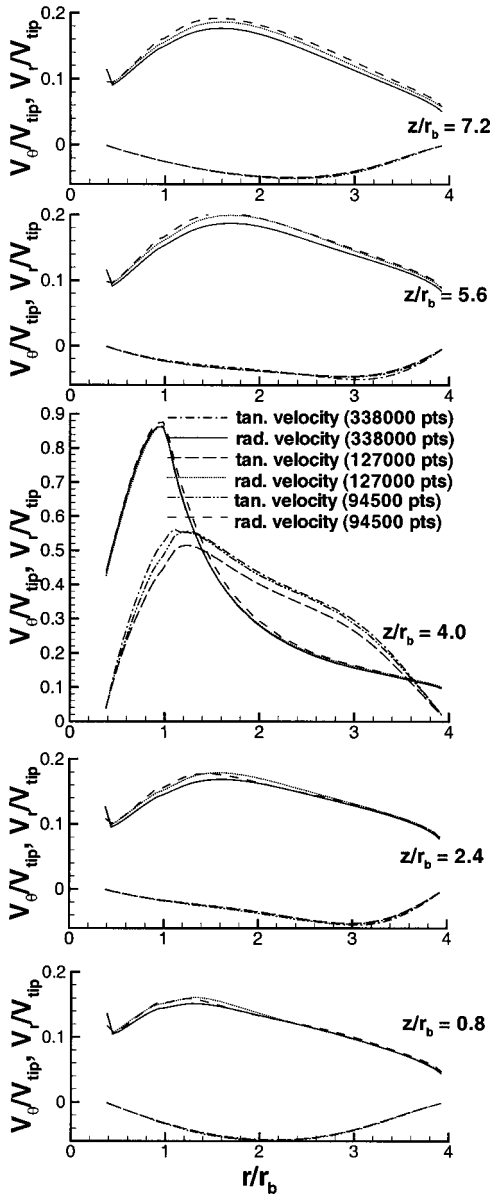

Fig. 3 Velocity profiles for grid independent study

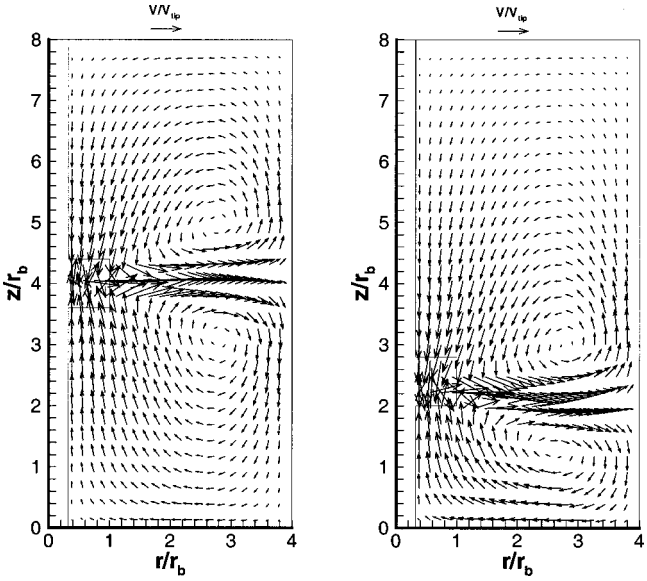

Fig. 4 Computed mean velocity field, modified k-ϵ, case 1 (left), case 2 (right)

characteristics similar to the Rushton impeller, and therefore these low-frequency motions are unlikely to be important in the present flow.

Figure 4 shows the computed mean velocity field for both cases using the modified k-ϵ (MKE) model. Predictions for all six models studied look qualitatively similar. The predicted flowfield is dominated by a radial jet emanating from the impeller which produces two major circulating regions in the tank, one above and one directly below the impeller. The two recirculating eddies are roughly symmetrical in Fig. 4, but the presence of the lower boundary surface leads to considerable asymmetry in case 2.

In Fig. 5 the tangential velocity component is compared with the experiment for cases 1 and 2. The tangential velocity in the impeller discharge region is accurately predicted by each model. However, near the shaft, above and below the impeller, the tangential velocity is severely underpredicted. It is also apparent that the k-ω model predictions near the shaft are better than the k-ϵ model predictions. This is presumably associated with the additional overprediction of the discharge velocity in the impeller region in the k-ω model predictions. In STR flows the angular momentum decreases in the radial direction and the flow has features similar to that of a free vortex (where swirl enhances turbulence). The recirculating flow leads to streamlines with concave curvature in the ξ-η plane near the shaft, which destabilizes turbulence. These complex effects are not properly represented by the turbulence models, which partly contributes to the poor performance observed.

Damping functions, which are needed by most two-equation models to accurately predict near wall turbulence, are formulated

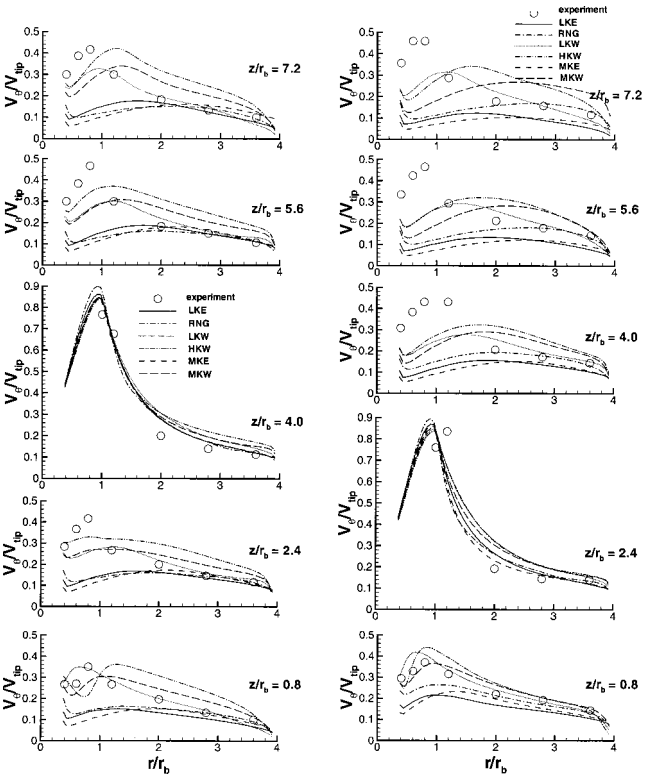

Fig. 5 Computed tangential velocity

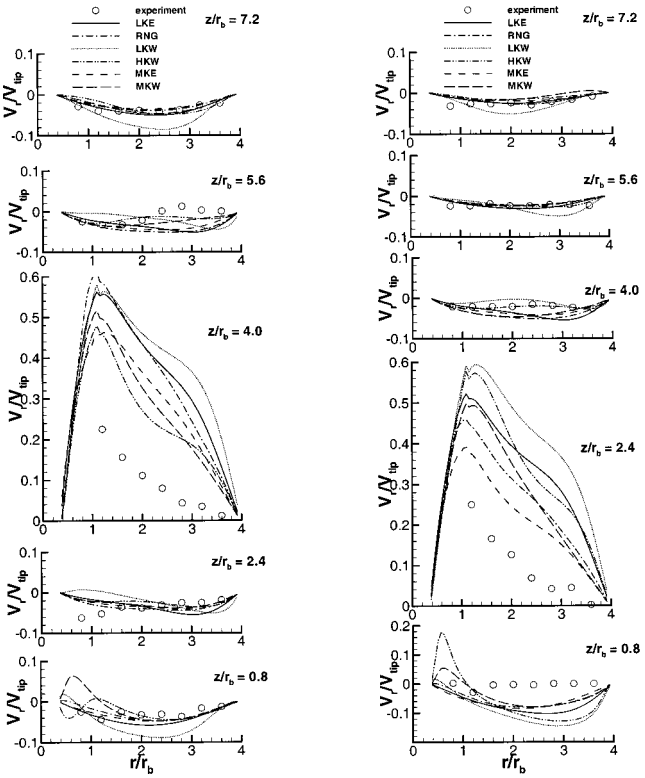

Fig. 6 Computed radial velocity profiles, case 1 (left), case 2 (right)

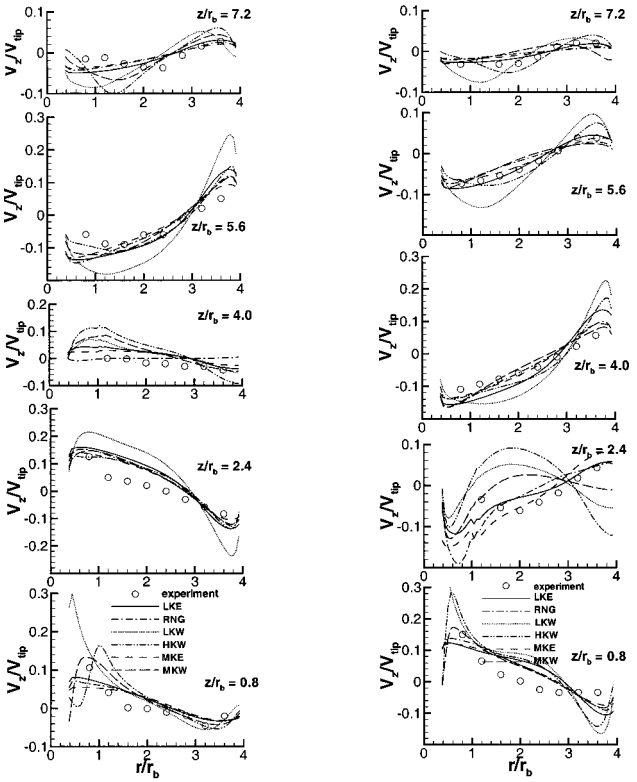

Fig. 7 Computed axial velocity profiles, case 1 (left), case 2 (right)

for wall bounded flows or flows with moderate separation. For flows of this nature, the turbulent Reynolds number, $\mathrm{Re}_t = k^2/\nu\epsilon$, is significant in the boundary layer region close to the wall and negligible in the freestream region away from walls. In more complex flows such as the flow in stirred tanks, Re_t can vary in magnitude along the tank walls and in the outer flow field. In these more complex flows the traditional damping functions are ill-suited and near wall turbulence may not be computed accurately. Near the shaft, the computed Re_t is not very large; thus, low Reynolds number effects in this region may not be represented properly. It seems as though all of the models, except for the HKW model, predict relaminarization of the flow near the shaft, which is not shown by experiments. This would cause the tangential velocity near the shaft to be underpredicted as observed in the current calculations. In the outer tank regions, above and below the impeller discharge, the tangential velocity is overpredicted. This is caused by an overprediction of the eddy viscosity in the outer region of the tank. The streamline curvature near the outer tank wall stabilizes turbulence. Since the models cannot represent these complex effects the eddy viscosity is overpredicted.

Figure 6 shows the computed radial velocity profiles compared with experimental data for cases 1 and 2. We can see that at $z/r_b = 4$ (impeller discharge region for case 1) and at $z/r_b = 2.4$ (impeller discharge region for case 2), the radial component of velocity has been overpredicted by each model. This overprediction of radial velocity is caused by an underprediction of the eddy viscosity in this region, which leads to a reduction of the lateral spreading rate of the impeller discharge. The experiments of Dong [12] show anisotropic turbulence near the shaft and in the impeller discharge region for case 1 and case 2. The curvature induced modifications to the ϵ-equation (given in Eq. (2)) and the correction to the ω-equation (given in Eq. (3)) appear to move the radial velocities in the right direction. The MKE model seems to show more of an overall improvement to the predictions for case 2 than for case 1, especially in the impeller discharge region. This is probably a result of the fact that the experiments of Dong [12], show that the level of anisotropy in this region for case 2 is slightly less than in case 1. At other axial locations, the radial velocities are considerably smaller in magnitude, and the agreement with the predictions is more satisfactory.

The predictions and experimental data for the axial velocity are shown in Fig. 7. The experimental data indicates that the impeller discharge is projected slightly downwards. The models do not seem to predict this downward projection accurately. Dong [7] indicated that the flow condition in the impeller stream and close to the rotor shaft changes rapidly downstream so that relaxational effects and stress convection may be important in the downstream region. Two equation models cannot correctly account for these effects. This is reflected by the significant overprediction in the axial velocity components. The extent of overprediction in Fig. 7 is directly correlated with the overpredictions of the radial velocities seen in Fig. 6. The LKW model shows the highest level of axial velocity overprediction. It should be noted that the k-ϵ models show lower levels of overprediction.

The turbulence kinetic energy profiles are shown in Fig. 8 for case 1 and case 2. As noted earlier, the predictions in the impeller jet region and near the shaft are rather unsatisfactory, and reflect the inability of the damping functions to properly represent low Reynolds number effects near solid walls. Inaccurate turbulent predictions by two-equation models can also be caused by improper representation of the streamline curvature. Two-equation models have been known to fail to reproduce, even qualitatively, several important features of swirling flows such as velocity component decay, jet spreading rate or diffusion rate, degree of entrainment, and kinetic energy levels. Near the impeller shaft in a stirred tank, the flow is highly curved and if the models are not suitably corrected for curvature then they will not produce accurate results.

In the present study, the gradient Richardson number is used in the modified k-ϵ model to account for swirl effects, while both the

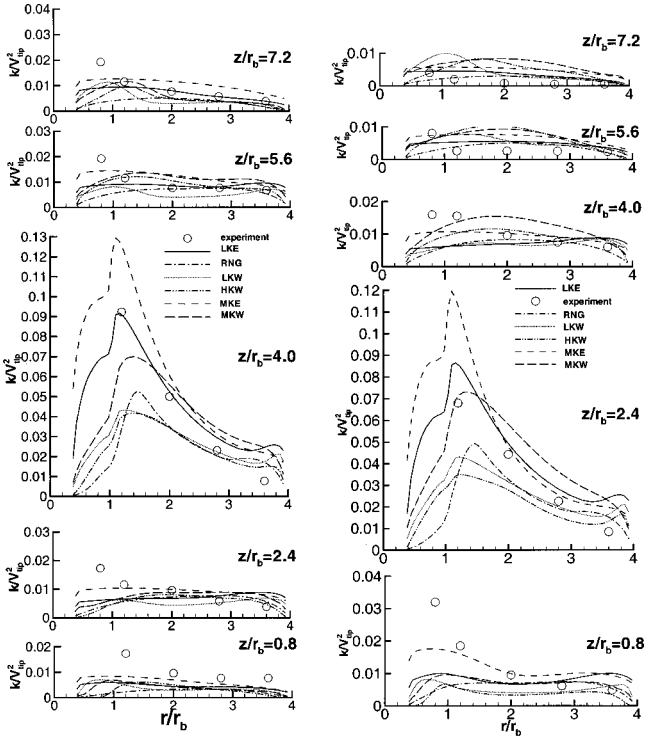

Fig. 8 Kinetic energy profiles, profiles, case 1 (left), case 2 (right)

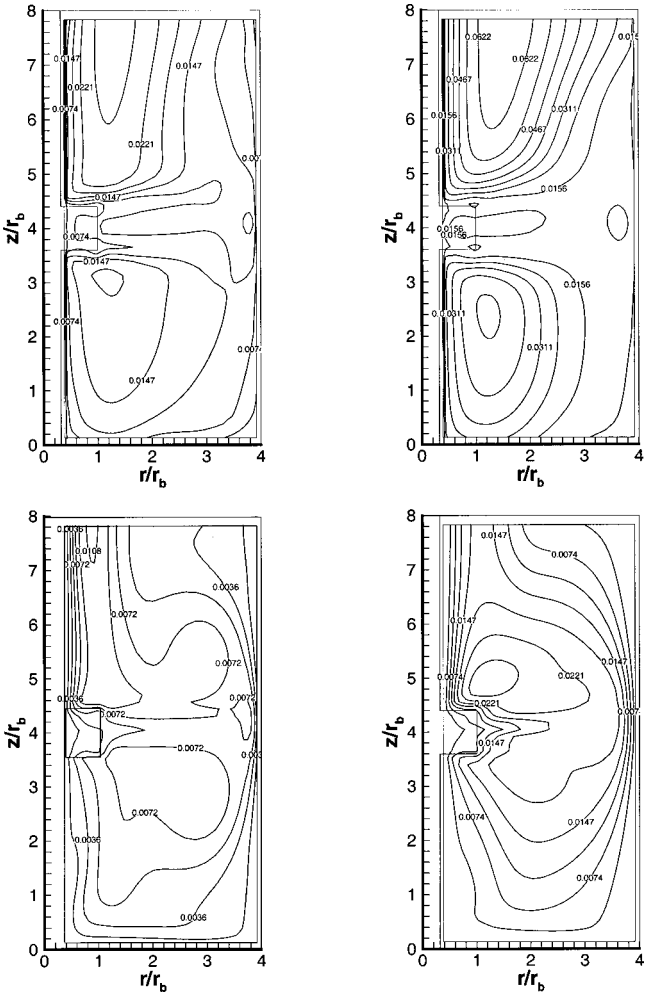

Fig. 9 Eddy viscosity contours, (*a*) LKW, (*b*) MKW, (*c*) LKE, (*d*) MKE model

gradient Richardson number and ζ-correction are used together in the modified k-ω model. It was found that the ζ correction helped to increase the kinetic energy in the impeller region of the tank and the gradient Richardson number correction increased the kinetic energy near the shaft. From Fig. 8 we see that the LKE model predicts the kinetic energy fairly accurately in the impeller discharge region. The kinetic energy near the shaft is not accurately predicted which motivates the present use of the gradient Richardson number correction in Eq. (2) leading to the MKE model. Some improvements in the shaft region are noted in the MKE predictions, but the k-values in the impeller discharge region are now overpredicted.

The LKW and HKW models underpredict the kinetic energy in the impeller discharge region and near the shaft. The MKW model therefore incorporates the gradient Richardson number and ζ-correction together. Although these corrections improved the kinetic energy predictions slightly, they did not show a significant global improvement to the results. These corrections are not universal and have been formulated for simple turbulent flows, not for complex flows such as the flow in stirred tanks.

Ducoste and Clark [6] report that vortices trailing from the impeller blades affect the local energy dissipation in the impeller region. In their simulations, they contribute this to their poor predictions of dissipation. We believe that the trailing vorticies also contribute to the poor predictions of kinetic energy in the impeller region for both case 1 and case 2. Ducoste and Clark [6] do not observe this because they have modeled the impeller region as a disk with experimental velocity and kinetic energy profiles as boundary conditions in this region. Thus their experimental profile for kinetic energy has already accounted for the additional dynamics of the trailing vortices, but they do not have experimental profiles for dissipation. In our simulations there are no ad hoc modeling of the impeller region, rather the velocity and turbulent quantities at the impeller discharge are computed in the same manner as in the bulk of the tank.

Figure 9 show the eddy viscosity computed using the LKE, the MKE, the LKW, and the MKW models. The LKE model shows high values above and below the impeller blades. Relatively lower values of the eddy viscosity are observed adjacent to the shaft and in the impeller region. The low values adjacent to the shaft are responsible for the underprediction of the tangential velocities by the LKE model. The curvature corrections, represented by the MKE model, appear to appropriately enhance the eddy viscosity in the impeller discharge region as well as the region around the shaft. However, the eddy viscosity in other regions appears to be enhanced as well. The LKW model also shows similar eddy viscosity trends as the LKE model, except that the eddy viscosity values are somewhat smaller than those predicted by the LKE model. The MKW model, incorporating both Richardson number and ζ-corrections, significantly enhances the eddy viscosity in the impeller discharge region. This explains the significant improvements in the radial velocities observed with the MKW model.

It is difficult to determine which model produces better predictions. If the impeller region is not predicted accurately, then the models will produce poor predictions in the remainder of the tank. For this reason, most researchers have prescribed experimental boundary conditions for the impeller region. Sahu et al. [29] have shown that if experimental boundary conditions are prescribed, then two-equation models will accurately predict the flow in the bulk of the tank. Therefore, one way to quantify the error between models is by analyzing the difference between the model predictions and experiments in the impeller region. Tables 1 and 2 contain the rms error of the results in the impeller region for both case 1 and case 2, respectively. The turbulent kinetic energy and mean

Table 1 Residual error (case 1, $z/r_b=4$)

Model	u_r	u_z	u_θ	k	k mean
HKW	0.1638	0.0674	0.0612	0.0272	0.0270
LKW	0.3267	0.0385	0.0502	0.0266	0.0280
LKE	0.2873	0.0343	0.0382	0.0093	0.0490
RNG	0.2777	0.0316	0.0411	0.0274	0.0263
MKW	0.2011	0.0463	0.0508	0.0161	0.0430
MKE	0.2106	0.0295	0.0382	0.0198	0.0608

velocity are compared with the mean kinetic energy in the impeller region. Table 1 indicates that at $z/r_b=4$, the HKW model produces the best prediction of radial velocity. However, this best prediction overpredicts the radial velocity by a factor of two close to the blade. Wilcox has shown that the HKW model fails to predict the sharp peak of kinetic energy near solid walls. This leads to an underprediction of the kinetic energy near the blade surface which can be observed at $z/r_b=4$ in Fig. 8. This underprediction of kinetic energy causes an underprediction of eddy viscosity, which in turn causes the radial velocity to be overpredicted. There are three damping functions in the LKW model: β^* in the k-equation, σ in the ω-equation, and σ^* in the eddy viscosity formulation. The damping function β^* is formulated to increase the kinetic energy near solid walls. At $z/r_b=4$ in Fig. 8 the kinetic energy predictions by the LKW model are similar to the predictions by the HKW model. This indicates that β^* is probably ill-suited for the complex flow in the impeller region since the kinetic energy is not increased near the blade surface. The damping function σ is formulated to increase the dissipation near the wall so that the increased kinetic energy does not cause the eddy viscosity to become overpredicted. A similar purpose is served by σ^*, which also helps to reduce the eddy viscosity near the wall. Turning attention back to Fig. 6, it can be seen that the largest overprediction of radial velocity at $z/r_b=4$ is produced by the LKW model. This indicates that although the kinetic energy is similar to the HKW model in this region, the eddy viscosity has been severely overdamped near the impeller blade surface causing the increased overprediction of radial velocity. This suggests that either σ has caused the dissipation to be excessively overpredicted near the blade surface, or σ^* has overdamped the eddy viscosity near the blade surface. Similar arguments can be made about the damping functions in the other models. As stated above, the rms error for the radial velocity prediction of the (HKW) model is low compared with the other models, but the rms error in the kinetic energy for the (HKW) model is high compared with the other models. This means that there must be significant error in the dissipation rate computed by the (HKW) model. Experimental data for turbulence dissipation is needed for a better assessment of the relationship between the the turbulence predictions and the velocity predictions. The combination of the ill-suited damping functions and the inability for two-equation models to accurately predict anisotropic turbulence, causes poor predictions of velocity and turbulence quantities in the impeller region.

From Table 1, it can be seen that the lowest rms error for u_r, u_z, u_θ, and k corresponds to the HKW, MKE, LKE, MKE, and LKE models, respectively. From Table 2, the MKE model has the lowest error in u_r, while the LKE model has the lowest error in u_z, u_θ, and k. Based on this simplistic measure of error, it appears that the LKE model provides the best description of the flowfield.

Table 2 Residual error (case 2, $z/r_b=2.4$)

Model	u_r	u_z	u_θ	k	k mean
HKW	0.2906	0.0995	0.1114	0.0182	0.0208
LKW	0.3633	0.0829	0.1114	0.0141	0.0268
LKE	0.2559	0.0196	0.0923	0.0135	0.0460
RNG	0.1846	0.0318	0.1760	0.0190	0.0230
MKW	0.2046	0.0552	0.1078	0.0134	0.0455
MKE	0.1239	0.0332	0.1316	0.0268	0.0525

Nonlinear models have allowed more accurate predictions of the turbulence quantities in nonisotropic regions of some flows without introducing any additional differential equations. Nonlinear models are usually numerically stiff compared with linear models, but would probably produce more accurate predictions of turbulent quantities in STRs, especially in the impeller discharge region.

Durbin [30] proposed a new elliptic relaxation model for the strongly inhomogeneous region near the wall in wall-bounded turbulent shear flows. The k-ϵ models fail to predict near wall turbulence because k^2/ϵ has the wrong profile as a function of y^+ near the wall. Durbin [30] suggests that the velocity scale near the wall is not k but $\overline{v^2}$, where $\overline{v^2}$ is the variance of the normal component of turbulent velocity. In Durbin's V2F model, the eddy viscosity is described as $\nu_t=C_\mu\overline{v^2}T$ instead of as in the traditional k-ϵ model formulation, and the model can be integrated all the way to the wall without any ad hoc damping functions. Verzicco et al. [31] applied the V2F model to the STR of Dong [12]. Their simulations show that the V2F model performs well near the shaft compared with the standard k-ϵ model, but overpredicts the radial velocity in the impeller region. They also show that the turbulent kinetic energy is underpredicted in the impeller swept region.

Applying a nonlinear version of the k-ϵ-$\overline{v^2}$ model is the subject of current research to improve predictions in stirred tank flows.

Concluding Remarks

The flow in an unbaffled stirred tank is investigated numerically using six different two-equation turbulence models. The mean velocity fields computed using the six models are compared with experimental LDV data. This is the first study on STR's which examines the performance of DNS-based low-Re k-ϵ models and the performance of low-Re k-ω models.

Specific observations made in this study are: 1) The radial velocity component in the impeller discharge region is overpredicted by each of the models. 2) The tangential velocity component in the impeller discharge region is predicted well by the models, but is underpredicted near the shaft. 3) The LKE model is the only model which produces reasonable kinetic energy predictions in the impeller discharge region.

Each model captures the qualitative circulation patterns in the STR. However, all of the models overpredict the mean radial discharge of the impeller due to an underprediction of the eddy viscosity. The experiments of Dong [9], show that the flow in this region is nonisotropic. To account for the nonisotropy in the flow, more sophisticated turbulence models must be employed. The recent work at CTR [31] suggest that more than one blade segment on the impeller must be modeled to capture the effects of neighboring blade vortex interactions.

Acknowledgments

The authors would like to thank Dr. Stuart E. Rogers of the Computational Algorithms Branch at NASA Ames Research Center for the use of the INS3D flow solver. This work was supported by a grant from Dow Chemical and the Louisiana Educational Quality Support Fund (LEQSF).

References

[1] Harvey, P. S., and Greaves, M., 1982, ''Turbulent Flow in an Agitated Vessel, Part II: Numerical Solution and Model Predictions,'' Trans. Inst. Chem. Eng., **60**, pp. 201–210.

[2] Ranade, V. V., and Joshi, J. B., 1989, ''Flow Generated by Pitched Blade Turbines II: Simulation Using k-ϵ Model,'' Chem. Eng. Commun., **81**, pp. 225–248.

[3] Ju, S. Y., Mulvahill, T. M., and Pike, R. W., 1990, ''Three-Dimensional Tur-

bulent Flow in Agitated Vessels with a Nonisotropic Viscosity Turbulence Model,'' Can. J. Chem. Eng., **68**, pp. 3–16.
[4] Kresta, S. M., and Wood, P. E., 1991, ''Prediction of the Three Dimensional Turbulent Flow in Stirred Tanks,'' AIChE J., **37**, pp. 448–460.
[5] Bakker, A., Myers, K. J., Ward, R. W., and Lee, C. K., 1996, ''The Laminar and Turbulent Flow Pattern of a Pitched Blade Turbine,'' Trans. Inst. Chem. Eng., **74**, pp. 485–491.
[6] Ducoste, J. J., and Clark, M. M., 1999, ''Turbulence in Flocculators: Comparison of Measurements and CFD Simulations,'' AIChE J., **45**, pp. 432–436.
[7] Dong, L., Johansen, S. T., and Engh, T. A., 1994b, ''Flow Induced by an Impeller in an Unbaffled Tank-II. Numerical Modeling,'' Chem. Eng. Sci., **49**, pp. 3511–3518.
[8] Harvey, A. D., Wood, S. P., and Leng, D. E., 1997, ''Experimental and Computational Study of Multiple Impeller Flows,'' Chem. Eng. Sci., **52**, pp. 1479–1491.
[9] Wechsler, K., Breuer, M., and Durst, F., 1999, ''Steady and Unsteady Computations of Turbulent Flows Induced by a 4/45° Pitched-Blade Impeller,'' ASME J. Fluids Eng., **121**, pp. 318–329.
[10] Dong, L., Johansen, S. T., and Engh, T. A., 1994a, ''Flow Induced by an Impeller in an Unbaffled Tank-I. Experimental,'' Chem. Eng. Sci., **49**, pp. 549–560.
[11] Wilcox, D. C., 1993, *Turbulence Modeling for CFD*, DCW Industries, La Cañada, CA.
[12] Rogers, S. E., Kwak, D., and Kiris, C., 1991, ''Steady and Unsteady Solutions of the Incompressible Navier-Stokes Equations,'' AIAA J., **29**, pp. 603–610.
[13] Rodi, W., and Mansour, N. N., 1993, ''Low Reynolds Number k-ϵ Modeling With the Aid of Direct Simulation Data,'' J. Fluid Mech., **250**, pp. 509–529.
[14] Sloan, D. G., Smith, P. J., and Smoot, L. D., 1986, ''Modeling of Swirl in Turbulent Flow Systems,'' Prog. Energy Combust. Sci., **12**, pp. 163–250.
[15] Yakhot, V., and Smith, L. M., 1992, ''The Renormalization Group, the ϵ-Expansion and Derivation of Turbulence Models,'' J. Sci. Comput., **7**, pp. 35–61.
[16] ''Fluent 4.4 User's Guide,'' 1997, Second Edition, Fluent Inc., Lebanon, NH., Chem. Eng. Sci., **52**, pp. 1479–1491.
[17] Wolfstein, M., 1969, ''The Velocity and Temperature Distribution of One-Dimensional Flow with Turbulence Augmentation and Pressure Gradient,'' Int. J. Heat Mass Transf., **12**, pp. 301–318.
[18] Reynolds, W. C., 1982, *Lectures on Turbulence*, presented as a short course at Los Alamos National Laboratories. Los Alamos, NM.
[19] Kresta, S. M., 1998, ''Turbulence in Stirred Tanks: Anisotropic, Approximate, and Applied,'' Chem. Eng. Sci., **76**, pp. 563–576.
[20] Kresta, S. M., and Wood, P. E., 1993, ''The Flow Field Produced by a Pitched Blade Turbine: Characterization of the Turbulence and Estimation of the Dissipation Rate,'' Chem. Eng. Sci., **48**, pp. 1761–1774.
[21] Fort, I. M., and Makovsky, T., 1993, ''Flow and Turbulence in Baffled System with Impeller with Inclined Blades,'' Collect. Czech. Chem. Commun., **33**, pp. 31–44.
[22] Zhou, Genwen, and Kresta, S. M., 1996, ''Distribution of Energy Between Convective and Turbulent Flow for Three Frequently Used Impellers,'' Trans. Inst. Chem. Eng., **74A**, pp. 379–389.
[23] Jaworski, Z., Nienow, A. W., and Dyster, K. N., 1996, ''An LDA Study of Turbulent Flow Field in a Baffled Vessel Agitated by an Axial, Down-Pumping Hydrofoil Impeller,'' Can. J. Chem. Eng., **74**, pp. 3–15.
[24] Hockey, R. M., and Nouri, J. M., 1996, ''Turbulent Flow in a Baffled Vessel Stirred by a 60° Pitched Blade Impeller,'' Chem. Eng. Sci., **51**, pp. 4405–4421.
[25] Brodkey, R. S., 1967, *The Phenomena of Fluid Motions*, Dover Edition 1995, New York, NY.
[26] Sreenivasan, K. R., 1984, ''On the Scaling of the Turbulence Energy Dissipation Rate,'' Phys. Fluids, **27**, pp. 1048–1051.
[27] Stoots, C. M., and Calabrese, R. C., 1995, ''Mean Velocity Field Relative to a Rushton Turbine Blade,'' AIChE J., **41**, pp. 1–11.
[28] Kresta, S. M., Roussinova, V. and Grgic, B., 1999, ASME/JSME Summer Meeting, July 18–23, San Francisco, CA.
[29] Sahu, A. K., and Joshi, J. B., 1995, ''Simulation of Flow in Stirred Vessels with Axial Flow Impellers: Effects of Various Numerical Schemes and Turbulence Model Parameters,'' Ind. Eng. Chem. Res., **34**, pp. 626–639.
[30] Durbin, P. A., 1991, ''Near-Wall Turbulence Closure Modeling Without Damping Functions,'' Theor. Comput. Fluid Dyn., **3**, pp. 1–13.
[31] Verzicco, R., Iaccarino, G., Fatica, G., and Orlandi, P., 2000, ''Flow in an impeller stirred tank using an immersed boundary method,'' *Annual Research Briefs*, Center for Turbulence Research, NASA Ames/Stanford Univ. pp. 251–261.

Effect of Body Aspect Ratio and Tank Size on the Hydrodynamics of a Rotating Bluff Body During the Initial Spin-Up Period

D. Maynes[1]
Assistant Professor
e-mail: maynesrd@et.byu.edu

M. Butcher
Research Assistant

Department of Mechanical Engineering,
435 CTB,
Brigham Young University,
Provo, UT 84602

Hydrodynamic torque measurements on rotating bluff bodies are presented for 32 different bodies and three different sized tanks for Reynolds numbers in the range 10^4-10^5. The present results focus on the initial period, build-up regime, where the torque remains constant before the tank walls have impacted the flow field in the vicinity of the body. The results show that during the build-up regime, the torque coefficient is a function only of the aspect ratio and increases to a maximum at an aspect ratio near unity, followed by a decrease for further increases in the aspect ratio. This behavior is similar to a uniform flow past rectangular cylinders of varied width and a physical description for the observed variation is proposed. A nondimensional time scale describing the time until the tank geometry impacts the flow field near the body is also presented. This time scaling is based on all of the measurements and appears to be quite general, predicting the spin-up time for bodies differing in volume by three orders of magnitude and tanks differing by two orders of magnitude. [DOI: 10.1115/1.1383550]

1 Introduction

Forces on immersed bluff bodies due to flow past them has long been of fundamental interest in the study of fluid dynamics. Such measurements are critical in the design and development of objects subjected to fluid mechanic loading. They are also critical in describing the associated flow field. Uniform flow past bluff bodies is a mature area. However, a related area has received relatively little attention in the literature. This area is the fluid mechanics associated with a rotating bluff body. Rotating bluff body flows are significantly different from flow fields caused by uniform flow past a bluff body. The primary differences are that the rotating body drives the flow, the body rotates through a self generated wake, the primary fluid direction is rotational, and a secondary flow is induced by the body rotation. For bounded flows (rotating bodies in a tank) the tank geometry is also important.

Much of the previous work related to bluff body flows has been in the broad area of stirred mixing tank flows. Of particular interest has been the effects of different impeller types on the flow field characteristics [1–5], the turbulence level in the bulk flow and in the impeller stream [6,7], and scale up of geometrically similar tanks [8,9]. A somewhat standard geometry for stirred mixing tanks operating in the turbulent regime was adopted by the early 1960s and continues to exist as the standard. Consequently, much of the literature addressing stirred tanks has focused on impeller and tank geometries similar to this standard. For most studies in the literature the aspect ratio (impeller height/impeller radius) ranges between 0.32 and 0.50, also, the ratios of impeller radius to tank radius and impeller height to tank height are typically between 0.33–0.5 and 0.05–0.07, respectively [10]. In addition, most studies have focused on unidirectional rotation without addressing the spin up transient.

The power required to rotate an impeller in a mixing tank is the product of the hydrodynamic torque and the rotation rate, Ω. At steady state the power is balanced by the rate of energy dissipation within the tank. During spin-up from rest, however, the measured torque is indicative of the different fluid mechanic regimes which exist in the transient process. Recently Maynes et al. [11,12] characterized the spin-up of an initially quiescent fluid in a tank due to the rotation of a bluff body (square impeller with a large aspect ratio). For spin-up of a bluff body from rest, three distinct temporal regimes were observed. The first regime was termed the build-up regime. In this regime, the hydrodynamic torque on the bluff body, and velocity fluctuations of the tangential velocity in the bulk flow remain relatively constant. The effects of the tank walls have not yet affected the flow near the body and the behavior is similar to what would occur if the body were rotated in an infinite fluid. The second regime was termed the decay regime. In this regime, the torque and velocity fluctuations decay with power law relations. The decay of the torque and the velocity fluctuations occur because, after some characteristic time, the effects of the tank walls impact the flow behavior near the rotating body. Decay continues until steady state is reached which is the third regime. At steady state, the average torque and the velocity fluctuations level off to approximately constant values. In this regime, the momentum added to the fluid by the rotating body is balanced by the destruction of momentum at the tank walls.

These previous rotating bluff body studies [11,12] were important with regards to the evolution of the flow field from rest. They were also leading in the development of a time scaling that described the temporal evolution of the flow field. However, this previous work presented torque measurements for only seven bluff bodies in a single sized tank and no other data can be found in the literature describing the torque or power requirements for impeller geometries during the build-up regime. Thus the focus of this paper is to present results that quantify the behavior of the torque over a large range of aspect ratios, body size to tank size ratio, and for three very different sized tanks. The results correspond to a Reynolds number range of 10^4-10^5. Specifically this paper will focus on the build-up regime or the initial rotation period before the effects of the tank walls have impacted the flow field. Another paper will focus on the decay dynamics and the steady state regime. Insights into how the flow field, during this initial period, depends on the above parameters will be addressed

[1]Author to whom correspondence should be addressed.

Contributed by the Fluids Engineering Division for publication in the JOURNAL OF FLUIDS ENGINEERING. Manuscript received by the Fluids Engineering Division May 16, 2000; revised manuscript received March 30, 2001. Associate Editor: D. R. Williams.

Table 1 Body specifications and Re ranges explored

L*	h/L	Re Range
Small Tank (R=0.105 m, H=.254 m, H*=2.42)		
0.67	0.42, 0.99, 1.41, 1.84, 2.26	3.1×10^4—2.8×10^5
0.39	0.56, 1.14, 1.4, 2.83, 4.25	4.8×10^4 –2.2×10^5
Medium Tank (R=0.294 m, H=0.42 m, H*=1.43)		
0.36	0.35, 0.71, 1.41, 1.89	2.5×10^4—2.6×10^5
0.24	0.42, 0.99, 1.41, 1.84, 2.26	2.5×10^4—2.6×10^5
0.14	0.56, 1.13, 1.41, 2.83, 4.24	2.5×10^4—1.5×10^5
Large Tank (R=0.457 m, H=1.52 m, H*=3.33)		
0.13	15.89	1×10^3—1×10^4
0.15	6.83	9×10^3—9×10^4
0.22	1.65, 4.55	2×10^4—1.5×10^5
0.31	0.71, 1.41	2.5×10^4—2.8×10^5
0.37	2.73	4×10^4—2.6×10^5
0.67	0.94	6×10^4—5.8×10^5

and the previously developed time scaling by Maynes et al. [12] will also be re-evaluated in light of the now much more extensive data.

2 Methodology

2.1 Tank Sizes and Body Geometries Employed. Experiments were conducted in three different tanks, the radius' of the tanks were $R=0.457$ m, 0.294 m, and 0.105 m. The corresponding heights for these tanks, and the tank aspect ratios, were $H=1.52$ m($H^*=H/R=3.33$), 0.42 m ($H^*=1.43$), and 0.254 m ($H^*=2.42$).

The characteristic length, L, of the bluff bodies utilized was defined to be the distance from the center of the body out to a corner in a horizontal plane. The aspect ratio of the body is the ratio of the body height over L. In the small tank, 10 different bluff bodies were used, ranging in aspect ratio from 0.42–2.83 with L values of 0.041–0.071 m ($L^*=L/R=0.39-0.68$). In the medium tank, fourteen bluff bodies were used. These bodies varied in aspect ratio from 0.35–4.24 where L varied from 0.041–0.11 m ($L^*=0.14-0.374$). In the large tank, seven bodies were used ranging in aspect ratio from 0.71–15.9 with L varying between 0.06–0.32 m ($L^*=0.13-0.67$). All of the bodies were square in cross section. Table 1 lists the bluff bodies used, the dimensions for each, the Reynolds number range ($\mathrm{Re}=\Omega L^2/\nu$) for each, and the tank in which it was used. The fluid used was water at approximately 20°C. For all experiments, the tank was completely filled so that a free surface did not exist.

2.2 Experimental Setup. Figure 1 shows a schematic diagram of the experimental setup and a typical bluff body. Regardless of the body or tank used, data acquisition was similar for all tests. The body was connected to a stepper motor, controlled by a Macintosh computer, via a shaft and located such that the center of the body coincided with the center of the tank. An in-line torque sensor that interfaced with a data acquisition system was mounted on the shaft between the body and the motor. After the fluid in the tank had completely come to rest, motion and data acquisition were initiated. Data was acquired for a time much longer than the time required for steady state to be attained. The acquisition rate was 100 HZ for all of the experiments. This sampling frequency was much greater than double the largest frequencies resolved by the sensor due to fluid motions. The maximum rotation rate for each body was limited by the upper limits of the torque sensors employed.

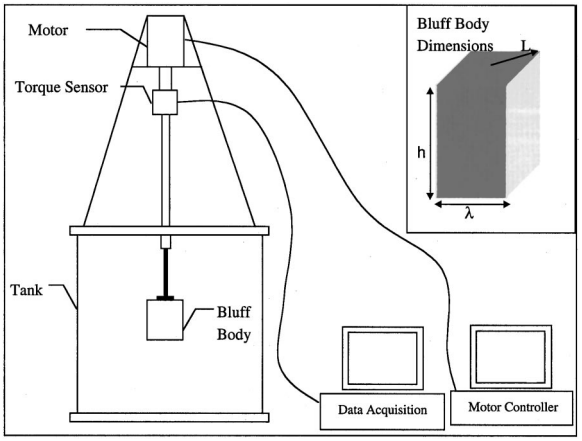

Fig. 1 Schematic of a typical experimental facility and an illustration of a bluff body

The motor utilized was an SX Series Compumotor manufactured by Parker Hannifin Corporation. It consisted of a programmable indexer and drive connected with a stepper motor. It allowed the acceleration, rotation rate, and number of revolutions to be specified. According to the manufacturer's specifications, the accuracy of the velocity and acceleration were within 0.02 percent.

Two Key Transducer torque meters were employed to obtain the torque measurements in the experiments. For the sensor used in the small and medium tanks, full scale corresponded to a torque value of 0.706 N-m. This sensor was also utilized in the large tank in addition to a second sensor where full scale corresponds to 22.6 N-m.

The signal from the torque sensor was connected to an A/D converter interfaced with a PC machine. The motor and acquisition program were initiated by the same trigger switch and when the switch was closed, the data acquisition system began collecting data and the motor began to rotate. The data collection process stopped shortly before the motor ceased rotating. The fluid was allowed to come to rest before the process was repeated.

2.3 Nondimensional Parameters. For fast accelerating flow the hydrodynamic torque can be written as $T=T(L,R,H,h,\Omega,\nu,\rho,t)$. Where T is the torque, L is the characteristic length of the body, h is the height of the body, R is the radius of the tank, H is the height of the tank, Ω is the rotation rate in radians/second, ν is the kinematic viscosity, ρ is the fluid density, and t is time. Standard dimensional analysis reduces the number of variables from nine to six. The following nondimensional parameters describe the flow field from startup.

$$C_m=\frac{T}{\frac{1}{2}\rho\Omega^2L^4h} \tag{1}$$

$$\mathrm{Re}=\Omega L^2/\nu \tag{2}$$

$$L^*=\frac{L}{R} \tag{3}$$

$$h^*=\frac{h}{R} \tag{4}$$

$$H^*=\frac{H}{R} \tag{5}$$

$$t^*=\Omega t/2\pi \tag{6}$$

C_m is the nondimensional torque coefficient, Re is the Reynolds number, t^* is the number of revolutions, and L^*, h^*, and H^* are geometric parameters for the body and tank. Values for the density and kinematic viscosity were obtained for water at 20°C.

3 Error Analysis

For instantaneous measurements of the torque, the torque coefficient can be expressed as $C_m \pm C_{me}$, where C_{me} represents the error associated with the torque measurements. The expression for

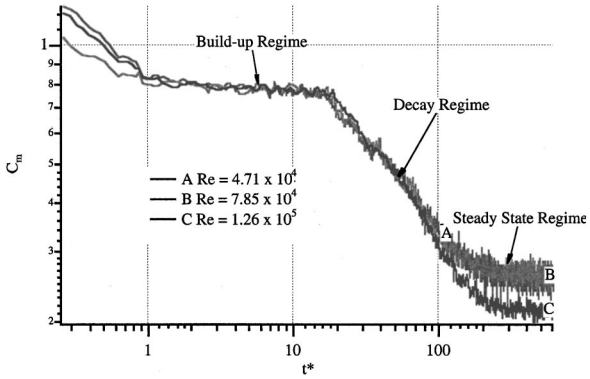

Fig. 2 C_m versus t^* for $L^*=0.24$ and $h/L=1.41$ for Re=4.71 $\times 10^4$, 7.85$\times 10^4$, and 1.26$\times 10^5$. This figure illustrates the three temporal regimes that exist in the spin up from rest to steady state of a rotating bluff body.

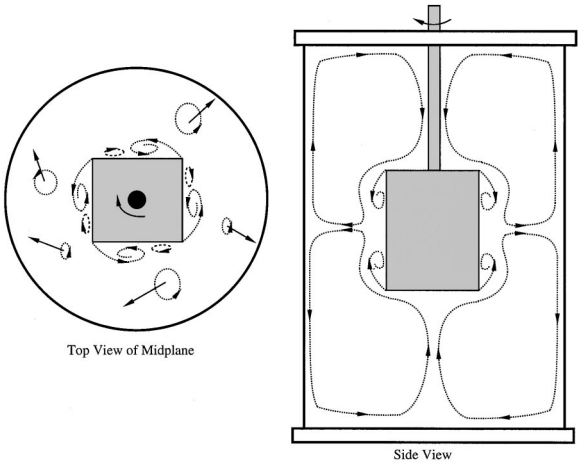

Fig. 3 Schematic illustration of the general behavior of the flow field at the body center in the r-θ plane and at a vertical plane passing through the center of the body in the r-z plane

C_m is given in Eq. (1) as a function of torque (T), density (ρ), rotation rate (Ω), characteristic body length (L), and body height (h). The error, C_{me}, is also a function of these parameters.

The primary source of error in the experiments was associated with the torque sensor employed. The output signal from both transducers was accurate to within ± 0.05 percent of full scale. This corresponds to bias errors of $\pm 3.53\times 10^{-4}$ N-m and $\pm 1.12 \times 10^{-2}$ N-m for the small and large sensors respectively. There was also some precision error in the torque measurement due to the electrical noise in the voltage signal. During the build-up and steady-state regimes, the precision error was minimized by computing the average torque over several data points. Using standard error analysis the maximum precision error for the small sensor was computed to be 0.0006 N-m. The total error from the torque measurement was then determined.

The density was determined by looking it up in a table at the given temperature and was assumed to be accurate within 0.5 kg/m^3. According to the manufacturer specifications on the motor, the rotation rate was accurate to within ± 0.02 percent of the rotation rate. The scale used to measure the characteristic length and height has a least count of 1 mm. So these measurements were assumed to be accurate to within 0.5 mm. The value of C_{me} was calculated for each data set. The maximum error was associated with the smallest body at the lowest rotation rate during the steady state regime. This was calculated to be 12.5 percent. The error for the rest of the measurements ranged from 1–10 percent with almost all of the measurements being accurate to within ± 5 percent.

4 Overview of the Flow Field During the Build-Up Regime

Figure 2 shows a sample of the data collected for a body in the medium tank with $L^*=0.24$ and $h/L=1.41$. This figure plots C_m versus the number of revolutions, t^*, on a log-log scale for three different Re. The data illustrate the three distinct temporal regimes that exist. The build-up regime, where the value of the C_m remains relatively constant, corresponds to $1\leqslant t^*\leqslant 20$. The decay regime, where C_m decays with a power law relation, corresponds to $20\leqslant t^*\leqslant 200$. And the steady-state regime, where the torque levels off to a constant mean value, corresponds to $t^*>200$. The results presented in this paper focus on the effects of body aspect ratio and tank geometry on the torque coefficient during the build-up regime and on the time elapsed before C_m begins to decay.

When the body begins to rotate, there is an initial inertial loading that causes the value of the torque to quickly reach a peak. When the body ceases to accelerate the value of the torque levels off to a constant value. The build-up regime lasts from the moment that this constant value is reached until the torque begins to decrease. A general illustration of the flow field during the start-up process is shown in Fig. 3. This illustration depicts the r-θ plane at a level coinciding with the center of the body (left), and the r-z plane (right). These schematics are formulated from flow visualization observations.

When the body first begins to rotate a starting vortex is formed on the leeside of each corner as viewed in the r-θ plane. These initial vortices are shed from the body and convect out into the bulk flow region. After the initial vortex is ejected a separation region is observed to exist and remain on the leeside of each corner. Also because of the low pressure which exists in these separation zones, a secondary flow is induced by the body rotation. Consequently, the separation regions near the top and bottom of the body represent three dimensional recirculation zones. It should be noted that axial velocity measurements near rotating bluff bodies [13] show that immediately after passage of a corner the observed motion (outside of the recirculation region) is towards the midplane. As the next corner approaches however, the fluid motion is away from the midplane. On average the secondary motion is toward the midplane above and below the body and radially outward at the midplane (often called impeller stream in mixing tank literature).

It is this secondary flow that accounts for much of the transport of momentum throughout the tank. Initially the fluid that is transported by the secondary flow into the region near the body has little or no angular momentum associated with it until it is acted on by the body. As long as this is the case, the torque on the body must remain relatively constant because the size of the recirculation, and thus low pressure, regions do not change. This is the condition that would exist if the body were to rotate in an infinite medium. Because the flow is confined, fluid that has been acted on by the body, either directly or indirectly, is transported by the secondary flow back to the region either above or below the body. At this time the fluid now transported into the region near the body again interacts with the body. However now the relative velocity between fluid and object is smaller leading to smaller recirculation, and low pressure regions. Consequently, the torque begins to decrease. As rotation continues, the torque decays until a condition is reached where the destruction of momentum at the tank walls, due to the wall boundary layers, is balanced by the addition of momentum by the rotating body. Also at this time, the power input must equal the rate of energy dissipation.

Based on the above quantitative description of the flow field dynamics, it would be expected that the only important parameters affecting the value of C_m in the build-up regime are the body

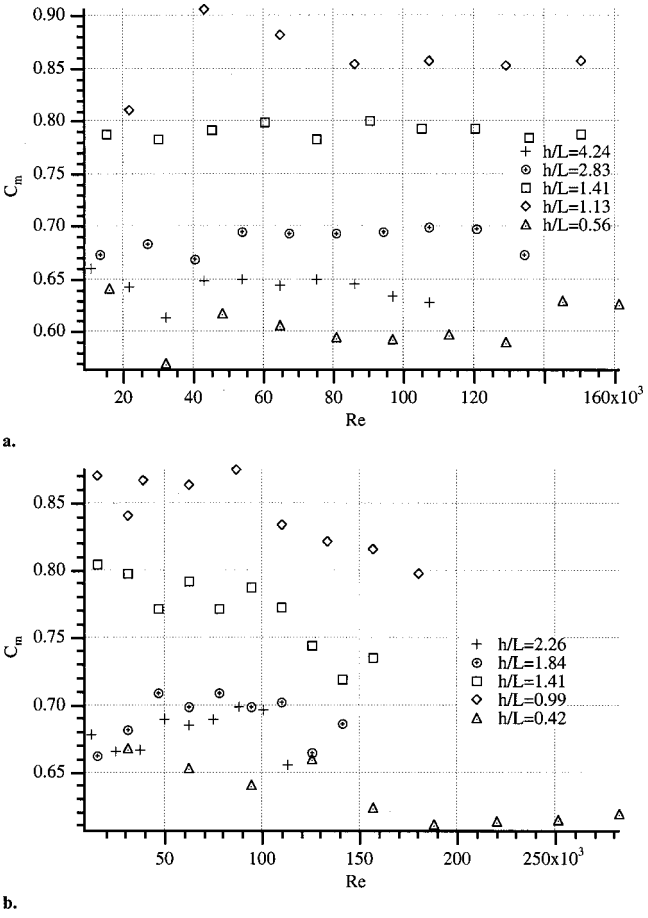

Fig. 4 Build-up regime torque coefficient versus Reynolds number in the medium tank for (a) $L^*=0.14$ and (b) $L^*=0.24$. For each L^*, results for five aspect ratios are shown.

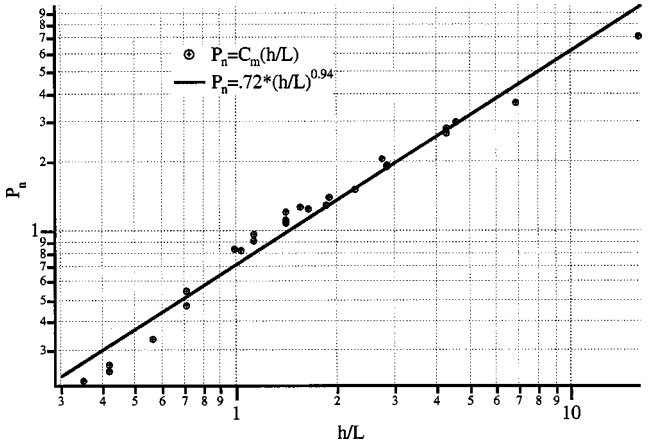

Fig. 5 Build-up regime value of P_n versus h/L for 32 different cases representing all three tanks

dimensions. The tank dimensions clearly are important with regards to the time over which the build-up regime behavior exists, however, with regards to the magnitude of the torque they should not be significant.

5 Build-Up Regime Results

5.1 Aspect Ratio Effects on C_m in Build-up Regime. Results are now presented that describe the effects of variations in the aspect ratio on the build-up regime value of C_m. The physical mechanisms causing the variations in C_m are also discussed.

Shown in Fig. 4(*a*) are build-up regime values of C_m plotted versus Re for $L^*=0.14$ and $h/L=0.56$, 1.13, 1.41, 2.83, and 4.24. Likewise Fig. 4(*b*) plots C_m versus Re for $L^*=0.24$ and $h/L=0.42$, 0.99, 1.41, 1.84, 2.26. Both of the above sets of data were obtained in the medium size tank, $H^*=1.43$. The value of C_m shown in these figures corresponds to a representative value averaged over several data points in the build-up regime. Note that over the Re range explored some variation exists for a fixed L^* and h/L. Within the range of experimental uncertainty for the C_m measurements ($\approx\pm5$ percent), however, C_m corresponding to a fixed L^* and h/L may be assumed to be constant for the Re range presented. Indeed all of our data obtained in all three tanks follow this same trend, where for a fixed value of L^* and h/L, C_m remains approximately constant.

Note from Fig. 4 that C_m is the lowest in magnitude for small h/L. For $L^*=0.14$ and $h/L=0.56$ $C_m\approx0.6$, likewise for $L^*=0.24$ and $h/L=0.42$ $C_m\approx0.62$. However, the maximum value does not occur for the largest h/L. For the data of Fig. 4 the maximum values of C_m occur at $h/L=1.13$ for $L^*=0.14$, and at $h/L=0.99$ for $L^*=0.24$. For larger h/L the magnitude of C_m decreases for both L^*.

In traditional stirred mixing tank studies the power number is defined to be

$$P_n=\frac{P}{\rho\Omega^3D^5} \tag{7}$$

where P is the power input and D is the impeller radius. Since $D=2L$ and $P=T\Omega$, the forms of P_n and C_m are similar only differing by a constant in the denominator and the ratio h/L as shown by comparing Eq. (8) with Eq. (1).

$$P_n=\frac{T}{\rho\Omega^2 16L^5} \tag{8}$$

Also, in computing P_n, Ω is often expressed in revolutions/second rather than radians/second as we do for C_m. Neglecting the differences in constant coefficients that appear in Eq. (1) and Eq. (8), and the difference in coefficients that would result when using revs/s instead of rad/s, a power number can simply be expressed as $P_n=C_m(h/L)$. Shown in Fig. 5 is data for P_n plotted versus h/L where the value for P_n represents an average over the Re ranges explored. Data corresponding to all of the bodies listed in Table 1 are displayed and represents the build-up regime value of P_n for 32 different cases in the three different tanks. The Re range is 10^4-10^5 for all of the bodies. The figure clearly shows as h/L increases, the required power input also increases. Also, the figure shows that tank size does not play an effect in the build-up regime. This is evident since the data were obtained in three tanks with vastly different volumes and all the data follows a similar curve.

Although P_n is monotonically increasing with increasing h/L, suggesting P_n is proportional to h, note from Fig. 5 that the relation is not linear. Much more significant insight into the flow field physics is obtained by plotting C_m versus h/L for the same cases shown in Fig. 5. This is done in Fig. 6. The torque coefficient represents a ratio of the measured torque over the product of the induced dynamic pressure due to body rotation, $1/2\rho(\Omega L)^2$, the body surface area, Lh, and the lever arm from the body center to a corner, L. Note from Fig. 6 that for h/L increasing from 0.3 to about 1 that C_m also increases. In this range of h/L a least squares curve fit to the data suggests

$$C_m=0.48+0.31\left(\frac{h}{L}\right)+0.15\left(\frac{h}{L}\right)^2 \tag{9}$$

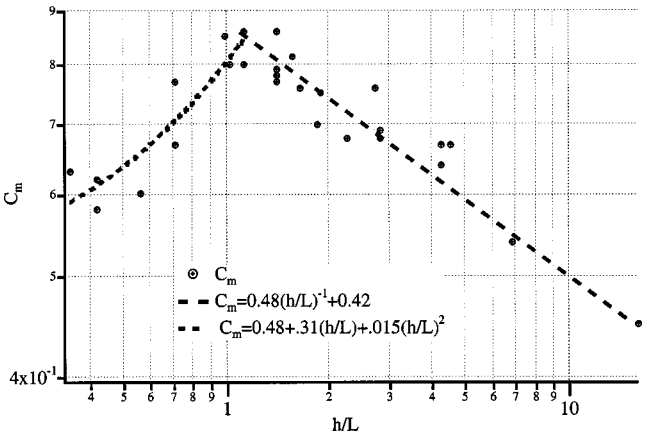

Fig. 6 Build-up regime value of C_m versus h/L for 32 different cases representing all three tanks

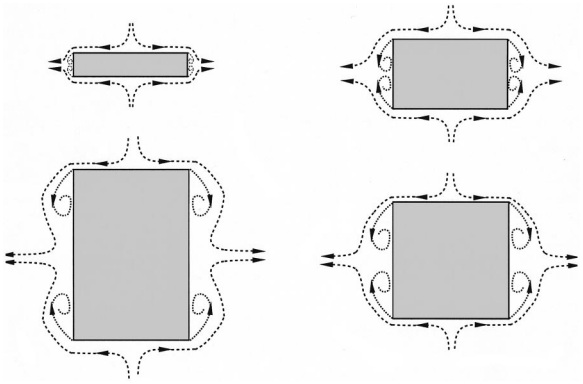

Fig. 8 Schematic of the *r-z* plane flow behavior in the vicinity of the body for four different bluff bodies with different aspect ratios

A maximum exists at $h/L \approx 1.1 (C_m \approx 0.9)$, but for h/L increasing above 1.1, C_m decreases as shown by the data. In this range a least squares curve fit to the data suggest the form

$$C_m = 0.48\left(\frac{h}{L}\right)^{-1} + 0.42 \tag{10}$$

Thus the torque per height increases with increasing h until h is about the same size as L, above which further increases in h leads to a decrease in the torque/height.

The above behavior is somewhat similar in form to drag coefficient, C_D, measurements due to uniform flow past rectangular cylinders (see Fig. 7 for illustration) reported by Nakaguchi et al. [14] and Bearman and Trueman [15]. C_D data for 2-D rectangular cylinders with different X/Y ratios are shown in Fig. 7 based on data from Blevins [15] and Courchesne and Laneville [16]. C_D is the ratio of the measured drag per length of cylinder over the product of the dynamic pressure, $1/2\rho U_\infty^2$, and cylinder height Y. For this flow the drag coefficient increases from the thin plate value of 1.9 to about 3.0 at $X/Y \approx 0.65$. Above $X/Y = 0.65$ C_D decreases with what appears to be a power law relation. The physical reason leading to this observed behavior was explained by Bearman and Trueman [15] and verified by flow visualization studies. For small X the characteristic size of the shed vortices scales with the height of the cylinder, Y. As X increases, however, the size of the shed vortices increases leading to a lower back pressure on the downstream cylinder face. This occurs because of separation at the front corners which results in a broadening of the dividing streamlines between the potential flow and the separated flow regions. At $X/Y \approx 0.65$ the size of the shed vortices in the wake decreases and continues to decrease for increasing h/L for the range $X/L < 3.0$. This results in an increasing back pressure on the cylinder and occurs because the length scales of the separated flow regions downstream from the front corners are now of the same scale as X. Consequently, as h/L increases, the direction of the potential flow is increasingly more parallel to the upper and lower faces resulting in smaller shed vortices behind the cylinder and thus a narrower wake.

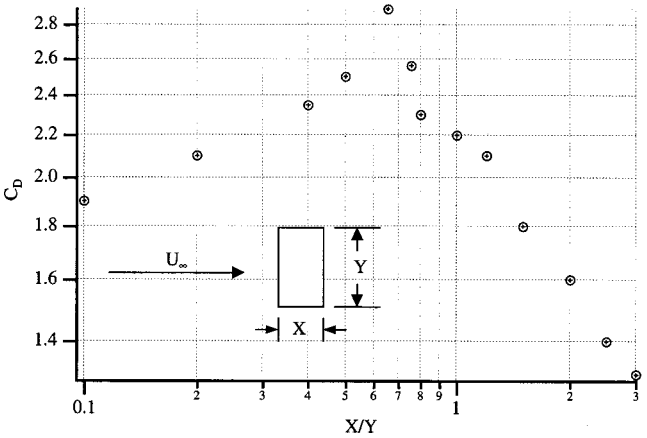

Fig. 7 C_D versus X/Y for uniform flow past 2-D rectangular cylinders

In a similar manner the aspect ratio of the rotating bluff body affects the size of the separated flow regions and thus the pressure drag exerted on the body. A schematic of the flow field in the *r-z* plane is shown in Fig. 8 for different h/L ratios. In the reference frame of the rotating body, the separated flow regions exist on the lee side of the corners due to tangential motion past the body and due to the secondary flow over the top and bottom of the body. For small h/L the size of the separated regions is limited by the height of the body. This is illustrated in Fig. 8 (upper left) where only the secondary motions are considered. Under these conditions the size of the separated flow regions is limited due to symmetry. As h/L increases the size of these recirculation zones increases thus resulting in a lower pressure and an increase in C_m. This continues until h approaches the same size as L. At greater h/L ratios the size of the vertical separation zones no longer increases but remains at a fixed size and scales with L. Consequently, for increasing h/L, the percentage of the body influenced by these vortices decreases resulting in a decrease in C_m. The above description considers only the secondary motion, however, the behavior should be similar for the real three dimensional flow and qualitatively describes the behavior of the C_m data.

The above description suggests that for $h/L > 1$ the characteristic size of the shed vortices on the leeside of the rotating body corners due to the coupled tangential and secondary flow is now independent of h. If this is the case, the torque on the body should equal the torque due to these shed vortices plus the torque due to the much smaller separated flow regions that exist in between these recirculation zones at the top and bottom of the body (see Fig. 8 lower left). If we make the assumption that in this ''middle'' region that the separated flow regions are 2-D so that the torque per unit height in this region is constant we can mathematically express the torque for $h/L > 1$ as

$$T = T(h = L) + T'_{\text{middle}}(h - L) \tag{11}$$

where $T(h=L)$ is the torque that would exist on a body with $h = L$, T'_{middle} is the torque per unit height in the midsection and *h-L* represents that portion of the body over which the separated flow regions are 2-D and h independent. Rewriting Eq. (11) in terms of torque coefficient as shown in Eq. (1) results in Eq. (12),

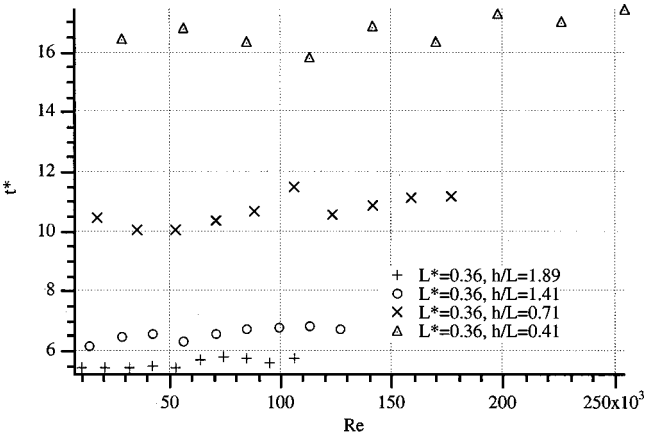

Fig. 9 Revolutions until decay regime begins plotted versus Re for $L^*=0.36$ and $h/L=1.89$, 1.41, 0.71, and 0.41 in the medium tank

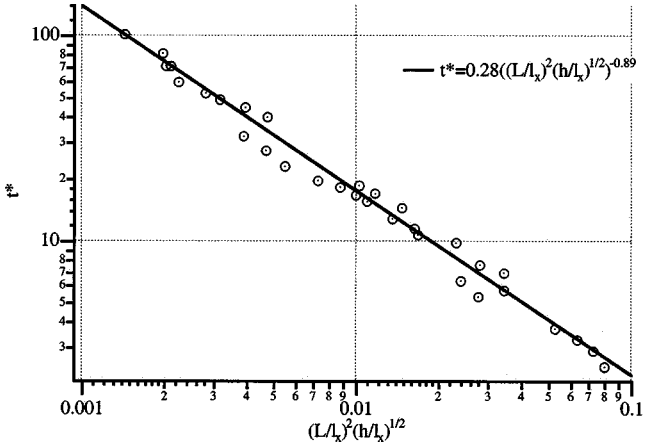

Fig. 11 t^* versus $(L^2/l_x^2)(h/l_x)^{1/2}$ for 32 different bodies in the three tanks

$$C_m = C_m(h=L)\frac{L}{h} + C_{m2-D}\frac{h-L}{h} \tag{12}$$

$C_m(h=L)$ is about 0.85, $C_{m2\text{-D}}$ is the C_m value that would exist for a truly 2-D body. We do not have data for such a body but the data show that for $h/L=16$, $C_m=0.45$. A reasonable approximation for a value approximating a 2-D body is 0.4. Substituting these values into Eq. (12) and simplifying results in

$$C_m = 0.45\left(\frac{h}{L}\right)^{-1} + 0.4 \tag{13}$$

Note that the values in the above expression differ only slightly from the values in Eq. (10). Equation (13) does not fit the data quite as well as Eq. (10) but it is based on the physical description above and provides evidence of the correctness of this description.

5.2 Build-Up Regime Time Scale. Shown in Fig. 9 is the number of revolutions, t^*, required until decay starts for $L^*=0.36$ and $h/L=1.89$, 1.41, 0.71, and 0.41 in the medium tank, plotted versus Re. The data show that the t^* until decay begins shows little, if any, dependence on Re for the Re range explored, but is a significant function of h/L. All of our data for all bodies utilized in all three tanks exhibit this same behavior. Plotted in Fig. 10 are values of the t^* where decay begins, averaged over the Re ranges explored, versus h/L for five different L^* and in the small and medium tanks. For each L^* the t^* value when decay begins, decreases with increasing h/L. It is also evident from the figure that the tank size, R and H, is also important. This is illustrated by the two cases where $L^*=0.36$ in the medium tank and $L^*=0.39$ in the small tank. For $L^*=0.36$ and $H^*=1.45$ the number of revolutions required is about 1/2 that required for $L^*=0.39$ and $H^*=2.33$.

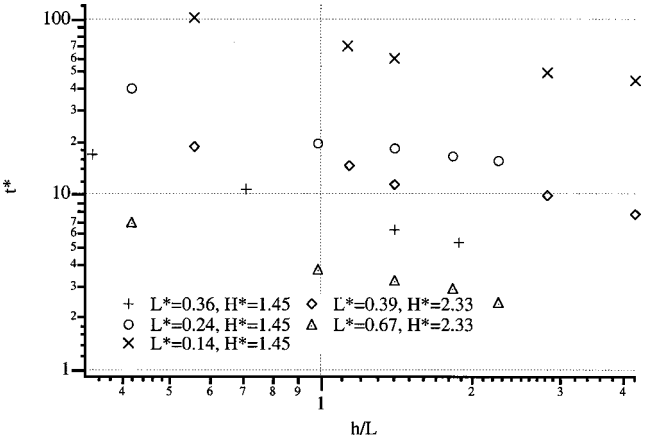

Fig. 10 Revolutions until decay begins versus h/L for 25 different bodies representing three L^* values in the medium tank and two L^* values in the small tank

Previously Maynes et al. [12] presented a time scale, based on standard turbulent scalings that describes the spin-up time from a quiescent fluid until the decay regime begins for eight bodies employed in the large tank. This time was expressed as $t_b \sim l_b^2/(\Omega L^2)$ where $l_b^2=(R-L)^2+(H/2-h/2)^2$. This time represents the time required for the entire flow field to be affected by turbulent motions, l_b is the largest distance in the tank over which turbulent motions will be transported, L represents the characteristic length scale of the turbulent motions, and the characteristic velocity of the turbulent motions was argued to scale with ΩL. When the dimensional time, t, is normalized by t_b the following nondimensional time scale results.

$$\tau_0 = t^*\frac{L^2}{(R-L)^2+\left(\frac{H-h}{2}\right)^2} \tag{14}$$

For the data in the large tank the τ_0 when decay begins is between 0.8 and 1.4 for eight different bluff bodies. However, the value of τ_0 varies between about 0.9–2.6 in the medium tank and 1.5–4 in the small tank, suggesting a different scaling may be more appropriate and universal for such a large range of body and tank geometries. Shown in Fig. 11 is the t^* until decay begins for 32 different bodies in the three tanks plotted versus $(L/l_x)^2(h/l_x)^{1/2}$. The characteristic length of the tank, l_x is taken here as $R+H/2$ and represents the distance from the center of the tank to the top (or bottom) corner of the tank following the path of the secondary motions. Thus from a scaling argument $l_x^2/(\Omega L^2)$ would be the time required for momentum to be transported due to turbulence over the entire tank volume. This scaling, however, includes no h dependence and illustrates the complexity of developing simple scaling relations in turbulent flows with multiple geometric length scales. The data exhibit a $(h/l_x)^{1/2}$ dependence and when plotted versus $(L/l_x)^2(h/l_x)^{1/2}$ the t^* data follows a power law relation quite closely. A power law curve fit to the data suggests a form

$$t^* = 0.28\left[\left(\frac{L}{l_x}\right)^2\sqrt{\frac{h}{l_x}}\right]^{-0.89} \tag{15}$$

or a nondimensional time scale of the form

$$\tau = \frac{t^*}{0.28}\left[\left(\frac{L}{l_x}\right)\sqrt{\frac{h}{l_x}}\right]^{0.89} \quad (16)$$

For all of our data the value of τ when decay begins ranges between 0.8–1.2 with the average being 1.0 and 67 percent of the data are within ± 0.12 of this value. This scaling is significant because it represents the spin up time until decay begins for bodies differing in volume from $7.8\times10^{-5}\,m^3$–$2.7\times10^{-2}\,m^3$ and tanks differing in volume from $8.8\times10^{-3}\,m^3$–$9.8\times10^{-1}\,m^3$ and for the Re range of order 10^4–10^5. Although all of our data correspond to square impellers over a wide range of aspect ratio, the time scaling trends should be similar for other radial flow impellers located in the center of a tank.

6 Conclusions

For a body that begins rotating in a quiescent confined fluid the measured hydrodynamic torque on the body remains constant, after constant rotation rate is attained, for some time dependent on the size of the body and tank. This time is referred to as the build-up regime and during this time C_m depends only on the ratio h/L. For $h/L \leqslant 1.1$ C_m increases with increasing h/L and is a maximum for $h/L \approx 1.1$. At greater h/L, C_m decreases with a power law relation. This behavior exists due to the effects of the body aspect ratio on the characteristic length of the shed vortices which results in pressure drag on the body. For $h/L \leqslant 1.1$ the characteristic size of the separated flow regions increases with increasing h and the value of C_m can be approximated by Eq. (9). For $h/L > 1.1$, the effects of the secondary flow on the separated flow regions is limited to a length that scales with L. Consequently, increases in h/L result in decreases in C_m and Eq. (10) describes C_m for h/L values in this range. A nondimensional time scale that describes the time over which C_m remains constant in this initial time period is given in Eq. (16) and all of our data fall within 20 percent of this relation. The data presented represent 32 different bodies differing in volume by three orders of magnitude and three different tanks differing in volume by two orders of magnitude. Also the Re range of the presented data was 10^4–10^5.

Nomenclature

C_D = drag coefficient
C_m = torque coefficient $(T/(1/2\rho\Omega^2L^4h))$
C_{me} = error in determining C_m
D = impeller diameter (m)
h = body height (m)
h^* = nondimensional body height (h/R)
H = fluid height in tank (m)
H^* = nondimensional fluid height (H/R)
l_b = characteristic tank length scale for previous large tank data
l_x = characteristic tank length scale
L = characteristic body length $(\lambda/2^{1/2})$, (m)
L^* = nondimensional body length (L/R)
P = power input (W)
P_n = power number $(P/(1/2\rho\Omega^3D^5))$
R = tank radius (m)
Re = Reynolds number (wL^2/ν)
t^* = nondimensional time (t^* = revolutions)
T = torque (N-m)
U_∞ = uniform freestream velocity
V = characteristic velocity $(\omega L, \text{cm/s})$
X = width of 2-D rectangular cylinder
Y = height of 2-D rectangular cylinder
α = angular acceleration $(1/s^2)$
λ = length of body face (m)
Ω = angular rotation rate (1/s)
ν = kinematic viscosity (m^2/s)
ρ = fluid density (kg/m^2)
τ_0 = normalized time scale from previous work
τ = normalized time scale describing length of build up regime $t^*(L/l_x)^2(h/l_x)^{1/2}$

References

[1] Rutherford, K., Mahmoudi, M. S., Lee, K. C., and Yianneskis, M., 1996, ''The Influence of Rushton Impeller Blade and Disk Thickness on the Mixing Characteristics of Stirred Vessels,'' Trans. Inst. Chem. Eng., Part A, **74**, pp. 369–378.

[2] Gunkel, A. A., and Weber, M. E., 1975, ''Flow Phenomena in Stirred Tanks,'' AIChE J., **21**, No. 5, pp. 931–949.

[3] Roberts, R. M., Gray, M. R., Thompson, R., and Kresta, S. M., 1995, ''The Effect of Impeller and Tank Geometry on Circulation Time Distributions in Stirred Tanks,'' Trans. Inst. Chem. Eng., Part A, **73**, pp. 78–86.

[4] Rushton, J. H., Costich, E. W., and Everett, H. J., 1950, ''Power Characteristics of Mixing Impellers Part I,'' Chem. Eng. Prog., **46**, No. 8, pp. 395–404.

[5] Rushton, J. H., Costich, E. W., and Everett, H. J., 1950, ''Power Characteristics of Mixing Impellers Part II,'' Chem. Eng. Prog., **46**, No. 8, pp. 467–477.

[6] Wu, H., and Patterson, G. K., 1989, ''Laser-Doppler Measurements of Turbulent-Flow Parameters in a Stirred Tank,'' Chem. Eng. Sci., **44**, No. 10, pp. 2207–2221.

[7] Costes, J., and Couderc, J. P., 1988, ''Study by Laser Doppler Anemometry of the Turbulent Flow Induced by a Rushton Trubine in a Sitrred Tank: Influence of the Size of the Units,'' Chem. Eng. Sci., **43**, No. 10, pp. 2765–2772.

[8] Rice, R. W., and Baud, R. E., 1990, ''The Role of Micromixing in the Scale-Up of Geometrically Similar Batch Reactors,'' AIChE J., **36**, No. 2, pp. 293–298.

[9] Bourne, J. R., and Dell'ava, P., 1987, ''Micro- and Macro-Mixing in Strired Tank Reactors of Different Sizes,'' Chem. Eng. Res. Des., **65**, pp. 180–186.

[10] Tatterson, G. B., 1991, *Fluid Mixing and Gas Dispersion in Agitated Tanks*, McGraw-Hill, pp. 23–50.

[11] Maynes, D., Klewicki, J. C., and McMurtry, P. A., 1998, ''Time Resolved Torque of Three Dimensional Rotating Bluff Bodies in a Cylindrical Tank,'' ASME J. Fluids Eng., **120**, pp. 23–28.

[12] Maynes, D., Klewicki, J., and McMurtry, P., 1999, ''Spin-up in a Tank Induced by a Rotating Bluff Body,'' J. Fluid Mech., **388**, pp. 49–68.

[13] Maynes, D., 2000, ''Molecular Tagging Velocimetry Characterization of Rapid KDP Crystal Growth,'' AIChE J., **46**, No. 3, pp. 450–461.

[14] Nakaguchi, H., Hashimoto, K., and Muto, S., 1968, ''An Experimental Study on Aerodynamic Drag of Rectangular Cylinders,'' Journal of the Japan Society of Aeronautical and Space Sciences, **16**, pp. 1–5.

[15] Blevins, R. D., 1984, *Applied Fluid Dynamics Handbook*, Van Nostrand Reinhold, pp. 319

[16] Courchesne, J., and Laneville, A., 1979, ''A Comparison of Correction Methods Used in the Evaluation of Drag Coefficient Measurements for Two-Dimensional Rectangular Cylinders,'' ASME J. Fluids Eng., **101**, pp. 506–510.

Scott K. Thomas[1]

Richard C. Lykins

Department of Mechanical
and Materials Engineering,
Wright State University,
Dayton, OH 45435-0001

Kirk L. Yerkes

Air Force Research Laboratory (PRPG),
Wright-Patterson AFB, OH 45433-7251

Fully-Developed Laminar Flow in Sinusoidal Grooves

The flow of a constant property fluid through a sinusoidal groove has been analyzed. A numerical solution of the conservation of mass and momentum equations for fully developed flow is presented. The mean velocity, volumetric flow rate, and Poiseuille number are presented as functions of the groove geometry, meniscus contact angle, and shear stress at the liquid-vapor interface. In addition, a semi-analytical solution for the normalized mean velocity in terms of the normalized shear stress at the meniscus is shown to agree with the numerical data quite well. [DOI: 10.1115/1.1385832]

1 Introduction

Isotropic materials such as quartz glass or borosilicate glass can be chemically etched to form micro-grooves for the enhancement of evaporative heat transfer in chip-level devices [1]. A typical etched profile in glass is shown in Fig. 1, where the profile is smooth instead of having sharp corners seen in the etching of crystalline materials such as silicon [2]. While many studies have been performed on sharp-cornered geometries (triangular grooves [3–7], rectangular grooves [8–10], and trapezoidal grooves [11]), very little information is available in the open literature on the flow of liquid in rounded-corner geometries. Stroes and Catton [12] compared the capillary performance of triangular and sinusoidal grooves by means of an experimental study. Two sets of grooves were machined into stainless steel test plates such that the cross-sectional areas of the grooves were equal. Strip heaters were placed under the plates to provide heat input. The test plates were placed at inclination angles of 4 and 6 deg and ethanol was added to the grooves until the liquid reached the lands of the grooves. The average wetted length of each set of grooves was recorded as the heat input was varied from 0 to 25 W. The study showed that the triangular grooves had a greater capillary pumping ability compared to the sinusoidal grooves with the same cross-sectional area, inclination angle, and heat input. Stroes and Catton postulated that this was due to the axial rate of change of the radius of curvature of the meniscus. Sinusoidal grooves, however, could dissipate a given heat input with a smaller wetted area than triangular grooves due to the larger wetted perimeter found with sinusoidal grooves.

The objective of the present study was to examine the fully-developed laminar flow of liquid in sinusoidal grooves. The effects of countercurrent and cocurrent vapor flow over the liquid-vapor interface were investigated by relating the liquid velocity gradient to the friction factor of the vapor. The variation of the shear stress on the liquid-vapor interface [10] was neglected, and the liquid-vapor interface was assumed to be circular ($Bo \ll 1$). The mean velocity, volumetric flow rate and Poiseuille number were determined as functions of the interfacial shear stress, the meniscus contact angle, the groove aspect ratio and the amount that the groove was filled.

2 Mathematical Model

A constant property liquid flows steadily in a sinusoidal groove as shown in Fig. 2. A meniscus, which is assumed to be circular, comprises the liquid-vapor interface. For fully developed laminar flow, the conservation of mass and momentum equations reduce to the classic Poisson equation in dimensionless form [13]

$$\frac{\partial^2 v^*}{\partial x^{*2}} + \frac{\partial^2 v^*}{\partial z^{*2}} = -1 \tag{1}$$

On the groove wall, the no-slip condition is in effect.

$$v^* = 0: \quad 0 \leqslant x^* \leqslant w_l^*/2, \quad z^* = \frac{1}{2}\left\{1 + \cos\left[-\pi\left(\frac{x^*}{\beta} + 1\right)\right]\right\} \tag{2}$$

At the line of symmetry, the velocity gradient is zero in the x^* direction

$$\frac{\partial v^*}{\partial x^*} = 0: \quad x^* = 0, \quad 0 \leqslant z^* \leqslant h_l^* + R^* \sqrt{1 - \left(\frac{w_l^*}{2R^*}\right)^2} - R^* \tag{3}$$

The dimensionless radius of curvature is given by

$$R^* = \left(\frac{w_l^*}{2}\right)\left[1 + \frac{(1 + d^* \tan\phi)^2}{(d^* - \tan\phi)^2}\right]^{1/2} \tag{4}$$

where

$$d^* = \frac{\pi}{2\beta}\sin\left[-\pi\left(\frac{w_l^*}{2\beta} + 1\right)\right] \tag{5}$$

The maximum value for the meniscus contact angle ϕ for a wetting fluid can be determined for a given geometry by allowing the radius of curvature to approach $R^* \to \infty$.

$$\phi_{\max} = \tan^{-1}\left\{\frac{\pi}{2\beta}\sin\left[-\pi\left(\frac{w_l^*}{2\beta} + 1\right)\right]\right\} \tag{6}$$

At the liquid-vapor interface, a uniform shear stress is imposed in the y direction.

$$\frac{\partial v^*}{\partial n^*} = \tau_{lv}^*: \quad 0 \leqslant x^* \leqslant w_l^*/2,$$

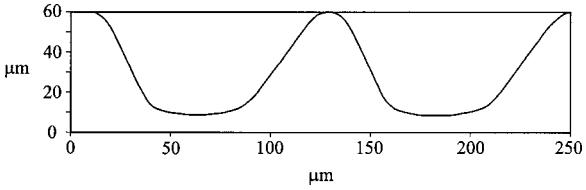

Fig. 1 Grooves chemically etched in glass (courtesy of D. Liepmann, University of California at Berkeley)

[1]Author to whom correspondence should be addressed.

Contributed by the Fluids Engineering Division for publication in the JOURNAL OF FLUIDS ENGINEERING. Manuscript received by the Fluids Engineering Division June 9, 2000; revised manuscript received April 16, 2001. Associate Editor: F. K. Wasden.

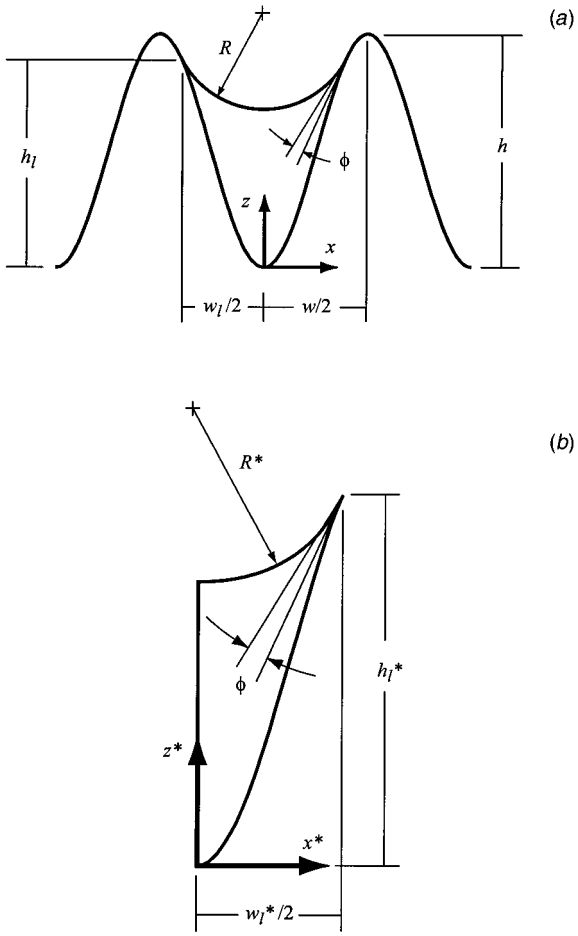

Fig. 2 Flow of liquid in a sinusoidal groove: (*a*) definition of geometric parameters; (*b*) dimensionless solution domain

$$z^* = h_l^* + R^* \sqrt{1-\left(\frac{w_l^*}{2R^*}\right)^2} - \sqrt{R^{*2}-x^{*2}} \tag{7}$$

The dimensional shear stress at the liquid-vapor interface can be cast in terms of the friction factor of the vapor.

$$\tau_{lv} = \begin{cases} \left[\dfrac{\rho_v(\overline{v_v})^2}{2}\right] f_v & \text{for cocurrent flow} \\ -\left[\dfrac{\rho_v(\overline{v_v})^2}{2}\right] f_v & \text{for countercurrent flow} \end{cases} \tag{8}$$

The Poiseuille number of the liquid in the groove is given by

$$\mathrm{Po} = f\,\mathrm{Re} = \frac{D_h^{*2}}{2\overline{v^*}} \tag{9}$$

The dimensionless hydraulic diameter for the flow of liquid in a sinusoidal groove with a circular meniscus is $D_h^* = 4A_l^*/P^*$, where the dimensionless cross-sectional area of the liquid is given by

Table 1 Poiseuille number versus sinusoidal duct aspect ratio: Comparison of the present solution with that given by Shah [15]

	Poiseuille number, Po	
β	Shah [15]	Present
1/4	14.553	14.479
1/3	14.022	13.931
1/2	13.023	12.935
$1/\sqrt{3}$	12.630	12.543
2/3	12.234	12.148
1	11.207	11.115
2	10.123	10.061
4	9.743	9.6373

$$A_l^* = \frac{w_l^*}{2}(2h_l^* - 1) - R^* \times \left[R^* \cos^{-1}\sqrt{1-\left(\frac{w_l^*}{2R^*}\right)^2} - \left(\frac{w_l^*}{2}\right)\sqrt{1-\left(\frac{w_l^*}{2R^*}\right)^2}\right] + \left(\frac{\beta}{\pi}\right)\sin\left[-\pi\left(\frac{w_l^*}{2\beta}+1\right)\right] \quad \text{for} \quad \phi < \phi_{\max} \tag{10}$$

$$A_l^* = \frac{w_l^*}{2}(2h_l^* - 1) + \left(\frac{\beta}{\pi}\right)\sin\left[-\pi\left(\frac{w_l^*}{2\beta}+1\right)\right] \quad \text{for} \quad \phi = \phi_{\max} \tag{11}$$

The dimensionless wetted perimeter is given by the following integral equation.

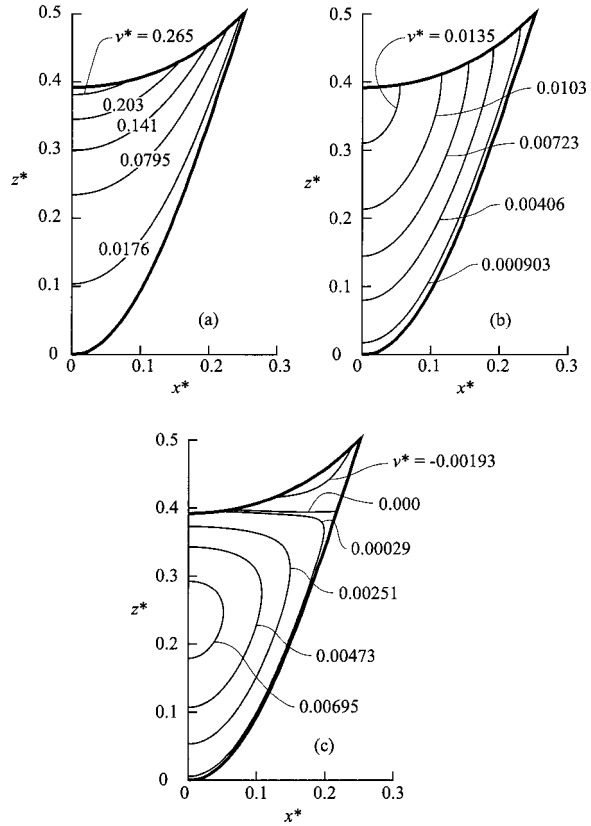

Fig. 3 Dimensionless velocity fields for laminar flow in a sinusoidal groove ($\beta = 0.5$, $w_l^*/2 = 0.25$, $\phi = 25°$): (*a*) $\tau_{lv}^* = 2.0$ (cocurrent flow); (*b*) $\tau_{lv}^* = 0.0$; (*c*) $\tau_{lv}^* = -0.1$ (countercurrent flow)

$$P^* = 2\int_0^{w_l^*/2} \sqrt{1+\left(\frac{\pi}{2\beta}\right)^2 \sin^2\left[-\pi\left(\frac{x^*}{\beta}+1\right)\right]}\,dx^* \quad (12)$$

The mean velocity is defined as

$$\overline{v^*} = \frac{2}{A_l^*}\int_0^{w_l^*/2}\int_0^{z^*} v^*\,dz^*\,dx^* \quad (13)$$

3 Numerical Model

The elliptic Poisson equation given by Eq. (1) with mixed boundary conditions [Eqs. (2), (3) and (7)] was solved using Gauss-Seidel iteration with a central differencing scheme and successive over-relaxation [14]. The convergence criteria for the iterative solution was set to $\epsilon = 10^{-10}$ for each case. A grid independence check was made in which the number of grids in each direction was doubled. When the value for the Poiseuille number did not change by more than 1 percent, grid independence was considered to be reached. The convergence criterion was then reduced by an order of magnitude while maintaining the highest number of grids. If the Poiseuille number did not change by more than 1 percent, the solution was considered to be independent of both grid size and ϵ. Otherwise, a grid independence check was made at the smaller value of ϵ until a converged solution was reached. The integral equation for the wetted perimeter [Eq. (12)] was integrated numerically since no closed-form solution exists.

The numerical model was tested against an existing solution in the archival literature. Shah [15] determined the friction factors for the laminar flow within ducts of various cross sections using a

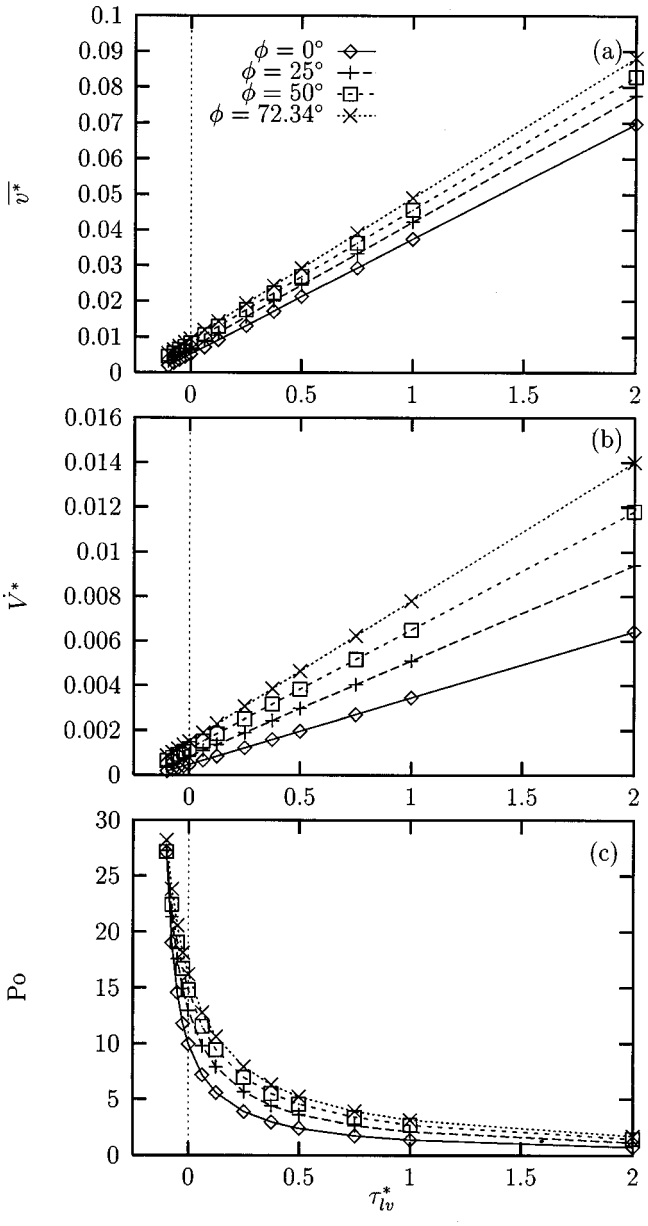

Fig. 4 Variation of the flow variables with shear stress at the liquid-vapor interface for various values of meniscus contact angle ($\beta = 0.5$, $w_l^*/2 = 0.25$, $P^* = 1.15245$): (*a*) mean velocity; (*b*) volumetric flow rate; (*c*) Poiseuille number

Table 2 Mean velocity, Poiseuille number and volumetric flow rate versus shear stress at the liquid-vapor interface for various values of meniscus contact angle ($\beta = 0.5$, $w_l^*/2 = 0.25$, $P^* = 1.15245$)

ϕ	τ_{lv}^*	$\overline{v^*}$	Po	$\dot{V}^*$
0°	−0.1	0.18878×10^{-2}	27.088	0.17394×10^{-3}
0°	−0.075	0.26896×10^{-2}	19.013	0.24782×10^{-3}
0°	−0.05	0.35104×10^{-2}	14.567	0.32344×10^{-3}
0°	−0.025	0.43465×10^{-2}	11.765	0.40048×10^{-3}
0°	0.0	0.51353×10^{-2}	9.9581	0.47316×10^{-3}
0°	0.0625	0.71345×10^{-2}	7.1676	0.65738×10^{-3}
0°	0.125	0.91525×10^{-2}	5.5873	0.84330×10^{-3}
0°	0.25	0.13188×10^{-1}	3.8774	0.12152×10^{-2}
0°	0.375	0.17224×10^{-1}	2.9689	0.15870×10^{-2}
0°	0.5	0.21260×10^{-1}	2.4053	0.19589×10^{-2}
0°	0.75	0.29332×10^{-1}	1.7434	0.27026×10^{-2}
0°	1.0	0.37404×10^{-1}	1.3672	0.34464×10^{-2}
0°	2.0	0.69691×10^{-1}	0.73377	0.64214×10^{-2}
25°	−0.1	0.32506×10^{-2}	27.245	0.39414×10^{-3}
25°	−0.075	0.41572×10^{-2}	21.303	0.50408×10^{-3}
25°	−0.05	0.50437×10^{-2}	17.559	0.61158×10^{-3}
25°	−0.025	0.59348×10^{-2}	14.923	0.71962×10^{-3}
25°	0.0	0.68259×10^{-2}	12.974	0.82768×10^{-3}
25°	0.0625	0.90536×10^{-2}	9.7820	0.10978×10^{-2}
25°	0.125	0.11229×10^{-1}	7.8870	0.13616×10^{-2}
25°	0.25	0.15650×10^{-1}	5.6588	0.18977×10^{-2}
25°	0.375	0.20072×10^{-1}	4.4123	0.24338×10^{-2}
25°	0.5	0.24493×10^{-1}	3.6158	0.29700×10^{-2}
25°	0.75	0.33336×10^{-1}	2.6566	0.40422×10^{-2}
25°	1.0	0.42179×10^{-1}	2.0997	0.51144×10^{-2}
25°	2.0	0.77551×10^{-1}	1.1420	0.94034×10^{-2}
50°	−0.1	0.45097×10^{-2}	27.149	0.64296×10^{-3}
50°	−0.075	0.54643×10^{-2}	22.406	0.77904×10^{-3}
50°	−0.05	0.64189×10^{-2}	19.074	0.91514×10^{-3}
50°	−0.025	0.73345×10^{-2}	16.693	0.10457×10^{-2}
50°	0.0	0.82746×10^{-2}	14.796	0.11797×10^{-2}
50°	0.0625	0.10625×10^{-1}	11.523	0.15148×10^{-2}
50°	0.125	0.12975×10^{-1}	9.4363	0.18498×10^{-2}
50°	0.25	0.17586×10^{-1}	6.9621	0.25072×10^{-2}
50°	0.375	0.22255×10^{-1}	5.5014	0.31728×10^{-2}
50°	0.5	0.26922×10^{-1}	4.5477	0.38382×10^{-2}
50°	0.75	0.36256×10^{-1}	3.3769	0.51690×10^{-2}
50°	1.0	0.45590×10^{-1}	2.6855	0.64998×10^{-2}
50°	2.0	0.82926×10^{-1}	1.4764	0.11823×10^{-1}
72.34°	−0.1	0.54127×10^{-2}	28.188	0.86146×10^{-3}
72.34°	−0.075	0.64152×10^{-2}	23.783	0.10210×10^{-2}
72.34°	−0.05	0.74177×10^{-2}	20.569	0.11805×10^{-2}
72.34°	−0.025	0.84202×10^{-2}	18.120	0.13401×10^{-2}
72.34°	0.0	0.94227×10^{-2}	16.192	0.14996×10^{-2}
72.34°	0.0625	0.11929×10^{-1}	12.790	0.18985×10^{-2}
72.34°	0.125	0.14354×10^{-1}	10.629	0.22844×10^{-2}
72.34°	0.25	0.19309×10^{-1}	7.9016	0.30730×10^{-2}
72.34°	0.375	0.24264×10^{-1}	6.2880	0.38618×10^{-2}
72.34°	0.5	0.29219×10^{-1}	5.2217	0.46504×10^{-2}
72.34°	0.75	0.39129×10^{-1}	3.8992	0.62276×10^{-2}
72.34°	1.0	0.49039×10^{-1}	3.1112	0.78048×10^{-2}
72.34°	2.0	0.88244×10^{-1}	1.7290	0.14044×10^{-1}

least-squares-matching technique. Table 1 shows the comparison of the Poiseuille number between the present solution and that given by Shah [15] for laminar flow in a family of sinusoidal ducts. The agreement is excellent, with a maximum difference of 1.1 percent.

4 Results and Discussion

A numerical study has been completed in which the flow of liquid in a sinusoidal groove has been solved. Figure 3 presents contour plots of the dimensionless liquid velocity. The maximum liquid velocity increases with cocurrent shear, and decreases with countercurrent shear, as expected. For countercurrent vapor flow, a portion of the liquid flows in the $-y$ direction, which is opposite to the direction of the pressure gradient. This flow reversal shows the potential of the vapor shear to drive the mean velocity of the liquid to zero, or to completely reverse the flow, depending on the magnitude of the pressure gradient.

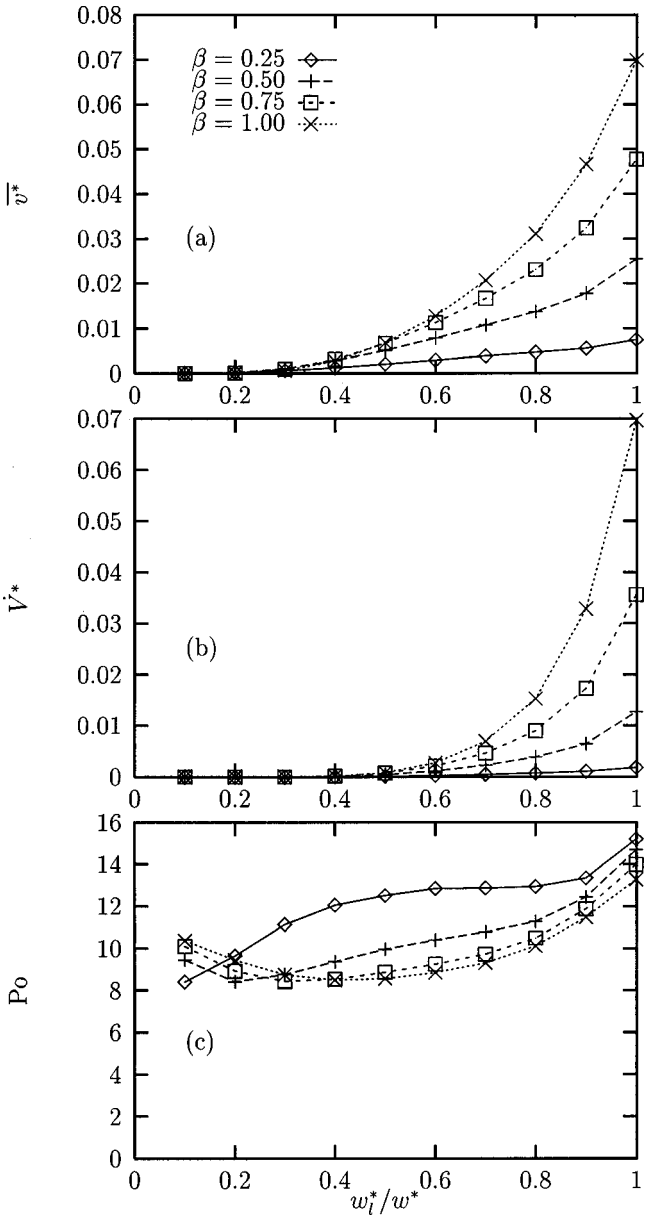

Fig. 5 Variation of the flow variables with groove fill ratio for various values of groove aspect ratio ($\tau_{lv}^*=0.0$, $\phi=0°$): (*a*) mean velocity; (*b*) volumetric flow rate; (*c*) Poiseuille number

Table 3 Wetted perimeter, mean velocity, Poiseuille number and volumetric flow rate versus groove fill ratio for various values of groove aspect ratio ($\tau_{lv}^*=0.0$, $\phi=0°$)

β	w_l^*/w^*	P^*	$\overline{v^*}$	Po	$\dot{V}^*$
0.25	0.1	0.0731191	0.13005×10^{-4}	8.4006	0.35142×10^{-8}
0.25	0.2	0.223950	0.20221×10^{-3}	9.6365	0.70676×10^{-6}
0.25	0.3	0.450806	0.63058×10^{-3}	11.141	0.84242×10^{-5}
0.25	0.4	0.734032	0.12616×10^{-2}	12.059	0.40386×10^{-4}
0.25	0.5	1.04707	0.20592×10^{-2}	12.514	0.12238×10^{-3}
0.25	0.6	1.36011	0.29299×10^{-2}	12.849	0.27336×10^{-3}
0.25	0.7	1.64333	0.38585×10^{-2}	12.871	0.49958×10^{-3}
0.25	0.8	1.87019	0.47149×10^{-2}	12.940	0.77004×10^{-3}
0.25	0.9	2.02102	0.55519×10^{-2}	13.346	0.10799×10^{-2}
0.25	0.999	2.09364	0.74536×10^{-2}	15.203	0.18573×10^{-2}
0.5	0.1	0.114187	0.35380×10^{-5}	9.4469	0.82578×10^{-9}
0.5	0.2	0.288528	0.19851×10^{-3}	8.4052	0.82718×10^{-6}
0.5	0.3	0.531454	0.10922×10^{-2}	8.7511	0.20062×10^{-4}
0.5	0.4	0.827649	0.28055×10^{-2}	9.3706	0.13311×10^{-3}
0.5	0.5	1.15245	0.51353×10^{-2}	9.9581	0.47316×10^{-3}
0.5	0.6	1.47724	0.78593×10^{-2}	10.398	0.11735×10^{-2}
0.5	0.7	1.77344	0.10755×10^{-1}	10.780	0.22962×10^{-2}
0.5	0.8	2.01636	0.13817×10^{-1}	11.282	0.38892×10^{-2}
0.5	0.9	2.19070	0.17762×10^{-1}	12.443	0.64680×10^{-2}
0.5	0.999	2.30389	0.25467×10^{-1}	14.698	0.12692×10^{-1}
0.75	0.1	0.160025	0.11137×10^{-5}	10.092	0.21124×10^{-9}
0.75	0.2	0.367435	0.10959×10^{-3}	8.9207	0.44516×10^{-6}
0.75	0.3	0.634966	0.93568×10^{-3}	8.4299	0.18655×10^{-4}
0.75	0.4	0.951588	0.31271×10^{-2}	8.5312	0.17184×10^{-3}
0.75	0.5	1.29509	0.67001×10^{-2}	8.8579	0.74738×10^{-3}
0.75	0.6	1.63860	0.11328×10^{-1}	9.2444	0.21238×10^{-2}
0.75	0.7	1.95522	0.16731×10^{-1}	9.7209	0.46642×10^{-2}
0.75	0.8	2.22275	0.23143×10^{-1}	10.489	0.89608×10^{-2}
0.75	0.9	2.43016	0.32404×10^{-1}	11.885	0.17278×10^{-1}
0.75	0.999	2.58868	0.47659×10^{-1}	13.997	0.35626×10^{-1}
1.0	0.1	0.207697	0.45992×10^{-6}	10.367	0.73744×10^{-10}
1.0	0.2	0.453879	0.59860×10^{-4}	9.4362	0.22830×10^{-6}
1.0	0.3	0.752420	0.66244×10^{-3}	8.7481	0.13415×10^{-4}
1.0	0.4	1.09559	0.27276×10^{-2}	8.4926	0.16081×10^{-3}
1.0	0.5	1.46369	0.67927×10^{-2}	8.5590	0.84758×10^{-3}
1.0	0.6	1.83180	0.12785×10^{-1}	8.8427	0.27842×10^{-2}
1.0	0.7	2.17497	0.20665×10^{-1}	9.3068	0.69688×10^{-2}
1.0	0.8	2.47351	0.31143×10^{-1}	10.106	0.15279×10^{-1}
1.0	0.9	2.71969	0.46597×10^{-1}	11.485	0.32778×10^{-1}
1.0	0.999	2.92539	0.69923×10^{-1}	13.281	0.69692×10^{-1}

Figure 4 and Table 2 show the mean velocity, volumetric flow rate and Poiseuille number versus shear stress at the liquid-vapor interface for several values of the meniscus contact angle. The mean velocity increases with both τ_{lv}^* and ϕ, but is a relatively weak function of ϕ. For a given value of meniscus contact angle, the mean velocity is linear with τ_{lv}^* due to an overall force balance on the liquid. The volumetric flow rate also increases with τ_{lv}^* and ϕ, but is a much stronger function of ϕ due to the increase in the cross-sectional area of the liquid. The Poiseuille number decreases as τ_{lv}^* increases. For cocurrent vapor flow ($\tau_{lv}^*>0$), Po decreases steadily with τ_{lv}^*. For countercurrent flow, Po increases dramatically with $-\tau_{lv}^*$ due to the mean velocity approaching zero. In general, Po increases with ϕ due to the increase in the hydraulic diameter of the liquid.

Figure 5 and Table 3 present the mean velocity, volumetric flow rate and Poiseuille number versus the groove fill ratio for several values of the groove aspect ratio. The mean velocity increases monotonically with area ratio and groove aspect ratio. The volumetric flow rate also increases with w_l^*/w^* and β, but drops off rapidly for $w_l^*/w^*<0.5$ due to the decrease in flow area. The Poiseuille number is relatively constant for this case. For $\beta \geqslant 0.5$, Po decreases and then increases with area ratio. For $\beta = 0.25$, Po increases over the range of w_l^*/w^* examined.

5 Semi-Analytical Solution for $\overline{v^*}$

As seen in Fig. 4(*a*), the mean velocity is a linear function of the imposed shear stress at the liquid-vapor interface. Since a direct numerical simulation of the liquid flow field for a number of values of the shear stress is computer resource intensive, it is appropriate to seek a semi-analytical expression for $\overline{v^*}$. Figure 6(*a*) shows the definition of the parameters involved, where the mean velocity when the shear stress is zero ($\overline{v_0^*}$) is given by the numerical solution. The value for the liquid-vapor shear for which the mean velocity is zero ($\tau^*_{lv,0}$) is given by the following force balance analysis. Figure 6(*b*) shows a differential element of the liquid in the groove. A force balance between the pressure drop and the shear forces at the liquid-vapor interface and at the wall results in the following relation.

$$p_y A_l - p_{y+dy} A_l + \tau_{lv} A_{lv} - \overline{\tau_w} A_w = 0 \tag{14}$$

The areas over which the shear stresses τ_{lv} and $\overline{\tau_w}$ act are $A_{lv} = P_{lv} dy$ and $A_w = P dy$, respectively. Using these areas and nondimensionalizing gives

$$A_l^* + \tau_{lv}^* P_{lv}^* - \overline{\tau_w^*} P^* = 0 \tag{15}$$

For Poiseuille flow in ducts of arbitrary cross section, and combined Couette-Poiseuille flow between flat plates, the shear stress at the wall is related to the mean velocity of the fluid by a constant (White [13]). Therefore, in the present analysis, it is assumed that this also holds for the flow of liquid in a sinusoidal groove with an imposed shear stress at the liquid-vapor interface.

$$\overline{\tau_w^*} = C_1 \overline{v^*} \tag{16}$$

It should be noted that the constant C_1 is probably a function of the groove geometry and meniscus contact angle. However, since the objective of this analysis is to determine the liquid-vapor shear stress when the mean liquid velocity is zero, this functionality is unimportant. The perimeter of the liquid-vapor interface is

$$P_{lv}^* = 2R^* \sin^{-1}\left(\frac{w_l^*}{2R^*}\right) \tag{17}$$

Substituting these relations into the force balance equation results in the following expression for mean velocity.

$$\overline{v^*} = \frac{1}{C_1 P^*}\left[A_l^* + 2\tau_{lv}^* R^* \sin^{-1}\left(\frac{w_l^*}{2R^*}\right)\right] \tag{18}$$

The mean velocity is zero when

$$\tau^*_{lv,0} = -\frac{A_l^*}{2R^* \sin^{-1}\left(\frac{w_l^*}{2R^*}\right)} \tag{19}$$

Figure 7(*a*) shows the results of Eq. (19). The numerical results shown in Fig. 4(*a*) were extrapolated to determine the values for shear stress at the liquid-vapor interface when $\overline{v^*} = 0$. Both curves indicate that $\tau^*_{lv,0}$ increases with ϕ due to the increasing depth of liquid in the groove. The prediction given by Eq. (19) is quite

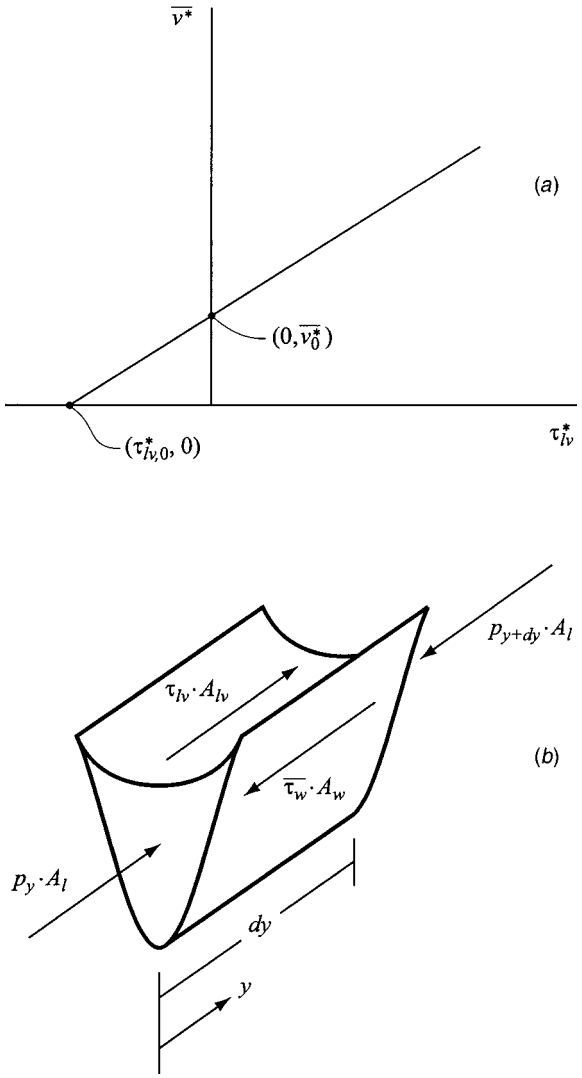

Fig. 6 Semi-analytical solution for $\overline{v^*}$: (*a*) definition of parameters; (*b*) force balance on the liquid in a sinusoidal groove

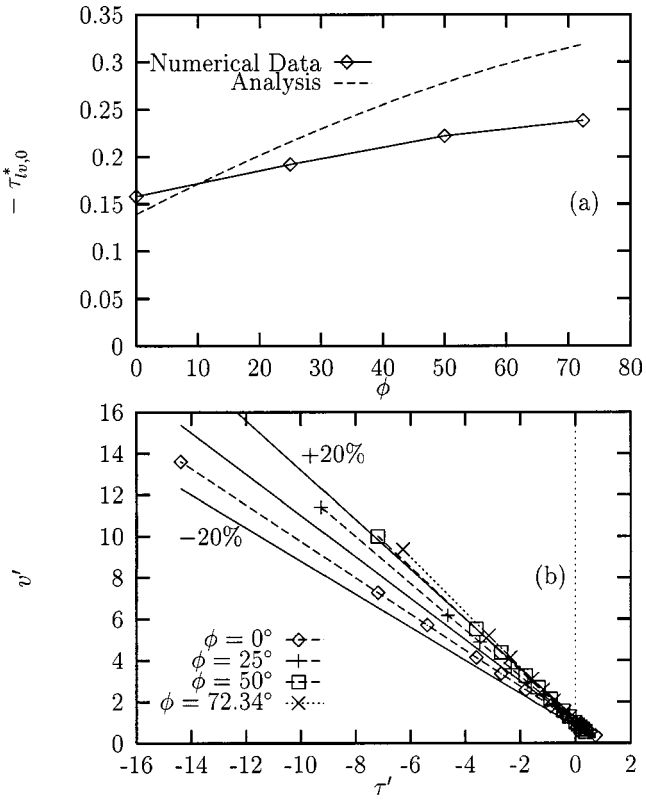

Fig. 7 Comparison of the semi-analytical solution with numerical data ($\beta = 0.5$, $w_l^*/2 = 0.25$): (*a*) countercurrent vapor shear stress required for $\overline{v^*} = 0$; (*b*) normalized mean velocity versus normalized shear stress at the liquid-vapor interface

good given the simplicity of the closed-form solution. The equation for the normalized mean velocity as a function of the normalized shear stress is given by

$$v' = \overline{v^*}/\overline{v_0^*} = 1 - \tau' \tag{20}$$

where $\tau' = \tau_{lv}^*/\tau_{lv,0}^*$. The semi-analytical solution for the normalized mean velocity is shown in Fig. 7(*b*) with the corresponding numerical data presented in Fig. 4(*a*). Equation (20) predicts 94 percent of the data to within ±20 percent over the range of meniscus contact angle examined.

6 Conclusions

Based on the results of the numerical model of the flow of liquid in a sinusoidal groove, the following conclusions have been made: For a given meniscus contact angle, the mean velocity was linear with imposed shear stress at the liquid-vapor interface. The volumetric flow rate in the groove was negligible for groove fill ratios of less than $w_l^*/w^* < 0.5$. The Poiseuille number was a strong function of the countercurrent shear stress. A semi-analytical expression was provided to approximate the mean velocity as a function of the shear stress at the liquid-vapor interface.

Acknowledgment

Funding for this work was provided by the Air Force Research Laboratory (PRPG) under Contract No. F33615-98-1-2844.

Nomenclature

A_l = cross-sectional area of the liquid, m^2
A_l^* = A_l/h^2
A_{lv} = area of the liquid-vapor interface, m^2
A_w = area of the groove wall, m^2
Bo = Bond number, $\rho g z_1^2/\sigma$
d^* = parameter defined in Eq. (5)
D_h = hydraulic diameter, $4A_l/P$, m
D_h^* = D_h/h
f = friction coefficient, $2\overline{\tau}/\rho\overline{v}^2$
g = acceleration due to gravity, m/s^2
h = groove height, m
h_l = height of liquid in the groove at the wall, m
h_l^* = h_l/h
n = coordinate normal to the liquid-vapor interface
n^* = n/h
p = pressure, N/m^2
P = wetted perimeter, m
P^* = P/h
P_{lv} = perimeter of the liquid-vapor interface, m
P_{lv}^* = P_{lv}/h
Po = Poiseuille number, f Re
R = radius of curvature of the meniscus, m
R^* = R/h
Re = Reynolds number, $\rho\overline{v}D_h/\mu$
v = y-direction velocity, m/s
$\overline{v}$ = average y-direction velocity, m/s
v^* = $\mu v/h^2(-dp/dy)$
$\overline{v^*}$ = dimensionless average y-direction velocity
$\overline{v_0^*}$ = dimensionless average y-direction velocity when $\tau_{lv}^* = 0$
v' = $\overline{v^*}/\overline{v_0^*}$
$\dot{V}$ = volumetric flow rate, $\overline{v}A_l$, m^3/s
$\dot{V}^*$ = $\mu\dot{V}/[h^4(-dp/dy)]$
w = period of the sinusoidal groove, m
w^* = w/h
w_l = width of the liquid in the groove, m
w_l^* = w_l/h
x, y, z = coordinate directions
x^* = x/h
z_1 = distance from the liquid-vapor interface to the groove bottom, m
z^* = z/h
β = groove aspect ratio, $w/2h$
ϵ = convergence criterion
μ = absolute viscosity, Pa-s
ρ = density, kg/m^3
σ = surface tension, N/m
τ_{lv} = shear stress at the liquid-vapor interface, N/m^2
τ_{lv}^* = $\tau_{lv}/h(-dp/dy)$
$\tau_{lv,0}^*$ = dimensionless shear stress at the liquid-vapor interface when $\overline{v^*} = 0$
$\overline{\tau}$ = average shear stress, $A_l(-dp/dy)/P$, N/m^2
$\overline{\tau}_w$ = average shear stress at the groove wall, N/m^2
$\overline{\tau}_w^*$ = $\overline{\tau}_w/h(-dp/dy)$
τ' = $\tau_{lv}^*/\tau_{lv,0}^*$
ϕ = meniscus contact angle, rad
ϕ_{max} = maximum meniscus contact angle, rad

References

[1] Kirshberg, J., Liepmann, D., and Yerkes, K., 1999, ''Micro-cooler for chip-level temperature control,'' *Proc. SAE Aerospace Power Systems Conf.*, Paper No. 1999-01-1407.
[2] Maluf, N., 2000, *An Introduction to Microelectromechanical Systems Engineering*, Artech House, Boston, pp. 41–83.
[3] Ayyaswamy, P., Catton, I., and Edwards, D., 1974, ''Capillary flow in triangular grooves,'' ASME J. Appl. Mech., **41**, 332–336.
[4] Ma, H., Peterson, G., and Lu, X., 1994, ''The influence of vapor-liquid interactions on the liquid pressure drop in triangular microgrooves,'' Int. J. Heat Mass Transf., **37**, pp. 2211–2219.
[5] Romero, L., and Yost, F., 1996, ''Flow in an open channel,'' J. Fluid Mech., **322**, pp. 109–129.
[6] Lin, L., and Faghri, A., 1997, ''Steady-state performance of a rotating miniature heat pipe,'' J. Thermophys. Heat Transfer, **11**, pp. 513–518.
[7] Kolodziej, J., Musielak, G., Kaczmarek, M., and Strek, T., 1999, ''Determination of free surface and gravitational flow of liquid in triangular groove,'' Computational Mechanics, **24**, pp. 110–117.
[8] DiCola, G., 1968, ''Soluzionne analitica, amezzo della transformata di Fourier, di un problema di fusso in un canale rettangolare,'' Euratom C.C.R. Ispra (Italy), C.E.T.I.S.
[9] Schneider, G., and DeVos, R., 1980, ''Non-dimensional analysis for the heat transport capability of axially grooved heat pipes including liquid/vapor interaction,'' AIAA Paper No. 80-0214.
[10] Khrustalev, D., and Faghri, A., 1999, ''Coupled liquid and vapor flow in miniature passages with micro grooves,'' ASME J. Heat Transfer, **121**, pp. 729–733.
[11] Hopkins, R., Faghri, A., and Khrustalev, D., 1999, ''Flat miniature heat pipes with micro capillary grooves,'' ASME J. Heat Transfer, **121**, pp. 102–109.
[12] Stroes, G., and Catton, I., 1997, ''An experimental investigation of the capillary performance of triangular versus sinusoidal channels,'' ASME J. Heat Transfer, **119**, pp. 851–853.
[13] White, F., 1991, *Viscous Fluid Flow*, 2nd edn., McGraw-Hill, New York, pp. 104–131.
[14] Anderson, D., Tannehill, J., and Pletcher, R., 1984, *Computational Fluid Mechanics and Heat Transfer*, Hemisphere, New York, pp. 87–169.
[15] Shah, R., 1975, ''Laminar flow friction and forced convection heat transfer in ducts of arbitrary geometry,'' Int. J. Heat Mass Transf., **18**, pp. 849–862.

P. Merati
Professor and Chair

M. J. Macelt
Research Assistant

Department of Mechanical and Aeronautical Engineering,
Western Michigan University,
Kalamazoo, Michigan,
Kalamazoo, MI 49008

R. B. Erickson
Vice President of Technology,
Goulds Pumps, Inc.,
Seneca Falls, NY 13148

Flow Investigation Around a V-Sector Ball Valve

Experimental and computational methods were used to study the structure and behavior of the shedded vortices around a V-ball valve. Strouhal frequency for shedded vortices around the valve over a range of operating conditions and flow rates using water as the medium were measured. The information gathered in this study would help to predict at what operating conditions pipe ruptures might occur. A dynamic pressure transducer was used to determine the Strouhal frequency. LDV was used to measure the mean velocity and turbulence magnitudes. FLUENT was used to develop a two dimensional fluid dynamics model. Flow was visualized using high-speed video photography. A dominant large three-dimensional vortex downstream of the valve was detected. The centerline of this vortex is a shadow of the valve lip. A fifth degree polynomial describing the relationship between the Strouhal number and Reynolds number is obtained.
[DOI: 10.1115/1.1385831]

1 Introduction

A V-ball valve is a common control valve used in many types of industrial situations. It is similar to a regular ball valve except it has a V-shaped notch in the lip of the valve. A case history is presented by Lewis et al. [1] pertaining to piping vibrations in a medium consistency paper pumping system at a large North American integrated pulp and paper mill that ultimately resulted in pipe rupture. The medium consistency range is from approximately 8 percent–15 percent oven-dry consistency. For this consistency, the fiber network is extremely strong and the pipes friction losses are relatively high due to high apparent viscosity. The system was designed to transfer pulp at 12 percent oven-dry consistency (12 percent fiber, 88 percent water by mass) from a washer stage to a storage tower through nearly 214 m of 51 cm diameter pipe. Initial tests indicated the piping had pressure pulsation of 687 kPa peak to peak which were exerting a shaking force of approximately 66.75 kN–133.6 kN peak to peak at each of seventeen 90 degree elbows in the piping system. The frequencies of the major pressure pulsation were at 1.3 Hz and 3.8 Hz which corresponds to the one-quarter and three-quarter (closed-open piping system) standing pressure waves in the piping system. The source of the pulsation energy was traced to the control valve located immediately downstream of the centrifugal pump. It was suspected that the frequency of the shedded vortices at the valve lip match the frequency of the standing waves in this particular piping system, generating the perfect condition for large piping system pressure pulsation. The pressure pulsation did not exist above 70 percent valve opening.

Specific Strouhal numbers at different operating conditions for V-ball valves have not been published, but it has been reported that the Strouhal number for V-ball valves range from 0.1–0.3 Hz (Lewis et al. [1]). This research was conducted due to lack of available data on variation of Strouhal number with Reynolds number and flow structure for V-ball valves. Although water is used as fluid medium in this research, the results can be used for estimating the V-ball Strouhal numbers for medium consistency pulp applications. The relationship providing the frequency of the quarter wave for Newtonian fluids in pipes is given by Sparks et al. [2]. This relationship depends on the acoustic velocity in an elastic container and the pipe length. The acoustic velocity depends on the fluid density, fluid bulk modulus of elasticity, mean pipe diameter, pipe wall thickness and pipe elastic modulus. The correction factors for variation of acoustic velocity with pulp consistency, pulp air content and its temperature are described by Wylie et al. [3].

2 Facilities, Instrumentation, and Techniques

A schematic of the experimental test setup is shown in Fig. 1. The picture in Fig. 2 is an overhead view of the test loop. The closed loop recirculating system includes a tank that holds about 189 liters of water. A heat exchanger made from copper tubing is wrapped around the inside wall of the tank. Tap water flows through the copper coil to cool the circulating fluid, to keep its temperature at a constant value.

A 50 horsepower, variable speed, centrifugal pump drives the fluid through the system. The test section of the setup, made of Plexiglas, allows for the use of optical flow measurement techniques and consists of two components glued together. The first part is modeled after a 5.08 cm. Fisher V150 V-Ball valve. The top and side views of the Plexiglas valve are shown in Figs. 3 and 4, respectfully. The second part is a 5.08 cm diameter, 50.8 cm long pipe. Pressure gauges are used to measure the pressure drop across the valve between the upstream and downstream of the test section.

A Kistler quartz dynamic pressure transducer is located downstream of the test section to measure the pressure fluctuations in the fluid. Power spectrum analysis is performed on the collected signals to determine the dominant frequencies. After the water leaves the test section, it is routed back to the tank. Two different flowmeters are used in the system. One is a zero to 3.7848 liters per second (lit/sec) RCM analog flowmeter. The other is a 3.7848 to 31.54 lit/s RCM analog flow meter. For different test situations, the meters are changed accordingly. Downstream of the flowmeter is a 7.62 cm, ball valve, followed by a 7.62 cm to 20.32 cm diffuser which decreases the velocity of the water before it enters the tank.

During initial trial runs of the system, cavitation was visualized around the V-ball valve at all test conditions. The vapor bubbles produced by cavitation interfered with the laser beams of the LDV system and produced noise that affected pressure transducer signal. The first method to correct the cavitation problem was using the ball valve to induce upstream backpressure. By adjusting the opening of the valve, the flow is restricted and the pressure increased. This corrected the complication for a few experimental situations, but it also induced severe cavitation around the ball valve, which was apparent in the pressure transducer signal. Closing the ball valve also reduced the flow to the point that most of the proposed cases could not be tested. This method was deemed insufficient. The second method of correction was to

Contributed by the Fluids Engineering Division for publication in the JOURNAL OF FLUIDS ENGINEERING. Manuscript received by the Fluids Engineering Division July 7, 2000; revised manuscript received February 9, 2001. Associate Editor: F. K. Wasden.

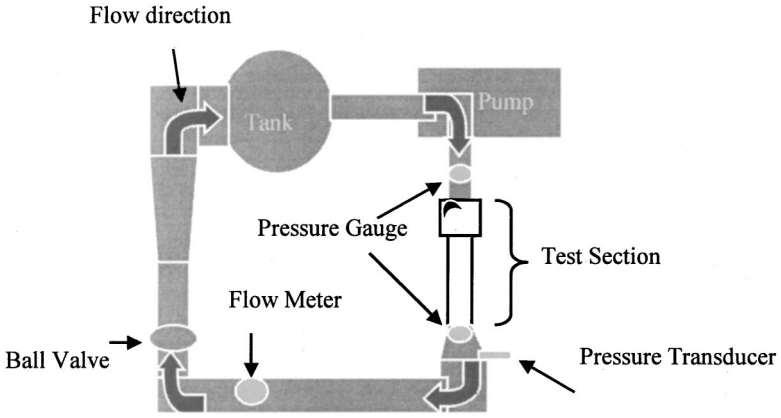

Fig. 1 Experimental test setup

Fig. 2 Overhead view of the test loop

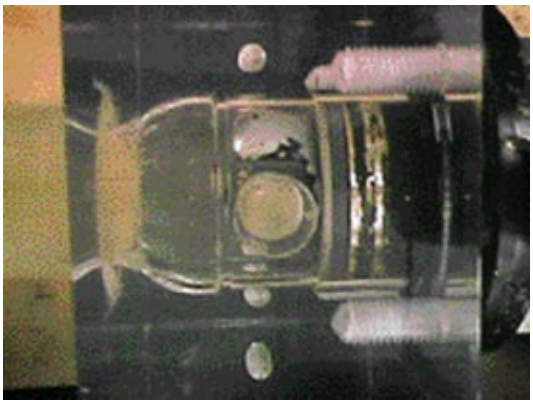

Fig. 3 Top view of Plexiglas valve

Fig. 4 Side view of Plexiglas valve

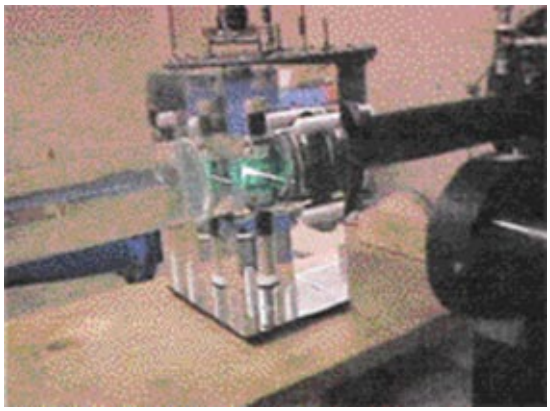

Fig. 5 LDV laser beams in valve region

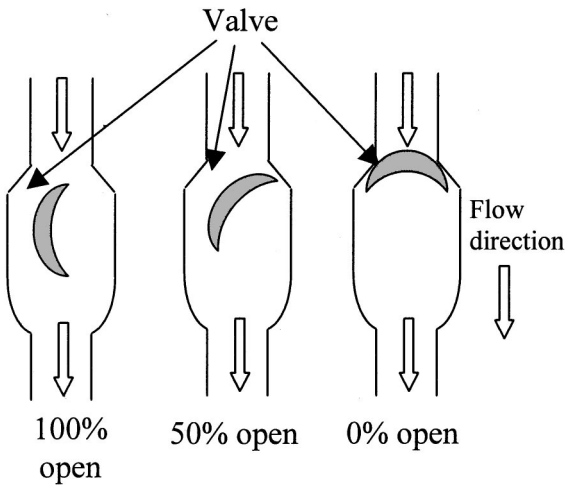

Fig. 6 Illustration of percent opening

modify the tank so that the entire system could be pressurized. The maximum safe operating pressure for the system was estimated to be about 309 kPa. Pressurizing the system beyond 309 kPa could lead to failure of the vertical weld running up the side of the tank. The tank was not originally designed to be a pressure vessel.

LDV was used to measure streamwise flow velocity and turbulence intensity downstream of the valve. A 100-mW Argon-Ion laser with a wavelength of 514 nm produced the beams used in this study. The laser beams in the valve region are shown in Fig. 5. Metallic, spherical particles with a mean diameter of 12 μm

Table 1 Test matrix

Delta P (kPa)	% open	20	30	40	50	60	70
	Cv	0.1266	0.3346	0.5560	0.8689	1.3190	1.8149
68.7	Flow rate(lit/sec), Test	1.05, 1	2.77, 3	4.61, 4	7.20, 6	10.93, 8	15.04, 10
137.9	Flow rate(lit/sec), Test	1.48, 2	-	6.52, 5	10.19, 7	15.46, 9	21.27, 11

were used to seed the flow. Signals from the photo detector are sent to the TSI's IFA 500, for analysis. A power spectrum analysis was performed on the LDV signal to determine the dominant frequencies of the flow.

A NAC-1000 high-speed video photography system was used to visualize the flow structure around the valve. The video camera was positioned so that it was looking down at the valve. Two strobe lights were used to provide the necessary light for the video camera and were synchronized to flash at the same frequency as the video camera's shutter. A sample rate of 500 frames per second was used.

The independent variables for each test are fluid flow rate and the valve position. Position is expressed as percent opening and is based on a 90-degree turn of the valve. Every 9-degree rotation is 10 percent as shown in Fig. 6. The valve manufacturer publishes data about their valves based on percent opening.

The test matrix is shown in Table 1. The volumetric flow rates are based on the following liquid sizing equation presented in the valve and actuator catalogs by Fisher [4].

$$Q = C_v \sqrt{\frac{\Delta P}{G}} \tag{1}$$

Q = flow rate (lit/s)
C_v = liquid sizing coefficient [lit/sec*(kPa)$^{-0.5}$]
ΔP = body differential pressure (kPa)
G = specific gravity

For each test, sets of pressure data were taken. Each set of data was analyzed by a Labview program to produce a power spectrum versus frequency graph. The power spectrum for each set was averaged to determine the Strouhal frequency. For each set of

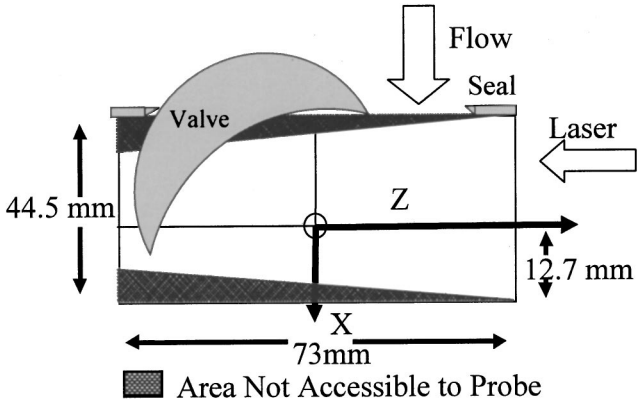

Fig. 7 Coordinate system for LDV measurements

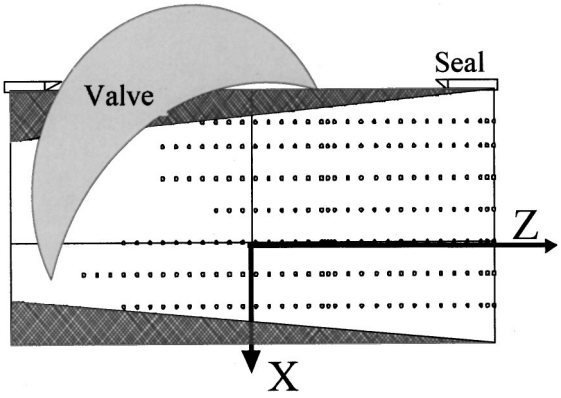

Fig. 8 Probe volume locations

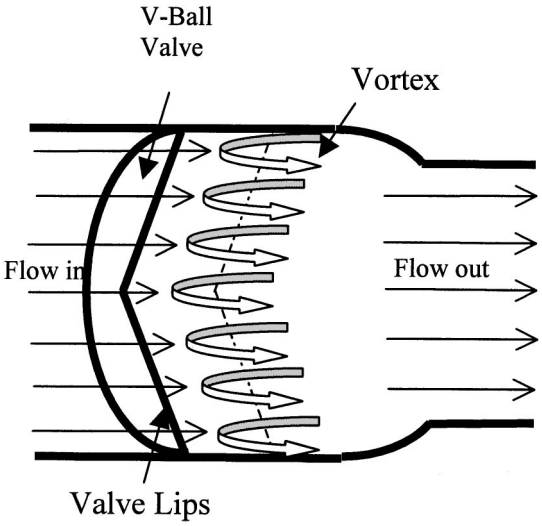

Fig. 9 Schematic of the V-ball valve vortex

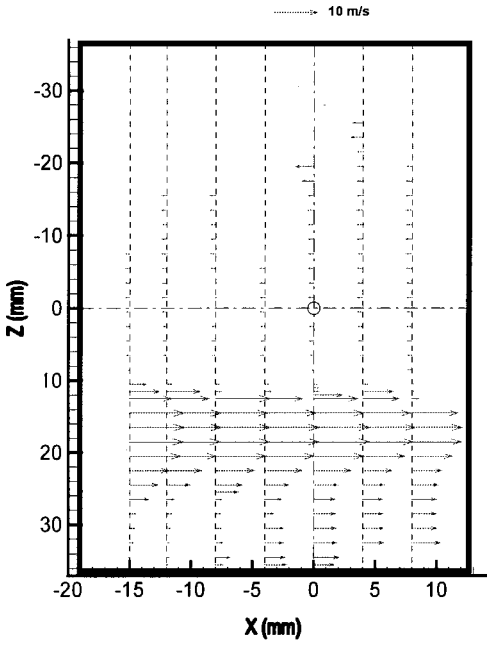

Fig. 10 Streamwise mean components of the flow velocity, 50 percent open and 4.42 lit/s

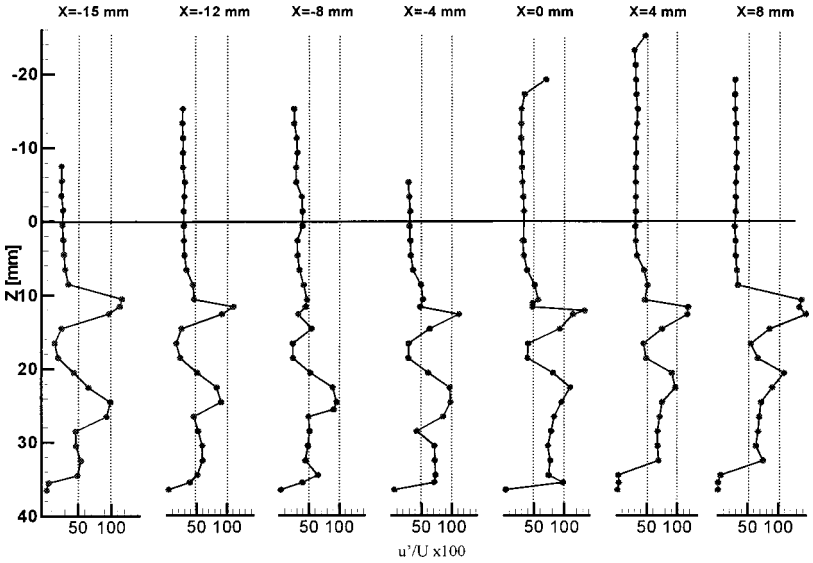

Fig. 11 Turbulence intensity profiles, 50 percent open and 4.42 lit/s

pressure data, 4096 data points were taken at 1024 samples per second.

For the LDV measurements, ten thousand data points were collected. The probe volume was positioned in an area of flow with high velocity and low turbulence to observe the effect of the dominant vortex. A Mathcad program was developed to determine the exact location of the probe volume in the water. This was necessary because the laser was passing through three different media; air, Plexiglas, and water. Each medium has a different index of refraction. Power spectrum analysis was performed on each data set using a Labview program.

The power spectra of the velocity signal obtained from LDV did not provide conclusive peaks that could be traced to the vortex shedding frequency. However, LDV was used to measure the mean velocity and turbulence intensity of the vortex flow of the valve at 50 percent open and 4.42 lit/s flow rate. The coordinate system for LDV measurements is shown in Fig. 7. The locations of the probe volume on a horizontal plane perpendicular to the shaft axis are shown in Fig. 8. At each location two thousand data points were acquired. The mean and standard deviation of two thousand data points provided the mean velocity and turbulence intensity profiles presented in this section.

3 Experimental Results

A large vortex was observed directly downstream of the valve. Close observation of the high-speed video has shown that the center of rotation of the main vortex follows the shape of the valve lip. This occurs because the flow that drives this vortex is following the contour of the valve. The general shape of the vortex is shown in Fig. 9.

Profiles of the streamwise component of the velocity are shown in Fig. 10. The largest components are observed at the valve opening and extend downstream. The negative components

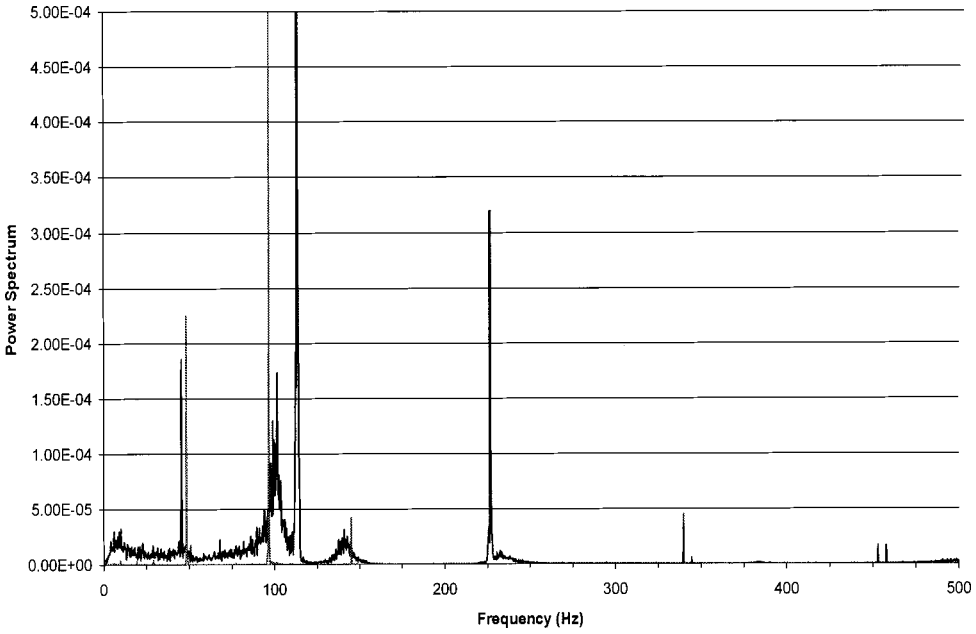

Fig. 12 Pressure power spectra for the valve at 50 percent and 100 percent open with 7.25 lit/s

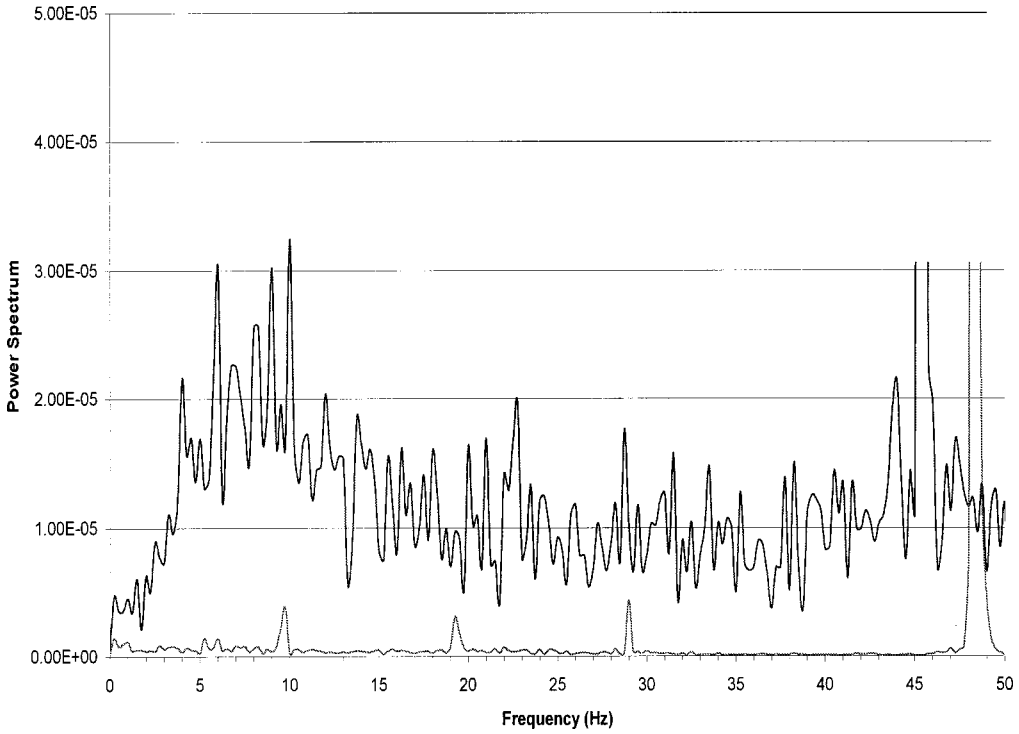

Fig. 13 Pressure power spectra for the valve at 50 percent and 100 percent open with 7.25 lit/s

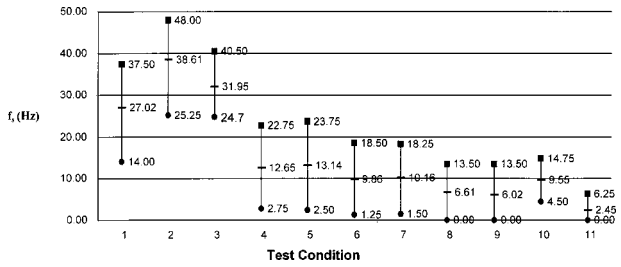

Fig. 14 Broadband Strouhal frequency

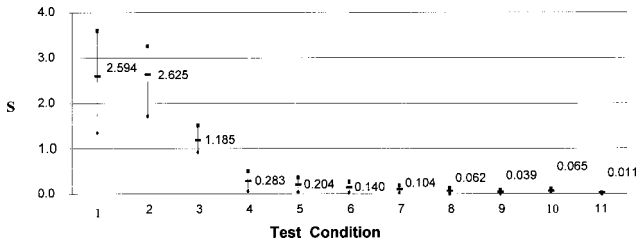

Fig. 15 Broadband Strouhal number

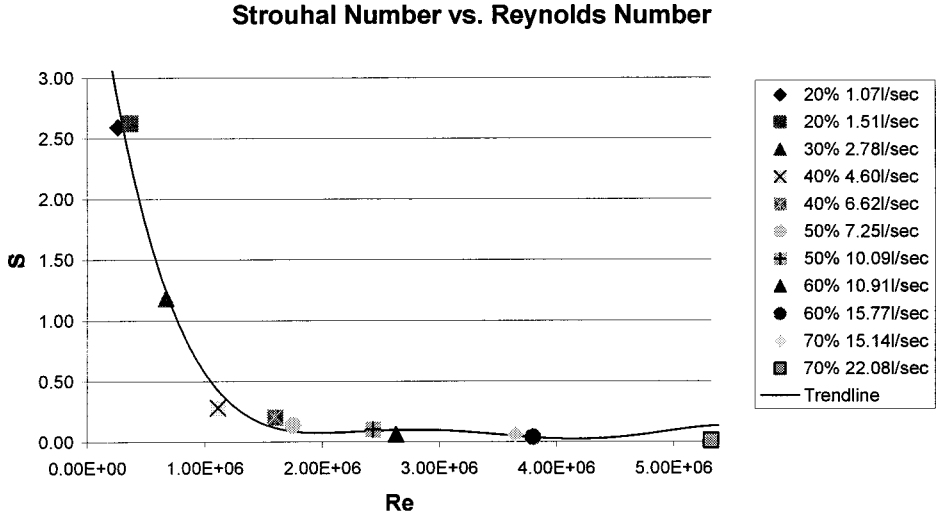

Fig. 16 Strouhal number versus Reynolds number at each test condition

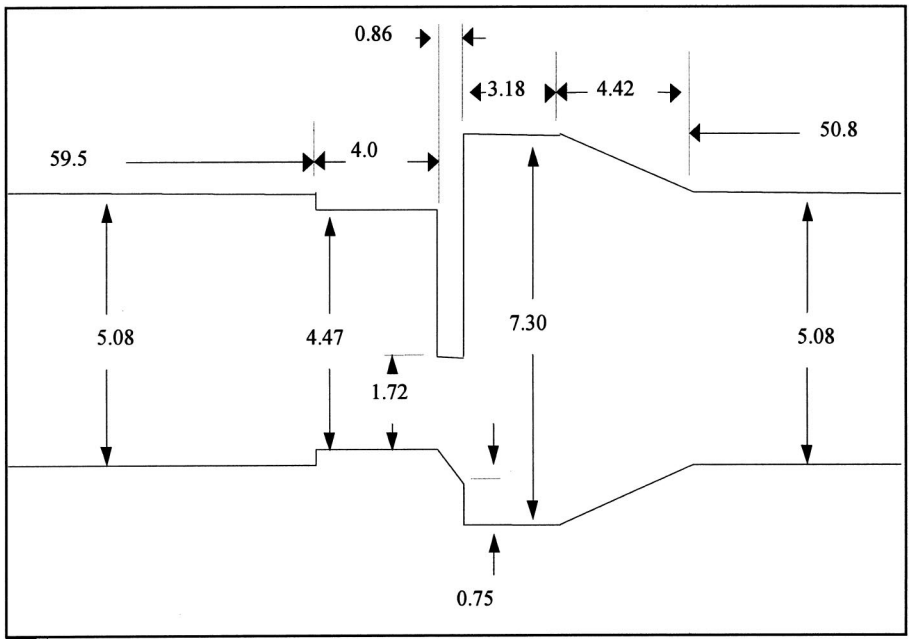

Fig. 17 Two-dimensional model of the valve and the piping system (units in cm)

show the flow reversal corresponding to the vortex flow of the valve. The turbulence intensity profiles are shown in Fig. 11. Turbulence intensity is defined as the ratio of the local RMS values of the velocity fluctuation and the mean velocity of the flow in the 5.08 cm pipe U, plotted on a percentage base. The largest magnitudes of turbulence intensities are observed in the separated shear layer region of the valve lip. The second weaker peak in the turbulence intensity profiles is due to the separated flow of the valve seat. The uncertainty for LDV measurements is ± 2 percent.

A typical pressure power spectrum is shown in Fig. 12. This figure shows a comparison of the power spectrum between valve positions of 100 percent open and 50 percent open at the same flow rate, 7.25 lit/s. Darker graph in Fig. 12 represents 50 percent valve opening. Sharp peaks represent the rotational frequency

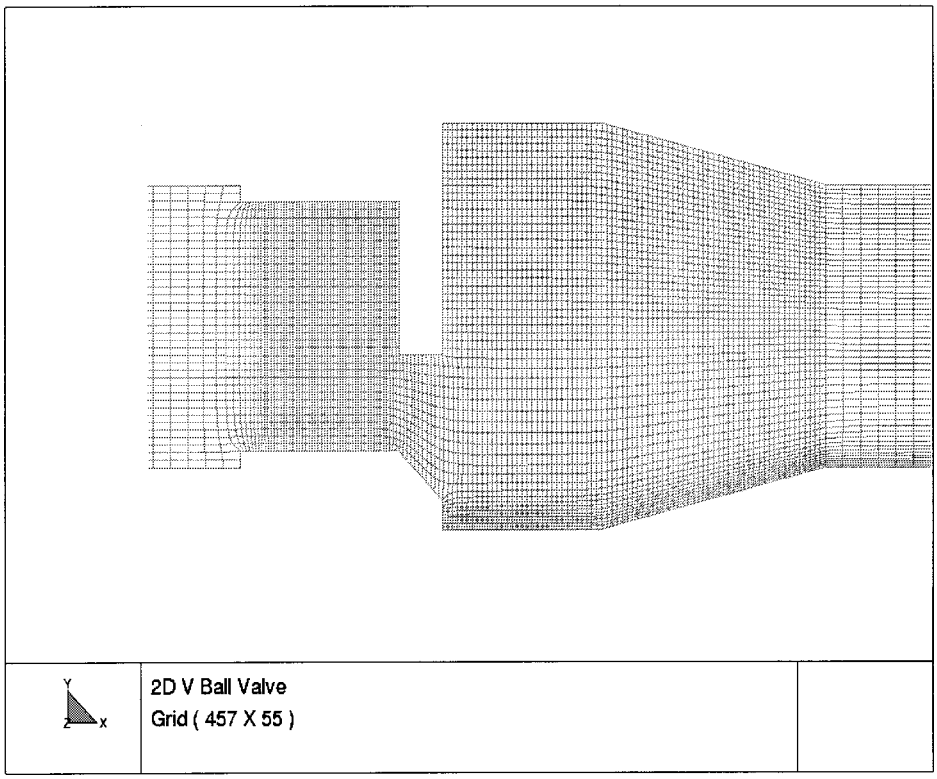

Fig. 18 Physical grid

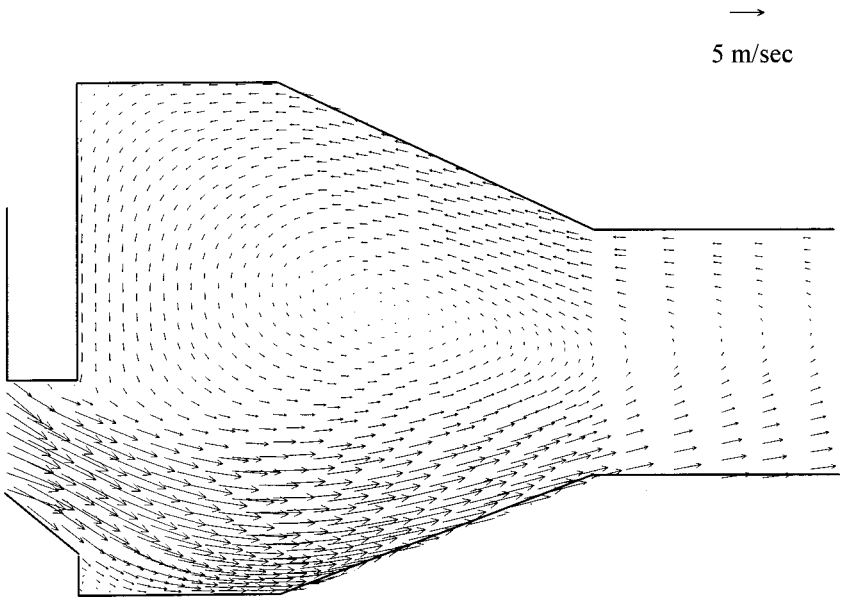

Fig. 19 Velocity vectors near the valve

of the individual impeller vanes and their harmonics. The uncertainty for pressure measurements is ± 0.1 percent.

Power spectrum analysis has revealed a broadband Strouhal frequency shown in Fig. 13. Broadband Strouhal frequency starts at about 1.25 Hz, the lower limit, and ends at about 18.50 Hz, the higher limit. The centroid of this region was calculated to be about 9.86 Hz. The formula used to calculate the centroid of the broadband Strouhal frequency on the x-axis is shown in Eq. (2). The x-axis is the frequency axis and the y-axis is the power spectrum axis. This method is used to calculate all of the Strouhal frequencies. The broadband Strouhal frequencies for each test condition are shown in Fig. 14.

$$\text{Centroid}(x \text{ axis}) = \frac{\int y \cdot x dx}{\int y dx} \tag{2}$$

As the flow rate and valve opening increase, the broadband Strouhal frequency generally decreases. Strouhal number for each test condition is shown in Fig. 15. Strouhal number S and Reynolds number Re are calculated based on the following relationships.

$$S = f_s D/U \tag{3}$$

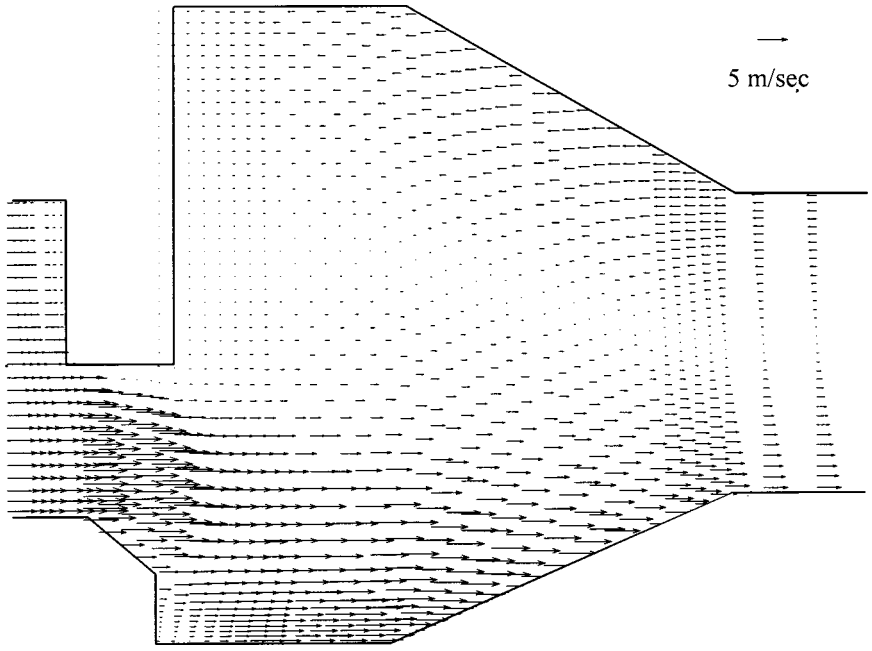

Fig. 20 Streamwise component of the velocity

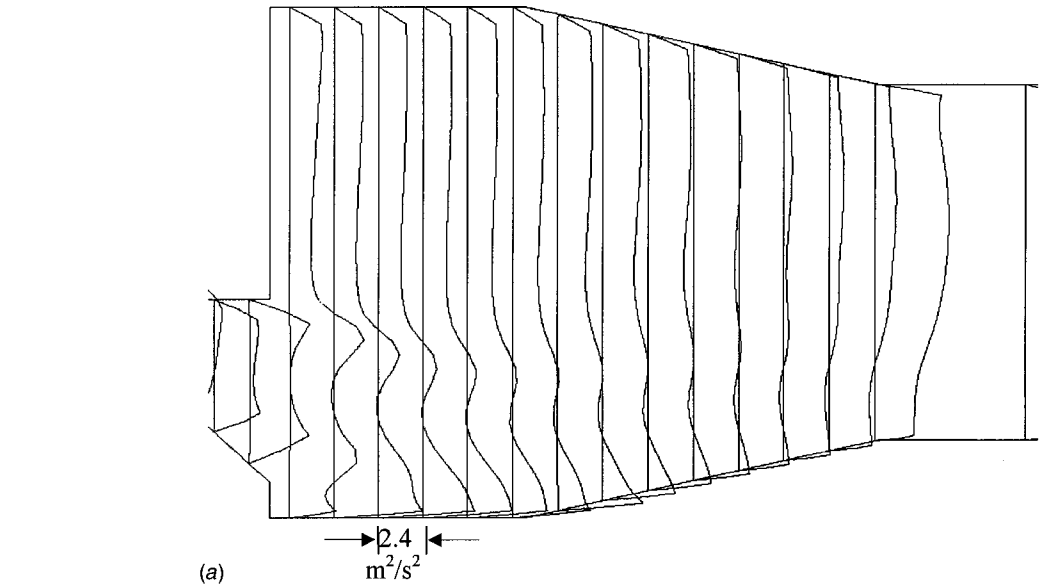

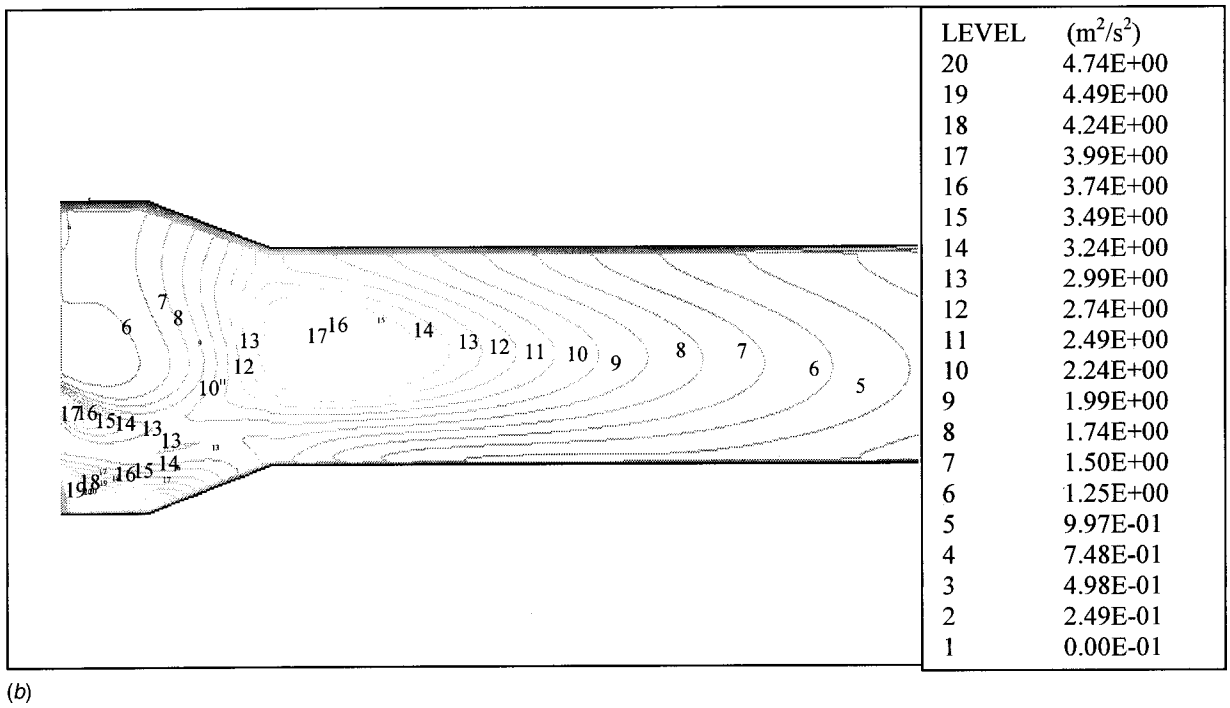

Fig. 21 (*a*) Turbulence kinetic energy profiles; (*b*) Constant contours of turbulence kinetic energy

$$\mathrm{Re} = UD/v \tag{4}$$

$$S = -1.17\times10^{-32}\,\mathrm{Re}^5 + 2.1\times10^{-25}\,\mathrm{Re}^4 - 1.44\times10^{-18}\,\mathrm{Re}^3 + 4.7\times10^{-12}\,\mathrm{Re}^2 - 7.3\times10^{-6}\,\mathrm{Re} + 4.41 \tag{5}$$

f_s = dominate vortex frequency, Strouhal frequency
U = mean streamwise velocity in 5.08 cm pipe
D = pipe diameter (5.08 cm)
v = kinematics viscosity

The uncertainty in measuring the mean velocity of the flow in the pipe and thus Re is ±0.5 percent. The same general trend shown in Fig. 14 is observed, but there is an even greater contrast in the Strouhal number as flow rate and valve opening increase. The Strouhal number S versus Reynolds number Re is shown in Fig. 16. The variation of S with Re can be described by a fifth degree polynomial obtained by least square curve fitting technique. This polynomial for $\mathrm{Re} \leqslant 5.32\times10^6$ is represented by Eq. (5) and the trendline is shown in Fig. 16.

Since the Strouhal number for different valve openings depends only on one independent variable, i.e., Reynolds number, the pipe diameter seems to be an appropriate length scale for defining S versus Re. The paper mill problems have been observed for pipe diameters 0.35 m to 0.91 m with pipe flow speeds of 0.15 m/s–0.45 m/s. This results in a Reynolds number of around 0.15×10^6 corresponding to S=3 and Strouhal frequencies of 0.5 Hz–3.86 Hz. This is consistent with the data presented by Lewis et al. [1].

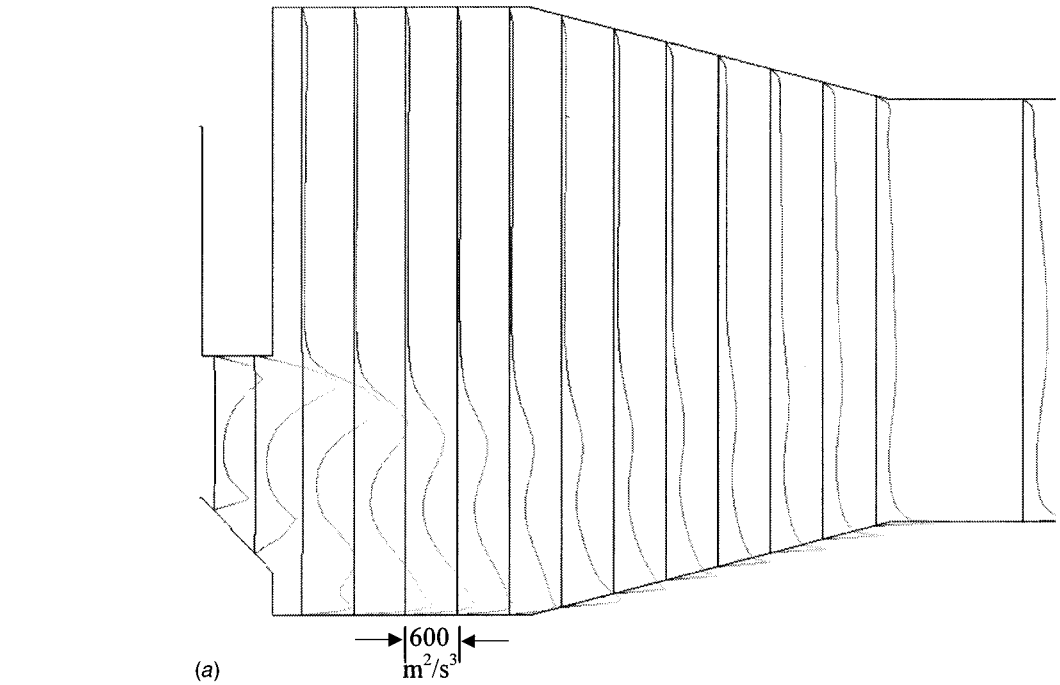

(a)

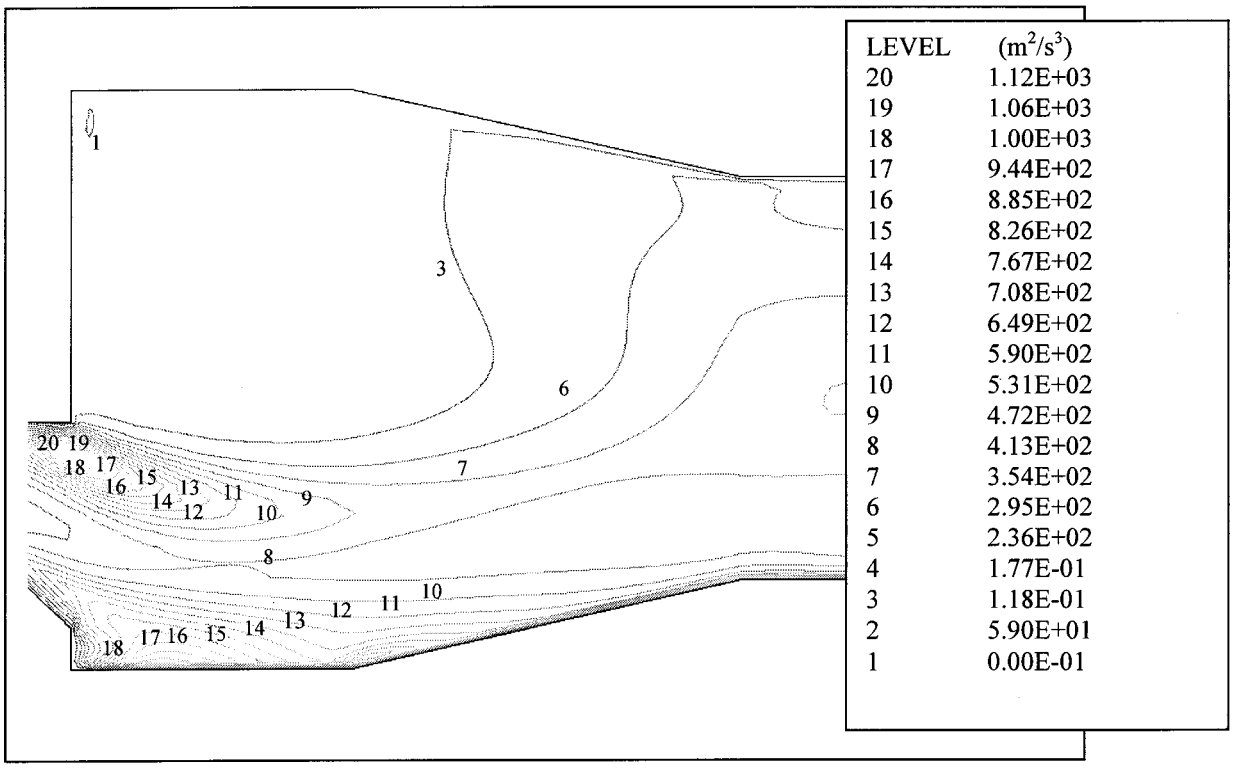

(b)

Fig. 22 (*a*) Eddy dissipation rate profiles; (*b*) Constant contours of eddy dissipation rate

4 Computational Fluid Dynamics (CFD)

Using FLUENT, a two dimensional model of the valve body and connecting pipes shown in Fig. 17 is created to investigate the flow. A structured grid made of 457×55 nodes, with k-ϵ turbulence model is used. The boundary conditions were obtained from the laboratory experiments. The inlet velocity of 2.2 m/s, corresponding to 4.42 lit/sec of flow rate and the outlet pressure of one atmosphere were used. This model provides flow properties, such as velocity, pressure, turbulence, and dissipation rate quantities. A section of the physical grid in the valve region is shown in Fig. 18. The grid concentration in the valve region is higher for resolving the vortex flow and the separated flow of the boundary layers. The valve seat is also modeled.

Flow velocity vectors in the valve region are shown in Fig. 19. The existence of a large vortex that extends downstream for several pipe diameters is clearly shown in this figure. A small

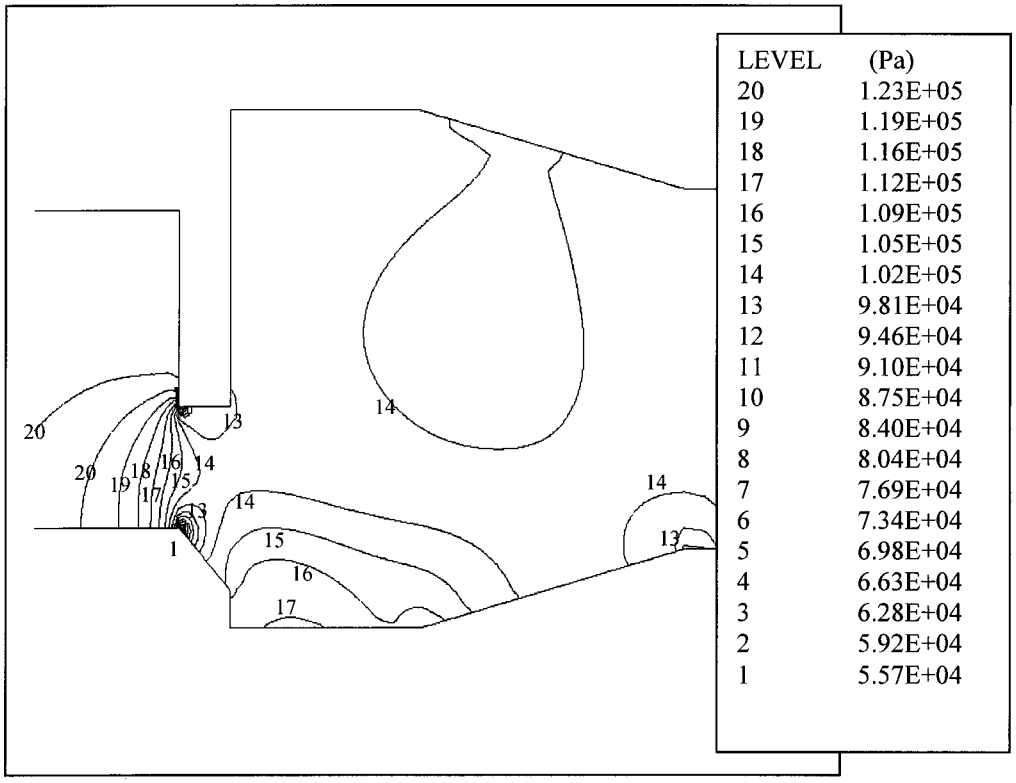

Fig. 23 Constant contours of absolute static pressure

recirculating zone at the corner region near the valve seat is observed. The dominant effect of the valve in the entire system is because of the large vortex with high energy and low frequency of oscillation.

Streamwise component of the velocity is shown in Fig. 20. The velocity profiles are very similar to the streamwise velocity components measured with LDV as shown in Fig. 10. The magnitude of the velocity components is smaller in the CFD results because flow is assumed two-dimensional. This assumption with corresponding boundary conditions creates lower pressure drop across the valve compared with the real flow condition. The lower pressure drop provides lower driving force for speeding up the flow in the valve region.

Turbulence kinetic energy profiles are shown in Fig. 21(*a*). The separated regions of the flow where shear layers exist have the highest magnitudes of the turbulence kinetic energy. There is close qualitative agreement between turbulence intensity measurements obtained by LDV as shown in Fig. 11 and kinetic energy profiles of Fig. 21(*a*). The constant contours for turbulence kinetic energy are shown in Fig. 21(*b*). The magnitude of the turbulence kinetic energy in the contracted region of the valve is high. This is due to creation of large shear layer of the vortex as it is squeezed into a smaller region of the downstream pipe. This increase in turbulence is obvious in the turbulence measurements shown in Fig. 11. The eddy dissipation rate profiles and contours are shown in Figs. 22(*a–b*). These figures show that energy is dissipated in the regions where turbulence is generated. The constant absolute static pressure contours are shown in Fig. 23. As the flow speeds up in the valve opening, the pressure drops and it losses some of its energy to viscous dissipation in the separated regions. The overall pressure difference is positive to drive the fluid downstream.

5 Conclusions

This work resulted from a need to better understand the fluid dynamics of stock piping systems, and how V-ball valves affect those dynamics. An experimental facility was developed to measure the vortex flow structure and its dominant Strouhal number for a V-ball valve. Pressurization of the entire system eliminated the valve cavitation and reduced the system noise drastically. High-speed video photography, LDV, dynamic pressure measurements, and CFD were used for this investigation.

There exists a dominant large three-dimensional vortex downstream of the valve. The centerline of this vortex is a shadow of the valve lip. There is close qualitative agreement between the CFD results and velocity and turbulence measurements. The Strouhal number for V-ball valves was found to be independent of valve opening. The appropriate characteristic length for Strouhal and Reynolds numbers is pipe diameter. A fifth-degree polynomial relationship between Strouhal number S and Reynolds number Re for different valve openings and flow rates have been obtained. The magnitude of S drops with Re. This drop is much faster for $Re<10^6$. Piping system designers can use the empirical relationship obtained in this research to obtain the dominant frequencies generated by V-sector ball valves to avoid resonance conditions. Changing the pipe diameter, modifying the flow restriction in the valve area, adding an orifice after the valve are some of the options to detune or attenuate the system resonance once the vortex frequency is known.

Acknowledgment

This research was supported by a grant from Goulds Pump, Inc. in Seneca Falls, New York.

References

[1] Lewis, A. L., Szenasi, F. R., and Roll, D. R., 1996, ''Control Valve Induced Pipeline Vibrations in a Paper Pulp Pumping System,'' *Proceedings of the 14th International Pump Users Symposium*, College Station, Texas.
[2] Sparks, C. R., and Wachel, J. C., 1977, ''Pulsation in Centrifugal Pump and Piping Systems,'' Hydrocarbon Process., pp. 183–189.
[3] Wylie, B. E., and Streeter, V. L., 1983, *Fluid Transients*, Feb Press, Ann Arbor, MI.
[4] ''Valve and Actuator Catalogs on CD-ROM,'' 1977, Fisher Controls International, Incorporated. Marshalltown, Iowa.

Gwo-Bin Lee
Assistant Professor
Department of Engineering Science,
National Cheng Kung University,
Tainan, Taiwan, Republic of China, 701
e-mail: gwobin@mail.ncku.edu.tr

Chen-I Hung
Professor

Bin-Jo Ke
Graduate Student

Department of Mechanical Engineering,
National Cheng Kung University,
Tainan, Taiwan, Republic of China, 701

Guan-Ruey Huang
Graduate Student

Bao-Herng Hwei
Senior Students

Hui-Fang Lai
Senior Students

Department of Engineering Science,
National Cheng Kung University,
Tainan, Taiwan, Republic of China, 701

Hydrodynamic Focusing for a Micromachined Flow Cytometer

This paper describes hydrodynamic focusing inside a micromachined flow cytometer. Flow cytometry is a process whereby cells are analyzed and sorted based on hydrodynamic focusing phenomenon and specific cellular characteristics. In this study, the hydrodynamic focusing phenomenon is first modeled by employing potential flow theory. Then the flow field inside the flow cytometer is numerically simulated. The effect of the device geometry and relative sheath and sample flow rate on the focusing of the center flow is explored systematically. At last, a micromachine-based flow chamber is designed and fabricated on plastic substrates as a micro flow cytometer. Hydrodynamic focusing is verified with the use of microscopic visualization of water sheath flows and dye-containing sample flow. Experimental data indicate that the size of focused sample stream can be reduced to about 3 μm, which is applicable to cell sorting and counting.
[DOI: 10.1115/1.1385514]

Introduction

Micromachining techniques and MEMS (Micro-Electro-Mechanical-Systems) technology have opened a number of opportunities for researchers in various fields. Micro-sensors, micro-actuators, and IC control circuits could all be integrated in a small area using batch-fabrication techniques. MEMS has been an enabling technology in various fields, revolutionizing existing fabrication techniques. The applications of MEMS technologies, for instance in the research of the drug discovery process in the pharmaceutical industry, or in analytical chemistry, are not only increasing the performance of the conventional analytical methods and helping our understanding of the analytical process but, much more important, it allows totally new access to information on the molecular level. A micro total analysis system (μ-TAS), which executes sampling, sample transportation, reaction, separation, and detection, can be realized by using microfabrication techniques [1–3].

In the past few years, microfabrication of miniature fluidic devices has attracted considerable interest in the field generally known as microfluids [4–5]. Miniaturization of the fluidic system has potential benefits including disposability, reduced size, improved performance, low cost, reduced sample and reagent volume, and reduced power consumption. Furthermore, the integration of the microfluidic system and detection circuitry can improve reliability and functionality. The present study will present an important microfluidic device—a micro flow cytometer. Special attention will be focused on the hydrodynamic focusing phenomenon inside the device.

Contributed by the Fluids Engineering Division for publication in the JOURNAL OF FLUIDS ENGINEERING. Manuscript received by the Fluids Engineering Division September 25, 2000; revised manuscript received April 18, 2001. Associate Editor: P. W. Bearman.

Flow cytometers have been widely used for cell sorting and counting for researchers working in the field of medical diagnosis [6–7]. Figure 1 shows a schematic diagram of a conventional flow cytometer. Typically, the particles are injected into an electrolyte and hydrodynamically focused into a single cell stream constrained by two concentric sheath flows. Subsequently, the focused cell stream is then passed through a detection region (optical or electrical detection) for cell counting or sorting. Several micro-chip flow cytometers using different substrates have been reported previously. Miyake et al. [8] reported a five-layer stainless steel/glass laminate sheath flow chamber. Hydrodynamic focusing was demonstrated by microscopic visualization of a water sheath and dye-containing sample. Similarly, Sobek et al. [9] demonstrated that microfabricated flow cytometry could be constructed on the quartz wafers, which utilized the principle of hydrodynamic sheath flow focusing in a manner similar to that used in conventional flow cytometers. Later, Larsen et al. [10] presented a micro particle counter based on Coulter principle and sheath flows. The cell counter was fabricated on silicon substrates using standard IC (Integrated Circuit) fabrication and anodic bonding techniques. Hydrodynamic focusing has been observed successfully during their experiments. Using similar concepts, Koch et al. [11] reported another micro-chip cell counting device. A novel technology based on silicon trench etching and subsequent deposition of metal electrodes over the trench edges has been applied for built-in electrode access.

Most of the microfabricated cytometers apply sheath flows for hydrodynamic focusing of the center flow. However, non-sheath-flow-based cell-counting device, which only uses a single flow channel etched into a silicon wafer, has also been reported previously. The ability for carrying out differential blood cell counts has been demonstrated by Altendorf et al. [12]. Even though micromachined flow cytometers have been demonstrated in the lit-

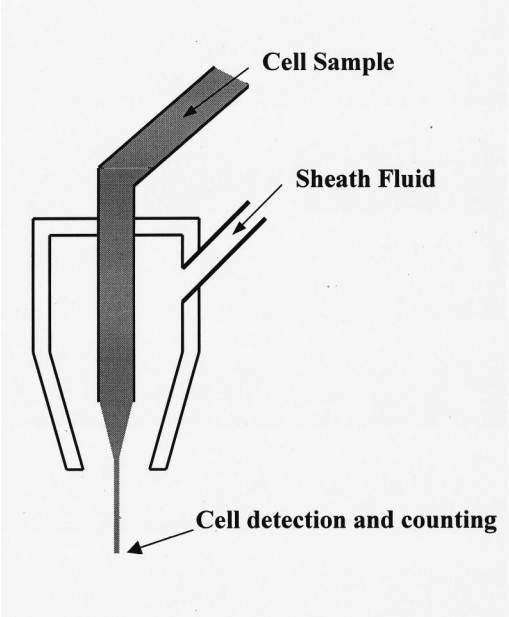

Fig. 1 Schematic representation of a conventional flow cytometer. Center flow is focused hydrodynamically into a single cell stream due to sheath flows

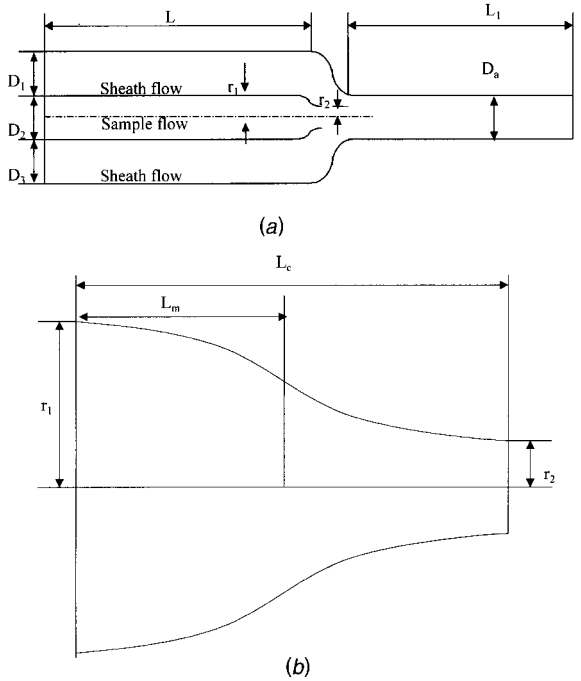

Fig. 2 Schematic representation of the micro flow cytometer (a), and close-up schematic of the convergent nozzle

erature, systematic investigation of the flow field inside the microfluidic device has not yet been reported, including theoretical and numerical analysis. The effect of the device geometry on the hydrodynamic focusing of the center flow has not been explored, neither. Furthermore, the relative sheath and sample flow rate plays an important role on the width of the focused cell stream. Besides, it is also crucial to fabricate a flow cytometer inside a small area such that the cost of microfabrication can be reduced. Consequently, the length of which the width of the focused stream reaches a cell size becomes a critical design parameter. The present study is therefore aimed at exploring the technique for achieving the focused flows, referred to as ''hydrodynamic focusing,'' inside a flow cytometer.

In order to mass-fabricate cheap, disposable microfluidic chips, a novel hot embossing method to duplicate microfluidic channels on plastic (Polymethylmethacrylate, PMMA) substrates has been developed [13]. Microfluidic devices can be fabricated with ease at low cost using this method. In addition, reliable bonding methods for PMMA plates have also been developed to seal the microfluidic devices. In the present study, these micromachining techniques have been applied to fabricate a micro flow cytometer for cell sorting and counting. Microfluidic devices have very smooth and reproducible features using the developed techniques. Details including design, fabrication, characterization, as well as operation of the micromachined flow cytometer, will be discussed in the following sections.

Design and Fabrication of Micro Flow Cytometry

Figure 2 represents a simplified micro flow cytometer. It is composed of three channels. The cell samples are injected from the center channel and focused hydrodynamically into a single cell stream constrained by flows from two sheath channels. The profile of the convergent part could be critical to the nozzle design. A smooth profile is applied to avoid potential loss of flow energy. The geometry of the inner and outer nozzles described by the following equations [14].

(i) $l<L_m$

$$r=(r_1-r_2)\left[1-\frac{\left(\frac{l}{L_c}\right)^3}{\left(\frac{L_m}{L_c}\right)^2}\right]+r_2 \tag{1}$$

(ii) $l>L_m$

$$r=(r_1-r_2)\left[\frac{\left(1-\frac{l}{L_c}\right)^3}{\left(1-\frac{L_m}{L_c}\right)^2}\right]+r_2, \quad L_m=L_c/2 \tag{2}$$

where r and l are radial and axial coordinates, respectively (Fig. 2).

Figure 3 shows a schematic representation of a simplified fabrication process for flow cytometers. A commercial blank photo mask substrate (Nanofilm, Inc.) consisting of three layers ($1-\mu$m photoresist, 1-μm Cr, and 2.3-mm quartz, respectively) was used as a master template on which microfluidic devices were fabricated. Microfluidic devices on the quartz substrate were formed by using wet etching (Buffered oxide etchant, BOE, 6:1) with Cr as etch masks. BOE was chosen due to the act that the fabricated micro structure has a smoother appearance than hydrofluoric acid (HF) etching. Quartz was etched in all areas except the masked area, and the resulting structure was inverse raised three-dimensional image of the channels. The micromachined quartz templates can then be used repeatedly to fabricate cheap and disposable plastic devices.

The microfluid devices were then imprinted on plastic blanks by placing quartz templates with inverse raised image on top of a PMMA blank. During the fabrication process, a hot embossing machine was used to apply uniform and reproducible pressure ($>1.25\times10^5$ N/m^2) on the templates (Fig. 4). During the compression process, both PMMA and quartz template were heated above transition temperature (105 °C) of the plastics for at least 10 minutes. Experimental data showed that hot embossing was an

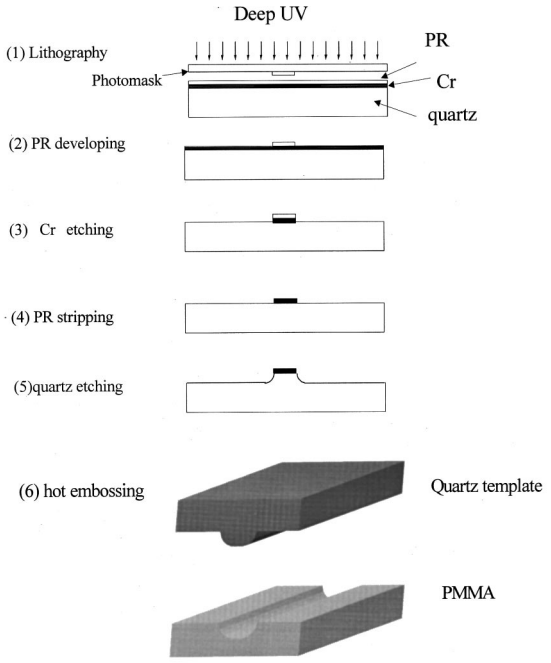

Fig. 3 Fabrication process for quartz master templates. Microfluidic devices on the quartz substrate were formed by using wet etching (buffered oxide etchant, BOE, 6:1) with Cr as etch masks

effective method to duplicate microfluidic devices on plastic substrates. The resulting structure shown in Fig. 5 was then clamped with another blank PMMA cover plate to form the sealed channels. The PMMA devices were heated at a higher temperature (108 °C) for at least 12 minutes for bonding. Prior to bonding,

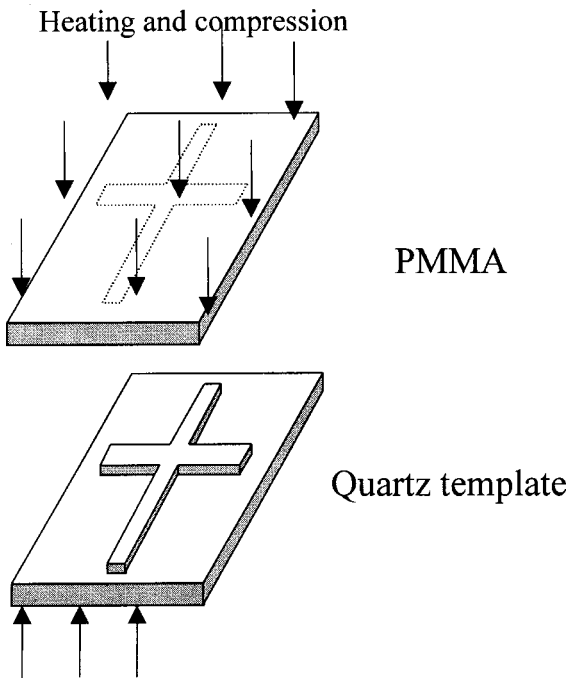

Fig. 4 Schematic diagram of hot embossing methods. A hot embossing machine was used to apply uniform and reproducible pressure on the surfaces. The entire devices were heated above transition temperature of the plastics for at least 10 minutes

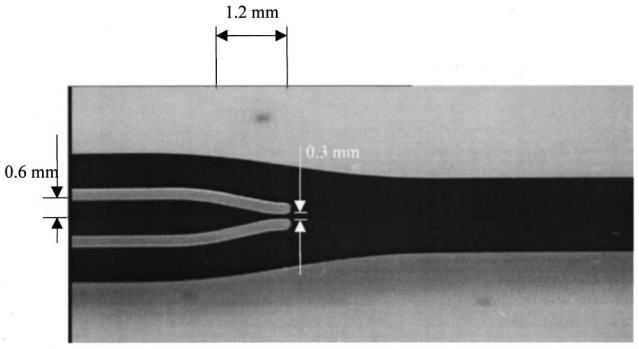

Fig. 5 Picture of a microfabricated flow cytometer. It was fabricated on PMMA substrates using hot embossing methods

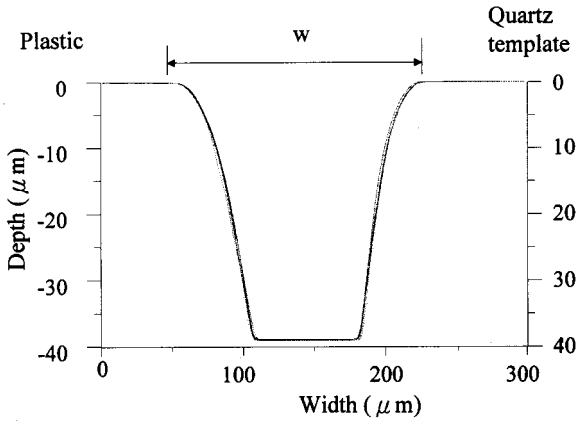

Fig. 6 Cross-sectional geometry of the micro channels. Note that 10 sets of data are plotted on the same figure along with one from a quartz template

four through holes (800 μm in diameter) were drilled on the cover plate as flow inlets and outlets. These holes were aligned under microscope with the ends of the channels. The good sealing of micro channels were observed. In the present study, the hot-embossing method was applied to fabricate a micro flow cytometer (Fig. 5).

The reproducibility of the microfabricated flow cytometers using hot embossing methods was evaluated by measuring 10 channels on different plastics. The channels were characterized on the basis of the depth of the channels, as well as the width of the channels at the surface of the plastic. The cross-sectional geometry of the channels was obtained from surface profilometer (alpha-step 500) and the results are shown in Fig. 6. It should be noted that 10 sets of data, along with that for a quartz template, have been plotted on the same figure. It can be clearly seen that the surface profile of the channel on PMMA plates corresponds well to that on the quartz template. The average depth of the channels is 38.12 μm and the relative standard deviation is less than 1%. The average with at the top of the surface is 102.9 μm, with a relative standard deviation of 2.17%. These data show that hot embossing is an effective method to duplicate microfluidic devices on plastic substrates.

Theoretical Model

The objective of the section is to propose a theoretical model to predict the width of focused center flow inside a micro flow cytometer. Kachel et al. reviewed hydrodynamic properties of conventional flow cytometry instruments using potential flow theory [15]. Consider an area in the reservoir (A) that is located a distance (s) from the inlet to the tube of radius (R) (Fig. 7). Assum-

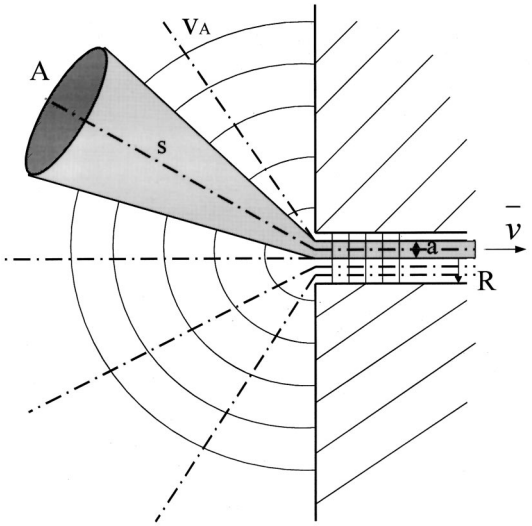

Fig. 7 The coordination of potential flow theory showing the fluid passing through the cross section (A) in the distance (s) is focused to a smaller cross section (a) inside a tube [15]

ing fluid passes through with the same velocity at each cross section, conservation of mass assures the following equation:

$$V_A 2\cdot\pi\cdot s^2=\overline{\nu}\cdot\pi R^2 \tag{3}$$

$$\frac{V_A}{\overline{\nu}}=\frac{R^2}{2s^2} \tag{4}$$

where V_A and $\overline{\nu}$ are velocities at point A and inlet of the tube, respectively. The above equation is the principle of ''hydrodynamic focusing'' which is used in most flow cytometric instruments. The area (A) represents the cross-sectional area of an injection tube containing cells in our case. These cells would be focused into a small stream cross the area (a) where detection of cells would be performed. Using the similar concept, one can derive the equation for flow inside a planar micromachined flow cytometer. In Fig. 8 consider the two-dimensional situation where sample flow is from a larger inner nozzle into a small focused cell stream. Likewise, conservation of mass requires that the amount of fluid crossing the center channel must equal the amount of fluid crossing the focused stream. It follows that

$$\overline{\nu_2}\cdot D_2=\nu_c\cdot d \tag{5}$$

$$d=\frac{\overline{\nu_2}}{\nu_c}\cdot D_2 \tag{6}$$

where D_2, d, $\overline{\nu_2}$, ν_2 are width of the center channel before focusing, width of the focused stream, velocities inside center channel and focused stream, respectively. The flow inside the micro cytometer is considered to be laminar, and the diffusion and mixing between focused stream and sheath flows is assumed negligible. With the above assumption, conservation of mass assures the following equations.

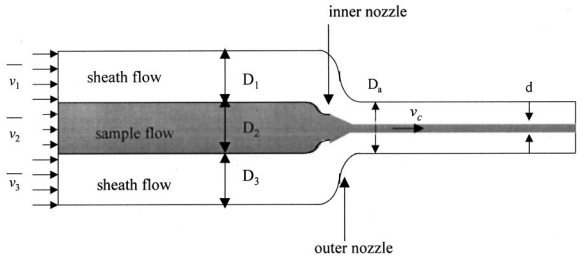

Fig. 8 Schematic representation of a micromachined flow cytometer. Note that inner and outer nozzles have a convergent profile

$$\dot{m}_{in}=\rho_1\overline{\nu}_1\cdot D_1+\rho_2\overline{\nu}_2\cdot D_2+\rho_3\overline{\nu}_3\cdot D_3 \tag{7}$$

$$\dot{m}_{out}=\rho_a J_a\cdot D_a \tag{8}$$

$$\overline{\nu}_a=\frac{(\rho_1\overline{\nu}_1 D_1+\rho_2\overline{\nu}_2 D_2+\rho_3\overline{\nu}_3 D_3)}{\rho_a D_a} \tag{9}$$

where $\dot{m}_{in}$ and $\dot{m}_{out}$ are mass flow rates of the inlet and outlet flows; D_1 and D_3 are width of the inlet channels 1 and 3, respectively; $\overline{\nu}_1$, $\overline{\nu}_2$, and $\overline{\nu}_3$ are velocities in sections 1, 2, and 3; $\overline{\nu}_a$ is average velocity inside outlet section D_a. Assuming that it is a fully-developed laminar flow inside the outlet channel, velocity profile inside the section D_a is parabolic-distributed. It follows that

$$\nu_c=\nu_{\max}=1.5\overline{\nu}_a \tag{10}$$

where ν_c is the velocity at the center line of the channel.

Therefore, the width of the focused center stream can be represented as

$$d=\frac{\overline{\nu}_2}{\nu_c}\cdot D_2=\frac{\rho_a\overline{\nu}_2\cdot D_2 D_a}{1.5\cdot(\rho_1\overline{\nu}_1 D_1+\rho_2\overline{\nu}_2 D_2+\rho_3\overline{\nu}_3 D_3)}$$

$$=\frac{\rho_a D_a}{1.5\left(\rho_1\dfrac{\overline{\nu}_1}{\overline{\nu}_2}\dfrac{D_1}{D_2}+\rho_2+\rho_3\dfrac{\overline{\nu}_3}{\overline{\nu}_2}\dfrac{D_{31}}{D_2}\right)} \tag{11}$$

The above equation is used to predict the width of the focused stream inside the flow cytometer. It indicates that the width of the focused stream is inversely proportional to the relative sheath and sample flow rate and proportional to volumetric flow rate of the sample flow. The results calculated from the above simple model have also been compared with numerical simulation and experimental data, which will be discussed in the following sections. The above equation provides a simple guideline to predict the width of the focused stream. It should be also noted that Eq. (11) does not provide any information regarding the effect of device geometry (such as relative location of the inner and outer nozzles) on the width of the focused stream. The numerical simulation method will be used to explore the geometry effect in the next section.

Numerical Simulation

The schematic diagram of the physical model for the micro flow cytometer is shown in Fig. 8. The following assumptions are made to simplify the mathematics without losing the essential physics:

1 The flow is Newtonian, steady, laminar, and incompressible.
2 Only two-dimensional flow is considered in the present study.
3 Neglect gravity force.
4 Nonslip condition applies on the solid boundary.
5 Isothermal distribution in temperature field is assumed.

Governing equations.

(a) Continuity equation

$$\frac{\partial}{\partial x_j}(\rho u_j)=0 \tag{12}$$

where ρ and u_j are density and velocity vector, respectively.

(b) Momentum equation

$$\frac{\partial}{\partial x_i}(\rho u_i u_j)=-\frac{\partial p}{\partial x_i}+\frac{\partial \tau_{ij}}{\partial x_i} \tag{13}$$

Table 1 Geometric parameters for the flow cytometer

r_1	r_2	$D_1=D_2=D_3$	D_a	L	L_1
0.6	0.3	1.2	2.4	10	8

Unit: mm

where p and τ_{ij} are pressure and stress tensor, respectively.

The Navier-Stokes equations along with appropriate boundary conditions are solved numerically using finite volume method with SIMPLEC (Semi-Implicit Method for Pressure-Linked Equations Consistent) algorithm [16]. Supplementary numerical calculations performed on grids ranging from 90×36 to 160×80 suggest that satisfactory grid independence could be achieved using a 150×60 grid. Table 1 lists all geometric parameters for the flow cytometers. The following sections will discuss the numerical results.

Geometry of Outer Nozzles. Three types of outer nozzles have been chosen to evaluate the effect of geometry on the hydrodynamic focusing. The relative sheath and sample flow rate is kept constant (10:1) to achieve reasonable flow focusing and the location of the inner nozzle is fixed for all cases. Table 2 shows the width of the focused stream for three cases. It has been found that the focusing effect becomes prominent as outer nozzle is shorten. For the third case ($L_c=2$ mm), the width of the focused stream can be scaled to 7.8 μm at the exit of the outer nozzle. The data indicate that appropriate design of the outer nozzle could appreciably improve the performance of hydrodynamic focusing. It also implies that one can achieve effective hydrodynamic focusing in a very short length.

Locations of the Inner Nozzle. The location of the inner nozzle for sample flow injection could also play an important role on hydrodynamic focusing. Three cases corresponding to three different locations of the inner nozzle in Table 3 are calculated for demonstration. It shows that the width of the focused stream is a strong function of the locations of the inner nozzle. While the exit of the inner nozzle is aligned with the inlet of the outer nozzle (case 1), the width of the focused stream is 42.3 μm at the exit of the outer nozzle. Furthermore, the width can be scaled down to 7.8 μm while inner nozzle is moved to the middle of the outer nozzle. However, it becomes larger (47.9 μm) as the inner nozzle is moved toward further downstream location.

Relative Sheath and Sample Flow Rate. The relative sheath and sample flow rate is another important parameter for operation of the flow cytometer. Equation (11) indicates that the width of the focused stream decreases as the relative sheath and sample flow rate increases. Figure 9 shows the variation of the width of the focused stream along with axial location for flows with different relative flow rate ratios. The trend is consistent with results predicted by Eq. (11). For the case with a relative flow rate ratio of 10, the focused width could be scaled down to 10 percent of the original width at a distance less than 300 μm. Figure 10 represents the variation of the width of the focused stream along with the relative flow rate while measured at the exit of the micro flow cytometer. It shows that the width of the focused stream is inversely proportional to relative sheath and sample flow rate. The width of the focused stream can be scaled down to 7.4 μm, while the flow rate ratio reaches 10.

Table 2 Geometry of the outer nozzles versus hydrodynamic focusing width. The widths of the focused stream (d_1 and d_2) are shown in the table for three cases. It has been found that the focusing effect becomes prominent as outer nozzle is narrowed down to a shorter length. In Tables 2–4, d_1 and d_2 are widths of the focused stream measured at the end of the convergent part of the outer nozzle and the outlet of the flow cytomter, respectively

	L_c (mm)	L_m (mm)	d_1 (μm)	d_2 (μm)
Case 1	6	3	27.95	24.73
Case 2	4	2	11.4	10.8
Case 3	2	1	7.8	7.5

Table 3 Locations of the near nozzle versus hydrodynamic focused width. It shows that the width of the focused stream is a strong function of the locations of the inner nozzle. The parameter x is the location of the inner nozzle, which is measured from the inlet of the sample flow

	x (mm)	d_1 (μm)	d_2 (μm)
Case1	10	42.3	20.6
Case2	11	7.8	7.5
Case3	11.2	47.9	44.9

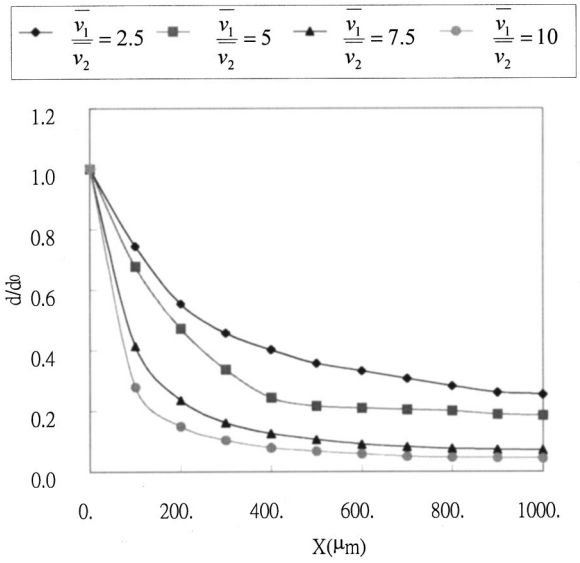

Fig. 9 Variation of the width of the focused stream along with axial location for flows with different relative flow rates. Note that the focused width (d) is normalized by a reference width (d_0), which is the width measured at the exit of the inner nozzle

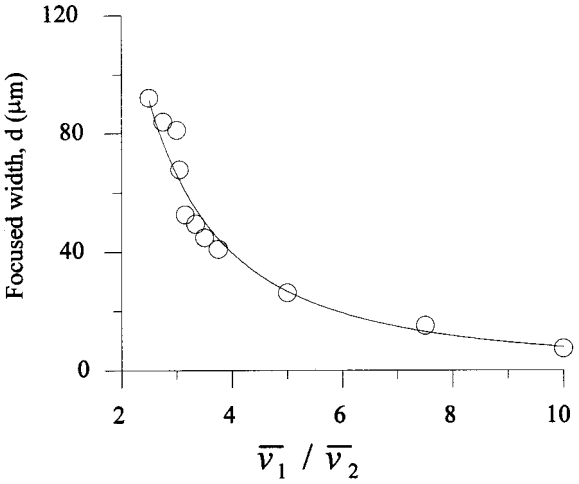

Fig. 10 The variation of the width of the focused stream along with relative flow rates while measured at the exit of the flow cytometer

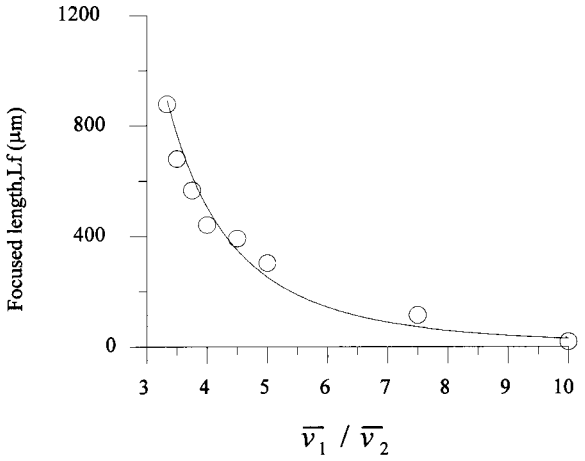

Fig. 11 The variation of the focused length along with the relative sheath and sample flow rates

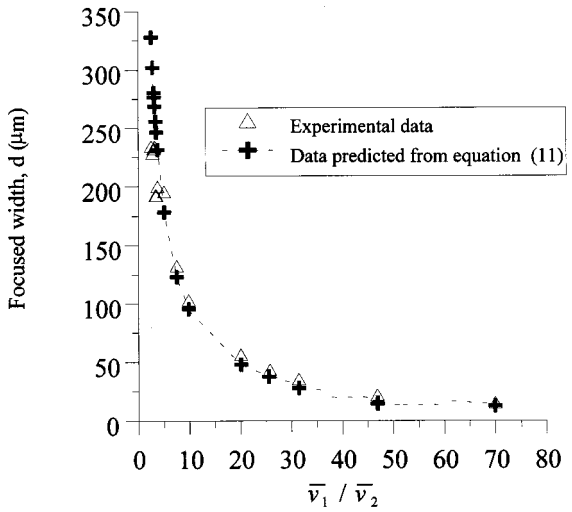

Fig. 13 The variation of the width of the focused stream along with relative flow rates

Another important issue for hydrodynamic focusing inside a flow cytometer is the length it takes to reach a focused stream. One would like to design a micro flow cytometer inside a smaller area such that the cost of the chip can be reduced. In this study, a ''focused length'' is defined as the length of which focused stream reaches 10 percent of the width at the exit of the inner nozzle. Figure 11 shows the variation of the focused length along with the relative sheath and sample flow rates. As expected, larger relative sheath and sample flow rates achieve shorter focused length. The focused length can be as short as 20 μm for a relative flow rate of 10.

Experimental Section

A micromachine-based flow cytometer has been fabricated using techniques described in the previous section. The flow cytometer has the same geometry as shown in Fig. 2. According to numerical simulation, one can best obtain hydrodynamic focusing of the center flow while the inner nozzle is placed at the middle location of the outer nozzle. Therefore, only this geometry has been chosen for hydrodynamic tests. Hydrodynamic focusing was investigated with water sheath flows and a dye-containing sample flow under a microscope. An image processing system, consisting of a high-resolution CCD video camera, an image interface card and a PC, was used for image acquisition.

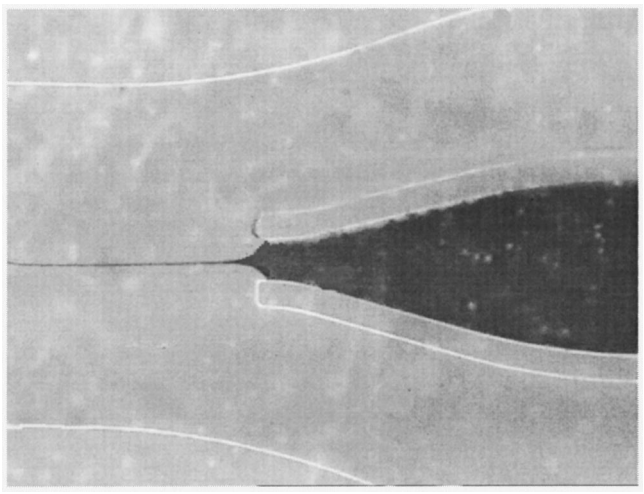

Fig. 12 Focused sample stream inside a flow cytometer. Hydrodynamic focsuing is verified with the use of microscopic visualization of water sheath flows and dye-containing sample flow

The sheath and sample flows are injected from inlets by syringe pumps. The velocity of the sample flow is fixed at 0.02 mm/s and the sheath flow velocity ranges from 0.05 mm/s–1.4 mm/s, resulting in a relative sheath and sample flow rate of 2.5–70. A stable focused sample stream could be formed while an appropriate relative sheath and sample flow rate is applied (Fig. 12). As the flow rate of the sheath flow increases, the width of the focused sample stream is reduced accordingly. Figure 13 represents the variation of the width of the sample stream along with the relative sheath and sample flow rates. It showed that the width of the center flow could be scaled to the size of a cell. For example, as the relative sheath and sample flow rate reaches 25, the width of the focused stream is about 10 μm. The width can be even scaled down to 3 μm while the relative sheath and sample flow rate reaches 70. The value is suitable for single cell sorting and counting application since the size of a red blood cell is on the same order.

It is noted that experimental data are higher than numerical results. In the present study, only two-dimensional flow is considered for numerical solvers. However, the flow inside the micro flow cytometer is truly three-dimensional in nature. It is speculated that the discrepancy comes from three-dimensional effect. Table 4 shows two cases considering 2-D and 3-D situations simulated by the same numerical solver. The width of the focused stream is higher in 3-D case (23.2 μm) than in 2-D case (7.5 μm). One possible reason is stated as follows: Since the depth of the channel is only 40 μm, the center flow cannot be constrained efficiently such that it will take longer length to achieve effective focusing. Besides, viscous forces on the upper and lower walls will also impose an adverse effect on hydrodynamic focusing. As a result, one can expect that experimental data are higher than numerical results. It also implies that micro flow cytometers with a higher aspect ratio could have better flow focusing effect.

The width of the focused stream calculated from Eq. (11) was also plotted on Fig. 13 for comparison. It is noted that experimental data are reasonably accordant with theoretical results predicted

Table 4 2D versus 3D cases in a flow cytometer

	v_1 (mm/s)	v_2 (mm/s)	d_1 (μm)	d_2 (μm)
Case1(2D)	20	2	7.8	7.5
Case2(3D)	20	2	30.8	23.2

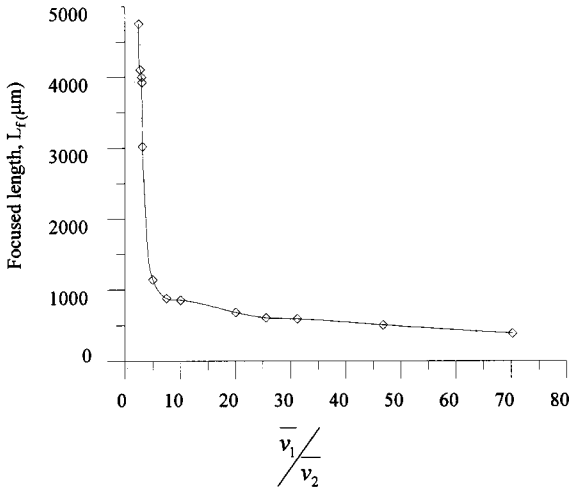

Fig. 14 The variation of the focused length along with the relative sheath and sample flow rates

by the simple model at high flow ratios. For example, the width of the focused stream is 17.2 μm and 20.8 μm for experimental and theoretical data, respectively, at a flow rate ratio of 45. It indicates that the simple model proposed by the present study is a reliable theoretical tool for predicting the performance of flow focusing inside a micromachined flow cytometer.

Similarly, using the same definition of ''focused length'' as shown in the previous section, one can obtain experimental data for focused length. Figure 14 shows the variation of the focused length along with the relative sheath and sample flow rates. As expected, larger relative sheath and sample flow rates achieves shorter focused length.

Conclusions

The working principle of the flow cytometer is the hydrodynamic focusing effect of a center flow, surrounded by two sheath flows. The width of the center cell flow will be decreased hydrodynamically such that only one cell is allowed to be located at the center region and ready for detection and sorting. In this study, the hydrodynamic focusing phenomenon is first investigated by employing potential flow theory. A theoretical model for prediction of the focused cell stream is proposed. Then the flow field inside the flow cytometer is simulated numerically. The effect of the device geometry and inlet velocities of the flow on the focusing of the center flow is explored systematically.

At last, a micromachine-based flow chamber is designed and fabricated on plastic substrates as a micro flow cytometer. Hydrodynamic focusing is verified with the use of microscopic visualization of water sheath flows and dye-containing sample flow. The width and length of the focused stream is measured. Experimental data indicate that the size of focused sample stream can be reduced to less than 10 μm, which is applicable to cell sorting and counting.

Efforts from this work will enable us to develop key technologies for the development of microfluidic chips capable of cell sorting and counting. Based on the results from the study, one will explore the possibility to apply the chips on the related fields, such as μ-TAS, clinical hematology and oncology.

Acknowledgments

Financial support from the National Science Council of the Republic of China is greatly acknowledged. We would also like to thank Dr. T. S. Leu for valuable discussions.

Nomenclature

A = area in the reservoir
a = area inside a tube
D_1 = width of the inlet channel 1 in the inlet section before focusing
D_2 = width of the inlet channel 2 in the inlet section before focusing
D_3 = width of the inlet channel 3 in the inlet section before focusing
D_a = width of the channel in the outlet section
d = width of the focused stream
d_0 = width of the focused stream measured at the exit of the inner nozzle
d_1 = width of the focused stream measured at the end of convergent part of the outer nozzle
d_2 = width of the focused stream measured at the exit of the flow cytometer
L = length of sample inlet section
L_1 = length of the sample outlet section
L_c = total length of the convergent part
L_m = length at inversion point of the convergent part
l = axial coordinate of the convergent part
p = pressure
R = radius of the tube
r = radial coordinate of the convergent part
r_1 = half width of the convergent part at starting location
r_2 = half width of the convergent part at ending location
s = distance from the inlet to the tube
V_A = velocity at point A
x = axial coordinate
$\bar{v}$ = velocity at the inlet of the tub
$\bar{v}_a$ = average velocity in the outlet section
$\bar{v}_c$ = velocity of the focused stream
$\bar{v}_1$ = velocity inside the first channel
$\bar{v}_2$ = velocity inside the second (center) channel
$\bar{v}_3$ = velcoity inside the third channel
$\dot{m}_{in}$ = mass flow rate of the inlet flow
$\dot{m}_{out}$ = mass flow rate of the outlet flow
ρ = denisty of the fluid
τ_{ij} = shear stress tensor

References

[1] Manz, A., Graber, N., and Widmer, H. M., 1990, ''Miniaturized Total Analysis Systems: A Novel Concept for Chemical Sensing,'' Sens. Actuators, **B1**, pp. 244–248.
[2] Chiem, N. C., Colyer, C., and Harrison, J. D., **1997**, ''Microfluidic Systems for Clinical Diagonstics,'' The International Conference on Solid-State Sensors and Actuators, TRANSDUCERS '97, Chicago, Vol. 1, pp. 183–186.
[3] Jed Harrison, D., and van den Berg, Albert, **1998**, *Micro Total Analysis Systems '98*, Kluwer Academic Publishers, the Netherlands.
[4] Shoji, S., and Esashi, M., 1994, ''Micro flow Devices and Systems,'' J. Micromech. Microeng., **4**, pp. 157–171.
[5] Gravesen, P., Branebjerg, J., and Lensen, O. S., 1993, ''Microfluidics—A Review,'' J. Micromech. Microeng., **3**, pp. 168–182.
[6] Melamed, M. R., Lindmo, T., and Mendelsohn, M. L. (ed), **1991**, *Flow Cytometry and Sorting*, 2nd Edition, Wiley, New York.
[7] Parks, D. R., Lanier, L. L., and Herzenberg, L. A., **1956** ''Flow Cytometry and Fluoresence Activated Cell Sorting (FACS),'' *Handbook of Experimental Immunology*, 4th Edition, Wier DM. Blackwell Scientific Publications, Oxford, Chap. 29.
[8] Miyake, R., Ohki, H., Yamazaki, I., and Yabe, R., **1991** ''A Development of Micro Sheath Flow Chambers,'' Proceedings of the IEEE Micro Electro Mechanical Systems Workshop, Nara, Japan, Jan., pp. 259–264.
[9] Sobek, D., Senturia, S. D., and Gray, M. L., **1994**, ''Microfabricated Fused Silica Flow Chambers for Flow Cytometry,'' Solid-State Sensor and Actuator Workshop, Hilton Head, South Carolina, June 13–16, pp. 260–263.
[10] Larsen, U. D., Blankenstein, G., and Branebjerg, J., 1997, ''Microchip Coulter Particle Counter,'' The International Conference on Solid-State Sensors and Actuators, TRANSDUCERS '97, Chicago, Vol. 2, pp. 1319–1322.
[11] Koch, M., Evans, A. G. R., and Brunnschweiler, A., 1999, ''Design and Fabrication of a Micromachined Coulter Counter,'' J. Micromech. Microeng., **9**, pp. 159–161.
[12] Altendorf, E., Zebert, D., Holl, M., and Yager, P., 1997, ''Differential Blood Cell Counts Obtained Using a Microchannel Based Flow Cytometer,'' Sens. Actuators, **1**, pp. 531–534.

[13] Lee, G. B., Huang, G. R., Lin, Y. H., Sung, W. C., and Chen, S. H., 2000, ''Microfabricated Plastic Chips by Hot Embossing Methods and Their Applications for DNA Separation and Detection,'' SPIE Micromachining and Microfabrication, Sept., **4177**, pp. 112–122.
[14] Chen, Y. F., 1996, ''The Evolution of Vortical Structure and Nonlinear Spectral Analysis in the Axisymmetric Jet,'' Ph.D. dissertation, Hydraulics and Ocean Department, National CHeng Kung University.
[15] Kachel, V., Fellner-Feldegg, H., and Menke, E., 1990, ''Hydrodyanmic Properties of Flow Cytometry Instruments,'' *Flow Cytometry and Sorting*, 2nd ed., Wiley-Liss, pp. 27–44.
[16] Van Doormaal, J. P., and Raithby, G. D., 1984, ''Enhancements of the SIMPLE method for predicting incompressible fluid flows,'' Numer. Heat Transfer, **7**, pp. 147–163.

Numerical Solution of Incompressible Unsteady Flows in Turbomachinery

L. He

K. Sato

School of Engineering,
University of Durham,
South Road, Durham, DH1 3LE, United Kingdom

A three-dimensional incompressible viscous flow solver of the thin-layer Navier-Stokes equations was developed for the unsteady turbomachinery flow computations. The solution algorithm for the unsteady flows combines the dual time stepping technique with the artificial compressibility approach for solving the incompressible unsteady flow governing equations. For time accurate calculations, subiterations are introduced by marching the equations in the pseudo-time to fully recover the incompressible continuity equation at each real time step, accelerated with a multi-grid technique. Computations of test cases show satisfactory agreements with corresponding theoretical and experimental results, demonstrating the validity and applicability of the present method to unsteady incompressible turbomachinery flows. [DOI: 10.1115/1.1383595]

Introduction

Computational Fluid Dynamics (CFD) techniques are very useful tools for design and analysis of complex fluid machinery. Although most of the current CFD research activities are on steady flows, there is an increasing interest in unsteady flow computations. Unsteady blade row interaction is an inherent phenomenon for all kinds of turbomachinery, due to relative motion of rotor/stator bladerows. The effects of the unsteadiness on time-averaged performance, as well as on blade forced responses, are of great interest for designs of modern turbomachinery.

As far as radial turbomachines are concerned, pronounced rotor-stator interactions are expected, since the spacing between impeller and diffuser rows is normally quite small. In centrifugal pumps and compressors, many researchers observed that a highly distorted flow was discharged from an impeller exit (Eckardt [1], Krain [2]). Also the pressure field in the frontal part of a diffuser passage may be very nonuniform. Both would result in a strong unsteady interaction between the blade rows.

There have been some experimental and numerical studies of the unsteady blade row interaction problems in centrifugal machines at a high-speed flow condition (Yamane and Nagashima [3], Filipenco et al. [4]). However most of research experiments are operated in a low speed (incompressible) flow condition (e.g., Inoue and Cumpsty [5] Ubaldi et al. [6]), because of limitation in costs and difficulties in instrumentation at high speeds. For pumps in which the working fluid is essentially incompressible, it was suggested that the amplitude of the pressure fluctuations due to the unsteady blade row interaction may have the same order of magnitude as the total pressure rise across the pump (Arndt et al. [7]). This would affect both the fluid dynamic and the structural performances, especially in relation to the minimum unsteady pressure associated cavitations. Bladerow interaction is also responsible for the noise generation in the pumping system (Akin and Rockwell [8]).

Currently, most numerical studies on unsteady turbomachinery flows are restricted in the compressible flows. It is probably because the most commonly used method for the unsteady computations is the density-based time-marching technique that is known to have severe restrictions at a low Mach number flow, due to the non-time-dependent form of the incompressible flow continuity equation. A widely used approach for steady incompressible flows is to introduce the pseudo-compressibility (Chorin [9]). This method was validated for various flow situations by many researchers (e.g., Rizzi and Eriksson [10], Farmer et al. [11]). The method was also applied to the turbomachinery flows (e.g., Walker and Dawes [12]). The advantage of the method is that it can be easily implemented in the frame of the conventional time-marching compressible flow solvers. However, this method is only applicable to steady flow computations since the modified governing equations with the pseudo-compressibility assumption lose the physical meaning until the converged solution is obtained.

The main objective of the present work is to simulate unsteady incompressible flows in turbomachinery by using a time marching based method. For time-accurate unsteady flow computations, the dual time-stepping technique (Jameson, [13]) is adopted to perform inner-iterations in order to satisfy the divergence condition of the incompressible continuity equation at each real time step. A similar approach has been adopted for 3D inviscid Euler calculations of free-surface problems by Belov et al. [14]. The focus of the present work is on a 3D unsteady thin-layer Navier-Stokes solver applicable to blade row interaction problems in low speed centrifugal compressors and pumps.

Computational Methodology

The unsteady three-dimensional incompressible thin-layer Navier-Stokes equations are adopted. The flow governing equations in absolute cylindrical coordinate system with a pseudo-compressibility has a form of,

$$\frac{\partial}{\partial \tau}\int\int\int_{\Delta v}\Theta dV+\oint\oint_{A}[Fn_x+(G-U_{\omega r})n_\theta+Hn_r]\cdot dA = \int\int\int_{\Delta V}(S_i+S_v)dV \tag{1}$$

where,

Contributed by the Fluids Engineering Division for publication in the JOURNAL OF FLUIDS ENGINEERING. Manuscript received by the Fluids Engineering Division March 23, 1999; revised manuscript received April 5, 2000. Associate Editor: V. Ghia.

$$\Theta=\begin{pmatrix} p/\beta^2 \\ \rho u \\ \rho v r \\ \rho w \end{pmatrix} F=\begin{pmatrix} \rho u \\ \rho uu+p \\ \rho uvr \\ \rho uw \end{pmatrix} G=\begin{pmatrix} \rho v \\ \rho uv \\ (\rho vv+p)r \\ \rho vw \end{pmatrix}$$

$$H=\begin{pmatrix} \rho w \\ \rho uw \\ \rho vwr \\ \rho ww+p \end{pmatrix} S_i=\begin{pmatrix} 0 \\ 0 \\ 0 \\ -(p+\rho vv)/r \end{pmatrix} \quad (2)$$

The term p/β^2 accounts for the pseudo-compressibility (Chorin [9]) introduced in the governing system. The parameter β has a dimension of velocity and determines the artificial acoustical speed. The convergence rate and stability of the method are dependent strongly upon the value of β chosen. In this solver, the value of β is kept constant through the flow field and it is determined by the formula:

$$\beta=c\sqrt{(u^2+v^2+w^2)_{\max}} \quad (3)$$

where c is the constant taken in the order of unity. It was found that *a small value of c was beneficial for fast convergence, however a value smaller than 1.0 could cause stability problems.* In the present work, *c was typically taken to be 1.2.* The pseudo-compressibility equations are integrated in the pseudo-time until the velocity divergence-free condition of the continuity equation is satisfied, where the convergence is decided by checking the error which is defined as the maximum pressure difference from the previous time step divided by the inlet dynamic head.

The effect of viscosity is taken into account in a form of source terms in S_v . They are modeled under the thin-layer assumption so that the viscous stress terms in the directions tangential to solid surfaces are included (He and Denton, [15]). The effect of the turbulent eddy viscosity is included by the Baldwin-Lomax mixing length model.

Since the governing equations with the pseudo-compressibility are marched in the pseudo-time, the transient part of the computation has no physical sense. In order to conduct unsteady flow computations, the dual-time stepping technique (Jameson [13]) was introduced and combined with the pseudo-compressibility method. In this scheme, the pseudo-compressibility method is a means to satisfy the continuity equation at every real time step, and the equations are marched in the real time by the fully implicit formulation. The complete formulation for the current time marching scheme with the second order real time derivative is:

$$\frac{\partial\Theta^{n+1}}{\partial\tilde{t}}+R^{n+1}+\frac{1}{2\Delta t}(3\tilde{\Theta}^{n+1}-4\tilde{\Theta}^{n}+\tilde{\Theta}^{n-1})=0 \quad (4)$$

where,

$$\tilde{\Theta}=\begin{pmatrix} 0 \\ \rho u \\ \rho v r \\ \rho w \end{pmatrix} \quad (5)$$

where superscript ''*n*'' denotes the real time level for the unsteady computations and *R* is the net fluxes. At a converged state, the first term with the pseudo-time derivative is driven to zero to fully satisfy the incompressible unsteady flow governing equations.

The flow equations are discretized in space in the cell-centred finite volume form and are integrated in the pseudo-time using the four-stage Runge-Kutta scheme. *Since no temporal accuracy is required for the pseudo time-marching, standard acceleration methods for steady flows can be directly applied. In the present work, a simple multi-grid technique (He [16]) is adopted, which typically enables an equivalent time-step around 50~80 times larger than that allowed by the numerical stability based on the smallest mesh spacing.* In solving the discretized governing equations, the forth-order artificial damping terms are added to avoid the oscillatory odd-even decoupling. To minimize unnecessary diffusion in the high shear region, the damping terms are scaled by the local convection speed with respect to the local eigen-value (Farmer et al., [11]).

Boundary conditions are applied at wall surfaces, inlet/exit, and circumferential boundaries. On solid surfaces, a slip condition is applied with an approximate form of the log law model (Denton, [17]). At the inlet of the computational domain, total pressure and flow angles are specified while, at the outflow boundary, static pressure is specified for the current version. Other unspecified components at the boundary are extrapolated from the interior domain. For the stage configurations with different blade numbers in each row, the number of passages will be taken to cover the same total circumferential length. At the interface between the rotating and stationary mesh frames, the flow fluxes are calculated based on the linear interpolation between two meshes, ensuring the instant information exchange across the interface.

Numerical Examples

The method has been implemented in a computer code based on a previous compressible flow solver for unsteady multi-stage turbomachinery flows (He [18,19]). A range of steady and unsteady computations were carried out for validation purposes (Sato [20]). Two unsteady flow cases are presented here.

Laminar Boundary Layer With Freestream Oscillation. An unsteady laminar boundary layer on a flat plate with a fluctuating main stream has been computed for the purpose of assessing the capability for the unsteady viscous flow computations. The laminar boundary layer is subject to a small sinusoidal fluctuation in the main stream flow, for which there is a well established semi-analytical solution (Ackerberg and Phillips [21]). For the computation, a two-dimensional mesh, which consists of the 66 × 50 points in streamwise and normal direction was used.

The grid points were arranged near the wall so that there were approximately 30 points across the boundary layer in order to resolve the boundary layer flow. The flow computations have been operated in very low speed where the mean free stream velocity of 5.6 m/s. The free-stream oscillation was realized by applying the sinusoidal exit static pressure fluctuation. The amplitude of the free-stream velocity fluctuation was taken to be very small (about 0.53 percent of the mean velocity) to ensure a linear behavior of the unsteady flow. Comparisons are made for the velocity profile and phase angle across the boundary layer in the complex form against the semi-analytical solution by Ackerberg and Phillips [21], as shown in Fig. 1. An excellent agreement is obtained.

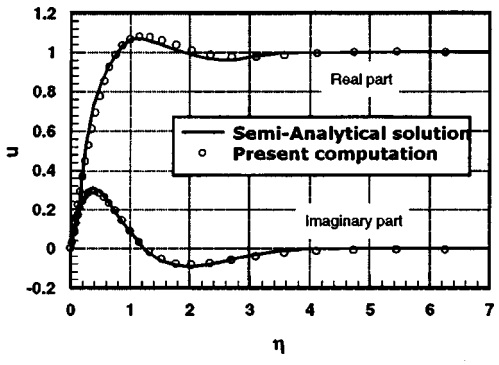

Fig. 1 Comparison of flow profile inside boundary layer in complex form

Table 1 Parameters of centrifugal pump case

Number of impeller blade	$z_i = 7$
Number of diffuser vanes	$z_d = 12$
Rotational speed	$n = 2000$ rpm
Flow rate coefficient	$\phi = 0.0475$
Total pressure rise coefficient	$\Psi = 0.65$
Reynolds number $\mathrm{Re} = U_2 L/\nu$	$\mathrm{Re} = 6.5 \times 10^5$

Centrifugal Pump Stage. An unsteady flow for a centrifugal impeller with a vaned diffuser, for which detail time-averaged and unsteady data were available (Ubaldi et al. [6]) was computed. This experimental centrifugal pump has a simplified 2-D configuration. Basic dimensions of the system and operating condition are given in the Table 1. In the experiment, instantaneous and ensemble-averaged velocity profiles were measured at the impeller outflow using the hot-wire technique. Instantaneous and ensemble averaged static pressure distribution on the shroud surface are also measured through the passage. In the present study, comparisons were made for the impeller outlet section.

In order to obtain unsteady solutions comparable to the experimental unsteady data, a numerical simulation is conducted on a computational domain including all the blade passages in the pump system. A H-type mesh (Fig. 2) that consisted of 874,000 nodal points ($50 \times 58 \times 20 \times 7$, $30 \times 65 \times 20 \times 12$ in pitchwise, streamwise, spanwise directions and the number of the passages for 1st and 2nd rows) was used. *The mesh points were clustered toward endwall and blade surfaces, with a typical ratio of 1.2 between adjacent mesh cells*. The number of real time steps in one impeller blade-passing period was 120.

The comparisons of the solutions were made at the same level of the mass flow rate, which is regulated by the careful adjustment of the exit static pressure. The final values of the time averaged flow rate coefficient and the total pressure rise coefficient measured at the exit of the computational domain were 0.048 and 0.69, respectively, in the computation.

Figure 3 shows the history of the blade forces acted on the impeller and diffuser in tangential direction. The computation was started from the solution given from a different blade count (7 impeller blades and 14 diffuser vanes) and then 14 impeller blade passing periods in total were computed. In the first 7 periods, the computation was performed with 40 inner iterations at each real time step. Then the number of the inner iterations was increased to a minimum of 50 in order to reduce the error in the real-time marching formulation. Concurrently, the maximum error was kept smaller than 0.05 percent through the computation. The total computational time required for 14 periods was approximately 390 hours on the SGI power challenge when dual-processors were used.

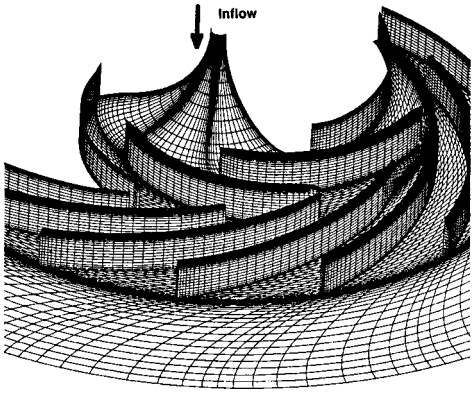

Fig. 2 Computational mesh

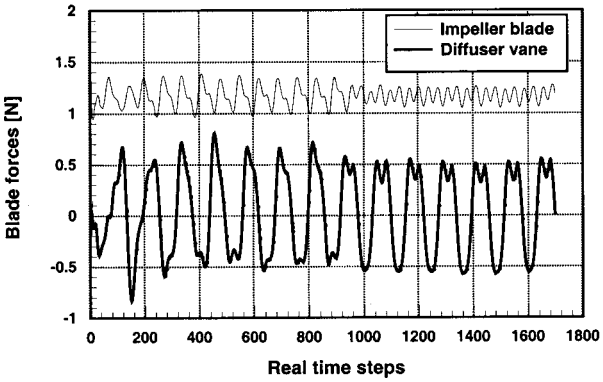

Fig. 3 Blade forces history in tangential direction

Figure 4 and Fig. 5 show the time averaged discharged flow profile at the impeller exit in the pitchwise direction at the mid-span from both the prediction and experiment. The relative locations of the impeller trailing edges are marked in the top of the figures. The computed radial velocity profile shows a qualitative agreement with the experiment. *However, the predicted velocity levels are a little less than that of the experiment. Since the same flow rate as the experiment was achieved, the computed mean radial velocity should be the same as the experimental one. Given that the radial velocity at the mid-span was underpredicted (Fig. 4), this seems to suggest that that the viscous blockage effect in*

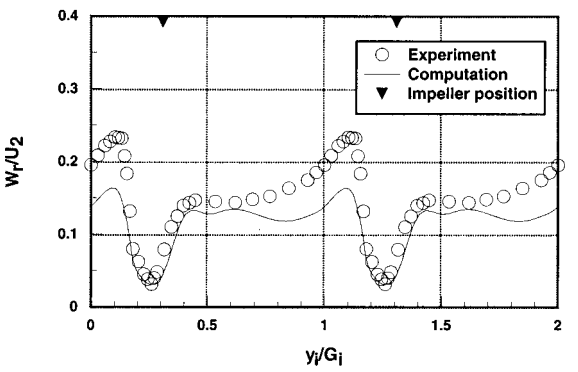

Fig. 4 Time-averaged Radial velocity profile at mid span of impeller outlet

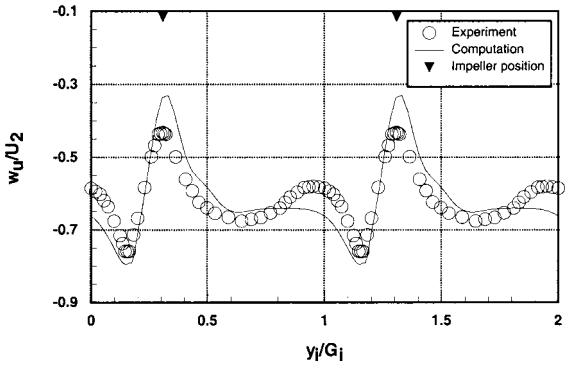

Fig. 5 Time-averaged relative tangential velocity profile at mid span of impeller outlet

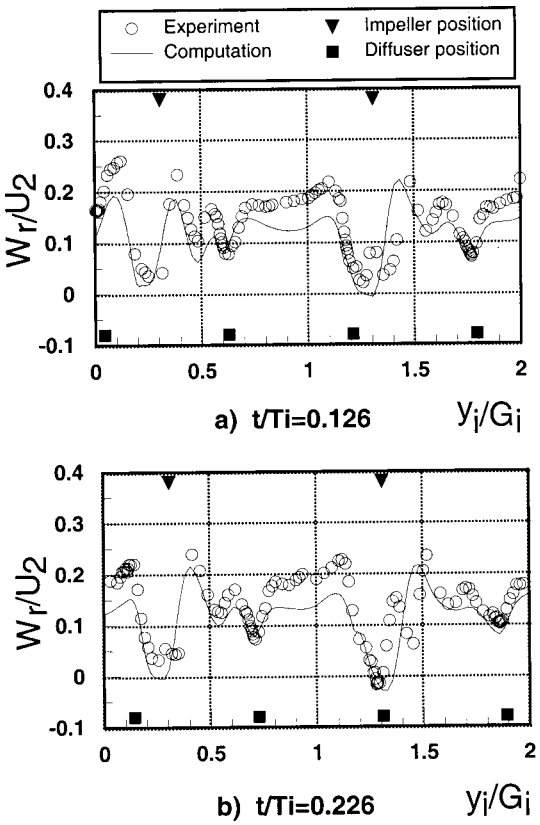

Fig. 6 Instantaneous radial velocity profile at impeller outlet, mid span

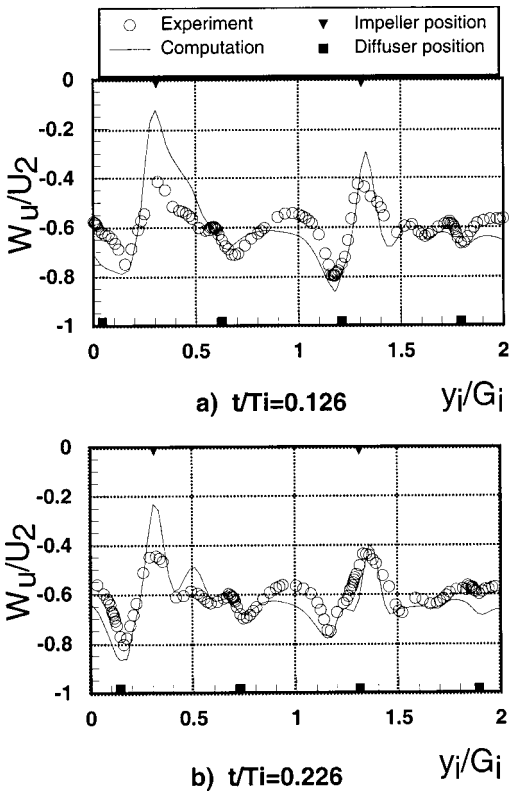

Fig. 7 Instantaneous relative tangential velocity profile at impeller outlet, mid span

the regions near end-walls be underpredicted, which might be because the viscous flow structures near the endwalls were not sufficiently well resolved with the current grids.

The comparison of the relative circumferential velocity profile shows that the computation under-predict a local low momentum fluid region near the mid-pitch toward the pressure surface ($y_i/G_i \approx 0.9$, in Fig. 5), which is observed in the experiment. Ubaldi et al. ([6]) suggested that this low momentum region is originated from the tip leakage flow. *For the computations, the tip clearance is implemented by a simple model with only one computational cell in the tip clearance region. A computation without tip clearance was also attempted. The tip-leakage flow is expected to be influential especially in the endwall region. In terms of the results of the velocity in the mid-span where the experimental data were available, the computations with and without the tip clearance did not show a marked difference.*

Figures 6 and 7 show unsteady radial and relative tangential velocity profiles at impeller outlet at certain time instant with the relative position of the impeller and diffuser vane indicated on top and bottom of the figures, respectively. The observation of the flow velocity vectors (not shown) seems to suggest that the two velocity deficits observed in the instantaneous radial velocity profiles near the diffuser vane is due to the interaction effect of the impeller blade wake and the diffuser leading edge. This effect is clearly captured in the numerical solutions. The interaction effect observed in the instantaneous relative tangential velocity profile in the computation is overestimated. The time averaged relative tangential velocity profile (Fig. 5) shows that the depth of the impeller blade wake is overestimated in the computation compared with that in the experiment. This seems to be responsible for the pronounced interaction effect in the computation. However, the computational results capture the trend of the experimental data quite well.

Sensitivity Study. A study has been performed to examine the mesh density dependency, the number of the real time steps per period and the number of the pseudo-time iterations every real time step. This study has been conducted with a modified pump configuration with 7 impeller blades and 14 diffuser vanes for the purpose of reducing the computational cost. For this case, only 1 impeller passage and 2 diffuser passages were used. The numerical test has been conducted by varying the parameters individually to examine those effects on the solutions. Due to the different diffuser vane number, the comparison of instantaneous experimental data that is defined in terms of the relative locations between the rotor and stator is no longer possible. As a result, the results presented here are only in the time averaged sense.

Mesh Density Dependency. Three meshes with different grid points in different directions were used:

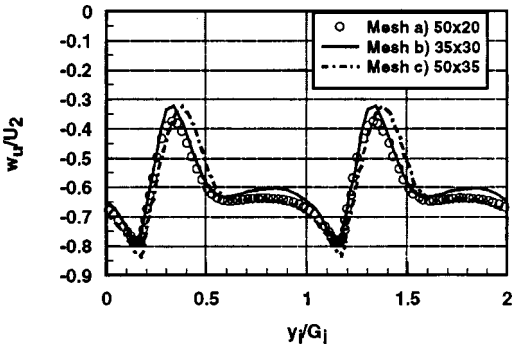

Fig. 8 Comparison of relative tangential velocities with different mesh densities

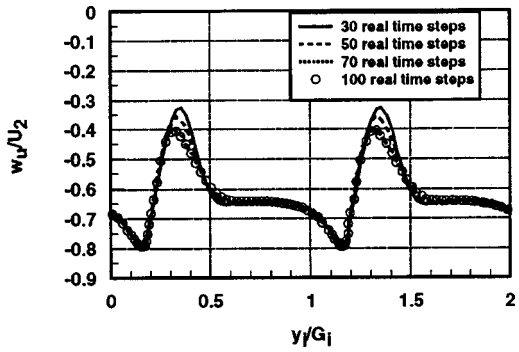

Fig. 9 Comparison of relative tangential velocities with different numbers of real time steps/period

Mesh (a): $50 \times 58 \times 20 \times 1+30 \times 65 \times 20 \times 2$
Mesh (b): $35 \times 58 \times 30 \times 1+26 \times 65 \times 30 \times 2$
Mesh (c): $50 \times 58 \times 35 \times 1+30 \times 65 \times 35 \times 2$

Figure 8 shows the time-averaged relative tangential velocity distributions obtained from the computations using these meshes. Slight difference is observed in the results partly because of the different flow level for those cases (flow rate coefficients: 0.0478, 0.0458, 0.0455 for mesh a, b, c, respectively). Overall the results agree with each other well and do not show significant mesh dependence. In the following studies, the computations have been conducted using the mesh type a).

Number of Real Time Steps Per Period. Different numbers of real time steps per period (30, 50, 70, and 100) were used in the computations and the results were compared (Fig. 9 and Fig. 10). The number of the pseudo-time iterations was fixed to 40 at each real time step where the maximum errors of less than 0.1 percent were obtained for all these computations. With an increased number of real time steps, the computations begin to capture the higher harmonic components, as a result of an improved time-wise resolution. The results show some slight difference in the time averaged solutions (Fig. 9) and suggest that, for this centrifugal pump stage, at least 70 real time steps per period is required to capture the effect of higher order unsteadiness. This is also confirmed by the comparison of the stator-generated unsteadiness (Fig. 10), showing that the calculations converge to a time-step independent solution with the real time steps of 70 or more per period. On the other hand, for the simple laminar boundary layer with a freestream fluctuation, where higher order harmonic unsteadiness is negligible, numerical tests showed that unsteady velocity profiles could be captured perfectly well with the real time steps as few as 10 in one period. This contrast suggests that the higher order harmonic component must be captured in order to obtain a reasonable ensemble averaged solution.

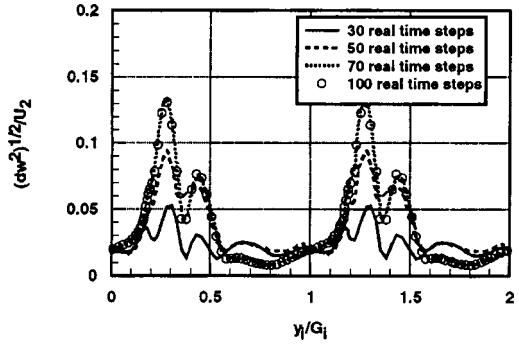

Fig. 10 Comparison of stator-generated unsteadiness with different number of real time steps/period

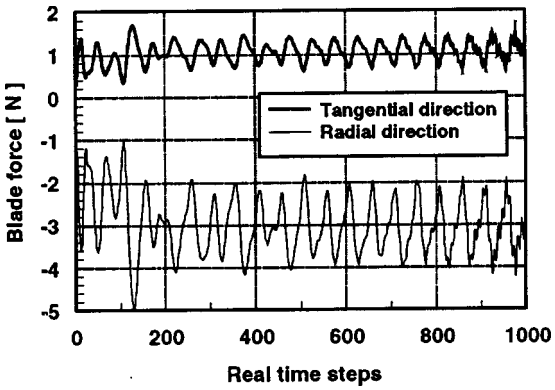

Fig. 11 Blade force histories with relatively smaller number of pseudo-time iterations

Number of Pseudo-Time Iterations. The number of the pseudo-time iterations at each real time-step was found to affect both accuracy and convergence. Generally, the number of the pseudo-time iterations needs to be increased with an increase in mesh density or a decrease in number of real-time steps per period.

In unsteady flow calculations, we would usually use the periodicity of flow variables as an indication of convergence. One needs to recognize that the inviscid part of the flow would converge at a very different rate compared to that of the near wall viscous flow region, because of different speeds of information propagation. A sufficient number of the pseudo-time iteration has to be performed so that the viscous as well as the inviscid parts of the flow field are fully converged at each real-time step. It was found that if the number of the subiterations at each real-time step was not sufficient, the accumulation of errors could lead a stability problem. Figure 11 shows an example of such a case. In this viscous flow computation, 20 pseudo-time iterations were performed at each real-time step. The time history of the blade force indicated a periodic behavior for a while before an oscillatory pattern started to grow. The solution eventually became divergent. For the same case, a converged solution was obtained if the number of the pseudo-time iterations was increased to 30 or more.

Through the numerical tests, it was found that for a typical unsteady case with 50 or more real-time steps per period, the inviscid solutions with relatively coarse meshes could be adequately obtained with about 20 pseudo-time iterations per each real step. The number needs to be increased up to 30 to 50 for the viscous computations with finer meshes (~100,000 per passage or more). As shown in Fig. 12 for a viscous computation with 50 real time steps per period, 30 pseudo-time iterations per each real time step seem to be sufficient. However, for computations with much finer meshes (e.g., the unsteady boundary layer computations in

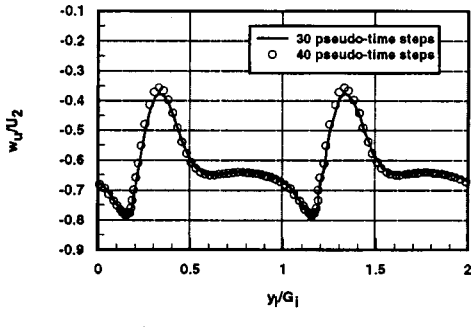

Fig. 12 Comparison of relative tangential velocity with different pseudo-time iteration numbers

which nearly 30 grid points were allocated inside the boundary layer), 100 or more pseudo-time iterations may be required at each real time step to achieve an adequately converged solution.

The results of these sensitivity studies provide useful guidance for large scale practical computational applications.

Concluding Remarks

A three dimensional incompressible thin-layer Navier-Stokes method has been developed for multi-stage unsteady turbomachinery flow calculations. The method is based on a combination between the pseudo-compressibility and the dual-time stepping technique.

Calculations were carried out for unsteady incompressible flow cases, and the results show satisfactory agreement with well-established theoretical and experimental data. Sensitivity of the solution to various numerical variables was assessed for a centrifugal pump stage. The effects of the mesh density, the number of the pseudo-time iterations and the real time step length were examined.

Nomenclature

C_p = static pressure coefficient
D = pump diameter
k = reduced frequency ($k=\omega x/U$)
G_i = impeller tangential pitch
t = real time
$\tilde{t}$ = pseudo time
T_i = impeller blade passing period
U_2 = peripheral velocity at impeller trailing edge
w = relative velocity
η = similarity variable ($\eta=y\sqrt{\rho U/\mu x}$)
ϕ = flow rate coefficient ($\phi=4Q/(U_2\pi D_2^2)$)
ψ = pressure rise coefficient ($\Psi=2(P_{t4}-P_{t0})/(\rho U_2^2)$)

Subscript

0 = at the inlet
r = in radial direction
t = stagnation parameter
u = in tangential direction

References

[1] Eckardt, D., 1976, ''Detailed Flow Investigations Within a High-Speed Centrifugal Compressor Impeller,'' ASME J. Fluids Eng., **88**, pp. 390–402.
[2] Krain, H., 1988, ''Swirling Impeller Flow,'' ASME J. Turbomach., **110**, pp. 122–128.
[3] Yamane, T., and Nagashima, T., 1997, ''High Speed Centrifugal Impeller and Diffuser Interaction near Stall Conditions,'' Proceedings of the 8th International Symposium, Stockholm, Sweden.
[4] Filipenco, V. G., Deniz, S., Johnston, J. M., Greitzer, E. M., and Cumpsty, N. A., 1998, ''Effects of Inlet Flow Field Conditions on the Performance of Centrifugal Compressor Diffusers Part 1: Discrete-Passage Diffuser,'' ASME Paper No. 98-GT-473.
[5] Inoue, M., Cumpsty, N. A., 1984, ''Experimental Study of Centrifugal Impeller Discharge Flow in Vaneless and Vaned Diffusers,'' ASME J. Eng. Gas Turbines Power, **106**, pp. 455–467.
[6] Ubaldi, M., Zunino, P., Barigozzi, G., and Cattanei, A., 1996, ''An experimental Investigation of Stator Induced Unsteadiness on Centrifugal Impeller Outflow,'' ASME J. Turbomach., **118**, pp. 41–54.
[7] Arndt, N., Acosta, A. J., Brennen, C. E., and Caughey, T. K., 1990, ''Experimental Investigation of Rotor-Stator Interaction in a Centrifugal Pump with Several Vaned Diffusers,'' ASME J. Turbomach., **112**, pp. 98–108.
[8] Akin, O., and Rockwell, D., 1994, ''Actively Controlled Radial Flow Pumping System: Manipulation of Spectral Content of Wakes and Wake-Blade Interactions,'' ASME J. Fluids Eng., **116**, pp. 528–537.
[9] Chorin, A. J., 1967, ''A Numerical Method for Solving Incompressible Viscous Flow Problems,'' J. of Computational Physics, **2**, pp. 12–26.
[10] Rizzi, A., and Eriksson, L. F., 1985, ''Computation of Inviscid Incompressible Flow with Rotation,'' J. Fluid Mech., **153**, pp. 275–312.
[11] Farmer, J., Martinelli, L., and Jameson, A., 1994, ''Fast Multigrid Method for Solving Incompressible Hydrodynamic Problems with Free Surfaces,'' AIAA J., **32**, 1175–1182.
[12] Walker, P. J., and Dawes, W. N., 1990, ''The extension and Application of Three-Dimensional Time-Marching Analyses to Incompressible Turbomachienry Flows,'' ASME J. Turbomach., **112**, pp. 385–390.
[13] Jameson, A., 1991, ''Time Dependent Calculations Using Multigrid, with Applications to Unsteady Flows Past Airfoils and Wings,'' AIAA Paper No. 91-1596.
[14] Belov, A., Martinelli, L., and Jameson, A., 1994, ''A Novel Fully Implicit Multigrid Driven Algorithm for Unsteady Incompressible Flow Calculations,'' Proceedings, Second European CFD Conference ECCOMAS 94.
[15] He, L., and Denton, J. D., 1994, ''Three-Dimensional Time-Marching Inviscid and Viscous Solutions for Unsteady Flows around Vibrating Blades,'' ASME J. Turbomach., **116**, pp. 469–476.
[16] He, L., 1996, ''II. Time-Marching Computations of Unsteady Flows, Bladerow Interaction and Flutte'' in Unsteady Flows in Turbomachinery, VKI Lecture Series 1996-05, von Karman Inst., Belgium, Mar.
[17] Denton, J. D., 1992, ''The Calculation of Three Dimensional Viscous Flow Through Multistage Trubomachines,'' ASME J. Turbomach., **114**, pp. 18–26.
[18] He, L., 1996, ''TF3D, a Program to Calculate Turbomachinery Flow in 3-Dimensions (User's Guide, version 1),'' University of Durham, UK.
[19] He, L., 2000, ''Three-Dimensional Unsteady Navier-Stokes Analysis of Stator-Rotor Interaction in Axial-Flow Turbines,'' IMechE Journal of Power and Energy **214**, Part A pp. 13–22.
[20] Sato, K., 1999, ''Blade Row Interaction in Radial Turbomachines,'' Ph.D. thesis, University of Durham, Oct.
[21] Ackerberg, R. C., and Phillips, J. H., 1972, ''The Unsteady Laminar Boundary Layer on a Semi-Infinite Flat Plate due to Small Fluctuations in the Magnitude of the Free-Stream Velocity,'' J. Fluid Mech., **51**, pp. 137–157.

H. Michallet[1]
C. Mathis
P. Maïssa
F. Dias[2]

Institut Non-Linéaire de Nice,
UMR 6618 - CNRS and UNSA,
1361, route des Lucioles, 06560 Valbonne,
France

Flow Filling a Curved Pipe

A small scale experiment was designed to study the propagation of the front of a viscous fluid filling a curved pipe. Several Newtonian fluids with different viscosities and a non-Newtonian fluid have been used. The experiments show that there exists a minimum speed for completely filling the pipe, which depends on the parameters of the experiment (diameter d and radius of curvature R of the pipe, kinematic viscosity ν of the fluid). Appropriate dimensionless numbers are introduced to characterize the flow and optimal filling conditions. [DOI: 10.1115/1.1374442]

Introduction

Prestressed concrete is commonly used in construction. To prevent the prestressed strands from any corrosion, a cement solution is generally injected in pipes of complex geometry. The pipe has to be completely filled in order to avoid weak zones in the structure. The aim of the present study is to observe experimentally the propagation of the front of a viscous fluid injected in a curved pipe, in order to understand the reasons for the appearance of unfilled zones. The solution used in construction is composed of cement, water, liquefier, and retarder. It is a non-Newtonian fluid with air bubbles and particles in suspension. As a first step, we mainly focus in this paper on the filling by Newtonian fluids.

Permanent flows in pipes have been widely studied [1], particularly in the case of curved pipes [2–4] and in engineering applications [5,6]. However, pipe flows involving a propagating front or interface remain poorly understood. The problem of an air-water interface propagating in straight inclined pipes has been addressed only recently [7,8]. As stated above, in industrial applications such as construction, the fluid is often mixed with air bubbles and the flow ought to be treated as a slug flow (see for example [9,10] for recent work on slug flows in pipes). But the emphasis of the present work is in the propagation of the interface which clearly separates the gas from the liquid.

The front propagation of a perfect fluid in a horizontal pipe was studied by Benjamin [11]. See also the review by Simpson [12] on gravity currents for related studies and Asavenant and Vanden-Broeck [13]. Benjamin analyzed the front in terms of a ''cavity flow'' displacing a fluid beneath it. The two-dimensional geometry is shown in Fig. 1(*a*) (Benjamin also considered the case of a circular cross-section). Note that Benjamin studied only the case where the free surface detaches with an angle of 60 degrees. By applying conservation of mass, momentum, and energy, he found that there is a unique solution, characterized by

$$\frac{U}{\sqrt{gd}}=\frac{1}{2},\quad \frac{u}{\sqrt{gh}}=\sqrt{2},\quad \frac{h}{d}=\frac{1}{2},$$

where the meaning of the various symbols is shown in Fig. 1. In other words, the cavity fills half of the box. An experiment was suggested by Benjamin to realize closely this flow. Liquid initially fills a long rectangular box closed at both ends and fixed horizontally. One end is then opened, and under the action of gravity the liquid flows out freely from this end. It can be expected that, after the transient effects of starting have disappeared, the air-filled cavity replacing the volume of the ejected fluid will progress steadily along the box. Observed in a frame of reference travelling with the front of the cavity, the motion of the liquid will appear to be steady, as shown in Fig. 1(*a*). If the effects of viscosity and surface tension are neglected, the velocity of the cavity relative to a stationary observer will be U, and, since $h=d/2$, the liquid will discharge from the open end with the same velocity. In addition to the solution studied by Benjamin, there is also a one-parameter family of solutions in which the free surface detaches from the box tangentially [14]. Such a solution is plotted in Fig. 1(*b*). At the exit of the box, the Froude number $u(gh)^{-1/2}$ for these solutions is between 1 and $\sqrt{2}$. The limit $\sqrt{2}$ corresponds to Benjamin's solution, while the limit 1 corresponds to the vanishing of the cavity. Using conservation of mass, momentum and energy, one finds the relation

$$\frac{u}{\sqrt{gh}}=\sqrt{\frac{d}{h}}. \tag{1}$$

Unfortunately, simple arguments based on conservation of mass, momentum and energy do not give as much information in the case of a curved channel.

It is nevertheless important to keep in mind that the Froude number prevails to determine the size of the cavity and thus the ability to fill the pipe. This point will be discussed in the section where we consider various dimensionless numbers. Before that, we first describe the manner in which the experiments have been conducted. Then we present and discuss the experimental results.

Experimental Setup

The experimental setup is shown in Fig. 2. Gravity acts downwards. A transparent PVC pipe (''Tubclair'') of inner diameter d is curved with a radius R. Different diameters and radii were considered: $0.6\leqslant d\leqslant 2$ cm; $5\leqslant R\leqslant 30$ cm. The special case of a horizontal straight pipe was also investigated. The fluid was injected with a centrifugal pump at a constant mean flow velocity (noted U).

Several fluids were considered in order to investigate the effects of density ρ, surface tension σ, and mainly kinematic viscosity ν (see Table 1). A series of runs has been performed with a non-Newtonian fluid (gel). Its viscosity has been measured with a plane-plane viscosimeter (see Fig. 3).

We assume that capillary effects are negligible, so that $d\gg L_c$ where $L_c=\sigma^{1/2}(\rho g)^{-1/2}$ is the capillary length ($\sigma=73$ gs^{-2} for water and $\sigma=21$ gs^{-2} for silicone). In the case of water $L_c=0.26$ cm and this assumption might be a shortcoming for small diameters. We nevertheless performed a few runs with water contaminated with wetting agents in order to diminish L_c: the behavior and the results were the same within measurements errors. Moreover, the results presented in this paper are limited to $d\geqslant 1$ cm.

[1]Permanent address: Laboratoire des Ecoulements Géophysiques et Industriels (UJF-INPG-CNRS), BP53, 38041 Grenoble Cedex 9, Fax: +33 4 76 82 52 71; E-mail: herve.michallet@hmg.inpg.fr.

[2]Corresponding author, present address: Ecole Normale Supérieure de Cachan - CNRS, CMLA UMR8536, 61 avenue du Président Wilson, 94235 Cachan Cedex; E-mail: dias@cmla.ens-cachan.fr.

Contributed by the Fluids Engineering Division for publication in the JOURNAL OF FLUIDS ENGINEERING. Manuscript received by the Fluids Engineering Division August 4, 1999; revised manuscript received February 28, 2001. Associate Editor: P. E. Raad.

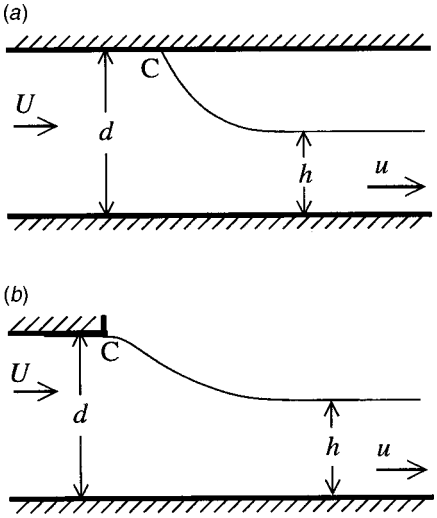

Fig. 1 Steady two-dimensional flow past a cavity. (*a*) Solution with the free surface leaving the wall with a 60 degree angle. (*b*) Solution with the free surface leaving the wall tangentially. The point C denotes the detachment point.

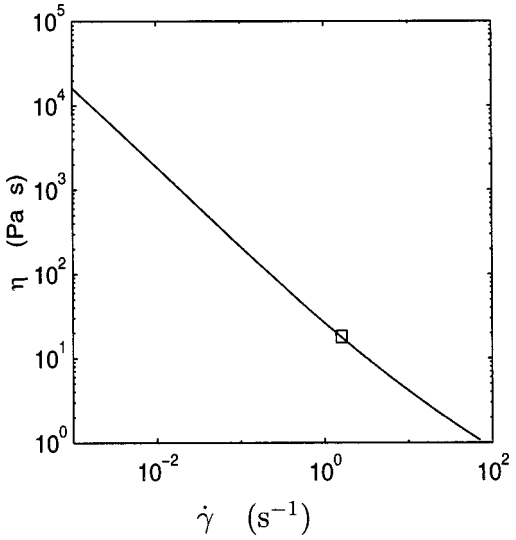

Fig. 3 Dynamic viscosity η of the gel versus the shear stress $\dot{\gamma}$. Its density is $\rho = 1.03$ g/cm^3. We note that this fluid is very viscous in the conditions of our experiments (we can estimate roughly that $\dot{\gamma} \sim 2U/d$ is less than 10 s^{-1}). Measurements have been performed with a plane-plane viscosimeter at Ecole des Mines de Paris (CEMEF, Sophia Antipolis).

Observations

For a very low flow rate (a typical mean flow velocity is $U \sim 0.1$ cm/s) and a sufficiently large pipe section (so that $d \gg L_c$) the interface is more or less horizontal in the upflow part of the pipe. The flow is dominated by gravity. In the downflow part of the pipe the liquid is creeping down the pipe.

If U is slightly increased, the interface becomes more or less perpendicular to the pipe when rising. At the top, the interface deforms as shown in Fig. 2. The intersection between the interface and the upper part of the pipe (point C in Fig. 2) is a stagnation point.

If U is increased, the point C moves (interface in dotted line in Fig. 2). As soon as U is decreased back to zero, the pipe is emptying and the interface moves back to the top.

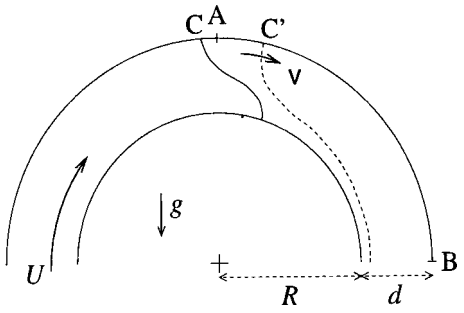

Fig. 2 Diagram of the flow and notation. The interface is shown at two different times in solid and dotted lines.

Table 1 Fluids used in the experiments.

Fluid	Density ρ (g/cm^3)	Viscosity ν (cm^2/s)	Symbol $R=5$ cm	$R=30$ cm	$R=\infty$
Water	1	0.01	●	○	⊙
Water (40 %) + glycerol (60 %)	1.16	0.086	▼	▽	▽
Silicone V50	1	0.5	▶	▷	
Silicone V100	1	1		△	
Silicone V300	1	3		◁	
Gel	1.03	(See Fig. 3)		□	

We consider that the pipe is completely filled when the point C has reached the point B (Fig. 2). We define U_c as the critical speed beyond which the interface moves until the pipe is completely filled. The speed v is the mean velocity of the point C moving from A to B (Fig. 2): if U is larger than U_c, then v is greater than zero.

For the special case of the non-Newtonian fluid gel, the viscosity is smaller where the shear stress is larger, that is near the boundaries. Away from the boundaries, the behavior of the fluid is similar to a solid core pushed by the flow. In other words, the characteristic time of deformation of the interface is very long.

Measurements

The mean flow velocity U was obtained by measuring the flow rate in the steady-state regime, i.e., when the pipe was completely filled. The flow rate and v were estimated by measuring the filling time of a graded beaker and the travelling time of point C from A to B (Fig. 2) with a stopwatch. We may consider that these simple techniques do not lead to any bias error. By repeating the same run (at least five times) for different flow rates, we have estimated that the precision limit and thus the uncertainty was always better than 10 percent on U and v.

We measured v as a function of U for different experiments using various fluids, pipes, and curvatures (see Table 1). In Fig. 4, v is plotted versus U for several runs in four different configurations. The line $v = U$ delimits the region where physical solutions exist: v cannot be larger than U. In all our experiments v apparently varies linearly with U. We may thus determine the critical velocity U_c (for $v = 0$), the slope $\alpha = dv/dU$ and the interfacial velocity $v(U=0)$, by rms fitting a straight line into the data for each fluid, pipe diameter and radius of curvature.

Let us first consider the slope α of the four straight lines in Fig. 4. The analysis presented in the Introduction considered a perfect fluid. It was assumed that the flow is identical in a reference frame moving with the front. In this framework, the filling of a pipe is similar to the emptying of the pipe. This would imply that α is equal to one: adding δU to the mean entrance flow velocity would add the same value to the front propagation velocity. It is therefore not surprising that the slopes of the straight lines in Fig. 4 related to water are close to one. When the fluid is far from perfect

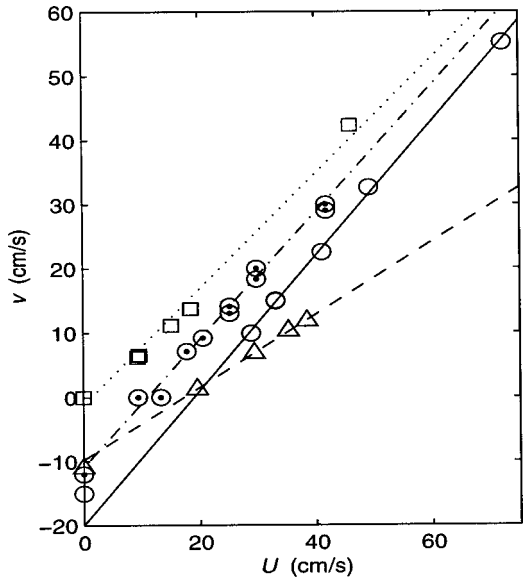

Fig. 4 Speed of the front propagation v versus the mean entrance velocity U (d=1.5 cm; see list of symbols in Table 1). The straight lines are fitted curves by quadratic means.

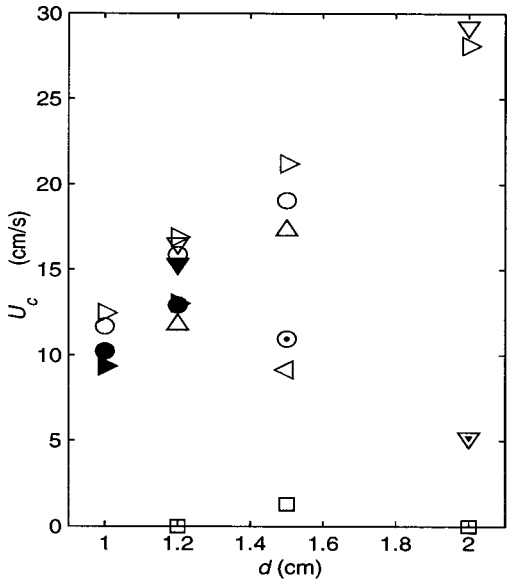

Fig. 5 Critical speed versus the pipe diameter (see list of symbols in Table 1)

but still Newtonian (case of the silicone oil V100 in Fig. 4), α is clearly smaller than one: when the viscosity is large, the deformation of the front strongly depends on U. For a low viscosity, the deformation of the interface takes place on a very short time scale and the propagation of the front apparently does not depend on the reference frame. In the other limit, that is for a very large viscosity, the deformation of the front takes place on a very long time scale and the slope is again close to one (this is the case of the non-Newtonian fluid).

The velocity $v(0)$ corresponds to the draining of the pipe. The measurements have been performed by bringing U to zero after filling the pipe: the flow is then from right to left in Fig. 2. It is important to emphasize that $v(0)$ is very small in the case of the non-Newtonian fluid. We have estimated that the draining velocity is about 1 cm per week. The deformation of the front is visible only when the fluid is sheared and U_c is therefore also close to zero for the gel. The agreement in $v(0)$ between the measured values and the values deduced from the fitted straight lines in Fig. 4 is rather good except in the case of water for $R=30$ cm. The discrepancy is probably due to measurement errors but also to wetting effects. The contact between the fluid and the PVC is indeed not the same when filling or emptying the pipe. It was not our purpose to investigate wetting effects and we did not test other materials for the pipe. We therefore have to consider that wetting effects may induce a bias error over U_c of about 10 percent in the worst case, i.e., an uncertainty of 20 percent in the water case.

The critical speed U_c (mean entrance velocity for which $v=0$) is plotted against the pipe diameter d in Fig. 5. U_c clearly tends to increase with d. Considering gravitational effects, the larger is d, the more efficient are gravity effects to deform the interface. It is thus not surprising that inertial effects have to be increased to compensate for it. Gravity effects could also reasonably depend on the radius of curvature. The interface deforms more rapidly when the pipe is curved: for a same diameter, U_c is therefore smaller when $R=\infty$. Otherwise, if R is large but not infinite, the travelling time of the front in the pipe is large and the mean entrance velocity has to be large for the front to propagate. In other words, for a very small radius, the front has not enough time to deform before the exit of the pipe. This would explain the fact that U_c is larger for $R=30$ cm than for $R=5$ cm.

In addition, above $\nu=1$ cm^2/s, viscous effects tend to maintain the shape of the interface and thus decrease U_c. This is noticeable for the silicone V100 and clearly visible for the silicone V300. Again the case of the gel requires specific comments. U_c is very close to zero because the front deforms only when the fluid is sheared as mentioned above. The graphical estimation of U_c gives a nonzero value only for $d=1.5$ cm. This configuration will allow us to estimate dimensionless numbers for the gel in the next section.

The data in Figs 4 and 5 are available in tabular form in Table 2.

Interpretation in Terms of Dimensionless Numbers

We may consider various dimensionless numbers that could characterize the flow in our special configuration. Note that in our experiments both the Bond number ($\mathrm{Bo}=d^2\rho g/\sigma$) and the Weber number ($\mathrm{We}=\rho d U^2/\sigma$) are very large: capillary effects are a lot weaker than inertial and gravitational effects.

Considering inertial and viscous effects in the framework of a curved pipe, we introduce a modified Reynolds number Re, which partly takes into account centrifugal effects, and is in fact the classical Reynolds number plus the Dean number [15]:

$$\mathrm{Re}=\frac{Ud}{\nu}\left(1+\sqrt{\frac{d}{R}}\right). \tag{2}$$

To balance inertial and gravity effects, we build a modified Froude number Fr, such as:

$$\mathrm{Fr}=\frac{U}{\sqrt{gd}}\left(1+\sqrt{\frac{d}{R}}\right). \tag{3}$$

The modification of the classical dimensionless numbers may be understood by considering that there is a need to add centrifugal effects to maintain the fluid against the concave side of the pipe. Note that (2) and (3) tend toward the classical Reynolds and Froude numbers in the limiting case of a straight pipe, i.e., when R tends toward infinity.

Let us finally define K, which measures the balance between gravity and viscosity:

$$K=\frac{\mathrm{Fr}}{\mathrm{Re}}=\frac{\nu}{\sqrt{gd^3}}. \tag{4}$$

Table 2 Measured values

Fluid	Radius of curvature R (cm)	Pipe diameter d (cm)	Speed of front v (cm/s)	Mean entrance velocity U (cm/s)
▶ Silicone V50	5	1.0	−8.6	0.0
-	5	1.0	0.6	10.2
-	5	1.0	3.2	14.1
-	5	1.0	11.8	28.7
-	5	1.0	18.9	36.6
-	5	1.2	−10.7	0.0
-	5	1.2	4.4	19.8
-	5	1.2	6.7	22.8
-	5	1.2	12.2	31.4
▷ -	30	1.0	−8.8	0.0
-	30	1.0	1.0	13.0
-	30	1.0	4.9	18.9
-	30	1.0	8.9	23.6
-	30	1.0	19.5	35.6
-	30	1.0	22.1	38.4
-	30	1.2	−10.8	0.0
-	30	1.2	1.4	19.1
-	30	1.2	4.5	24.0
-	30	1.2	8.9	31.0
-	30	1.2	16.9	43.6
-	30	1.5	−13.6	0.0
-	30	1.5	2.2	24.2
-	30	1.5	7.3	34.2
-	30	1.5	16.4	49.2
-	30	1.5	22.5	57.0
-	30	2.0	−18.0	0.0
-	30	2.0	2.0	34.6
-	30	2.0	3.4	38.4
-	30	2.0	4.8	41.6
-	30	2.0	6.4	46.3
-	30	2.0	11.2	62.4
Δ silcone V100	30	1.2	−8.5	0.0
-	30	1.2	2.3	14.7
-	30	1.2	2.3	14.7
-	30	1.2	3.9	17.1
-	30	1.2	5.0	18.0
-	30	1.5	−11.0	0.0
-	30	1.5	1.3	19.6
-	30	1.5	6.8	29.4
-	30	1.5	10.3	35.3
-	30	1.5	11.8	38.5
◁ Silicone V300	30	1.5	−6.2	0.0
-	30	1.5	0.9	10.5
● water	5	1.0	−9.5	0.0
-	5	1.0	3.0	12.4
-	5	1.0	7.2	15.5
-	5	1.0	10.8	18.1
-	5	1.2	−10.3	0.0
-	5	1.2	0.7	13.7
-	5	1.2	1.4	14.0
-	5	1.2	7.0	19.1
-	5	1.5	−11.9	0.0
○ -	30	1.0	−9.8	0.0
-	30	1.0	3.2	14.8
-	30	1.0	9.6	19.4
-	30	1.0	13.5	23.1
-	30	1.0	41.3	47.1
-	30	1.2	−12.0	0.0
-	0	1.2	0.5	16.9
-	30	1.2	4.6	19.5
-	30	1.2	5.6	22.5
-	30	1.2	9.2	23.2
-	30	1.2	14.1	29.0
-	30	1.2	28.0	42.3
-	30	1.2	28.8	44.9
-	30	1.2	52.7	66.6
-	30	1.5	−15.0	0.0
-	30	1.5	9.9	28.9
-	30	1.5	15.0	33.1
-	30	1.5	14.9	33.1
-	30	1.5	22.5	41.1
-	30	1.5	32.6	49.2
-	30	1.5	55.2	72.2
⊙ -	∞	1.5	−12.0	0.0
-	∞	1.5	0.0	9.4
-	∞	1.5	0.0	13.3
-	∞	1.5	7.1	17.8
-	∞	1.5	9.2	20.6
-	∞	1.5	13.0	25.2

Table 2 (Continued)

Fluid	Radius of curvature R (cm)	Pipe diameter d (cm)	Speed of front v (cm/s)	Mean entrance velocity U (cm/s)
-	∞	1.5	14.1	25.2
-	∞	1.5	18.3	29.8
-	∞	1.5	20.0	29.8
-	∞	1.5	29.0	41.8
-	∞	1.5	30.0	41.8
▼ water (40%) + glyc. (60%)	5	1.2	1.6	16.7
-	5	1.2	4.8	20.2
-	5	1.2	12.6	27.5
▽ -	30	1.2	6.1	26.7
-	30	1.2	15.0	38.8
-	30	1.2	14.9	38.8
-	30	1.2	29.5	63.2
-	30	1.2	51.6	95.7
	30	2.0	5.7	39.3
-	30	2.0	3.3	42.4
-	30	2.0	10.2	56.8
-	30	2.0	15.2	64.2
-	∞	2.0	0.0	6.9
▽	∞	2.0	0.0	8.2
-	∞	2.0	16.4	24.8
-	∞	2.0	22.7	32.1
-	∞	2.0	34.9	47.1
-	∞	2.0	45.3	69.2
-	∞	2.0	57.0	80.4
□ gel	30	1.2	0.0	0.0
-	30	1.2	1.8	2.0
-	30	1.2	20.3	23.1
-	30	1.2	22.3	27.8
-	30	1.5	0.0	0.0
-	30	1.5	6.2	9.3
-	30	1.5	6.5	9.6
-	30	1.5	11.1	15.1
-	30	1.5	13.7	18.5
-	30	1.5	42.3	46.0
-	30	2.0	0.0	0.0
-	30	2.0	38.7	49.6
-	30	2.0	35.9	53.6
-	30	2.0	31.0	55.6
-	30	2.0	44.1	64.0
-	30	2.0	55.9	88.9

Note that K does not depend on the mean flow velocity U. Re and Fr are computed for $U=U_c$ and plotted against K in Figs. 6 and 7.

We may consider two kinds of estimation of the dimensionless numbers for the gel. First we may use the graphical estimation of U_c from Fig. 4 for $d=1.5$ cm: $U_c \sim 1.2$ cm/s, leading to $\nu \sim 200$ cm^2/s from Fig. 3 (assuming that $\dot{\gamma} \sim 2U_c/d$). This allows us to plot the squares in Figs. 6 and 7. Second, we may estimate from our measurement that $U_c \sim v(0)$ is nonzero but very small (six orders of magnitude less than the other values of velocity). In that case, the squares would be far off the bottom right-hand corners of Figs. 6 and 7. In any case, the gel is possibly following the trend of Newtonian fluids with very large viscosity.

In Fig. 6, the data can be separated into two regions corresponding to partially (below the data) and completely (above the data) filled pipes. In a situation where the flow is characterized by a point belonging to the border line between the two regions, the filling would be effective over an infinite time, using an infinite amount of fluid. In the frame of a linear approximation, the data follow approximatively the (-1) slope, showing that Fr$(U=U_c)$ is constant from Eq. (4).

Another way to represent the same results is given in Fig. 7. One sees that Fr is of the same order of magnitude for all experiments while K varies over four orders of magnitude, but Fr is not rigorously constant. In the range of diameters we investigated, we can say roughly that Fr characterizes the ability to fill the pipes

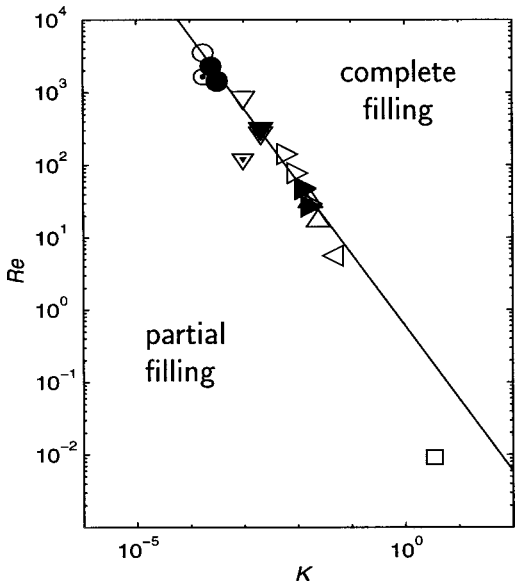

Fig. 6 Modified Reynolds number (2) computed for $U=U_c$ versus K (4) (see list of symbols in Table 1.)

(Fr=1 corresponds to the theoretical limit (1) where the flow detaches tangentially at the exit of a horizontal box, as suggested above in the introduction). Setting a flow rate leading to Fr$\geqslant$1 would certainly fill any straight pipe.

A careful examination of Fig. 7 leads to several remarks. For Newtonian fluids, the dotted symbols, which correspond to straight pipes, lie below the points corresponding to curved pipes. The latter are gathered with no obvious dependence on the radius of curvature R. Therefore the modified Froude number, which takes into account centrifugal effects, can predict the effective filling of the curved pipes, but is of less interest in the limit of straight pipes. Each group of points corresponds to a different fluid, i.e., viscosity. The tendency for Fr($U=U_c$) to increase with d is clearly visible in each group of points. For $K\geqslant 10^{-2}$, Fr($U=U_c$) is apparently decreasing with K and the flow would eventually tend to follow a non Newtonian behavior.

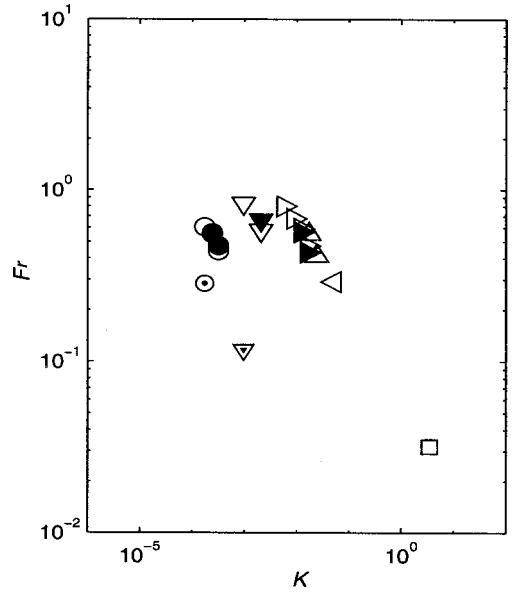

Fig. 7 Modified Froude number (3) computed for $U=U_c$ versus K (4) (see list of symbols in Table 1.)

In almost all our experiments, Re is larger than 10 (see Fig. 6) indicating that viscous effects are smaller than inertial ones. Meanwhile, the data on Fr indicate that both inertial and gravitational effects are comparable.

Conclusion

In order to understand the failure in filling curved pipes, we performed a series of experiments using various fluids. We measured the velocity of propagation of the front v and we deduced from its linear dependence with the mean flow velocity U a critical value U_c, below which there is no longer a complete filling of the pipe. This critical velocity U_c is increasing with d for each fluid.

Results are presented in a synthetic way as relations between dimensionless numbers. We have shown, in the scope of our work, that a modified Froude number determines the ability of the flow to fill a curved pipe. In all our experiments and for Newtonian fluids of different viscosities, the filling was complete for Fr $\geqslant 0.6\pm 0.2$.

We also performed experiments with a non-Newtonian fluid whose rheological behavior is similar to the one of cement suspensions. The front deforms very slowly when the shear is weak because this increases the viscosity of the fluid. In that case, the complete filling may be obtained for Fr very small. Following [16,17], a more extensive study would be needed in order to understand the detail of the non-Newtonian effects.

For industrial applications we advise considering pipes of small diameters and injecting the solution at a relatively low flow rate in order to increase its effective viscosity. However, a future study of interest will be to repeat the present experiments in the context of slug flows.

Acknowledgments

The authors thank C. Peiti at Ecole des Mines de Paris (CEMEF, Sophia Antipolis) for his help, and R. Leroy and O. Coussy for providing helpful comments. The authors are grateful to J.Ch. Bery for his help in the conception and realization of the experimental apparatus. This study was part of a contract with the Laboratoire Central des Ponts et Chaussées.

Nomenclature

d	=	diameter of pipe
R	=	radius of curvature
g	=	acceleration of gravity
ν	=	kinematic viscosity
ρ	=	density
U	=	mean entrance velocity
u	=	mean exit velocity
v	=	velocity of the upper point of the front
$U_c=U(v=0)$	=	critical mean velocity
h	=	height of the exit flow
$\mathrm{Fr}=U(1+(d/R)^{1/2})/(gd)^{1/2}$	=	modified Froude number
$\mathrm{Re}=Ud(1+(d/R)^{1/2})/\nu$	=	modified Reynolds number
K	=	Fr/Re
σ	=	surface tension
$L_c=\sigma^{1/2}(\rho g)^{-1/2}$	=	capillary length
$\mathrm{Bo}=d^2\rho g/\sigma$	=	Bond number
$\mathrm{We}=\rho d U^2/\sigma$	=	Weber number

References

[1] Berger, S. A., Talbot, L., and Yao, L.-S., 1983, ''Flow in curved pipes,'' Annu. Rev. Fluid Mech., **15**, pp. 461–512.
[2] Soh, W. Y., and Berger, S. A., 1984, ''Laminar entrance flow in a curved pipe,'' J. Fluid Mech., **148**, pp. 109–135.
[3] Olson, D. E., and Snyder, B., 1985, ''The upstream scale of flow development in curved circular pipes,'' J. Fluid Mech., **150**, pp. 139–158.
[4] Ishigaki, H., 1994, ''Analogy between laminar flows in curved pipes and orthogonally rotating pipes,'' J. Fluid Mech., **268**, pp. 133–145.

[5] Popiel, C. O., and van der Merwe, D. F., 1996, ''Friction factor in sine-pipe flow,'' ASME J. Fluids Eng., **118**, pp. 341–345.
[6] Majumdar, B., Mohan, R., Singh, S. M., and Agrawal, D. P., 1998, ''Experimental study of flow in a high aspect ratio 90 deg curved diffuser,'' ASME J. Fluids Eng., **120**, pp. 83–89.
[7] Chanson, H., 1997 ''Air-water flows in partially-filled conduits,'' J. Hydraul. Res. **35**, No. 5, pp. 591–602.
[8] Capart, H., Sillen, X., and Zech, Y., 1997, ''The design of sewage sludge pumping systems,'' J. Hydraul. Res., **35**, No. 5, pp. 659–672.
[9] Woods, B. D., and Hanratty, T. J., 1999, ''Influence of Froude number on physical processes determining frequency of slugging in horizontal gas-liquid flows,'' Int. J. Multiphase Flow, **25**, No. 6-7, pp. 1195–1223.
[10] Taitel, Y., Sarica, C., and Brill, J. P., 2000, ''Slug flow modeling for downward inclined pipe flow: theoretical considerations,'' Int. J. Multiphase Flow, **26**, No. 5, pp. 833–844.
[11] Benjamin, T. B., 1968, ''Gravity currents and related phenomena,'' J. Fluid Mech., **31**, pp. 209–248.
[12] Simpson, J. E., 1982, ''Gravity currents in the laboratory, atmosphere, and ocean,'' Annu. Rev. Fluid Mech., **14**, pp. 213–234.
[13] Asavenant, J., and Vanden-Broeck, J.-M., 1996, ''Nonlinear free-surface flows emerging from vessels and flows under a sluice gate,'' J. Austral. Math. Soc., B **38**, pp. 63–86.
[14] Vanden-Broeck, J.-M., and Keller, J. B., 1987, ''Weir flows,'' J. Fluid Mech., **176**, pp. 283–293.
[15] Dean, W. R., 1927, ''Note on the motion of fluid in a curved pipe,'' Philos. Mag., **20**, pp. 208–223.
[16] Chilton, R., Stainsby, R., and Thompson, S., 1996, ''The design of sewage sludge pumping systems,'' J. Hydraul. Res., **34**, No. 3, pp. 395–408.
[17] Chilton, R., and Stainsby, R., 1998, ''Pressure loss equations for laminar and turbulent non-Newtonian pipe flow,'' J. Hydraul. Eng., **124**, No. 5, pp. 522–529.

Satoshi Watanabe
Associate Professor,
Faculty of Engineering,
Kyushu University,
6-10-1 Hakozaki,
Higashi-ku,
Fukuoka 812-8581, Japan
e-mail: fmnabe@mech.kyushu-u.ac.jp

Yoshinobu Tsujimoto
Professor,
Graduate School of Engineering Science,
Osaka University,
1-3 Machikaneyama,
Toyonaka 560-8581, Japan
e-mail: tujimoto@me.es.osaka-u.ac.jp

Akinori Furukawa
Professor,
Faculty of Engineering,
Kyushu University,
6-10-1 Hakozaki,
Higashi-ku,
Fukuoka 812-8581, Japan
e-mail: fmfuru@mech.kyushu-u.ac.jp

Theoretical Analysis of Transitional and Partial Cavity Instabilities

This paper describes a new time marching calculation of blade surface cavitation based on a linearized free streamline theory using a singularity method. In this calculation, closed cavity models for partial and super cavities are combined to simulate the transitional cavity oscillation between partial and super cavities. The results for an isolated hydrofoil located in a 2-D channel are presented. Although the re-entrant jet is not taken into account, the transitional cavity oscillation with large amplitude, which is known to occur when the cavity length exceeds 75 percent of the chord length, was simulated fairly well. The partial cavity oscillation with relatively high frequency was simulated as damping oscillations. The frequency of the damping oscillation agrees with that of a stability analysis and of experiments. The present calculation can be easily extended to simulate other cavity instabilities in pumps or cascades. [DOI: 10.1115/1.1378295]

Introduction

It is well known that the blade surface cavity becomes unstable and causes a strong vibration when the cavity length exceeds about 75 percent of the chord length (Wade and Acosta [1] and Kawanami et al. [2], etc.). Under the oscillation, the cavity dramatically changes between small partial cavity and large super cavity, and it often accompanies the large cloud cavity shedding with the re-entrant jet. Here, we call this oscillation ''transitional cavity oscillation.'' The frequency of this type of oscillation is usually low. Through visual observations and pressure measurements carefully carried out by several researchers (Le et al. [3], Arndt et al. [4], Sato et al. [5]), it is also well known that the small partial cavity also oscillates with smaller amplitude and relatively high frequency, herein called ''partial cavity oscillation.'' Under partial cavity oscillation, it is often observed that cloud cavities are shed from the cavity trailing edge. The frequency increases as the cavity becomes smaller, keeping the Strouhal number based on cavity length nearly constant. Generally speaking the cavity oscillations seem to be classified by the frequency characteristics of the cavity oscillations into the two types mentioned above.

There have been a number of theoretical studies on these cavity oscillations, from the classical linearized theory proposed by Tulin and Hsu [6] to the recent numerical calculations (Kubota et al. [7] and Dang and Kuiper [8]). Based on a linearized cavity model, Nishiyama and Shiire [9] have proposed a stability analysis using a singularity method for self-excited cavity oscillation and have calculated the unsteady fluid forces. Their stability analysis employs a semi-closed cavity terminus model and a free source wake. It is assumed that the cavity length is constant, and the experimental data are used to determine the cavity thickness at the trailing edge. Recently, Watanabe et al. [10] have proposed a stability analysis based on a singularity method and applied it to partial cavities. In the analysis, a closed cavity model is used which allows the cavity length freely to change, and no experimental data are needed to close the analysis. It was found that partial cavities longer than 75 percent of chord length are statically unstable; that is the frequency obtained is zero. This is due to the negative cavitation compliance—for those cavities, the cavity volume decreases when the ambient pressure is reduced. Moreover, it was found that for a small partial cavity, unstable modes with high frequencies exist. These results are thought to correspond to the transitional and partial cavity oscillations, but the frequencies obtained do not agree with experimental ones. This stability analysis [10], which assumes a small disturbance on the steady cavity, simply shows that the branch of the steady partial cavity solution longer than 75 percent of the chordlength is statically unstable, with a mode exponentially shifting to the stable branch which has shorter cavity length. In experiments, we observe the transitional cavity oscillation when we lower the cavitation number below a certain value corresponding to the minimum value for partial cavitation number predicted by a linear steady cavity analysis. This suggests that we need to depart from the assumption of ''small disturbance'' on the steady solution to a finite amplitude oscillation, to simulate the transitional cavity oscillation.

In the present study, a new time marching calculation is proposed for the simulation of cavity oscillations. To simplify the calculations, we still assume a linear closed cavity model, but the cavity length is allowed to change, largely covering partial and super cavities. It should be noted that the cavity shedding and re-entrant jet dynamics are not considered due to the restriction of linearized closed cavity model. In this paper, a single hydrofoil located in a semi-infinite 2-D channel is considered to determine if the obtained instability is system dependent or not.

Fundamental Flow Field. As shown in Fig. 1, we analyze the flow around a flat plate hydrofoil with the angle of attack α located in a two-dimensional semi-infinite duct (width H and upstream duct length L) and its inlet connected to a space with constant pressure. The cavity of length l is assumed on the suction surface of the blade. Assuming that the disturbances of blade and cavity are small, the flow field can be represented by a main flow U, a source distribution q representing the cavity, a bound vortex

Contributed by the Fluids Engineering Division for publication in the JOURNAL OF FLUIDS ENGINEERING. Manuscript received by the Fluids Engineering Division November 15, 2000; revised manuscript received March 30, 2001. Associate Editor: J. Katz.

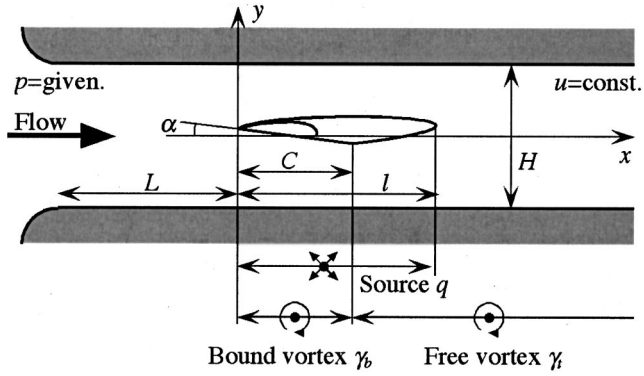

Fig. 1 Cavity model in semi-infinite 2-D channel

distribution γ_b representing the blade, and a free vortex distribution γ_t representing the vortex wake. Taking account of wall effects by introducing mirror images of singularities, and considering that the flow disturbance vanishes downstream, the complex potential W can be represented as follows:

$$W(z)=Uz+\frac{1}{2\pi}\left\{\int_0^l q(\xi)F_q(z,\xi)d\xi+i\int_0^C \gamma_b(\xi)F_\gamma(z,\xi)d\xi + i\int_C^\infty \gamma_t(\xi)F_\gamma(z,\xi)d\xi\right\} \quad (1)$$

$$F_q(z,\xi)=\log\left\{\frac{2H}{\pi}\sinh\left[\frac{\pi}{2H}(z-\xi)\right]\right\} + \log\left\{-i\frac{2H}{\pi}\sinh\left[\frac{\pi}{2H}(z-\xi)\right]\right\}-\frac{\pi}{H}z$$

$$F_\gamma(z,\xi)=\log\left\{\frac{2H}{\pi}\sinh\left[\frac{\pi}{2H}(z-\xi)\right]\right\} - \log\left\{-i\frac{2H}{\pi}\sinh\left[\frac{\pi}{2H}(z-\xi)\right]\right\} \quad (2)$$

It should be noted that all singularities are distributed on the chord of the hydrofoil, and located on the centerline of the channel, based on the assumption of the small cavity thickness and small flow angle downstream of the blade.

Taking the z-derivative of complex potential, we can obtain the following complex conjugate velocity:

$$w(z)=u-i\nu=dW/dz=U+\frac{1}{2\pi}\left\{\int_0^l q(\xi)f_q(z,\xi)d\xi + i\int_0^C \gamma_b(\xi)f_\gamma(z,\xi)d\xi+i\int_C^\infty \gamma_t(\xi)f_\gamma(z,\xi)d\xi\right\} \quad (3)$$

$$f_q(z,\xi)=\frac{\pi}{2H}\left\{\coth\left[\frac{\pi}{2H}(z-\xi)\right]+\tanh\left[\frac{\pi}{2H}(z-\xi)\right]-2\right\}$$

$$f_\gamma(z,\xi)=\frac{\pi}{2H}\left\{\coth\left[\frac{\pi}{2H}(z-\xi)\right]-\tanh\left[\frac{\pi}{2H}(z-\xi)\right]\right\} \quad (4)$$

The complex potential $W(z)$ and complex conjugate velocity $w(z)$ can be determined by the boundary and complementary conditions in the following section.

Boundary and Complementary Conditions

Boundary Conditions on the Cavity Surface. It is assumed that the pressure on the cavity surface is constant with the vapor pressure p_v. This condition results in the following boundary condition, which is derived from the linearized momentum equation on the cavity surface:

$$\frac{\partial u_c}{\partial t}+U\frac{\partial u_c}{\partial x}=-\frac{1}{\rho}\frac{\partial \rho}{\partial x}=0 \quad (5)$$

where $U+u_c$ with $U\gg|u_c|$ is the velocity on the cavity surface. Here, $U+u_c$ corresponds to u expressed in Eq. (3). The velocity at the leading edge of cavity surface $u_c(0)$, which is needed to solve Eq. (5), can be obtained by applying the unsteady version of linearized Bernoulli's equation between the leading edge and the inlet of upstream duct:

$$\frac{u_c(0)}{U}=\frac{u_c(-L)}{U}+\frac{2}{U^2}\frac{\partial\,\mathrm{Re}[W(-L)-W(0)]}{\partial t}+\sigma_{-L}. \quad (6)$$

where $\sigma_{-L}=2(p_{-L}-p_v)/\rho U^2$ is the cavitation number at the duct inlet.

The condition described here is applied only on the upper surface of the cavity as follows:

$$u(x+0i)=\mathrm{Re}[w(x+0i)]=U+u_c(x) \quad (7)$$

The boundary condition on the lower surface of the cavity can be satisfied automatically because, as described later, we consider only the free vortex distribution inside the cavity which does not induce any pressure difference across the x-axis.

Boundary Condition on the Wetted Surface. On the wetted surface of the blade, flow tangency condition is applied as follows:

$$\nu(x\pm 0i)=\mathrm{Im}[w(x\pm 0i)]=-U\alpha \quad (8)$$

Unsteady Kutta's Condition. We assume that the pressure difference across the blade vanishes at the trailing edge of the blade. By applying the linearized momentum equation, this condition can be expressed as follows:

$$\frac{d}{dt}\int_0^C \gamma_b(\xi)d\xi+U\gamma_t(C)=0 \quad (9)$$

Equation (9) is equivalent to Kelvin's circulation conservation law and signifies that the free vortex of strength $\gamma_t(C)$ is shed on the mean velocity U from the trailing edge of the blade, corresponding to the change in the blade circulation.

We assume that the trailing free vorticity $\gamma_t(x)$ is transported on the free stream:

$$\frac{\partial \gamma_t}{\partial t}+U\frac{\partial \gamma_t}{\partial x}=0 \quad (10)$$

For the case of a super cavity, it is assumed that the free vorticity is convected inside the cavity following the above equation and then shed from the trailing edge of the cavity.

Kinematic Boundary Condition on Cavity Surface. We consider a closed curve fitting around the blade and cavity. Denoting the y-location of the upper part of the curve by η^+ and the lower by η^-, the kinematic condition on cavity surfaces can be expressed as follows:

$$\frac{\partial \eta^\pm}{\partial t}+U\frac{\partial \eta^\pm}{\partial x}=\nu(x\pm 0i) \quad (11)$$

Subtracting Eq. (11) applied to the lower part from that applied to the upper part, we obtain the following equation:

$$\frac{\partial[\eta^+(\xi)-\eta^-(\xi)]}{\partial t}+U\frac{\partial[\eta^+(\xi)-\eta^-(\xi)]}{\partial x}=q(x) \quad (12)$$

Cavity Closure Condition. We employ a closed cavity model. Thus, the cavity closure condition is

$$\eta^+(l)-\eta^-(l)=0 \tag{13}$$

Analytical Procedure

The unknown quantities in this problem are the singularity distributions $q(x), \gamma_b(x), \gamma_t(x)$, the cavity length l, the velocity distribution on cavity surface $u_c(x)$, and the cavity thickness $\eta^+(x)-\eta^-(x)$ at the time $t+\Delta t$. These distributions at each time step are discretized in space, and a numerical solution is obtained by applying a time marching method. The values of $q(x)$, $\gamma_b(x)$, $u_c(x)$ and $\eta^+(x)-\eta^-(x)$ are defined on the following nodes X_k. For the case of a partial cavity ($l<C$),

$$X_k=\frac{l}{2}\left[1-\cos\left(\frac{k-1}{N_1-1}\pi\right)\right] \quad (0<x<l, k=1,2,\ldots,N_1)$$

$$X_k=l+\frac{C-l}{2}\left[1-\cos\left(\frac{k-N_1-1}{N_2-1}\pi\right)\right]$$

$$(l<x<C, k=N_1+1, N_1+2,\ldots,N_1+N_2) \tag{14}$$

For the case of a super cavity ($l>C$),

$$X_k=\frac{C}{2}\left[1-\cos\left(\frac{k-1}{N_1-1}\pi\right)\right] \quad (0<x<l, k=1,2,\ldots,N_1)$$

$$X_k=C+\frac{l-C}{2}\left[1-\cos\left(\frac{k-N_1-1}{N_2-1}\pi\right)\right]$$

$$(l<x<C, k=N_1+1, N_1+2,\ldots,N_1+N_2) \tag{15}$$

where N_1 and N_2 are the numbers of nodes. We have employed the cos-laws to obtain fine node distributions around the leading edge, the trailing edge, and the cavity closure. It should be noted that nodes move in accord with the change in cavity length.

Considering that the vortices are convected on the free stream U, the strength of the free vortex wake $\gamma_t(x)$ can be determined at $x=C+nU\Delta t$. Solving Eq. (10) explicitly with the first upwind difference, we can determine $\gamma_t(x)$ accurately.

The strengths of singularities are assumed to be linear between nodes, except for the regions near the leading and trailing edges of the cavity. In these regions the singular behavior of linearized cavitating flow obtained by Geurst [11,12] should be taken into account. It is assumed that $q(x)\sim x^{-1/4}$ and $\gamma_b(x)\sim x^{-1/4}$ near the leading edge, and $q(x)\sim(l-x)^{-1/2}$ near the trailing edge of cavity. Moreover, for the case of a partial cavity, $\gamma_b(x)\sim(x-l)^{-1/2}$ is assumed just downstream of the trailing edge of the cavity.

All unknowns are determined from Eqs. (5)–(13). Equations (5), (7), (9), and (12) are solved by Euler's first implicit scheme using the first upwind difference for the evaluation of convective terms. Boundary conditions (6) and (8) are satisfied at $t=t+\Delta t$ on the control points, at the middle of each node. Then, we can express all boundary and complementary conditions in the following matrix form:

$$[A(l^{t+\Delta t})]\{Q^{l+\Delta t}\}=[B(l^t)]\{Q^t\}+\{D(t+\Delta t)\} \tag{16}$$

$$Q=\{q(X_1),\ldots,\gamma_b(X_1),\ldots,\gamma_t(C+U\Delta t),\ldots,u_c(X_1),\ldots,\eta^+(X_1)-\eta^+(X_1),\ldots\}^T \tag{17}$$

Because the coefficient matrix A includes the unknown $l^{t+\Delta t}$, Eq. (16) is not a set of linear equations. To obtain the solution of Eq. (16), we need the following iterative procedure: (i) assume the value of cavity length $l^{t+\Delta t}$; (ii) solve Eq. (16) without the cavity closure condition Eq. (13); (iii) estimate the error of $l^{t+\Delta t}$ from Eq. (13); (iv) modify the value of $l^{t+\Delta t}$; and (v) repeat (i)–(iv) until the cavity closure condition is satisfied.

The numbers of nodes and the time increment were set as $N_1=N_2=37$ and $\Delta t=0.05C/U$ in the present calculation. It was confirmed in the steady analysis that the steady cavity length obtained with $N_1=N_2=37$ agrees with that of $N_1=N_2=100$ to three decimal places, indicating that $N_1=N_2=37$ is gives satisfactory results for the present time marching calculation. It was confirmed that the cavity behavior does not change significantly if we decrease the time increment below $\Delta t=0.05C/U$. This time increment is also small enough, compared to the minimum period of oscillation of $1.3C/U$ for partial cavity oscillation and $7.4C/U$ for the transitional oscillations in the present calculations.

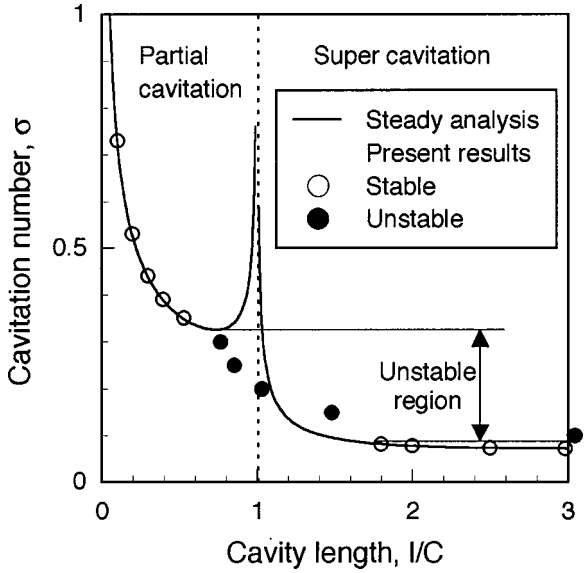

Fig. 2 Steady cavity length and mean cavity length of present analysis

Numerical results are shown mainly for the case with $C/H=0.7$, $L/C=9.6$, $a=1.5$[deg]. The results of the steady analysis are shown by the solid line in Fig. 2. We have a discontinuity between partial and super cavity solutions, as always observed with a linear cavity model. The stability analysis (Watanabe et al. [10]) shows that the partial cavity longer than 73 percent of chord length is statically unstable for the case with $C/H=0.7$.

Results and Discussions

Partial Cavity Oscillation. When a small disturbance is applied to the steady small partial cavity, the solution moves immediately to another equilibrium. However, on the way to the new equilibrium, a few swings with high frequency are observed. Figure 3 shows a typical example, in which a step change in the inlet cavitation number from $\sigma_{-L}=0.523(l/C=0.2)$ to 0.53 is given at $t=0$. Time histories of σ_{-L}, normalized cavity length l/C, normalized cavity volume V_c/C^2 and the pressure coefficient at the leading edge C_p are shown in the figure. The pressure coefficient C_p is evaluated by subtracting the inertia effect of the upstream duct from the pressure at the duct inlet, assuming one-dimensional flow in the duct:

$$C_p=\frac{2(p_0-p_v)}{\rho U^2}=\frac{2(p_{-L}-\rho L\,du/dt-p_v)}{\rho U^2}=\sigma_{-L}+\frac{L}{H}\frac{2}{U^2}\frac{d^2V_c}{dt^2} \tag{18}$$

From this definition, the pressure coefficient C_p can be thought of as the cavitation number at the leading edge. Figure 3 shows that the cavity executes a few swings before settling in a new equilibrium with $l/C=0.197$. The swings have high frequency, which is found to agree with that of partial cavity oscillation in the experiment, which will be shown later. Similar results are obtained for other cases with $l/C<0.7$. It was confirmed that the size of small initial disturbance did not affect the frequency at all.

Transitional Cavity Oscillation. In experiments, transitional cavity oscillation occurs when we decrease the cavitation number below a certain value corresponding to the minimum cavitation

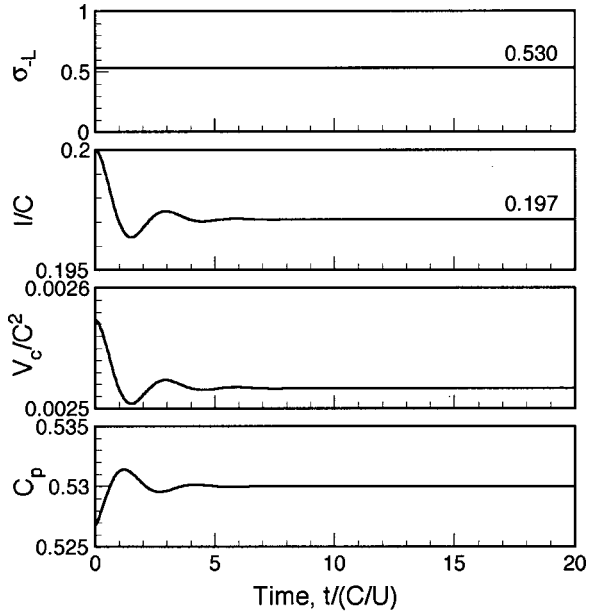

Fig. 3 Time histories of cavitation number at duct inlet, cavity length, cavity volume, and pressure coefficient for the case of step change in cavitation number from $\sigma_{-L}=0.523$ to 0.530 at $t=0$

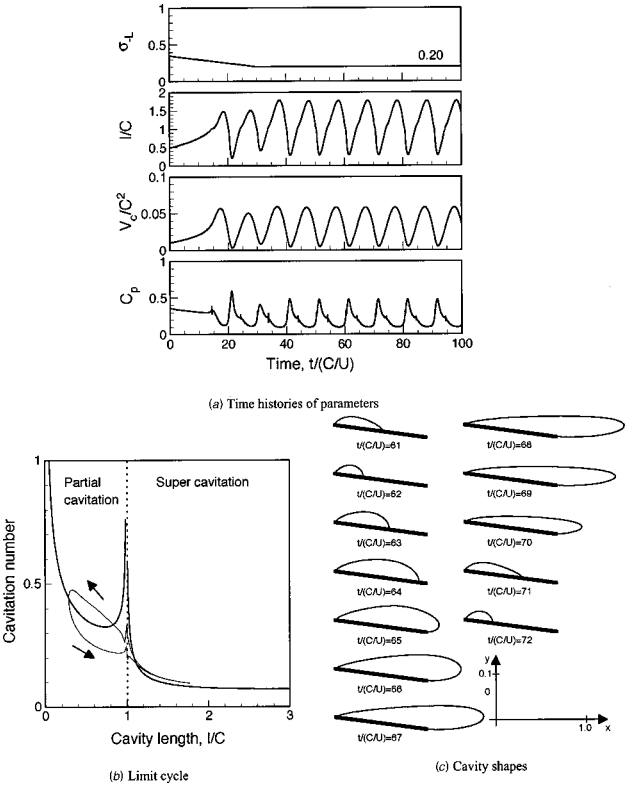

Fig. 4 Results of linearly decreasing cavitation number from $\sigma_{-L}=0.35$ to 0.2 within $t=0-30C/U$. (*a*) Time histories of parameters; (*b*) limit cycle; (*c*) cavity shapes.

number for the steady partial cavitation predicted by a linear stability flow analysis. This occurs when the cavity length is about 75 percent of chord length, as shown in Fig. 2. However, the cavitation number of the steady cavity solution longer than 75 percent of chord length is larger than the minimum value. The stability analysis assuming a small disturbance [10] shows simply that this branch of the steady solution is statically unstable. So we must depart from the steady solution. For this reason we employ the time marching calculation, which allows finite amplitude cavity oscillations. The calculation is made by gradually decreasing the upstream cavitation number below the minimum value. Figure 4 shows a typical example of the results, in which the cavitation number is linearly decreased from $\sigma_{-L}=0.35$ ($l/C=0.5$) to 0.2 within $t=0-30C/U$, and kept constant thereafter.

The results in Fig. 4(*a*) show that the cavity oscillates largely between $l/C=0.2$ to 1.8, with the normalized frequency fC/U of approximately 0.1. Figure 4(*b*) shows the limit cycle in σ_0-l/C plane, where the limit cycle is drawn by using the pressure coefficient C_p at the leading edge. Figure 4(*c*) shows the instantaneous cavity shape. Despite a linearized closed cavity model, the growing and shrinking processes of the cavity are reasonably simulated.

Once the cavity gets into steady oscillation, the frequency and the amplitude are not affected by the size of the initial disturbance applied.

Comparisons With Experiments and Stability Analysis. Returning to Fig. 2, the mean cavity length obtained by the present calculation is shown by symbols for various cavitation numbers. As we decrease the cavitation number, the mean cavity length smoothly transits from partial to super cavitation regime. However, in the present calculation, the mean cavity length can become as large as $l/C=3$. As we can see from the plot of steady cavity length in Fig. 2, long super cavities extend quite rapidly as we decrease the cavitation number. Perhaps associated with this characteristic, the amplitude of cavity oscillation grows very large and the mean cavity length becomes as large as $l/C=3$. For steady flows, the smooth transition between partial and super cavity is obtained by applying a nonlinear cavity model (Wu [13]). If we neglect the case of extremely large mean cavity length caused by large amplitude oscillations, the present result may suggest that the unsteadiness can also explain the transition between partial and super cavities.

It is well known experimentally that longer super cavities are stable. A linear stability analysis of super cavities similar to Watanabe et al. [10] shows that super cavities longer than $l/C=1.8$ is stable. If we start the present time marching calculation from an initial condition of steady super cavity with a small disturbance, the result approaches the equilibrium on the steady cavitation number-cavity length plot. Those results are also shown in Fig. 2.

Figure 5 shows the normalized frequency fC/U and the amplitude of cavity length fluctuation plotted against the mean cavity length for various inlet duct lengths. Figure 5(*a*) shows the results of present calculations, in which the frequencies of damping oscillations of shorter partial cavities are shown by open symbols, and the frequencies of steady oscillation are shown by closed symbols. Figure 5(*b*) shows the results of experiments (Arndt et al. [4] and Sato et al. [5]). Sato et al.'s experiments are for a flat plate hydrofoil with a sharp leading edge, and the results for the case of the incidence angle of 1.5 [deg] are plotted. For this incidence angle a clear blade surface cavity is observed. The inlet pressure fluctuation shows a rather broadband spectrum and the peak frequency of the spectrum is plotted. Reasonable agreement can be observed between the present calculation and Sato et al.'s results. However, the calculated frequency of the transitional cavity oscillation depends on the inlet duct length, while no such dependence was observed in the experiment. This difference might be caused by the fact that the cavity shed from the cavity trailing edge, usually observed in experiments, is totally neglected in the present calculation. If we have the shed-off cavities, the change of total cavity volume would be much smaller. We believe that this is the cause of the independence of the experimentally observed transitional cavity oscillation on the system.

Arndt et al.'s experiments [4] are made using a NACA0015

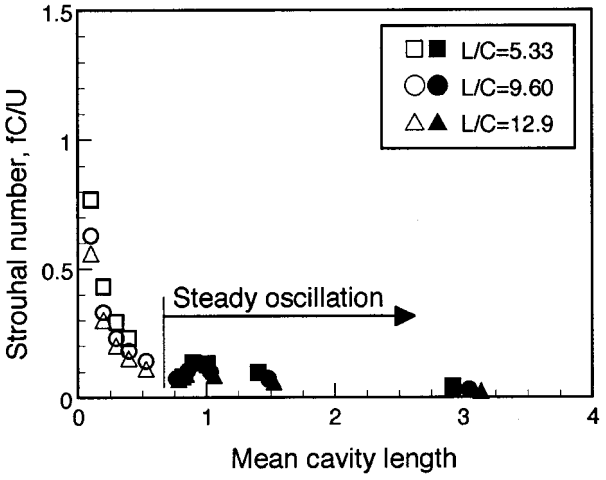

(*a*) Present study

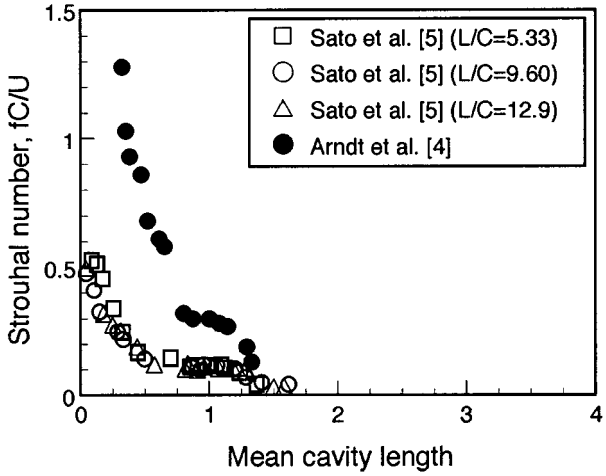

(*b*) Experimental results

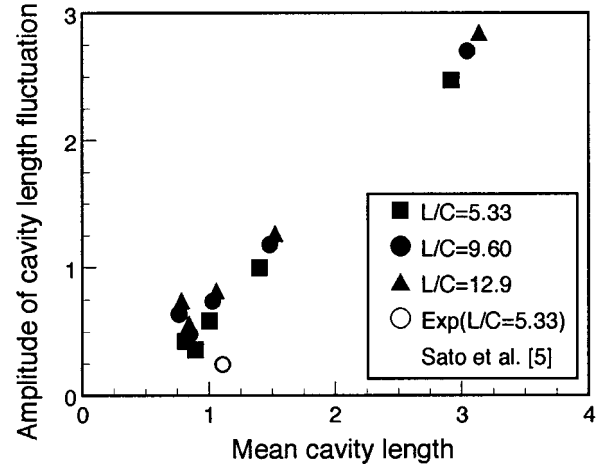

(*c*) Amplitude of cavity length fluctuation

Fig. 5 Comparisons of Strouhal number between present study and experiments. (*a*) Present study; (*b*) experimental results; (*c*) amplitude of cavity length fluctuation.

hydrofoil. The frequency observed is significantly higher than the results of present calculations and of Sato et al.'s experiment. The reason for the discrepancy of the frequency is not known but it is

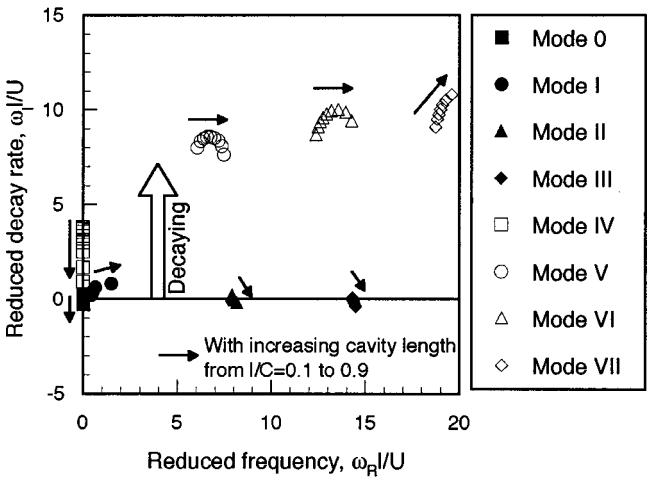

Fig. 6 Results of stability analysis for various cavity lengths

interesting to note that the two types of cavity oscillation, partial cavity oscillation and the transitional cavity oscillation, are also observed in this experiment.

Figure 5(*c*) shows the amplitude of the cavity length fluctuation. We observe that the present calculation overestimates the oscillation amplitude. This might be caused by neglecting the fluid viscosity and the cavity shedding in the calculation.

Finally, we examine the relationship between the present results and those of the linear stability analysis (Watanabe et al. [10]). In the stability analysis, the flow is separated into uniform steady flow, a small steady disturbance, and a small unsteady disturbance. The flow disturbances are represented by the steady and unsteady components of a source distribution on the cavity, vortex distributions on the blade surface and the wake, in the same way as the present calculations. The boundary conditions are linearized based on the assumptions of the small disturbance. If we separate the boundary conditions into steady and unsteady components, the unsteady components are represented as a system of homogeneous linear equations in terms of the unsteady component of the source and vortex distributions. The complex frequency determined under the condition that the determinant of the coefficient matrix of the linear equations should be zero, so that the system has nontrivial solutions. The complex frequency is composed of a real part ω_R showing the frequency of the oscillation and an imaginary part ω_I showing the decaying rate. Figure 6 shows the complex frequencies of the obtained modes including damping ones, for various cavity lengths, after normalizing them using the mean cavity length l and the free-stream velocity U. Those modes are decaying if the imaginary part ω_I is positive. They are named Mode 0-Mode VII, depending on the value of their frequency ω_R. Mode 0, with frequency zero, becomes amplifying for $l/C > 0.73$, corresponding to the static instability of longer partial cavities, or the transitional cavity oscillation. Figure 7 shows the comparison of the frequency of the damping mode of Mode I with that of the damping oscillation in the present time marching calculations. They agree with each other for cases with various inlet duct lengths. This shows that the partial cavity oscillation observed in experiments may correspond to the damping mode. No explanation is given at this moment why the amplifying modes Mode II and III shown in Fig. 6 have never appeared in the present calculation and in the experiments.

Conclusions

(a) A new time marching calculation of unsteady cavitation is proposed by combining unsteady linear closed cavity models of partial and super cavities.

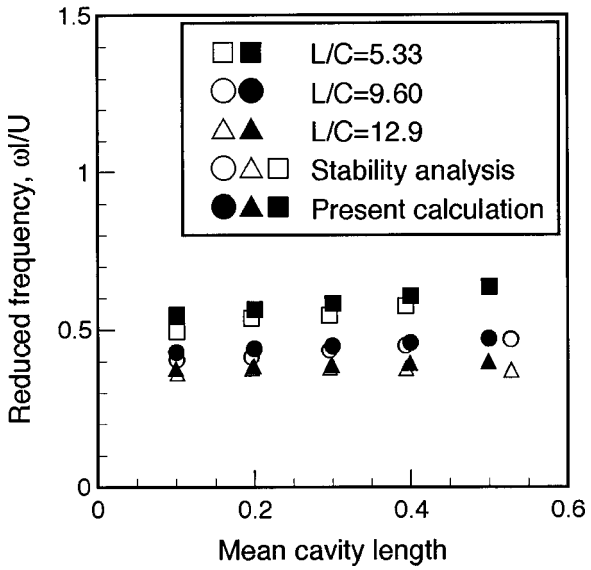

Fig. 7 Comparisons of reduced frequency based on mean cavity length between present results and Mode I in Fig. 6

(b) The partial cavity oscillation observed in experiments corresponds to the damping oscillation simulated by the present calculation. However, why the damping oscillation appears in experiments still remains unknown.

(c) Transitional cavity oscillation is well simulated by the present calculation, although cavity shedding and re-entrant jet are not included in the analysis. However, the system dependence is more significant in the calculation than in the experiment.

(d) The transition between partial and super cavities is also well simulated by the present analysis with a linear unsteady closed cavity model, except that the mean cavity length becomes significantly larger owing to the large amplitude of the oscillation in the regime of shorter super cavitation. This result may imply that the unsteadiness can also explain the transition between partial and super cavities, as well as nonlinear cavity models.

(e) The damping oscillation of a partial cavity is found to correspond to one of the damping modes predicted by the previous stability analysis. However, it remains unclear why other amplifying modes do not appear in the experiments and in the present calculation.

Acknowledgments

This study was partly supported by the Grant-in-Aid for Scientific Research of the Ministry of Education, Science, Sports and Culture.

Nomenclature

A,B = coefficient matrices in Eq. (16)
C = chord length
C_p = pressure coefficient defined in Eq. (18)
D = constant vector in Eq. (16)
$F_q(z,\xi), F\gamma(z,\xi)$ = functions defined in Eq. (2)
f = frequency
$f_q(z,\xi), f_\gamma(z,\xi)$ = functions defined in Eq. (4)
i = imaginary unit in space
j = imaginary unit in time
L = upstream duct length
l = cavity length
l_m = mean cavity length
N_1, N_2 = numbers of nodes
p = pressure
p_v = vapor pressure
Q = unknown vector
q = strength of source distribution
t = time
U = mean flow velocity
u, v = velocity components in the x- and y-directions
u_c = disturbance component of velocity on the cavity surface
V_c = cavity volume
W = complex potential
w = complex conjugate velocity, $=u-iv$
X = location of the discrete points
α = angle of attack
γ_b, γ_t = strengths of vortex distributions representing blade and wake
Δt = time increment
η^+ = upper part of closed curve fitted with blade and cavity
η^- = lower part of closed curve fitted with blade and cavity
ρ = density
σ = cavitation number
ξ = location from blade leading edge
ω_R = angular frequency of the eigen-modes obtained by stability analysis
ω_I = decaying rate of the eigen-modes obtained by stability analysis

Superscripts

$t, t+\Delta t$ = variables at t and $t=t+\Delta t$

Subscripts

$-L$ = inlet of the upstream duct

References

[1] Wade, R. B., and Acosta, A. J., 1966, ''Experimental Observations on the Flow Past a Plano-Convex Hydrofoil,'' ASME J. Basic Eng., **88**, pp. 273–283.
[2] Kawanami, Y., Kato, H., Yamaguchi, H., Tanimura, M., and Tagaya, Y., 1997, ''Mechanism and Control of Cloud Cavitation,'' ASME J. Fluids Eng., **119**, pp. 788–794.
[3] Le, Q., Franc, J. P., and Michel, J. M., 1993, ''Partial Cavities: Global and Mean Pressure Distribution,'' ASME J. Fluids Eng., **115**, pp. 243–248.
[4] Arndt, R. E. A., Song, C. C. S., Kjeldsen, M., He, J., and Keller, A., 2000, ''Instability of Partial Cavitation: A Numerical/Experimental Approach,'' Proceedings, 23rd Symposium on Naval Hydrodynamics, Val de Reuli.
[5] Sato, K., Tanada, M., Monden, S., and Tsujimoto, Y., 1999, ''Observations of Oscillating Cavitation on a Flat Plate Hydrofoil,'' (in Japanese), Trans. Jpn. Soc. Mech. Eng., Ser. B, **65**, No. 639, pp. 3659–3667.
[6] Tulin M. P., and Hsu, C. C., 1980, ''New Applications of Cavity Flow Theory,'' Proceedings, 13th Symposium on Naval Hydrodynamics, pp. 107–131.
[7] Kubota, A., Kato, H., and Yamaguchi, H., 1992, ''New Modeling of Cavitating Flows: A Numerical Study of Unsteady Cavitation on a Hydrofoil Section,'' J. Fluid Mech., **240**, pp. 59–96.
[8] Dang, J., and Kuiper, G., 1999, ''Re-Entrant Jet Modeling of Partial Cavity Flow on Two-Dimensional Hydrofoils,'' ASME J. Fluids Eng., **121**, pp. 773–780.
[9] Nishiyama, T., and Shire, M., 1985, ''Self-Excited Oscillation of the Cavity on a Hydrofoil and Lift Fluctuation (Linear Analysis by a Singularity Method),'' (in Japanese), Trans. Jpn. Soc. Mech. Eng., Ser. B, **59**, No. 561, pp. 2796–2804.
[10] Watanabe, S., Tsujimoto, Y., Franc, J. P., and Michel, J. M., 1998, ''Linear Analysis of Cavitation Instabilities,'' Proceedings, 3rd International Symposium on Cavitation, Vol. **I**, pp. 347–352.
[11] Geurst, J. A., 1959, ''Linearized Theory for Partially Cavitated Hydrofoils,'' International Shipbuilding Progress, **6**, No. 60, pp. 369–384.
[12] Geurst, J. A., 1960, ''Linearized Theory for Fully Cavitated Hydrofoils,'' International Shipbuilding Progress, **7**, No. 65, pp. 12–27.
[13] Wu, T. Y., 1962, ''A Wake Model for Free-Streamline Flow Theory, Part 1,'' J. Fluid Mech., **13**, pp. 161–181.

Journal of Fluids Engineering

Technical Briefs

Developing Film Flow on an Inclined Plane With a Critical Point

Kenneth J. Ruschak
Senior Research Associate

Steven J. Weinstein
Research Associate

Manufacturing Research and Engineering Organization, Eastman Kodak Company, Rochester, NY 14652-3701

Kam Ng
Research Associate, Research Laboratories, Eastman Kodak Company, Rochester, NY 14650-2142

Viscous, laminar, gravitationally-driven flow of a thin film on an inclined plane is analyzed for moderate Reynolds number under critical conditions. A previous analysis of film flow utilized a momentum integral approach with a semiparabolic velocity profile to obtain an ordinary differential equation for the film thickness for flow over a round-crested weir, and the singularity associated with the critical point for a subcritical-to-supercritical transition was removable. For developing flow on a plane with a supercritical-to-subcritical transition, however, the same approach leads to a nonremovable singularity. To eliminate the singularity, the film equations are modified for a velocity profile of changing shape. The resulting predictions compare favorably with those from the two-dimensional boundary-layer equation obtained by finite differences and with those from the Navier-Stokes equation obtained by finite elements. [DOI: 10.1115/1.1385516]

Introduction

Laminar flow in thin films at moderate Reynolds number has many practical applications including liquid film coating [1]. Frequently such flows are designed such that film thickness varies gradually in the flow direction. In that case, the classical boundary-layer approximation to the Navier-Stokes equation is justified [2]. However, the boundary-layer equation is still a formidable nonlinear, two-dimensional, partial differential equation that must generally be solved numerically [3].

A standard approach to the boundary-layer equation, attractive for ease of use, is assuming a velocity profile, frequently fixed in shape but variable in magnitude, and minimizing the resulting residual to obtain an ordinary differential equation for the film profile. An inherent drawback is that the initial velocity profile can no longer be arbitrary. Another limitation is the occurrence of a critical point with a singularity, and typically this situation is avoided (for example, [4]) or accommodated (for example, [5]). The film-profile equations are typically first order in the derivative of film thickness when surface tension is neglected [6–8]. The time-dependent film-profile equation, linearized about a steady solution, is hyperbolic and admits wave solutions travelling at the speed of the characteristics [6]. For subcritical flow, waves travel upstream and downstream. For supercritical flow, waves travel downstream only. At a critical point, the coefficient of the derivative of film thickness vanishes. If the rest of the equation can vanish there as well, the singularity may be removable. For developing flow on an inclined plane with a supercritical-to-subcritical transition, the singularity is not removable and the film-profile equation fails, although numerical solutions to the Navier-Stokes and boundary-layer equations can be generated. Similarly, numerical solutions to the boundary-layer equation for decelerating flow on a horizontal plane have been generated [9]. Because the numerical solutions do not require surface tension, it is not key to resolving the breakdown of the film equation and is neglected here. As shown below, the solutions do show that the velocity profile changes shape in the region of the critical point. In light of that observation, the residual approach to the boundary-layer equation is modified here to accommodate a velocity profile of changing shape. The resulting equations for film flow are more complicated but remain tractable. The flow predictions thereby obtained compare favorably to numerical solutions of the boundary-layer and Navier-Stokes equations. With this modification, the residual approach is restored as an option when a velocity profile of fixed shape leads to a critical point with a nonremovable singularity.

Ruyer-Quil and Manneville [10] used a height-averaged approach, and demonstrated that a non-self-similar velocity profile, in which the wall shear stress is different from that predicted from a parabolic velocity profile, yields improved agreement between theoretical and experimental predictions of wave propagation down inclined planes. They obtain additional equations to resolve additional degrees of freedom by evaluating the boundary-layer equation along the boundaries of the film. The approach here is similar, but the focus is on critical flow. The simplest geometry for a transition from supercritical to subcritical flow is considered, and new equations for the film profile are proposed that are not singular. The approach is motivated by numerical solutions to the boundary-layer and Navier-Stokes equations that show a velocity profile of nonconstant shape. Altering the shape of the velocity profile is common in classical boundary-layer flows [2] to improve the accuracy of the predicted wall shear stress and to predict boundary-layer separation; however, the motivation here is avoiding a breakdown of the film-profile equation for a supercritical-to-subcritical transition.

Contributed by the Fluids Engineering Division of THE AMERICAN SOCIETY OF MECHANICAL ENGINEERS. Manuscript received by the Fluids Engineering Division July 28, 2000; revised manuscript received April 16, 2001. Associate Editor: F. K. Wasden.

Experimental Observation

A qualitative experiment was conducted to show a standing wave where laminar flow passes from supercritical to subcritical on a planar, inclined wall. Supercritical flow was distinguished by stationary waves in the wake of a needle touching the surface of the liquid. Subcritical flow was distinguished by periodic flow disturbances, induced by a small, rotating agitator, radiating in all directions. A film in supercritical flow was produced by pumping aqueous glycerol to a distribution die with a slot of height 0.012 cm. The lower half of the die extended from the slot outlet in the flow direction to serve as the inclined plane. Surface tension and surface-tension gradients were reduced by the addition of the surfactant Aerosol® OT (Cytec Industries, Inc.) at high concentration. A small amount of slurry of titanium dioxide was added to the liquid to make it white and opaque. The liquid had a viscosity of 11.8 mPa·s and a specific gravity of 1.11. Lighting by two synchronized strobe lights was adjusted to create shadows revealing the shape of the film. Volumetric flow rate per unit width was fixed at 1.7 cc/s/cm and the inclination of the plane was varied. At sufficiently low angles of inclination, the fully developed flow reached downstream is subcritical. The flow passes from supercritical to subcritical, and the transition is marked by a two-dimensional stationary wave. As inclination increases, the wave moves farther from the slot outlet and becomes less distinct. At sufficiently high angles of inclination, the flow remains supercritical and no wave is apparent. Figure 1 is a photograph showing this evolution for inclinations of 1, 1.5, and 2 degrees.

Equations

A Newtonian liquid with viscosity μ and density ρ flows down a plane inclined at angle θ to horizontal as shown in Fig. 2. The flow evolves from a prescribed initial state and becomes fully developed downstream. Coordinate x increases down the plane, and coordinate y is normal to the plane and outwardly directed. The corresponding velocity components are u and v respectively, and pressure is p. With gravitational acceleration denoted G and volumetric flow rate per unit width q, the film thickness in fully developed, gravitationally driven viscous flow is $h_\infty = [3\mu q/\rho G \sin(\theta)]^{1/3}$. The Reynolds number, $\mathrm{Re}=\rho q/\mu$, significantly exceeds unity so that the length scale along the plane significantly exceeds h_∞.

For gradually varying film thickness, the boundary-layer approximation to the Navier-Stokes equation is justified [7,11,12]:

$$\rho\left[u\frac{\partial u}{\partial x}+v\frac{\partial u}{\partial y}\right]=-\frac{\partial p}{\partial x}+\rho G\sin(\theta)+\mu\frac{\partial^2 u}{\partial y^2} \tag{1}$$

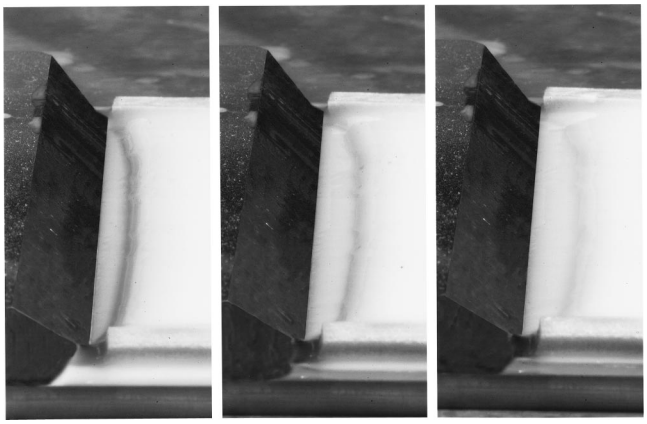

Fig. 1 Photograph showing the standing wave at wall inclinations of 1, 1.5, and 2 degrees. The Reynolds number is 16.

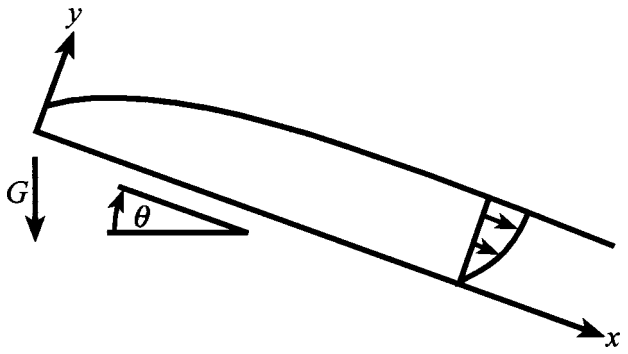

Fig. 2 Definition sketch

$$0=-\frac{\partial p}{\partial y}-\rho G\cos(\theta) \tag{2}$$

The continuity equation is

$$\frac{\partial u}{\partial x}+\frac{\partial v}{\partial y}=0 \tag{3}$$

The surface of the film, $y=h(x)$, is a streamline and free of stress

$$q=\int_0^h u\,dy,\quad \partial u/\partial y=0,\quad p=0\quad (y=h) \tag{4}$$

Velocity is zero at the stationary wall.

$$u=0,\quad v=0\quad (y=0) \tag{5}$$

Finally, the initial film thickness and velocity profile are prescribed.

$$h=h_0,\quad u=u_0(y),\quad (x=0) \tag{6}$$

The following dimensionless variables are introduced:

$$\chi=x/\mathrm{Re}\,h_\infty,\quad H=h/h_\infty,\quad \beta=h_0/h_\infty \tag{7}$$

In applying Eqs. (1)–(6) to film flow, a rectangular domain can be obtained by replacing the coordinate y with y/h. Here, a rectangular domain is obtained through the von Mises transformation [2,12]. In this transformation, the stream function ψ, defined such that $u=\partial\psi/\partial y$ and $v=-\partial\psi/\partial x$, replaces the cross-film coordinate y, and the dependent variable is proportional to the square of the x-component of velocity, $\phi=(uh_\infty/q)^2$. This transformation maps the interface to a fixed boundary location $0\leq\psi\leq q$. With $\Psi=\psi/q$, the resulting nonlinear boundary-value problem for $\phi(\chi,\Psi)$ is:

$$\frac{\partial\phi}{\partial\chi}+\frac{6}{\mathrm{Re}\tan(\theta)}\frac{dH}{d\chi}=\sqrt{\phi}\frac{\partial^2\phi}{\partial\Psi^2}+6 \tag{8}$$

$$\frac{y}{h_\infty}=\int_0^\Psi\frac{dz}{\sqrt{\phi(\chi,z)}},\quad H=\int_0^1\frac{dz}{\sqrt{\phi(\chi,z)}} \tag{9}$$

$$\phi=0\ \ (\Psi=0),\quad \partial\phi/\partial\Psi=0\ \ (\Psi=1) \tag{10}$$

The initial velocity profile ($\chi=0$) is chosen to be either a plug

$$\phi=\beta^{-2} \tag{11}$$

or a half parabola

$$\phi=\beta[1-\cos(\gamma/3)+\sqrt{3}\sin(\gamma/3)],\qquad \gamma=\tan^{-1}[\sqrt{1-(1-\Psi)^2}/(1-\Psi)] \tag{12}$$

For the case of a vertical wall, Eq. (8) becomes that given in [12].

Equations (8)–(10) with either Eq. (11) or (12) were solved by finite differences. It proved necessary to add a second-derivative term to the right-hand side of Eq. (8) of the form $\varepsilon\partial^2\phi/\partial\chi^2$,

where $\varepsilon \ll 1$ is a small number taken to be 10^{-4} in the calculations below. This additional term permits the additional constraint that $H=1$ at the downstream end of the grid $\chi=L$ and thereby suppresses a solution describing a horizontal interface in which the derivative of film thickness on the left-hand side of Eq. (8) balances the constant on the right-hand side.

To implement finite differences, new variables χ' and Ψ' are defined that permit more mesh points to be located near $\chi=0$ and $\Psi=0$, namely, $\chi'=[\log(\chi+\delta_\chi)-\log(\delta_\chi)]/[\log(L+\delta_\chi)-\log(\delta_\chi)]$ and $\Psi'=[\log(\Psi+\delta_\Psi)-\log(\delta_\Psi)]/[\log(1+\delta_\Psi)-\log(\delta_\Psi)]$, where δ_χ and δ_Ψ are constants. In the calculations, $\delta_\chi=10^{-6}$ and $\delta_\Psi=10^{-2}$, and the numbers of uniform segments in the χ' and Ψ' directions were 100 and 50, respectively. The solution was obtained iteratively in MATLAB by Newton's method. For most cases, a solution of Eq. (8) without the term in $dH/d\chi$, obtained as previously described [3], provided an initial guess. As $\mathrm{Re}\tan(\theta)$ was set to smaller values, the previously converged solution supplied an initial guess. In addition to numerical solutions of the boundary-layer equation, solutions of the Navier-Stokes equation were generated by the finite element method [3].

An approach simpler than the Von Mises transformation is to assume a velocity profile and to integrate Eq. (1) across the film. The partial differential equation thereby reduces to an ordinary differential equation. A frequent assumption is that the velocity profiles at all cross sections are geometrically similar, and a common choice for the shape is a half parabola. For the problem at hand, however, a geometrically similar profile fails if there is a critical point, and to avoid this outcome a more general velocity profile is employed. With $\eta=y/h$,

$$uh/q=A[\eta-5\eta^2/2+4\eta^3/3]+3[\eta-\eta^2/2] \quad (0\leqslant\eta\leqslant 1) \tag{13}$$

The function $A(x)$ alters the shape of the velocity profile and is determined as part of the solution. This profile is a cubic polynomial that reduces to a half parabola for $A=0$, and in the present problem A asymptotes to zero downstream. Eq. (13) is consistent with Eqs. (4) and (5). Velocity component v follows from Eqs. (13), (3), and (5), and pressure follows from Eqs. (2) and (4).

$$p=\rho G\cos(\theta)(h-y) \tag{14}$$

Equation (1), evaluated from these expressions for u, v, and p, leaves residual R. The two equations required to solve for H and A are generated by requiring the average of the residual to be zero over two intervals.

$$\frac{1}{\omega}\int_0^\omega R\,d\eta=0 \tag{15}$$

The extent of an interval is specified by ω, $0<\omega\leqslant 1$. The choice $\omega=1$ gives an overall momentum balance.

$$\left[\frac{3}{\mathrm{Re}\tan(\theta)}-\frac{\alpha}{H^3}\right]\frac{dH}{d\chi}+\frac{1}{H^2}\frac{d\alpha}{d\chi}=3-\frac{3+A}{H^3} \tag{16}$$

$$\alpha=6/5-A/15+A^2/105 \tag{17}$$

Computational experiments were carried out over the range of second values for ω. The outcome, summarized below, leads to the limit of Eq. (15) as $\omega\to 0$ with the result $R=0$ at $\eta=0$.

$$0=-1+\frac{1}{\mathrm{Re}\tan(\theta)}\frac{dH}{d\chi}+\frac{5A/3+1}{H^3} \tag{18}$$

Eqs. (16) and (18) can be rearranged as

$$-\alpha\frac{dH}{d\chi}+H\frac{d\alpha}{d\chi}=4A \tag{19}$$

$$\frac{dH}{d\chi}=\mathrm{Re}\tan(\theta)\left[1-\frac{5A/3+1}{H^3}\right] \tag{20}$$

A solution to Eqs. (19) and (20) is sought for H and A that asymptotes to fully developed flow downstream, $A\to 0(\chi\to\infty)$ and from Eq. (20) $H\to 1(\chi\to\infty)$. A numerical integration is started from an asymptotic solution obtained by linearizing Eqs. (19) and (20) about fully developed flow. The asymptotic solution comprises terms in $e^{m\chi}$ where m is the root of a quadratic equation. For θ positive and less than 90 deg, there is one positive and one negative real root, and the negative root is selected so that the departure from fully developed flow decays downstream.

For a velocity profile that is geometrically similar at each cross section, A is a constant and Eq. (16), the overall momentum balance, reduces to

$$\left[\frac{3}{\mathrm{Re}\tan(\theta)}-\frac{\alpha}{H^3}\right]\frac{dH}{d\chi}=3-\frac{3+A}{H^3} \tag{21}$$

The coefficient of $dH/d\chi$ in this equation determines whether flow is subcritical (coefficient positive) or supercritical (coefficient negative) according to wave propagation [6]. The fully developed flow is critical whenever $\mathrm{Re}\tan(\theta)=3/\alpha$. For flow that is everywhere supercritical, Eq. (21) admits a solution that tends to fully developed flow. On the other hand, if the flow is everywhere subcritical, or if the flow passes from supercritical to subcritical, there is no solution to Eq. (21) tending to fully developed flow. Moreover, the singularity at the critical point cannot be removed by requiring that the right-hand-side of Eq. (21) vanish at the critical point. Therefore, a velocity profile of fixed shape fails in the problem at hand.

Results

When the initial film thickness is much less than that far downstream ($H\ll 1$), gravitational effects are initially negligible and the solution is a well known similarity solution for which film thickness grows linearly [3]. This similarity solution is a Jeffery-Hamel flow, an exact solution of the Navier-Stokes equation for radially diverging streamlines [13]. Equations (16)–(18) admit such a solution, specifically $A=-3/5$, $\alpha=1088/875$, and $dH/d\chi=525/272$, if the terms arising from gravity are dropped or, equivalently, if just the leading terms are retained as $H\to 0$. Choices for ω in Eq. (15) other than $\omega\to 0$ do not produce this limiting case and so are less useful. Figure 3 illustrates this outcome for $\mathrm{Re}=50$ and $\theta=3$ deg. Different nonzero values for ω yield similarly shaped but truncated solution curves that abruptly

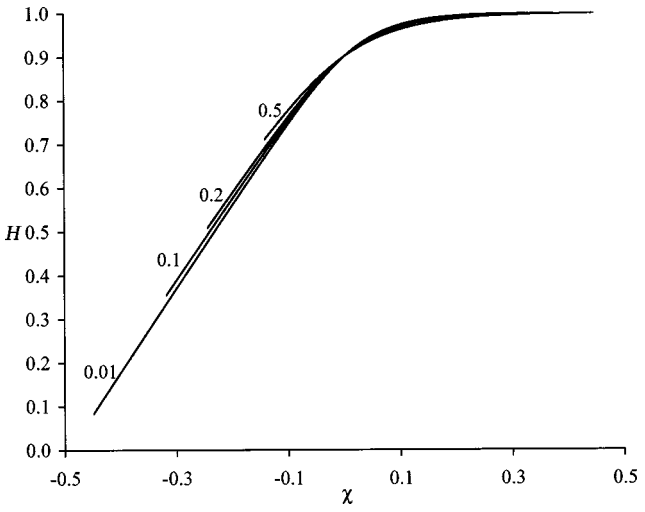

Fig. 3 Film profiles for Re=50 and θ=3 deg at four values of ω in Eq. (15). The profiles terminate abruptly because of a zero determinant.

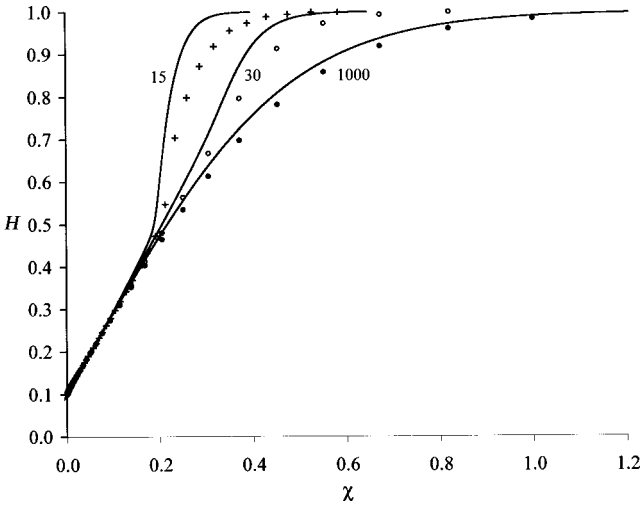

Fig. 4 Film profiles for three values of Re at θ=3 deg from Eqs. (19) and (20) (solid lines) and from the boundary-layer equation (points)

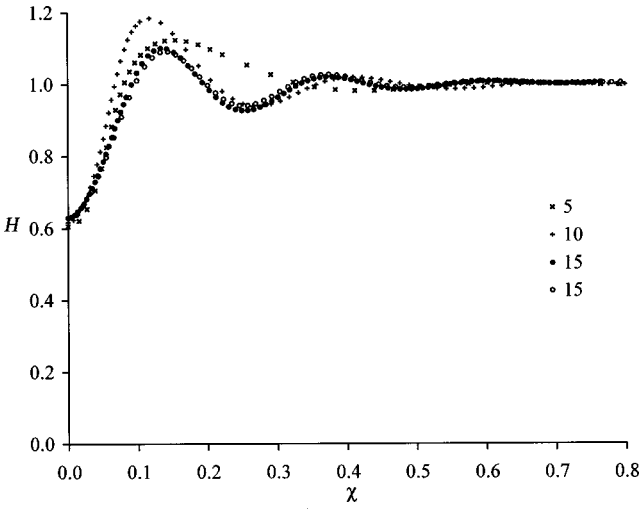

Fig. 5 Film profiles by the finite element method for three values of Re at θ=3 deg. Results for two meshes at Re=15 support a conclusion that the waves are not a numerical artifact.

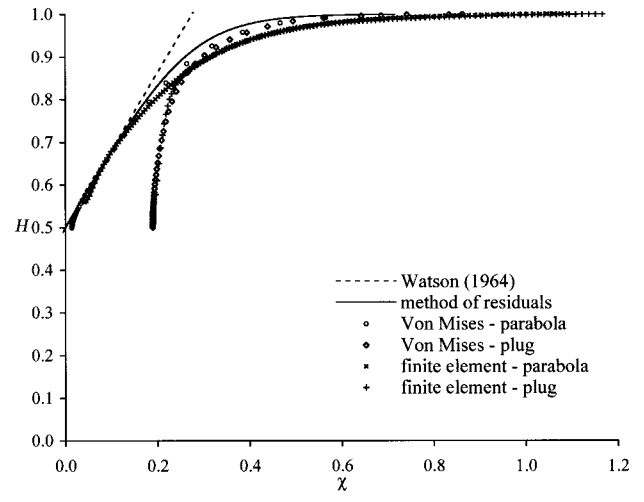

Fig. 6 Film profiles for Re=50 and θ=3 deg from the solution of the boundary layer equation by the method of residuals, from the solution of the boundary layer equation by the Von Mises transformation, and from the solution of the Navier-Stokes equation by the finite-element method. Also shown is the linear profile for negligible gravity [14].

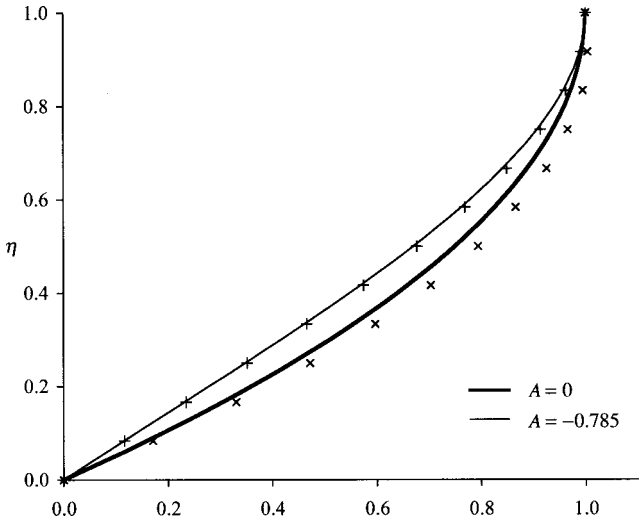

Fig. 7 Extreme velocity profiles for Re=30 and θ=3 deg from the method of residuals (solid curves) and from the finite element method (points)

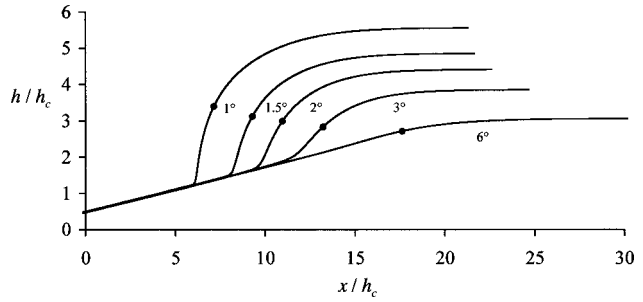

Fig. 8 Film profiles at five angles of inclination for the conditions of the photo. The circles show the location where the coefficient of $dH/d\chi$ in Eq. (16) vanishes.

end where the determinant of the equations becomes zero. Consequently, all of the following results are for the choices ω=1 and $\omega \rightarrow 0$ in Eq. (15).

Equations (19) and (20) admit a solution at Reynolds numbers of order unity and greater as shown in Fig. 4 for θ=3 deg. Also shown in Fig. 4 are solutions of the boundary layer equation by the Von Mises transformation with an initial parabolic velocity profile. The agreement improves as Re increases. The dimensionless profile does not change for values of Re exceeding 1000. At Reynolds numbers of order unity, the small-slope assumption breaks down, and solutions to the Navier-Stokes equation by the finite-element method produce film profiles that oscillate spatially as shown in Fig. 5. The boundary-layer equations do not capture these standing waves.

A more detailed comparison for Re=50 and θ=3 deg is shown in Fig. 6. The linear profile for negligible gravitational effects [14] is shown and is closely approached by the profile from the method of residuals, Eqs. (19) and (20). Solutions of the Navier-Stokes equation by the finite element method and of the boundary-layer equation by the Von Mises transformation for the cases of initial plug and parabolic velocity profiles are also shown and are nearly indistinguishable. The film profile in the parabolic case quickly approaches the Jeffery-Hamel similarity solution, but that in the plug case approaches fully developed flow directly. The method of residuals cannot capture differences arising from initial velocity profiles.

Velocity profiles according to the method of residuals are com-

pared with those from the finite element method in Fig. 7 for Re=30 and θ=3 deg. Velocity profiles for the extreme values of A, 0 and −0.785, are plotted as smooth curves. The extreme profiles from the finite-element method are plotted as points. The method of residuals captures the range of velocity profiles reasonably well, and this agreement supports the conclusion that a velocity profile of fixed shape is unworkable in the present problem.

Figure 8 shows film profiles by the method of residuals at Re =16, the value for the conditions of the experimental observation. In accordance with Fig. 1, the profiles show a prominent standing wave that shifts downstream and fades as the inclination of the plane increases.

Concluding Remarks

Although the shape of the velocity profile changes in the transition from supercritical to subcritical flow, the change is modest according to Fig. 7. Nonetheless, any inference that a half parabola should suffice for the velocity profile is incorrect. There is a region in the flow where the dominant terms in Eqs. (19) and (20) nearly cancel. The small difference is offset by the term related to the changing shape of the profile, the term in $d\alpha/d\chi$. This term precludes a singular solution and provides access to fully developed flow downstream.

The cubic velocity profile approximates Jeffery-Hamel flow more accurately than a parabolic velocity profile. The slope of the linear film profile determined above, 1.93, is near the expected value, 1.81 [14]. On the other hand, a parabolic velocity profile gives 2.5 [3]. A cubic profile, unlike a parabolic profile, can accommodate the inflection point at the wall inherent in the Jeffrey-Hamel solution.

The choice $\omega \rightarrow 0$ in Eq. (15) is equivalent to evaluating the Navier-Stokes equation at the wall, a common step in classical boundary-layer analysis. The inertial terms vanish at the wall, and it is that outcome that precludes a vanishing determinant. So, our findings support the classical approach to providing an additional equation.

Flow is everywhere supercritical in the case of a vertical plane, and consequently the many analyses of that special case have not encountered a critical point.

The evident success of the present approach suggests that it be generalized to more complicated flows and explored more extensively. Such work is in progress.

Acknowledgment

The photograph was taken by Paul DeVries of Eastman Kodak Company.

References

[1] Kistler, S. F., and Schweizer, P. M., eds., 1997, *Liquid Film Coating*, Chapman & Hall, New York.

[2] Schlichting, H., 1979, *Boundary-Layer Theory*, 7th edition, McGraw-Hill, New York, pp. 157–158.

[3] Ruschak, K. J., and Weinstein, S. J., 2000, ''Thin-Film Flow at Moderate Reynolds Number,'' ASME J. Fluids Eng., **122**, pp. 774–778.

[4] Alekseenko, S. V., Nakoryakov, V. E., and Pokusaev, B. G., 1994, *Wave Flow of Liquid Films*, Begell House, Inc., New York.

[5] Thomas, S., Hankey, W., and Faghri, A., 1990 ''One-Dimensional Analysis of the Hydrodynamic and Thermal Characteristics of Thin Film Flows Including the Hydraulic Jump and Rotation,'' ASME J. Heat Transfer, **112**, pp. 728–735.

[6] Ruschak, K. J., and Weinstein, S. J., 1999, ''Viscous Thin-Film Flow Over a Round-Crested Weir,'' ASME J. Fluids Eng., **121**, pp. 673–677.

[7] Anderson, H. I., 1984, ''On Integral Method Predictions of Laminar Film Flow,'' Chem. Eng. Sci., **39**, pp. 1005–1010.

[8] Anderson, H. I., 1987, ''The Momentum Integral Approach to Laminar Thin-Film Flow,'' Proc. ASME Symposium on Thin Films, Vol. **48**, pp. 7–13.

[9] Higuera, F. J., 1994, ''The hydraulic jump in viscous laminar flow,'' J. Fluid Mech., **274**, pp. 69–92.

[10] Ruyer-Quil, C., and Manneville, P., 1998, ''Modeling film flows down inclined planes,'' The European Physical Journal B, **6**, pp. 277–292.

[11] Bruley, D. F., 1965, ''Predicting Vertical Film Flow Characteristics in the Entrance Region,'' AIChE J., **11**, 945–950.

[12] Cerro, R. L., and Whitaker, S., 1971, ''Entrance Region Flows With a Free Surface: the Falling Liquid Film,'' Chem. Eng. Sci., **26**, pp. 785–798.

[13] Rosenhead, L., 1940, ''The Steady Two-Dimensional Radial Flow of Viscous Fluid Between Two Inclined Plane Walls,'' Proc. R. Soc. London, Ser. A, **175**, pp. 436–467.

[14] Watson, E. J., 1964, ''The Radial Spread of a Liquid Jet Over a Horizontal Plane,'' J. Fluid Mech., **20**, pp. 481–499.

On Preferred Perturbations Selected by Centrifugal Instability

Oleg A. Likhachev
Research Associate Professor, The University of Arizona, Department of Aerospace and Mechanical Engineering, 1130 N. Mountain, P. O. Box 210119, Tucson, AZ 85721-0119
e-mail: oleg@u.arizona.edu

Introduction

A new theoretical treatment of the Taylor-Gortler instability of laminar boundary layers with streamline curvature is brought to the reader's attention in the present note. It is well established that a boundary layer over a concave surface is unstable with respect to centrifugal instability, manifested by the presence of a spanwise vortex array consisting of evenly spaced counter-rotating vortices. One notices a plethora of theoretical analyses devoted to the problem while reviewing the literature (see, e.g., reviews by Floryan [1] and Saric [2]). It was a concern about a disparity in the theoretical predictions that stimulated the study of Floryan and Saric [3]. They elaborated a general approach to the problem by formulating the boundary layer and disturbance equations in a general, orthogonal, curvilinear system of coordinates and the order-of-magnitude analysis of the equations. Recently, Bottaro and Luchini [4] took a fresh look at local theories in the hope of obtaining a more consistent formulation of the problem. However, the existing theories predict nothing about which characteristic wavelength of the vortices will actually appear for a given experimental setup. Based on the experimental findings of Tani and Sakagami [5] and Bippes [6], it became apparent that a flow with a favorable streamline curvature is indifferent to a perturbation wavenumber. This experimental observation seems to be consistent with the theory, which does not provide any preferred wavelength of the instability. Due to Swearingen and Blackwelder [7], the only mechanism of wavelength selection is a competition of perturbations with different amplification rates. Only those corresponding to the most-amplified ones are remained. However, in spite of the widely accepted success of the quasi-parallel theory, some of the theoretical predictions remain in question. An existence of the critical Gortler number at a finite spanwise wavenumber is yet unresolved. In fact, the first manifestations of the presence of spanwise vortices are noticed for the Gortler numbers that are an order of magnitude larger than the long-wavelength asymptote predicted by the theory.

In the present study, an attempt was made to simplify a formulation of the theoretical problem as much as possible while retaining the most-important features of the phenomenon. These features can be outlined as follows: First of all, one deals with *a secondary steady flow* imposed on the primary laminar boundary layer. Analysis of this coherent small-intensity motion can be carried out along lines similar to the regular similarity approach used for the initial boundary layer. Second, the nature of the centrifugal

Contributed by the Fluids Engineering Division for publication in the JOURNAL OF FLUIDS ENGINEERING. Manuscript received by the Fluids Engineering Division October 5, 2000; revised manuscript received March 27, 2001. Associate Editor: D. R. Williams.

instability is *inviscid*. It means that one can consider, without loss of generality, the limit $\varepsilon \ll 1$ and $\mathrm{Re} \gg 1$ while keeping the appropriate combination of the parameters constant. Here, $\varepsilon (\equiv \delta/R)$ is the curvature parameter, which is a ratio of two length scales that govern boundary layer type flows with streamline curvature: the radius of curvature $R(x)$ and the boundary layer thickness $\delta(x)$. It is customary to use ε as a small parameter in the order-of-magnitude analysis. The Reynolds number, $\mathrm{Re} = \delta U_\infty/\nu$, is based on the local reference scales of the mean flow. Finally, *nonparallel effects* due to a divergence of the boundary layer need to be addressed in the stability analysis. It must be admitted here that great attention was paid to the asymptotic solution and the nonparallel effects in previous studies. However, as shown below, not all terms due to the first assumption were involved in the solution. These extra terms significantly affect stability characteristics of the laminar boundary layer with streamline curvature.

Governing Equations

Consider the stability of a laminar boundary layer flowing along a concave wall. The analysis begins with the equations of motion and continuity in an orthogonal body-oriented coordinate system introduced by Goldstein [8]. When the curvature parameter is small, $\varepsilon \ll 1$, all of the curvature terms in the equations of a basic state may be neglected and the mean flow in the boundary layer approximation is represented by the Blasius boundary layer. It is anticipated that a three-dimensional, steady, spatially growing disturbance imposed on the primary boundary layer can be represented in a form of the asymptotic expansion:

$$\begin{aligned}(u', v') = U_\infty \{ & A(\varphi)[\hat{u}(\eta), v(\eta)] \\ & + \varepsilon [u_1(\varphi, \eta), v_1(\varphi, \eta)] + O(\varepsilon^2)\} \\ & \times \cos(\beta z) \exp\left(\int_{\varphi_0}^{\varphi} \hat{\gamma} d\varphi \right)\end{aligned}$$

$$w' = U_\infty [A(\varphi) w(\eta) + \varepsilon w_1(\varphi, \eta) + O(\varepsilon^2)] \sin(\beta z) \exp\left(\int_{\varphi_0}^{\varphi} \hat{\gamma} d\varphi \right) \tag{1}$$

$$p' = U_\infty^2 [A(\varphi) p(\eta) + \varepsilon p_1(\varphi, \eta) + O(\varepsilon^2)] \cos(\beta z) \exp\left(\int_{\varphi_0}^{\varphi} \hat{\gamma} d\varphi \right)$$

Here, the slow variable $d\varphi = dx/R(x)$ is introduced, where x is a coordinate along a surface; η and z are coordinates at right angles to a surface and in the spanwise direction, made dimensionless with the length scale $\delta = C(\nu x/U_\infty)^{1/2}$; U_∞ is the free-stream velocity; and $\hat{\gamma}$ and β are the dimensionless amplification rate and the spanwise wavenumber, respectively. Based on experimental evidence, it is generally recognized that the quasi-exponential growth of the linear amplification phase persists far downstream. It is also assumed here that, at leading order on a small parameter, the steady perturbations are self-similar ones, along lines similar to the basic flow, and one should remember while taking derivatives along the flow that the perturbation field implicitly depends on x as a function of $\eta = y/\delta(x)$. In a number of studies (e.g., Ragab and Nayfeh [9], Floryan and Saric [3], Finnis and Brown [10], Bottaro and Luchini [4] only the nonparallel effects associated with a mean flow divergence were taken into account at the stability analysis. Substituting solution (1) into perturbation equations in body-oriented coordinates and making use of the transformations $\gamma = \varepsilon\ \mathrm{Re}\ \hat{\gamma}$, $u = \varepsilon\ \mathrm{Re}\ \hat{u}$, and $q = \mathrm{Re}\ p$, one gets, at leading order on the small curvature parameter, $\varepsilon \ll 1$, the linear stability equations of the form

$$\begin{aligned} \gamma U u + Go^2 U' v - B f u' &= u'' - \beta^2 u \\ \gamma U v + V' v - B f v' + 2Uu + q' &= v'' - \beta^2 v \\ \gamma U w - B f w' - \beta q &= w'' - \beta^2 w \\ \gamma u + Go^2 (v' + \beta w) &= \beta \eta U u' \end{aligned} \tag{2}$$

Here, the prime denotes the derivative with respect to η; $Go = \mathrm{Re}\sqrt{\varepsilon}$ is the Gortler number; $B = C^2/2 (\equiv \mathrm{Re}\ \delta/2x)$, the constant factor that is $B = 1.481$, if the displacements thickness, δ_*, is the reference length scale; while $f(\eta)$ is the dimensionless stream function of the basic state, $\vec{U}/U_\infty = (U, V/\mathrm{Re})$, where $U = f'$ and $V = B(\eta U - f)$. The system (2) that is subject to homogeneous boundary conditions

$$\begin{aligned} u = v = w = 0 \quad & \text{at} \quad \eta = 0 \\ u = v = w = 0 \quad & \text{at} \quad \eta \to \infty \end{aligned} \tag{3}$$

represents the eigenvalue problem with respect to $\gamma(\beta, Go)$, and the Riccati factorization method was used for its solution. It becomes apparent from (2) that nonparallel effects are already taken into account at leading order on the curvature parameter. Solutions to Eqs. (2) depend explicitly neither on the curvature parameter nor on the Reynolds number; however, the growth rate and a scale of the downstream velocity perturbation do depend on a particular experimental setup even for the same value of the Gortler number.

The amplitude function $A(\varphi)$ is arbitrary at leading order on the small parameter, however, it is determined by imposing the solvability condition at the next order (see, e.g., Nayfeh [11]). By using the notation

$$\{\psi_{1j} : j = 1, \ldots, 6\} \Rightarrow \{v, u, w, q, Du, Dw\} \tag{4}$$

equations (2) can be rewritten in the compact form

$$D\psi_{1j} - \sum_{k=1}^{6} a_{jk} \psi_{1k} = 0 \quad \text{for} \quad j = 1, \ldots, 6 \tag{5}$$

where $D = \partial/\partial\eta$. Making use of Goldstein's equations, the next order problem is written as

$$D\psi_{2j} - \sum_{k=1}^{6} a_{jk} \psi_{2k} = E_j (dA/d\varphi) + G_j A \quad \text{for} \quad j = 1, \ldots, 6 \tag{6}$$

where E_j and G_j are known functions of the primary and the secondary flow quantities (see Appendix). According to the asymptotic expansion (1), functions ψ_{2j} are defined by the expression

$$\{\psi_{2j} : j = 1, \ldots, 6\} \Rightarrow \{v_1, u_1, w_1, q_1, Du_1, Dw_1\}$$

which is similar to (4). Since the homogeneous parts of (6) are the same as (5) and since the latter have a nontrivial solution, the inhomogeneous equations (6) have a solution if and only if the homogeneous parts are orthogonal to every solution of the adjoint homogeneous problem, that is

$$\int_0^\infty \sum_{j=1}^{6} [E_j (dA/d\varphi) + G_j A] \zeta_j d\eta = 0 \tag{7}$$

where the $\zeta_j(\eta)$ are solutions of the adjoint homogeneous problem

$$\begin{aligned} D\zeta_j + \sum_{k=1}^{6} a_{kj} \zeta_k = 0 \qquad & \text{for} \quad j = 1, \ldots, 6 \\ \zeta_4 = \zeta_5 = \zeta_6 = 0 \qquad & \text{at} \quad \eta = 0 \\ \zeta_4, \zeta_5, \zeta_6 \to 0 \quad & \text{as} \quad \eta \to \infty \end{aligned} \tag{8}$$

The equation for the amplitude $A(\varphi)$ comes from the solvability condition (7)

$$M(\varphi) dA/d\varphi + N(\varphi) A = 0 \tag{9}$$

where

$$M(\varphi)=\int_0^\infty \sum_{j=1}^{6} E_j \zeta_j d\eta, \quad N(\varphi)=\int_0^\infty \sum_{j=1}^{6} G_j \zeta_j d\eta \qquad (10)$$

Thus an expression for the disturbances to leading order has the exponential form

$$\vec{u}' \propto A_0 \vec{u}(\eta) \exp\left[\int_{\varphi_0}^{\varphi} (\hat{\gamma} - N/M) d\varphi\right] \qquad (11)$$

where $\vec{u}(\eta)$ is the eigenvector (4) calculated for the given x-location and A_0 is an arbitrary constant due to the linearity of the problem.

Results and Discussion

Two neutral stability curves, $\hat{\gamma}=0$, in the linear approximation are shown in Fig. 1. The dashed line represents the classical treatment of the problem by Gortler, which is a solution to Eqs. (2)–(3), when the factor B is equated to zero. The calculation reproduces Gortler's corrected neutral curve due to Herbert [12]. The neutral curve calculated in the framework of the present model is shown with the solid line. Since the perturbation growth/decay rate depends on a particular experimental setup, $\hat{\gamma} = \gamma(\beta, Go)/(\varepsilon\ \mathrm{Re})$ (not a linear neutral curve!), the curves of a constant amplification rate, $\hat{\gamma}=const$, may be given here only as an arbitrary example, in our case for $\varepsilon(x)\equiv 0.01$. As should be expected, both neutral curves have the same short-wave asymptote. However, contrary to the locally parallel approach, the latter neutral curve has a minimum at a finite value of the spanwise wavenumber. One can see from Fig. 1 that the theoretical predictions are consistent with the experimental observations. It is also well established experimentally that longitudinal vortices, occurring due to centrifugal instability, preserve their spanwise scale while developing downstream. This feature of the vortices can be exploited to relate the local Gortler number to the measured local dimensionless spanwise wavenumber. Thus, based on the definition of the Gortler number, one obtains the relationship $Go \propto \beta^{3/2}$ since $\beta=(2\pi/\lambda_0)\delta$, where λ_0 is the dimensional spanwise wavelength of the vortices. According to Fig. 1, the straight lines

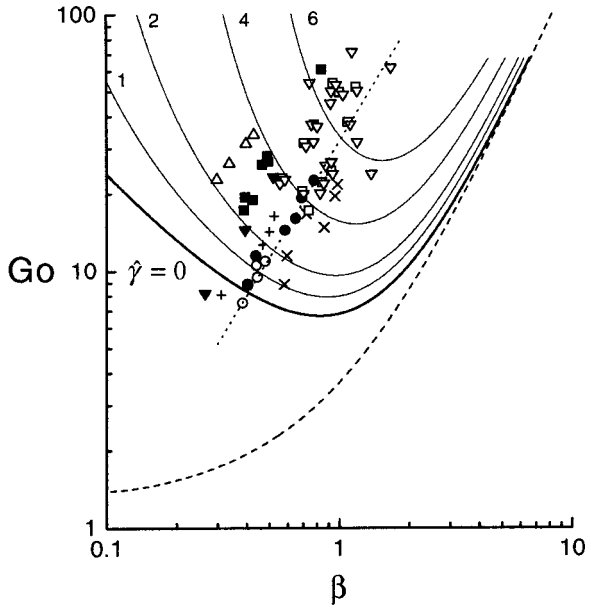

Fig. 1 Neutral stability curves obtained from the Gortler model, ----, and in the present study, —. Experimental points due to Tani [13]: ○, +, ▼, ■, △; Winoto and Crane [14]: □; Crane and Sabzvari [15]: ▽; Finnis and Brown [10]: ×, ●. The dotted line represents a function $Go \sim \beta^{3/2}$ corresponding to a constant dimensional wavenumber.

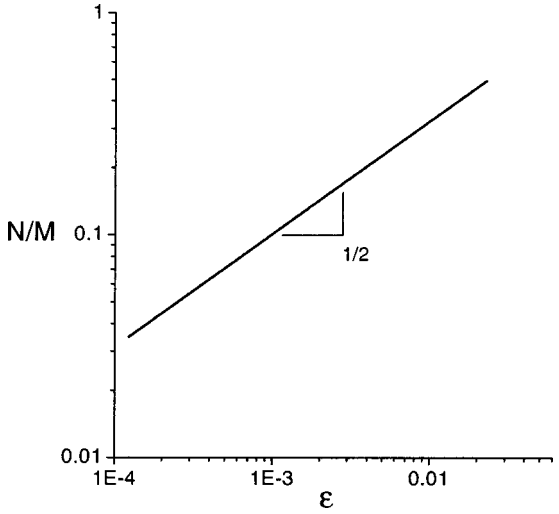

Fig. 2 Nonlinear correction to the amplification rate for β=0.4 and Go=8.282

with slope 3/2, which correspond to a constant dimensional wavenumber, cross the neutral curve at almost a right angle over a wide range of the parameters (Go,β). Small external perturbations with β from this range have almost the same amplification rate and, hence, an equal chance of observation. The large scattering of experimental data in this region supports this finding. On the other hand, based on the present calculations, a preferred naturally occurring perturbation does exist, and, according to Fig. 1, has a spanwise wavenumber, $\beta\approx 0.4$, and is a neutral one at $Go\approx 8.28$. However, any external factor imposed on the flow may give rise to a perturbation with a wavenumber from the instability region whenever the flow Gortler number is large enough, $Go_{\delta_*} > 6.8$ (or for the generally used Gortler number based on the momentum thickness, $Go_\theta > 1.63$, since for the Blasius boundary layer the shape factor is $\delta_*/\theta = 2.59$).

Correction to the amplification rate due to a slight nonlinearity, represented by the ratio N/M in Eq. (11), depends on both the curvature parameter and the Reynolds number. This also may explain a large scattering of the data since they correspond to different experimental setups. It is easily seen from Eq. (10) and expressions for the functions E_j and G_j that $N/M = F(\beta, Go)/\mathrm{Re}$. Consequently, for a constant β and Go, the correction is proportional to a square-root of the curvature parameter, $N/M \sim \sqrt{\varepsilon}$. As follows from the linear approach analyzed above, a divergence of the boundary layer has a stabilizing effect on centrifugal instability in the first-order approximation. However, the same stabilizing effect has a slightly nonlinear correction, adding to the stability of the laminar boundary layer flowing over a concave wall. The correction to the linearly neutral perturbation corresponding to β=0.4 and Go=8.282 is shown in Fig. 2 versus ε. It is seen from the plot that the stabilizing effect due to the flow divergence is more pronounced for larger curvature parameters. For example, for the small curvature parameter used by Finnis and Brown [10] in their experiments, $\varepsilon(=\delta_{*1}/R)\approx 5\cdot 10^{-4}$, the correction to the linear neutral parameters β and Go does not exceed 1 percent.

Conclusions

It has been shown in a number of theoretical studies devoted to the linear analysis of the centrifugal instability of a laminar boundary layer over a concave surface that a divergence of the mean flow contributes to the flow instability. In the present study, a new treatment of the centrifugal instability is proposed. It is assumed that the secondary steady flow in the form of counter-rotating vortices is imposed on the primary boundary layer and

has a self-similar form if rendered nondimensional with the local reference scales. Contrary to the existing nonparallel approaches, the opposite conclusion is drawn—the nonparallel effects are strongly stabilizing. The calculated linear neutral stability curve is in a very good agreement with experimental data regarding the flow parameters at the first manifestation of the instability. The preferred naturally occurring perturbation wavelength was also identified. The calculated critical Gortler number is, by an order of magnitude, larger than that provided by recent theoretical investigations and is consistent with the data. Finally, it was also shown that the slightly nonlinear correction to the amplification rate due to a divergence of the mean flow is sufficiently small to change the flow stability characteristics for moderate curvature parameters.

Appendix

$$E_1 = -u, \quad E_2 = E_3 = 0, \quad E_4 = -\mathrm{Re}\ Uv,$$

$$E_5 = \mathrm{Re}Uu, \quad E_6 = \mathrm{Re}\ Uw$$

$$G_1 = v + i\beta\eta w, \quad G_2 = G_3 = 0,$$

$$G_4 = (\beta^2 + BDV)\eta v - (1 - B\eta V)Dv + \eta Dq$$

$$G_5 = -Go^2 D(\eta U)v - (\beta^2\eta + BV)u + \gamma q + (1 - B\eta V)Du$$

$$G_6 = -\beta^2\eta w + (1 - B\eta V)Dw - i\beta\eta q$$

Acknowledgments

This work was supported by a grant from the Office of Naval Research (contract number N00014-991-0883) monitored by Dr. Patrick Purtell.

References

[1] Floryan, J. M., 1991, ''On the Gortler Instability of Boundary Layers,'' Prog. Aerosp. Sci., **28**, pp. 235–271.
[2] Saric, W. S., 1994, ''Gortler Vortices,'' Annu. Rev. Fluid Mech., **26**, pp. 379–409.
[3] Floryan, J. M., and Saric, W. S., 1982, ''Stability of Gortler Vortices in Boundary Layers,'' AIAA J., **20**, No. 3, pp. 316–324.
[4] Bottaro, A., and Luchini, P., 1999, ''Gortler Vortices: Are They Amenable to Local Eigenvalue Analysis?'' Eur. J. Mech. B/Fluids, **18**, pp. 47–65.
[5] Tani, I., and Sakagami, J., 1964, ''Boundary-Layer Instability at Subsonic Speeds,'' *Proceedings of Third Congress of International Council of Aerospace Sciences*, Spartan, Washington, DC, pp. 391–403.
[6] Bippes, H., 1972, ''Experimentelle Untersuchung des laminar-turbulenten Umschlags an einer parallel angestromten konkaven Wand,'' *Mathematisch-naturwissenschaftliche klass, Heidelberger Akademie der Wissenschaften*, Sitzungsberichte, **3**, pp. 103–180; translated as ''Experimental Study of the Laminar-Turbulent Transition of a Concave Wall in Parallel Flow,'' NASA-TM-75243.
[7] Swearingen, J. D., and Blackwelder, R. F., 1986, ''Spacing of Streamwise Vortices on Concave Walls,'' AIAA J., **24**, pp. 1706–1709.
[8] Goldstein, S., 1938, *Modern Developments in Fluid Dynamics, Vol. I.*, Oxford University Press.
[9] Ragab, S. A., and Nayfeh, A. H., 1981, ''Gortler Instability,'' Phys. Fluids, **24**, pp. 1405–1417.
[10] Finnis, M. V., and Brown, A., 1989, ''Stability of a Laminar Boundary Layer Flowing Along a Concave Surface,'' ASME J. Turbomach., **11**, pp. 376–386.
[11] Nayfeh, A. H., 1980, ''Stability of Three-Dimensional Boundary Layers,'' AIAA J., **18**, pp. 1706–1709.
[12] Herbert, T. H., 1979, ''Higher Eigenstates of Gortler Vortices,'' *Recent Developments in Theoretical and Experimental Fluid Mechanics*, U. Muller, K. G. Roesner, and B. Schmidt, eds., Springer-Verlag, New York, pp. 331–338.
[13] Tani, I., 1962, ''Production of Longitudinal Vortices in the Boundary Layer Along a Concave Wall,'' J. Geophys. Res., **67**, pp. 3075–3081.
[14] Winoto, S. H., and Crane, R. I., 1980, ''Vortex Structure in Laminar Boundary Layers on a Concave Wall,'' Int. J. Heat Fluid Flow, **2**, pp. 221–231.
[15] Crane, R. I., and Sabzvari, J., 1984, ''Laser-Doppler Measurements of Gortler Vortices in Laminar and Low-Reynolds-Number-Turbulent Boundary Layers,'' *1st Int. Symp. on Applications of Laser-Doppler Anemometry to Fluid Mechanics*, Lisbon; also, 1984, *Laser Anemometry in Fluid Mechanics*, R. J. Adrian et al., eds., Lladoan-Inst. Sup. Tec., Lisbon, pp. 19–35.

The Transient for MHD Stokes's Oscillating Plate: An Exact Solution

R. K. Deka and U. N. Das
Department of Mathematics, Gauhati University, Guwahati(Assam) 781 014, India

V. M. Soundalgekar
31A-12, Brindavan Society, Thane, 400 601, India

1 Introduction

Stokes [1] first presented an exact solution to the Navier-Stokes equation. The first solution is for the flow of a viscous incompressible fluid past an impulsively started infinite horizontal plate in its own plane and is known as Stokes's first problem, whereas the second solution was also presented by Stokes [1] in case of the flow of a viscous incompressible fluid past an infinite horizontal plate oscillating in its own plane and is also known as Stokes's second problem. These problems being of fundamental nature, these are referred in all the textbooks on viscous flow e.g., Schlichting [2]. However, this solution is not a complete solution because it does not satisfy the initial condition. Hence Stokes's solution is the steady-state solution, which applies after the effect of any initial velocity profiles has died out. The knowledge of the initial or the transient solution is essential in order to understand the full solution of flow past an oscillating plate in its own plane.

Since it is a fundamental solution, it has many applications, e.g., (i) acoustic streaming around an oscillating body, (ii) effect of fluctuating free stream on the boundary layer flow past a body; in this case, Stokes's result is considered as a perturbation in the high frequency limit. This is because for an incompressible fluid flow, it is immaterial whether the plate oscillates in a stagnant fluid or the plate is fixed and the fluid oscillates. The transient solution is also important in certain unsteady boundary layers e.g., those starting from rest or those with an external velocity having an arbitrary time dependence. Hence to understand the exact nature of these problems, the knowledge of the transient and the steady-state components is significant.

Panton [3] first presented the solution to transient problem in exact form in terms of standard mathematical functions. Panton [3] presented the transient and starting phase velocity distributions for the plate either oscillating as $\sin(T)$ or $-\cos(T)$. Physically the $\sin(T)$ or $-\cos(T)$ represents a standing wave passing through the origin or not passing through the origin. The effect of transversely applied magnetic field on the transient component of Stokes's solution, when induced magnetic field is negligible has not been studied in the literature. Hence the motivation to undertake this study. In Section 2, the mathematical analysis is presented; a solution to transient component is presented in terms of standard mathematical functions. The transient and starting velocity distributions are shown graphically. The results are discussed by comparing with those of Panton.

2 Mathematical Analysis

We assume that a viscous electrically conducting incompressible fluid surrounds a nonconducting horizontal plate. At time $t \leqslant 0$, the plate and the fluid are in a stationary state. At time $t > 0$, the plate starts oscillating in its own plane and a uniform magnetic filed of strength B_0 is applied in a direction transverse to the direction of the horizontal plate. The x-axis is taken

Contributed by the Fluids Engineering Division of THE AMERICAN SOCIETY OF MECHANICAL ENGINEERS. Manuscript received by the Fluids Engineering Division March 17, 1999; revised manuscript received May 1, 2001. Associate Editor: D. P. Telionis.

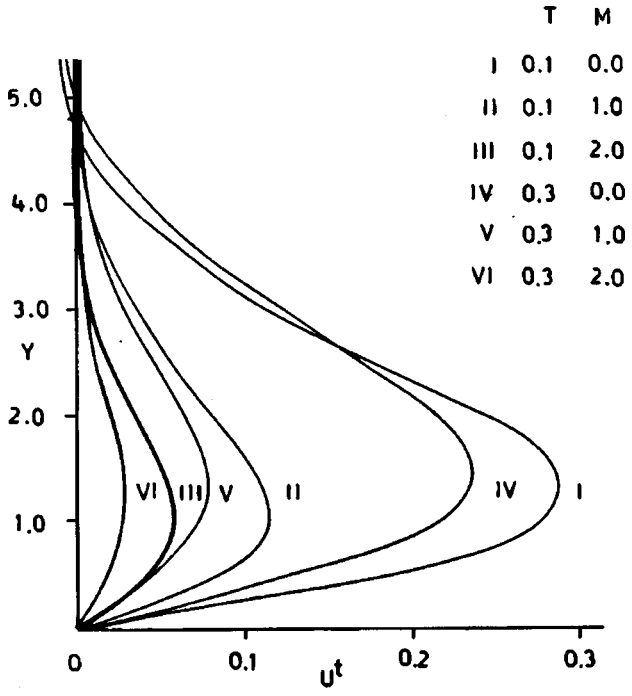

Fig. 1 Transient velocity distribution, plate velocity sin(*T*)

along the plate and the *y*-axis is taken normal to the plate. The velocity satisfies the nondimensional equation and boundary conditions:

$$\frac{\partial U}{\partial T}=\frac{\partial^2 U}{\partial Y^2}-MU \tag{1}$$

$$U\langle Y,0\rangle=0 \tag{2a}$$

$$U(0,T)=\sin(T) \tag{2b}$$

$$U(\infty,T)<\infty \tag{2c}$$

where the capital letters denote nondimensional variables which are defined by

$$U=u/u_0,\quad T=\omega t,\quad Y=y\sqrt{\omega/\nu},\quad M=(\sigma B_0^2)/\langle\rho\omega\rangle$$

where u_0 is the amplitude, ω the frequency, ν the kinematic viscosity, σ the electrical conductivity, ρ the density of fluid, and B_0 is the strength of the transverse magnetic field.

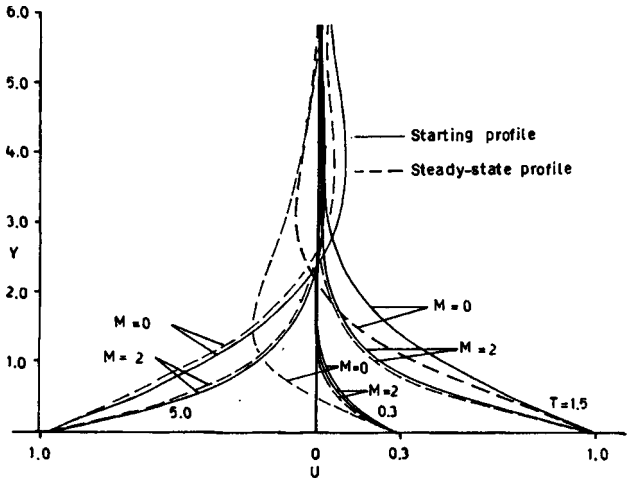

Fig. 2 Starting phase velocity profiles, plate velocity sin(*T*)

The velocity may be decomposed into a steady-state and transient component satisfying Eq. (1) as:

$$U=U^s+U^t \tag{3}$$

The steady-state component can be derived in the following form:

$$U=e^{-aY/\sqrt{2}}\sin\langle T-bY/\sqrt{2}\rangle \tag{4}$$

where

$$a=\sqrt{M+\sqrt{1+M^2}},\quad b=1/a$$

This solution (4) satisfies the boundary conditions (2*b*,*c*) but not the initial condition (2*a*). If the transient solution satisfies the boundary conditions:

$$U^t(Y,0)=-e^{-aY/\sqrt{2}}\sin(-bY/\sqrt{2})=\mathrm{Im}\,e^{-CY/\sqrt{2}} \tag{5a}$$

$$U^t(\infty,T)<\infty \tag{5b}$$

$$U^t(0,T)=0 \tag{5c}$$

where C is the complex constant $C=a-ib$, then the composition of the transient and steady-state solutions will completely satisfy Eqs. (1) and (2*a*,*b*,*c*,).

The general transient problem is solved by Laplace transform technique using the conditions (5*a*,*b*,*c*) as:

$$U^t(Y,T)=\mathrm{Im}\left[\frac{1}{2}e^{-(CY/\sqrt{2})-iT}\,erfc\sqrt{\frac{T}{2}}\left(C-\frac{Y}{T\sqrt{2}}\right)-\frac{1}{2}e^{(CY/\sqrt{2})-iT}\,erfc\sqrt{\frac{T}{2}}\left(C+\frac{Y}{T\sqrt{2}}\right)\right] \tag{6}$$

By plotting the transient solution we can get an idea of just how rapidly the dying character happens. The transient component of the velocity is given in Fig. 1. The curves decay rapidly as M increases and the maximum point moves further into the fluid. It is observed that the maximum velocity has been reduced to less than 0.03 even for smaller time $T=0.3$ for $M=2$, which indicates further that as M increases the maximum velocity reduces further for smaller time.

The complete starting velocity profiles are shown on Fig. 2. Velocity profiles are given for the case when the fluid is initially still and the plate is moved so that the velocity varies as sin(T). For comparison the steady-state solutions are plotted as dashed lines. The first set of curves at $T=0.3$ shows the viscous ''wave'' has penetrated only slightly into fluid and the penetration reduces as M increases. The corresponding steady-state velocity profile shows that the fluid does not show negative velocity as M increases as a departure from the case of Panton. The next curve at $T=1.5$ shows a deeper penetration and the fluid propagates inward sharply at $T=5.0$ as M increases. It is noticeable that the transient and steady-state curves are almost the same even for $T=0.3$, $M=2$ as observed in Fig. 1 and this is true for $T=1.5$, 5 for $M=2$ also. Thus in the presence of magnetic field the oscillation does not require longer time for the transition to decay.

3 Conclusions

(a) In the presence of magnetic field, maximum velocity falls rapidly and approaches the plate.
(b) The difference between the starting and the steady-state solutions is quite insignificant in the presence of magnetic field.

References

[1] Stokes, G. C., 1851, ''On the Effect of the Internal Friction of Fluids on the Motion of Pendulums,'' Trans. Cambridge Philos. Soc., **9**, pp. 8–106.
[2] Schlichting, H., 1960, *Boundary Layer Theory*, McGraw-Hill, New York.
[3] Panton, R., 1968, ''The Transient for Stoke's Oscillating Plate: A solution in Terms of Tabulated Functions,'' J. Fluid Mech., **31**, pp. 819–825.

Approximate Similarity of Confined Turbulent Coaxial Jets

P. J. Foster, J. M. MacInnes, and F. Schubnell
Department of Chemical and Process Engineering,
University of Sheffield, Sheffield S1 3JD, United Kingdom

Introduction

The turbulent flow produced when a jet of fluid is confined by an enclosure has many practical analogues in combusting furnace flows, arterial blood flows, and the ventilation of lungs, Slutsky and Menon [1]. The importance of this flow has led to investigations of the simplified case of the coaxial jet in a cylindrical duct as defined in Fig. 1. An analysis of enclosed coaxial jets is made here which unifies two previous theories of the approximate similarity of such flows. Also, computational fluid dynamics is used to investigate the flow to clarify the extent of similarity, the role of the static pressure boundary condition, and the choice of the density scale.

The flow is produced by an inner jet flow with nozzle radius, r_1, and uniform density and velocity, ρ_1 and u_1, and a secondary outer flow in the annular region between r_1 and r_2 with uniform conditions ρ_2 and u_2. The flow develops over a length, L, before exiting from the duct through an outlet. The principal feature of the flow which is of interest is the formation of a toroidal recirculation eddy, a section of which is shown in Fig. 1.

Previous work has emphasized the conditions under which the flows produced by two different coaxial jet flows could be expected to be similar. This has been a particular concern in the development of combustion devices, where preliminary testing of combustion enclosure designs with cold models is useful if the model flow can be satisfactorily linked with that in the actual combustion device. Thring and Newby [2] used physical and dimensional reasoning to derive a single nondimensional parameter

$$\theta_0=\frac{\dot{m}_1+\dot{m}_2}{\sqrt{G_1\rho_m\pi r_2^2}} \tag{1}$$

where $\dot{m}_1$ and $\dot{m}_2$ are the jet and secondary mass flow rates, respectively, G_1 is the axial momentum flow rate of the jet, and ρ_m is the density of the two streams when fully mixed. Matching this ''Thring-Newby'' parameter would lead to approximately similar flows away from the initial region of the jet.

Barchilon and Curtet [3] developed a one-dimensional model for the jet velocity excess, the jet width and the velocity in the outer flow and arrived at the similarity parameter, the ''Craya-Curtet number'':

$$C_t=\frac{U_k}{\sqrt{U_d^2-U_k^2/2}} \tag{2}$$

in which U_k and U_d are velocity scales arising from the flow rates of mass and momentum at the inlet:

$$U_k=\frac{1}{A}\int_A u\ dA \tag{3}$$

$$U_d^2=\frac{1}{A}\int_A\left(u^2+\frac{p}{\rho}\right)dA \tag{4}$$

Contributed by the Fluids Engineering Division of THE AMERICAN SOCIETY OF MECHANICAL ENGINEERS. Manuscript received by the Fluids Engineering Division December 16, 1998; revised manuscript received March 1, 2001. Associate Editor: P. E. Raad.

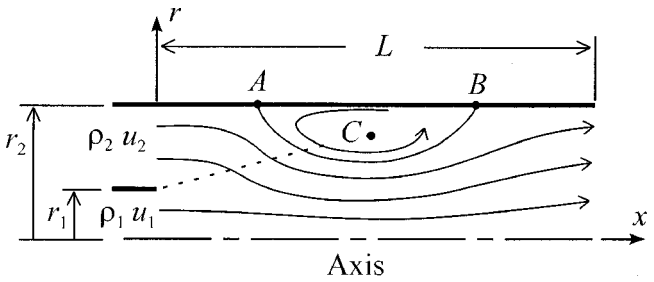

Fig. 1 The coaxial jet

Integration is over the entire cross-section of the inlet flow (at $x=0$) and u, p and ρ are the axial velocity, static pressure and density.

Theory

The conditions under which precise similarity of the flows in two different coaxial jets occurs can be determined by nondimensionalizing the exact governing equations. For low speed flow the parameters which arise are the Reynolds number, and when heat and mass transfer are important, the Prandtl and Schmidt numbers. In addition, the inlet boundary conditions lead to the ratios of velocity, density and radius of the two streams. Thus, in addition to the Reynolds number, the following nondimensional ratios must be matched to produce precisely similar flows:

$$r^*=\frac{r_2}{r_1}\quad u^*=\frac{u_2}{u_1}\quad \rho^*=\frac{\rho_2}{\rho_1} \tag{5}$$

The idea of approximate similarity of coaxial jets originates from the work of Thring and Newby [2] who were concerned with modeling combustion systems using isothermal conditions. Replacing an actual jet of cool, dense reactant gases issuing from a burner, with a jet of gases of the same low density as the hot gases in the combustion chamber, was of interest as a first step in setting up an isothermal scale model. The Thring-Newby parameter and the Craya-Curtet number are results of efforts to develop a criterion for approximate similarity. Both parameters may be expressed in terms of a common parameter, β, involving the inlet momentum flow rate G and mass flow rate $\dot{m}$ where:

$$\beta=\frac{\dot{G}}{\dot{m}U}$$

with

$$U\equiv\frac{\dot{m}}{\rho_m A} \tag{6}$$

This parameter is a nondimensional inlet momentum flow rate. In the case of the Craya-Curtet number, the density has been taken as uniform so $\rho_m=\rho_1=\rho_2$ and one can express β using the definitions of Eqs. (3) and (4) as $\beta=U_d^2/U_k^2$ which on substitution into Eq. (2) gives the relation

$$C_t=\frac{1}{\sqrt{\beta-\frac{1}{2}}} \tag{7}$$

Thus β and C_t are directly linked and one can equivalently match either β or C_t. A generalized Thring-Newby parameter can also be expressed in terms of β as

$$\theta=\frac{1}{\sqrt{\beta}} \tag{8}$$

This will be termed the momentum parameter. Equation (8) reduces to the Thring-Newby parameter, Eq. (1), when the momen-

tum flow rate, $\dot{G}$, used in β excludes the secondary flow momentum. In the combustion systems which Thring and Newby had in mind the secondary air stream generally has low momentum in relation to the burner jet flow.

The appearance of the effective density, ρ_m, in the dimensionless momentum flow rate is important when the densities of the jet and secondary fluids differ. Thring and Newby took ρ_m, in effect, to be the density of the mixture formed by combining the jet and secondary streams at constant pressure and adiabatically, a plausible approximation for small secondary flow where the jet largely encounters the hot low density combustion gases recirculated from upstream.

A further issue is the way in which the static pressure at the inlet surface is represented. Differences between the pressure at the inlet and within the duct beyond the inlet will either increase the momentum flow rate or decrease it, depending on whether that pressure difference is positive or negative. It is this effect which is represented by the inclusion of pressure in Eq. (4). Becker et al. [4] use the negative of the dynamic pressure of the secondary stream as the pressure difference. This appears to be motivated by consideration of cases for which θ is small. These have large recirculation eddies for which the secondary flow encounters a rise in pressure, approximately equal to its initial dynamic pressure. Of course it would be more appropriate to take the pressure difference as zero in cases where θ is large and the eddy moves further downstream and becomes smaller.

The Craya-Curtet number and the Thring-Newby parameter each may be expressed in terms of β as shown above. The Craya-Curtet number does not apply to cases with nonuniform density. The Thring-Newby parameter does not include the momentum of the secondary stream. These restrictions are avoided using the momentum parameter, θ, defined by Eqs. (8) and (6) in terms of the general momentum and mass flow rates:

$$\dot{G} = \int_A (\rho u^2 + p - p_c)\, dA \tag{9}$$

$$\dot{m} = \int_A \rho u\, dA \tag{10}$$

The pressure, p_c is the ''appropriate'' chamber pressure, here taken to be the stagnation pressure of the secondary stream, following Becker et al.

The particular case of a coaxial jet in a cylindrical duct is considered here. With each stream having uniform conditions, β may then be written using the ratios defined in Eqs. (5) as

$$\beta = \frac{\left\{ \dfrac{1}{r^{*2}} + \rho^* u^{*2}\left(1 - \dfrac{1}{r^{*2}}\right) - \dfrac{1}{2}\rho^* u^{*2} \right\} \dfrac{\rho_m}{\rho_1}}{\left[\dfrac{1}{r^{*2}} + \rho^* u^* \left(1 - \dfrac{1}{r^{*2}}\right) \right]^2} \tag{11}$$

In the curly brackets the three terms represent the jet momentum, the secondary stream momentum and the pressure, respectively.

Computations and Results

A large number of computations were made using the standard k-ϵ turbulence model of Launder and Spalding [5], with a logarithmic boundary wall treatment. The mean flow and turbulence equations were solved numerically using the Fluent [6] code. The domain for all computations is the axisymmetric chamber of Fig. 1 with length $L = 12.0$ m and radius $r_2 = 1.0$ m. For most of the computations the jet radius $r_1 = 0.05$ m is used, although some computations have also been made with jet radii of 0.03 and 0.1 m. A grid giving a solution with numerical error within a few percent has been used. The fluid used is taken to be a perfect gas and a temperature difference between the streams is used to produce the density difference. The mixture density required in Eq. (11) can then be expressed as

$$\frac{\rho_m}{\rho_1} = \frac{1 + \rho^* u^* (r^{*2} - 1)}{1 + u^* (r^{*2} - 1)} \tag{12}$$

In the computations each parameter affecting the flow was varied to produce a range of different values of the momentum parameter, θ. The parameters varied were jet velocity, secondary velocity, jet radius and the stream temperature (density) ratio. The values used and the corresponding values of the momentum parameter are listed in Table 1. Each computation uses the reference case values for the parameters not being varied.

Figure 2 shows computed stream function contours for values of θ from 0.05–0.597. As the momentum parameter increases, the recirculation eddy moves progressively downstream and its size decreases. A computation for $\theta = 0.776$ produced no eddy.

The accuracy with which the nondimensional momentum flow rate, β, can collapse the computed results over the range of conditions of Table 1 may be examined using a plot of the change in the position of the stagnation points characterizing the recirculation eddy. These points are labeled A, B, and C on Fig. 1, corresponding to the upstream separation point, the downstream reattachment point and the point of zero mean velocity in the center of the eddy.

Figure 3 shows all data plotted in this way. Ignoring the open circles and the crosses, the collapse of the results is generally good. The collapse is excellent for the position of the separation point, A, with the results deviating by less than 1 percent from a universal curve. The results for the position of the eddy center, and the reattachment position further downstream, show less satisfactory collapse. As the axial numerical cell size increases in the downstream direction, it is likely that interpolation errors cause some of the poorer collapse for points B and C.

The crosses correspond to changes in the radius ratio, and the resulting eddy positions show the largest differences from correlation. The larger jet diameter produces the greatest difference, which is expected since the jet diameter in relation to the duct size is increased and the condition of small jet to duct diameter ratio is less well satisfied. The case with smaller jet diameter than the reference condition is acceptably well correlated with the other results but is still less accurately correlated than with the other

Table 1 Conditions of the computations

Parameter	Reference Case $\theta = 0.372$	Other values used
U_1 (m/s)	30	20 (θ=0.517) 40 (0.294) 50 (0.247) 60 (0.214)
U_2 (m/s)	0.5	0.0 (θ=0.050) 0.15 (0.149) 0.3 (0.247) 0.7 (0.489) 0.9 (0.597) 1.0 (0.647) 1.13 (0.708) 1.29 (0.776)
r_1 (m)	0.05	0.03 (θ=0.544) 0.1 (0.263)
$T_2/T_1 = \rho_1/\rho_2$	1.0	4.0 (θ=0.224) 0.6 (0.460) 0.33 (0.586) 0.25 (0.657)

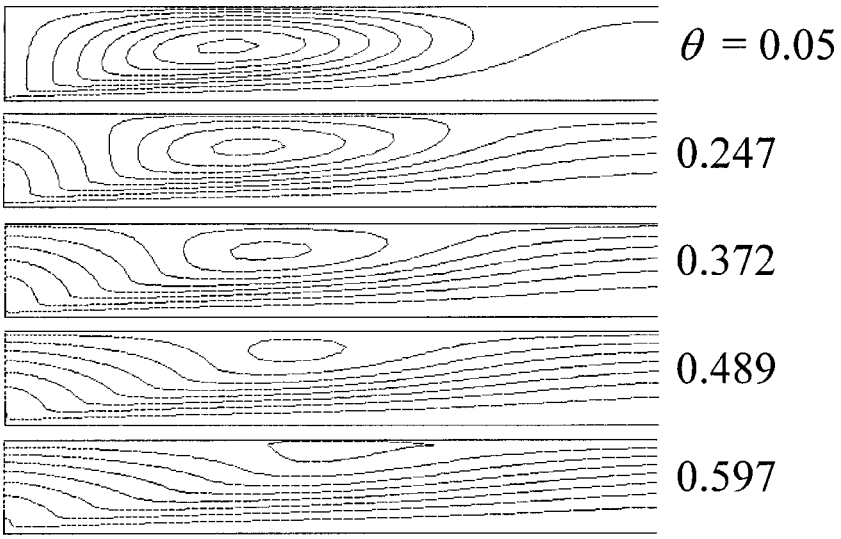

Fig. 2 Variation of computed stream function contours with momentum parameter, θ

varied parameters. This indicates a particular sensitivity to a departure from precise geometric similarity. This is consistent with the fact that if Reynolds number influences are small, the collapse would be precise for all results except those where the radius ratio or density ratio is varied.

Some evidence is also available in Fig. 3, regarding the choice of the density scale ρ_m. The filled circles are those resulting when the mixture density, Eq. (12), is used to determine θ for the cases of nonuniform density. The same results are also plotted in the figure with open circles showing the effect of using the secondary stream density for ρ_m. While use of the mixture density gives somewhat better collapse at large θ and the secondary stream density at small θ, each gives a similar, acceptable collapse overall.

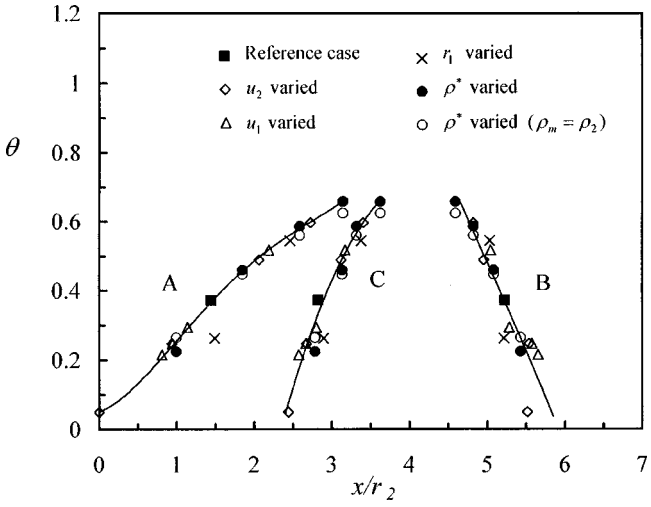

Fig. 3 The computed stagnation positions for a range of values of the momentum parameter, θ, produced by varying inlet velocity ratio, u^*, density ratio, ρ^*, and radius ratio, r^*. The nondimensional momentum flow rate, β, is determined using Eq. (11).

The form of β used in the momentum parameter in Fig. 3 is that used by Becker et al. and Barchilon and Curtet and given by Eq. (11). This definition includes the momentum of the secondary stream and also adopts the approximation that the pressure difference acting on the emerging fluid is equal to the dynamic pressure of the secondary stream. This is in contrast to the form used by Thring and Newby in which neither of these effects is included. The data were replotted with, first, the dynamic pressure and then the secondary momentum excluded from calculated β values. The degree of correlation was found to be entirely unaffected by whether these effects were included or excluded from β.

References

[1] Slutsky, A. S., and Menon, A. S., 1987, ''Catheter Position and Blood Gases During Constant-Flow Ventilation,'' J. Appl. Physiol. **62**, No. 2, pp. 513–519.
[2] Thring, M. W., and Newby, M. P., 1953, ''Combustion Length of Enclosed Turbulent Jet Flames,'' *Fourth Symposium (International) on Combustion*, Williams and Wilkins, Baltimore, pp. 789–796.
[3] Barchilon, M., and Curtet, R., 1964, ''Some Details of the Structure of an Axisymmetric Confined Jet with Backflow,'' ASME J. Basic Eng. **86**, No. 4, pp. 777–787.
[4] Becker, H. A., Hottel, H. C., and Williams, G. C., 1963, ''Mixing and Flow in Ducted Turbulent Jets,'' *Ninth Symposium (International) on Combustion*, Academic Press, London, pp. 7–20.
[5] Launder, B. E., and Spalding, D. B., 1974, ''The numerical computation of turbulent flows,'' Comput. Methods Appl. Mech. Eng. **3**, pp. 269–289.
[6] Fluent, Version 4.4, 1996, Fluent Incorporated, Lebanon, New Hampshire.

Journal of Fluids Engineering

Errata

Erratum: ''Computation of Particle and Scalar Transport for Complex Geometry Turbulent Flows'' [ASME J. Fluids Engineering, 123, No. 2, pp. 372–381]

P. G. Tucker

In the above paper, Table 2 was printed incorrectly. The correct Table 2 appears below.

Table 2 Gradient arguments for direction cosines of $\hat{n}$

Argument	Direction cosines
$\left\|\frac{\partial L}{\partial x}\right\| > \max\left[\left\|\frac{\partial L}{\partial y}\right\|, \left\|\frac{\partial L}{\partial z}\right\|\right], \quad \frac{\partial L}{\partial x} > 0$	$n_1 = 1,\ n_2 = 0,\ n_3 = 0$
$\left\|\frac{\partial L}{\partial x}\right\| > \max\left[\left\|\frac{\partial L}{\partial y}\right\|, \left\|\frac{\partial L}{\partial z}\right\|\right], \quad \frac{\partial L}{\partial x} < 0$	$n_1 = -1,\ n_2 = 0,\ n_3 = 0$
$\left\|\frac{\partial L}{\partial y}\right\| > \max\left[\left\|\frac{\partial L}{\partial x}\right\|, \left\|\frac{\partial L}{\partial z}\right\|\right], \quad \frac{\partial L}{\partial y} > 0$	$n_1 = 0,\ n_2 = 1,\ n_3 = 0$
$\left\|\frac{\partial L}{\partial y}\right\| > \max\left[\left\|\frac{\partial L}{\partial x}\right\|, \left\|\frac{\partial L}{\partial z}\right\|\right], \quad \frac{\partial L}{\partial y} < 0$	$n_1 = 0,\ n_2 = -1,\ n_3 = 0$
$\left\|\frac{\partial L}{\partial z}\right\| > \max\left[\left\|\frac{\partial L}{\partial x}\right\|, \left\|\frac{\partial L}{\partial y}\right\|\right], \quad \frac{\partial L}{\partial z} > 0$	$n_1 = 0,\ n_2 = 0,\ n_3 = 1$
$\left\|\frac{\partial L}{\partial z}\right\| > \max\left[\left\|\frac{\partial L}{\partial x}\right\|, \left\|\frac{\partial L}{\partial y}\right\|\right], \quad \frac{\partial L}{\partial z} < 0$	$n_1 = 0,\ n_2 = 0,\ n_3 = -1$

Erratum: ''The Production of Shear Flow Profiles in a Wind Tunnel by a Shaped Honeycomb Technique'' [ASME J. Fluids Eng., 119, No. 3, p. 713]

F. Ahmed and B. Lee

In the online version of the above Technical Brief, the initial of the first author is incorrect. The correct name is F. Ahmed. The print version of this Technical Brief has the correct initial.

